



This project has received funding from the European Union's Horizon 2020 research and innovation programme under grant agreement No. 700748

LIQUEFACT

Assessment and mitigation of Liquefaction potential across Europe: a holistic approach to protect structures/infrastructure for improved resilience to earthquake-induced Liquefaction disasters.

H2020-DRA-2015

GA no. 700748



DELIVERABLE D3.2

Methodology for the liquefaction fragility analysis of critical structures and infrastructures: description and case studies

Author(s):	António Viana da Fonseca, Maxim Millen, Xavier Romão, Julieth Quintero, Sara Rios, Cristiana Ferreira, Fabrizio Panico, Carlos Azeredo, Nuno Pereira Janko Logar, Aleš Oblak, Matjaž Dolšek, Mirko Kosič, Sebastjan Kuder, Matej Logar Sadik Oztoprak, M. Kubilay Kelesoglu, Sinan Sargin, Cihan Oser, Ilknur Bozbey Alessandro Flora, Emilio Billota, Andrea Prota, Marco Di Ludovico, Anna Chiaradonna Giuseppe Modoni, Luca Paoletta, Rose Line Spacagna Carlo G. Lai, Simantini Shinde, Francesca Bozzoni
Responsible Partner:	University of Porto (UPorto)
Version:	1.0
Date:	31/12/2018
Distribution Level (CO, PU)	PU



This project has received funding from the European Union's Horizon 2020 research and innovation programme under grant agreement No. 700748

DOCUMENT REVISION HISTORY

Version	Editor	Comments	Status
31/12/2018	1	First Draft	Draft

LIST OF PARTNERS

Name	Country
UPORTO Universidade do Porto	Portugal
Istan-Uni Istanbul Universitesi	Turkey
ULJ Univerza V Ljubljani	Slovenia
UNINA Universita degli Studi di Napoli Federico II	Italy
NORSAR Stiftelsen Norsar	Norway
ARU Anglia Ruskin University Higher Education Corporation	United Kingdom
UNIPV Università degli Studi di Pavia	Italy
UNICAS Universita degli Studi di Cassino e del Lazio Meridionale	Italy



This project has received funding from the European Union's Horizon 2020 research and innovation programme under grant agreement No. 700748

CONTENTS

EXECUTIVE SUMMARY	22
SCOPE AND PURPOSE	25
1. INTRODUCTION	26
1.1 REPORT LAYOUT	26
2. MACRO-MECHANISM APPROACH FOR BUILDINGS ON SHALLOW FOUNDATIONS	28
2.1 OVERVIEW OF DIFFERENT MODELING STRATEGIES AND KEY PARAMETERS.....	28
2.1.1 KEY MECHANISMS IN SOIL-LIQUEFACTION-FOUNDATION-STRUCTURE INTERACTION.....	30
2.1.2 VULNERABILITY ASSESSMENT OF CONCRETE FRAME BUILDINGS VIA MACRO MECHANISM APPROACH	37
2.2 MODELLING OF BUILDINGS ON LIQUEFIABLE DEPOSITS.....	38
2.2.1 INTRODUCTION	38
2.2.2 KEY FEATURES OF THE PHYSICAL MODEL.....	39
2.2.3 GROUND MOTIONS	43
2.2.4 SUPERSTRUCTURE MODEL.....	43
2.2.5 FOUNDATION MODEL.....	45
2.2.6 ADDITIONAL ASPECTS FOR NUMERICAL MODELLING	46
2.2.7 CASE STUDY EXAMPLE	46
2.2.8 VARIATIONS IN SOIL-FOUNDATION STRUCTURE INTERACTION MODELS	48
2.2.9 ESTIMATING THE FOUNDATION LOAD-SETTLEMENT BEHAVIOUR.....	56
2.2.10 MODELLING SETTLEMENTS	57
2.2.11 MODELLING SOIL HETEROGENEITY	59
2.2.12 MODELLING RECOMMENDATIONS.....	60
2.2.13 CONCLUSIONS.....	61
2.3 SIMPLIFIED PROCEDURE TO CLASSIFY SOIL PROFILES.....	61
2.3.1 OVERVIEW	61
2.3.2 RATIONALE FOR THE SELECTION OF THE GOVERNING PARAMETERS.....	64
2.3.3 PROCEDURE TO DEFINE ESP FROM CPT	67
2.3.4 DEFINITION OF EQUIVALENT SOIL PROFILE	68
2.3.5 EXAMPLE SITE RESULTS	69
2.3.6 APPLICATION OF THE PROCEDURE TO REAL CASE STUDIES	72
Christchurch Earthquake Sequence 2010-2011.....	73
San Carlo Emilia Romagna (2012).....	84



This project has received funding from the European Union's Horizon 2020 research and innovation programme under grant agreement No. 700748

Conclusions.....	90
2.3.7 ARTIFICIAL EQUIVALENT SOIL PROFILES	90
2.3.8 SUMMARY.....	93
2.4 ESTIMATION OF SITE RESPONSE AND SOIL-STRUCTURE INTERACTION USING EFFECTIVE STRESS ANALYSIS.....	93
2.4.1 INTRODUCTION	93
2.4.2 OVERVIEW OF FLAC MODEL	94
2.4.3 VALIDATION IN 2D ANALYSIS.....	98
2.4.4 CONCLUSIONS.....	101
2.5 SIMPLIFIED PROCEDURE TO ESTIMATE PORE PRESSURE IN FREE FIELD	101
2.5.1 INTRODUCTION	101
2.5.2 BACKGROUND	102
Stress-based methods	103
Energy-based methods.....	104
2.5.3 DIFFERENT APPROACHES TO ESTIMATE PORE PRESSURE BUILD UP	108
Numerical analysis	109
Simplified stress based method (SBM).....	113
Simplified dissipated energy based methods	113
2.5.4 COMPARISON OF THE METHODS FOR A SINGLE CASE	114
2.5.5 COMPARISON OF THE METHODS FOR THE 500 CASES.....	119
2.5.6 MODELLING RECOMMENDATIONS.....	120
2.5.7 CONCLUSIONS.....	121
2.6 SIMPLIFIED PROCEDURE TO ESTIMATE SETTLEMENTS OF BUILDINGS	121
2.6.1 EXISTING METHODOLOGIES FOR ESTIMATING SETTLEMENTS.....	121
2.6.2 PARAMETRIC STUDY.....	124
2.6.3. SETTLEMENTS OF BUILDINGS RESULTS.....	130
2.6.4. MODELLING RECOMMENDATIONS AND CONCLUSIONS.....	132
2.7 SIMPLIFIED PROCEDURE TO ESTIMATE SURFACE GROUND MOTION.....	133
2.7.1 INTRODUCTION	133
2.7.2 TIME-FREQUENCY FILTERING	137
2.7.3 THE STOCKWELL TRANSFER FUNCTION METHOD	139
2.7.4 COMPARISON OF METHODS.....	142
2.7.5 MODELLING RECCOMENDATIONS AND CONCLUSIONS.....	146
2.8 APPLICATION IN SPECIFIC CASE STUDY – PIEVE DI CENTO.....	147



This project has received funding from the European Union's Horizon 2020 research and innovation programme under grant agreement No. 700748

Methodology for the liquefaction fragility analysis of critical structures and infrastructures: description and case studies

2.8.1	LOCATION OF THE CASE STUDY SITE	147
2.8.2	ANALYSIS PROCEDURE.....	148
2.8.3	SOIL PROFILES DESCRIPTION	149
2.8.4	GROUND MOTIONS DESCRIPTION.....	157
2.8.5	FLAC 1-D NUMERICAL MODEL SETUP.....	159
2.8.6	PORE PRESSURE ESTIMATION.....	160
2.8.7	SETTLEMENTS ESTIMATION.....	161
2.8.8	BUILDINGS DESCRIPTION.....	162
2.8.9	RESULTS.....	162
2.9	RAPID RISK IDENTIFICATION OF SOIL LIQUEFACTION AND STRUCTURAL DAMAGE	171
2.9.1	INTRODUCTION AND MOTIVATION.....	171
2.9.2	OVERVIEW OF PROCESSES OF THE METHOD FOR RAPID RISK IDENTIFICATION OF SOIL LIQUEFACTION AND STRUCTURAL DAMAGE	172
2.9.3	SIMPLIFIED MODEL FOR SOIL-STRUCTURE INTERACTION WITH CONSIDERATION OF LIQUEFACTION	173
	Overview	173
	Model for prediction of pre-liquefaction foundation ultimate moment capacity.....	177
	Model for prediction of foundation secant stiffness at 50% of moment capacity	179
	Model for prediction of time-dependent and ground-motion dependent triggering of liquefaction.....	180
	Model for prediction of post-liquefaction foundation moment capacity.....	183
	Model for prediction of strength degradation in case of liquefaction	184
	Model for prediction of building settlement	186
2.9.4	CASE STUDY: APPLICATION OF RAPID RISK IDENTIFICATION METHOD TO A CODE-CONFORMING BUILDING WITH CONSIDERATION OF LIQUEFACTION AND DIFFERENT LEVELS OF SEISMIC HAZARD	188
	STEP 1: Definition of input data	188
	STEP 2: Simplified fragility analysis of the soil-structure configuration with consideration of liquefaction	193
	STEP 3: Risk assessment.....	194
	STEP 4: Risk-based decision making regarding the need for detailed analysis of soil liquefaction.....	195
2.9.5	CONCLUSIONS.....	196
	REFERENCES.....	199
3.	VULNERABILITY ASSESSMENT OF EMBANKMENTS USING FINITE ELEMENT MODELING.....	207
3.1	MODELING OF EMBANKMENTS ON LIQUEFIABLE DEPOSITS	207
3.1.1	INTRODUCTION	207
3.1.2	LITERATURE REVIEW.....	208
3.1.3	METHODOLOGY FOR THE VULNERABILITY ASSESSMENT OF EMBANKMENTS.....	209
3.1.3.1	Methods for deriving fragility curve	209



This project has received funding from the European Union's Horizon 2020 research and innovation programme under grant agreement No. 700748

3.1.3.2	<i>Damage states</i>	211
3.1.3.3	<i>Intensity measures</i>	214
3.1.3.4	<i>Uncertainties</i>	215
3.1.4	<i>NUMERICAL PROCEDURE TO DEVELOP FRAGILITY CURVES FOR EMBANKMENTS</i>	216
3.1.4.1	<i>Validation procedure</i>	216
3.1.4.2	<i>Description of the numerical model used for the derivation of fragility curves</i>	223
3.1.4.3	<i>Results of numerical analyses</i>	230
3.1.4.4	<i>Multiple Stripe Analysis and few examples of fragility curves</i>	232
3.1.4.4.1	<i>Road embankments</i>	236
3.1.4.4.2	<i>Railway embankments</i>	239
3.1.4.4.3	<i>Further considerations</i>	240
3.1.4.5	<i>The use of Artificial Neural Networks for the assessment of fragility curves</i>	243
3.1.4.5.1	<i>Training data and pre-processing</i>	244
3.1.4.5.2	<i>ANN simulations: Regression and Classification technique</i>	247
3.1.4.5.2.1	<i>ANN regression technique</i>	248
3.1.4.5.2.2	<i>ANN classification technique</i>	253
3.1.4.5.3	<i>Conclusions on ANN study</i>	259
3.1.5	<i>CONCLUSION</i>	260
3.2	<i>APPLICATION TO A CASE STUDY OF EMBANKMENTS - TURKEY</i>	261
3.2.1	<i>CARK CANAL SITE</i>	261
3.2.2	<i>POLICE STATION SITE</i>	271
3.2.3	<i>CONCLUSION</i>	275
	<i>REFERENCES</i>	275
4.	<i>VULNERABILITY ASSESSMENT OF MASONRY BUILDINGS USING HISTORICAL DATA</i>	279
4.1	<i>INTRODUCTION</i>	279
4.2	<i>EMILIA EARTHQUAKE</i>	280
4.2.1	<i>RECONSTRUCTION PROCESS</i>	280
4.2.2	<i>DATA COLLECTION ON DAMAGED BUILDINGS</i>	280
4.2.3	<i>LIQUEFACTION INDUCED DAMAGE</i>	283
4.2.4	<i>EMPIRICAL DAMAGE: US vs. LS BUILDINGS</i>	283
4.2.5	<i>EFFECTS OF STRUCTURAL VULNERABILITY ON EMPIRICAL DAMAGE</i>	285
4.2.6	<i>PREDICTION OF REPAIR COSTS</i>	287
4.3	<i>EMPIRICAL FRAGILITY CURVES</i>	287
4.3.1	<i>DAMAGE GRADES</i>	288



This project has received funding from the European Union's Horizon 2020 research and innovation programme under grant agreement No. 700748

4.3.2	LIQUEFACTION INDICES	288
4.3.3	LIQUEFACTION FRAGILITY CURVES	294
4.4	CONCLUSIONS	295
	REFERENCES.....	296
5.	VULNERABILITY ASSESSMENT OF PIPELINES USING HISTORICAL DATA	300
5.1	INTRODUCTION	300
5.2	LITERATURE REVIEW.....	301
5.2.1	EGUCHI ET AL., 1991.....	301
5.2.2	HONEGGAR ET AL., 1992	307
5.2.3	NIBS, 2004	307
5.2.4	EIDINGER, 1998	308
5.2.5	O'ROURKE ET AL., 1998	309
5.2.6	ISOYAMA ET AL., 2000.....	310
5.2.7	ALA, 2001.....	312
5.2.8	TERZI ET AL., 2006	313
5.2.9	TERZI ET AL., 2007	315
5.2.10	O'ROURKE, 2012.....	316
5.2.11	O'ROURKE ET AL., 2014	319
5.2.12	TOPRAK ET AL., 2014	321
5.2.13	SHERSON ET AL., 2015.....	322
5.2.14	TOPRAK ET AL., 2015	324
5.2.15	TOPRAK ET AL., 2017.....	326
5.2.16	D. BOUZIOU ET AL., 2017.....	327
5.2.17	O'ROURKE ET AL., 2018	329
5.2.18	TOPRAK ET AL., 2018	330
5.3	CHRISTCHURCH CITY CASE STUDY.....	331
5.3.1	THE 2010-2011 CANTERBURY EARTHQUAKE SEQUENCE CES	331
5.3.2	WIDESPREAD LIQUEFACTION MANIFESTATIONS DURING CES.....	332
5.3.3	INDICATORS OF LIQUEFACTION SEVERITY.....	337
5.3.4	DAMAGE TO WATER SUPPLY NETWORK IN CHRISTCHURCH DURING CES.....	338
5.4	METHODOLOGY TO DEVELOP EMPIRICAL FRAGILITY CURVES FOR PIPELINES	343
5.5	CONCLUDING REMARKS.....	370
	REFERENCES.....	371
6.	FINAL REMARKS.....	374



This project has received funding from the European Union's Horizon 2020 research and innovation programme under grant agreement No. 700748

6.1	NOTES OF ONGOING AND EMERGING STUDIES.....	376
	REFERENCES.....	377
	APPENDICES.....	379
A.1	APPENDICES TO SECTION 2.9	379
	<i>A-1.1 CALIBRATION OF THE SIMPLIFIED MODEL FOR THE SOIL SPRING</i>	<i>379</i>
	<i>A-1.1.1 Description of the FLAC 2D model and results.....</i>	<i>380</i>
	<i>A-1.1.2 Results of model calibration</i>	<i>381</i>
	<i>A-1.2 CALIBRATION OF INPUT MOTION FOR FRAGILITY ANALYSIS.....</i>	<i>389</i>
	<i>A-1.3 VALIDATION OF THE SIMPLIFIED MODEL FOR THE SOIL SPRING.....</i>	<i>390</i>
	<i>A-1.3.1 Methodology.....</i>	<i>390</i>
	<i>A-1.3.2 Results of model validation</i>	<i>390</i>
A.2	APPENDICES TO CHAPTER 3 - SECTION 3.2	400
	<i>A-2.1 PROPOSED FRAGILITY CURVES TRAFFIC EMBANKMENTS WITH PGA AS INTENSITY.....</i>	<i>400</i>



This project has received funding from the European Union's Horizon 2020 research and innovation programme under grant agreement No. 700748

LIST OF FIGURES AND TABLES

FIGURES

Figure 2.1: Different modelling approaches for soil-liquefaction-foundation-structure interaction 29

Figure 2.2: Soil, foundation and structure response from centrifuge experiment SHD02-04 adapted from Dashti et al. (2010) 30

Figure 2.3: Displacement-based Assessment with SFSI (Millen. 2016)..... 31

Figure 2.4: RSN3317_2 motion (a) Response of Elastic systems (b) Time series and significant duration (from Millen et al. (2018)) 32

Figure 2.5: Occurrence of response displacement of elastic systems (from Millen et al. (2018))..... 33

Figure 2.6: Shift in response spectra due to site effects 34

Figure 2.7: Rigid-body and differential movements of the foundation (taken from Millen, 2016)..... 36

Figure 2.8: Expected influence of differential settlements on the pushover response of a building..... 36

Figure 2.9: Problem domain and numerical model..... 38

Figure 2.10: Bivariate Gaussian copula correlating beam height and span 39

Figure 2.11: Example of physical model of the reference structure 41

Figure 2.12: Foundation-soil systems: (a) rigid foundation on bedrock; (b) rigid foundation on compressible soil; (c) isolated footings on compressible soil..... 43

Figure 2.13: Numerical model for cases (a) and (b) and detail of the beam-column joints configuration..... 44

Figure 2.14: Numerical model for structure with isolated footings..... 46

Figure 2.15: Case study building and soil profile..... 47

Figure 2.16: Example of linear elastic model response..... 50

Figure 2.17: Example of linear spring-damper system response 51

Figure 2.18: Example of footings settlements for a linear spring-damper system 52

Figure 2.19: Model for vertical stiffness degradation..... 53

Figure 2.20: Example of non-linear spring-damper system response 55

Figure 2.21: Example of footings settlements in non-linear spring-damper system 56

Figure 2.22: Results with equal incremental settlements..... 58

Figure 2.23: Results with random factors applied to incremental settlements..... 60

Figure 2.24: Equivalent Soil Profile: definition of the three governing parameters 62

Figure 2.25: Different real soil profiles with distinct CRR profiles but identical LSN value..... 63

Figure 2.26: Different building widths and soil profiles 63

Figure 2.27: Influence of crust properties on bearing capacity 65

Figure 2.28: Parametric acceleration response spectra (ARS) ratios 66

Figure 2.29: Procedure to implement the CRR-fitted method..... 68

Figure 2.30: Equivalent soil profile classification: a) range definition; b) classes 69

Figure 2.31: Example site, around Sullivan Park (Christchurch), where 100 CPTus were selected 70

Figure 2.32: Case study single profile classified 71

Figure 2.33: Equivalent soil profile distribution for the example site..... 72

Figure 2.34: a) Epicenter locations and faults of the seismic events characterizing the 2010-2011 Christchurch Earthquake Sequence (as at June 2011). Projected surface locations of major blind faults in yellow and location of mapped surface ruptures in red. (b,c,d) Example of liquefaction-induced damage on buildings,



This project has received funding from the European Union's Horizon 2020 research and innovation programme under grant agreement No. 700748

road and networks. Major cracks with ejecta sands (b) affected residential houses and infrastruvture (c,d).
 73

Figure 2.35. Summary scheme of the available investigations in the New Zealand Geotechnical Database. Thanks to the data sharing between a huge number of data owners, who have approved the publication of their factual geotechnical data, the NZGD is continuous updated. 74

Figure 2.36. a) Available specific scenario (the 22 FEB 2001 Mw 6.2 Christchurch Earthquake) Shakemap; b) Map of the Groundwater Table depth (from the NZGD). 75

Figure 2.37. a) The histograms show that the equivalent soil profile method is globally adequate in the schematization of real profiles: in fact, of the 8 200 tests analyzed for the Christchurch case study, only 1.2% need further engineering evaluations; b) Considering the Std_normed_error (evaluated as Std Normed Err= Normed error*20/Max depth.) the percentage of CPTs showing an error greater than 0.15 becomes around 15%. 76

Figure 2.38. The Map shows the position of the CPTs with an average error greater than 0.15. Most of them are located in the South of the City, while no further assessment is required in the so called "Red Area" along the Avon River. 77

Figure 2.39. The Map shows the position of the CPTs with an average error greater than 0.15. Most of them are located in the South of the City, while no further assessment is required in the so called "Red Area" along the Avon River. 77

Figure 2.40. Example of CPT for which the equivalent soil profile method is consistent with the real soil profile (N.E.<0.05). 78

Figure 2.41. Example of CPT profile showing a quite good agreement between the equivalent soil profile and the real one (0.05<N.E.<0.15). 79

Figure 2.42. CPT_220 represents an example of profile where a specific engineering evaluation is required. (0.15<N.E.) 80

Figure 2.43. Liquefaction-induced land damage observations across Christchurch after the February 2011 earthquake, with the February 2011 magnitude-weighted equivalent Mw = 7.5 PGA contours overlaid (van Ballegooy, 2014 after Bradley & Hughes, 2012)..... 81

Figure 2.44. Statistical distribution of each equivalent soil profile..... 82

Figure 2.45. General overview of the ESP spatial distribution. It can be observed that many of the weak and moderate profiles are located along the two Rivers of the City. 83

Figure 2.46. Histograms of the ESP parameters and comparison of LSN from ESP and CPT. 84

Figure 2.47. Digital Elevation Model (on the left) shows that the district of S. Carlo is located along f the old Reno River Paleochannel. Geological features of San Carlo area (on the right). 85

Figure 2.48. a) Summary scheme of the available investigations in the Emilia Romagna Region Geotechnical Database; b) available CPTs (around 1000) and boreholes (≈200) in the whole S. Agostino and Mirabello municipality 85

Figure 2.49. a) Available specific scenario (the 22 FEB 2001 Mw 6.2 Christchurch Earthquake) Shakemap; b) Map of the Groundwater Table depth (from the NZGD). 86

Figure 2.50. a) Histogram of the ESP normal error; b) Histograms of the ESP Std_normed_error (*Std Normed Err = Normed error * 20/Max depth*) show that the ESP_method performs well for all the analysed CPTs..... 87

Figure 2.51. The Map shows the position of the CPTs available in the S. Carlo district 88



This project has received funding from the European Union's Horizon 2020 research and innovation programme under grant agreement No. 700748

Figure 2.52. Liquefaction-induced land damage observations across S. Carlo district after the 20 May 2012 earthquake. 88

Figure 2.53. The statistical distribution of each equivalent soil profile is here shown; most of the analyzed CPTs highlights the widespread presence of a thin/midsize, deep and low resistance three strata equivalent soil profile (48% of all the CPTs). 89

Figure 2.54. General overview of the ESP spatial distribution..... 90

Figure 2.55. LSN vs equivalent soil profile classes at different seismic demand levels 91

Figure 2.56. Liquefaction severity vs equivalent soil profile class for different levels of seismic hazard 92

Figure 2.57: Numerical model of Dashti centrifuge test 95

Figure 2.58: Motions applied in the numerical model of centrifuge experiments 96

Figure 2.59: Comparison between numerical and experimental values of settlements of the building..... 98

Figure 2.60: Comparison between numerical and experimental settlement for the experiment T3-30 98

Figure 2.61: Comparison between numerical and experimental values of pore pressure..... 99

Figure 2.62: Comparison between numerical and experimental pore pressure for the experiment T3-30 .. 99

Figure 2.63: Comparison between numerical and experimental response spectra of the surface acceleration (free-field)..... 100

Figure 2.64: Surface acceleration (free-field) comparison for the experiment T3-30 100

Figure 2.65: Surface acceleration (free-field) comparison for the experiment T6-30 101

Figure 2.66: Pore pressure time series for two different cases 102

Figure 2.67: Relationship between normalised dissipated energy and CSR_{20} (Kokusho, 2013) 106

Figure 2.68: Calculation of NSE graphically 107

Figure 2.69: CSR from element tests versus equivalent SPT blow count..... 109

Figure 2.70: Ground motion SDOF response spectra..... 111

Figure 2.71: Element tests results for the case 37 116

Figure 2.72: Equivalent number of cycles time series (a) and acceleration base record (b) for the case 37 117

Figure 2.73: Normalised dissipated energy time series for the case 37 118

Figure 2.74: Normalised strain energy time series for the case 37..... 118

Figure 2.75: Pore pressure ratio predicted by each method for the case 37 119

Figure 2.76: Accuracy of the methods in terms of pore pressure ratio (r_u) and time to liquefy (t_{liq}): a) SBM; b) SEBM..... 120

Figure 2.77: 2D Flac model considerations 124

Figure 2.78: Calibration of the factor in Equation (2.64) 126

Figure 2.79: Clay theoretical tau gamma backbone..... 129

Figure 2.80: Comparison between numerical and analytical results of total settlements 130

Figure 2.81: Comparison between numerical and analytical settlements for Soil Profile: 8 – Foundation: 1 – Ground motion: 2– Scale factor: 0.25 131

Figure 2.82: Comparison between numerical and analytical settlements for Soil Profile: 8 – Foundation: 1 – Ground motion: 2– Scale factor: 0.25 132

Figure 2.83: Natural seismic isolation due to liquefaction..... 133

Figure 2.84: Standing wave modes that cause site amplification 134

Figure 2.85: Site amplification in liquefied deposit..... 135

Figure 2.86: Two a frequency harmonic signal 137



This project has received funding from the European Union's Horizon 2020 research and innovation programme under grant agreement No. 700748

Figure 2.87: Stockwell transform of two a frequency harmonic signal 138

Figure 2.88: Stockwell transform of two a frequency harmonic signal 138

Figure 2.89: Two a frequency harmonic signal 139

Figure 2.90: Influence of liquefaction on surface acceleration..... 140

Figure 2.91: Transfer functions for Stockwell transfer function method 141

Figure 2.92: Stockwell explained example 142

Figure 2.93: Comparison of time series for STF method..... 143

Figure 2.94: Comparison of spectral quantities for STF method..... 144

Figure 2.95: Comparison of time series for STF method - late liquefaction 145

Figure 2.96: Comparison of spectral quantities for STF method - later liquefaction 146

Figure 2.97: Location of Pieve di Cento: a) within Italy map; b) geological map of the region (in blue is represented the fine-grained deposits and in yellow sand deposits from Appenninic rivers 147

Figure 2.98: Location of Pieve di Cento (indicated by a star) and 35 km long segment in the Po Plain where deep downhole investigations were made (after Minarelli et al., 2016)..... 148

Figure 2.99: Logic tree of inputs and modelling decisions 149

Figure 2.100: CPTu results..... 150

Figure 2.101: Soil profile 1 from CPTu 1..... 150

Figure 2.102: Soil profile 2 from CPTu 2..... 151

Figure 2.103: Soil profile 3 from CPTu 3..... 151

Figure 2.104: Soil profile 4 from CPTu 4..... 152

Figure 2.105: Soil profile 5 from CPTu 5..... 152

Figure 2.106: Unit weight (γ_{dry}) for the 5 soil profiles 153

Figure 2.107: Maximum shear modulus ($G=G_{max}$) for the 5 soil profiles..... 153

Figure 2.108: Permeability (k_H) for the 5 soil profiles 154

Figure 2.109: Relative density (D_r) for the 5 soil profiles..... 154

Figure 2.110: Undrained strength ($S_u=c_u$) for the 5 soil profiles. 155

Figure 2.111: Calibration of factor value to calculate the input shear stress in numerical models 159

Figure 2.112: Histogram of the maximum pore pressure ratio 161

Figure 2.113: Settlement results 161

Figure 2.114: Physical model of the reference structure..... 162

Figure 2.115: Performance measures versus peak intensity measures..... 163

Figure 2.116: Performance measures versus cumulative intensity measures..... 164

Figure 2.117: Fragility curves for peak intensity measures..... 165

Figure 2.118: Fragility curves for cumulative intensity measures..... 165

Figure 2.119: influence of load redistribution model 167

Figure 2.120: Influence of settlement model..... 168

Figure 2.121: Influence of pore pressure build-up method 169

Figure 2.122: Influence of surface ground motion method 170

Figure 2.123: Influence of CPT 170

Figure 2.124: Influence of ground water level 171

Figure 2.125: Processes of the method for Rapid Risk Identification (RRI) of soil liquefaction and structural damage..... 173



This project has received funding from the European Union's Horizon 2020 research and innovation programme under grant agreement No. 700748

Figure 2.126: Schematic presentation of the simplified model for soil-structure interaction (SSI) with consideration of liquefaction. 174

Figure 2.127: Pushover curve, idealized pushover curve and force-displacement relationship of the equivalent SDOF model of the structure (left), and (right) the corresponding moment-rotation relationship of the equivalent SDOF model of the structure. 176

Figure 2.128: Moment-rotation relationship of the inelastic soil spring. 176

Figure 2.129: Schematic presentation of the procedure for simulation of the degradation of strength in case liquefaction is triggered for a given ground motion. 176

Figure 2.130: Assumed distribution of forces for computation of foundation ultimate moment capacity. 178

Figure 2.131: Mechanism of bearing capacity of two-layer soils according to Meyerhof and Hanna (1978): a) strong layer overlaying a weak layer, and b) weak layer overlaying a strong layer. 178

Figure 2.132: Relation between elastic and nonlinear rotational stiffness of strip foundations according to Gazetas et al. (2013). 180

Figure 2.133: Schematic presentation of the Kramer’s et al. (2016) procedure for time-dependent and ground-motion dependent triggering of liquefaction. 181

Figure 2.134: Estimation of the equivalent number of cycles of a signal using the peak counting method and the mean of the DSS+ and DSS– normalization curves according to Liu et al. (2001). 183

Figure 2.135: Proposed model for the degradation of strength due to liquefaction. 185

Figure 2.136: Example of (left) the relationship between the foundation moment capacity and the pore pressure ratio in the liquefiable layer for different thicknesses of the non-liquefiable crust and (right) the relationship between the pore pressure ratio and the degraded friction angle of the liquefiable layer. 186

Figure 2.137: Cumulative rotation-settlement relationship based on FLAC analyses for liquefaction (blue color) and non-liquefaction cases (red color). The proposed settlement – cumulative rotation relationships are presented with dashed lines. 187

Figure 2.138: Geometry and characteristics of the investigated case study example. 189

Figure 2.139: Force-displacement relationship and the corresponding equivalent moment rotation relationship of the SDOF model of the building. 190

Figure 2.140: Moment-rotation relationship of the inelastic soil spring. 190

Figure 2.141: Comparison of seismic hazard curve from SHARE hazard data (Giardini et al., 2013) for the selected locations: Benavente (red) and Düsseldorf (blue). 191

Figure 2.142: Acceleration response spectra (5% damping) of the selected set of ground motions (GMs) used for fragility analysis. 191

Figure 2.143: Schematic representation of the definition of limit states related to structural damage. 192

Figure 2.144: Fragility curves for designated limit states (left) and the liquefaction fragility curve (right) obtained based on the assumption of lognormal distribution of the fragility function (thin lines) and based on the empirical CDF (thick lines). 194

Figure 3.1: General procedure for deriving numerical fragility curves for road elements (SYNER-G, 2011). 211

Figure 3.2: Naruse River Levee site location with damaged levees and epicentre marks (Takahashi and Sugita, 2009 - modified). 217

Figure 3.3: Cross section of Naruse river levee and locations of sensors (Takahashi and Sugita, 2009). 218

Figure 3.4: Borehole data and SPT-N value distribution – Naruse river levee (Takahashi and Sugita, 2009). 219



This project has received funding from the European Union's Horizon 2020 research and innovation programme under grant agreement No. 700748

Figure 3.5: Numerical model of Naruse river levees..... 219

Figure 3.6: Recorded acceleration time history at the top of base layer – Naruse river levee (Cubrinovski, 2011)..... 221

Figure 3.7: EPWP in the unimproved zone: recorded and calculated values by Cubrinovski (2011) and from FLAC analysis (model: FLAC m1). 221

Figure 3.8: EPWP in the unimproved zone: recorded and calculated values by Cubrinovski (2011) and from FLAC analysis (model: FLAC m2). 222

Figure 3.9: EPWP in the SCP zone: recorded and calculated values by Cubrinovski (2011) and from FLAC analysis (model: FLAC m1). 222

Figure 3.10: EPWP in the SCP zone: recorded and calculated values by Cubrinovski (2011) and from FLAC analysis (model: FLAC m2). 222

Figure 3.11: a) Crest settlement and b) horizontal displacement at left toe – Naruse river levee (FLAC models). 223

Figure 3.12: Geometry variations for parametric study of embankment. 224

Figure 3.13: Spectra of used ground motions. 226

Figure 3.14: Numerical model in FLAC. 228

Figure 3.15: Locations of time history points. 230

Figure 3.16: Typical embankment displacements. 230

Figure 3.17: a) Pore water pressure ratio (R_u) at final calculated state and b) maximum R_u during analysis. 231

Figure 3.18: Correlations with vertical displacement at central top point of embankment. 232

Figure 3.19: Multiple stripe analysis procedure for derivation of »ds2« fragility curve – case H4B24-S5. ... 233

Figure 3.20: Fragility curves for different crest widths (road embankments). 237

Figure 3.21: Fragility curves for different embankment height (road embankments). 237

Figure 3.22: Fragility curves for different soil profiles (road embankments). 238

Figure 3.23: Fragility curves for different relative density of liquefiable sandy layer (road embankments). 238

Figure 3.24: Fragility curves for different crest width (railway embankments). 239

Figure 3.25: Fragility curves for different embankment height (railway embankments). 239

Figure 3.26: Fragility curves for different soil profiles (railway embankments). 240

Figure 3.27: Fragility curves for different relative density in sandy layer (railway embankments). 240

Figure 3.28: Crest deformation shapes for crest width $B = 6$ m and $B = 24$ m. 241

Figure 3.29: Fragility curves based on horizontal displacements - at crest and medium dense soil. 242

Figure 3.30: Fragility curves based on horizontal displacements - at ground level and medium dense soil. 242

Figure 3.31: Fragility curves based on horizontal displacements - at crest and loose soil. 242

Figure 3.32: Fragility curves based on horizontal displacements - at ground level and loose soil. 243

Figure 3.33: Predicted versus true results on the 20 % of the data as test set. 248

Figure 3.34: Evaluation diagram for data set 1. Graphs show the performance of ANN with respect to the percentage of data included in training set (D_t/D). Subdivision into training and testing data set is made randomly. 249

Figure 3.35: Evaluation diagram for data set 1. Graphs show the performance of ANN with respect to the percentage of data included in training set (D_t/D). Subdivision into training and testing data set is made



This project has received funding from the European Union's Horizon 2020 research and innovation programme under grant agreement No. 700748

randomly under condition that all data points from single FLAC analysis are included either in training or in testing data set. 249

Figure 3.36: Fragility curve fitting parameters μ and σ for unseen geometry and regression technique. .. 250

Figure 3.37: Examples of fragility curves for unseen geometry and regression technique. 251

Figure 3.38: Examples of ANN predictions of embankment settlement by regression technique for unseen geometry. 252

Figure 3.39: ANN predictions of embankment settlement by regression technique for data sets 2 and 3 based on training with data set 1. 252

Figure 3.40: ANN predictions of embankment settlement by regression technique for unseen geometry. Left: prediction for data set 3 based on training with data sets 1 and 2. Right: prediction for data set 2 based on training with data sets 1 and 3. 253

Figure 3.41: Fragility curve fitting parameters μ and σ – unseen random samples and classification technique. 254

Figure 3.42: Examples of fragility curves μ and σ – unseen random samples and classification technique. 255

Figure 3.43: Fragility curve fitting parameters μ and σ – unseen geometry and classification technique. . 256

Figure 3.44: Confusion matrices for highway embankment damage states - predicting both new data sets (Logar, 2018). 257

Figure 3.45: Confusion matrices for railway embankment damage states - predicting both new data sets (Logar, 2018). 258

Figure 3.46: The location of the sites. 261

Figure 3.47: Map of Adapazari showing the location of Cark and Sakarya Rivers, Cark Canal site and CPT Line 1 (Bray et al. 2001, Youd et al. 2009). 262

Figure 3.48: Plan view of the CPT tests and the boreholes (Bray et al. 2001). 263

Figure 3.49: q_c and I_c profile of SCPTU 1-24. 263

Figure 3.50: Section view of the river embankment and soil profile (Youd et al. 2009). 264

Figure 3.51: General cross section view with; soil stratification, soil type and the groundwater level (Bray et al. 2001). 264

Figure 3.52: A north to south view of the canalized river (Bay and Cox 2001, Photo by Brady Cox). 265

Figure 3.53: Current (November 2018) view of canal from the bridge. 265

Figure 3.54: Actual and idealized section and soil profile of the canal case. 267

Figure 3.55: Fragility curve used for the Cark Canal case. 267

Figure 3.56: Numerical model of the Cark Canal site. 268

Figure 3.57: PM4Sand model results with the parameters given in **Table 3.25**. 269

Figure 3.58: r_u values at the end of the dynamic model. 270

Figure 3.59: Vertical displacement profile at the embankment crest. 270

Figure 3.60: The effect of embankment slope (a) 1V:1H and (b) 1V:2H in terms of total displacements. 271

Figure 3.61: Ground displacement map observed at the Police Station site (Cetin et al. 2004). 272

Figure 3.62: Ground displacements in the will (embankment) (Cetin et al. 2004). 272

Figure 3.63: Soil profile is presented by CPT-PS-2 and SPT-PS-2 (Cetin et al. 2004). 273

Figure 3.64: SPT-PS-2 borehole data (Cetin et al. 2004). 273

Figure 3.65: Fragility curve for crest of the embankment at loose sand. 274

Figure 3.66: Fragility curve for the bottom of the embankment at loose sand. 275



This project has received funding from the European Union's Horizon 2020 research and innovation programme under grant agreement No. 700748

Figure 4.1: ShakeMap (<http://shakemap.rm.ingv.it/shake/index.html>) representing the spatial distribution of peak ground acceleration (PGA) and the buildings affected by liquefaction (a); San Carlo (b) and Mirabello (c) dataset with geological maps. 281

Figure 4.2: Distribution and cumulative percentage of the buildings as a function of the construction age (a), number of stories (b) and average story surface area (c). 282

Figure 4.3: Damage induced by liquefaction..... 283

Figure 4.4: Section 4- AeDES form: Damage to structural elements and existing short term countermeasures 284

Figure 4.5: Vertical structure C-DPMs: US class (a); LS class (b). 284

Figure 4.6: Mean empirical damage as a function of the vulnerability categories of buildings. 286

Figure 4.7: Minimum, Z_{min} , and maximum, Z_{max} , depths of the uppermost saturated, potentially liquefiable, soil layer..... 291

Figure 4.8: Minimum depth isolines of the first potentially liquefiable soil layer under the surface, z_{min} (in meters), superimposed on the geological map, vs. the observed building damage induced by liquefaction (red symbols) in the municipalities of S. Carlo (a) and Mirabello (b). 293

Figure 4.9: I_{AM} index isolines superimposed on the geological map, vs. the observed building damage induced by liquefaction (red symbols) in the municipalities of S. Carlo (a) and Mirabello (b). 293

Figure 4.10: Geological map with I_{AM} values adopted for the municipalities of S. Carlo (a) and Mirabello (b). 294

Figure 4.11: Lognormal and exponential fragility curves (*solid lines*) fitting observed fragility data (*circles*) for all the buildings and the adopted regression techniques (MLE and LSE). 295

Figure 5.1: Earthquake vulnerability relationships for underground pipelines in liquefaction areas (Eguchi, 1991)..... 307

Figure 5.2: Ground Deformation Damage Model for Cast Iron Pipes by HAZUS (NIBS, 2004) 308

Figure 5.3: Pipe repair-rate fragility curve versus permanent ground deformation (Eidinger, 1998)..... 309

Figure 5.4: Distribution of CI Repair Rate and Ground strain (T. O'Rourke S. T.-S., 1998) 310

Figure 5.5: Correlation between Ground Strain and CI Repair Rate (T. O'Rourke S. T.-S., 199) 310

Figure 5.6: Relation between PGA and damage rate of CIP (R. Isoyama, 2000)..... 311

Figure 5.7: Relation between PGV and damage rate of CIPb (R. Isoyama, 2000)..... 311

Figure 5.8: Relation between PGA and damage rate of DIP (R. Isoyama, 2000)..... 312

Figure 5.9: Relation between PGV and damage rate of DIP (R. Isoyama, 2000)..... 312

Figure 5.10: Analytical fragility curve for different width of liquefied zone (V. Terzi M. A., 2006) 315

Figure 5.11: Comparison of empirical and analytical fragility curves (V. Terzi M. A., 2006) 315

Figure 5.12: Comparison of empirical and analytical fragility curve (V. Terzi M. A., 2007) 316

Figure 5.13: Repair Rate vs. angular distortion of AC, CI and PVC pipelines for Christchurch earthquake (T. O'Rourke S.-S. J., 2012)..... 317

Figure 5.14: Repair Rate vs. lateral ground strain correlations for different pipe materials (T. O'Rourke S.-S. J., 2012)..... 318

Figure 5.15: Repair Rate vs. lateral ground strain and Angular distortion of AC pipelines for Christchurch earthquake (T. O'Rourke S.-S. J., 2012) 318

Figure 5.16: Repair rate vs angular distortion of (a) AC, (b) CI, (c) PVC water pipelines for the 22nd February earthquake (T. O'Rourke S.-S. J., 2014) 319



This project has received funding from the European Union's Horizon 2020 research and innovation programme under grant agreement No. 700748

Figure 5.17: Repair rate vs angular distortion of (a) earthenware(EW), (b) reinforced concrete rubber ring(RCRR), (c) concrete(CONC) wastewater pipelines for the 22nd February earthquake (T. O'Rourke S.-S. J., 2014)..... 319

Figure 5.18: Repair rate vs lateral ground strain of (a) AC, (b) CI, (c) PVC water pipelines for the 22nd February earthquake (T. O'Rourke S.-S. J., 2014) 320

Figure 5.19: Repair rate vs Lateral Ground Strain of (a) earthenware(EW), (b) PVC and UPVC wastewater pipelines for the 22nd February earthquake (T. O'Rourke S.-S. J., 2014) 320

Figure 5.20: Comparison of repair rate vs angular distortion and lateral ground strain UPVC wastewater pipelines for the 22nd February earthquake (T. O'Rourke S.-S. J., 2014) 321

Figure 5.21: Repair rate vs. lateral strain, and angular distortion for AC and CI pipelines (T. O'Rourke S.-S. J., 2014)..... 321

Figure 5.22: Repair Rate values obtained from LiDAR and air photo measurements (S. Toprak E. N.-S., 2014) 322

Figure 5.23: Christchurch water and wastewater pipes break rates for the different combinations of pipe material and size, calculated for different shaking intensity levels and ground liquefaction susceptibilities. Small wastewater pipes are smaller than 150mm and small water supply pipes are smaller than 100mm (A.K. Sherson, 2015) 324

Figure 5.24: Repair Rate vs Lateral Strain relationships for AC pipes (S. Toprak E. N.-S., 2014) 325

Figure 5.25: Repair Rate vs Lateral Strain relationships for CI pipes (S. Toprak E. N.-S., 2014)..... 325

Figure 5.26: Repair Rate vs Angular Distortion for AC and CI pipes (S. Toprak E. N.-S., 2014)..... 325

Figure 5.27: Repair Rate vs LSN for CI pipes (S. Toprak E. N., 2017) 326

Figure 5.28: Repair Rate vs LSN for PVC pipes (S. Toprak E. N., 2017)..... 327

Figure 5.29: Repair Rate vs LSN for AC pipes (S. Toprak E. N., 2017)..... 327

Figure 5.30: Repair rate vs. angular distortion for AC, CI and PVC pipelines: a) Results with updated measurements, b) Comparison of current and previous results (D. Bouziou, 2017)..... 328

Figure 5.31: Correlations of repair rate with lateral ground strain at 4-m and 56-m spacing for a) AC, b) CI and c) PVC pie materials for the 22nd Feb. 2011 earthquake and d) comparison of repair rate with lateral ground strain at 4-m spacing with previous work by O'Rourke et al. (2014) (D. Bouziou, 2017) 329

Figure 5.32: Repair rate vs. lateral ground strain and ground angular distortion for a) AC and b) CI pipelines (D. Bouziou, 2017) 329

Figure 5.33: Comparison Between Empirical and Analytical Fragility Relations for Various Cast Iron Pipe Diameters. High Ground Strain Model (T. O'Rourke T. V.-L., 2018) 330

Figure 5.34: RR vs. lateral ground strain for AC pipes (S. Toprak E. N., 2018) 330

Figure 5.35: RR vs. lateral ground strain for CI pipes (S. Toprak E. N., 2018) 331

Figure 5.36: Map showing CES events (Cubrinovski et al., 2015) 332

Figure 5.37: Liquefaction Map of Christchurch as produced by Curbrinovski and Taylor , 2011 (Reproduced from Cubrinovski et al., 2014) 333

Figure 5.38: Liquefaction map showing the areas of liquefaction and severity observed from different earthquakes. 4th Sept 2010 (white contours), 22nd February 2011 (red, yellow, magenta areas; Cubrinovski and Taylor, 2011) and 13th June 2011(black contours; Cubrinovski and Hughes, 2011). 334



This project has received funding from the European Union's Horizon 2020 research and innovation programme under grant agreement No. 700748

Figure 5.39: Liquefaction induced Land Damage observations across Christchurch after the February 2011 earthquake, with Feb 2011 magnitude-weighted equivalent $M_w = 7.5$ PGA contours overlaid based on Bradley & Hughes (2012) (Reproduced from Van Ballegooy et al., 2014) 335

Figure 5.40: Field Photographs of sand blows at study site following (A) Darfield $M_L = 7.1$ earthquake, (B) 22nd February 2011 $M_L 6.3, 5.8$ and 5.9 earthquakes, (C) 16 April 2011 $M_L 5.5$ earthquake, (D) 13 June 2011-a $M_L 5.6$ earthquake, (E) 13 June 2011-b $M_L 6.4$ earthquake and (F) 23 December 2011 $M_L 5.8$ and 6.0 earthquakes. All images were taken within 3 hours of the last inducing earthquake (Reproduced from Quigley et al., (2013)) 335

Figure 5.41: Observed liquefaction-induced land damage and dwelling foundation damage due to Christchurch earthquakes: (a) Extensive liquefaction in low-lying Christchurch suburbs (23rd February 2011), (b) Suburban Christchurch street covered with liquefaction ejecta (23 February 2011), (c) Pavement completely buried by liquefaction ejecta and ponded water after liquefaction (24th February 2011), (d) Surface water flowing over liquefaction ejecta with collapsed concrete block wall (22 February 2011), (e) Liquefaction ejecta next to brick house that subsided (25 May 2011), and (f) Uplift of concrete floor inside house with liquefaction ejecta and water mark around base of walls (01 March 2011). (Reproduced from Van Ballegooy et al., 2014) 336

Figure 5.42: Typical layout of watermains and submains in the carriageways and footpaths of Christchurch (reproduced from Cubrinovski et al., 2011). Typical layout of watermains and submains in the carriageways and footpaths of Christchurch (reproduced from Cubrinovski et al., 2011). 338

Figure 5.43: Illustration of backfill and pipe-laying details (units in mm) (Reproduced from Cubrinovski et., 2011)..... 339

Figure 5.44: (a) Circumferential split on AC main, Rowan Avenue (Picture reproduced from Cubrinovski et al., 2015), (b) AC main broken collar and longitudinal split (Reproduced from Cubrinovski et al., 2015).... 341

Figure 5.45: (a) Longitudinal split on AC main, (b) Broken CI main (Reproduced from Curbrinovski et al., 2014) 342

Figure 5.46: (a) bursts in the wall (indicated) of a CLS, (b) PVC mains (Reproduced from Cubrinovski et al., 2014)..... 342

Figure 5.47: (a) Compression effects in AC pipe joint, Sewell Street Kaiapoi, (b) Tension effects in AC pipe joint, Sewell Street Kaiapoi (Reproduced from Toprak et., 2017) 343

Figure 5.48: framework for development of the fragility model..... 344

Figure 5.49: Water Supply Network of Christchurch 345

Figure 5.50: Water Supply Network of Christchurch with different pipe types 346

Figure 5.51: Water Supply Network of Christchurch with different pipe materials 346

Figure 5.52: Water Supply Network of Christchurch with repairs 347

Figure 5.53: Sample LDP Map showing the data points where CPT tests were conducted. 348

Figure 5.54: Sample 20m buffer superimposed with water supply pipelines. 349

Figure 5.55: Intersected LDP points with buffer superimposed with Total LDP data points..... 350

Figure 5.56: LDP points showing superimposed with LDP zonation 350

Figure 5.57: Figure showing conversion of pipelines to points..... 351

Figure 5.58: Sample Pipeline points superimposed with LDP zonation map 351

Figure 5.59: (a) RR vs Settlement, (b) RR vs LSN 354

Figure 5.60: (a) RR vs LPIish, (b) RR vs LPI 354



This project has received funding from the European Union's Horizon 2020 research and innovation programme under grant agreement No. 700748

Methodology for the liquefaction fragility analysis of critical structures and infrastructures: description and case studies

Figure 5.61: (a) RR vs Settlement, (b) RR vs LSN 355

Figure 5.62: (a) RR vs LPIish, (b) RR vs LPI 355

Figure 5.63: (a) RR vs Settlement, (b) RR vs LSN 356

Figure 5.64: (a) RR vs LPIish, (b) RR vs LPI 356

Figure 5.65: (a) RR vs Settlement, (b) RR vs LSN 357

Figure 5.66: (a) RR vs LPIish, (b) RR vs LPI 357

Figure 5.67:Efficiency results for (a) Settlement, (b) LSN 358

Figure 5.68:Efficiency results for (a) LPIish, (b) LPI 358

Figure 5.69: Efficiency results for (a) Settlement, (b) LSN 359

Figure 5.70: Efficiency results for (a) LPIish, (b) LPI 359

Figure 5.71: Efficiency results for (a) Settlement, (b) LSN 360

Figure 5.72: Efficiency results for (a) LPIish, (b) LPI 360

Figure 5.73: Efficiency results for (a) Settlement, (b) LSN..... 361

Figure 5.74: Efficiency results for (a) LPIish, (b) LPI 361

Figure 5.75: Sample Magnitude Sufficiency results for Settlement..... 362

Figure 5.76: Sample Magnitude Sufficiency results for Settlement..... 362

Figure 5.77: Sample Magnitude Sufficiency results for Settlement..... 363

Figure 5.78: Sample Magnitude Sufficiency results for Settlement..... 363

Figure 5.79: Distance Sufficiency results for (a) Settlement, (b) LSN..... 364

Figure 5.80: Distance Sufficiency results for (a) LPIish, (b) LPI..... 364

Figure 5.81: Distance Sufficiency results for (a) Settlement, (b) LSN..... 365

Figure 5.82: Distance Sufficiency results for (a) LPIish, (b) LPI..... 365

Figure 5.83: Distance Sufficiency results for (a) Settlement, (b) LSN..... 366

Figure 5.84: Distance Sufficiency results for (a) LPIish, (b) LPI..... 366

Figure 5.85: Distance Sufficiency results for (a) Settlement, (b) LSN..... 367

Figure 5.86: Distance Sufficiency results for (a) LPIish, (b) LPI..... 367

Figure 5.87:Architecture of the ANN network (Calabrese et al., 2013) 368

Figure 5.88: *Confusion Matrix of the ANN model* 369



This project has received funding from the European Union's Horizon 2020 research and innovation programme under grant agreement No. 700748

TABLES

Table 2.1: Probabilistic distributions for the geometrical properties of the structural model.....	41
Table 2.2: Random distributions for the material properties of the structural model.....	41
Table 2.3: Random distributions for the gravity loads associated to the structural model for the design and seismic combinations	42
Table 2.4: Example of three selected profiles showing respectively low, medium and high normed error. .	78
Table 2.5: Liquefaction severity classes for ESP classification from macro-zonation	92
Table 2.6: Mohr-Coulomb parameters in numerical model from Dashti centrifuge experiment	97
Table 2.7: PM4Sand parameters in numerical model from Dashti centrifuge experiments	97
Table 2.8: Soil profile parameters	110
Table 2.9: Input ground motions.....	112
Table 2.10: Conditions of the selected case.....	114
Table 2.11: Soil profile properties considered in parametric study.....	125
Table 2.12: Soil profile properties.....	126
Table 2.13: Foundation properties considered in parametric study	127
Table 2.14: Mohr-Coulomb parameters for 2D parametric study	128
Table 2.15: Parameters for the three soil profiles with 2 layers.....	155
Table 2.16: Parameters for the two soil profiles with 3 layers	156
Table 2.17: Additional ground motions considered in the case study.....	158
Table 2.18: Input parameters of the hysteretic damping model	160
Table 2.19: Natural frequency of the liquefied site	160
Table 2.20: Geometric parameters for the reference model.....	162
Table 2.21: Median and standar desviation of each intensity measure.	166
Table 2.22: Definition of limit state related to ground deformations, i.e. peak rigid-body foundation rotations and settlements. Adapted after Bird et al. (2006).	192
Table 2.23: Comparison of the fragility parameters $\tilde{\alpha}_{g,LS}$ and β_{LS} , annual probabilities of exceeding designated limit states P_{LS} , and probabilities of exceeding designated limit states in 50 years ($P_{LS,50}$) obtained for the building located in Benavente (Portugal) and Düsseldorf (Germany), respectively.....	196
Table 3.1: Damage state criteria by Maruyama et al (2010).....	212
Table 3.2: Damage state criteria by RISK-UE approach (SYNER-G, 2011).....	212
Table 3.3: Damage state criteria by Argyroudis et al (2018).....	213
Table 3.4: Damage state criteria by Werner (2006) (summarized by SYNER-G, 2011).....	213
Table 3.5: Damage state criteria by Lagaros et al (2009).....	214
Table 3.6: Soil properties – Naruse river levee (Takahashi and Sugita, 2009).....	218
Table 3.7: Material parameters used in numerical analyses – Naruse river Levee.	220
Table 3.8: Soil profiles used in numerical calculations.	224
Table 3.9: Material properties for numerical simulations – general parameters.....	225
Table 3.10: Material properties for numerical simulations – PM4 parameters.	225
Table 3.11: Set of used ground motions	227
Table 3.12: Matrices with all performed analyses in FLAC.	229
Table 3.13: Fragility curve parameters in terms of PGA – medium dense soil (road embankments).	234



This project has received funding from the European Union's Horizon 2020 research and innovation programme under grant agreement No. 700748

Table 3.14: Fragility curve parameters in terms of PGA – loose soil (road embankments). 234

Table 3.15: Fragility curve parameters in terms of PGA – medium dense soil and crest width variations (road embankments)..... 234

Table 3.16: Fragility curve parameters in terms of PGA – medium dense soil (railway embankments)..... 234

Table 3.17: Fragility curve parameters in terms of PGA – loose soil (railway embankments). 235

Table 3.18: Fragility curve parameters in terms of PGA – medium dense soil and crest width variations (railway embankments)..... 235

Table 3.19: Fragility curve parameters in terms of Arias intensity – medium dense soil (road embankments). 235

Table 3.20: Fragility curve parameters in terms of Arias intensity – loose soil (road embankments). 235

Table 3.21: Fragility curve parameters in terms of Arias intensity – medium dense soil (railway embankments)..... 236

Table 3.22: Fragility curve parameters in terms of Arias intensity – loose soil (railway embankments). 236

Table 3.23: Additional numerical analyses data set 2..... 246

Table 3.24: Additional numerical analyses data set 3..... 247

Table 3.25: Calibrate PM4Sand parameters for the liquefiable (3) Silt (NP) layer at the Cark Canal site. ... 269

Table 4.1: DG (EMS-98) and corresponding damage levels to VSs according to the AEDES survey forms (Baggio et al. 2007)..... 289

Table 5.1: List of Fragility Functions..... 302

Table 5.2: Damage algorithms for water pipelines (NIBS, 2004) 307

Table 5.3: Damage algorithms for Oil pipelines (NIBS, 2004) 308

Table 5.4: Number of repairs for type of hazard (Eidinger, 1998)..... 309

Table 5.5: Earthquake and Number of Points in PGD Database (Alliance, 2001) 313

Table 5.6: Buried Pipe Vulnerability Functions (Alliance, 2001) 313

Table 5.7: Constants for fragility curve (Alliance, 2001) 314

Table 5.8: Wastewater pipes break rates for the combined and averaged data (Both Feb and June) (A.K. Sherson, 2015)..... 323

Table 5.9: Break rates for water pipes in the February and June earthquakes (A.K. Sherson, 2015)..... 323

Table 5.10: Table showing CES events with their magnitudes and epicentral depths (Callaghan 2014; Cubrinovski et al., 2015) 332

Table 5.11: Types of Pipe Materials and its mode of failure..... 340

Table 5.12: Repair Count for different Pipe Materials 340

Table 5.13: Repair Count for different Pipe Diameters..... 341

Table 5.14: Table showing (a) Lengths of different pipe types (b) Repairs conducted after each event of CES (c) Lengths of different Pipe Materials..... 345

Table 5.15: Results of Luco & Cornell Method (2002) 353

Table 5.16: Table showing pipeline attributes..... 368



This project has received funding from the European Union's Horizon 2020 research and innovation programme under grant agreement No. 700748

EXECUTIVE SUMMARY

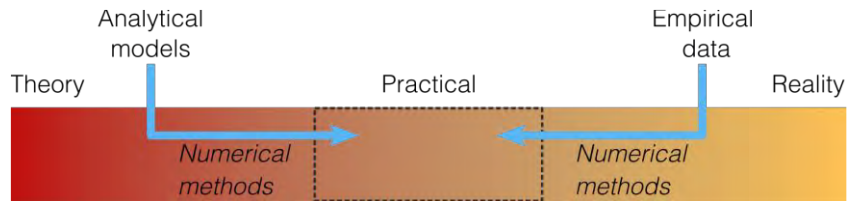
This report addresses the objective 3.2 of the Liquefact project to develop an efficient probabilistic numerical procedure for the simulation of liquefaction-induced damage and fragility analysis of critical structures and infrastructures. Different modelling strategies to simulate liquefaction-induced structural damage including uncertain/random factors with relevant effects on the behaviour of liquefiable soils and of interacting structure-soil systems, were developed and existing techniques were evaluated. Based on the studies presented in this report, the key factors that contribute to the occurrence of liquefaction and its impacts on critical structures and infrastructures were identified, to enable the development, evaluation and implementation of the most appropriate mitigation strategies to improve community resilience to against Earthquake Induced Liquefaction Damage (EILD) event.

The complexity of soil-liquefaction-foundation-structure interaction (SLFSI) is a challenge for both geotechnical and structural engineers. To cope with this complexity, both analytical and empirical approaches were taken to develop practical models for different asset types that had an adequate balance between complexity and accuracy specifically suited to probabilistic vulnerability analysis. The vulnerability analysis forms a key step of the loss assessment procedure developed in the final deliverable of this LIQUEFACT work package (Deliverable 3.3).

To adequately demonstrate the developed procedures, each approach was demonstrated on two different asset types (point/individual assets and distributed assets). Figure below illustrates the asset types and approaches covered in this report: (a) two analytical models, one for an individual asset (reinforced concrete building) and another for distributed asset (a road embankment); while, (b) two empirical database models were used, one for an individual asset (masonry structure building) and another for distributed asset (a road embankment).



This project has received funding from the European Union's Horizon 2020 research and innovation programme under grant agreement No. 700748



- Point (reinforced concrete buildings)
- Point (masonry structures Emilia-Romagna)



- Distribute (road embankment)



- Distribute (pipelines Christchurch)



(a)

(b)

Type of critical structures and infrastructures modelled during this workpackage: (a) analytical approaches with calibrated numerical simulations; (b) empirical approaches.

In this Deliverable the four major chapters will describe these novel approaches.

Chapter 2 presents the methodologies for considering the three factors that condition the behaviour of low-rise structures (residential and public like governmental offices, health facilities like hospital, fire stations, transport stations, terminals) during an EILD event. This work has involved both geotechnical and structural engineers working together to develop a modular analysis framework based on the key mechanisms involved in SLFSI (macro-mechanism approach): the first aspect covers the building structural/conditions (section 2.2), the second is covers the soil profile classes (2.3) and, the third, the ground motion intensity (2.4). It is also explained how the excess pore pressure time series – responsible for the development of this instability – can be estimated by a simplified procedure (2.5), and also how settlements of buildings (2.6) and the modified surface ground motions (2.7) time series generated under these conditions can be estimated with expeditious and simplified methods. This numerical modelling approach is able to represent the damage and the complex behaviour of interacting structure-soil systems and can be applied where the risk of soil liquefaction and structural damage has been evaluated as sufficiently high, through application of an initial Rapid Risk Identification (RRI) procedure (2.9). A pilot case in Emilia-Romagna - Italy, in Pieve-di-Cento - has been selected in view of the availability of sufficient data to apply the macro-mechanism approach that was developed in the last months in WP3, under UPorto team coordination (2.8).



This project has received funding from the European Union's Horizon 2020 research and innovation programme under grant agreement No. 700748

Regarding the specific modelling of Soil-Foundation-Structure Interaction (SFSI) effects, the advantages and drawbacks of different types of approaches were analysed in an attempt to find the most efficient modelling approach for probabilistic analyses. A novel mathematical technique for the simulation of site response including liquefaction without needing a constitutive model was developed. A simplified strain-energy liquefaction triggering procedure was developed for assessing the time of liquefaction. A substructuring approach was developed for modelling differential settlements and soil-foundation-structure interaction, overcoming some of the issues of super-position by considering rates of deformation rather than loads and forces. A new classification system was developed for quantifying liquefaction susceptibility independent of the ground motion demand. New settlement-vs-time relationships were developed for better accounting for the rate of settlement development. A new modular framework and procedure (macro-mechanism approach) was developed for vulnerability assessment of buildings considering liquefaction and shaking related damage that incorporated all of these new techniques, as well as existing techniques from literature and accounted for their uncertainties. Finally, a novel rapid risk assessment procedure was developed to quickly assess liquefaction and shaking related damage using a single-degree-of-freedom system to determine when the macro-mechanism approach should be applied. All of the methods were developed inside a probabilistic framework such that the factors associated to sources of uncertainty were established at a good level of confidence. Some of the factors that can condition the present framework are being further developed and analysed.

Chapter 3 presents the work done on vulnerability assessment of transport embankments with an emphasis on development of the fragility functions from extensive numerical simulations. This work used two-dimension nonlinear fully coupled effective stress finite different analyses to evaluate the performance of the embankments. Furthermore, a feasibility study on the possible use of artificial neural networks for interpolation / extrapolation of numerical results to different geometrical situations. These fragility curves were validated against two well documented case histories from Turkey.

In Chapter 4 empirical damage and liquefaction fragility curves are proposed based on Seismic Damage Grades, resulting from the analyses of 1,000 private residential masonry buildings located in several municipalities struck by 2012 Emilia earthquake,

Chapter 5 follows an empirical procedure to develop fragility models for earthquake-induced liquefaction damage in pipeline networks, based on the extensive data collection followed by the 2010-2011 Canterbury Earthquake Sequence CES in the city of Christchurch.



This project has received funding from the European Union's Horizon 2020 research and innovation programme under grant agreement No. 700748

SCOPE AND PURPOSE

The consideration that soil liquefaction is not exclusively in the problem domain of geotechnical engineering, but also there is a clear interaction between liquefiable soil profiles and the superstructure loading systems, provides the main focus of this report. The development of excess pore pressure and liquefaction can lead to a change in the shaking demands on the structure, impacting in the soil-liquefaction-foundation-structure interaction (SLFSI), also impact structural performance through further factors, like settlements, tilt, lateral spreading, etc. This SLFSI is a challenge from both geotechnical and structural engineers. Regarding the specific modelling of soil-structure interaction effects, the advantages and drawbacks of different types of approaches were analysed in an attempt to find the most efficient modelling approach for probabilistic analyses. Sub-structuring techniques were tested in order to use suitable modelling strategies for the structures and for the ground where liquefaction effects can develop. Adequate modelling of the more relevant sources of uncertainty for the vulnerability analysis problem have also been carried out by first identifying those sources using suitable statistical techniques and sensitivity analyses. Probabilistic models of the factors associated to those sources of uncertainty have been established and efficient statistical simulation strategies were used to propagate these uncertainties to the structural damage measures used in the vulnerability analyses.

The work developed aimed at investigating the vulnerability of critical infrastructures, specifically buildings with shallow foundations, to the impacts of liquefaction, using suitable statistical techniques and sensitivity analyses. A novel framework allowed to quantify settlement and soil stiffness as time series to allow SLFSI to be considered in structural modelling in a simplified manner. Further studies were performed on other infrastructure including embankments, pipelines and masonry buildings following different modelling techniques to evaluate a range of different approaches to assess vulnerability of buildings and infrastructure.

For the vulnerability analysis framework developed for buildings the framework offers a numerical efficient approach for engineers to considering the impacts of liquefaction (Millen et al., 2019). The efficiency of the procedure and the decoupling of the liquefaction analysis and structural analysis, allows engineers to consider a variation of the material properties and of underlying assumptions to obtain the inputs for the structural analysis. Using this probabilistic procedure, the liquefaction vulnerability analysis of selected case studies representative of real critical structures and infrastructures were carried out using analysis procedures which are typical of performance-based earthquake analysis. The selected cases studies have focused on shallow-founded buildings and embankments for transportation network or protection levees in free and no-free field conditions, but now focusing specifically in the two field trial tests at the two pilot sites (in Emilia Romagna, in Italy and in Adapazari, in Turkey), considering the parameters deduced from the characterization tests conducted in the natural ground conditions. The first one was directly associated to Pieve di Cento pilot test sites selected to conduct the activities in WP4, while the embankments were selected in Adapazari sites where data from Kocaeli 1999 earthquake induced liquefaction damages were observed. General archetypes of those case studies were defined, establishing different classes of structures for each case study, with different soil profiles and with the two types of geotechnical solutions. The outcomes of the vulnerability analysis were expressed in a set of fragility curves that were defined for specific performance levels addressing the type of damage expected from earthquake-induced liquefaction.



This project has received funding from the European Union's Horizon 2020 research and innovation programme under grant agreement No. 700748

1. INTRODUCTION

1.1 REPORT LAYOUT

This report presents the development of procedures to perform vulnerability analysis of buildings and infrastructure on liquefied soils, this report includes the following steps.

Chapter 2 presents the development of a numerically efficient modular approach for vulnerability for buildings (macro-mechanism approach). An overview of soil, foundation and building performance on liquefiable soil is presented, and how the consideration of an advance performance-based framework for estimating the settlement of shallow-founded structures on liquefiable deposits for such a highly nonlinear Soil-Foundation-Structure-Interaction (SFSI) requires robust numerical studies to evaluate SFSI effects and changes in the seismic demand imposed on the foundation through a liquefiable soil deposit.

For that, numerical parametric studies have identified the structural and soil input parameters that most influence foundation settlement of a single-degree-of-freedom (SDOF) building on liquefiable ground. Seismic demand at the foundation level is compared with those at the free-field soil surface and at the elastic bedrock level through time-frequency domain analyses of the accelerations. This analysis helps to evaluate the timing of liquefaction and how it influences the frequency content and amplitude of free-field and foundation accelerations, to control the demand imposed on the superstructure, and the timing and extent of foundation settlement.

This chapter explicitly addresses the three main work package objectives and describe the advantages of the adopted rational approaches:

- Development of an efficient numerical procedure for the simulation of liquefaction-induced damage of buildings.

Macro-mechanism approach dramatically reduces analysis time through a modular assessment of the major mechanisms, rather than performing fully coupled nonlinear dynamic analysis of a building soil system

- Development of an efficient probabilistic framework for liquefaction vulnerability analysis of buildings.
Combination of building and soil profile classes with defined criteria allows an intuitive physics-based approach to assess vulnerability where uncertainties and probabilities in inputs and in simplifying assumptions can be explicitly assessed

- General framework procedure for users and owners of buildings to assess subsoil properties and evaluate vulnerability.

Vulnerability analysis framework works for regional and building specific studies, the equivalent soil profile that classifies liquefaction susceptibility independent of the hazard means rapid and physically consistent vulnerability analysis can be performed. The modular design of the macro-mechanism approach means additional accuracy or multiple approaches can be considered for each step

Existing and newly-developed simplified procedures and nonlinear effective stress analysis procedures using FLAC2D (ITASCA, 2017) were implemented, calibrated against well documented centrifuge tests from Dashti



This project has received funding from the European Union's Horizon 2020 research and innovation programme under grant agreement No. 700748

and Bray (2010) and empirical functions from Boulanger and Idriss (2016), and evaluated to estimate pore-pressure in free-field, settlements of buildings and surface ground motions.

A Rapid Risk Identification method was developed in section 2.9, and can be applied as an initial screening tool to rapidly assess the risk associated with liquefaction to decide whether further more detailed analyses are warranted. This is based on risk assessment of a simplified SSI model, allowing for a rapid risk assessment without the need to perform time-consuming analyses. This method can be used as a screening tool in the case of low- to mid-rise structures on shallow foundations.

Chapter 3 presents the work done on vulnerability assessment of traffic embankments with an emphasis on development of the fragility functions for such facilities. It can be divided into the following parts – theoretical background, presentation of numerical work and subsequent evaluation of sample fragility curves for traffic embankments, feasibility study on the possible use of artificial neural networks for interpolation / extrapolation of numerical results to different geometrical situations. Finally, the produced fragility curves were validated against two well documented case histories from Turkey.

Chapter 4 proposed empirical damage and liquefaction fragility curves, based on Seismic Damage Grades, resulting from the analyses of 1,000 private residential masonry buildings located in several municipalities struck by 2012 Emilia earthquake. A thorough discussion is made on which parameters should be used for the interpretation of this extensive database of masonry buildings (several cases presented both typical damage induced by inertial forces and settlements associated to liquefaction) and fragility curves were developed.

Chapter 5 propose new empirical fragility models for earthquake-induced liquefaction damage in pipeline networks, based on the extensive data collection followed by the 2010-2011 Canterbury Earthquake Sequence (CES) in the city of Christchurch. The extensive damage to infrastructures and lifelines registered allowed to study the most appropriate liquefaction demand parameters. Correlations between repair rates, pipeline network and liquefaction severity indicators (settlement, LSN, Liquefaction Potential Index (LPI) and Liquefaction Potential Index as given by Ishihara (LPI_{ish}), were evaluated to propose the most appropriate liquefaction demand parameters.



This project has received funding from the European Union's Horizon 2020 research and innovation programme under grant agreement No. 700748

2. MACRO-MECHANISM APPROACH FOR BUILDINGS ON SHALLOW FOUNDATIONS

In this chapter a rational procedure to estimate the expected losses to a building on a liquefiable soil deposit due to seismic activity is defined and developed in a soil-structure system approach (SSS approach), considering the liquefiable soil deposit to be part of the topology rather than considering liquefaction directly as a hazard.

Several Unique Interaction Issues (UII) were considered to estimate losses in the presence of liquefaction: (UII 1) the extent of ground shaking is dependent on the extent and depth of liquefaction (it can dramatically reduce or in some cases amplify ground shaking); (UII 2) The extent of liquefaction is dependent on the presence of the building (large static vertical stresses under the foundation can prohibit full liquefaction from occurring); (UII 3) Both ground shaking and liquefaction cause nonlinear deformation to buildings (differential settlement can cause the premature yielding, modifying the dynamic response and extent of damage) (UII 4) The manifestation of liquefaction near a building can modify the dynamic properties of the building-foundation-soil system.

By considering the liquefiable nature of the soil deposit as part of the typology this approach can account for the above issues by modelling the performance of a building and soil profile to an upward propagating shear wave and accounting for the interaction. It can also be applicable at both the individual building scale and regional level, and can account for different levels of accuracy and criticality with more detailed models used for assets of greater importance.

The alternative “liquefaction-as-a-hazard” approach requires a complex “interaction function” to reduce the level of shaking in the presence of liquefaction to overcome each of the conditions in UII 1. As for the UII 2, it is required to make some modification to the liquefaction hazard to account for different building typologies. For issues UII 3 & 4, an additional interaction function is needed to assess the modification of buildings to each of the hazards in presence of others and further interaction function to account for the damage from two different sources.

To account for liquefaction in this procedure, the influence of liquefaction compared to a conventional SFSI problem can be considered through three aspects: (i) changes in the ground shaking hazard; (ii) changes in the soil-foundation-structure system (modification to the effective stiffness properties of the soil-foundation interface); and, (iii) increases in the soil-foundation permanent deformations (modification to local damage and the structural yield and ultimate displacements due to differential settlement, changes in overall performance due to rigid body tilt and settlement).

2.1 OVERVIEW OF DIFFERENT MODELING STRATEGIES AND KEY PARAMETERS

Figure 2.1 explores three different approaches to considering soil-liquefaction-foundation-structure interaction (“SLFSI”). The building-soil system can either be assessed directly through modelling the soil and the building in a single numerical or experimental model (Full model) or in a modular approach where different macro-mechanisms are first quantified and then connected through consideration of their



This project has received funding from the European Union's Horizon 2020 research and innovation programme under grant agreement No. 700748

interactions (Macro-mechanism) or completely de-coupled where shaking and liquefaction damage are assessed independently and then combined through an interaction function (Separate hazards).

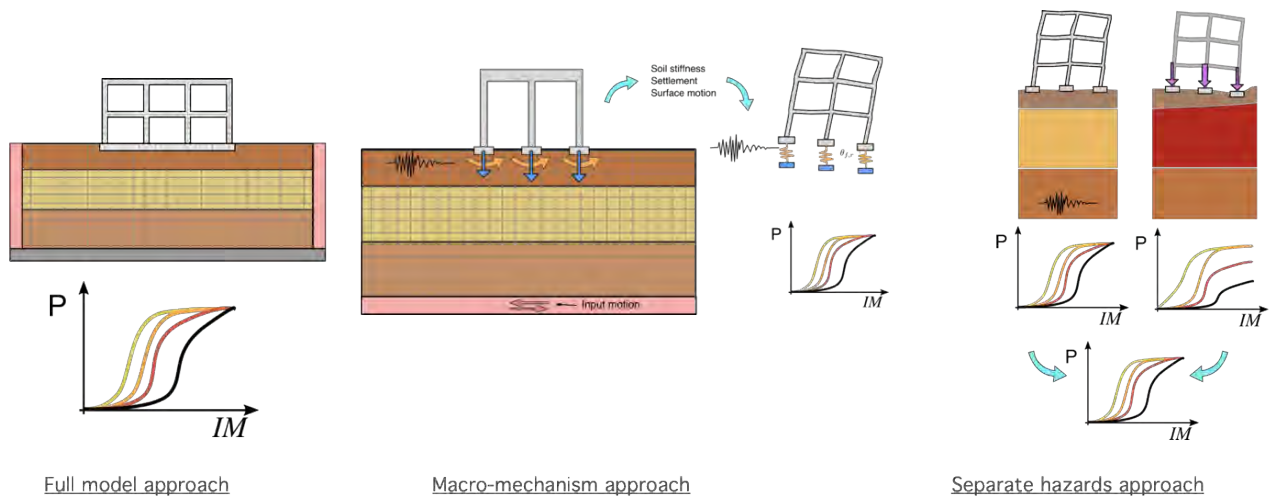


Figure 2.1: Different modelling approaches for soil-liquefaction-foundation-structure interaction

The full model is advantageous in that the interactions between all the mechanisms are implicitly accounted for. However, it is practically impossible to capture experimentally a detailed soil model and a detailed nonlinear structural model across a wide range of ground motions, even with a centrifuge, due to scaling laws and costs of experiments. Numerically a direct model is possible although none of the widely used state-compatible constitutive models exist in any widely used software that also contains suitable constitutive models for structural model. Therefore, a trade-off must be made in reduced accuracy for the soil or structure. The direct approach is computationally demanding as stiff structural elements often require a very small time step, while the large soil domain means there are many elements to be assessed at each time step. Also a direct approach does not benefit from generalising behaviour, in that a change in one assumption would require the numerical model to be completely re-run. Finally it is difficult to assess uncertainties the evaluation of uncertainties of the complete model would require extensive field or experimental data to validate against.

The macro-mechanism approach that was adopted for the performance of buildings in this chapter is further explained in section 2.2. The macro-mechanism approach captures the macro behaviour of the soil profile and building using submodels (e.g. pore pressure model, settlement model), and the explicitly accounts for their interaction.

The separate hazards approach, although numerical efficient and can make use of existing fragility curves for shaking damage, suffers from some significant drawbacks. The use of an interaction function to combine shaking and liquefaction damage is non trivial as well be explored in the next section when different mechanisms are explored. Essentially liquefaction modifies the shaking demand and differential settlements modifying the resistance capacity of the building which influences the shaking damage. Meanwhile the liquefaction damage (settlement and tilt) is dependent on the inertial load (shaking) of the building. Furthermore, liquefaction is directly dependent on the strength and therefore the shaking and liquefaction damage are highly correlated.



This project has received funding from the European Union's Horizon 2020 research and innovation programme under grant agreement No. 700748

2.1.1 KEY MECHANISMS IN SOIL-LIQUEFACTION-FOUNDATION-STRUCTURE INTERACTION

The influence of earthquake induced liquefaction on settlements, tilting or lateral spreading of footings resting on liquefiable and associated dynamic soil impedance (stiffness and damping) has high impact on the performance of a building on liquefiable soil. Any procedure that aims to consider these induced damaging factors will have to consider the change in shaking demand and changes to the natural vibration modes of the systems due to liquefaction, and should use a displacement-based assessment procedure that considers nonlinear SLFSI. The extension to the effects of liquefaction rely on several assumptions about the behaviour of the soil, site response and the structure, which require extensive research to improve the robustness of the performance assessment of buildings.

A strong focus on damage related to soil and foundation deformation is usually assumed, disregarding the damage associated to strong ground shaking, justified by the natural isolation that can occur due to the weakening of the soil during liquefaction (Millen et al. 2018). However, complete liquefaction does not occur instantly at the beginning of shaking (e.g. Wildlife record from the 1987 Superstition Hills earthquake, Kramer et al., 2011), and therefore the building can be exposed to intense shaking prior to liquefaction or while the soil is in a semi-liquefied state. The partial development of liquefaction under a building causes modification to the dynamic properties of both the soil deposit and soil-foundation-structure system and could potentially amplify the response beyond the non-liquefied conditions. Centrifuge experiments (e.g. Dobry and Liu, 1994) and numerical simulations (e.g. Karamitros et al., 2013a, b,c) have also highlighted that high vertical stress from the foundation limits the build-up of pore pressure to the extent that negative pore pressures can even develop directly under the foundation. As emphasized by Millen et al. (2018), the limitation of pore pressure build-up under high vertical stress can result in buildings being subjected to strong shaking even though liquefaction occurs in nearby free-field conditions. The strong shaking response is seen in the centrifuge experiments by (Dashti et al., 2007, 2010) shown in **Figure 2.2**, for the centrifuge experiment titled SHD02-04. The results show that even after pore pressure build up, the building still had a strong shaking response as seen in **Figure 2.2** (a).

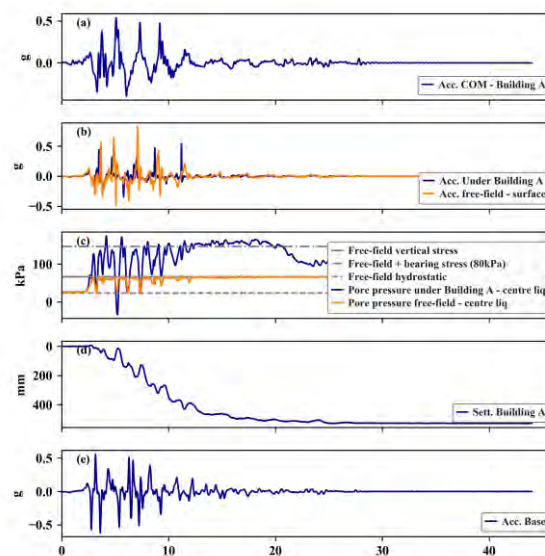


Figure 2.2: Soil, foundation and structure response from centrifuge experiment SHD02-04 adapted from Dashti et al. (2010)



This project has received funding from the European Union's Horizon 2020 research and innovation programme under grant agreement No. 700748

It is clearly not acceptable to disregard strong shaking when liquefaction occurs and there is a need to better understand SLFSI, as well as to develop a framework to consider the combined damage of both soil-foundation deformation and ground shaking. Furthermore, the development of liquefaction mitigation techniques that focus only on limiting pore pressure development (e.g. several methods in MBIE (2016)), should be re-assessed in regards to both soil/foundation deformation and ground shaking.

The numerical simulation of buildings on liquefiable soil that can simulate both the fully-coupled soil-fluid effective stress behaviour of the soil and the degradation and collapse of the structure are still beyond the capabilities of the majority of available engineering software. However, simple analytical and empirical techniques can provide useful insights into the expected level of damage from soil-foundation deformation and damage from ground shaking, which can help the engineer focus on the most critical parts of the building (Millen et al. 2018).

As described in deliverable 3.1, the extension of the displacement-based assessment procedure (**Figure 2.3**) to account for liquefaction relies on several assumptions about the behaviour of the soil, site response and the structure, which require an extensive research to improve the robustness of the assessment (Millen et al., 2018):

1. Assess the pushover response of the structure to determine the yielding and the ultimate force and displacement
2. Determine the displacements from the foundation at the point of structural failure
3. Convert the soil-foundation-structure system to an SDOF with an equivalent mass, height, stiffness and a factor to reduce the elastic displacement spectrum to account for energy dissipation
4. Reduce the spectrum and assess whether the displacement capacity of the SDOF is greater than the spectral demand.

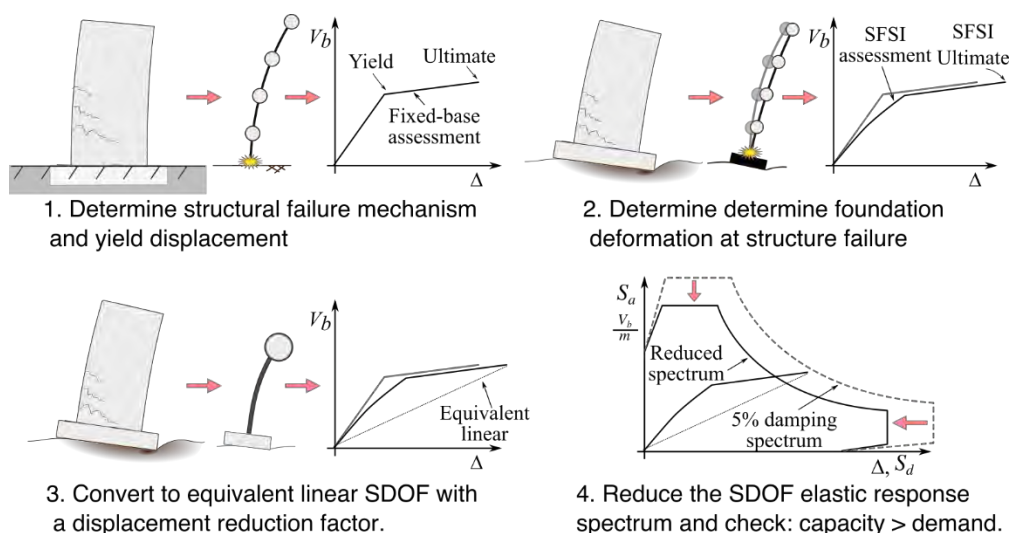


Figure 2.3: Displacement-based Assessment with SFSI (Millen. 2016)

The application of the displacement-based assessment framework highlighted current deficiencies in the SFSI procedure (Millen et al. 2018), and the difficulties to examine the magnitude of their influence were identified as described in the following sub-sections:



This project has received funding from the European Union's Horizon 2020 research and innovation programme under grant agreement No. 700748

Changes in ground shaking hazard (modify the displacement spectrum and displacement reduction factors)

The displacement-based assessment procedure is concerned with the maximum ductility demand of the structure. If the strongest shaking occurs prior to the development of liquefaction, it could be expected that the building performance in terms of maximum ductility demand would be similar to assessing the building in non-liquefied conditions. However, the strongest shaking (at the base of the deposit) may occur after liquefaction, meaning that the liquefied soil would modify the surface shaking. Liquefaction tends to reduce high frequency ground shaking and can potentially increase low frequency shaking.

Deterministically, it is impossible to accurately determine the maximum shaking demand on the building as the development of excess pore pressure is highly sensitive to the soil conditions, and the soil properties after liquefaction are poorly understood. However, two simple studies can highlight the relative importance of these two concepts (peak response before liquefaction occurs, and amplified low frequency content).

The first study uses the second set of 40 ground motions from Millen (2016) that were selected from site with $V_{s,30}$ values of between 120-360m/s from the ground motion data from Ancheta et al. (2013). A series of elastic SDOF analyses were conducted at various periods to determine when the peak displacement would occur in relation to the significant duration of the record, determined using the cumulative acceleration according to Trifunac and Brady (1975). The maximum response for two periods (0.5 seconds and 4.0 seconds) and a critical damping of 20% for the ground motion RSN3317_2 are shown in **Figure 2.4(a)**, and the corresponding input acceleration and significant duration are shown in **Figure 2.4 (b)**.

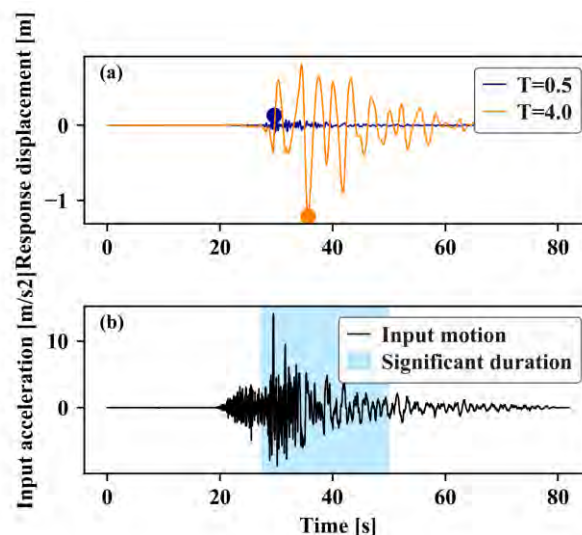


Figure 2.4: RSN3317_2 motion (a) Response of Elastic systems (b) Time series and significant duration (from Millen et al. (2018))

The results of the 40 ground motions for SDOF periods between 0.1-5 seconds and critical damping ξ of 20% are shown in **Figure 2.5** (Millen et al. 2018). It can be seen that short period structures typically experience their peak displacement earlier in the motion, while for longer period structures the peak displacement



This project has received funding from the European Union's Horizon 2020 research and innovation programme under grant agreement No. 700748

occurs later. **Figure 2.5** also highlights that for short period structures (less than 1.5 seconds), the peak response typically occurs in the first 30% of the strong shaking.

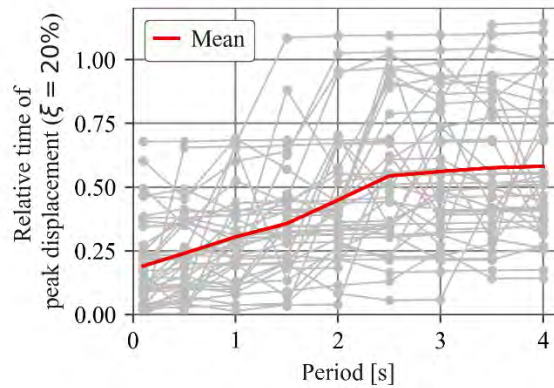


Figure 2.5: Occurrence of response displacement of elastic systems (from Millen et al. (2018))

While this study uses only elastic systems and therefore may only be appropriate for low-ductility systems, a study by Gazetas (2012) investigated the response of nonlinear systems. Gazetas (2012) showed that linear systems typically develop their peak response through the cumulative excitation of shaking, while the peak response of rigid-inelastic (sliding-block) systems develop their peak response due to the excitation of a single pulse. Therefore, it could be expected that the peak response of a nonlinear system would occur earlier in a record than for an equivalent linear system, since the cumulative excitation is less important if the nonlinearity increases. However, the characteristics of the individual ground motion in terms of the occurrence of pulses and the rate of pore pressure development in soil would govern the actual peak response of the structure. This study highlights the importance of the time of liquefaction, as early liquefaction may substantially reduce the seismic displacement of a building if liquefaction sufficiently reduces the amplitude of shaking.

The second study investigates how liquefaction can modify the amplitude of shaking. The study performs site response analysis using simple assumptions of the change in soil stiffness and energy dissipation due to liquefaction and modelled the response using linear elastic analysis following assumptions by Miwa and Ikeda (2006). Liquefaction is a highly nonlinear phenomenon; however, the frequency content of the surface motion is largely dependent on two parameters: the shear wave velocity and energy dissipation (or viscous damping).

Ground motions are modified as they travel up through a soil deposit, and some frequency content is amplified while other frequencies are de-amplified, largely based on the natural period of the site and the standing waves that develop. The natural period of a site (T_{site}) can be determined through equation (2.1), where $H_{profile}$ is the height of the soil profile and $V_{s,av}$ is the average shear wave velocity of the profile.

$$T_{site} = \frac{4H_{profile}}{V_{s,av}} \quad (2.1)$$



This project has received funding from the European Union's Horizon 2020 research and innovation programme under grant agreement No. 700748

As the shear stiffness of the soil deteriorates, the site period increases and subsequently can amplify longer period motion (Bouckovalas et al., 2016). In this study, a 20m soil profile is modelled over an elastic bedrock ($V_s=800\text{m/s}$). In the first analysis, the soil is modelled with a shear wave velocity of 120m/s , a unit weight of 18kN/m^3 and a critical damping ratio of 5% to simulate non-liquefied conditions. In the second study, the shear wave velocity is reduced to 30% of the original value and the critical damping ratio is increased to 25% over the lower 10 metres of the deposit to simulate liquefaction. The first five ground motions from the previous study (motion codes: RSN3271_1, RSN3317_2, RSN3512_1, RSN3663_1, RSN3670_1) were first scaled to match the design spectrum with a hazard factor of 0.3 and a soil class C and then were input at the base of the soil profile. The response spectra of the surface shaking compared to the original scaled motions are shown in **Figure 2.6**. It can clearly be seen that for the non-liquefied case the soil deposit amplifies the response around the period range of 0.8 seconds and is relatively unchanged over the remainder of the spectrum. The liquefied deposit shows a reduction in response in the low period range, due to the increase in damping, however, there is strong amplification in the period range around 3 seconds. This analysis is extremely simplistic and an elastic analysis is not suitable for simulating the highly nonlinear liquefaction phenomenon, the main drawback being that an elastic analysis means that the standing waves are at a constant frequency through the whole motion and therefore a strong amplification develops at these frequencies. In a profile that is liquefying, the natural frequency of the deposit is constantly changing so amplification does not develop at a single period. However, a recent proposal by Bouckovalas et al. (2017) suggests the elastic design spectra can be obtained from the envelope of two equivalent linear analyses. The first analysis considers the response of pre-liquefaction ground motion and site conditions and the second analysis considers the ground motion after liquefaction using post-liquefaction site conditions and the response spectra are combined based on the time of liquefaction.

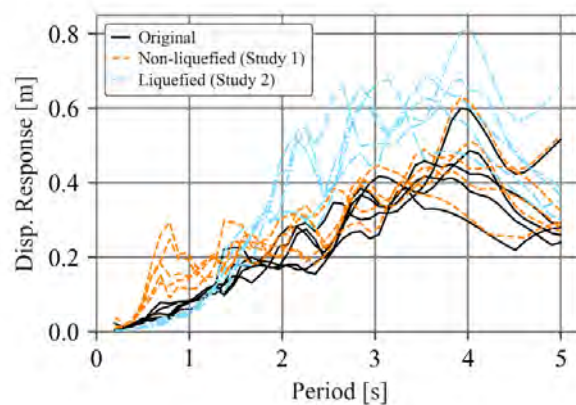


Figure 2.6: Shift in response spectra due to site effects

Changes in the soil-foundation-structure system (modification to the effective stiffness properties of the soil-foundation interface)

Once liquefaction has occurred, the soil has softened considerably, which alters the foundation impedance. Karatzia et al. (2017) developed expressions to quantify the small strain foundation impedance (stiffness and damping) for circular and equivalent circular surface foundations on liquefied soil deposits with a clay crust (a rigid footing lying on a three-layer liquefiable soil profile was numerically investigated, considering all three



This project has received funding from the European Union's Horizon 2020 research and innovation programme under grant agreement No. 700748

planar oscillation modes: vertical, horizontal and rocking). Notwithstanding the non-linear nature of the liquefaction phenomenon, Karatzia et al. (2017) showed that elastodynamic analysis can be employed as an engineering approach to the problem in the substructuring sense, assuming appropriate values for the shear wave velocity and material damping of the liquefied soil stratum, and considering a kind of “permanent” liquefied condition during the seismic event.

The results showed a decrease in the rocking stiffness of almost 40% for a shallow crust (foundation width to crust depth ratio of 0.5). The nonlinear stiffness in terms of uplift behaviour and soil yielding would also be expected to change. The nonlinear response at large strains is also expected to change as the strength of the liquefied layer has also decreased. Among the parameters explored, the thickness of the surface non-liquefiable soil layer is the one that seems to control the change in dynamic stiffness and damping. Based on the boundary element results, regression formulae for the vertical, horizontal and rocking static stiffness were obtained. These will be used for an initial assessment of the static stiffness of a surface foundation on liquefied soil in the methodology described below.

Research by Argeri (2018) investigated the change in the load-settlement and moment-rotation behaviour of a shallow foundation due to reduced stiffness and strength of a simulated liquefied layer under a surficial non-liquefying crust layer in PLAXIS. Argeri (2018) demonstrated a significant drop in initial rotational stiffness due to liquefaction, however, the maximum moment was similar to the non-liquefied case, since the stress bulb at the peak moment response was largely contained within the surficial crust. Dynamic analyses were also performed in PLAXIS using the liquefied and non-liquefied soil profiles and compared to a displacement-based assessment procedure that used the moment-rotation behaviour obtained from push-over based PLAXIS simulations, a sufficient match was obtained to suggest that assumptions could adequately account for the dynamic assessment of simple structures.

Increases in the soil-foundation permanent deformations (modification to local damage and the structural yield and ultimate displacements due to differential settlement, changes in overall performance due to rigid body tilt and settlement)

Liquefaction produces a dramatic reduction in stiffness and strength which often results in settlement and tilting of the foundation (See **Figure 2.2(d)** settlement results from Dashti et al., 2010). The level of deformation depends on numerous factors ranging from pore water flow rates, to soil heterogeneity or stress fields from adjacent buildings. Some of this deformation can occur in a uniform manner such as rigid-body settlement and rigid-body tilting (**Figure 2.7**– upper schematics), which can cause health issues for building occupants (Keino and Kohiyama, 2012). However, when the deformation happens in a non-uniform manner it cannot only cause health-related effects but can also introduce additional stresses and strains in the superstructure (**Figure 2.7**– lower schematics).



This project has received funding from the European Union's Horizon 2020 research and innovation programme under grant agreement No. 700748

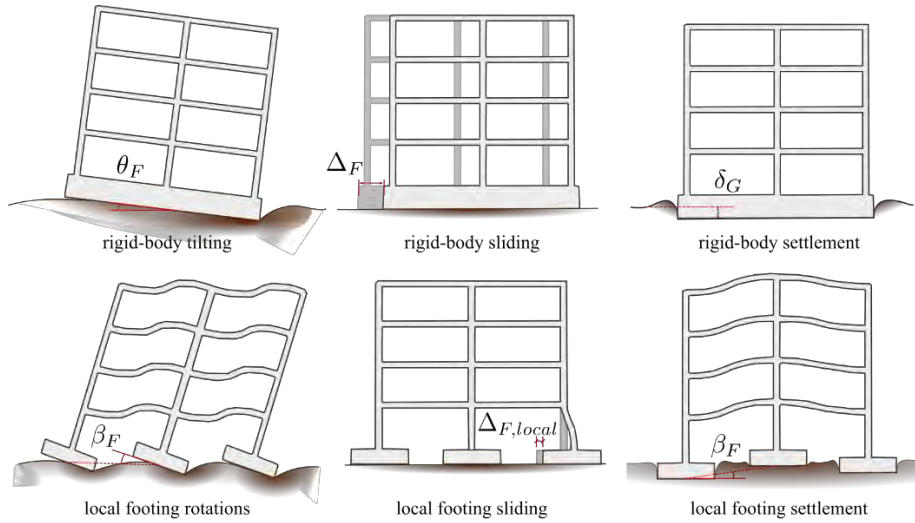


Figure 2.7: Rigid-body and differential movements of the foundation (taken from Millen, 2016)

The additional stresses in the superstructure result in an earlier onset of yielding and failure of members. **Figure 2.8** shows the conceptual change in the push over response of a structure due to differential settlements, where the yielding response is smoother due to earlier yielding of some members, while others are delayed until the stresses are redistributed and eventually failure occurs earlier due to the higher strains in the earlier yielding members (Millen et al., 2018).

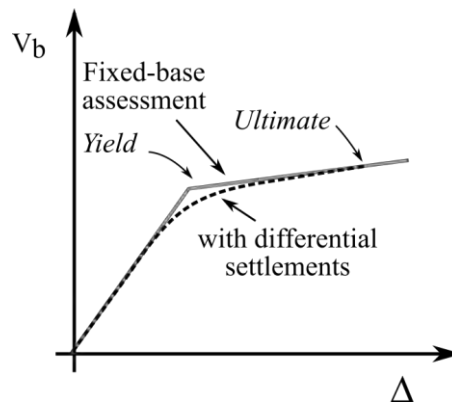


Figure 2.8: Expected influence of differential settlements on the pushover response of a building

The level of shear demand on the beams due to the complete loss of bearing under one footing, compared to the demands of seismic action, can be estimated using the Equation (2.2) from Gomez et al. (2018):

$$\zeta_v = \frac{\chi \beta^n n L}{U_b (n + f_b) \left[\frac{L}{2} + \lambda h \frac{S_a(T)}{g} \left(n - \frac{1}{2n} \right) \right]} \quad (2.2)$$

Where,

- χ switches from the maximum free settlement to the real one (see Gomez et al., 2018 how to calculate);



This project has received funding from the European Union's Horizon 2020 research and innovation programme under grant agreement No. 700748

- β , suggested to be 1.02, corrects the overestimation of seismic demand due to the “cantilever effect” and the distortion of V_s due to decompression of the settled column;
- U_b is the number of effective beams joining the settled column at each level, in any direction;
- f_b accounts for the presence of foundation beams (see Gomez et al., 2018 how to calculate);
- λ is the relative participating mass of the MDOF (see Gomez et al., 2018 how to calculate);
- n : number of storeys; L : beam span length; h : interstorey height; $S_a(T)/g$: elastic seismic demand spectral acceleration.

Equation (2.2) does not correspond directly to a reduction in yield and ultimate displacement capacity, and requires a nonlinear analysis of individual buildings to assess how stresses and strains would be redistributed within the structure.

2.1.2 VULNERABILITY ASSESSMENT OF CONCRETE FRAME BUILDINGS VIA MACRO MECHANISM APPROACH

In the proposed modelling macro-mechanism modelling approach, the issues of time of liquefaction, modification to surface acceleration, soil-foundation stiffness, differential settlement and load redistribution, are considered in detail to better estimate the expected demands and deformations of the foundation and the building. The modelling procedure developed in the workpackage 3 of Liquefact was based on a sub-structuring approach and overcomes some of the issues of superposition by considering the rate of deformation rather than imposing displacement and forces. It has been developed to provide an efficient procedure to consider the impact of liquefaction on the performance of buildings.

The development of the model requires four sub-steps:

1. Quantify the liquefaction potential of the soil profile in terms of depth and thickness of the liquefiable layer(s) and the resistance to liquefaction
2. Estimate the expected level of surface shaking considering the dynamic site response
3. Approximate the soil foundation stiffness using springs and dashpots that account for nonlinear soil behaviour and the change in soil characteristics due to liquefaction
4. Estimate the expected load-settlement behaviour of each footing accounting for the build-up of pore pressure

The four sub-steps can either be performed separately or in combination. The following sections describe an approach to estimate the sub-steps using FLAC2D (ITASCA, 2017) and a series of simplified expressions.

The key aspects of the numerical model can be seen in **Figure 2.9**, where lumped plasticity is used to capture the nonlinear behaviour in the beams, columns, joints, infills and soil. Distributed gravity load is used to capture the expected static moment and shear demand on the elements.

The input motion is the expected surface motion from sub step 2 and the expected differential settlement behaviour is captured through a combination of imposed settlement and changes in the stiffness of the soil springs. The full details of the numerical model are described in the following sections.



This project has received funding from the European Union's Horizon 2020 research and innovation programme under grant agreement No. 700748

2.2 MODELLING OF BUILDINGS ON LIQUEFIABLE DEPOSITS

2.2.1 INTRODUCTION

Liquefaction impacts the seismic surface motion, it modifies the soil-foundation settlement and can cause large settlement and tilt. The impact of these modifications requires a careful investigation of their interactions during a shaking event. To achieve this, a nonlinear time history analysis procedure has been developed that models the macro-mechanisms of the soil, foundation and structure. The procedure largely follows the modelling approach by Millen et al. (2019) with further exploration of some details related to settlement and load re-distribution.

The modelling procedure developed in this document is a sub-structuring approach and has been developed to provide an efficient procedure to consider the impact of liquefaction on the performance of buildings. The model presented here is for the problem domain prescribed in **Figure 2.9**, where the building is a Pre-1970's European reinforced concrete building on shallow foundations on flat ground, and subject to a ground motion only in one principle direction of the building.

The key aspects of the numerical model can be seen in **Figure 2.9**, where lumped plasticity is used to capture the nonlinear behaviour in the beams, columns, joints, infills and soil. Distributed gravity load is used to capture the expected static moment and shear demand on the elements. The input motion is the expected surface motion from sub step 2 and the expected differential settlement behaviour is captured through a combination of imposed settlement and changes in the stiffness of the soil springs.

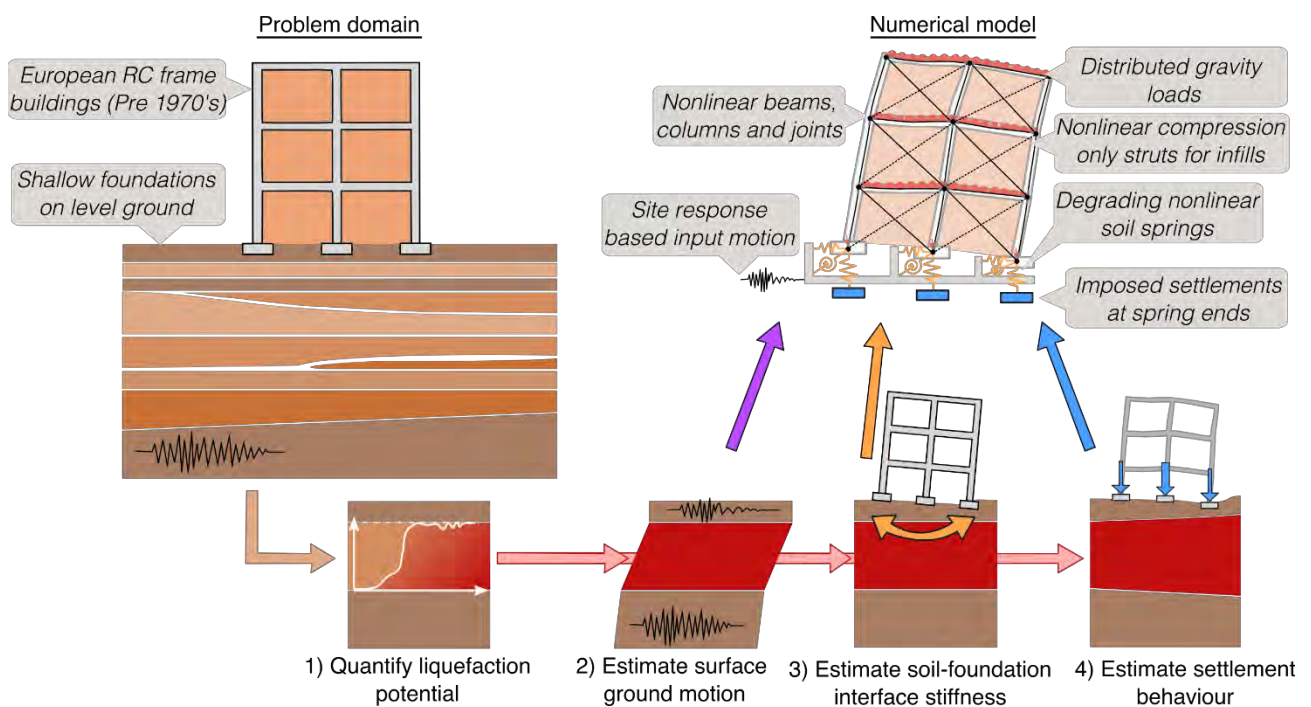


Figure 2.9: Problem domain and numerical model



This project has received funding from the European Union's Horizon 2020 research and innovation programme under grant agreement No. 700748

The structural model was implemented in a numerical form using the open source software OpenSees (McKenna et al., 2000). This software framework uses the finite element method for simulating the response of structural and geotechnical systems subjected to earthquakes.

This section outlines the key aspects of the structural model and various validation and verification steps in the development of the model.

2.2.2 KEY FEATURES OF THE PHYSICAL MODEL

A three-storey reinforced concrete (RC) building (with or without masonry infills) was considered as reference class of structures for analysis. The structural model is composed of a 2D reinforced concrete frame (example of a 3-storey 3-bay frame in **Figure 2.11**) and a specific configuration of the soil-foundation-structure interface, described in the subsequent sections.

The building class variability has been represented using a random generation of the building characteristics, and adopting a gravity-only design. Such design strategy is referred to as low-code design and it is based on the consideration of static loads, neglecting the dynamic features of the structure, in order to obtain a portfolio of non-seismic RC buildings.

The random building characteristics are referred to the geometric dimensions of the structural elements, to the material (steel and concrete) properties, and to the distributed gravity loads used in the design phase and associated to the seismic combination of actions. The probabilistic distributions from which the characteristics are generated are reported in **Table 2.1**, **Table 2.2**, and **Table 2.3**, respectively. Truncation levels are imposed to avoid extreme values. Beam height and beam span (or bay length) are correlated by a bivariate Gaussian copula and the minimum value of the former is truncated to 1/10 of the value of the latter. This correlation is as shown in the example of **Figure 2.10**, where 1000 values of the two variables were generated. The generated dimensions of the sections of columns and beams were rounded at 0.05 m.

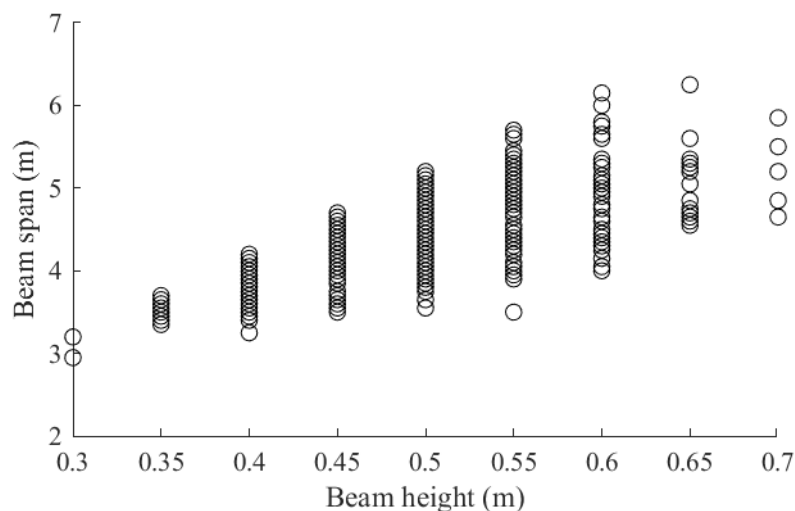


Figure 2.10: Bivariate Gaussian copula correlating beam height and span



This project has received funding from the European Union's Horizon 2020 research and innovation programme under grant agreement No. 700748

A simulated design coded in Matlab generated a set of input design parameters (geometry, material strength, gravity loads) from these distributions and then performed a gravity load (non ductile) design. The simulated design was performed by running a static gravity analysis in Opensees on the building with the generated characteristics and using a gravity load for a design combination of actions uniformly distributed on the beams, and a fixed base structure. The value of the gravity load for design was randomly generated from the probabilistic distribution presented in **Table 2.3**. The moment and shear demand in the beams and columns from the gravity analysis was used to size the reinforcing in the sections and joints and sized the foundation footings. All columns have been designed with the same reinforcement; while a specific reinforcement was designed for central and end sections of each beam. The properties of the sections corresponding to the calculated reinforcement were used to develop an OpenSees model for seismic assessment.

A second gravity analysis was then performed on the same building with the updated elements, using the value of uniform gravity load (also in this case uniformly distributed on the beams) associated to a seismic combination of actions. The value of this load is calculated as a fraction of the correspondent load for design combination. The ratio of the loads in seismic over design combination is randomly generated from the distributions presented in **Table 2.3**. The additional weight of the infills (if present) are summed to this load, in order to calculate the loads transmitted to the foundation and the nodal masses for the subsequent calculation of settlement and dynamic analysis. The nodal masses were calculated according to the axial load levels at the top of each column, by subtracting the total axial load of the above floors to the axial load at the lower storey.

Opensees does not associate masses to gravitational load; thus, the uniform gravity load for seismic combination of actions was statically applied in the subsequent dynamic analysis, in order to model the vertical static load, prior and during the dynamic application of the horizontal ground motion. The P-delta effects (second-order forces due to a displacement of the vertical load from its support), were explicitly modelled with a leaning column (**Figure 2.13**). The leaning column has a very high axial stiffness, a very low bending stiffness and it was linked to the structure by axially rigid truss elements, in order to not transfer relevant bending moments to the frame structure. A concentrated vertical load was applied to the leaning column at the level of each floor of the structure, equal to the weight of that floor.

The building mechanical and geometrical properties were stored in a file for subsequent analysis. By applying this procedure for a specified number of buildings, a population of non-seismic RC buildings can be generated.



This project has received funding from the European Union's Horizon 2020 research and innovation programme under grant agreement No. 700748

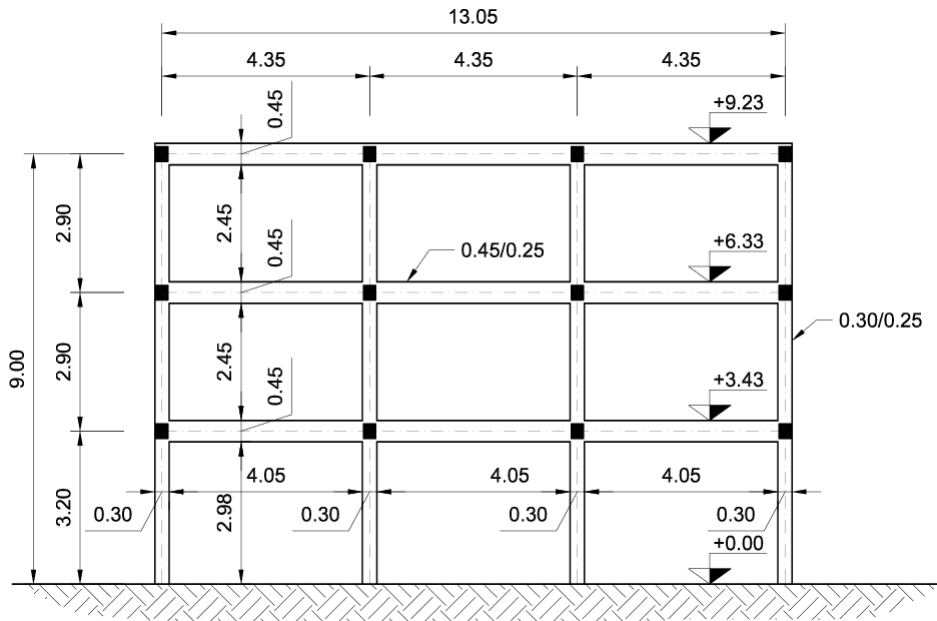


Figure 2.11: Example of physical model of the reference structure

Table 2.1: Probabilistic distributions for the geometrical properties of the structural model

Parameter	Type of distribution	Mean value (μ)	Std. deviation (σ)	Trunc. (min)	Trunc. (max)	Notes
Number of bays	Uniform	3		2	5	
Bay length (m)	Lognormal inv. cum.	4.37	0.11			Correlated to beam height by bivariate Gaussian copula
Ground floor height (m)	Lognormal	3.21	0.13	2.75	4.00	
Regular height (m)	Normal	2.88	0.20	2.75	3.50	
Beam height (m)	Normal inv. cum.	0.44	0.01	$L_{bay}/10$		Correlated to bay length by bivariate Gaussian copula
Beam width (m)	Lognormal	0.27	0.16	0.25	0.40	
Column depth (m)	Lognormal	0.28	0.15	0.20	0.44	
Column width (m)	Lognormal	0.27	0.16	0.20	0.53	

Table 2.2: Random distributions for the material properties of the structural model

Parameter	Type of distribution	Mean value (μ)	Std. deviation (σ)	Trunc. (min)	Trunc. (max)	Notes
Strength of concrete (MPa)	Gamma	24		12	70	Shape=6 Scale=4



This project has received funding from the European Union's Horizon 2020 research and innovation programme under grant agreement No. 700748

Steel class	Triangular	2		1	3	s1=25% s2=50% s3=25%
Yield strength of steel (class s1) (MPa)	Normal	344	68.8	230	500	
Yield strength of steel (class s2) (MPa)	Normal	495	22	400	550	
Yield strength of steel (class s3) (MPa)	Normal	589	30	500	670	

Table 2.3: Random distributions for the gravity loads associated to the structural model for the design and seismic combinations

Parameter	Type of distribution	Mean value (μ)	Std. deviation (σ)	Trunc. (min)	Trunc. (max)	Notes
Gravity load for design combination of actions (kN/m)	Triangular	50		35	65	
Ratio of gravity loads in seismic/design combination of actions	Triangular	0.30		0.25	0.35	

The soil-foundation-structure interaction was modelled with a complex non-linear dynamic model. The different features of this model are presented in the next sections, where the generic benchmark structure response has been studied in different foundation-soil configurations, from the simpler to the more advanced, in order to study the influence of each aspect of the model.

Three examples of soil-structure interactions are shown in **Figure 2.12**. In case a, the building foundations laid on a very stiff layer (bedrock), which prevented any displacement/rotation of the structure foundation. In such conditions, the bedrock ground motions do not undergo any amplification or modification in frequency content and intersect the soil surface unaltered. In case b, the soil beneath the foundation level corresponded to a multi-layer soil profile with a granular liquefiable layer and two non-liquefiable layers. The foundation was a very stiff continuous shallow foundation, which prevented differential settlements and/or base tilt. Case c presents the same soil layers of case b. The foundation system was composed of shallow isolated footings, which were prone to differential settlements/rotations.

Case c requires a complex soil-foundation-structure interaction model that includes a non-linear spring-damper system and imposed settlement at the base of the foundation nodes, as explained in section 2.2.4.



This project has received funding from the European Union's Horizon 2020 research and innovation programme under grant agreement No. 700748

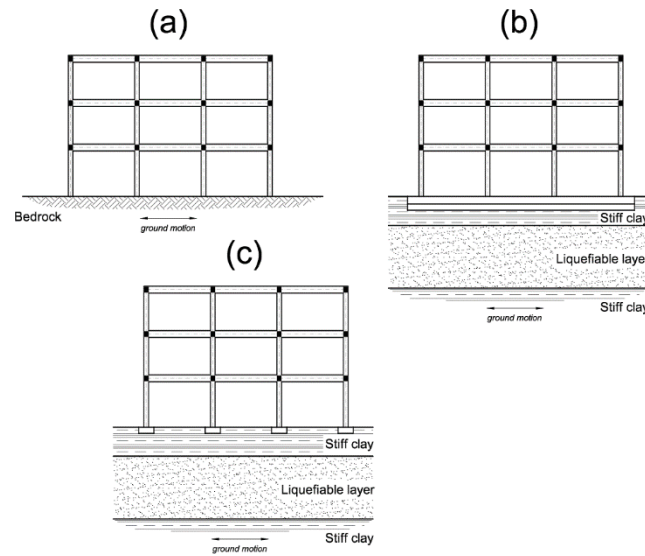


Figure 2.12: Foundation-soil systems: (a) rigid foundation on bedrock; (b) rigid foundation on compressible soil; (c) isolated footings on compressible soil

2.2.3 GROUND MOTIONS

For the case of bedrock (**Figure 2.12 a**), motions should be recorded rock motions, whereas for cases where the building is on liquefiable soil (**Figure 2.12 b and c**), a suitable site response analysis is required to obtain the surface motion as input. For the rigid mat foundation, the input motion can be applied directly to the base nodes of the structure, while for isolated footings the motion should be applied at the end of horizontal springs that represent the soil-foundation interface shear stiffness. Two procedures for performing site response analysis are detailed in section 2.7, the first is one-dimensional effective stress analysis. The surface motions obtained from these analyses should be filtered using a 4th order Butterworth lowpass filter at 15Hz, because the numerical noise due to rapid changes in stiffness becomes especially prominent above this frequency. The second procedure is a simplified mathematical method, the Stockwell transfer function method. Where a time-frequency filter is applied to the upward propagating motion in mimic the effects of liquefaction.

2.2.4 SUPERSTRUCTURE MODEL

The general modelling strategy adopted for the frame elements involved an association of nonlinear springs and elastic elements in series combined with a nonlinear moment-rotation joint model, following the main assumptions and strategies proposed Elwood (2004), Ibarra et al. (2005), Lignos and Krawinkler (2011), Baradaran Shoraka and Elwood (2013), Jeon et al. (2015) and Haselton et al. (2016).

BEAMS AND COLUMNS

The structure in elevation was modelled in OpenSees with a 2D model with 3 degrees of freedom (DOFs). The configuration for the fixed-base case (without soil-structure interaction) is reported in **Figure 2.13** for a 3-storey 3-bay structure. In each analysis, this model is the same used in the design phase. The RC frame was



This project has received funding from the European Union's Horizon 2020 research and innovation programme under grant agreement No. 700748

represented using 21 elastic beam-column elements (linear elastic), 9 for the beams and 12 for the columns (referred to as elasticBeamColumn elements in OpenSees).

BEAM-COLUMNS JOINTS

The linear elements were connected by nonlinear beam-column joints (Joint2D elements), connecting the end sections of beams and columns. The two-dimensional beam-column joints were modelled as parallelogram-shaped shear panels (rotational springs) with adjacent elements connected to their mid-points (detail in **Figure 2.13**). Each beam or column was connected to the shear panel through a shear and a rotational spring (ZeroLength elements). The system composed by the shear panel and the four spring elements at the external nodes was able to reproduce the nonlinear response of the structure under monotonic and cyclic strain, thanks to the specific properties of the materials associated to each component.

The central rotational spring was modelled with a hysteretic material (uniaxial Material Hysteretic), with pinching of force and deformation, damage due to ductility and energy, and degraded unloading stiffness based on ductility. The external rotational springs were modelled with a material (ModIMKPeakOriented) that simulates the modified Ibarra-Medina-Krawinkler deterioration model with peak-oriented hysteretic response (Lignos and Krawinkler, 2012). The strength and stiffness associated to these materials was a function of the physical characteristics of the sections of the corresponding elements (beams or columns), that were determined in the design phase, where the reinforcement of the structural elements was calculated.

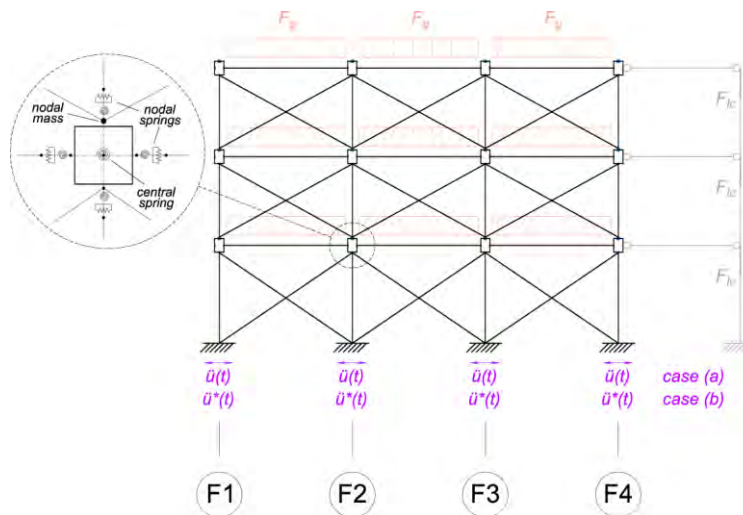


Figure 2.13: Numerical model for cases (a) and (b) and detail of the beam-column joints configuration

MASONRY INFILLS

Masonry infills were modelled with the equivalent strut approach, which is one of the commonly used principles when developing nonlinear mathematical models of infilled frames for earthquake analysis (Zarnic and Gostic, 1998).

The elements used were nonlinear truss elements that were assigned a nonlinear stress-strain material model simulating the infill behaviour. Two diagonal struts (as shown in **Figure 2.13**) were used to simulate one infill and were connected to the beam-column joints at the column level. The equivalent area of each strut



This project has received funding from the European Union's Horizon 2020 research and innovation programme under grant agreement No. 700748

was established based on the maximum lateral force of the infill (Zarnic and Gostic, 1997), transformed to the direction of the diagonal, and on the masonry compressive stress f_m . Maximum strength was assumed to be reached at an inter-storey drift of 0.2% (Dolsek and Fajfar, 2008). The lateral displacement of each infill was transformed into the diagonal displacement for the subsequent definition of the strain of the strut.

The parameters obtained, i.e. the maximum stress and strain, were used to define the masonry material with zero tensile strength simulated by the Concrete01 material (Noh et al., 2017). The peak compression strength f_m was equal to 3.1 MPa and all infills had a thickness of 0.1 m. Additionally, a residual strength equal to 10% of the peak strength was considered for numerical stability, which was reached at an inter-storey drift five times the peak inter-storey drift.

Openings were modelled following the proposal of Tasnimi and Mohebkah (2011), which consider a reduction factor for the equivalent truss width and peak load capacity. Such factor is a function of the ratio of the area of the openings of a panel to the area of the infilled panel. One door was considered in the central panel of the ground floor and a window for each panel of all the storeys in the two external bays (each panel between columns F1-F2 and F3-F4 in the model of **Figure 2.13**).

The infills were included in the structural model to involve realistic values of stiffness, strength and mass. Nevertheless, the damage of the infills during the application of the seismic load was not explicitly considered as a performance criterion in the subsequent assessment of the performance of the structure, where only the shear failure of beams, columns and joints, and inter-storey peak and residual drift and foundation tilt were considered.

2.2.5 FOUNDATION MODEL

For soil-foundation configurations similar to those of **Figure 2.12** a and b, foundations were modelled in OpenSees as infinitely rigid in the two displacement directions and in the rotational component (**Figure 2.13**). Thus, the nodes corresponding to the foundation level were constrained in the three components. Rock ground motions (a) and the surface ground motions (b) were applied at these nodes as acceleration time series ($\ddot{u}(t)$ and $\ddot{u}^*(t)$, respectively).

In a configuration similar to **Figure 2.12** c (isolated foundation on liquefiable soil), the more complex soil-foundation-structure interaction required the model shown in **Figure 2.14**. The dimensions of the isolated pads were determined for each building in the non-seismic design phase, along with the superstructure design. The footings were designed to be all equal, by considering the most loaded column and applying Meyerhof (1963) method to design a square section. In the numerical model, the base node of each column of the ground floor was connected to the constrained node by means of a nonlinear spring-damper system acting along the three degrees of freedom. The surface motions $\ddot{u}^*(t)$ were applied at the fixed nodes.

The spring system was composed of a vertical, a horizontal, and a rotational component. The damping (dashpot) system (not shown in **Figure 2.14**) acted in parallel with the spring system, and it was composed of three components as the spring system. The system was modelled in OpenSees by two ZeroLength elements, one for the spring and one for the dashpot element. The materials used for modelling the behaviour of these elements in each of the three components are described in the following sections.



This project has received funding from the European Union's Horizon 2020 research and innovation programme under grant agreement No. 700748

2.2.6 ADDITIONAL ASPECTS FOR NUMERICAL MODELLING

As referred, a design phase was carried out for each building before the dynamic analysis, in order to calculate the design properties of the structural elements, and to calculate the equivalent lumped masses. The lumped masses for dynamic response calculated in the design phase were located in the nodes above the shear panels, as shown in **Figure 2.13**.

For infilled structures, the extra masses and gravity loads due to the infills were added to the previously calculated nodal masses and distributed gravity load. A unit weight of 6.87 kN/m^3 was considered for the infills (Hak et al., 2012).

For the structures supported by the non-linear spring-damper system at the footings (**Figure 2.14**), a nodal mass corresponding to a half the vertical distributed load acting on the tributary span of the ground floor was placed in correspondence of each footing at the node between the spring-damper system and the column. The remaining 50% of the load was supposed to be directly transmitted to the ground between the footings and was not accounted in the structural analysis.

During the dynamic analyses, the gravitational loads for the seismic combination of actions was imposed as a uniform distributed load on each of the nine beam elements, and a horizontal ground motion was applied at the foundation level.

After the end of analysis, the maximum shear force of the end sections of all the beams and columns was checked against the Limit State of Near Collapse (NC) prescribed in Eurocode 8 – part 3 (CEN, 2005) (expression A.12) to assess whether shear failure occurred during the analysis.

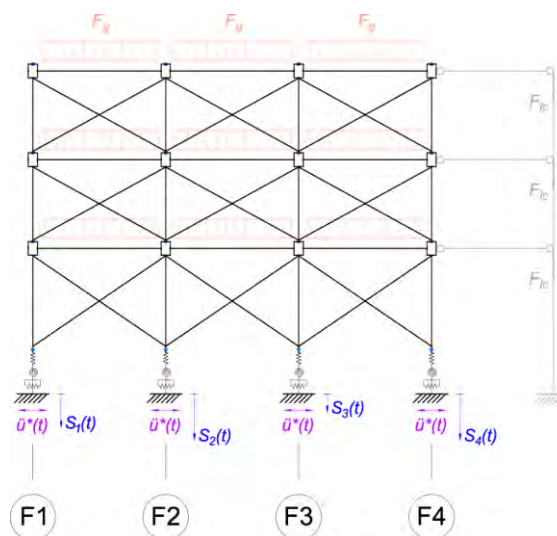


Figure 2.14: Numerical model for structure with isolated footings

2.2.7 CASE STUDY EXAMPLE

To demonstrate the difference in response for the different situations and different modelling assumptions, a simple case study building is considered. The simple three-storey three-bay case study building and soil



This project has received funding from the European Union's Horizon 2020 research and innovation programme under grant agreement No. 700748

profile can be seen in **Figure 2.15**. The building had a first storey height of 3.2m and other storeys of 2.9m. The beams were 0.45m deep and 0.25m wide and the columns were 0.3m deep and 0.25m wide. The design concrete and steel strength were 16MPa and 230MPa respectively. The structural elements (beams, columns, joints, foundation footings) were all sized using the simulated design process described in section 2.2.1 where the elements were designed using the factored gravity loads on the beams of 50kN/m. All columns have been designed with constant reinforcement with 4 12 mm diameter rebars and 6mm stirrups with a spacing of 0.15m to give a column yield moment of 35 kNm. A specific reinforcement was designed for central and end sections of each beam. 16mm longitudinal rebars were used with 8 mm stirrups in all the sections of all the beams. The yield moment of the beams was between 72 and 156 kNm at the end sections. The footings were designed to be equal by considering the most loaded column and applying the Meyerhof (1963) method to design a squared section of (B=L) 1.4 m with a depth of 0.55 m. A second gravity analysis was then performed using a uniform load associated to the seismic combination of actions (15.5 kN/m) and additional weight of the infills, in order to calculate the footing loads and nodal masses for the subsequent calculation of settlement and dynamic analysis.

For the examples presented in the chapter, the ground motion recorded from Dinar station during the Dinar Earthquake 1995 ($M_w=6.4$) in Turkey has been used. This motion is characterised by a site time-averaged shear-wave velocity in the top 30 m (V_{s30}) of 220m/s, and was taken from the NGA2-west strong motion database from Ancheta et al. (2013) number 1141.

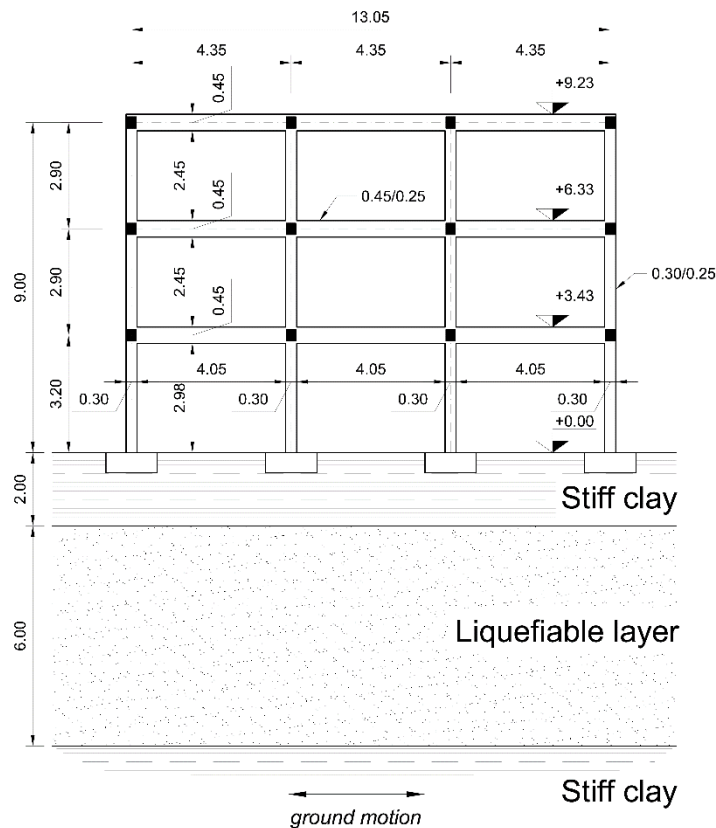


Figure 2.15: Case study building and soil profile



This project has received funding from the European Union's Horizon 2020 research and innovation programme under grant agreement No. 700748

2.2.8 VARIATIONS IN SOIL-FOUNDATION STRUCTURE INTERACTION MODELS

LINEAR ELASTIC MODEL FOR SPRING AND DASHPOT ELEMENTS

The initial soil-foundation impedance properties was determined using the formulations proposed in Gazetas (1991) (Equation (2.3)-(2.5)). The proposal takes into account the properties of the supporting soil, the geometry and inertia of the foundation and superstructure, and the nature of the dynamic excitation. The foundation response in a 2D problem is composed of three degrees of freedom in the vertical, horizontal, and rocking direction. Each degree of freedom associated to an elastic ("spring") and a viscous ("dashpot") response.

$$K_h = \frac{2Gl}{1-\nu} (2 + 2.50\chi^{0.85})k_y \quad (2.3)$$

$$K_v = \frac{2Gl}{2-\nu} (0.73 + 1.54\chi^{0.75})k_z \quad (2.4)$$

$$K_r = \frac{G}{2-\nu} I_{bx}^{0.75} \left(\frac{l}{b}\right)^{0.25} \left(2.4 + 0.5\frac{b}{l}\right)k_{rx} \quad (2.5)$$

where:

- $\chi = \frac{A_b}{4l^2}$
- $A_b = 4bl$ is the area of the foundation-soil contact surface
- $b = B/2$ and $l = L/2$ are the foundation semi-width and semi-length, respectively
- $I_{bx} = \frac{1}{12} (2l)(2b)^3 = \frac{1}{12} LB^3$ is the area moment of inertia of the foundation-soil contact surface around an axis parallel to the direction of the foundation length

k_y , k_z , and k_{rx} are dynamic coefficients, depending on the frequency-dependent term a_0 :

$$a_0 = \frac{\omega b}{V_s} \quad (2.6)$$

where $\omega = 2\pi f$ is the circular frequency of the applied force (from the structure to the foundation soil), and V_s is the shear wave velocity of the foundation soil. The relation between the dynamic coefficient and a_0 was provided by the author in form of graph. For the present case, imposing a period $T = 1/f$ of 1s it is

$$k_y = k_z = k_{rx} = 1 \quad (2.7)$$

Vertical springs are unable to resist tensile actions. Therefore, the material adopted was an elastic no-tension material (ENT material), with a constant stiffness modulus in compression (equation (2.4)), which drops to zero if the spring is loaded in extension. The horizontal and rocking component are modelled with the linear elastic material denominated "Elastic" in Opensees.



This project has received funding from the European Union's Horizon 2020 research and innovation programme under grant agreement No. 700748

The dashpots were modelled in OpenSees with a ZeroLength element acting in the horizontal and vertical components. As referred in the previous section, the rocking viscous component was coupled with the elastic element of the same component, due to the particular material used. The rocking viscous component of PyLiq1 material requires the definition of the damping coefficient. The materials associated to the ZeroLength elements were two Viscous type materials, which require the definition of a damping coefficient and a power factor (which was set equal to 1). The damping coefficients for the horizontal, vertical, and rocking components were calculated according to Gazetas (1991):

$$C_h = \rho V_s A_b c_y \quad (2.8)$$

$$C_v = \rho V_{La} A_b c_z \quad (2.9)$$

$$C_r = \rho V_{La} I_{bx} c_{rz} \quad (2.10)$$

where:

- A_b is the area of the footing
- $V_s = \sqrt{G/\rho}$ is the shear wave velocity of the upper soil layer
- $V_{La} = 3.4/(\pi(1 - \nu))V_s$ is Lysmer's analog wave velocity of the upper soil layer
- ρ is the density of the upper soil layer

Coefficient $c_y(a_0)$, $c_z(a_0)$, and $c_{rx}(a_0)$ are the dynamic coefficients, which depend on the frequency-dependent term a_0 . For the particular soil studied (imposing a period of 1s), it was:

$$c_y = 1; c_z = 1; c_{rx} = 0.1 \quad (2.11)$$

An example of response of the structure using linear springs is shown in **Figure 2.16**, through the inter-storey drifts of the superstructure and the global tilt of the foundation plane. For the i -th storey, inter-storey drift $\theta_{ss,i}$ is defined as the following time series:

$$\theta_{ss,i}(t) = \frac{\Delta_i(t) - \Delta_{i-1}(t)}{h_i} \quad (2.12)$$

Where Δ_i is the horizontal displacement of the i -th floor and h_i is the height of the i -th floor. The peak and residual inter-storey drifts of the i -th storey are the maximum and the last element in absolute value of this time series, respectively.

The global tilt of the foundation is:

$$\theta_f(t) = \frac{\Delta y_n - \Delta y_1}{L_{build}} \quad (2.13)$$

where Δy_1 and Δy_n are the settlements of the footings relative to the most external columns (F1 and F4 in the example of **Figure 2.14**), and L_{build} is the horizontal dimension of the building in the direction of the applied motion (which is shown as a time series of the acceleration in the second plot of **Figure 2.16**).



This project has received funding from the European Union's Horizon 2020 research and innovation programme under grant agreement No. 700748

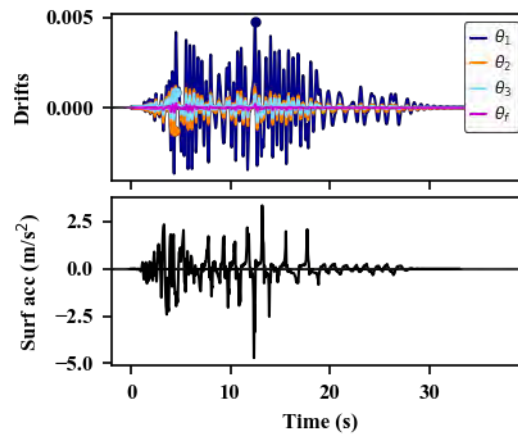


Figure 2.16: Example of linear elastic model response

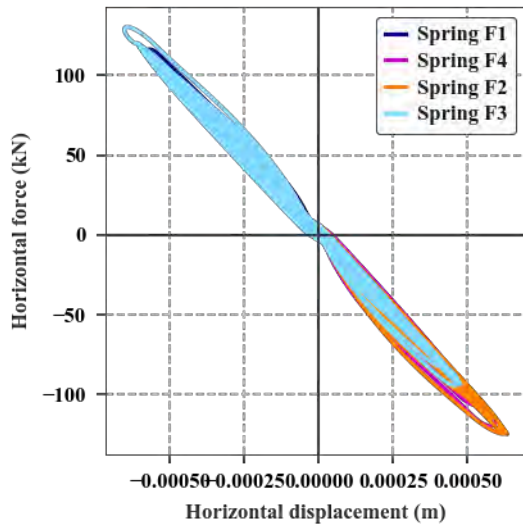
The results show that the drift is maximum at the ground floor, and decreases for higher storeys. The foundation tilt is comparatively low. A symmetric oscillation with respect to the initial configuration of the structure is observed in the drifts of all storeys and in the global tilt of the foundation. In this example, the intensity of the applied motion is not enough to cause permanent deformation in the superstructure or permanent tilt in the foundation.

The force-displacement and moment-rotation response of the linear elastic spring-damper system for the same analysis is shown in **Figure 2.17**. The unsymmetrical force of the vertical springs in compression and extension is shown. The slight force in extension is due to the dashpot response. The horizontal and rocking components are symmetrical in compression and extension. Their response is centred around the origin of the axes, while the vertical component presents a pre-load due to the initial gravitational load imposed. It is possible to note the higher role played by the dampers in the vertical and horizontal component than in the rocking component. This is an effect of the different coefficients in expressions (2.11).

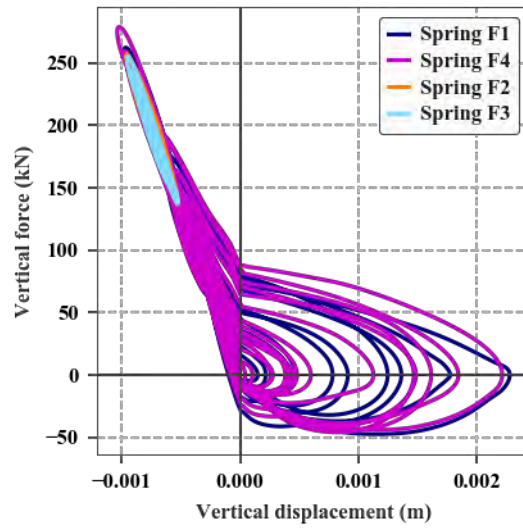
The settlements of the footings with time are shown in **Figure 2.18**. The footings relative to the external columns (F1 and F4) are loaded with a smaller static vertical load than the internal springs (F2 and F3). Therefore, the former deform less than the latter. On the other hand, during the shaking, the external nodes undergo higher strain induced by the dynamic forces, while the internal springs are less prone to extreme strain. The static load remains constant throughout the whole record (no load redistribution occurs).



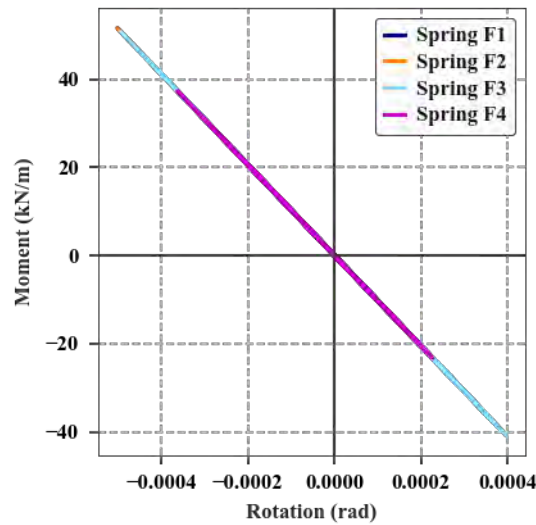
This project has received funding from the European Union's Horizon 2020 research and innovation programme under grant agreement No. 700748



(a) Horizontal component



(b) Vertical component



(c) Rocking component

Figure 2.17: Example of linear spring-damper system response



This project has received funding from the European Union's Horizon 2020 research and innovation programme under grant agreement No. 700748

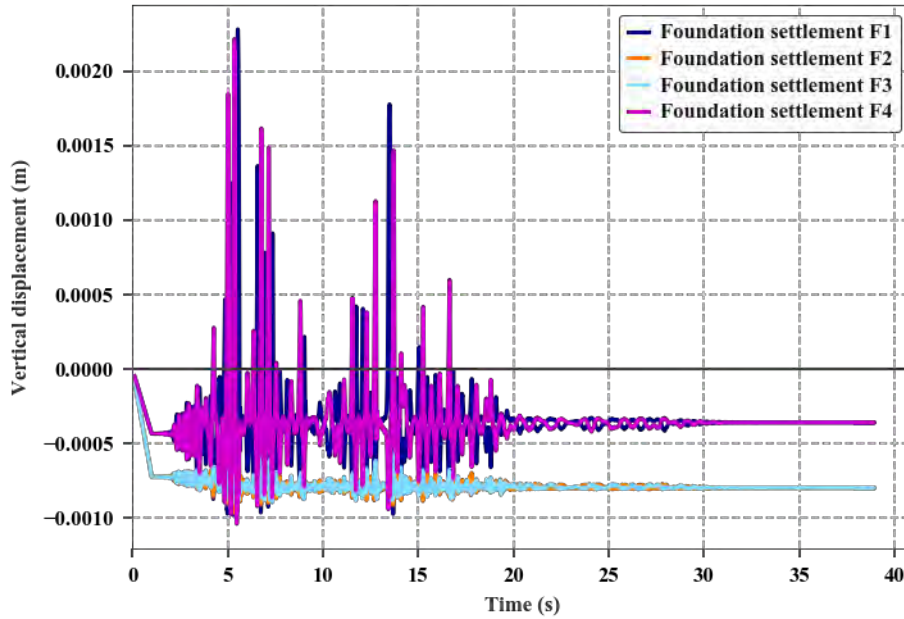


Figure 2.18: Example of footings settlements for a linear spring-damper system

NON-LINEAR MATERIAL MODELS FOR SPRING AND DASHPOT ELEMENTS

The behaviour of the soil-foundation-structure interaction laying on a liquefiable soil profile requires a more advanced model. Thus, in the non-linear foundation model, the materials associated to the spring-dashpot system were not linear and depended on the key variable r_u , accounting for the change of pore water pressure in the soil. This parameter is calculated as a pore pressure time series (see section 2.4).

In order to input the r_u time series in OpenSees, this should be transformed into a measure of the mean effective stress. The r_u time series can be related to the mean effective stress if a normalized form of this is considered:

$$p'_{norm} = \frac{p'}{p'_i} \quad (2.14)$$

where p'_i was the mean effective stress before the application of the ground motion. Adopting this definition, p'_{norm} depended on r_u through the following:

$$p'_{norm} = 1 - r_u \quad (2.15)$$

At the beginning of the analysis it was $r_u = 0$ and $p'_{norm} = 1$. When the pore pressure increased as an effect of the applied dynamic load, r_u increased, p'_{norm} decreased, and the soil tended towards liquefaction for $r_u = 1$ and $p'_{norm} = 0$.

Horizontal spring was still modelled with a linear elastic material. Thus, the stiffness modulus K_h defined in the previous section was kept as a constant.



This project has received funding from the European Union's Horizon 2020 research and innovation programme under grant agreement No. 700748

Vertical elastic component depended on the characteristics of the soil, which in turn varied with the mean effective stress. The material adopted was an elastic no-tension material (ENT material), characterized by a stiffness modulus K_v , dependent on the mean effective stress p' .

Vertical stiffness modulus assumed an initial value $K_{v,i}$ corresponding to $p'_{norm} = 1$ and coincident with Gazetas (1991) formulation expressed in equation (2.4). This value decreased linearly up to a residual value $K_{v,res} = r_v K_{v,i}$ when $p'_{norm} = 0$. Parameter r_v is a ratio of the initial over residual stiffness. The linear relation was:

$$K_v = K_{v,i} \cdot [1 - (1 - p'_{norm})(1 - r_v)] \quad (2.16)$$

If p'_{norm} was outside the interval $[0, 1]$ (e.g. when the soil manifested dilatant behaviour), the stiffness modulus did not exceed the interval between the initial and the residual value, as shown in **Figure 2.19**.

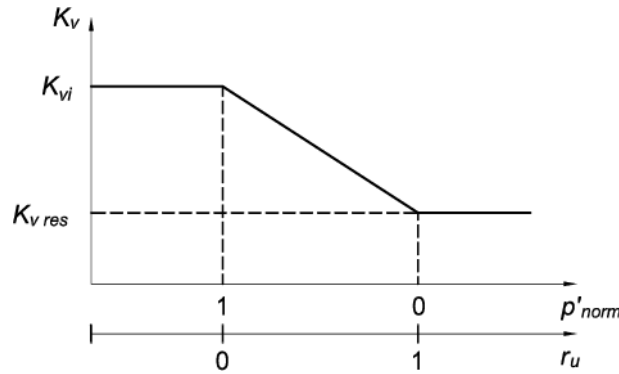


Figure 2.19: Model for vertical stiffness degradation

The same behaviour is adopted for rocking stiffness ($K_{r,res} = r_r K_{r,i}$). The initial values of rocking stiffness is expressed in equation (2.5).

Karadzia et al. (2017) presented the results for the dimensionless static stiffness ratio \tilde{K}_{ij}/K_{ij} of a multilayer configuration with a shallow non-liquefiable layer (crust) and a second liquefiable layer (similarly to the configuration shown in **Figure 2.12** b and c). The stiffness ratio was presented as a function of the crust and liquefiable layer heights, foundation width, and ratio of shear wave velocity measured in the crust and in the second layer in liquefied conditions. Term \tilde{K}_{ij} indicates the post-liquefied dynamic stiffness matrix, while K_{ij} indicates the pre-liquefied stiffness matrix. This ratio (of the vertical components of the respective matrices) was adopted as parameter r_v to be introduced in expression (2.16) (same procedure was adopted for the rocking component, where r_r is the ratio of the rocking components of the matrices defined above).

In the OpenSees implementation, p'_{norm} was introduced as a time series and it was calculated from the r_u time series, which was imported from the analysis results performed in FLAC. Hence, the value of K_v was calculated at each analysis step through expression (2.16), and the corresponding updated value was input in the analysis.



This project has received funding from the European Union's Horizon 2020 research and innovation programme under grant agreement No. 700748

Rotational springs were modelled in OpenSees using material PyLiq1. This is an elastic hardening-plastic material with ultimate capacity that incorporates liquefaction effects. It was described in Boulanger et al. (1999). The constitutive response of PyLiq1 (in terms of ultimate capacity and stiffness) was scaled in proportion to the mean effective stress time series. Both stiffness and ultimate capacity reduction were modelled with the same linear interpolation of **Figure 2.19**. Nevertheless, the material definition prescribes a zero value for the residual stiffness. Initial stiffness was calculated according to Gazetas (1991) proposal (2.5). When $p'_{norm} = 0$, rotational ultimate capacity was considered to be coincident with:

$$M_{cap,i} = M_y = N \frac{B}{2} \left(1 - \frac{N}{N_{cap}} \right) \quad (2.17)$$

where $N_{cap} = BLq_{ult}$ is the foundation bearing capacity in static conditions, calculated with Meyerhof (1963) method; and N is the vertical load due to the self-weight of the tributary area of each footing, calculated in static conditions.

As aforementioned, ultimate capacity decreased linearly with p'_{norm} , from $M_{cap,i}$ to $M_{cap,res}$, following qualitatively the scheme of **Figure 2.19**. The ratio of the capacities was calculated following Karatzia et al.(2017) formulation, although this was developed for stiffness reduction computation. Alternatively, the moment-rotation backbone response can be obtained from push-over analyses of a fine element model using degraded strength and stiffness for the soil (See Argeri, 2018).

PyLiq1 material incorporates a component for viscous damping. Thus, for the rotational component, only one element was necessary in the model, as the material used accounts for both elastic and dashpot components. The properties of the viscous damping are detailed in the next section.

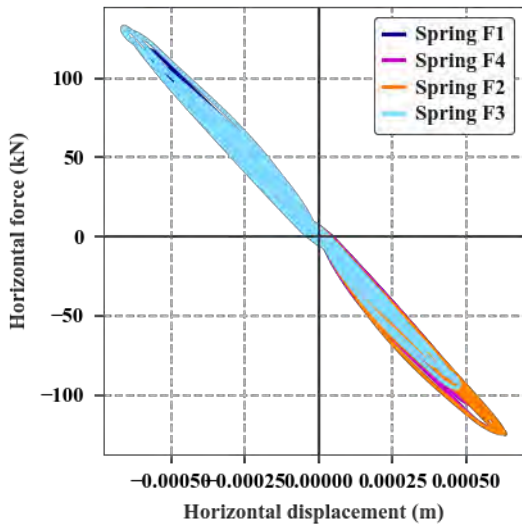
It is worth noting that material PyLiq1 is a symmetric material (behaving equally in tension and compression) which was designed to best behave in symmetric cyclic conditions (cycles around 0 shear stress). For this reason, it is not suitable to be used for modelling vertical springs behaviour, which presented an initial compressive stress due to the static vertical loads.

The response of the non-linear model is shown in **Figure 2.20**. The horizontal response is linear as the precedent case, while the vertical and rocking response are now dependent on r_u and therefore show a decrease in stiffness as the pore water pressure increases. The rocking stiffness shows higher stiffness degradation, due to the impossibility of imposing a residual stiffness higher than zero for material PyLiq1.

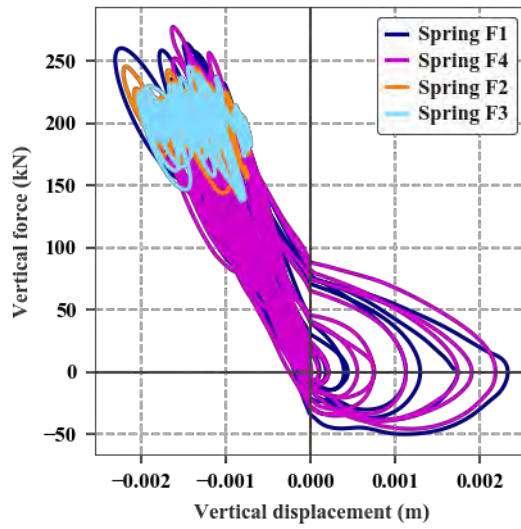
The footing settlements are shown against time in **Figure 2.21**. The response of the springs relative to the static gravitational load is the same as in the linear case (**Figure 2.18**). During the shaking, the degradation in stiffness due to the pore pressure build up causes an additional strain accumulating progressively during the shaking. In the linear model, the final settlement of the footings was around 0.4 mm for external base nodes and around 0.65 mm for internal base nodes. In the present non-linear model, the same settlements are around 1.0 and 1.8 mm, respectively. Thus, the liquefaction induced settlements are not captured in the springs, but provide a better characterisation of the dynamic properties of the building-soil system.



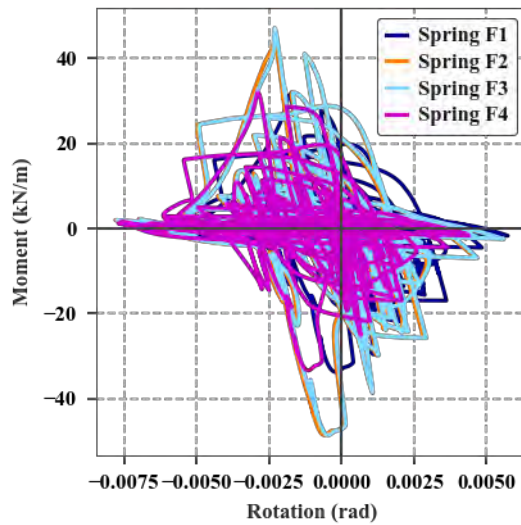
This project has received funding from the European Union's Horizon 2020 research and innovation programme under grant agreement No. 700748



(a) Horizontal component



(b) Vertical component



(c) Rocking component

Figure 2.20: Example of non-linear spring-damper system response



This project has received funding from the European Union's Horizon 2020 research and innovation programme under grant agreement No. 700748

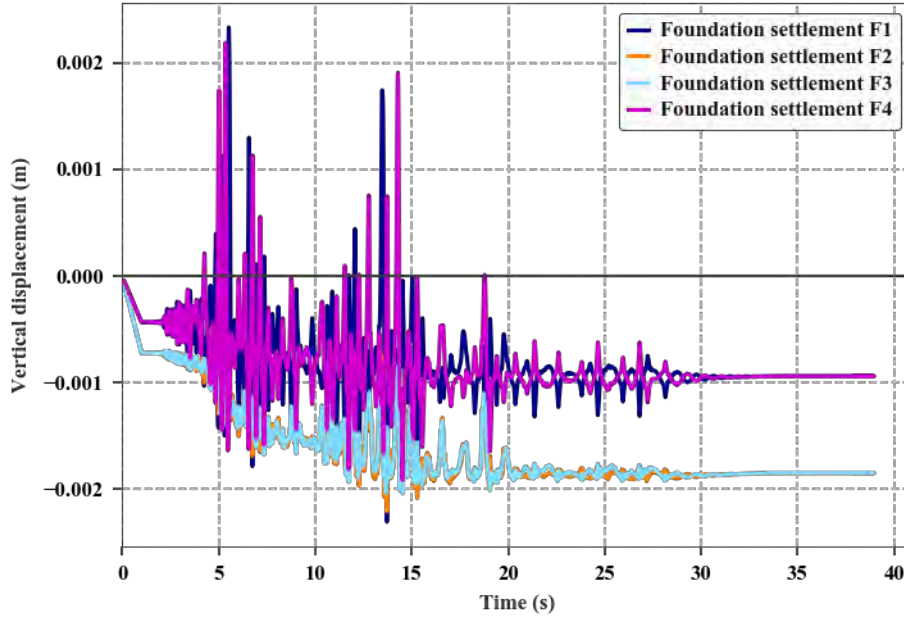


Figure 2.21: Example of footings settlements in non-linear spring-damper system

2.2.9 ESTIMATING THE FOUNDATION LOAD-SETTLEMENT BEHAVIOUR

The seismically-induced dynamic settlement (S_{dyn}) of a foundation is dependent on the vertical load and bearing capacity as well as the cyclic shear and moment loads imposed on the soil from soil site response and kinematic and inertia interaction between the soil and building. This settlement behaviour has been captured in simplified models by Karamitros et al. (2013a) and by Bray and Macedo (2017). The two methods and their adaptations are briefly described herein; they are described in detail in section 2.6.

Karamitros et al. (2013a) method is expressed in equation (2.18), where v is the velocity time series, Z_{liq} is the height of the liquefiable layer, and FS_{deg} is the degraded bearing capacity factor of safety calculated according to Karamitros et al. (2013a). The integral of the velocity time series corresponds to the cumulative absolute displacement (CAD).

$$S = \int |v^2| dt \cdot (Z_{liq})^{1.5} \left(\frac{1}{FS_{deg}} \right)^3 = CAD \cdot (Z_{liq})^{1.5} \left(\frac{1}{FS_{deg}} \right)^3 \quad (2.18)$$

The simplified model is intended to estimate the final settlement value, while for modelling the interaction between settlement and dynamic structural loads, a time series of settlement is required. The settlement model from Karamitros et al. (2013a) quantifies the seismic demand through the integral of the absolute velocity time series and therefore can produce a time series of settlement relative to the velocity time series. However, the rate of settlement is not constant as it is dependent on the extent of pore pressure build up. The pore pressure build up results in a reduction in the factor of safety that subsequently increases the rate of settlement. While this increase is dependent on how close the foundation is to bearing capacity failure, an arbitrary weighting factor equal to the pore pressure ratio was applied to the settlement equation to reflect the change in settlement rate with pore pressure (equation (2.19)).



This project has received funding from the European Union's Horizon 2020 research and innovation programme under grant agreement No. 700748

$$S_i = \frac{\sum_0^i |v_i| \cdot r_{u,i}}{\sum_0^n |v_i| \cdot r_{u,i}} \cdot CAD \cdot (Z_{liq})^{1.5} \left(\frac{1}{FS_{deg}} \right)^3 \quad (2.19)$$

The degraded bearing capacity factor of safety is taken as a constant in the approach presented in Karamitros et al. (2013a), where the applied vertical load is the load transmitted from each column to the foundation soil at the beginning of the ground motion. Nevertheless, such simplification does not take into account the stress redistributions among the footings due to the non-linearity of the system and the applied load. This could lead to undesirable detachments between the footing and the respective foundation soil.

A more thorough analysis would be achieved by considering FS_{deg} as being a time series and not a constant value. Since the value of the vertical loads is analysis-dependent and cannot be known a priori, the factor of safety time series should be built in an iterative manner. For each footing at each time step of the dynamic analysis using the results of the previous time step, the factor of safety is updated, and the resulting incremental settlement should be applied at each step to the respective footing. The degraded bearing capacity can be kept the same as from Karamitros et al. (2013a), as the degradation was already partially considered through the weighting factor based on the pore pressure, but the vertical load on the footing can be taken from Opensees at each time step to recompute the factor of safety and the expected change in displacement. Equation (2.19) was therefore modified to consider the differential of the settlement with respect to CAD . The change in CAD , the pore pressure ratio and the vertical load at each time step were then used to calculate the expected change in settlement over a time step. While these adaptations allow for the consideration of load redistribution and settlement during a seismic event, the adaptations have not been calibrated and were made in a way to best reflect the original work by Karamitros et al. (2013a).

The original formulation of the Bray and Macedo (2017) method (equation (2.20)) was intended to estimate the final settlement value and not the settlement time series and therefore needed extension to produce the time series, which was defined as:

$$S = \exp(c + \ln(CAV_{dp}) + 4.59 \ln q - 0.42 \ln(q)^2) \quad (2.20)$$

In this expression, c indicated a constant value including different factors, q is the vertical stress transmitted from the foundation to the soil, and CAV_{dp} is a standardized version of the cumulative absolute velocity (defined in Campbell and Bozorgnia, 2011), which in turn is the integral of the absolute value of acceleration. As in the precedent method, the absolute acceleration time series can produce a time series of settlement relative to the acceleration time series. The formulation can be applied in a simplified form by considering the vertical stress as a constant, or in a more thorough and numerically demanding way by iteratively calculating the vertical stress during the Opensees analysis, and using the result to compute the settlement increment of the subsequent step. As mentioned before, the iterative method is more accurate because takes into account load redistribution during the earthquake.

2.2.10 MODELLING SETTLEMENTS

For the structures with isolated footings, the imposed settlement time series $S(t)$ was applied at each constrained node, in order to take into account the liquefaction effects calculated in the FLAC analysis. The time series was calculated using one of the two methods described in the previous section, selecting the constant load or the varying load formulation. In the first case the settlement time series is pre-calculated



This project has received funding from the European Union's Horizon 2020 research and innovation programme under grant agreement No. 700748

and passed to the Opensees model, in the second case the time series is calculated at each analysis step as expressed in the precedent section.

The results for the analyses performed with constant load settlement (pre-calculated settlement time series) are reported in **Figure 2.22**. In the example, a 3-storey 3-bay building had been considered and settlement was calculated using Karamitros et al. (2013a) method. In the case of the structure without infills (**Figure 2.22 a**), a soft storey is observed at the ground floor; in fact, the maximum value of drift θ_1 is approximately equal to 4% (blue dots in figure), much higher than the drifts of the upper floors and the foundation tilt (<1%). Thus, the distortion is located in the columns of the ground floor, which during and after the shaking are not perpendicular to the foundation plane and to the beams of the first floor. The settlement time series show that the contribution of the imposed settlement is much higher than the spring strain, which in the figures is not significant. The flexibility of the structure is visible in the settlement of the footings, which is higher for the central footings (F2 and F3), and smaller for the external footings (F1 and F4). This is the effect of load redistribution: central footings, which initially take the higher share of the gravity load are subjected to a higher settlement than the external footings. This causes the vertical load to be transferred from the central to the external footings, until the load is equally shared among the four pads. The symmetry of the structure and the homogeneity of the foundation soil cause the settlement to be equal for the two central footings and for the two external footings. This, as expected, produces an almost nil global tilt of the foundation.

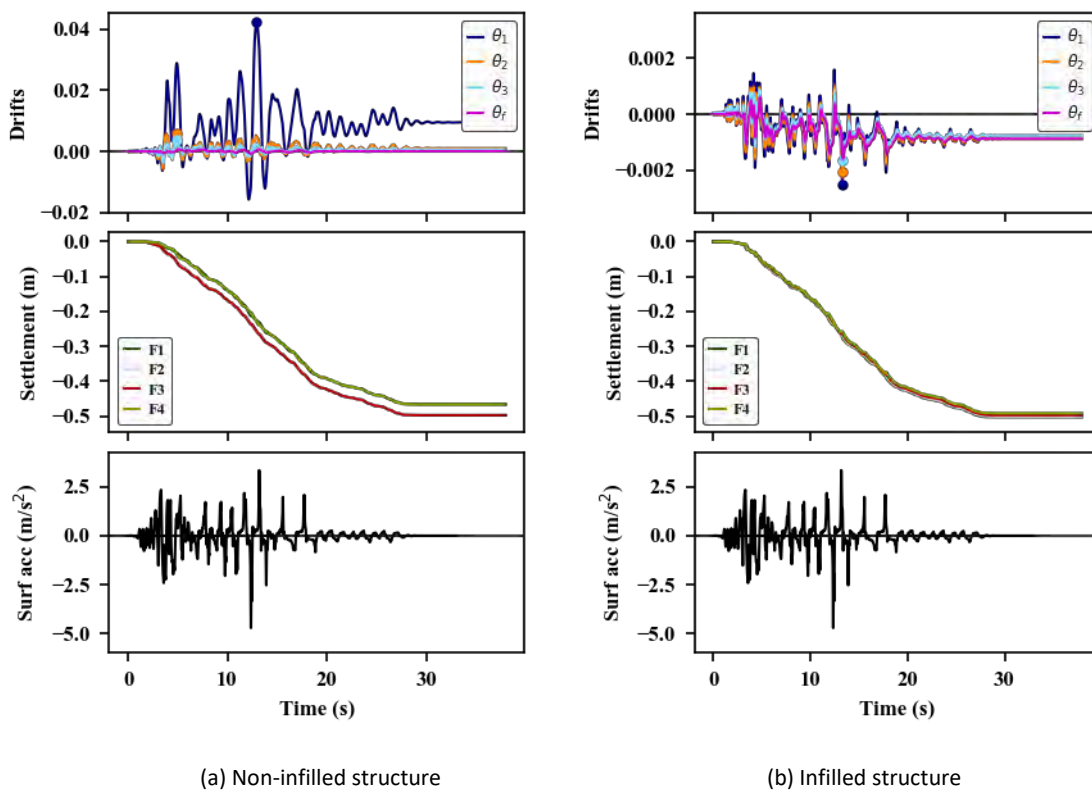


Figure 2.22: Results with equal incremental settlements



This project has received funding from the European Union's Horizon 2020 research and innovation programme under grant agreement No. 700748

The analysis performed considering the structure equipped with the infills described in section 2.2.6 is reported in **Figure 2.22 b**. The rigidity of the structure is clearly higher with respect to the precedent case. The inter-storey drifts and the foundation tilt are in phase and present similar values. The maximum values are less than 0.3%, ten times less than in the precedent case. The similar response of the inter-storey drifts and foundation tilt produces rigid movements of the structure rather than angular distortions between structural elements (e.g. the angles between columns and beams do not diverge significantly from the perpendicularity). The footings settlements are around 50 cm as the previous case, but the rigidity of the superstructure makes the settlements equal for all the footings. The analysis shows a small residual foundation tilt (around 0.1%).

2.2.11 MODELLING SOIL HETEROGENEITY

In order to include the effects of soil heterogeneity, at each footing the settlement time series was multiplied by a constant coefficient. A specific coefficient c_i was assigned at each footing, selected from a uniform distribution included in the interval [0.7-1.2]:

$$S_i(t) = c_i S(t) \quad (2.21)$$

with $i = 1...4$. The four randomly generated coefficients c_i are [1.107, 1.153, 0.763, 1.157], for footings from F1 to F4 (as in **Figure 2.14**), respectively. These values were used in all the analyses performed on structures supported by the spring-damper systems. Future analyses could aggravate these coefficients in view of additional factors like ejecta and sedimentation.

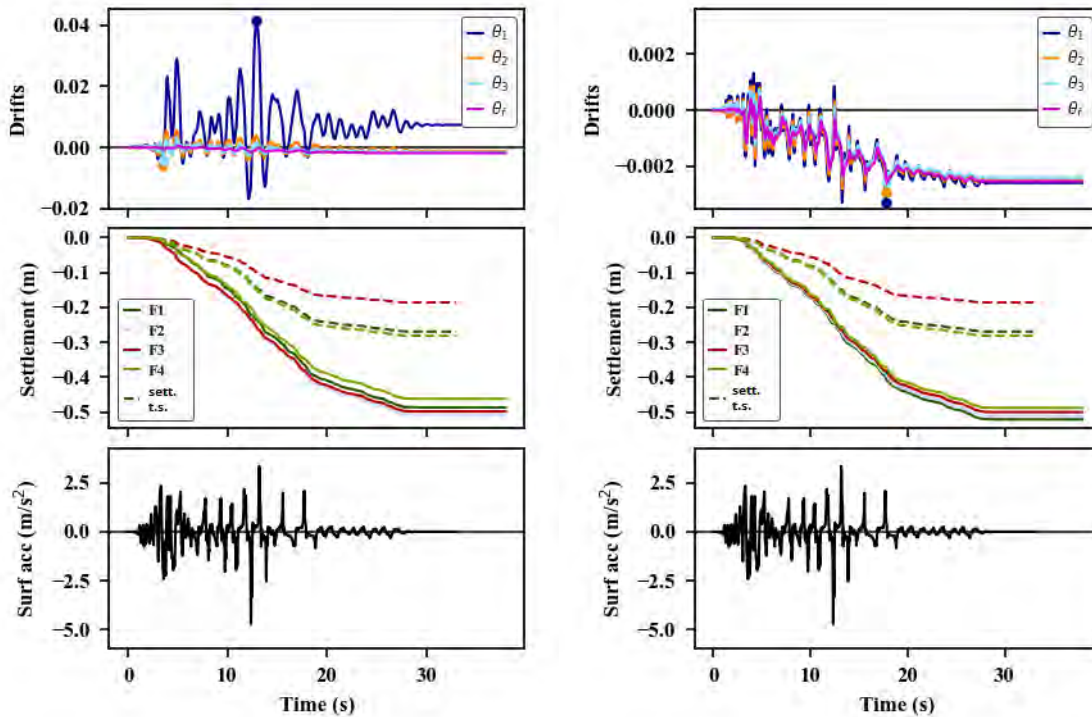
The results of the analyses performed imposing random coefficient to the varying load settlements (settlement increment calculated at each time step) are reported in Figure 2.23. Also for this case, the analyses were performed considering the superstructure with and without masonry infills. For each analysis, the drifts of the superstructure are very similar to the corresponding drifts of the precedent case. The foundation tilt in this case is not nil, being approximately equal to 0.2% in the negative (counter clockwise) direction. The distortion of the ground floor in the case of structure without infills is aggravated by the foundation tilt (which is in the opposite direction). As for the structure with infills, the rigid rotation of the foundation plane is associated with a congruent rotation of the superstructure, which tilts without major distortion between the structural elements.

As expected, the settlements of the four footings shows a higher dispersion than in the previous case. It is interesting to note that the tilt of the foundation plane is in both cases in the counter clockwise direction, although the coefficient of foundation F1 is lower than the coefficient of F4, which would suggest a rotation in the opposite sense. Nevertheless, examining the vertical load on the footings at the end of shaking, one can see that footing F3 is the most loaded, followed by F1, F2, and F4, respectively. This reflects the order of the random coefficients from the minimum to the maximum. Since the superstructure has a certain rigidity (with or without infills), its vertical reaction is governed by the two more loaded (i.e. prone to less settlement) footings, F3 and F1. Footings F2 and F4 have a higher allowable settlement rate, thus, their load is progressively redistributed by the superstructure to the F1 and F3. If the foundation tilt is calculated between F1 and F3, a negative value (i.e. in the counter clockwise direction) is obtained. This reflects the fact that the coefficient associated to F3 is lower than the coefficient associated to F1.



This project has received funding from the European Union's Horizon 2020 research and innovation programme under grant agreement No. 700748

The dashed lines in Figure 2.23 represent the settlement time series for the four footings calculated using the Karamitros et al. (2013a) method as a pre-calculated time series, scaled with the four constant random coefficients reported earlier. Thus, the dashed lines are calculated considering a factor of safety FS_{deg} equal to the degraded factor of safety in initial conditions (only gravity load applied). The continuous lines are calculated at each time step, by considering the vertical load acting on each footing in the previous step. The dashed lines present a higher dispersion than the continuous lines. This effect is due to the load redistribution in the second case from the more loaded springs to the less loaded and the consequent change in factor of safety. The average settlement calculated with constant FS_{deg} is approximately half the settlement calculated at each analysis step. The first is calculated by considering only the static load acting on the footings, while the second settlement considers the dynamic loads. The analysis of the results shows that the dynamic load reached, in some cases, peaks equal to twice the corresponding static load. Hence, the reduced factor of safety and the increased settlements in the second case.



(a) Non-infilled structure

(b) Infilled structure

Figure 2.23: Results with random factors applied to incremental settlements

2.2.12 MODELLING RECOMMENDATIONS

This chapter has presented a viable option for modelling gravity designed European reinforced concrete buildings. The model properties outlined in **Table 2.1**, **Table 2.2**, and **Table 2.3** should be used as inputs into a simulated design process if the actual design properties of a building cannot be directly obtained. The soil-foundation structure interaction (springs, dashpots and settlements) should follow either the constant load (pre-calculated settlement) or varying load (settlement increment calculated at each step) using the nonlinear springs described in section 2.2.7 (second part).



This project has received funding from the European Union's Horizon 2020 research and innovation programme under grant agreement No. 700748

2.2.13 CONCLUSIONS

The framework and procedure presented in this section offers a numerical efficient approach for engineers to considering the impacts of liquefaction on buildings. Although some of the inputs (e.g. rate of settlement) are not yet well calibrated, the efficiency of the procedure and the decoupling of the liquefaction analysis and structural analysis, allows engineers to consider a variation of the material properties and of underlying assumptions to obtain the inputs for the structural analysis. A case study building that was investigated with the above procedure did not suffer from large differential settlement and the infills provided significant additional capacity to resist differential settlements and inter-storey drifts. The model required a quantification of the modification of seismic shaking, settlement rate and soil-foundation impedance due to liquefaction. In the following, all these different factors will be explored in greater detail.

2.3 SIMPLIFIED PROCEDURE TO CLASSIFY SOIL PROFILES

2.3.1 OVERVIEW

A key measure in the context of this research refers to the expected level of damage to a building on shallow foundations after liquefaction. For this purpose, it is necessary to define a systematic process of classifying liquefaction resistance of soil profiles, using a standard seismic hazard or independent of seismic hazard. The hazard-independent classification of liquefaction resistance (e.g. the cyclic resistance ratio to liquefaction in 15 uniform cycles) is a key step in the context of performance-based design and assessment and loss assessment frameworks, where a range of seismic hazard levels are considered. The ability to rapidly evaluate the time of triggering for different ground motions would allow the development of more robust estimates of liquefaction damage using pre- and post-liquefaction, ground intensity measures (Kramer et al., 2016). The quantification of liquefaction, in terms of the key parameters that influence the performance of the building, should also reduce uncertainty when considering the influence of liquefaction on building performance.

The two most important parameters identified in recent literature are the thickness of the crust and the height of the liquefied (or liquefiable) layer. These two parameters are shown to influence building settlement (e.g. Liu and Dobry, 1997; Shahir and Pak, 2010; Karamitros et al., 2013a; Bertalot and Brennan, 2015; Lu, 2017), the characteristics and intensity of ground surface shaking (Bouckovalas et al., 2017), the manifestation of liquefaction at the surface (Ishihara, 1985; Ishihara et al., 1990) and the soil stiffness or foundation impedance (Karatzia et al., 2017).

While liquefaction classification in terms of triggering is useful for mapping, the hazard-independent classification does not preclude these assessments, since triggering can readily be obtained by applying the seismic hazard. This has the distinct advantage of being independent of seismic hazard maps, many of which are regularly updated. Furthermore, liquefaction triggering assessments that use different assumptions can provide considerably different results. Recent investigations of the performance of soil deposits in Christchurch during the 2011 earthquake by Cubrinovski et al. (2017) identified the role of pore water flow and seismic isolation as key differences between the CPT-based simplified triggering procedure from Boulanger and Idriss (2016) and nonlinear effective stress analyses. In turn, soil layers in terms of the normalised cone tip resistance and the information criterion were readily identified and consistent across both assessment procedures.



This project has received funding from the European Union's Horizon 2020 research and innovation programme under grant agreement No. 700748

In this section, a simple three criteria, hazard-independent liquefaction classification system is proposed for performance and loss assessment of buildings on shallow foundations, using the height (H_{liq}) and depth to the critical liquefiable layer (D_{liq}), as well as the average cyclic resistance of the layer for 15 cycles of uniform load (CRR_{n15}). **Figure 2.24** schematically summarises the concept of Equivalent Soil Profiles (ESP), in which a stratified multi-layered soil profile is converted into an simplified soil profile, with equivalent liquefaction response, based on the three governing parameters.

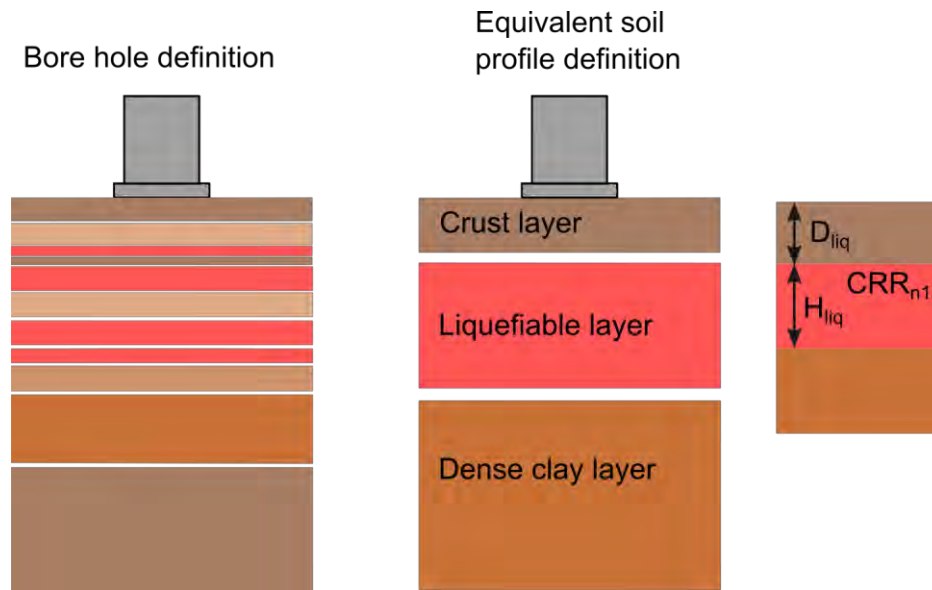


Figure 2.24. Equivalent Soil Profile: definition of the three governing parameters

The influence of these properties on ground surface shaking and bearing capacity has been briefly explored, however, further investigations on the impact of these parameters on liquefaction triggering, surface ground motions, soil foundation stiffness and settlement can be found in sections 2.5, 2.7, 2.2, 2.6 respectively. The generation of a simplified soil profile from a CPT record has implemented as an algorithm (available in the next release of the open-source Python package Liquepy, at <https://pypi.org/project/liquepy>) and also identifies difficulties in developing the equivalent profile, particularly in highly stratified soil. A set of criteria for classification of soil profiles for regional scale loss assessment are also presented and demonstrated on an example site in Christchurch, and subsequently implemented in two real case studies: Christchurch (New Zealand) and San Carlo (Italy).

The classification is used to develop building-soil profile classes for vulnerability analysis. The main advantages of this approach are:

- Can be exactly determined from CPT, DMT, SPT seismic waves surveys or borehole data
- Captures the soil profile behaviour across the full hazard range using just three values
- Information is directly related to building performance
- Can capture complex system effects (e.g. vertical pore water flow)
- Intuitive parameters are used (soil layering vs foundation geometry and hazard level), rather than strains or quality indexes (e.g. LPI or LSN)



This project has received funding from the European Union's Horizon 2020 research and innovation programme under grant agreement No. 700748

- Can provide a definition of the profile without knowing the seismic hazard at the site

To illustrate the limitation of existing approaches, an example is provided in **Figure 2.25** for a series of different soil profiles with distinct CRR at the liquefiable layer, but which result in the same LSN of 20, for a PGA of 0.15g. While this value of LSN is indicative of a moderate superficial manifestation of liquefaction, it fails to take into account the effects of liquefaction in the presence of buildings or the time to liquefaction. This is clearly evidenced in **Figure 2.26**, where the two buildings of different width are located in two of the previous soil profiles. Since the depth of influence of each building is different, the effects of liquefaction will be distinct, despite the same soil profile.

CRR profile for LSN = 20 @ PGA = 0.15g

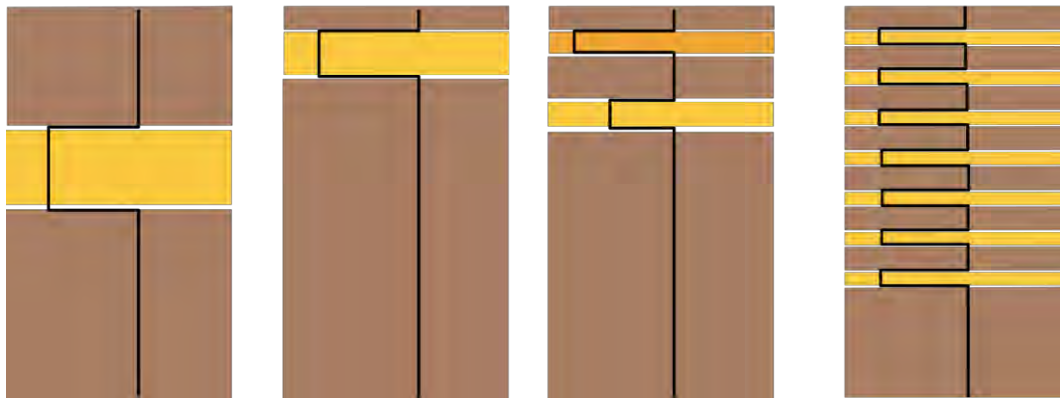


Figure 2.25. Different real soil profiles with distinct CRR profiles but identical LSN value

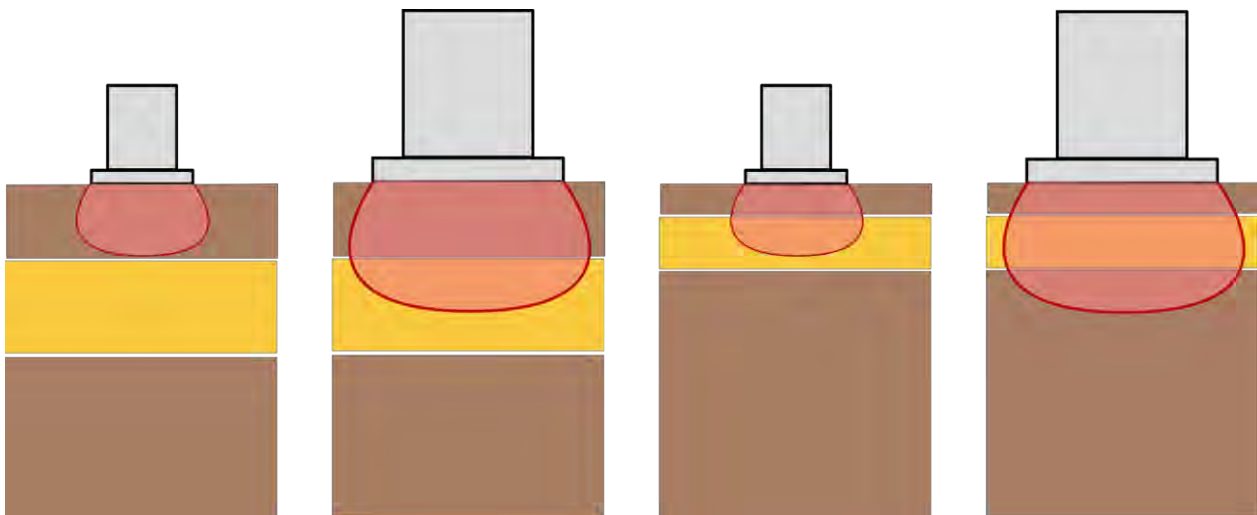


Figure 2.26. Different building widths and soil profiles

The fact that existing methods provide information of non-unique soil profiles means that it is not possible to directly estimate the expected level of damage to a building, for which a new approach is needed.

In short, the new classification for liquefaction potential provides a three-layered equivalent soil profile, where three governing parameters are considered:



This project has received funding from the European Union's Horizon 2020 research and innovation programme under grant agreement No. 700748

- D_{liq} , depth of the liquefiable layer, also referred to as H_{crust} , height of the crust, which influences ground motion characteristics, bearing capacity and settlement
- H_{liq} , height of the liquefiable layer, which also influences ground motion characteristics, bearing capacity and settlement
- CRR_{n15} , cyclic resistance ration, which influences timing of liquefaction

The use of a simplified geometry for the soil profile, based on well-selected parameters, also means that the assessment of the performance of buildings on liquefiable soil becomes more intuitive and easier to understand and predict.

2.3.2 RATIONALE FOR THE SELECTION OF THE GOVERNING PARAMETERS

Influence on bearing capacity

The bearing capacity of a foundation on a soil deposit in its liquefied state (degraded bearing capacity) is a key indicator of expected settlement and tilt (e.g. Karamitros et al., 2013a; Bray and Macedo, 2017; Bullock et al., 2018). According to Karamitros et al. (2013a) and Bray and Macedo (2017), the degraded bearing capacity can be computed according to Meyerhof and Hanna (1978), for a strong soil crust underlain by a weak soil layer. The degraded bearing capacity depends on the shear strength of the crust and the residual shear strength of the liquefied sand (Karamitros et al., 2013a), at least for cases where the stress bulb of the foundation does not reach deeper more resistant and non-liquefiable soils.

To demonstrate the importance of the crust height, **Figure 2.27** shows a series of calculations performed using Meyerhof and Hanna (1978) for different crust heights (H_{crust}), different crust undrained or total stress resistances – “cohesive” strengths (C_{crust}), different liquefied/degraded layer angle of shearing resistance – “equivalent” angle (ϕ_{deg}) and different foundation widths (B_f).



This project has received funding from the European Union's Horizon 2020 research and innovation programme under grant agreement No. 700748

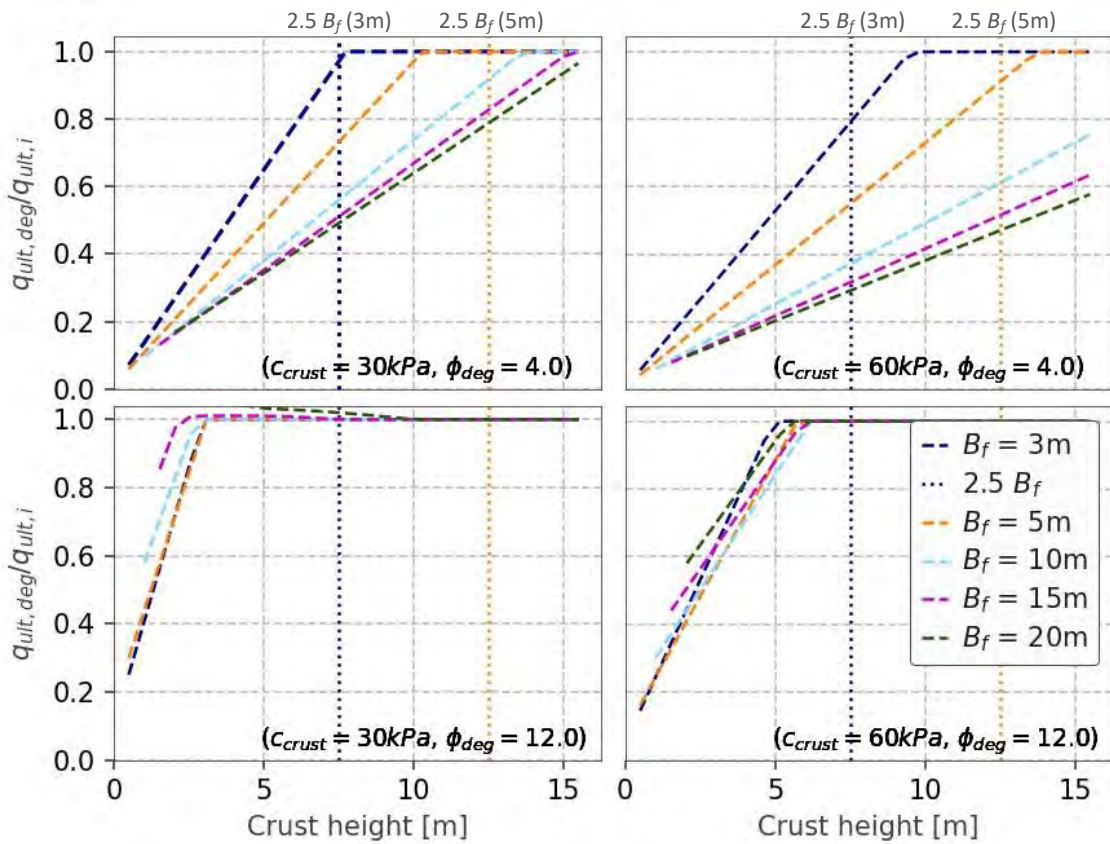


Figure 2.27. Influence of crust properties on bearing capacity

As illustrated in **Figure 2.27**, what is apparent is that for a strong crust and weak liquefiable layer strength, the thickness of the crust has great influence on the degradation of the bearing capacity ($q_{ult,deg}/q_{ult,i}$). The influence of the crust becomes less important with increasing strength of the liquefiable layer with respect to the crust. Also shown in **Figure 2.27** are the lines corresponding to 2.5 times the foundation width. This is approximately equal to the point where the thickness of the crust no longer has an influence on the bearing capacity. This influence is less than this limit for deeper foundations, if the liquefied soil is modelled with an equivalent friction angle, since the strength of this layer increases with depth, whereas assuming an equivalent cohesive strength (undrained or other derived in total stresses) would mean constant strength with depth. While the liquefied shear strength is a key parameter in the estimation of bearing capacity, it could also be expected to be highly correlated to the liquefaction resistance, as increased density typically results in increased liquefaction resistance and increased dilative behaviour.

Influence on surface shaking

Bouckovalas et al. (2017) proposed the Spectral Envelope Method, for approximating ground surface response spectra for a liquefied deposit where the liquefied and non-liquefied deposits are analysed with equivalent linear analyses and the envelope of the response spectrum from the pre and post liquefaction segments of the ground motion is considered the total surface response spectrum. This simple procedure provides unique insights into how the thickness of the crust, liquefiable layer and post-liquefaction stiffness



This project has received funding from the European Union's Horizon 2020 research and innovation programme under grant agreement No. 700748

influence the surface ground motion. While the liquefied shear stiffness is an influential parameter for estimation of the modification to the surface motion, it could also be highly correlated to the liquefaction resistance. A simple study is presented in **Figure 2.28**, where a series of linear analyses using the python package were performed using the python package Pysra (Kottke, 2018). The crust height, liquefiable layer height and ratio of shear stiffness between the liquefied and non-liquefied layers were adjusted. The total height of the soil profile was kept constant at 40 m and properties of the non-liquefied soil profile had all layers with 3% damping, unit weight of 17.5 kN/m³, and shear modulus of 30 MPa, 50 MPa and 70 MPa for the crust, liquefiable layer and base layer, respectively. An additional 15% damping was added to the liquefiable layer for the liquefied analyses.

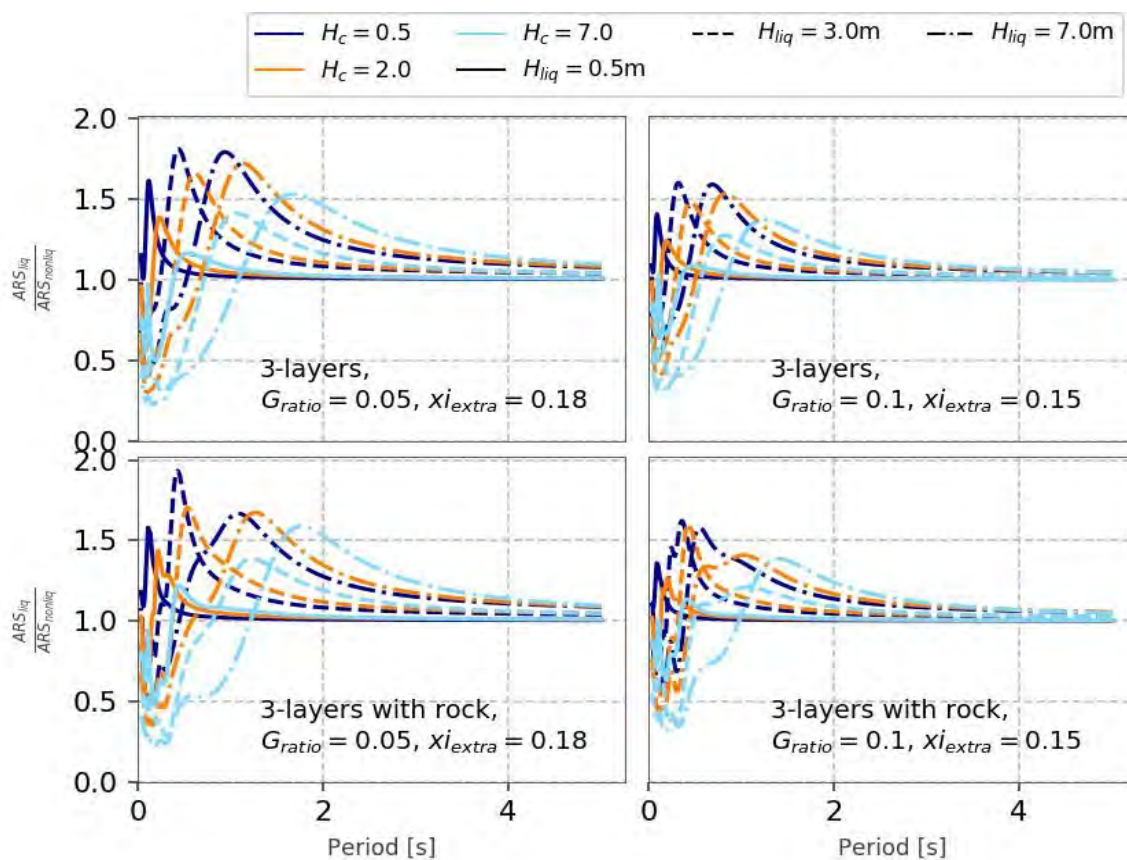


Figure 2.28. Parametric acceleration response spectra (ARS) ratios

The ratio of acceleration response spectra is shown between the liquefied and non-liquefied soil deposits. As expected, at low periods (high frequency) there is a strong reduction in the amplitude of shaking. For longer periods, this reduction switches to become an amplification, and eventually tends to no change in amplitude. The extent of periods that are amplified and de-amplified, as well as the magnitude of the amplification is clearly a function of the height of the crust, height of the liquefiable layer and the stiffness of the liquefiable layer. With a general shift to longer periods and for increasing crust and liquefied layer thickness, as well as decrease in liquefied layer stiffness.



This project has received funding from the European Union's Horizon 2020 research and innovation programme under grant agreement No. 700748

Strength of the liquefiable layer

The definition of the liquefaction resistance of the soil layers can be made using a variety of liquefaction triggering methods, namely with the computation of a factor of safety, in which the seismic hazard is considered and directly applied. However, different assumptions form the base of those methods and, therefore, considerably distinct results are to be expected. Examples from recent events also have shown that there may be substantial differences from simplified approaches and non-linear stress (or energy) analyses. In addition, seismic hazard maps are frequently revised, meaning that the derived liquefaction triggering results would need subsequent updating.

In order to address this issue in detail, Gerace (2018) analysed three possible parameters for the definition of the strength of the liquefiable layer, namely the factor of safety against liquefaction (FS_{liq}), the normalised clean-sand equivalent cone resistance (q_{c1NCS}) and the cyclic resistance ratio to liquefaction in 15 uniform cycles (CRR_{n15}), based on Boulanger and Idriss (2014) method. Liquefaction risk indexes, such as LPI and LSN were also studied and compared. After a preliminary analysis of the three strength parameters, and taking into account the need to back-calculate the remaining parameters from the specific selected parameter, it was concluded that the most appropriate parameter for correcting defining the strength of the liquefiable layer was CRR_{n15} , in terms of processing accuracy and speed, and representativeness of the actual soil profile. This parameter has the advantage of being independent of the seismic hazard, which is particularly convenient in the context of performance-based design and assessment and loss assessment frameworks, where a range of seismic hazard levels are usually considered.

2.3.3 PROCEDURE TO DEFINE ESP FROM CPT

The classification of a soil profile can be performed through cyclic element testing in the laboratory to identify key layers, but to allow efficient classification, it is more convenient and reliable to use continuous field data, namely through CPTu results. The procedure can be semi-automated by computing the CRR for a magnitude 7.5 earthquake using a simplified triggering procedure (e.g. Boulanger and Idriss, 2014), and fitting a three-layered profile to the CRR values, using a specifically designed Python code. The procedure proposed here consists of computing every possible three-layered profile so as to minimise the difference between the CRR values of the computed and the equivalent three-layered profiles, as schematically illustrated in **Figure 2.29**. The calculation of error is sensitive to the choice of value set to be the non-liquefying limit of CRR and the maximum depth of the profile. The non-liquefying limit was set to $CRR=0.6$, as this is a common limit used in simplified procedures (e.g. Youd et al., 2001; Boulanger and Idriss, 2014). Using a higher value means that soil layers with high CRR would generate some error during fitting (Gerace, 2018). The maximum depth was taken as 20 metres, since surficial consequences of liquefaction below such depths are negligible (Maurer et al., 2015). The increment of depths and CRR should be set small enough that they are not influential on the final results. The depth increment was set to 0.1m and the CRR increments were determined by setting the equivalent cone tip resistance for clean sand to range from 0 to 175 kPa in increments of 5kPa to give a CRR range from 0.061 to 0.6. The algorithm will be released in the next version of the open-source python package (Liquepy).



This project has received funding from the European Union's Horizon 2020 research and innovation programme under grant agreement No. 700748

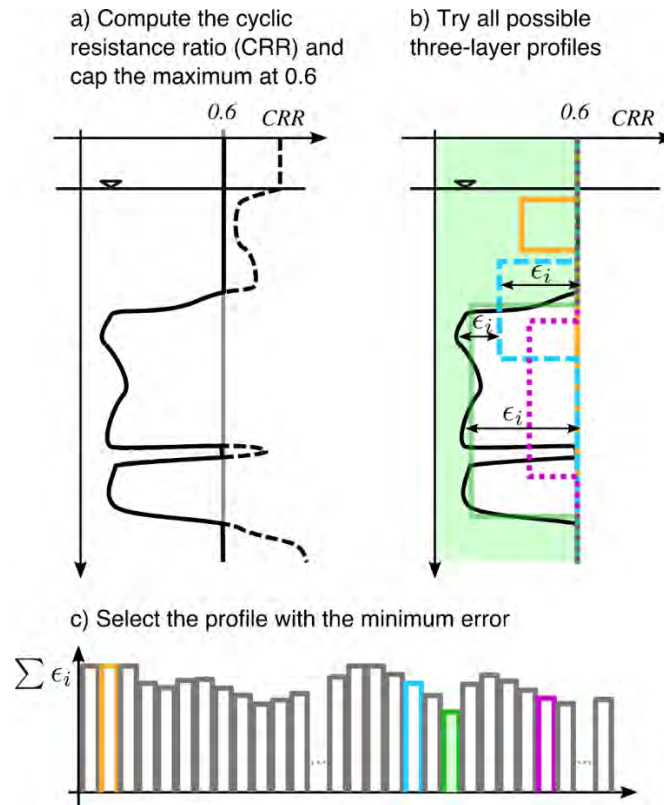


Figure 2.29. Procedure to implement the CRR-fitted method

The implemented algorithm (**Figure 2.29**) minimised the normalised difference $\tilde{\delta}$ (Equation (2.16)), where CRR_{calc} and CRR_{fitted} are the calculated and fitted CRR values, ΔH is the depth increment of the calculated values, $CRR_{non-liq}$ is the non-liquefiable limit and H_{total} is the total height of the profile, capped at the maximum value of 20m.

$$\tilde{\delta} = \frac{\sum (CRR_{calc,i} - CRR_{fitted,i}) \cdot \Delta H}{CRR_{non-liq} \cdot H_{total}} \quad (2.22)$$

The representativeness of the ESP with respect to the actual soil profile can be assessed by calculating and comparing the respective LSN values.

2.3.4 DEFINITION OF EQUIVALENT SOIL PROFILE

The classification for loss assessment was developed in Millen et al. (2019), the justification has been repeated here for completeness. The influence of the layer thicknesses and the liquefied soil strength and stiffness are continuous relationships, whereas regional scale loss modelling requires classification of the soil profile in discrete parts. The class limits for the cyclic resistance ratio are set to provide a reasonable split between the different classes based on previously investigated CPT data presented in Boulanger and Idriss (2016). The limits are therefore arbitrary, but provide an intuitive tool for discussion of the performance buildings as well as the time of liquefaction and post-liquefaction stiffness and strength.



This project has received funding from the European Union's Horizon 2020 research and innovation programme under grant agreement No. 700748

The limits for delineating the depth and height of the liquefiable layer were proposed for the performance of idealised upper and lower limits of low-rise buildings (less than six storeys) on shallow foundations. While some aspects of the performance are independent of the building height, very tall buildings or buildings on piled foundations may have less dispersion in performance if different criteria are chosen.

The minimum capacity of a soil deposit with a fully liquefied (zero liquefied strength) is approximately equal to two times the crust thickness times the equivalent cohesive strength of the crust. Therefore, a 2m thick 50kPa cohesive strength could sustain a minimum load of a 4m foundation with 50kPa load and a 7m crust could sustain 10m foundation of 70kPa. Thus, the majority of buildings would have bearing capacity factors of safety less than one for the shallow liquefaction class and greater than one for the deep liquefaction class. The 2m crust and 3m liquefiable layer also corresponds to a change from de-amplification to amplification of surface spectral acceleration for periods greater than 0.25s, which represents approximately the maximum first mode period for a low-rise building if the infills remain intact. Whereas the 7m crust and 7m liquefiable layer corresponds to the change at 1s, which is approximately the upper limit for the first mode period for low-rise buildings with damaged infills and limited ductility. Therefore, if the infills remain intact, then liquefaction would generally decrease the shaking demand on the building for even the shallow thin liquefaction classes, however, if the infill is damaged then significant amplification could be expected unless the liquefaction is large. Obviously, because the relationships are continuous, each class is not homogenous and no major change in behaviour should be expected when a slight change in depth resulting in a change in soil class. The parameter definitions lead to 22 different equivalent soil profile (ESP) types (**Figure 2.30**).

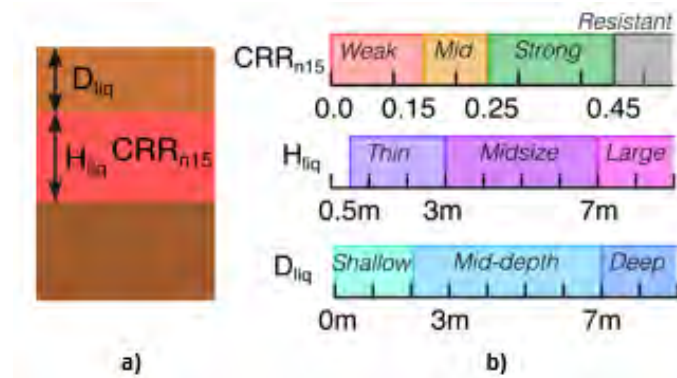


Figure 2.30. Equivalent soil profile classification: a) range definition; b) classes

2.3.5 EXAMPLE SITE RESULTS

In the 2010-2011 Canterbury Earthquake Sequence, severe and widespread liquefaction occurred over nearly half of the urban area of Christchurch (Cubrinovski et al., 2011). The liquefaction manifestation ranged from low or moderate to severe across various suburbs, and often was non-uniform even within a given suburb. Particularly severe liquefaction occurred in the eastern suburbs of Christchurch along the Avon River where lateral spreading also occurred (Cubrinovski and Robinson, 2016). Subsequently, extensive damage inspections and field investigations were carried out, especially where liquefaction occurred, providing a vast database of CPTu results. Further research studies have also been performed for in-depth analysis of particular aspects of soil liquefaction and its effects on buildings and infrastructure (Rhodes, 2017).



This project has received funding from the European Union's Horizon 2020 research and innovation programme under grant agreement No. 700748

One of the sites in Christchurch where liquefaction phenomena occurred was around Sullivan Park, along the Avon River (**Figure 2.31**). At this site, more than 500 CPTu tests were performed and the data results are available (via NZGD: www.nzgd.org.nz), from which 100 CPTu results have been randomly selected as the example site.

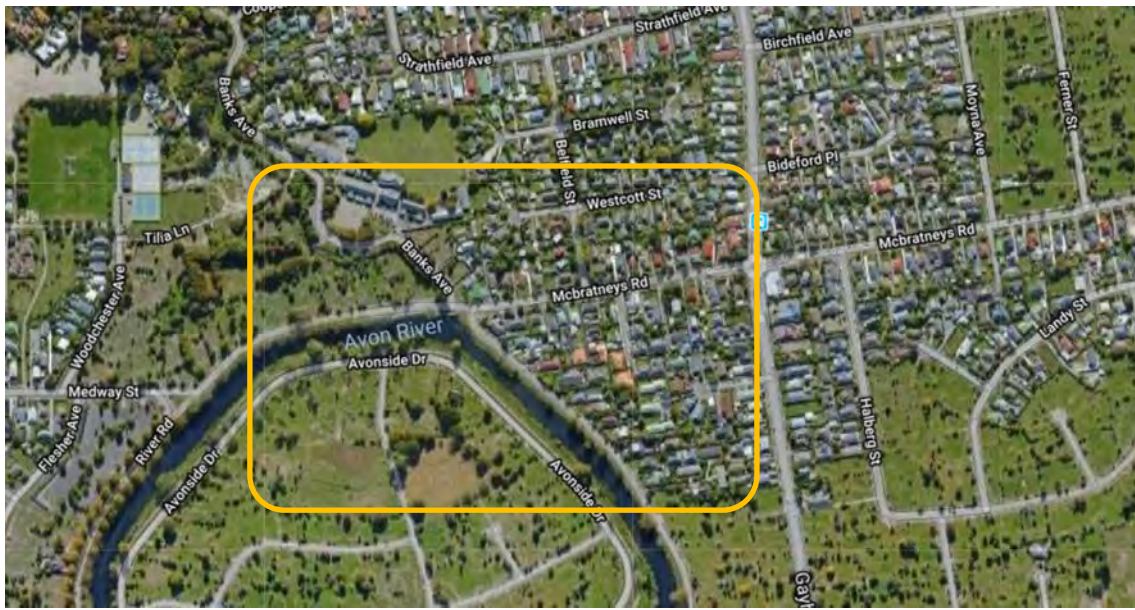


Figure 2.31. Example site, around Sullivan Park (Christchurch), where 100 CPTus were selected

The procedure developed for ESP has been applied to these results, in order to assess the applicability of the classification algorithm. An example of the algorithm output for a single soil profile from Christchurch is provided in **Figure 2.32**. In this figure, the parameters representing the equivalent soil profile are also indicated.



This project has received funding from the European Union's Horizon 2020 research and innovation programme under grant agreement No. 700748

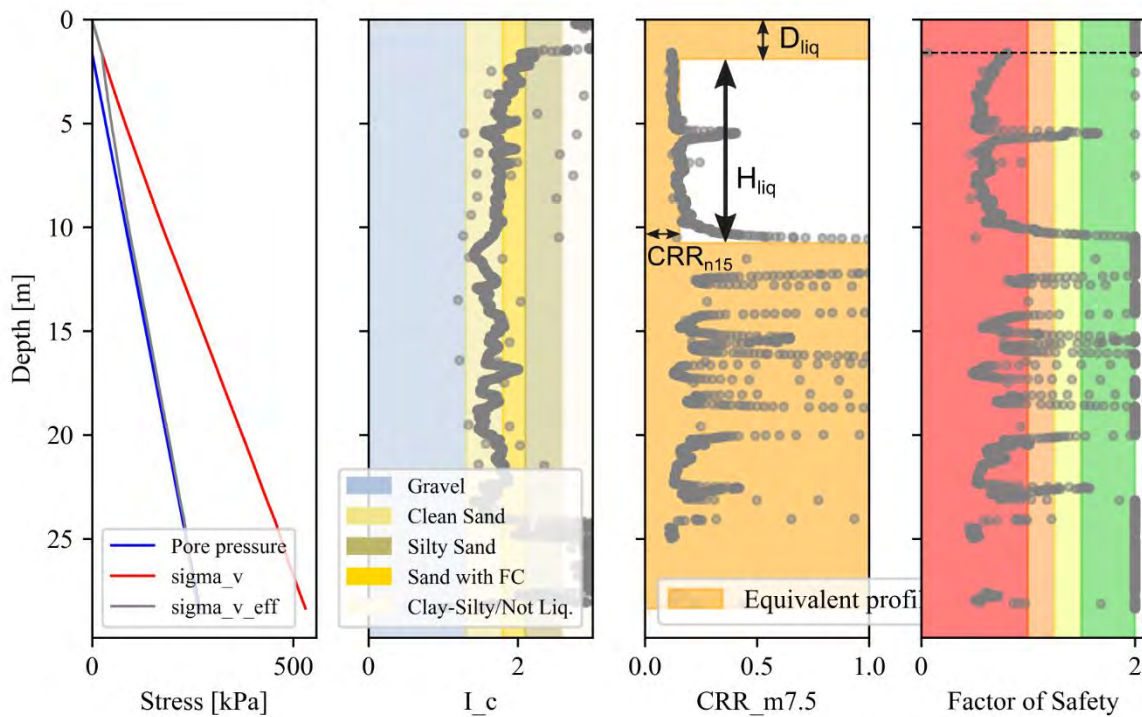


Figure 2.32. Case study single profile classified

To assess the representativeness of the obtained ESP, the computed error is analysed and a visual comparison of the actual and equivalent CRR profile is made. In addition, the LSN values of both profiles can be computed and compared, as a means to check the quality of the fit.

From the analysis of the 100 CPTus database of the example site, the distribution of the soil profile classification has been computed, as shown in **Figure 2.33**. Looking at this example site in Christchurch, this leads to the following breakdown on equivalent profile types: 34% of weak soil profiles, 65% of mid-strength, predominantly shallow, profiles and only 2% of strong soil profiles.



This project has received funding from the European Union's Horizon 2020 research and innovation programme under grant agreement No. 700748

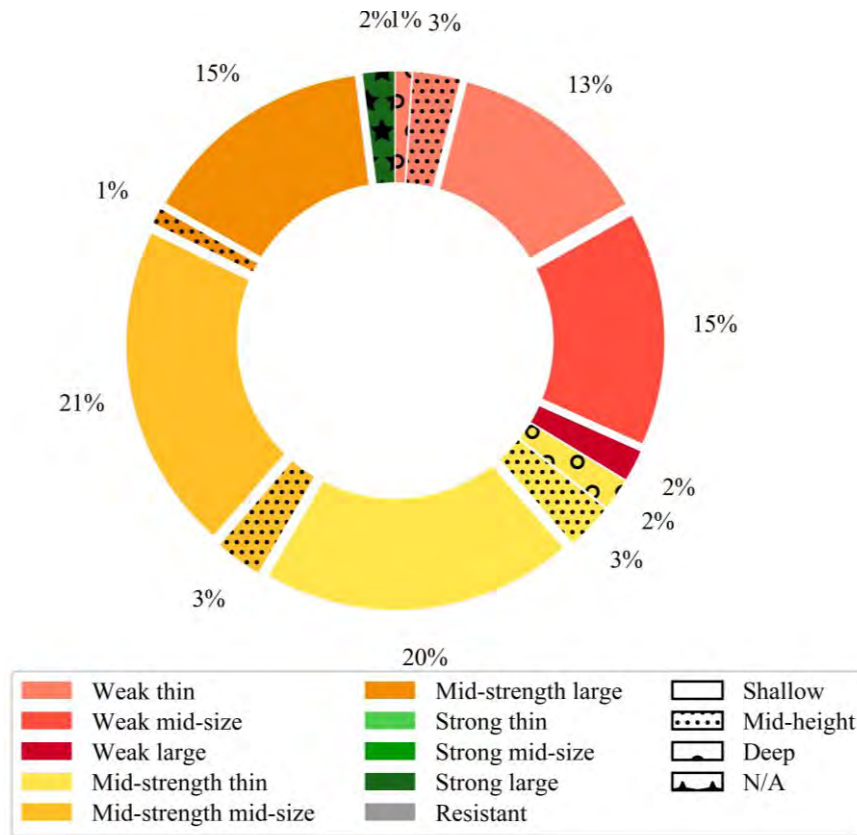


Figure 2.33. Equivalent soil profile distribution for the example site

The statistical breakdown of Equivalent Soil Profiles (ESP) in a region can be used to inform macro liquefaction maps as in region-level estimation (microzonation), enabling susceptibility to be connected to vulnerability of buildings and critical infrastructures. At the region-level, a distribution of ESPs could be used to reflect the variability of the soil across a large area.

Recognizing that this methodology has some limitations, particularly using just three layers, limits the ability to investigate the influence of pore waterflow and effects such as lensing.

2.3.6 APPLICATION OF THE PROCEDURE TO REAL CASE STUDIES

The applicability of the above described procedure has been tested versus two real case studies, Christchurch (New Zealand) and San Carlo (Italy), struck by severe earthquakes that caused extensive liquefaction. The large number of subsoil investigations performed in the two cases for reconstruction purposes coupled with the reconnaissance of damages caused by liquefaction provide exceptional collections of real scale experiments that enables to confirm or deny assumptions and more generally to validate the procedures defined in the Liquefact project. For this application, data coming from CPT and CPTU tests have been collected, their format homogenised and processed automatically to reconstruct the Equivalent Soil Profiles, measure each time the error accompanying equivalence and calculate traditional indicators.



This project has received funding from the European Union's Horizon 2020 research and innovation programme under grant agreement No. 700748

Considering that the procedures are automatically applied on large scale analyses (districts, regions etc.) treating each time large amounts of data, and considering the various uncertainties affecting geotechnical investigations, the validation process has been carried out on a statistical basis.

Christchurch Earthquake Sequence 2010-2011

Christchurch (pop. 366.100, 2013) is an important industrial and agricultural centre in the South Island of New Zealand and is the second largest city of the country. It is located on the eastern (Pacific) coast of the South Island, in the Canterbury Region. From the geological viewpoint, the City is situated over recent deposits of alluvial gravels laid down by the Waimakariri River, and fine marine sediments deposited on the coastal margin of the floodplain and in estuaries and lagoons. The sediments are about 700 metres deep: principally coarse-grained fluvial greywacke sands, gravels and silts, but with extensive sands in the eastern, seaward part of the city and with intermingled estuarine deposits especially in the central, south, and south eastern areas. The sediments lie on 200-300 meters of volcanic rock overlying greywacke basement at about 1000 m depth. To the south of the city, the sediments become shallower against the weathered volcanic cone of Banks Peninsula. The Port Hills are mantled with loess soils over the basalt rock.

In 2010-2011, the Canterbury region suffered a severe earthquake sequence known as Christchurch Earthquake Sequence (CES) that produced huge damage to buildings and infrastructural assets mostly caused by liquefaction (**Figure 2.34**). The 2010 – 2011 Canterbury earthquake sequence includes several thousands of events, four of them with $M_w \geq 6$. The event occurred on September 4th 2010 ($M_w 7.1$), named Darfield earthquake due to the location of the epicentre, and the subsequent earthquake of February 22nd 2011 ($M_w 6.2$) named Christchurch earthquake as its epicentre was located just below the city, resulted in 185 fatalities. Among all events, the earthquake of February 2011 was more devastating to central and eastern Christchurch due to the close proximity of the fault rupture.

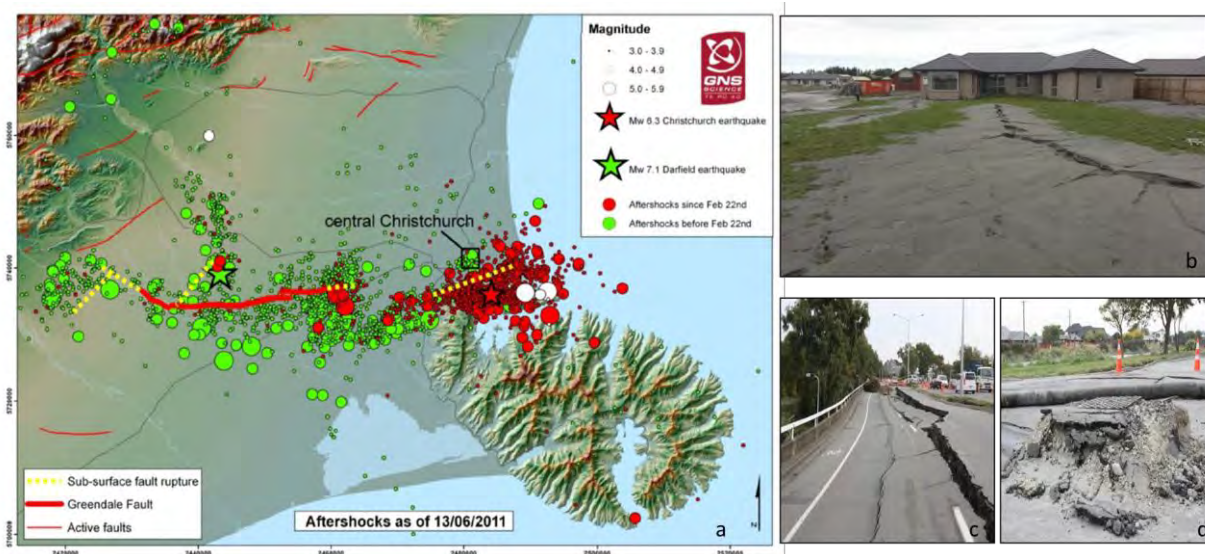


Figure 2.34. a) Epicenter locations and faults of the seismic events characterizing the 2010-2011 Christchurch Earthquake Sequence (as at June 2011). Projected surface locations of major blind faults in yellow and location of mapped surface ruptures in red. (b,c,d) Example of liquefaction-induced damage on buildings, road and networks. Major cracks with ejecta sands (b) affected residential houses and infrastructure (c,d).



This project has received funding from the European Union's Horizon 2020 research and innovation programme under grant agreement No. 700748

Methodology for the liquefaction fragility analysis of critical structures and infrastructures: description and case studies

v. 1.0

After the Christchurch Earthquake Sequence, the New Zealand Government (MBIE and EC) founded the building of the Canterbury Geotechnical Database (CGD), which later became NZGD (<https://www.nzgd.org.nz>). This database was primarily aimed at providing more efficient access to geotechnical information, but it can also be used for more strategic purposes, such as assisting with natural disaster recovery, increasing resilience around New Zealand, catastrophe loss modelling and informing land planning and regulatory processes. It was designed as a tool for technical professionals to share and use geotechnical data for the rebuilding of Christchurch. The information provided by the CGD is mostly a collection of raw data including scientific and engineering characterisation of the ground conditions (because the data is normally gathered, interpreted and conveyed to the client by a geotechnical engineer). Following the success of the Canterbury Geotechnical Database (CGD), a bigger database (New Zealand Geotechnical Database) was established that incorporated other data previously stored in the Auckland Geotechnical Database. The databases are continuously updated with new investigations. In October 2018, the NZGD included a huge number of: Cone Penetration Tests CPT (more than 30 000) and boreholes (16 000), 1 000 piezometric installations, more than 6 000 laboratory tests and around 10 000 other tests (**Figure 2.35**).

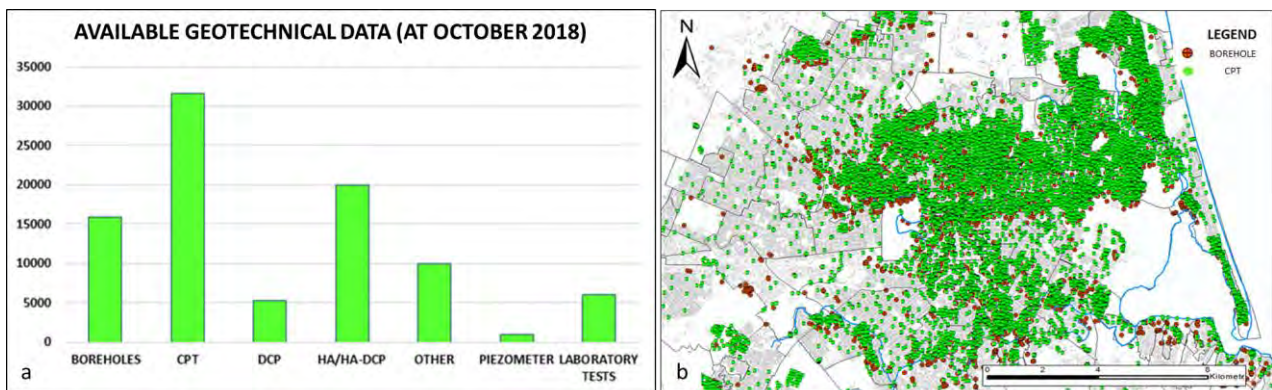


Figure 2.35. Summary scheme of the available investigations in the New Zealand Geotechnical Database. Thanks to the data sharing between a huge number of data owners, who have approved the publication of their factual geotechnical data, the NZGD is continuous updated.

Around 13 000 CPT profiles were available for the whole area of Christchurch City. Considering the Magnitude and GNS strong motion Map of the 22 February 2011 earthquake and accounting for the specific event Groundwater depth (**Figure 2.36**), these CPTs were processed applying the ESP methodology.



This project has received funding from the European Union's Horizon 2020 research and innovation programme under grant agreement No. 700748

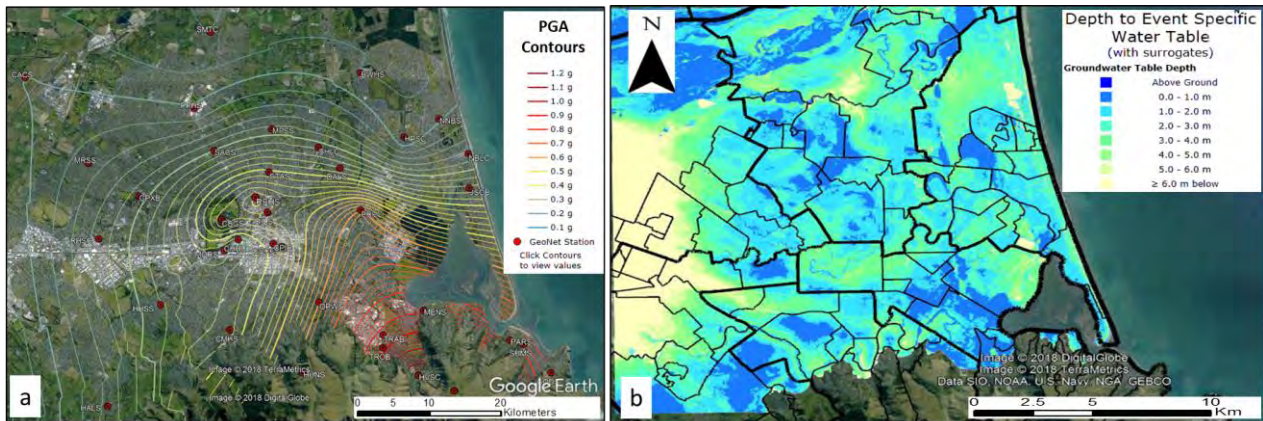


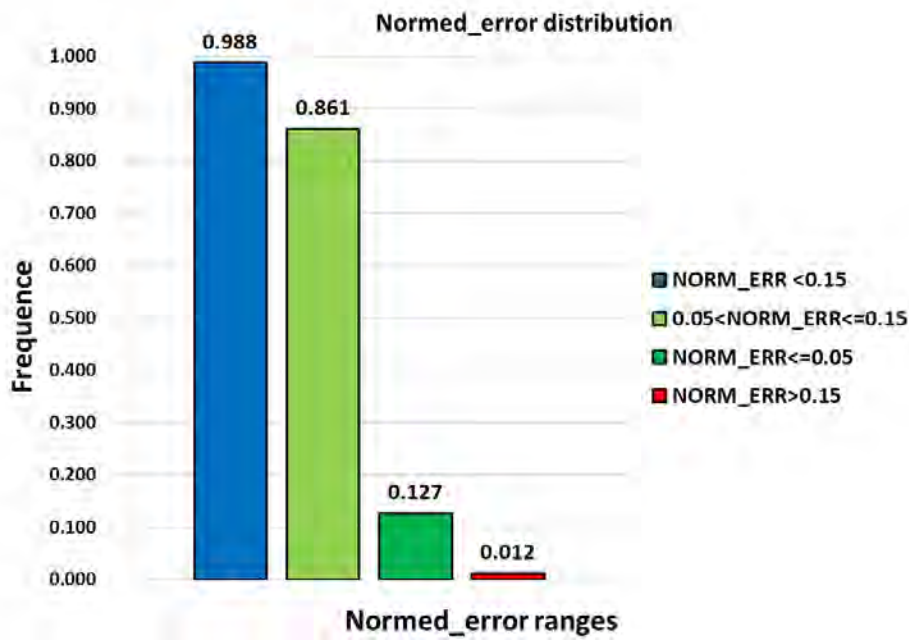
Figure 2.36. a) Available specific scenario (the 22 FEB 2001 Mw 6.2 Christchurch Earthquake) Shakemap; b) Map of the Groundwater Table depth (from the NZGD).

Representativeness of the equivalent soil profile

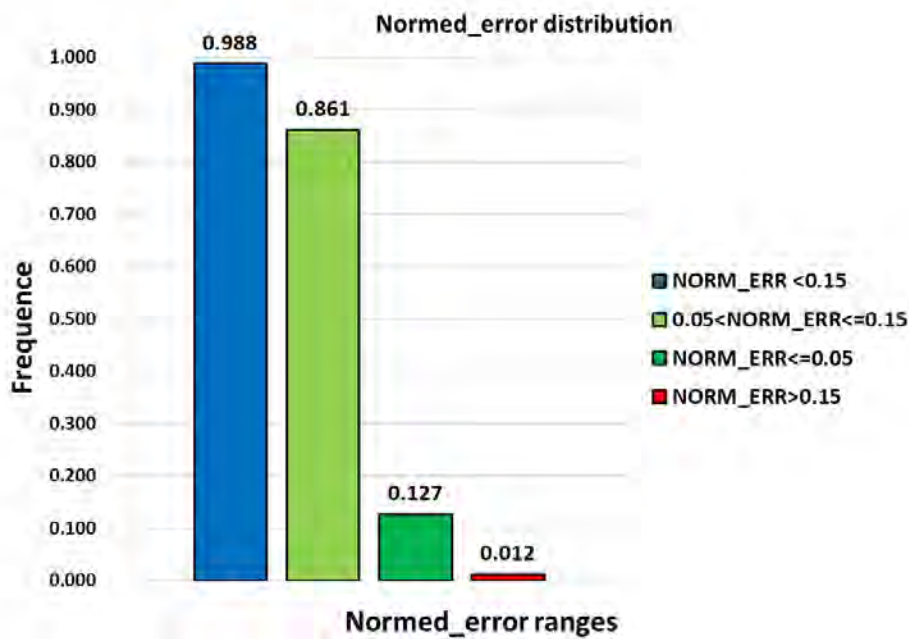
Out of 13 000 CPTs processed during the project, the analysis has been performed on 8818 CPTs considering only those that reach a depth larger than 10m. The ESP procedure has been applied automatically on each of these tests. As shown before, the ESP procedure finds from a CPT profile the combination of H_{crust} , H_{liq} and CRR that give the lowest normed error. Therefore, this parameter has been here used as an estimate of the validity of this method. **Figure 2.37** shows the frequency distribution of the normed errors. The fitting of soil profiles with a three layers ESP model that gives errors lower than 0.05 is optimal; when error is contained in the range 0.05-0.15 the fitting is acceptable; for errors larger than 0.15 the fitting with the three layers model is not applicable, typically due to the presence of multiple liquefiable layers separated by large non-liquefiable layers. The figure shows that over the 8818 processed CPT profiles, only 106 (1.2%) give errors larger than 0.15. However, the scattered position of these tests over the map (**Figure 2.38**) shows that the equivalence is rather affected by uncertainties linked to the execution and interpretation of the tests more than by local systematic variations of the stratigraphy. In all cases, engineering judgement is needed to focus on these tests and make a decision on the acceptance/rejection of the equivalence.



This project has received funding from the European Union's Horizon 2020 research and innovation programme under grant agreement No. 700748



(a)



(b)

Figure 2.37. a) The histograms show that the equivalent soil profile method is globally adequate in the schematization of real profiles: in fact, of the 8 200 tests analyzed for the Christchurch case study, only 1.2% need further engineering evaluations; b) Considering the Std_normed_error (evaluated as Std Normed Err= Normed error*20/Max depth.) the percentage of CPTs showing an error greater than 0.15 becomes around 15%.



This project has received funding from the European Union's Horizon 2020 research and innovation programme under grant agreement No. 700748

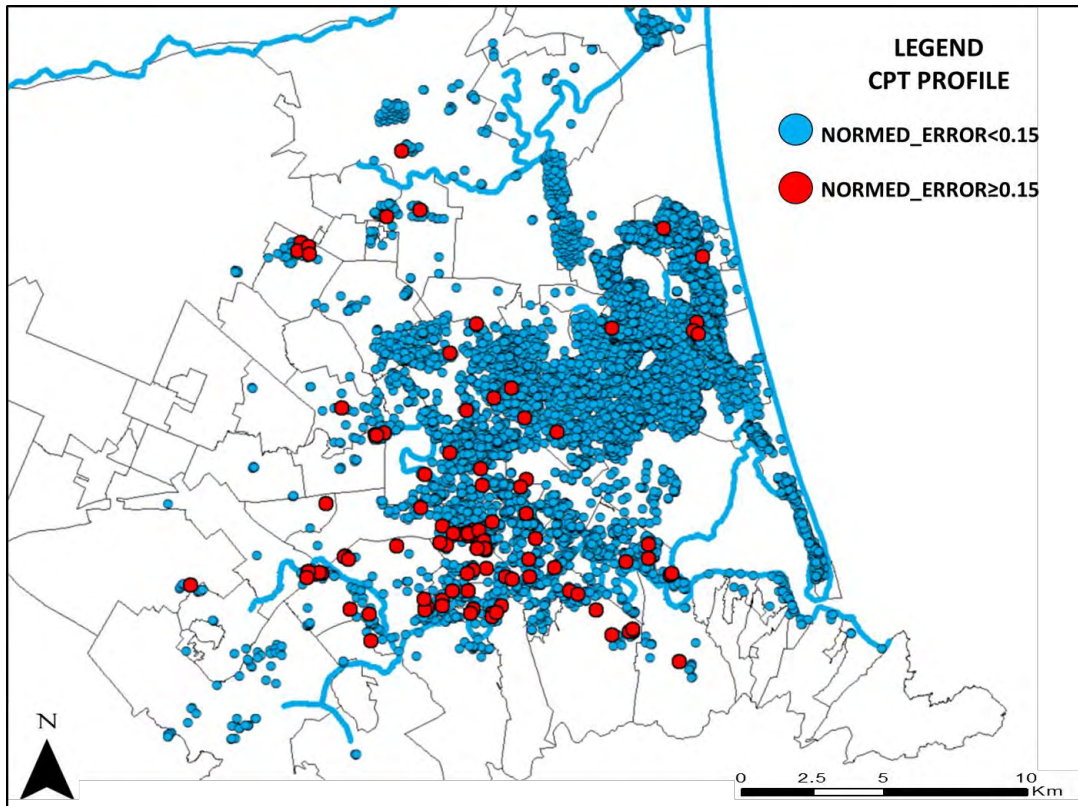


Figure 2.38. The Map shows the position of the CPTs with an average error greater than 0.15. Most of them are located in the South of the City, while no further assessment is required in the so called “Red Area” along the Avon River.

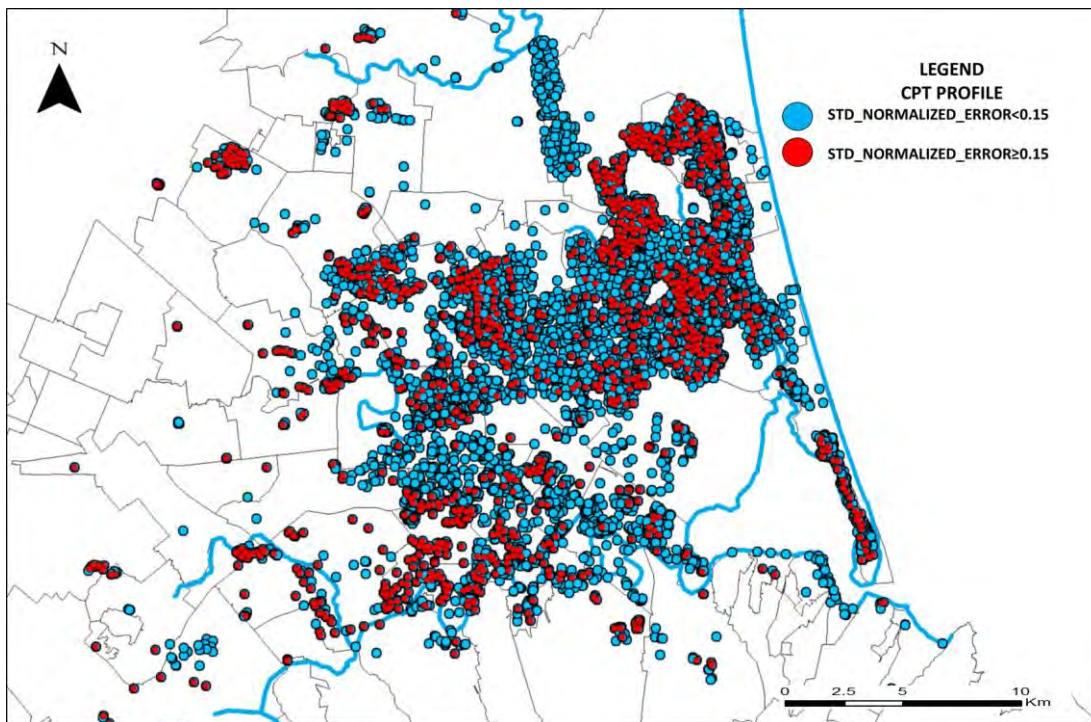


Figure 2.39. The Map shows the position of the CPTs with an average error greater than 0.15. Most of them are located in the South of the City, while no further assessment is required in the so called “Red Area” along the Avon River.



This project has received funding from the European Union's Horizon 2020 research and innovation programme under grant agreement No. 700748

In the following part, three representative profiles are analysed in detail to understand the meaning of normed errors. In fact, **Table 2.4** shows that the three selected profiles are representative of the above defined classes (with normed errors respectively $N.E.<0.05$, $0.05<N.E.<0.15$, $0.15<N.E.$).

Table 2.4: Example of three selected profiles showing respectively low, medium and high normed error.

LogID	Max_depth [m]	GWT [m]	GWT [m]	Pga [g]	H_crust [m]	H_liq [m]	CRR	Class	LSN_direct	LSN_esp	normed_error
912	38.1	1.71	1.71	0.50	1.71	8.20	0.161	MLS	33.6	36.6	0.016
2	40.5	2.51	2.51	0.54	7.51	4.80	0.371	SMX	11.2	1.1	0.111
220	24.3	1.06	1.06	0.45	9.26	10.60	0.131	WLD	55.2	18.6	0.175

As can be observed in **Figure 2.40** showing a case with low error (0.016), the ESP method is very accurate and the characterization of the soil profile with three layers is appropriate as there is only one and easily recognizable liquefiable layer. In fact, the plot of the Factor of Safety against Liquefaction (FS) highlights the presence of a continuous surficial sandy layer, having FS less than 1, extended up to a depth of 10 m. From the same plot, points having FS less than 1 can be recognised, but they cannot be classified as a continuous layer. This profile is adequately described through a crust thickness (H_crust) equal to 1.71 m, a thickness of the liquefiable layer (H_liq) equal to 8.2 m and an average CRR of 0.16. Therefore, according to the equivalent soil profile method, the CPT 912 is classified as MLS, since it is characterized by a large (thicker than 7 m) shallow (less than 2 m deep) liquefiable layer, having an intermediate resistance (where CRR_{n15} in 0.15-0.25 range).

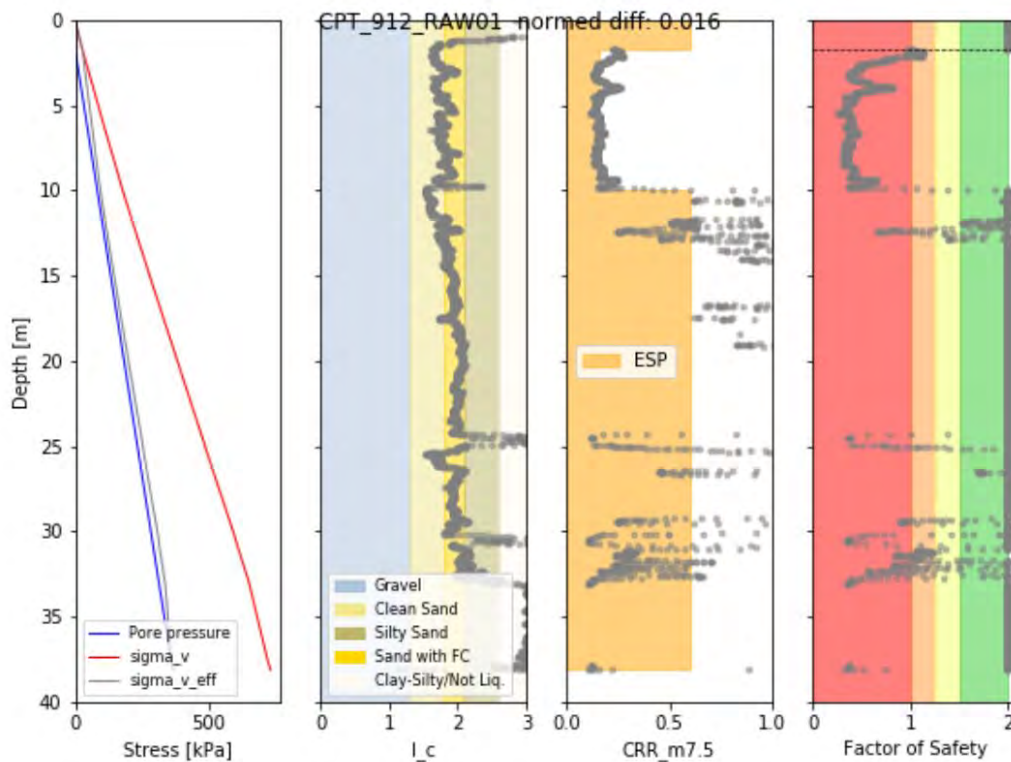


Figure 2.40. Example of CPT for which the equivalent soil profile method is consistent with the real soil profile ($N.E.<0.05$).



This project has received funding from the European Union's Horizon 2020 research and innovation programme under grant agreement No. 700748

The results are still acceptable but with a lesser extent, in the case of CPT_002, that gives a normed error of 0.111 (**Figure 2.41**). Here, two distinct liquefiable layers can be identified within the first 20 m, an upper one at 7-12 meters depth and a lower at 15-20 metres depth. A non-liquefiable layer around 2-3 meters thick can be recognised between them. In the ESP method, the second layer is not considered and the CPT_002 is classified as SMX type: strong since it is characterized by a relatively high CRR (0.25-0.5) and midsize because the liquefiable thickness H_{liq} is around 5 meters.

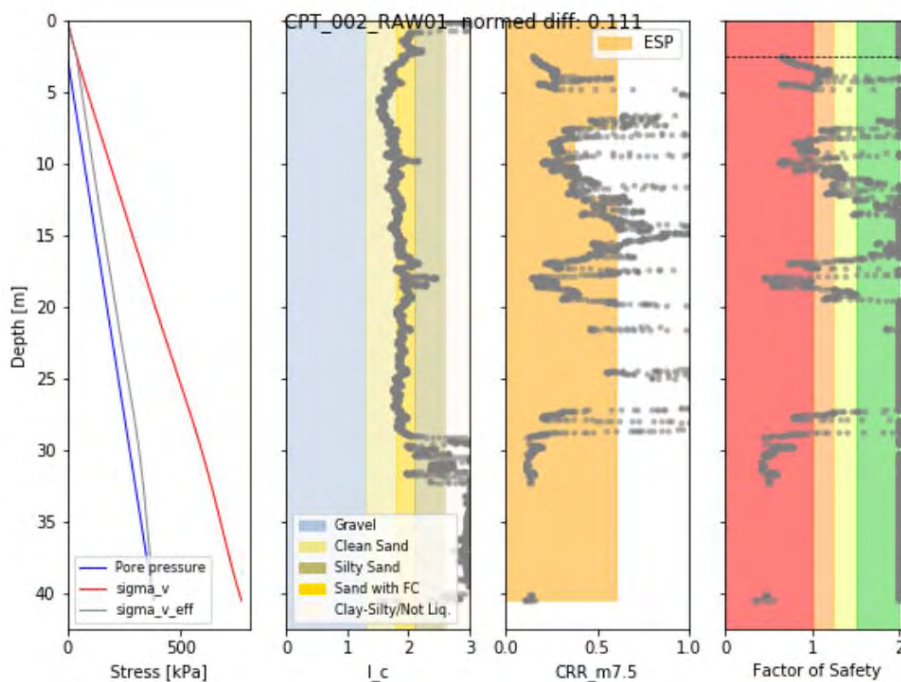


Figure 2.41. Example of CPT profile showing a quite good agreement between the equivalent soil profile and the real one ($0.05 < N.E. < 0.15$).

Finally, an example of test where the ESP method needs further analysis is the CPT_220 (**Figure 2.42**). In fact, the results of such CPT are characterized by an average error of 0.175. Even if the profile is classified as WLD according to the presence of a large weak liquefiable layer, the method does not account for the presence of a thick shallow liquefiable layer extended in the first 2-4 m of depth from the ground. Moreover, the same CPT profile highlights the presence of a second liquefiable lens 5-7m deep.

On the contrary, the ESP method gives a thickness of the crust (H_{crust}) larger than 9 m that implies a deep liquefaction phenomenon. The large normed error clearly identifies a poor fit and engineering judgement would be required to generate a suitable equivalent profile.



This project has received funding from the European Union's Horizon 2020 research and innovation programme under grant agreement No. 700748

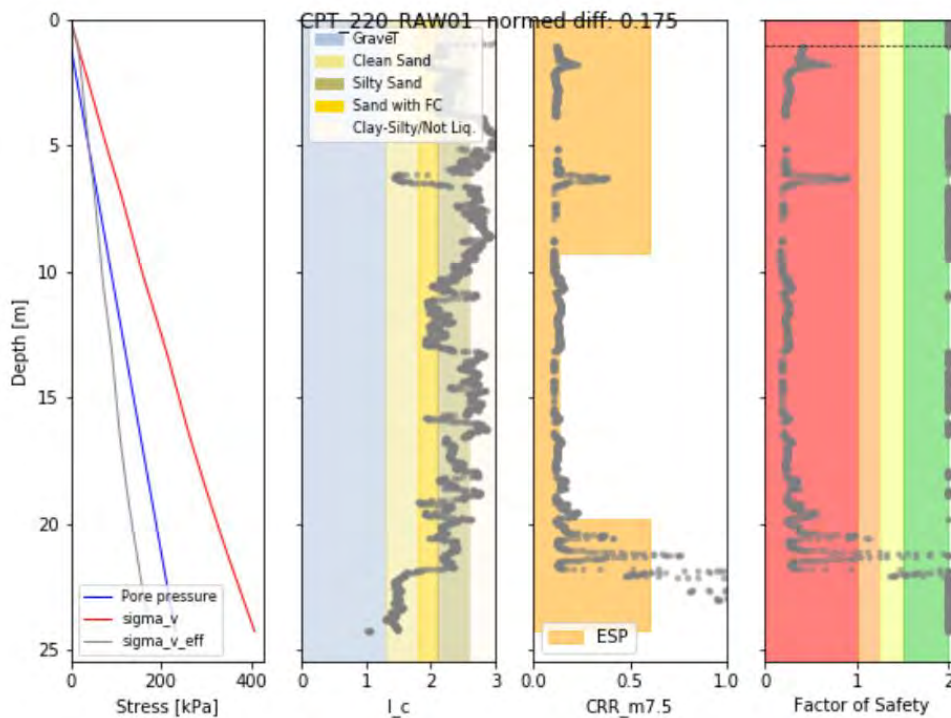


Figure 2.42. CPT_220 represents an example of profile where a specific engineering evaluation is required. ($0.15 < N.E.$).

Preliminary validation

Following the major Canterbury earthquake events, a qualitative survey of land damage and dwelling foundation damage was undertaken as part of the coordinated response by agencies of the NZ government. Liquefaction-induced land damage mapping of residential properties was carried out immediately after the September 2010, February 2011, and June 2011 earthquakes to assess the extent and severity of the surface effects of liquefaction.

The map in **Figure 2.43**, also available from the NZGD, represents an example of the land damage distribution from the February 2011 earthquake. Most of the ejected liquefied material was generally removed and major cracks filled (but not repaired) between each of the events. Therefore, the qualitative land damage mapping generally recorded the incremental effects of each earthquake. In particular, in the map of liquefaction ground observations: the blue (level 1 of damage) and green areas (level 2, only shaking-induced damage) represent zones where no liquefaction was observed; yellow areas are characterized by minor to moderate liquefaction and cracks, but no lateral spreading (level 3 of damage), while in the red zones (level 4 of damage) severe liquefaction, including major cracks and lateral spreading, occurred.



This project has received funding from the European Union's Horizon 2020 research and innovation programme under grant agreement No. 700748

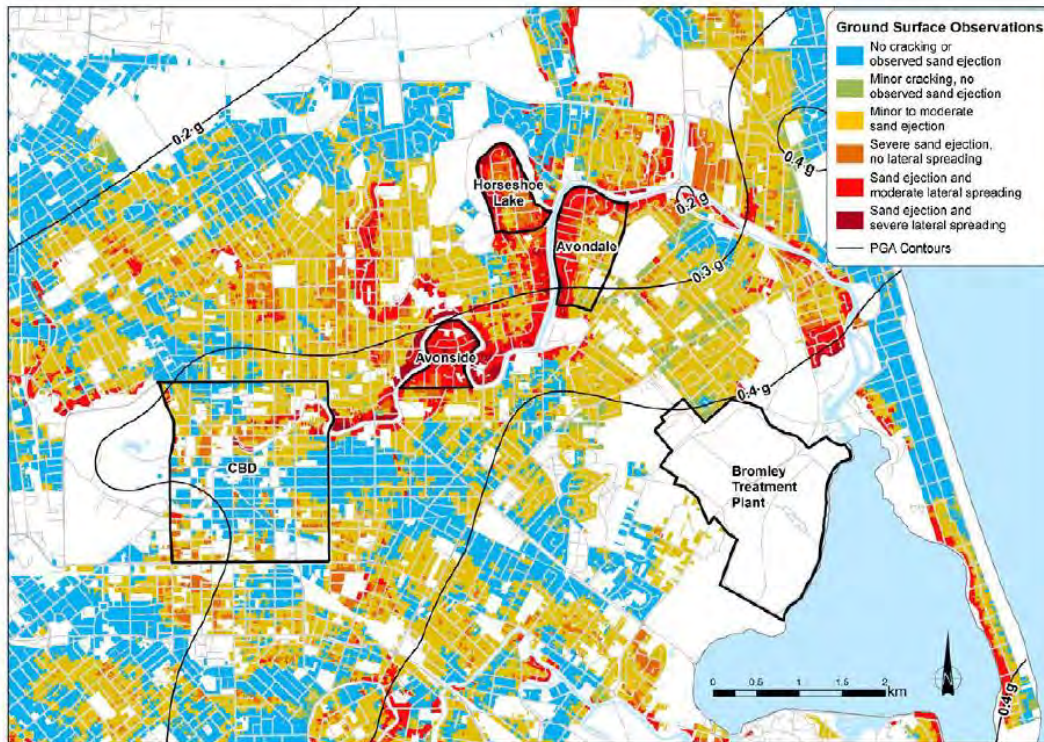


Figure 2.43. Liquefaction-induced land damage observations across Christchurch after the February 2011 earthquake, with the February 2011 magnitude-weighted equivalent $M_w = 7.5$ PGA contours overlaid (van Ballegooy, 2014 after Bradley & Hughes, 2012).

In addition to the land damage mapping, a more detailed land damage inspection program was undertaken on each of some 65.000 insured residential properties by a team of engineers for insurance claim damage assessment purposes. The CPT data processing allowed to evaluate, for each profile: the non-liquefiable crust thickness, the thickness of the liquefiable layer, the average CRR and both the LSN_{esp} and the traditional LSN. Based on these parameters (h_{crust} , H_{liq} and CRR), each CPT can be classified with an equivalent soil profile (ESP), accounting for the depth, the size and the resistance of the liquefiable layer. The distribution of the obtained ESPs is plotted in the following graph.



This project has received funding from the European Union's Horizon 2020 research and innovation programme under grant agreement No. 700748

		WEAK	%	MID	%	STRONG	%	RESIST	%
LARGE	Shallow	WLS	2.15	MLS	11.59	SLX	14.84	RXX	0.51
	Mid.	WLM	1.00	MLM	6.87				
	Deep	WLD	0.11	MLD	3.25				
MIDSIZE	Shallow	WMS	2.91	MMS	4.17	SMX	4.56		
	Mid.	WMM	1.98	MMM	4.52				
	Deep	WMD	0.40	MMD	3.38				
THIN	Shallow	WTS	1.66	MTS	1.94	STX	3.12		
	Mid.	WTM	1.92	MTM	2.54				
	Deep	WTD	1.34	MTD	3.20				

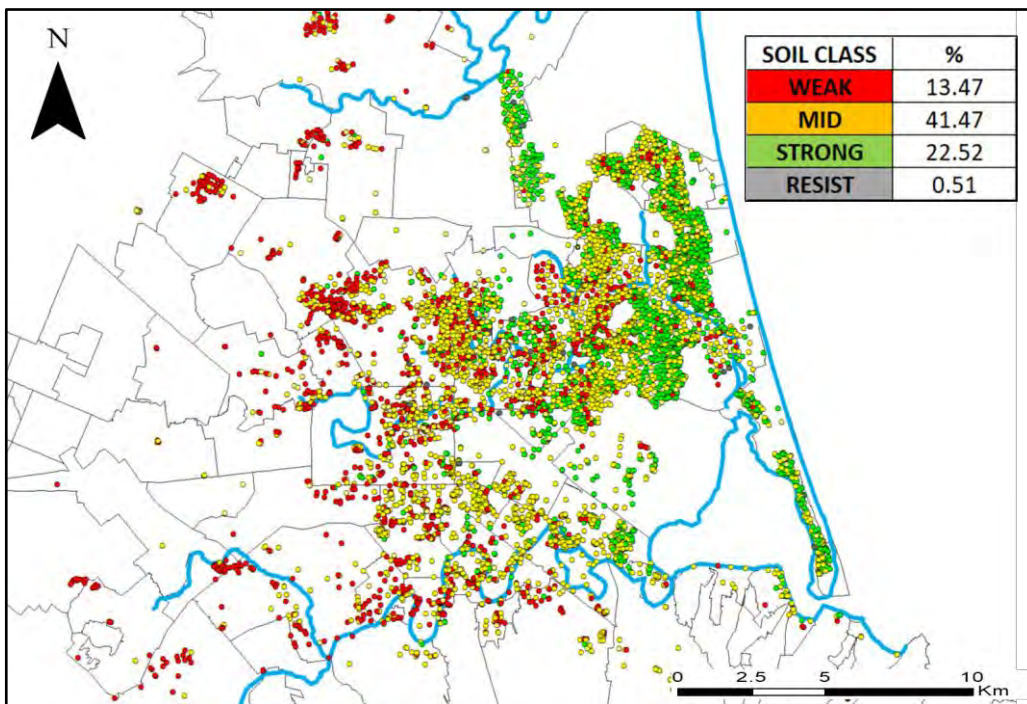


Figure 2.45. General overview of the ESP spatial distribution. It can be observed that many of the weak and moderate profiles are located along the two Rivers of the City.



This project has received funding from the European Union's Horizon 2020 research and innovation programme under grant agreement No. 700748

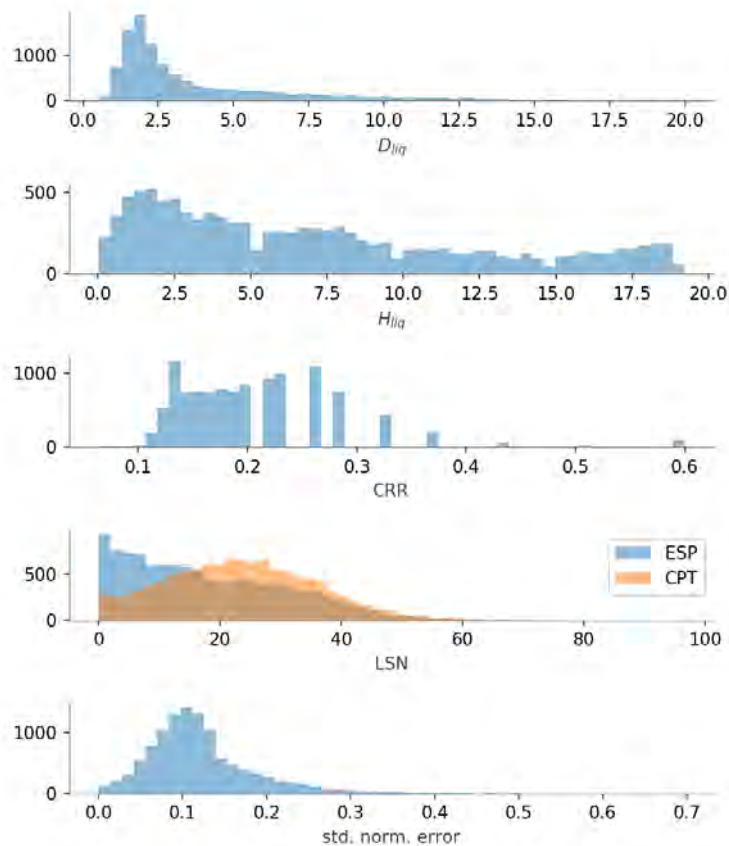


Figure 2.46. Histograms of the ESP parameters and comparison of LSN from ESP and CPT.

The classification using ESP also allows the distribution of key parameters to be investigated. **Figure 2.46** shows that the liquefiable layer is typically shallow, consistent with the low ground water level in Christchurch, while the height of the liquefiable layer is almost an uniform distribution, with a slight increase for thin layers. The cyclic resistance was nearly always above 0.1 with the majority of values between 0.1 and 0.2. The LSN from the ESP was skewed to the left, in general the ESP would have a lower LSN value than the CPT trace and in many cases would produce LSN equal to zero. Finally, the standard normalised error was typically around 0.1 with a small number of values above 0.2.

San Carlo Emilia Romagna (2012)

The district of San Carlo in the municipality of Sant'Agostino (Italy), was hit by the May-June 2012 seismic sequence. On 20th May a Mw 5.9 earthquake caused damages (186 buildings damaged at different levels only in San Carlo district) and extensive soil liquefaction (sand boils and cracks) in the whole municipality of S. Agostino and Mirabello. At that time, San Carlo district hosted: approximately 1500 inhabitants, housed in 660 buildings (ISTAT, 2018).

Reminding soil liquefaction occurs in areas with specific geological features, it is worth highlighting that Galli, et al. (2012) showed the presence of hidden paleochannels in that district (**Figure 2.47**, left side) and the topographical survey of the area (**Figure 2.35**, right side) evidenced the presence of hidden paleo-levees; thus, the area was clearly susceptible to soil liquefaction.



This project has received funding from the European Union's Horizon 2020 research and innovation programme under grant agreement No. 700748

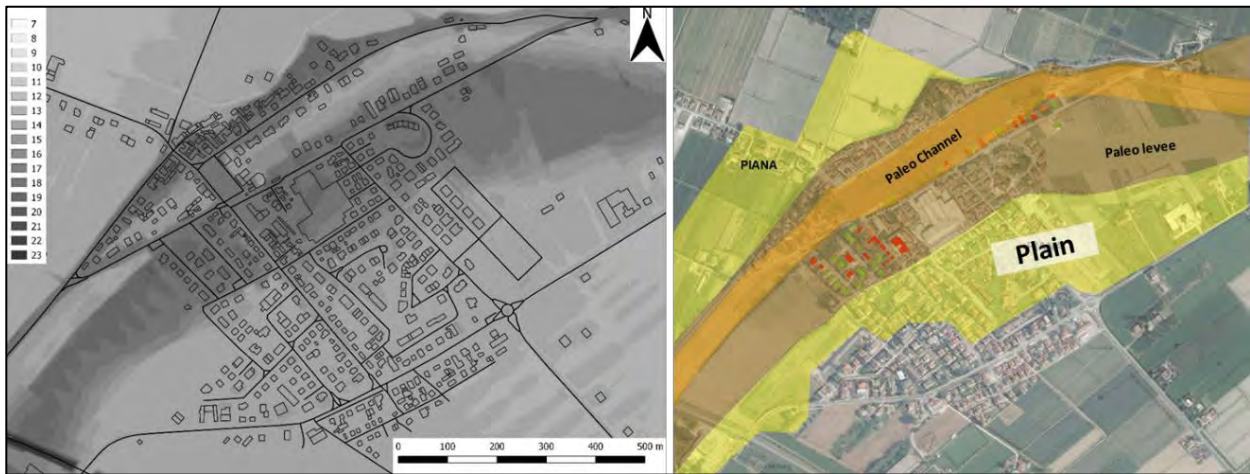


Figure 2.47. Digital Elevation Model (on the left) shows that the district of S. Carlo is located along f the old Reno River Paleochannel. Geological features of San Carlo area (on the right).

The Emilia Romagna Region encouraged the collection of the existing data and their loading into numerical archives that are constantly updated. After the May-June 2012 seismic sequence, a lot of new geotechnical information and surveys have been added to the already existing information. The Geognostic Database covers the entire regional plain territory and, at January 2018, more than 85 000 tests are publicly available (Figure 2.48.a).

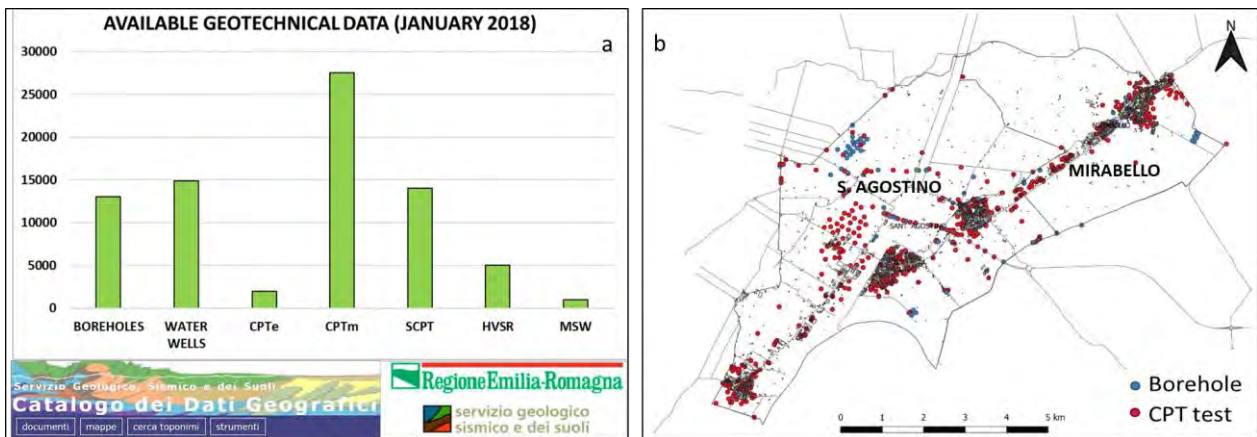


Figure 2.48. a) Summary scheme of the available investigations in the Emilia Romagna Region Geotechnical Database; b) available CPTs (around 1000) and boreholes (≈200) in the whole S. Agostino and Mirabello municipality

Around 1 000 CPT profiles were available for the whole area of Sant’Agostino and Mirabello, 150 of them located in the S. Carlo district. Considering the Magnitude and INGV strong motion Map of the 20 May 2012 earthquake and accounting for the specific event Groundwater depth (Figure 2.36), these CPTs were processed applying the equivalent soil profile method. Moreover, the traditional Liquefaction Severity Number LSN (van Ballegooy., 2014) was evaluated according to Boulanger and Idriss, 2014 procedure.



This project has received funding from the European Union's Horizon 2020 research and innovation programme under grant agreement No. 700748

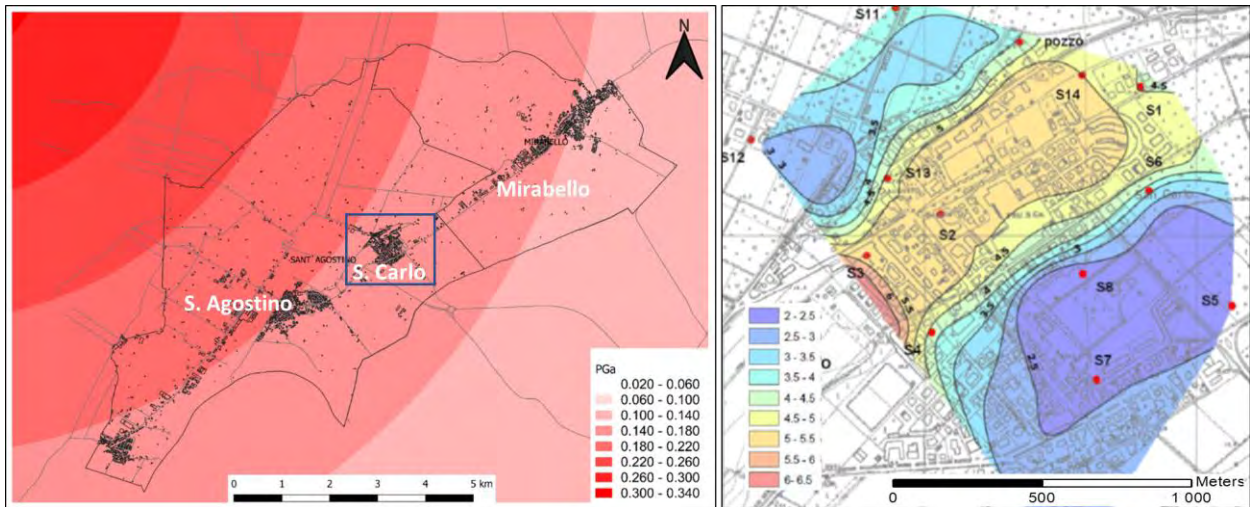


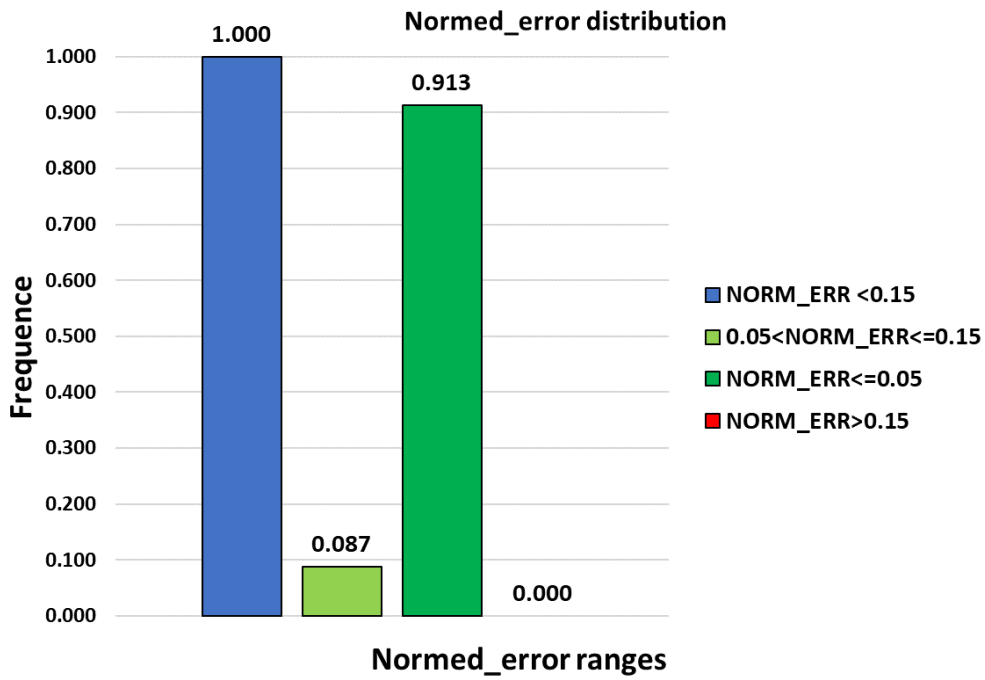
Figure 2.49. a) Available specific scenario (the 22 FEB 2001 Mw 6.2 Christchurch Earthquake) Shakesmap; b) Map of the Groundwater Table depth (from the NZGD).

Representativeness of the Equivalent Soil Profile

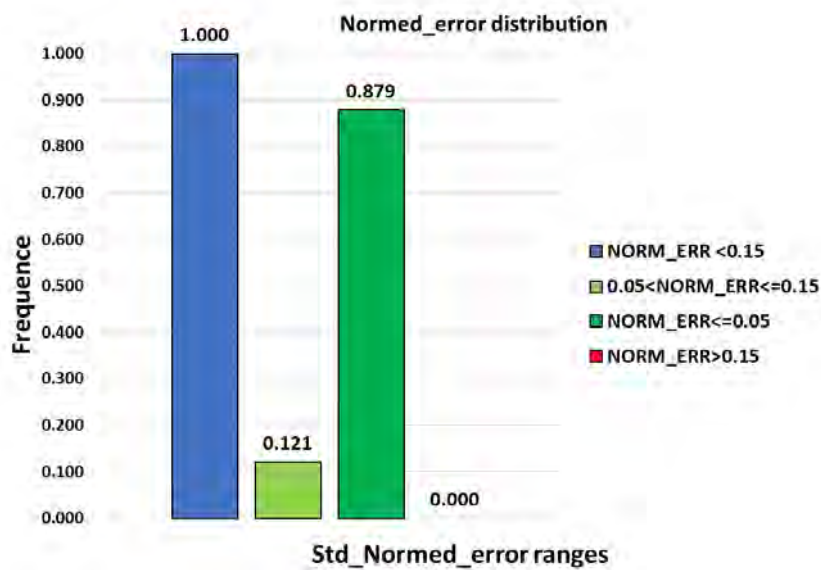
Within the study area 150 CPTs, having a depth larger than 10m, were processed according to the ESP method which define the best combination of (H_{crust} , H_{liq} , CRR) as the one with the lowest normed error. In the following histograms showing the average error are shown in order to estimate the consistency of this method. The fitting of soil profiles with a three layers ESP model that gives errors lower than 0.05 is optimal; when error is contained in the range 0.05-0.15 the fitting is acceptable; for errors larger than 0.15 the fitting with the three layers model is not applicable. Looking at **Figure 2.50**, the normed error for all CPT profiles distributed over the area, as shown in **Figure 2.51**, is lower than 0.15. Moreover, most of the analyzed CPT show an average error smaller than 0.05. This result implies that the three layers model defined by the ESP is well representative of the situation in San Carlo.



This project has received funding from the European Union's Horizon 2020 research and innovation programme under grant agreement No. 700748



(a)



(b)

Figure 2.50. a) Histogram of the ESP normal error; b) Histograms of the ESP Std_normed_error (*Std Normed Err = Normed error * 20/Max depth*) show that the ESP_method performs well for all the analysed CPTs.



This project has received funding from the European Union's Horizon 2020 research and innovation programme under grant agreement No. 700748

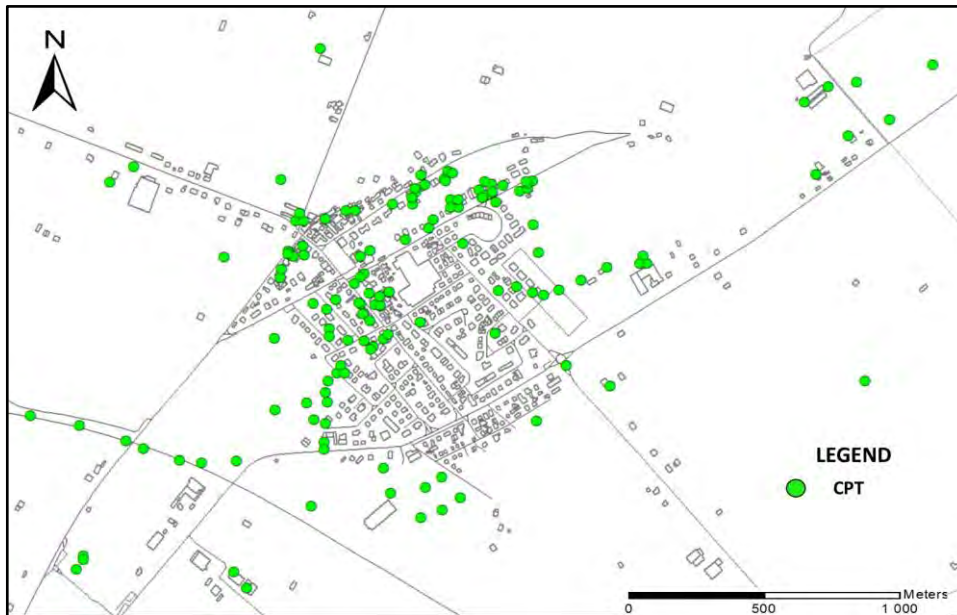


Figure 2.51. The Map shows the position of the CPTs available in the S. Carlo district

Preliminary Validation

For the study area of S. Carlo, punctual liquefaction (sand boils) and extensive cracking observations were merged to obtain a liquefaction-induced damage Map (Figure 2.52), built through a regular grid accounting for the distance between each centroids from such observations.

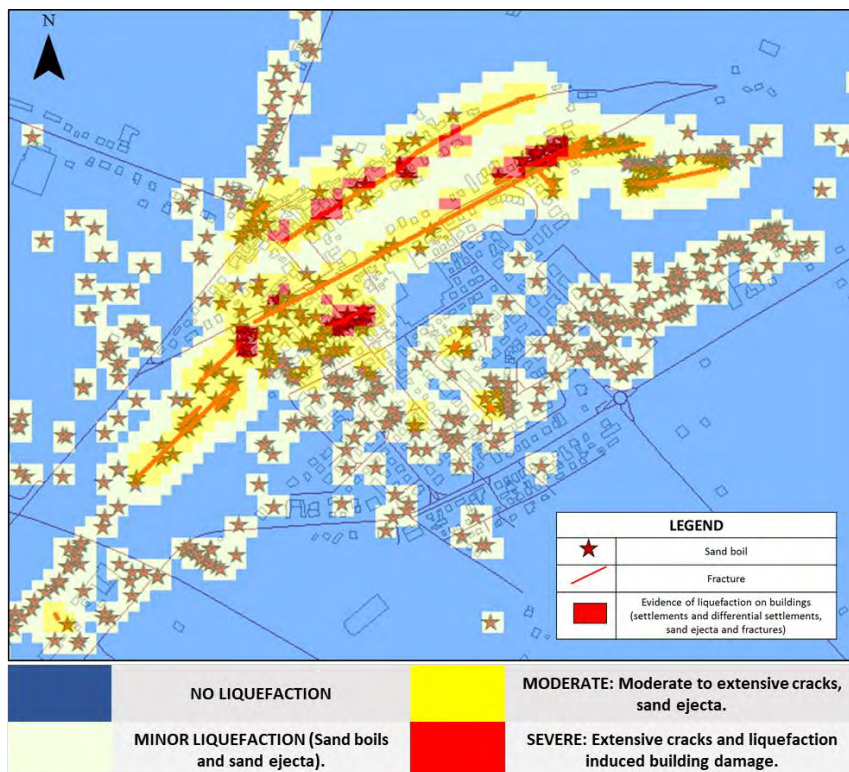


Figure 2.52. Liquefaction-induced land damage observations across S. Carlo district after the 20 May 2012 earthquake.



This project has received funding from the European Union's Horizon 2020 research and innovation programme under grant agreement No. 700748

The CPT data processing allowed to evaluate, for each profile: the non-liquefiable crust thickness, the thickness of the liquefiable layer, the average CRR.

Based on these parameters (H_{crust} , H_{liq} and CRR), each CPT can be classified with an equivalent soil profile (ESP), accounting for the depth, the size and the resistance of the liquefiable layer. The spatial distribution of the obtained ESPs plotted in **Figure 2.54** show a good consistency with the observation of damage on the studied area.

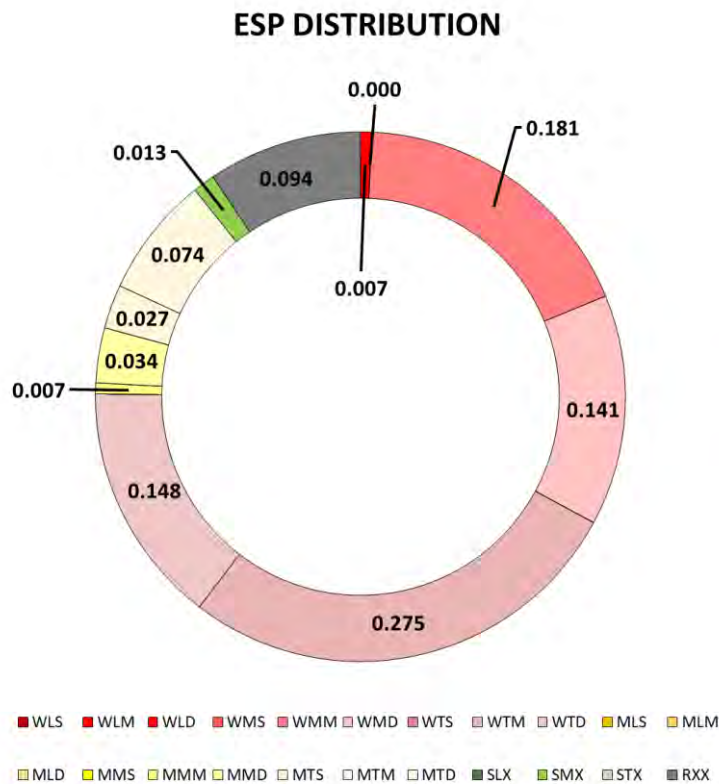


Figure 2.53. The statistical distribution of each equivalent soil profile is here shown; most of the analyzed CPTs highlights the widespread presence of a thin/midsized, deep and low resistance three strata equivalent soil profile (48% of all the CPTs).



This project has received funding from the European Union's Horizon 2020 research and innovation programme under grant agreement No. 700748

		WEAK	%	MID	%	STRONG	%	RESIST	%
LARGE	Shallow	WLS	0.00	MLS	0.00	SLX	0.00	RXX	9.40
	Mid.	WLM	0.00	MLM	0.00				
	Deep	WLD	0.67	MLD	0.00				
MIDSIZE	Shallow	WMS	0.00	MMS	0.00	SMX	1.34		
	Mid.	WMM	18.12	MMM	0.67				
	Deep	WMD	14.09	MMD	3.36				
THIN	Shallow	WTS	0.00	MTS	0.00	STX	0.00		
	Mid.	WTM	0.00	MTM	2.68				
	Deep	WTD	14.77	MTD	7.38				

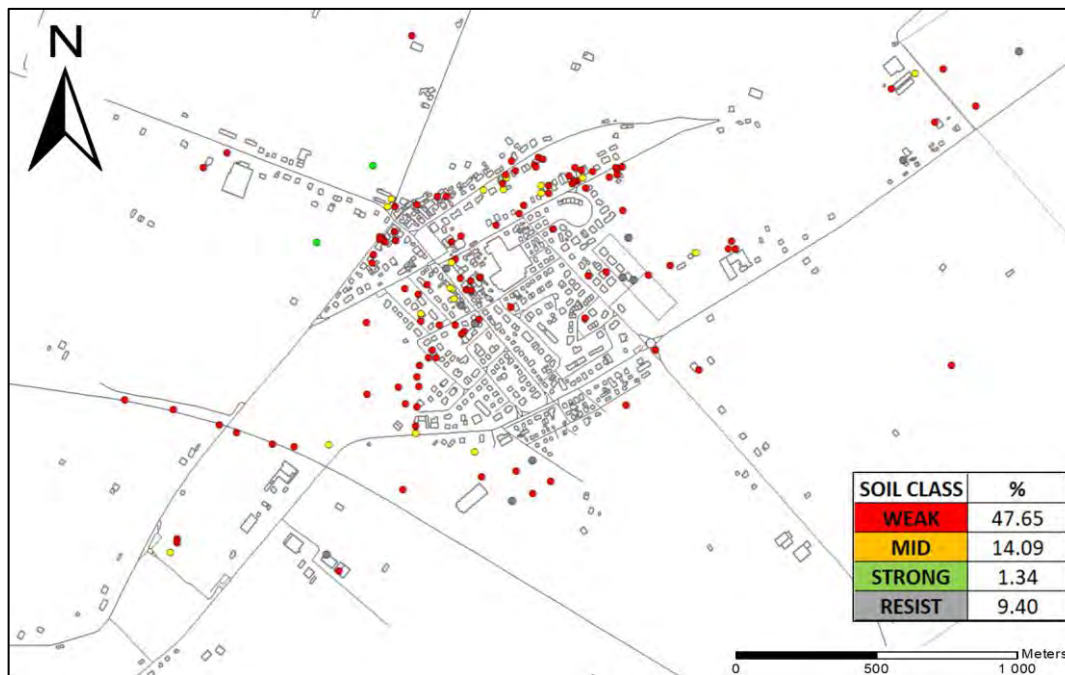


Figure 2.54. General overview of the ESP spatial distribution.

Conclusions

The ESP method has been applied to CPT records from two case studies, Christchurch (15000 CPTs) and San Carlo (150 CPTs). For the Christchurch study, the use of the normed error parameter suitably identified poor fitting of the ESP to indicate the possibility of multiple liquefiable layers and that human intervention would be required. Whereas for the San Carlo study all CPT records produced low normed error suggesting that a single liquefiable layer was suitable for classifying the deposits. In both case studies damage reports from recent earthquakes were used to evaluate the correlation between the ESP classification and reported damage. The ESP which classifies a soil profile based on the liquefaction resistance of a liquefiable layer, as well as the depth and thickness of the liquefiable layer provided a strong indicator of expected damage.

2.3.7 ARTIFICIAL EQUIVALENT SOIL PROFILES

An estimate of the correspondence between ESP classes and LSN values has been made to allow the backward estimate of likely ESPs in a region given a liquefaction severity estimate from a macro- or micro-zonation study. The study generated 200 random instances of each class, aggregated classes were sampled



This project has received funding from the European Union's Horizon 2020 research and innovation programme under grant agreement No. 700748

based on the number of aggregated classes (e.g. SLX was sampled 600 times, since the three thickness classes (shallow, mid-height and deep) were aggregated). For each instance the LSN was computed for four different hazard levels representing low moderate, high and severe seismicity (PGA values of 0.1g, 0.2g 0.35g and 0.5g for a magnitude 7.5 earthquake). The LSN values were then binned and through Bayes theorem, the percentage of each class in each bin represents the likely chance of that ESP given that LSN and PGA assuming the uniform sampling distribution is representative (see **Figure 2.55**). Therefore given an equivalent magnitude 7.5 PGA and LSN value the likely distribution of ESPs can be selected from the charts in **Figure 2.55**. The PGA values from different magnitude events can be converted to an equivalent magnitude 7.5 event using the magnitude scaling factor (Idriss and Boulanger (2008)). In fact, in cases where the soil is highly stratified and the CRR-fitted method (section 2.3.3) provides a poor fit, then an alternative LSN-compatible classification could be achieved by triangulation using the charts. The LSN value can be computed for the CPT or SPT record at each of the four different equivalent PGA levels and then averaging the percentages for each class from each chart to obtain the class with the highest percentage.

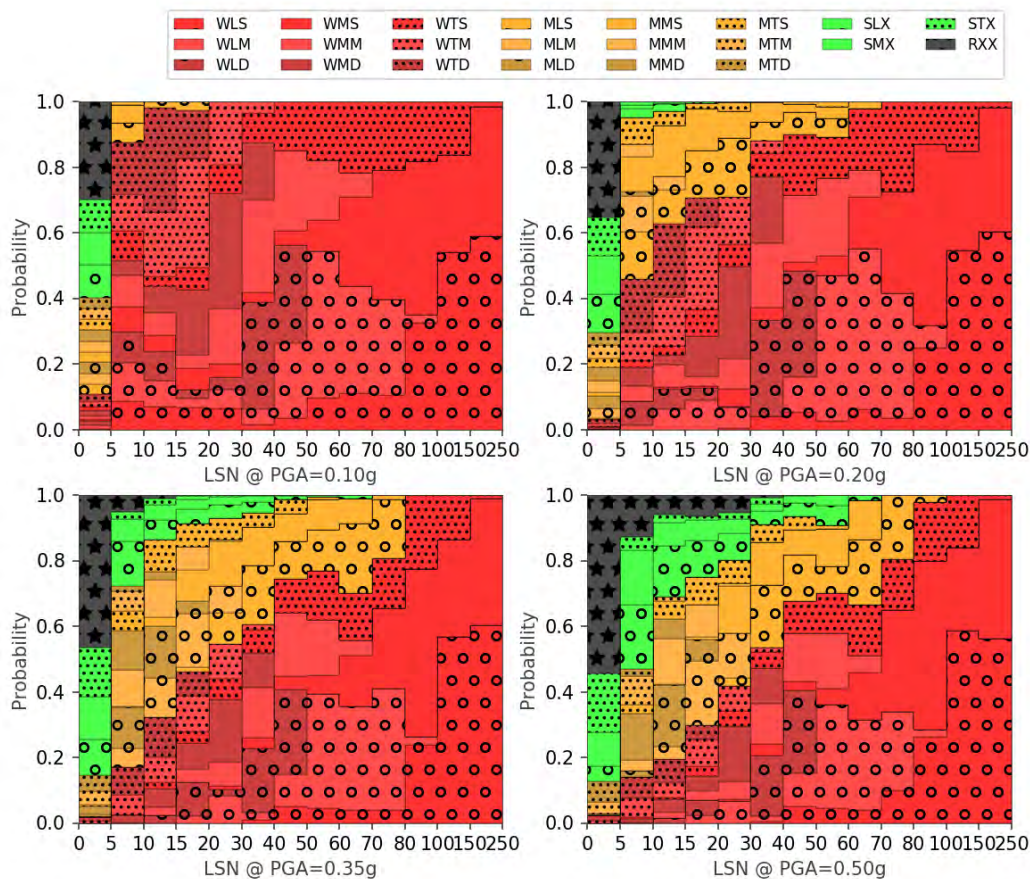


Figure 2.55. LSN vs equivalent soil profile classes at different seismic demand levels

The charts can be further simplified into severity classes where the original classes from Tonkin and Taylor (2013) were aggregated to provide just four severity classes (**Table 2.5**). The simplified charts are shown in **Figure 2.56** for the different expected seismic and liquefaction severity.



This project has received funding from the European Union's Horizon 2020 research and innovation programme under grant agreement No. 700748

Table 2.5: Liquefaction severity classes for ESP classification from macro-zonation

Severity	LSN range	Tonkin and Taylor (2013) description
Low	0 – 10	“Little to no expression of liquefaction, minor effects”
Moderate	10 - 30	“Minor expression of liquefaction, some sand boils” to “Moderate expression of liquefaction, with sand boils and some structural damage”
High	30 - 50	“Moderate to severe expression of liquefaction, settlement can cause structural damage” to “Major expression of liquefaction, undulations and damage to ground surface, severe total and differential settlement of structures”
Severe	>50	“Severe damage, extensive evidence of liquefaction at surface, severe total and differential settlements affecting structures, damage to services.”

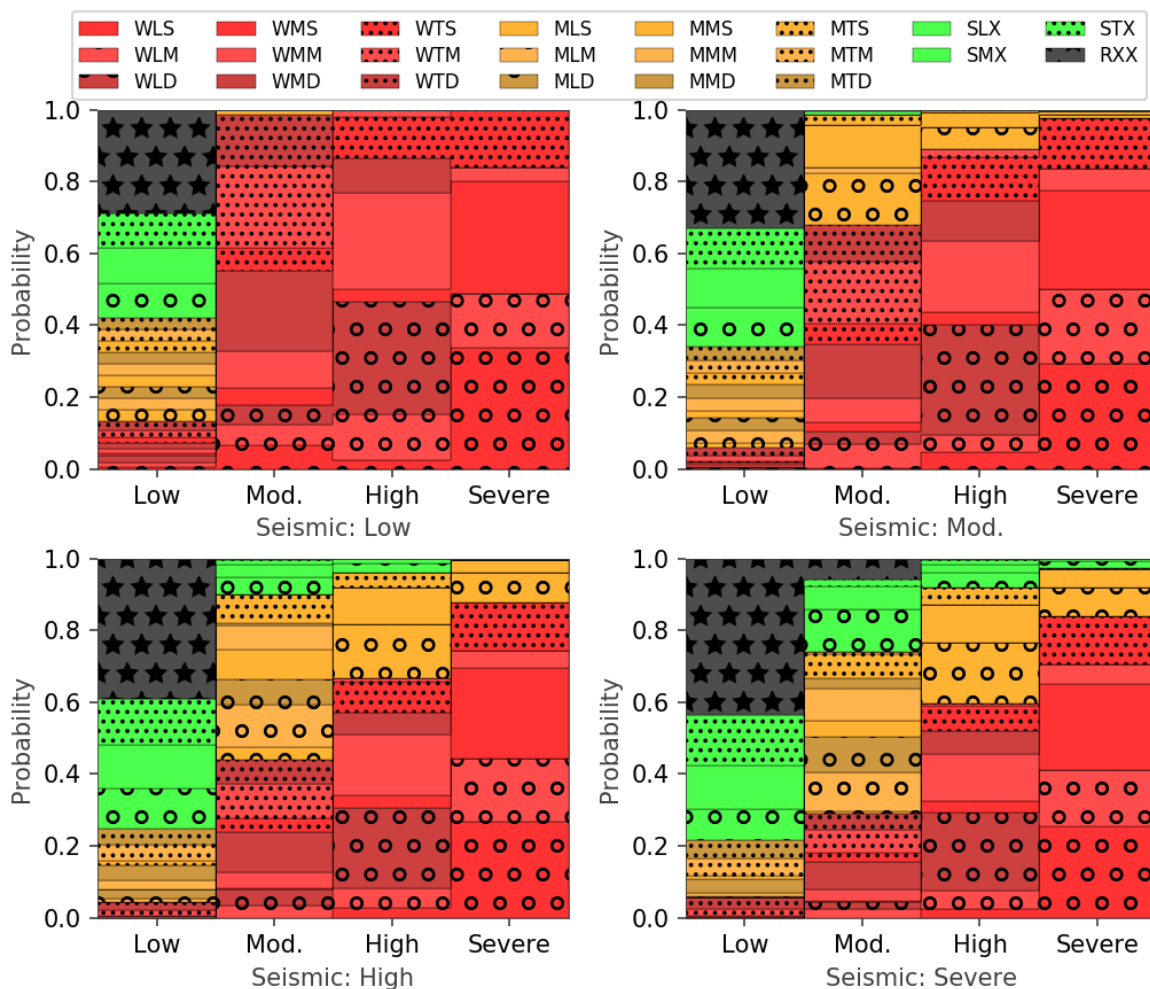


Figure 2.56. Liquefaction severity vs equivalent soil profile class for different levels of seismic hazard

From **Figure 2.56** it can be seen that in all cases there are many different ESP classes present. In the case where seismic and liquefaction severity are provided at multiple return periods then average of multiple charts can be used to estimate the distribution of profiles. However, this still provides a poorly defined



This project has received funding from the European Union's Horizon 2020 research and innovation programme under grant agreement No. 700748

liquefaction classification as weak deep profiles gives very different response to shallow strong profiles. Therefore it is highly recommended that further field testing (e.g. CPT or SPT) is performed to reduce the uncertainty in any vulnerability analysis.

2.3.8 SUMMARY

This section focused on introducing a new methodology for obtaining a simplified equivalent three-layered soil profile based on the liquefaction assessment of the soil profile from CPT data. The equivalent soil profile (ESP) is defined as a soil profile classification tool for the purpose of the seismic response of shallow-founded buildings in liquefied soils. This methodology uses three governing parameters: the depth of the crust (D_{liq}), the thickness of the liquefied layer (H_{liq}) and its shear strength (CRR_{n15}). Typical ranges of values for each of these variables have been defined, from which 22 different soil profile classes are derived.

The calibration of the methodology was based on the analysis of 8818 CPT tests at a site in Christchurch and 150 CPT tests in San Carlo, in which a majority of mid-strength shallow profiles were classified. The comparison between the generated equivalent soil profiles and the respective LSN classification was established to demonstrate the applicability of this new simplified approach to the assessment of severity liquefaction-induced damages. The use of this ESP classification for bearing capacity analysis in liquefied soils has the advantages of being capable of reproducing the actual response of the soil profile across the full hazard range using just three intuitive parameters, while providing simple implementation for numerical simulations, as the information can be directly related to the performance of shallow-founded buildings.

2.4 ESTIMATION OF SITE RESPONSE AND SOIL-STRUCTURE INTERACTION USING EFFECTIVE STRESS ANALYSIS

2.4.1 INTRODUCTION

Numerical modelling can be employed to simulate the seismic response of buildings on liquefiable soils given a suite of acceleration time histories for a specified earthquake scenario. This approach has been used in this research to estimate the behaviour of structures founded on soils profiles containing three layers, a crust, a liquefiable sand and a clayey deeper layer. This procedure requires the use of an advanced constitutive model that is able to reproduce liquefaction stress-strain behaviour and pore water pressure generation.

The PM4Sand constitutive model (Boulanger and Ziotopoulou, 2017) was implemented in the commercial software, FLAC 8.0 (Itasca, 2016) as a user defined material in a dynamic link library (DLL). This computer platform uses the finite difference method to solve the equations of motion and uses an explicit Lagrangian solution scheme, which allows large deformations problems to be solved (Itasca, 2016). The bulk modulus of the fluid as well as drained, undrained, or fully coupled stress-flow conditions may be specified.

PM4Sand is a sand plasticity model for geotechnical earthquake engineering applications. This model follows the basic framework of the stress-ratio controlled, critical state compatible, bounding surface plasticity model for sand presented by Dafalias and Manzari (2004). Modifications to the model were developed and implemented by Boulanger (2010) (version 1), Boulanger and Ziotopoulou (2012) (version 2), Boulanger and Ziotopoulou (2015) (version 3), and further by Boulanger and Ziotopoulou (2017) (version 3.1) to improve its



This project has received funding from the European Union's Horizon 2020 research and innovation programme under grant agreement No. 700748

ability to approximate the stress-strain responses important to geotechnical earthquake engineering applications.

The model parameters are grouped into two categories; a primary set of six parameters (three properties, two flags, and atmospheric pressure) that are most important for model calibration, and a secondary set of parameters that may be modified from their default values in special circumstances (Boulanger and Ziotopoulou, 2017). The primary model input properties of soil are:

- D_r - an apparent relative density which affects the peak drained and undrained strengths and the rate of strain accumulation during cyclic loading
- G_o - the shear modulus coefficient related with the shear modulus (G , this one corresponding $G_{max} = Vs^2$) which should be calibrated to the estimated or measured in-situ shear wave velocity
- h_{po} - the contraction rate parameter which is used to calibrate to the estimated in-situ cyclic resistance ratio (CRR) after all other properties have been set.

A detailed description about the constitutive model characteristics can be found in Boulanger and Ziotopoulou (2017).

To validate the efficacy of the numerical modelling, numerical platform and the constitutive model that will be used in this study, centrifuge experiments involving soil-structure systems were replicated in the software mentioned. Two cases of the centrifuge tests (T3-30 and T6-30) performed by Dashti et al (2010) were selected to be simulated. The analyses were performed in the prototype scale. These centrifuge experiments were already modelled numerically by Dashti and Bray (2013) and Ziotopoulou and Montgomery (2017). This section outlines the key aspects of the numerical modelling that were taken in the development of the model.

2.4.2 OVERVIEW OF FLAC MODEL

A nonlinear dynamic SSI effective stress analysis of the response of one of the structures of the centrifuge tests was performed. The structural models in the centrifuge experiments acted essentially as independent systems because the distance centre to centre was approximately four times their widths.

Model construction

The considered soil profile has three distinguishable layers with a total model thickness of 26 m and width of 90 m, sufficiently large to capture free-field conditions, avoid wave reflections and reduce the influence of the lateral boundaries on the response of the footing. In the T3-30 case, the first layer (surface) is 2.0 m thick, the second layer is 3.0 m thick and the third layer is 21.0 m thick. In the T6-30 case, the first layer (surface) is 2.0 m thick, the second layer is 6.0 m thick and the third layer is 18.0 m thick. The water table was set at a depth of 2.0 m. The considered numerical model is shown in **Figure 2.57**.



This project has received funding from the European Union's Horizon 2020 research and innovation programme under grant agreement No. 700748

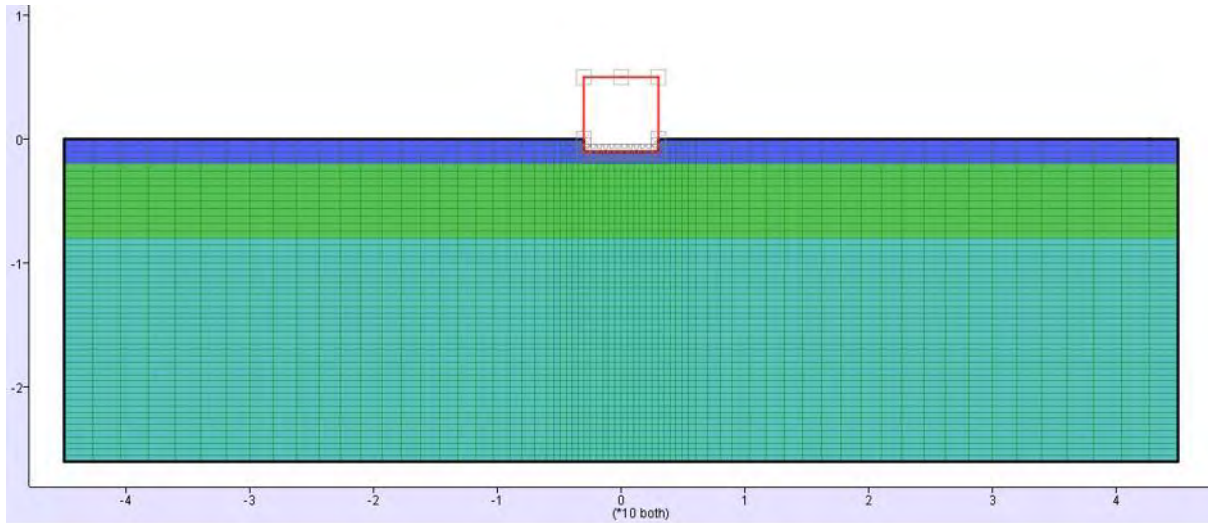


Figure 2.57: Numerical model of Dashti centrifuge test

The finite difference mesh was refined in the region closer to the footing and gradually coarsened towards the left and right boundaries to provide a better discretization in the area of interest. The lateral nodes at each depth were attached so they moved together.

Input of an earthquake motion into this software is typically done using either a 'rigid base' or a 'compliant base (also referred to as absorbing)'. In this case, the base was considered as rigid to represent the base of the centrifuge box. For a rigid base, a time-history of acceleration (or velocity or displacement) is specified for grid points along the base of the mesh (Mejia and Dawson, 2006).

Ground motions

Three shaking events were applied in the centrifuge experiments. The input motions consisted of a sequence of scaled versions of the North-South, fault-normal component of the ground motion recorded at a depth of 83 m in the Kobe Port Island down-hole array during the 1995 Kobe Earthquake. The moderate and large Port Island events were used for this numerical study. The peak acceleration PGAs of the moderate and large motions is approximately 0.15 and 0.55 g, respectively (Dashti et al, 2010). **Figure 2.58** shows the input acceleration-time histories.



This project has received funding from the European Union's Horizon 2020 research and innovation programme under grant agreement No. 700748

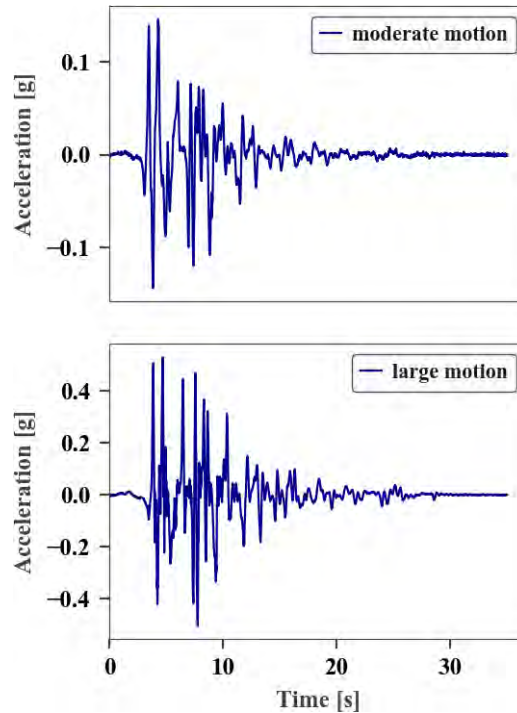


Figure 2.58: Motions applied in the numerical model of centrifuge experiments

Structure

The structure A in Dashti et al (2010) was selected to be used in the numerical model. The height and width of the structure was 6.0 metres. The building elements were modelled as beam elements available in the software (Figure 2.57). The building contact pressure ($q=80\text{kPa}$) in the experiments was distributed in four elements, 40% for the foundation, 5% for each column and 50% for the top element, allowing calculate the density of each beam element. The stiffness of the columns was adjusted to obtain the fundamental period for the structure ($T=0.21$ sec) in the experiments by means of Equation (2.23) and (2.24) where K is the stiffness of a portal frame deforming only in shear, L is the length of the columns (6 metres), I is the moment of inertia, m is the mass and T is the period of the structure. The top and bottom beams were 100 times stiffer than the column elements.

$$E = \frac{K \cdot L^3}{2 \cdot 12} \quad (2.23)$$

$$K = \frac{4 \cdot \pi^2 \cdot m}{T^2} \quad (2.24)$$

Unglued interface elements were applied between the footing and the surrounding soil to account for the frictional interaction between the two. A friction and dilation angle of 33 degrees and 0 degrees respectively were assigned and slip was allowed. Within the code, the interface is represented as a series of normal and shear springs that connect the opposing surfaces at interacting nodes. The corresponding normal and shear stiffnesses of the springs were both set to 20 MPa.



This project has received funding from the European Union's Horizon 2020 research and innovation programme under grant agreement No. 700748

Material models

All the layers are composed of sandy material. Both, static and dynamic parameters were taken from Ziotopoulou and Montgomery (2017). Mohr-Coulomb constitutive model was used in the three layers to calculate the initial stresses in the soil profile before the dynamic load to be applied. **Table 2.6** gives the list of input parameters for the static phase.

Table 2.6: Mohr-Coulomb parameters in numerical model from Dashti centrifuge experiment

Parameter	Unit	Layer 1	Layer 2	Layer 3
Density (ρ_{dry})	kg/m^3	1927	1669	1978
Shear modulus (tt)	kPa	1.11×10^5	5.35×10^4	1.18×10^5
Friction angle (φ)	$^\circ$	33.0	33.0	33.0
Cohesion (c)	kPa	0.0	0.0	0.0
Porosity (η)	–	0.270	0.375	0.259
Permeability (k_H)	m/s	1.7×10^{-5}	1.7×10^{-5}	1.73×10^{-5}

The permeability of any material should be set by the mobility coefficient (coefficient of the pore pressure term in Darcy's law) required by FLAC and designated by k ($m^2/Pa \cdot sec$) (Itasca, 2016).

This mobility coefficient could be related to hydraulic conductivity, designated by k_H (m/s), usually termed as “coefficient of permeability”, by means of:

$$k = \frac{k_H}{g \cdot \rho_w} \tag{2.25}$$

where g is the gravitational acceleration and ρ_w is the water density. It could also be specified an anisotropic permeability related to the components k_{xx} , k_{yy} and k_{xy} .

The PM4Sand constitutive model (Boulangier and Ziotopoulou, 2017) was adopted to simulate the three layers in the dynamic phase. **Table 2.7** gives the list of the input primary properties, while the secondary set of parameters were kept default.

Table 2.7: PM4Sand parameters in numerical model from Dashti centrifuge experiments

Parameter	Unit	Layer 1	Layer 2	Layer 3
Relative density (D_R)	–	0.86	0.30	0.90
Shear modulus coefficient (Go)	–	1092	427	1162
Contraction rate parameter (h_{po})	–	0.56	0.055	0.06



This project has received funding from the European Union's Horizon 2020 research and innovation programme under grant agreement No. 700748

2.4.3 VALIDATION IN 2D ANALYSIS

Results between the numerical simulations and centrifuge tests were compared in terms of settlements of the building and the pore pressure generation in the centre of the liquefiable layer (under the building and in free-field). The settlements results for the centre of the footing are shown in **Figure 2.59**. The time history of building settlement from the numerical simulation is compared with the centrifuge results in **Figure 2.60** for the experiment T3-30 using the Moderate ground motion.

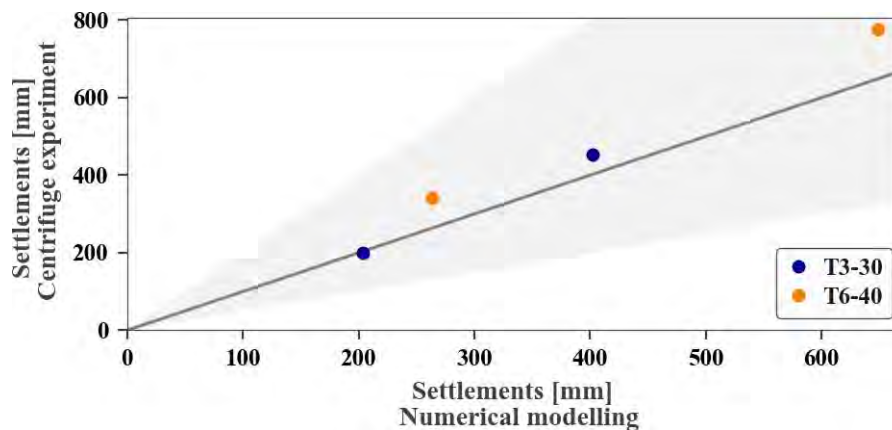


Figure 2.59: Comparison between numerical and experimental values of settlements of the building

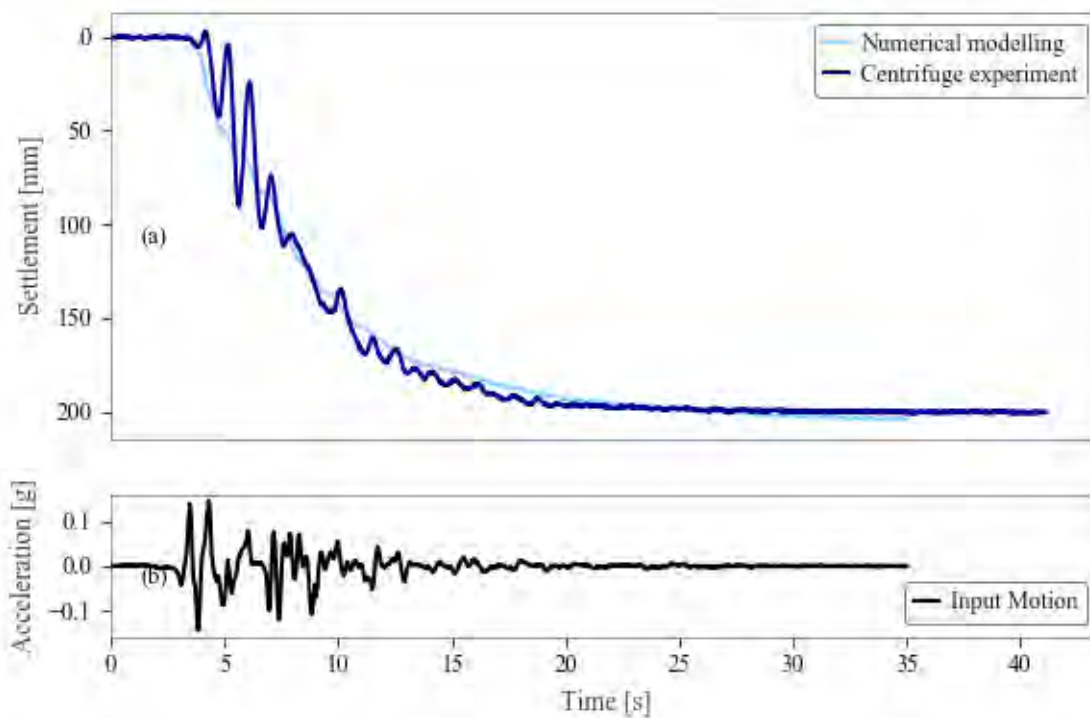


Figure 2.60: Comparison between numerical and experimental settlement for the experiment T3-30



This project has received funding from the European Union's Horizon 2020 research and innovation programme under grant agreement No. 700748

The comparison between the numerical and experimental values of pore pressure under the building and in free-field is shown in **Figure 2.61**. The time history of pore pressure from the numerical simulation is compared with the centrifuge results in **Figure 2.62** for the experiment T3-30 using the Moderate ground motion.

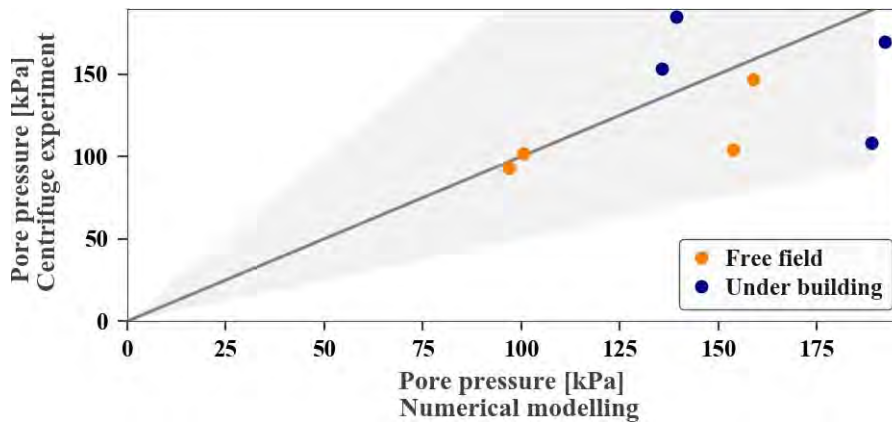


Figure 2.61: Comparison between numerical and experimental values of pore pressure

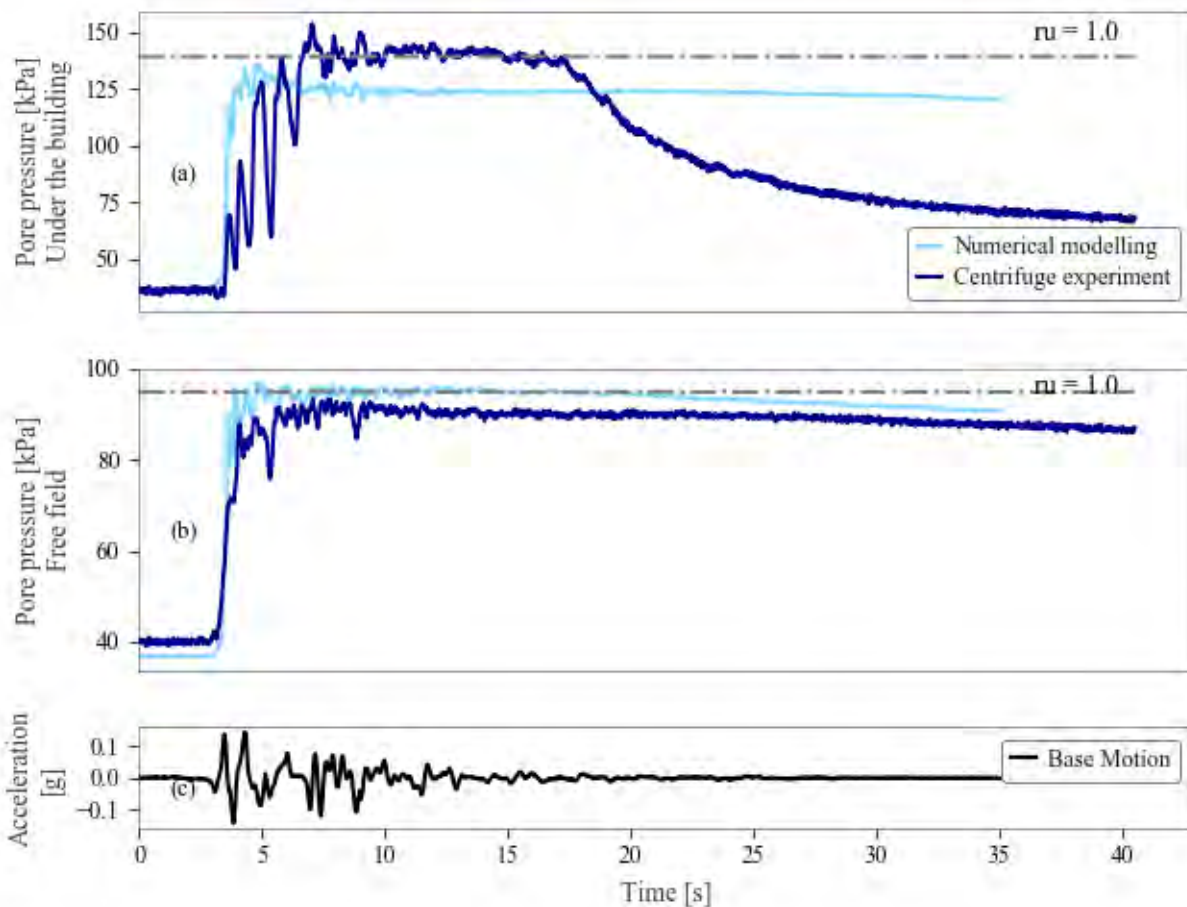


Figure 2.62: Comparison between numerical and experimental pore pressure for the experiment T3-30



This project has received funding from the European Union's Horizon 2020 research and innovation programme under grant agreement No. 700748

The surface acceleration in free-field were also compared through the response spectra (S_a). **Figure 2.63** shows the comparison between acceleration response spectra at the surface of the model for the recorded motions in the centrifuge experiment and the calculated in the numerical analyses for both experiments and ground motions. The Moderate ground motion was captured reasonably well but the Large ground motion is significantly underestimated. **Figure 2.64** and **Figure 2.65** show the acceleration signal in the surface (free-field) and the Stockwell transform.

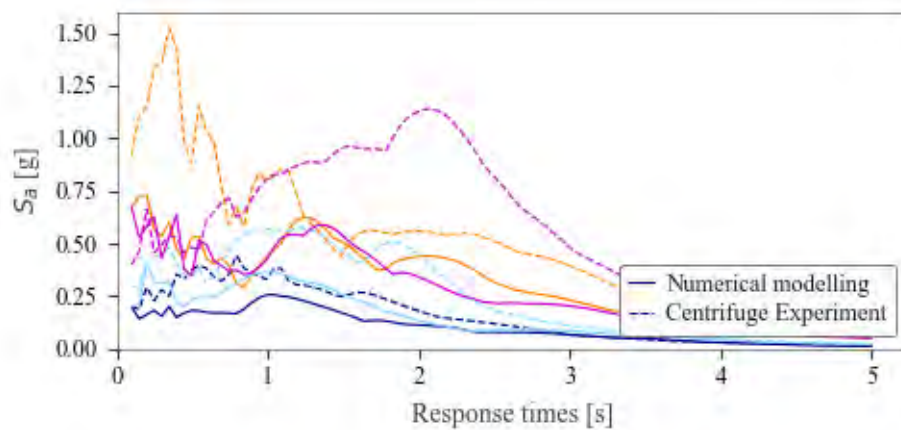


Figure 2.63: Comparison between numerical and experimental response spectra of the surface acceleration (free-field)

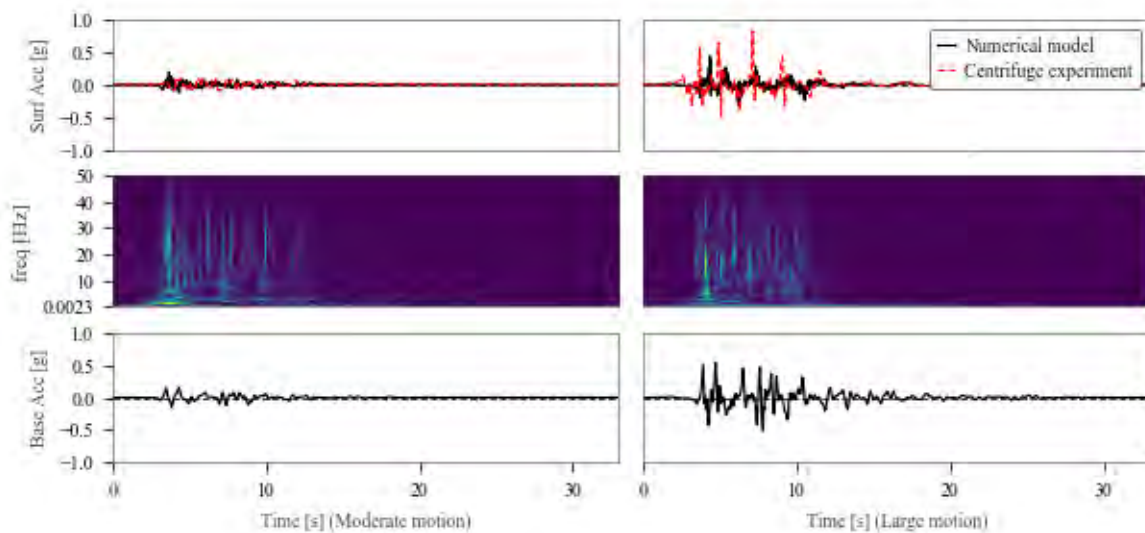


Figure 2.64: Surface acceleration (free-field) comparison for the experiment T3-30



This project has received funding from the European Union's Horizon 2020 research and innovation programme under grant agreement No. 700748

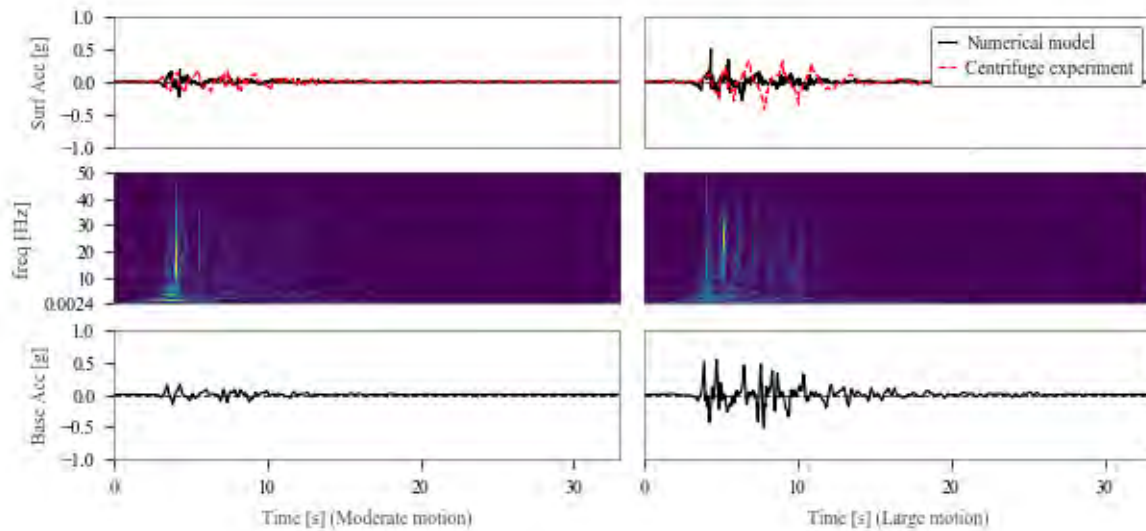


Figure 2.65: Surface acceleration (free-field) comparison for the experiment T6-30

2.4.4 CONCLUSIONS

A procedure for modelling pore pressure, site response and settlement using effective stress analysis with FLAC and PM4Sand was presented and validated against centrifuge tests. Settlement results are in relatively close agreement with the centrifuge test for both experiments and ground motions. The validation results show that pore pressures in the free-field are in more close agreement than the pore pressures under the building, but these validation results were considered satisfactory for the scope of this study.

2.5 SIMPLIFIED PROCEDURE TO ESTIMATE PORE PRESSURE IN FREE FIELD

2.5.1 INTRODUCTION

Earthquake-induced liquefaction can cause significant damages to buildings as seen by recent events in Christchurch (Diaz, 2016) (Bray et al., 2017). Although important technical achievements in understanding and mitigating liquefaction have been accomplished in the last decades, significant damage still occurs in seismic areas around the world. The generation of excess pore water pressure and liquefaction can dramatically change the dynamic response of a soil deposit and interacting structures. Thus, the time at which liquefaction occurs, may have a significant influence on the performance of a structure during a seismic event (Kramer et al., 2016). In fact, the amplification or reduction of the surface shaking due to liquefaction, in terms of peak values, as well as the frequency content of the modified motion and the geotechnical specificities of the site affects the ground motion arriving at the surface (Kramer et al., 2011). For that reason, liquefiable soils may result in bearing capacity degradation and seismic settlement accumulation of shallow foundations (Jafarian et al., 2017).

For that reason, the value of estimating the pore pressure evolution during an event is recognized. First, this allows the definition of the time to liquefaction (t_{liq}), i.e., the point when there is a change in state from solid to liquid. The information of whether liquefaction happens early or late in a particular ground motion can be invaluable for estimating surface damage. On the other hand, the pore pressure time series will allow the



This project has received funding from the European Union's Horizon 2020 research and innovation programme under grant agreement No. 700748

estimation of flow rates between layers and also the extent of pore pressure build up whether it reaches a state of liquefaction or not. In fact, a partially liquefied soil can still experience considerable softening behaviour that can alter the dynamic properties of soil-structure systems as well as modify the upward propagating shear waves. While liquefaction triggering depends on the liquefaction criteria (for example, the achievement of a certain pore pressure ratio defined by the ratio between the excess pore pressure and the initial effective stress) the pore pressure time series shows to what extent liquefaction occurs. As an example, **Figure 2.66** presents two different pore pressure time series, in terms of the pore pressure ratio defined as the ratio of the excess pore pressure by the initial effective vertical stress ($r_u = \Delta u / \sigma'_{v0}$). While the second clearly liquefies no matter which liquefaction criteria is applied, the first has a slower pore pressure build up that does not reach $r_u = 1$. Still, there is a significant pore pressure ratio ($r_u = 0.7$) which may result in partial liquefaction, liquefaction of part of the layer or even the supply of pore water to other layers that may liquefy. There are advanced nonlinear effective stress analysis techniques for evaluating the time of liquefaction. Unfortunately, these approaches require an extensive number of soil parameters, and non-trivial decisions about constraining the domain of the analysis (e.g. depth of the model). Whereas, simplified methods that have been developed for the assessment of liquefaction triggering, often have biases or simplifications that are suitable for triggering assessment, but provide a significant drawback for the more sensitive assessment of the time of triggering. In this section different approaches to estimate pore pressure from the simplified methods to the more complex numerical analysis will be discussed in terms of their advantages, limitations and uncertainties.

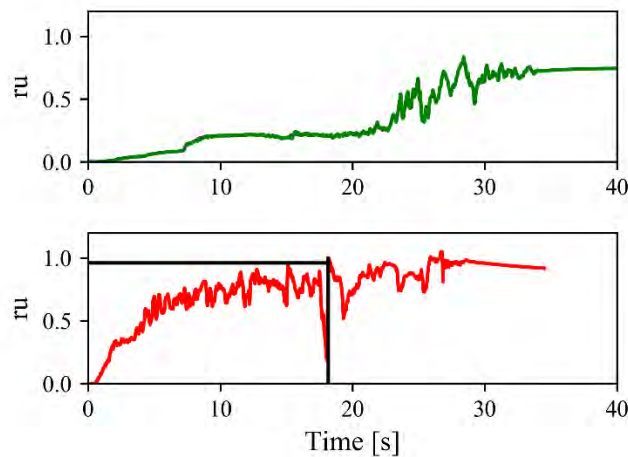


Figure 2.66: Pore pressure time series for two different cases

2.5.2 BACKGROUND

The prediction excess pore pressure has been extensively studied in the past decades due to its importance in triggering liquefaction and several simple empirical methods have been developed. These can be divided in three main groups: stress based, strain based and energy based. Stress-based methods were the first to be developed resulting from observations made on stress-controlled cyclic triaxial tests where an uniform shear stress is applied measuring the build- up of pore pressure with increasing number or cycles. It was shown that the build- up of pore pressure is more accurately predicted by cyclic shear strains and therefore



This project has received funding from the European Union's Horizon 2020 research and innovation programme under grant agreement No. 700748

strain controlled cyclic simple shear tests have been used to measure pore pressure build-up. In addition, strain based methods from numerical analysis have been proposed (Dobry et al., 1985) (Ivšić, 2006). On a different perspective, several energy based methods have been presented, following the assumption made by Nemat-Nasser et al. (1979) that pore water pressure generation can be uniquely related to the cumulative energy dissipation per unit volume of soil up to the onset of liquefaction. The stress based method will be described in detail due to its wide application, as well as the energy based methods that have some promising advantages.

Stress-based methods

The stress based method started with Seed et al. (1975), proposing equation (2.25) for the pore pressure model, which was simplified by Booker et al. (1976) with equation (2.27):

$$r_u = \frac{1}{2} + \frac{1}{\pi} \arcsin \left[2 \left(\frac{N}{N_L} \right)^{1/\beta} - 1 \right] \quad (2.26)$$

$$r_u = \frac{2}{\pi} \arcsin \left[\left(\frac{N}{N_L} \right)^{1/2\beta} \right] \quad (2.27)$$

where,

r_u is the pore pressure ratio

N is the equivalent number of uniform cycles

N_L is the number of cycles required to cause liquefaction

β is an empirical parameter

N_L and β , can be determined by cyclic triaxial tests. For a given soil, N_L increases as relative density increases and decreases as the magnitude of loading increases, with the magnitude of loading expressed in terms of Cyclic stress ratio (CSR). The use of N_L has its drawbacks as it can only be applied to liquefiable soils (Polito et al., 2008). However, “nonliquefiable” soils, such as dense sands and soils with plastic fines, can still undergo significant pore pressure increases and deformations as a result of cyclic softening (Boulanger et al., 2006). Booker et al. (1976) proposed a value of 0.7 for β , while Polito et al. (2008) proposed the following empirical equation:

$$\beta = c_1 FC + c_2 Dr + c_3 CSR + c_4 \quad (2.28)$$

where FC is the fines content, Dr is the soil relative density, and c_1 , c_2 , c_3 and c_4 are regression constants which vary with the fines content. For $FC < 35\%$: $c_1=0.01166$; $c_2=0.007397$; $c_3=0.01034$; and $c_4=0.5058$; and for $FC \geq 35\%$: $c_1=0.002149$; $c_2=-0.0009398$; $c_3=1.667$; and $c_4=0.4285$.

The number of uniform cycles (N) equivalent to an irregular earthquake ground motion can be obtained by the weighting scheme proposed by Seed et al. (1975) which was later used by Idriss (1999), Liu et al. (2001), Boulanger et al. (2006), Kishida et al. (2014). The Seed stress based model considers a power relationship between the cyclic stress ratio and the number of cycles – equation (2.29):

$$CSR = a \cdot N^{-b} \quad (2.29)$$



This project has received funding from the European Union's Horizon 2020 research and innovation programme under grant agreement No. 700748

where a and b are fitting parameters

Therefore, for two individual stress cycles with CSR_A and CSR_B , the relative number of cycles to cause failure at these two stress ratios is easily obtained (equation (2.30)). Assuming a reference value of uniform cycles for the magnitude of 7.5 ($N_{M=7.5}$), the obtained ratios of CSR correspond to the definition of a magnitude scaling factor (MSF) used in the Seed simplified procedure to calculate the seismic demand of liquefaction potential with equation (2.31). Also the MSF can be calculated using equation (2.32) from Idriss et al. (2008) or material dependent equations for MSF can be found in Boulanger et al. (2016). There have been several proposals for the b parameter such as $b=0.34$ for sands (Idriss, 1999) and $b=0.135$ for clays and plastic silts (Boulanger et al., 2006).

$$\frac{N_A}{N_B} = \left(\frac{CSR_B}{CSR_A} \right)^{1/b} \Leftrightarrow MSF = \frac{CSR_M}{CSR_{M=7.5}} = \left(\frac{N_{M=7.5}}{N_M} \right)^b \quad (2.30)$$

$$CSR_{M=7.5} = 0.65 \cdot PGA \cdot \frac{\sigma_{v0}}{\sigma'_{v0}} \cdot r_d \cdot \frac{1}{MSF} \quad (2.31)$$

$$MSF = 6.9 \cdot e^{-M/4} - 0.058 \leq 1.8 \quad (2.32)$$

where

PGA is the peak ground acceleration in g

r_d is parameter related with the depth

$\frac{\sigma_{v0}}{\sigma'_{v0}}$ is the overburden stress ratio

More recently a simple approach by Kramer et al. (2016) adapts the stress-based procedure from Boulanger et al. (2016) to obtain a time dependent, magnitude corrected peak ground acceleration that could be used to estimate the time of liquefaction.

To avoid the evaluation of the equivalent number of cycles corresponding to an earthquake of given magnitude, other formulations were proposed within the framework of the “endochronic theory” (e.g., Finn et al., 1982) expressing the pore pressure build up as a function of the so called “damaged parameter” which can be computed for both uniform or irregular time histories. Following Finn et al. (1982) other authors proposed additional formulations: Ivšić (2006), Park et al. (2015), Chiaradonna et al. (2018)

Energy-based methods

Energy based methods are formulated on different set of assumptions to stress based methods and therefore have some unique advantages:

- While stress based methods typically rely on instantaneous quantities such as peak ground acceleration (PGA), energy based methods use cumulative intensity measures, which typically have lower dispersion.
- Energy based methods are typically load amplitude independent, and therefore can quantify liquefaction resistance as a single value, compared to stress based methods which use a relationship between amplitude and number of constant stress cycles.



This project has received funding from the European Union's Horizon 2020 research and innovation programme under grant agreement No. 700748

- For constant amplitude input motion, stresses decrease as pore pressure increases, whereas energy is conserved;

The development of an energy-based liquefaction triggering method was first proposed by Davis et al. (1982) following the assumption made by Nemat-Nasser et al. (1979) that the pore pressure build-up is linearly correlated to the amount of dissipated seismic energy per unit volume of soil, which is a function of the standard penetration value, the initial effective overburden stress and the energy arriving at a site. The full expression for the pore pressure increase is the following:

$$\Delta u = \frac{C(N_1)}{r^2 \sqrt{\sigma'_0}} 10^{1.5M} \quad (2.33)$$

where,

M is the earthquake magnitude

r is the distance of a site from the centre of energy release

σ'_0 is the initial effective overburden stress

$C(N_1) = c_1 \cdot c_2 \cdot \lambda(N_1) \cdot 10^{1.8}$ determined empirically from a study of liquefaction case histories being N_1 the average corrected standard penetration value

Later on, Berril et al. (1985) have proposed another relationship:

$$r_u = \beta \cdot W^\xi \quad (2.34)$$

where W is the energy dissipated per unit volume of the soil normalized by the initial effective confining pressure, defined as follows:

$$W = \frac{1}{\sigma'_0} \int_0^t \tau \cdot d\gamma \quad (2.35)$$

being τ the shear stress and γ the shear strain. For undrained cyclic triaxial test loadings W is the cumulative enclosed area of the shear stress–strain loops, which can be computed by:

$$W = \frac{1}{2\sigma'_0} \sum_{i=1}^{n-1} (\sigma_{d,i+1} + \sigma_{d,i}) (\varepsilon_{a,i+1} - \varepsilon_{a,i}) \quad (2.36)$$

where σ_d is the applied deviator stress at a load increment and ε_a is the axial strain at a load increment.

Green et al. (2000) proposed a simplified relationship to estimate pore pressure based on the dissipated energy and PEC the “pseudoenergy capacity”:

$$r_u = \sqrt{\frac{W}{PEC}} \leq 1 \quad (2.37)$$



This project has received funding from the European Union's Horizon 2020 research and innovation programme under grant agreement No. 700748

where, PEC is basically the dissipated energy at liquefaction and it can be determined from cyclic test data by simply dividing the value of W at $r_u=0.65$ by 0.4225. In 2008, Polito et al. (2008) proposed a new equation to calculate PEC.

More recently, Kokusho (2013) proposed a simplified liquefaction triggering procedure. For the estimation of the soil capacity, CSR_{20} is evaluated with correlations with SPT blow counts and then normalised dissipated energy is estimated as indicated by **Figure 2.67** for two different liquefaction criteria defined by double amplitude axial strains of 2% and 5%.

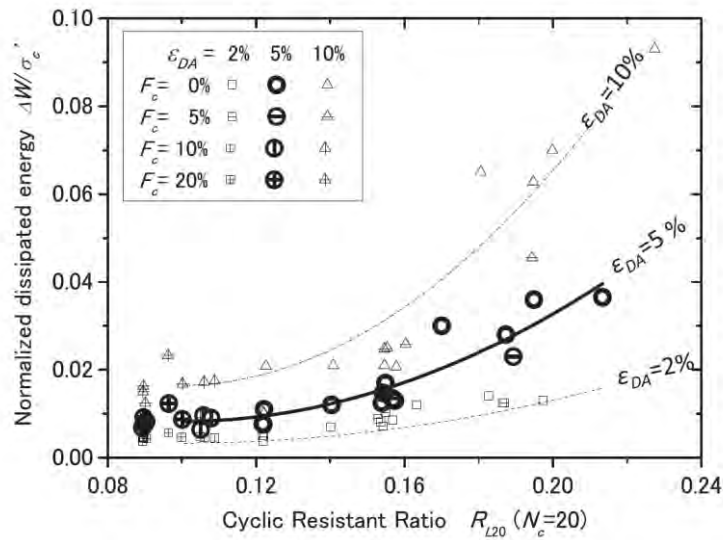


Figure 2.67: Relationship between normalised dissipated energy and CSR_{20} (Kokusho, 2013)

The dissipated energy (ΔW) is then converted to the strain energy (W) by the following equation:

$$\frac{W}{\sigma'_c} = 5.4 \times 10^{1.25 \cdot \log(\Delta W / \sigma'_c)} \quad (2.38)$$

From the strain energy, the strain capacity of the soil is computed by multiplying the strain energy by the thickness of the layer, which is compared to the upward energy.

In fact, in this method the demand is estimated by the upward energy density calculated by equation (2.39)

$$E_u = \rho V_s \int (\ddot{u})^2 dt \quad (2.39)$$

where,

\ddot{u} is the particle velocity of seismic waves propagating in the upward direction, obtained by integration of base acceleration;

ρ is the soil density;

V_s is the S-wave velocity.

To identify liquefaction triggering the energy ratios of individual layers are numbered sequentially starting from the lowest ratio and summed up. According to Kokusho (2013) liquefaction occurs in that sequence and



This project has received funding from the European Union's Horizon 2020 research and innovation programme under grant agreement No. 700748

in those layers for which the sum is lower than 1, because the upward energy can liquefy individual sand layers in the mentioned sequence until it is totally used by the energy capacities.

Methods that adopt dissipated energy have two major drawbacks, one is that the estimation of the dissipated energy within a soil profile from a seismic shear wave is far from trivial and very dependent on soil characteristics and changes as pore pressure increases. Secondly, the dissipated energy rapidly increases as the soil approaches liquefaction, and therefore a small change in the criteria for liquefaction triggering (e.g. change the limiting pore pressure ratio from 0.95 to 0.98), can have a large impact on the evaluated capacity. In order to overcome this problem, Millen et al. (2019) proposed a new method to estimate pore pressure development based on the principles of conservation of energy. The liquefaction resistance is measured in terms of normalised cumulative absolute strain energy (NSE), which is shown to be constant with loading amplitude but sensitive to soil properties. On the estimation of demand, the intensity measure selected was the cumulative absolute kinetic energy, used to provide an exact solution for the NSE at any depth in a homogenous purely linear elastic soil deposit using the nodal surface energy spectrum (NSES). NSE was calculated as the cumulative change in absolute elastic strain energy divided by the vertical effective stress – equation (2.42). Graphically it can be obtained as the sum of the absolute change in elastic strain energy between two peaks in the response (**Figure 2.68**). The peak points (local maxima and minima) were determined as the intercepts of the derivative shear strain using equation (2.40). Before applying equation (2.40) the derivatives equal to zero were removed from the time series to avoid flat peaks. NSE was then calculated as the average absolute stress multiplied by the change in strain between the peak points or the area enclosed between the peak points using equation (2.42).

$$peak_j = \Delta\gamma_i \cdot \Delta\gamma_{i+1} > 0 \quad (2.40)$$

$$|\tau_{av,j}| = \begin{cases} \frac{|\tau_{j+1} + \tau_j|}{2} & \tau_{j+1} + \tau_j > 0 \\ \frac{\tau_{j+1}^2 + \tau_j^2}{2|\tau_{j+1} - \tau_j|} & \tau_{j+1} + \tau_j < 0 \end{cases} \quad (2.41)$$

$$NSE = \sum_{j=0}^{n_{peaks}} |\tau_{av,j}| \cdot |\gamma_{j+1} - \gamma_j| / \sigma'_{v0} \quad (2.42)$$

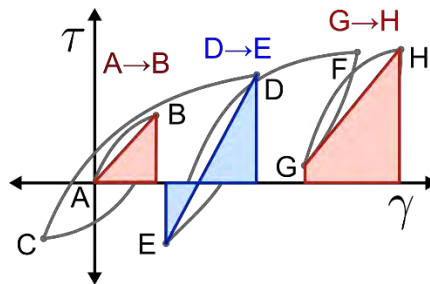


Figure 2.68: Calculation of NSE graphically

The cumulative absolute kinetic energy (KE) is the total kinetic energy given and taken from a soil element. It is computed as the sum of the cumulative absolute change in kinetic energy or for a continuous function it



This project has received funding from the European Union's Horizon 2020 research and innovation programme under grant agreement No. 700748

is the integral of absolute power – equation (2.43). As a ground motion intensity measure, it can be computed as the unit kinetic energy (UKE), where the soil mass density (ρ) is taken as 1.0.

$$KE = \rho \cdot \sum_{i=1}^n \Delta(u_i \cdot |u_i|) = \rho \int \left| \frac{du_i}{dt} \right|^2 dt \quad (2.43)$$

The strain energy which can be accurately predicted at any depth with the nodal surface energy spectrum (NSES). The upward and downward motion are converted into a time shifted motion at a particular depth, where the time shift corresponds to two times the travel time from the surface. For each time shift increment, the unit kinetic energy of the time shifted motion can then be computed to produce the strain energy at a particular travel time from the surface and can be repeated to obtain a spectrum. Since the strain energy and kinetic energy are complimentary, the spectrum gives the strain energy at the ground surface. Currently there are no predicting equations are available for UKE, however, Millen et al. (2019) suggests conditionally selecting ground motions based on the earthquake magnitude, distance and either expected cumulative absolute velocity after application of 5 cm/sec threshold acceleration (CAV_5) (Kramer et al., 2006) or Arias Intensity.

The pore pressure time series can be computed by the square root relationship presented in equation (2.44) where the NSE at liquefaction (NSE_{liq}) can be obtained by equation (2.45):

$$r_{u,i} = \sqrt{\frac{NSE_i}{NSE_{liq}}} \cdot r_{u,liq} \quad (2.44)$$

$$NSE_{liq} = \frac{2 \cdot CSR^2 \cdot \sigma'_{v0} \cdot n_{liq}}{G_i \cdot \left(1 - \frac{CSR}{\sin(\phi_{cv})}\right)} \cdot \kappa \quad (2.45)$$

Where κ is a calibrating parameter that can be taken equal to 3 for PM4sand model and n_{liq} is the reference number of cycles at liquefaction corresponding to the cyclic stress ratio (CSR).

2.5.3 DIFFERENT APPROACHES TO ESTIMATE PORE PRESSURE BUILD UP

In this section different approaches to estimate the pore pressure time series from a specific ground motion will be compared in terms of complexity, advantages and limitations but also on the uncertainties and simplifications involved in each step. The following approaches are considered:

- 1D nonlinear dynamic analysis performed using the commercial software FLAC® with the PM4Sand constitutive model (Boulanger et al., 2015)
- Simplified stress based method from Seed et al. (1975)
- Simplified dissipated energy based method adapted from Kokusho (2013)
- Simplified strain energy based method from Millen et al. (2019)



This project has received funding from the European Union's Horizon 2020 research and innovation programme under grant agreement No. 700748

Numerical analysis

The results from a series of 500 soil profiles that were generated and analysed using equivalent linear, and nonlinear analysis in Millen et al. (2019) are described in this section. The nonlinear analysis were performed in a 1D model to simulate the free field condition, but it followed the same procedures as the 2D model described in section 2.4. Two different non linear calculations were performed: effective stress analysis (ESA) and also non linear analysis (NLA) assuming the bulk modulus of the water to be null. This latter intends to simulate the case where the soil does not liquefy to compare assumptions related to stresses and dissipated energy. The soil profile consisted of three soil layers: two non-liquefiable layers made of hard clay located at the top and at the bottom while the middle layer, was made of sand. The water table was assumed at the interface of the first and second layers. In the numerical analysis the input upward propagating motion was used at the bottom of the model. The properties were randomly generated within the ranges shown in **Table 2.8**. The same random number was used for sampling the undrained strength, shear modulus and void ratio of layers 1 and 3, to account for the correlation between these parameters. By keeping the same ratio between these parameters the soil could be considered as a clay with a plasticity index of 30% and the shear modulus reduction curves used for this layer were based on the expression from Vardanega et al. (2013) for plasticity of 30%. The soil relative density, normalised shear modulus, and the PM4Sand contraction rate parameter (h_{p0}), were also correlated through the calculation of an equivalent normalised SPT blow count ($(N_1)_{60}$). Equation (2.48) was developed through a regression analysis where the h_{p0} , relative density and shear modulus were systematically varied with a confining stress of 100 kPa, and the CSR for 15 cycles was obtained through element tests. The equation provided a fast way to set the h_{p0} within realistic bounds (**Figure 2.69**). The CSR_{target} was randomly sampled between a lower limit of 55% of the cyclic resistance ratio from Boulanger et al. (2014) using the equivalent normalised SPT and an upper limit of equation (2.48).

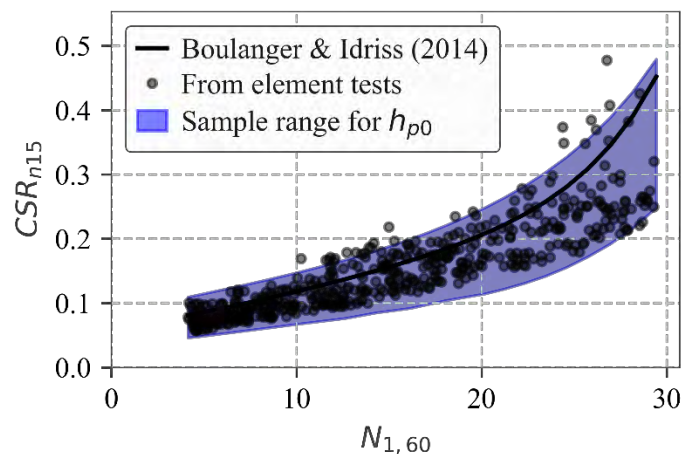


Figure 2.69: CSR from element tests versus equivalent SPT blow count



This project has received funding from the European Union's Horizon 2020 research and innovation programme under grant agreement No. 700748

Methodology for the liquefaction fragility analysis of critical structures and infrastructures: description and case studies

Table 2.8: Soil profile parameters

Parameter	Range
Height of L1, H_1	[0.5 – 8.5] m
Height of L2, H_2	[0.5 – 10]m
Total profile height, H_{total}	[20 – max(2.5 · ($H_1 + H_2$), 30)] m
Permeability of L1, k_1	$8 \cdot 10^{-8}$ m/s
Permeability of L2, k_2	$1.6 \cdot 10^{-5}$ m/s
Permeability of L3, k_3	10^{-9} m/s
Dilatancy, ψ	0°
Properties of layer 2	
Specific gravity, G_s	2.65
Poisson ratio, ν	0.3
Internal friction angle, ϕ	33°
Minimum void ratio, e_{min}	0.5
Maximum void ratio, e_{max}	0.8
Relative density, D_r	[0.3 – 0.8]
Normalised SPT, $N_{1,60}$	$46 \cdot D_r^2$
Normalised shear modulus, G_0	Equation 2 [Pa]
PM4Sand hpo factor	Equation 4
Other properties of layers 1 and 3	
Poisson ratio, ν_1	0.4
Specific gravity, G_s	2.7
Angle of shearing resistance, ϕ	0°
Undrained strength of L1	[30 – 34] kPa
Undrained strength of L3	[180 – 200] kPa
Void ratio of L1	[0.6 – 0.8]
Void ratio of L3	[0.5 – 0.7]
Initial shear modulus, G_i	1000 · Undrained strength

$$G_0 = 167\sqrt{(N_1)_{60} + 2.5} \cdot [0.7 - 1.5] \quad (2.46)$$

$$G = G_0 \cdot P_{atm} \sqrt{\frac{p'}{P_{atm}}} \quad (2.47)$$

$$h_{po} = \frac{CSR_{target} \cdot (2.05 - (2.4 * D_r))}{1 - CSR_{target} \cdot (12.0 - (12.5 * D_r))} \quad (2.48)$$

Each of the 500 profiles was evaluated against one of 49 ground motions selected from the NGAWest ground motion database (Ancheta et al., 2013) to select the ground motions the database was filtered by the following criteria, and then one motion was randomly selected as the closest to a set of 49 equally spaced PGA values between 0.1 and 0.49, so that an even distribution of PGA values would be present in the database. No other criteria were used for the selection to attempt to provide a wide unbiased selection of ground motions. The two horizontal components were combined together to obtain the maximum rotated Arias intensity (Arias, 1970) considering 100 potential angles. The following ground motion selection criteria were used:

1. Vs30 range: 180 - 400 m/s
2. Not a foreshock or aftershock event
3. From earthquake events with a magnitude larger than 5



This project has received funding from the European Union's Horizon 2020 research and innovation programme under grant agreement No. 700748

4. Ground motion has a PGA higher than 0.10
5. Have a usable frequency less than or equal to 0.25
6. Are available from the PEER ground motion database
7. Have the start of the earthquake record
8. Did not suffer from excessive disturbance during recording

The list of ground motions can be seen in **Table 2.9** and the acceleration and displacement single degree-of-freedom (SDOF) spectra of the motions is shown in **Figure 2.70**. No deconvolution was performed as the characteristics of the site where the recording was taken were unknown, therefore the energy in these records at the depth of the base of the model may be slightly lower than expected for the same distance and magnitude of earthquake.

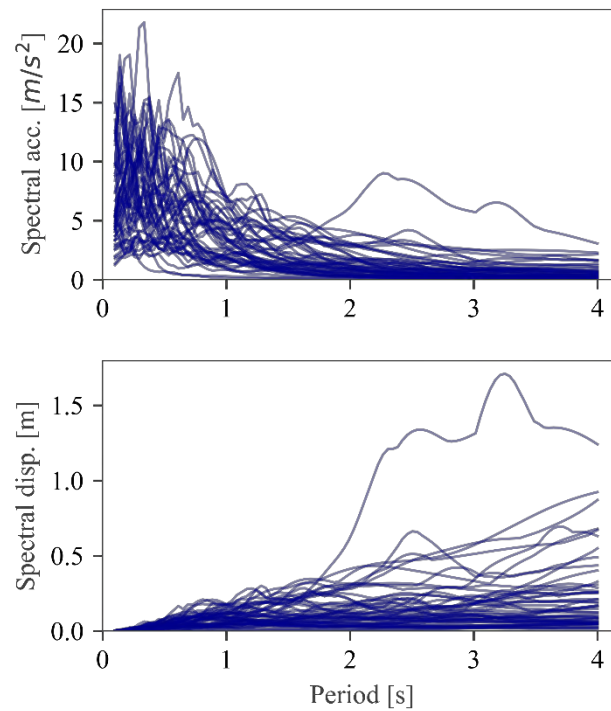


Figure 2.70: Ground motion SDOF response spectra



This project has received funding from the European Union's Horizon 2020 research and innovation programme under grant agreement No. 700748

Table 2.9: Input ground motions

ID	Record	E. dist [km]	Mw	Vs30 [m/s]	PGA [g]	Earthquake	Year	Station
1	148	9.6	5.74	350	0.26	Coyote Lake	1979	Gilroy Array #3
2	159	2.6	6.53	242	0.32	Imperial Valley-06	1979	Agrarias
3	175	32.0	6.53	197	0.14	Imperial Valley-06	1979	El Centro Array #12
4	240	2.8	5.7	382	0.55	Mammoth Lakes-04	1980	Convict Creek
5	313	19.9	6.6	361	0.35	Corinth, Greece	1981	Corinth
6	449	43.6	6.19	289	0.14	Morgan Hill	1984	Capitola
7	457	38.2	6.19	350	0.26	Morgan Hill	1984	Gilroy Array #3
8	461	3.9	6.19	282	0.32	Morgan Hill	1984	Halls Valley
9	558	14.3	6.19	316	0.42	Chalfant Valley-02	1986	Zack Brothers Ranch
10	592	9.9	5.99	368	0.31	Whittier Narrows-01	1987	Arcadia - Campus Dr
11	626	21.3	5.99	301	0.40	Whittier Narrows-01	1987	LA - 116th St School
12	692	11.7	5.99	339	0.43	Whittier Narrows-01	1987	Santa Fe Springs - E.Joslin
13	767	31.4	6.93	350	0.55	Loma Prieta	1989	Gilroy Array #3
14	770	39.9	6.93	334	0.32	Loma Prieta	1989	Gilroy Array #7
15	802	27.2	6.93	381	0.48	Loma Prieta	1989	Saratoga - Aloha Ave
16	803	27.1	6.93	348	0.42	Loma Prieta	1989	Saratoga - W Valley Coll.
17	838	94.8	7.28	370	0.14	Landers	1992	Barstow
18	848	82.1	7.28	353	0.38	Landers	1992	Coolwater
19	960	26.5	6.69	326	0.48	Northridge-01	1994	W Lost Canyon
20	1035	38.7	6.69	352	0.17	Northridge-01	1994	Manhattan Beach – Man.
21	1082	12.4	6.69	321	0.37	Northridge-01	1994	Sun Valley - Roscoe Blvd
22	1115	42.1	6.9	256	0.15	Kobe, Japan	1995	Sakai
23	1155	95.0	7.51	290	0.10	Kocaeli, Turkey	1999	Bursa Tofas
24	1158	98.2	7.51	282	0.40	Kocaeli, Turkey	1999	Duzce
25	1513	7.6	7.62	364	0.59	Chi-Chi, Taiwan	1999	TCU079
26	1605	1.6	7.14	282	0.48	Duzce, Turkey	1999	Duzce
27	2007	54.6	5.31	196	0.14	CA/Baja Border Area	2002	El Centro Array #11
28	3636	68.2	6.32	315	0.19	Taiwan SMART1(40)	1986	SMART1 I04
29	3643	69.2	6.32	307	0.22	Taiwan SMART1(40)	1986	SMART1 M02
30	3653	70.0	6.32	285	0.20	Taiwan SMART1(40)	1986	SMART1 O02
31	4066	15.1	6	227	0.55	Parkfield-02, CA	2004	PARKFIELD - FROELICH
32	4146	12.2	6	342	0.38	Parkfield-02, CA	2004	PARKFIELD - UPSAR 10
33	4159	42.3	6.63	306	0.19	Niigata, Japan	2004	FKS028
34	4169	42.5	6.63	365	0.35	Niigata, Japan	2004	FKSH21
35	4210	13.6	6.63	332	0.64	Niigata, Japan	2004	NIG020
36	4212	30.1	6.63	193	0.33	Niigata, Japan	2004	NIG022
37	4866	8.5	6.8	338	0.35	Chuetsu-oki	2007	Kawanishi Izumozaki
38	4889	58.1	6.8	315	0.37	Chuetsu-oki	2007	Joetsu Otemachi
39	5263	22.6	6.8	274	0.26	Chuetsu-oki	2007	NIG017
40	5495	39.2	6.9	288	0.25	Iwate	2008	AKTH19
41	5616	88.6	6.9	364	0.20	Iwate	2008	IWT007
42	5664	32.1	6.9	361	0.43	Iwate	2008	MYG005
43	5669	75.3	6.9	275	0.11	Iwate	2008	MYG010
44	5814	51.2	6.9	248	0.34	Iwate	2008	Furukawa Osaki City
45	5827	18.8	7.2	242	0.54	El Mayor-Cucapah	2010	MICHOACAN DE OCAMPO
46	5829	32.4	7.2	242	0.41	El Mayor-Cucapah	2010	RIITO
47	5836	55.3	7.2	265	0.45	El Mayor-Cucapah	2010	Meloland Geot. Array
48	6927	33.8	7	263	0.42	Darfield, New Zealand	2010	LINC
49	6962	26.9	7	296	0.45	Darfield, New Zealand	2010	ROLC



This project has received funding from the European Union's Horizon 2020 research and innovation programme under grant agreement No. 700748

Finally a series of numerical constant stress cyclic simple shear element tests were performed in FLAC on the liquefiable soil at the stress state corresponding to the stress state at the centre of the liquefiable layer. The soil was assessed at a large range of cyclic stress ratios from 0.04 to 0.6.

Simplified stress based method (SBM)

This method was implemented using equation (2.27) suggested by Booker (1976). The N/N_L ratio was calculated by equation (2.49) assuming an N_{ref} equal to 15 cycles. The CSR was calculated with equation (2.50) where a peak counting method was used to identify the acceleration peaks (acc_{peaks}), counting the largest peak between successive zero crossing. The stress-based method uses the surface acceleration, however, in this case only the upward propagating motion at the base was available and therefore the acceleration peaks were from two-times the upward base motion assuming that upward energy is half the surface motion due to the outcropping effect. The CRR was CSR_{15} (i.e., the cyclic stress ratio that the sand can sustain until it liquefies with 15 constant stress amplitude cycles) obtained from the element tests. There are several equations in the literature for the r_d parameter but in this work equations (2.51), (2.52) and (2.53) were used, being M the magnitude and z the depth.

$$\frac{N_L}{N} = \sum N_{ref} \cdot \left(\frac{CRR}{CSR} \right)^{1/b} \quad (2.49)$$

$$CSR = |acc_{peaks}| \cdot \frac{\sigma_{v0}}{\sigma'_{v0}} \cdot r_d \quad (2.50)$$

$$r_d = e^{[f(z)+g(z) \cdot M]} \quad (2.51)$$

$$f(z) = -1.012 - 1.126 \cdot \sin\left(\frac{z}{11.73} + 5.133\right) \quad (2.52)$$

$$g(z) = 0.106 + 0.118 \cdot \sin\left(\frac{z}{11.28} + 5.142\right) \quad (2.53)$$

Simplified dissipated energy based methods

In this work the dissipated energy based method from Kokusho (2013) was adapted to provide the estimation of the pore pressure time series. The demand was estimated by computing the strain energy in the layer of interesting from equivalent linear analysis using an open-source python package, Pysra v0.3.0 (Kottke, 2018). The clay layers were modelled with the Modified Hyperbolic Soil Type using the expressions from Vardanega et al. (2013) and a minimum damping of 2%. The sand layer was modelled using the Modified Hyperbolic Soil Type where the curvature factor was set to 1.0 and the reference strain, γ_{ref} , was set so that the maximum shear stress was reached at 20 times the reference strain. The strain energy (W) was calculated from the shear stresses and strains obtained in the equivalent linear analysis, being then inserted in equation (2.54) from Kokusho (2013) to obtain the dissipated energy (ΔW). The original formulation from Kokusho (2013) used the energy density of the upward propagating motion to estimate the strain energy. However, this resulted in a large discrepancy with the effective stress results, since the strain energy is highly dependent on frequency content and the interaction with the downward wave (Millen et al., 2019). The strain energy corresponds to four times the area of the triangle in Kokusho 2013 as indicated in **Figure 2.68**. This method is identified as EqLin+Kok



This project has received funding from the European Union's Horizon 2020 research and innovation programme under grant agreement No. 700748

$$\frac{\Delta W}{\sigma'_{v0}} = 10^{\frac{\log(W/\sigma'_{v0}) - \log(5.4)}{1.25}} \quad (2.54)$$

To evaluate the influence of equation (2.54), this relationship was compared to the hysteretic damping ratio (ξ) definition ($\xi = \Delta W / (W \cdot \pi)$). In this method the equivalent linear analysis is used again to calculate the strain energy which is then converted to the dissipated energy by the damping relationship, and so this was called EqLin+Damp. The damping ratio used in this relationship is the one from the equivalent linear analysis.

$$\xi = \frac{\Delta W}{W \cdot \pi} \quad (2.55)$$

In both methods, a simple pore pressure model, inspired in Green et al. (2000), was used since it does not need any calibrating parameters:

$$r_u = \sqrt{\frac{\Delta W}{\Delta W_{liq}}} \quad (2.56)$$

Additionally, the strain energy based method (SEBM) presented recently by Millen et al. (2019), was also implemented for comparison following the assumptions indicated before. In equation (2.45) k was considered equal to 3, the n_{liq} was 15, and the angle of shearing resistance at critical state equal to 33°.

2.5.4 COMPARISON OF THE METHODS FOR A SINGLE CASE

The methods presented above were first compared just for one soil profile and corresponding ground motion, selected from the 500 database, so that a direct view of the differences provided by each method could be clear. **Table 2.10** summarised the main parameters of the selected case. There are several cases where the results provided by the methods are very similar, and therefore the impact of the underlying assumptions are not obvious. For that reason, the case herein presented was selected so that the impact of the assumptions and simplifications considered implicitly or explicitly in each method can be analysed and discussed.

Table 2.10: Conditions of the selected case

Case ID	37
Ground motion record number	5836
Maxim shear modulus of the sand layer (MPa)	186
Relative density of the sand layer	70%
hpo	0.11
Thickness of top layer (m)	5
Thickness of centre layer (m)	8
Thickness of bottom layer (m)	13

First, the results of the element tests are presented together with some parameters used by the methods such as the b and β values used by the SBM (equations (2.26) to (2.29)), and also the liquefaction criteria



This project has received funding from the European Union's Horizon 2020 research and innovation programme under grant agreement No. 700748

defined by Kokusho (2013) in terms of the double amplitude axial strain (DA) for a given cyclic stress ratio at 20 cycles as indicated in **Figure 2.67**. In **Figure 2.71a)** the element tests results for a liquefaction criterion of $r_u=0.98$ are plotted against equation (2.29) using an upper and lower bound for b of [0.2-0.45]. The data obtained by Okamura et al. (2003) show that the most dense and strongest sands had b values of 0.45, 0.50, and 0.54, whereas the looser and weaker sands had b values of 0.13, 0.15, and 0.21. Since the sand of the present case has an intermediate $Dr=70\%$, the upper value of the weaker sands and the lower value of the dense sands was used. The b value obtained from fitting a curve to the element tests results at a $r_u=0.98$ was 0.36, close to the value of 0.34 proposed by Idriss (1999). All the curves cross at the point ($n=15$; CSR_{15}) and the impact of different b values is explored in **Figure 2.71a)** as this parameter is often poorly characterised unless a significant number of laboratory tests are performed. It was shown that the CSR_{15} did not change significantly with the pore pressure criteria. For this case, the following CSR_{15} values were obtained 0.1685, 0.1689, 0.1708 for a limit pore pressure ratio of 0.9, 0.95 and 0.98 respectively.

In **Figure 2.71b)** the element tests results were plotted in terms of the pore pressure ratio against the number of cycles normalized by the number of cycles required to liquefy that layer. The same plot shows the Booker et al. (1976), equation (2.27) with two different β values. The value of $\beta=0.7$ is suggested as a generic value by the author, while the value of 1.02 was obtained by equation (2.28) for the sand layer using $CSR=CSR_{15}=0.17$. In fact, the trend defined by numerical results has higher curvature than the simplified proposals which reflects the different base assumptions between the simple empirical equations by Booker et al. (1976) compared to the numerical analyses.

In **Figure 2.71c)** the normalized dissipated energy obtained from the element tests for different liquefaction criteria is compared to the same parameter obtained by the equations proposed by Kokusho (2013), for a $CSR_{20}=0.16$ obtained in the element tests. It seems that the 2% double amplitude axial strain results obtained by Kokusho (2013) agrees well with the data. However, using the 5% double amplitude axial strain dramatically increases the perceived resistance capacity of the soil. The use of different pore pressure ratios had minor impact on the calculated capacity in this example, but larger differences were observed for large pore pressure ratios in other cases, since the hysteresis loops tend to increase with increasing pore pressure.

In **Figure 2.71d)** the pore pressure ratio is plotted against the ratio of the normalized dissipated energy by the same parameter at liquefaction. Although this relation is usually assumed to be hyperbolic (Liang et al., 1995), potential ((Berril et al., 1985) (Hsu, 1995)) or exponential ((Davis et al., 2001), these laws do not provide a good fit as indicated on **Figure 2.71d)** for an hypothetical hyperbolic law, which may be source of error in the simplified methods.



This project has received funding from the European Union's Horizon 2020 research and innovation programme under grant agreement No. 700748

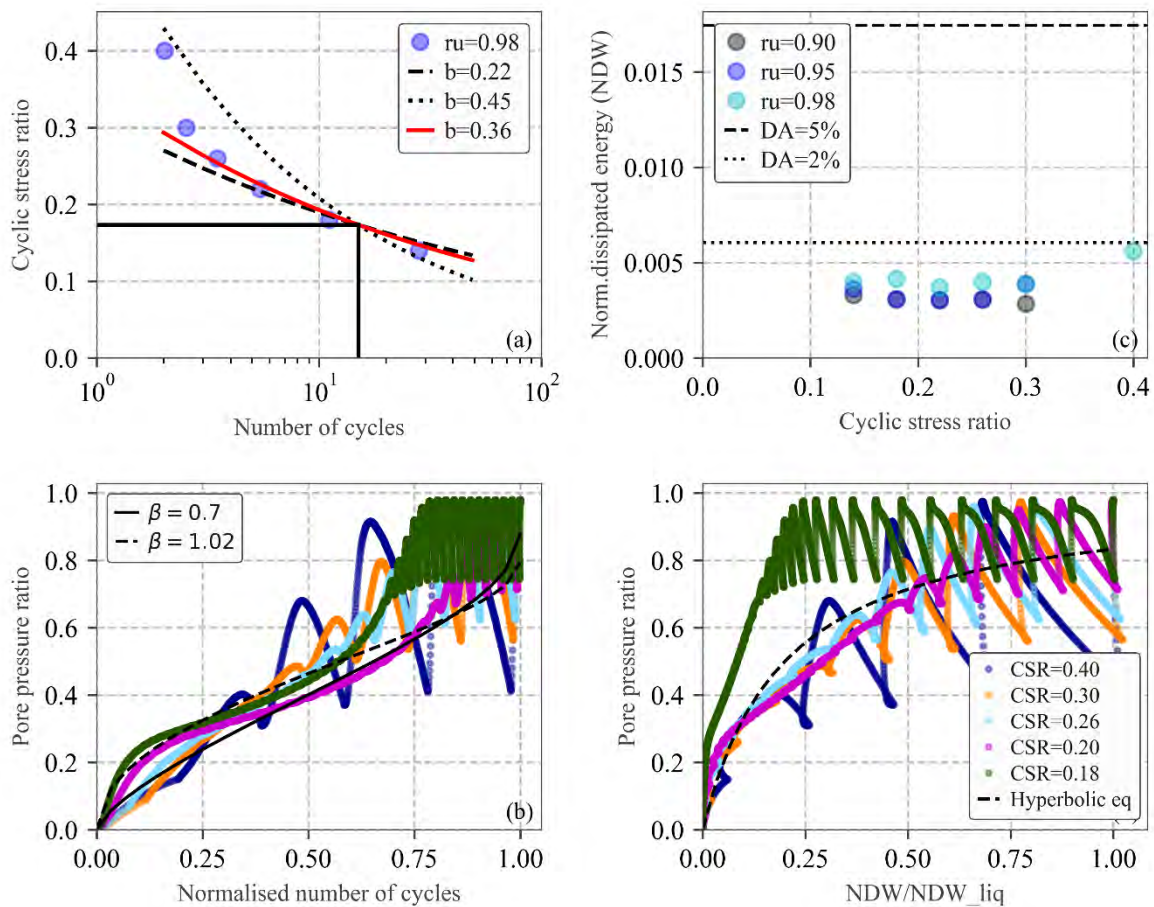


Figure 2.71: Element tests results for the case 37

As mentioned before, stress based method needs a conversion to the equivalent number of cycles, which is dependent on the soil capacity through the CSR_{15} and b value, and limits the efficiency of this method. In **Figure 2.72** the equivalent number of cycles obtained by the simplified stress based method (SBM) is compared to the numerical analysis (ESA and NLA). The equivalent number of cycles from the numerical analysis was calculated by converting the shear stresses into cyclic stress ratios and then applying equation (2.30). Both the SBM and the numerical analysis were calculated for the same range of b values [0.22-0.45] so that the uncertainty associated to this value could be observed. This equivalent conversion procedure has several uncertainties related to rd equation, and to the estimation of surface acceleration. In this work, rd was calculated by equation (2.51) but there are several other proposals in the literature. The surface acceleration was assumed as the double of the input upward energy but this is also a source of uncertainty. Finally, this equivalent cycle procedure assumes the shear stress to be constant throughout the earthquake, whereas typically shear stresses reduce due to softening of the soil with increased excess pore water pressure. According to the stress based method an equivalent number of cycles of 15 corresponds to liquefaction. As can be seen in **Figure 2.72** the variation in b value has a large impact on the calculation of number of cycles and time of liquefaction. The b value of 0.22 gives 262 equivalent number of cycles compared to 24 for the $b=0.45$. However, a b around 0.22 was obtained by several authors for clean sands with relative densities around 65-70% (Silver et al., 1976) (Carraro et al., 2003). In any case, it should be



This project has received funding from the European Union's Horizon 2020 research and innovation programme under grant agreement No. 700748

pointed out that for many other cases out of the 500 database this b value of 0.22 did not give such high number of cycles. From now on the SBM for this example will be calculated with the best fit $b=0.36$.

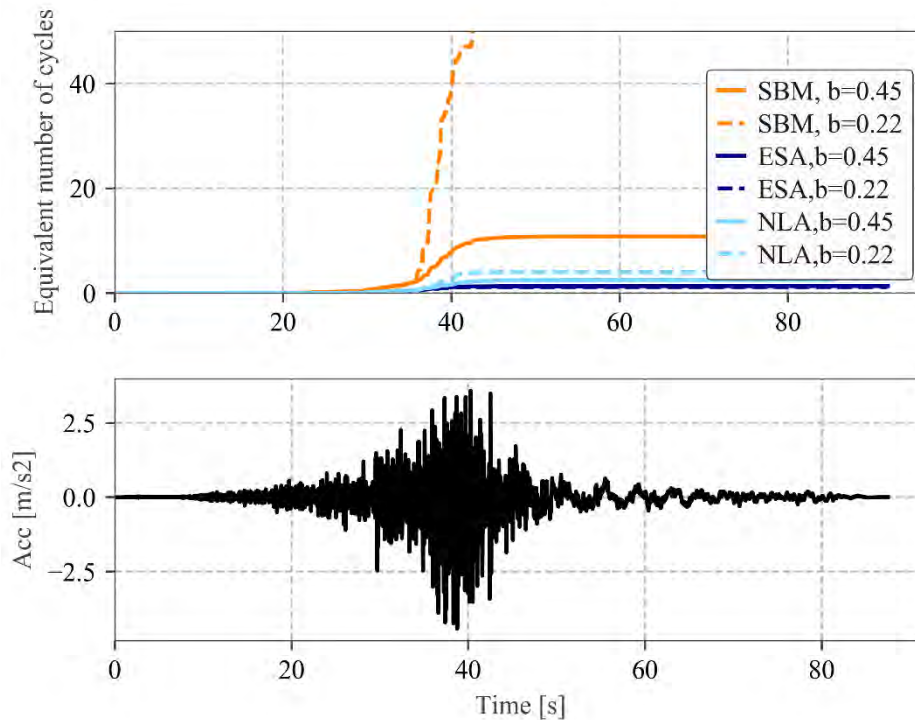


Figure 2.72: Equivalent number of cycles time series (a) and acceleration base record (b) for the case 37

Since there are several simplified energy based methods based on the evaluation of the dissipated energy, it is interesting to compare the dissipated energy from the numerical analyses (ESA and NLA) with the simplified method adapted from Kokusho (2013) - EqLin+Kok - and the one using the damping equation (EqLin+Damp). In **Figure 2.73** those methods are presented together with the normalized dissipated energies at liquefaction proposed by Kokusho (2013) based on CSR_{20} for the two liquefaction criteria as presented in **Figure 2.67**. The EqLin+Damp method and NLA are very similar with a slight overprediction of the NLA. None of the presented simplified methods predicts liquefaction as they are below the $DA=2\%$ threshold, conversely to the ESA that stand above the threshold. The dissipated energy from the ESA is similar to the EqLin+Kok up until the onset of liquefaction (approximately 40 seconds according to **Figure 2.73**), but increases further due to liquefaction weakening the soil.



This project has received funding from the European Union's Horizon 2020 research and innovation programme under grant agreement No. 700748

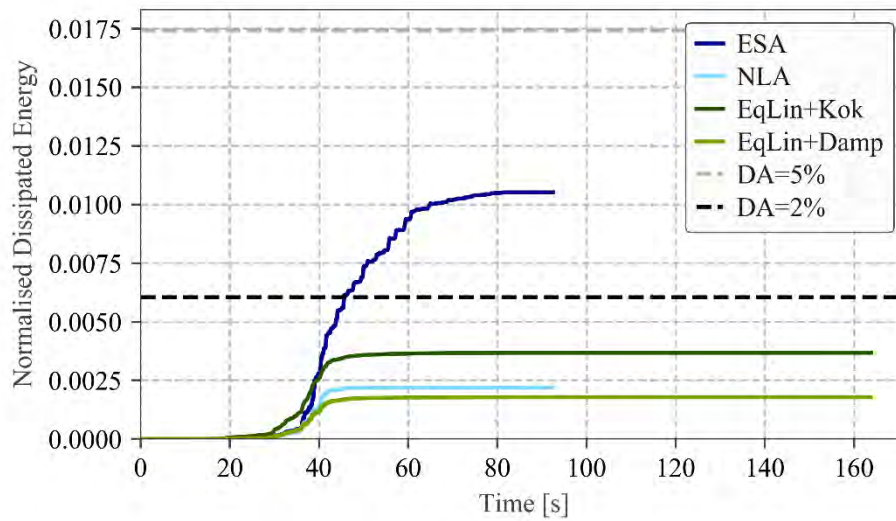


Figure 2.73: Normalised dissipated energy time series for the case 37

In addition, since both Kokusho (2013) and (Millen et al., 2019) use the strain energy, this parameter normalised by the effective stress was compared to the numerical analysis (**Figure 2.74**). Again the equivalent linear analysis plots very close to the NLA while the SEBM provides a bit higher energy. However, the energy estimated by the simplified methods did not achieve the values obtained in the ESA after liquefaction triggering.

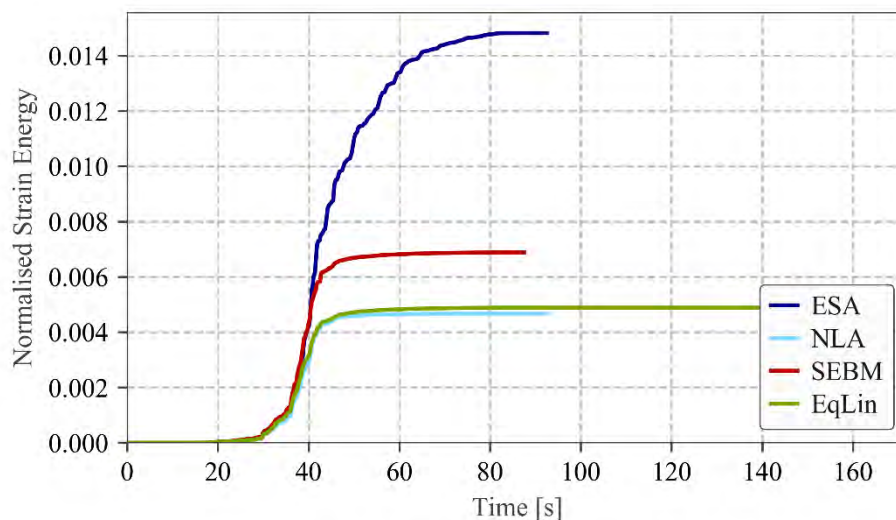


Figure 2.74: Normalised strain energy time series for the case 37

Finally, **Figure 2.74** compares the simplified methods with the ESA in terms of the estimation of the pore pressure time series. For the SBM the β value was calculated with equation (2.28) obtaining 1.02 and for b the optimum fit was assumed (0.36). The SBM predicts liquefaction at 32.2 s, and the SEBM at 38.5 s, where for ESA it is approximately 40 s. As mentioned before none of the equivalent linear methods predicts



This project has received funding from the European Union's Horizon 2020 research and innovation programme under grant agreement No. 700748

liquefaction for this case. However, it should be noted that from the 500 cases generated in this work there are some cases where the equivalent linear methods predict liquefaction together with ESA, being the EqLin+Kok apparently more accurate than EqLin+Damp as also recognised by the author (Kokusho, 2013).

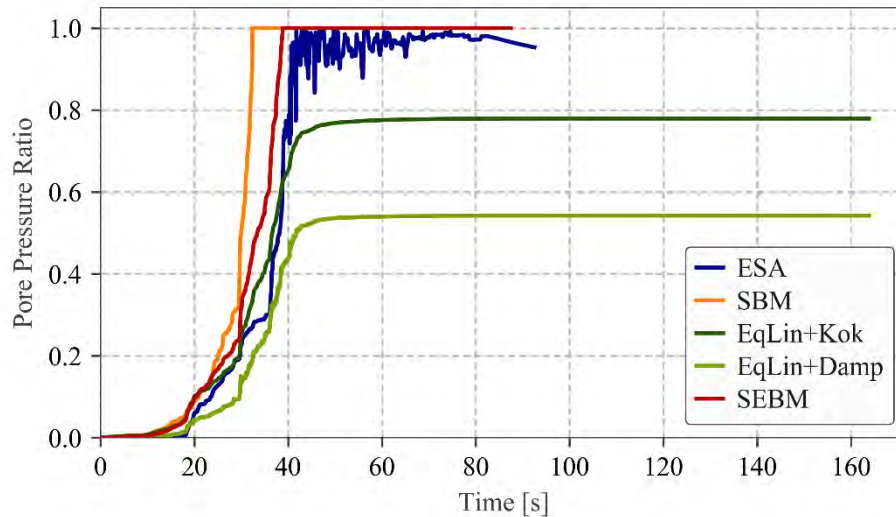


Figure 2.75: Pore pressure ratio predicted by each method for the case 37

2.5.5 COMPARISON OF THE METHODS FOR THE 500 CASES

In this section the results obtained for the 500 cases are presented in terms of the comparison between the effective stress analysis (ESA) and the simplified methods that performed better, namely the stress based method (SBM) and the strain energy based method (SEBM). The SBM was calculated using a b value of 0.34 and a β of 0.7. In **Figure 2.76** the top graphs represent the cases that did not liquefy in ESA and for which the maximum pore pressure ratio was calculated for both ESA and the simplified methods. The bottom graphs represent the cases that liquefied in ESA and for which the time of liquefaction was obtained both for ESA and the simplified analysis. The triggering of liquefaction was determined when the vertical effective stress dropped to below 5kPa, this was considered near complete collapse of the soil. From these analyses and assuming the non-linear effective stress analysis as reference, the SBM has an accuracy of 79% while the SEBM has an accuracy of 86%. The accuracy of the simplified methods was measured as the ratio between the number of analysis that did not give the same estimation as ESA (in terms of triggering or no triggering) by the total number of analysis.



This project has received funding from the European Union's Horizon 2020 research and innovation programme under grant agreement No. 700748

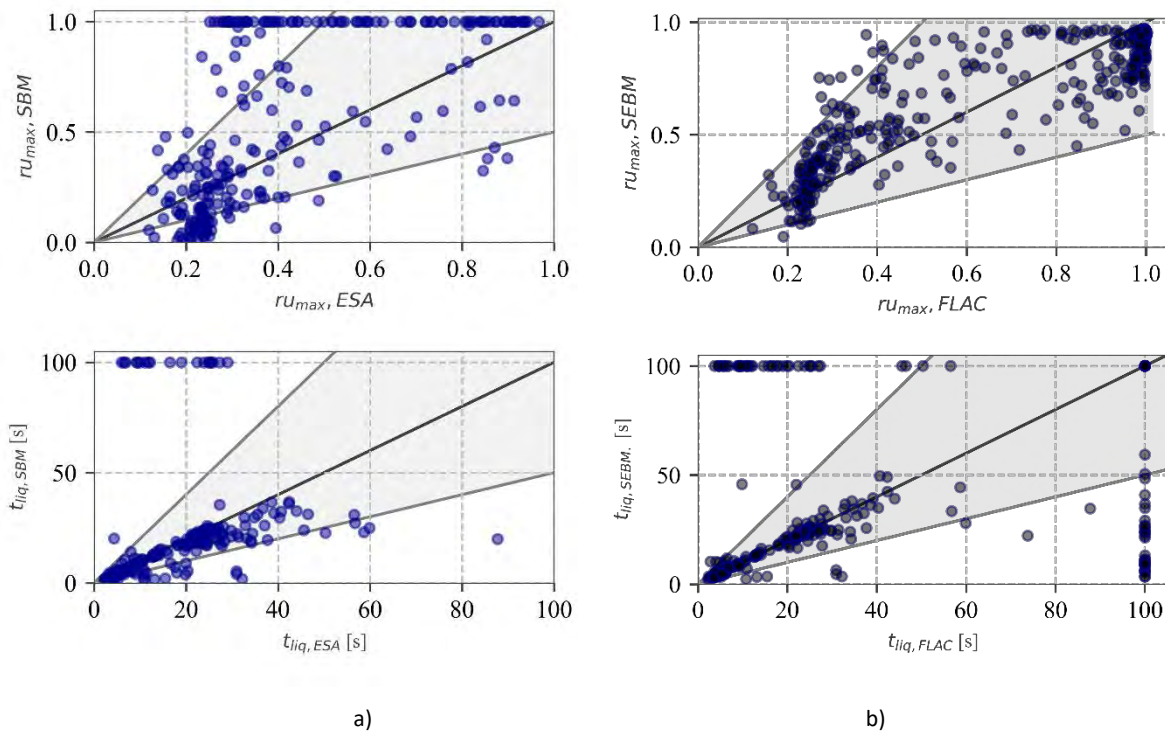


Figure 2.76: Accuracy of the methods in terms of pore pressure ratio (r_u) and time to liquefy (t_{liq}): a) SBM; b) SEBM

2.5.6 MODELLING RECOMMENDATIONS

From the four methods explored in this chapter, three methods have provided viable options for efficiently assessing the build-up of pore pressure.

Nonlinear effective stress analysis has the advantage of implicitly considering the shear demand and site response, without the need for simplifying assumptions, as well as considering pore water flow and can be expanded to two-dimensional and three-dimensional models. However, the model is the least computational efficient method. The pore pressure build-up also relies on the underlying assumptions and calibration of the constitutive model, where discrepancies between empirical curves by Booker et al. (1976) for the build-up of pore pressure with number of cycles provided a different relationship when using the model calibration approach from Millen et al. (2019). For this approach, it is recommended to use the PM4Sand with the default parameters, and set the contraction rate parameter using (equation (2.48), hp_0). The remaining aspects of the model should follow the procedure outlined in section 2.4.

The stress-based method should follow the steps outlined in section 2.5.3. In the absence of laboratory tests, the b value should be taken as 0.34 to be consistent with Boulanger et al. (2016) and the pore pressure build-up should use the beta value calculated for each specific case using equation (2.28) based on the relative density, cyclic stress ratio and fines content. If no information is available the value of 0.7 proposed by Booker et al. (1976) is a valid option.

The strain energy method from Millen et al. (2019) should be used with the normalised strain energy being calculated using equation (2.45) in the absence of laboratory tests.



This project has received funding from the European Union's Horizon 2020 research and innovation programme under grant agreement No. 700748

The dissipated energy method is not recommended due to the large variation in the capacity with changes in the liquefaction criteria and the lack of formal validation of the complete method.

2.5.7 CONCLUSIONS

A key aspect of the proposed macro-mechanism approach is the estimation of the build-up of pore pressure. This section 2.5 investigates the existing literature for estimating excess pore pressure and presents four methods based on different underlying assumptions. One approach is nonlinear effective stress analysis which implicitly considers the dynamic response of the soil deposit and the resistance capacity is considering through a constitutive model. The other methods (stress-based, dissipated energy based, strain-energy based) are simple models that use analytical or empirical equations to estimate the demand and capacity. There are other simplified methods based on damage parameters but they were not considered as they either require specific software or more complex implementation than the other simplified methods assessed here. The assumptions for the inputs of the methods were first evaluated to understand their impacts and then the methods were evaluated against each other. Three methods were proposed as viable models for estimating pore pressure build up, whereas the dissipated energy model was not recommended due to a lack of formal validation.

2.6 SIMPLIFIED PROCEDURE TO ESTIMATE SETTLEMENTS OF BUILDINGS

Settlements and tilting of structures that are not supported by deep foundations are the main types of liquefaction-induced damages, because those deformations can significantly affect the building operability (Yoshimi and Tokimatsu, 1977; Tokimatsu and Seed, 1987; Acacio et al., 2001). Due to that, several methodologies have been developed to study their effects on building with shallow foundations (Yoshimi and Tokimatsu, 1977; Liu and Dobry, 1997; Karamitros et al., 2013a). These methodologies have been based on field observations, centrifuge experiments, numerical simulations, or a combination of them.

2.6.1 EXISTING METHODOLOGIES FOR ESTIMATING SETTLEMENTS

Several attempts to provide simplified procedures able to estimate liquefaction-induced building settlements during seismic shaking have been proposed so far, especially in the last decade. In this section, a selection of three main procedures is shown.

Karamitros et al. (2013a)

The authors proposed an analytical method with strong physical basis whose main advantage is to account for each relevant influencing parameter separately. This methodology can only be used to calculate the total seismic settlement of isolated buildings during shaking.

Following a thorough review of numerical predictions, along with observations from relevant centrifuge and large-scale experiments published in the literature, Karamitros et al. (2013a) demonstrated that the majority of liquefaction-induced settlements is not due to an accumulated sand densification, but associated to a Newmark-type “sliding block” mechanism.

The sliding-block settlement accumulation mechanism proposed by Karamitros et al. (2013a) allows the identification of the following two groups of basic problem parameters:



This project has received funding from the European Union's Horizon 2020 research and innovation programme under grant agreement No. 700748

- a) Loading and strength parameters, related to the activated failure mechanism, namely: the average foundation bearing pressure q , the normalized thickness H/B and the undrained shear strength S_u (or c_u) of the clay crust, as well as the normalized thickness of the liquefiable sand layer Z_{liq}/B and the relative density D_r of the underlying liquefiable sand layer.
- b) Excitation characteristics, which control the amount of settlement accumulated when the above failure mechanism is activated, namely: the peak bedrock acceleration a_{max} , the peak bedrock velocity v_{max} (or, alternatively, the excitation period T) and the number of significant loading cycles N .

The proposed expression for the dynamic settlement ρ_{dyn} (i.e. the settlement during shaking) is shown in Equation (2.57), being c a foundation aspect ratio correction (Equation (2.58) where $c'=0.003$), a_{max} the peak bedrock acceleration, T the representative period of the motion, N the number of cycles of the excitation, Z_{liq} the thickness of the liquefiable sand layer, B the structure width and FS_{deg} the degraded static factor of safety of the foundation due to liquefaction.

$$\rho_{dyn} = c \cdot a_{max} \cdot T^2 \cdot N \cdot \left(\frac{Z_{liq}}{B}\right)^{1.5} \cdot \left(\frac{1}{FS_{deg}}\right)^3 \quad (2.57)$$

$$c = c' \left(1 + 1.65 \frac{L}{B}\right) \leq 11.65 \cdot c' \quad (2.58)$$

$$a_{max} \cdot T^2 \cdot N = \pi^2 \cdot \int_{t=0}^{N \cdot T} |v(t)| dt \quad (2.59)$$

FS_{deg} can be calculated through of the static loading ratio, the degraded bearing capacity ($q_{ult,deg}$) divided by the bearing pressure (q).

The foundation bearing capacity failure mechanism is simulated by the Meyerhof and Hanna (1978) model for a crust on a weak layer using the degraded friction angle in Equation (2.60) where U is the average excess pore pressure ratio of the liquefied sand and φ_0 is the initial friction angle. Superficial crust is beneficial and there is an upper bound beyond where failure occurs entirely within the crust and does not get affected by the liquefiable layer.

$$\varphi_{deg} = \tan^{-1}[(1 - U) \cdot \tan \varphi_0] \quad (2.60)$$

Even though the methodology is based on theoretical concepts and principles, it remains empirical. Hence, its application should respect the range of problem parameters considered in the numerical analyses. In this sense, this expression is strictly relevant to an infinitely extending and purely cohesive crust, as well as to an adequately thick liquefiable sand layer which will heavily modify the seismic motion at the foundation level. The variables corresponding to the input motion refer to an equivalent sinusoidal excitation but any heterogeneous seismic record can be used by relating those variables to the velocity time-history.

Bray and Macedo (2017)

The simplified procedure proposed by Bray and Macedo (2017) is the result of an extensive in-situ, experimental and analytical work. As a result of it, a numerical procedure has been satisfactorily calibrated



This project has received funding from the European Union's Horizon 2020 research and innovation programme under grant agreement No. 700748

for the evaluation of liquefaction in soil below buildings; and simultaneously, it has been identified which intensity measures provide better prediction of total settlements.

Consequently, a parametric set of over a thousand numerical analyses was conducted, and the influence of the different parameters on the deviatoric settlement was disaggregated, showing rather consistent trends. The influence of the degraded bearing capacity was shown to be very important: buildings near to the liquefaction-induced bearing collapse show a dramatic increment of settlement. Hence, the authors suggest that, for low bearing capacity factors of safety, the evaluation of settlements is not applicable.

A purely empirical expression for the deviatoric settlement (see Equation (2.61)) is obtained as a best-fitting regression of the results of the parametric analyses.

$$\ln(D_S) = c_1 + 4.59 \cdot \ln(Q) - 0.42 \cdot \ln(Q)^2 + c_2 \cdot LBS + 0.58 \cdot \ln(\tanh(H_L)) - 0.02 \cdot B + 0.84 \cdot \ln(CAVdp) + 0.41 \cdot \ln(S_a) + \varepsilon \quad (2.61)$$

$$CAVdp = \sum_{i=1}^N (H(x) \int_{t_{i-1}}^i |a(t)| dt) \quad (2.62)$$

$$LBS = \int W \cdot \frac{\varepsilon_{shear}}{z} dz \quad (2.63)$$

where c_1 and c_2 assume values of -8.35 and 0.072 for LBS smaller than 16, respectively, and -7.48 and 0.014 otherwise; Q is the foundation contact pressure, H_L is the liquefiable layer thickness; B is the building width; S_a is the spectral acceleration at a period equal to 1 second and ε is a normal random variable with 0.0 mean and 0.50 standard deviation in \ln units.

For determination of $CAVdp$, the standardised Cumulate Absolute Velocity as defined in Campbell and Bozorgnia (2012), Equation (2.62) was used where N is the number of discrete 1 second time intervals, x is $PGA_i - 0.025$ (PGA_i is the value of the peak ground acceleration (g) in time interval i , inclusive of the first and last values) and $H(x)$ is 0 if $x < 0$ or 1 otherwise.

Equation (2.63) was used for determination of LBS, an index of equivalent liquefaction-induced shear strain on the free-field (ε_{shear}), defined as the integration along the soil column of the strain estimated by means of the CPT-based procedure proposed in Zhang et al. (2004), weighted by the depth in order to provide more importance to the soil close to the foundation). ε_{shear} is calculated based on the estimated D_r of the liquefied soil layer and the calculated safety factor against liquefaction triggering (F_{SL}). $z(m)$ is the depth measured from the ground surface (> 0) and W is a foundation-weighting factor wherein $W = 0.0$ for z less than D_f , which is the embedment depth of the foundation, and $W = 1.0$ otherwise.

FLAC (Itasca, 2016)

In section 2.4 was demonstrated that Flac (Itasca, 2016), a numerical modelling software for advanced geotechnical analysis is able to get liquefaction-induced settlements. Settlements time-series obtained using 2D numerical models in this software were in relatively close agreement with centrifuge experiments results (see section 2.4). A description about the construction of the model in Flac can be found in section 2.4.1.



This project has received funding from the European Union's Horizon 2020 research and innovation programme under grant agreement No. 700748

2.6.2 PARAMETRIC STUDY

A parametric set of over a thousand nonlinear dynamic SSI effective stress 2D numerical analyses was performed to identify the key parameters controlling liquefaction-induced settlement for buildings with shallow foundations and compare the results in terms of settlement of the footing with Karamitros et al. (2013a) and Bray and Macedo (2017) approaches. Nine soil profiles, five foundations types and ten ground motions for three different scale factors were used to perform the 1350 analyses. The commercial software, FLAC 8.0 (Itasca, 2016) was used to perform the analyses (see section 2.4).

Model construction

The considered soil profile has three distinguishable layers with a total model thickness of 32 m and total width of 150 m, sufficiently large to capture free-field conditions, avoid wave reflections and reduce the influence of the lateral boundaries on the response of the footing (**Figure 2.77**). The first layer (crust) and third layer are composed of clay and the second layer (liquefiable layer) is composed of sand. Several parameters in the soil profile and foundation element were systematically varied in this study. **Table 2.11** shows the nine soil profiles considered. The water table is always located at a depth of 2.0 m.

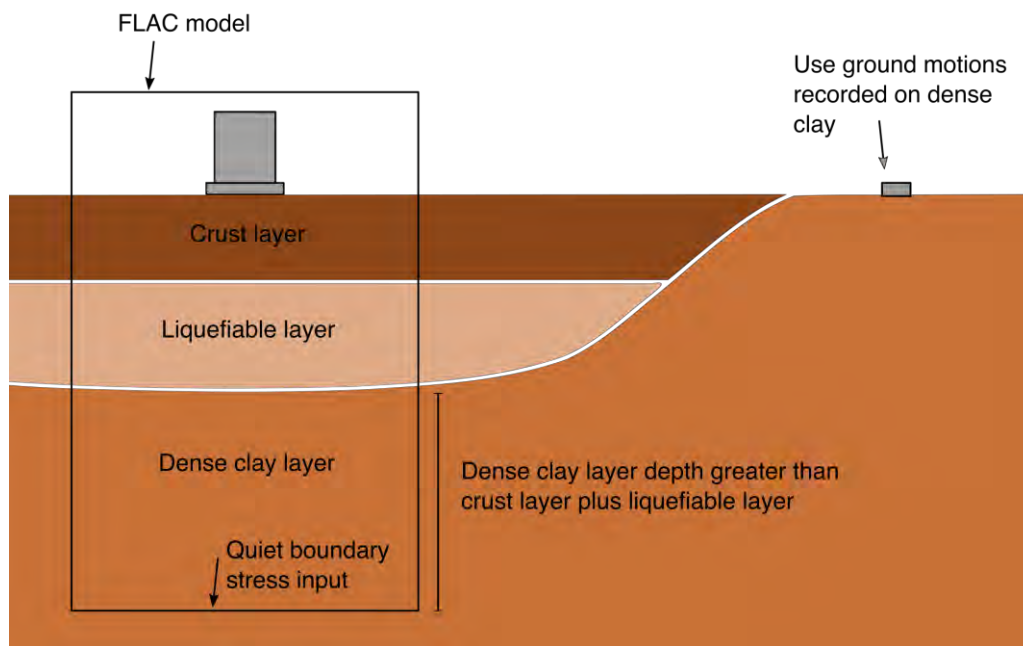


Figure 2.77: 2D Flac model considerations

The finite difference mesh was refined in the region closer to the footing and gradually coarsened towards the left and right boundaries to provide a better discretization in the area of interest. The lateral nodes at each depth were attached so they moved together and a compliant (also referred to as absorbing) base was used in the bottom boundary (Mejia and Dawson, 2006).



This project has received funding from the European Union's Horizon 2020 research and innovation programme under grant agreement No. 700748

Table 2.11: Soil profile properties considered in parametric study

Soil Profile	Layer 1 height [m]	Layer 2 height [m]	Layer 3 height [m]	Layer 2 Dr	Layer 1 strength [kPa]
1	3.88	4.85	23.27	0.55	50.0
2	1.94	4.85	25.21	0.55	50.0
3	7.76	4.85	19.39	0.55	50.0
4	3.66	4.57	23.77	0.55	50.0
5	4.41	5.52	22.07	0.55	50.0
6	3.88	4.85	23.27	0.55	30.0
7	3.88	4.85	23.27	0.35	50.0
8	4.00	2.00	26.00	0.55	50.0
9	4.00	8.00	20.00	0.55	50.0

Since a compliant boundary was used, a shear stress is specified for grid points along the base of the mesh (Mejia and Dawson, 2006) by converting the velocity time series using Equation (2.64) where σ_s is the applied shear stress, ρ is the mass density of the bottom layer, C_s is the velocity of shear wave propagation velocity and v_s is the input shear particle velocity.

$$\sigma_s = -factor \cdot \rho \cdot C_s \cdot v_s \quad (2.64)$$

Note that the factor in Equation (2.64) accounts for the input energy dividing into downward and upward propagating waves. The factor required calibration so that the input stress wave would produce the appropriate velocities at the bottom of the model that corresponds to the input velocity (Itasca, 2016). In the calibration procedure followed (Mejia and Dawson, 2006), an elastic analysis was conducted in DeepSoil (Hashash et al., 2016) and in FLAC, where the surface accelerations were compared to ensure that they matched. In Deepsoil the ground motion was applied as an acceleration time-history signal, and in FLAC the motion was input as a shear stress time-history corresponding to the same acceleration. The computed acceleration time series at top of the soil profile is shown in **Figure 2.78**. To obtain the same record in the surface, the factor was set to 1.1.



This project has received funding from the European Union's Horizon 2020 research and innovation programme under grant agreement No. 700748

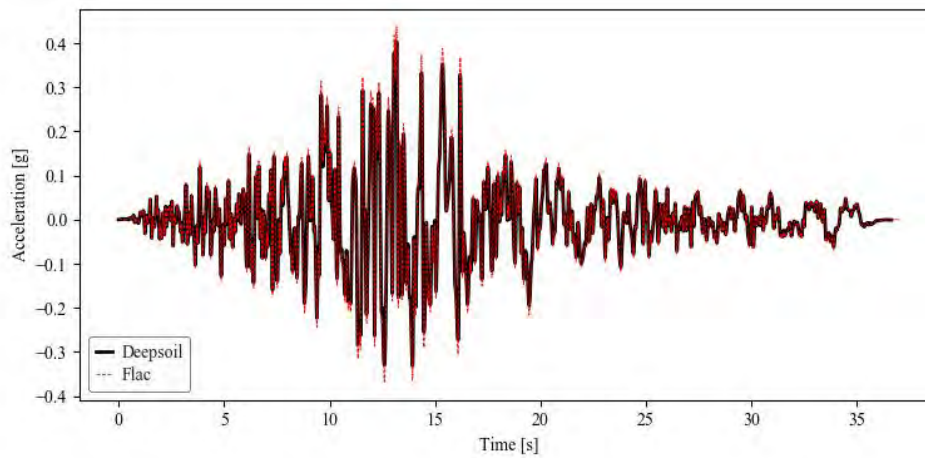


Figure 2.78: Calibration of the factor in Equation (2.64)

Ground motions

The European Ground Motions Database (Ambraseys et al., 2002) was used to select the ground motions. From this database, it was computed the error comparing the displacement spectra of each ground motion and the design spectra, according to Eurocode 8 – Part 1 (CEN, 2004a). The ground motions were selected according the following criteria:

- Vs measured at bottom between 250 and 400 m/s
- Magnitude between 5.5 and 7.6
- Distance greater than 20 kms to epicentre

Scale factors set to a range of values from 0.3 to 3.0. The range period of interest was set from 0.6 to 2.0 seconds. 10 ground motions were selected with an error smaller than 0.6. For the analyses in total were use 40 ground motions, the 10 in **Table 2.12** for three different scale factors (0.1, 0.25 and 0.4).

Table 2.12: Soil profile properties

id	Record	Time [sec]	SF	Error	Magnitude	Name
1	EURO127 1	41.33	3.0	0.23879	6.4	Friuli
2	EURO197 1	34.98	2.4	0.13967	7.4	Tabas
3	EURO531 2	28.185	1.4	0.46361	6.6	Pasinler
4	EURO844 2	22.99	1.8	0.26955	6.7	Spitak
5	EURO935 1	29.505	2.3	0.1338	7.4	Manjil
6	EURO5684 1	33.87	1.9	0.31591	7.1	Duzce
7	EURO5687 2	53.96	0.5	0.42016	7.1	Duzce
8	EURO9289 2	46.455	3.0	0.40616	6.5	Avej
9	EURO17405 1	68.25	3.0	0.46154	5.9	Simav
10	EURO17423 1	73.864	1.7	0.09369	7.1	Van



This project has received funding from the European Union's Horizon 2020 research and innovation programme under grant agreement No. 700748

Foundation

For this study only a mat footing was modelled to represent the building. The five foundations in **Table 2.13** were considered. The width of the foundations and the building contact pressure were varied.

Table 2.13: Foundation properties considered in parametric study

Foundation	Width [m]	Load [kPa]
1	10.0	80.0
2	3.0	80.0
3	16.0	80.0
4	10.0	40.0
5	10.0	130.0

The mat footing was modeled as a RC structure, for which the density of the concrete was assumed to be 2500kg/m^3 and the elastic Young's modulus (E) is $3.3\text{E}7$ kPa. The structural element was modeled as a beam element available in the software. The footing bearing pressure was applied as a distributed force to the nodes along the beam element.

Unglued interface elements were applied between the footing and the surrounding soil to account for the frictional interaction between the two. A friction and dilation angle of 33 degrees and 0 degrees respectively were assigned and slip was allowed. Within the code, the interface is represented as a series of normal and shear springs that connect the opposing surfaces at interacting nodes. The corresponding normal and shear stiffnesses of the springs were both set to 20 MPa.

Material models

Mohr-Coulomb constitutive model was used in the three layers to calculate the initial stresses in the soil profile before the dynamic load to be applied. **Table 2.14** gives the list of input parameters for the static phase. The shear modulus for the sandy layer was calculate from the normalised shear modulus (G_0), the atmosphere pressure (p_{atm}), and the effective confining pressure (p') in the middle of the layer.



This project has received funding from the European Union's Horizon 2020 research and innovation programme under grant agreement No. 700748

Table 2.14: Mohr-Coulomb parameters for 2D parametric study

Parameter	Unit	Layer 1	Layer 2	Layer 3
Density(ρ_{dry})	kg/m ³	$\frac{G_s \cdot 1000}{1 + e}$	$\frac{G_s \cdot 1000}{1 + e}$	$\frac{G_s \cdot 1000}{1 + e}$
G_s	-	2.70	2.65	2.70
e	-	0.7	$\frac{e_{max} - D_r}{e_{max} - e_{min}}$	0.6
e_{max}	-	-	0.8	-
e_{min}	-	-	0.5	-
Shear modulus(G_{max})	MPa	Undrained strength*1000	$G_o p_A \left(\frac{p'}{p_A}\right)^{1/2}$	Undrained strength*1000
Constant volume friction angle (ϕ_{cv})	°	0	33	0
Permeability (k_H)	m/s	8.00x10-8	1.60x10-5	1.00x10-9

The permeability of any material should be set by the mobility coefficient (coefficient of the pore pressure term in Darcy's law) required by FLAC and designated by k (m²/Pa.sec) (see section 2.4).

During the dynamic load in the clayey layers (crust and bottom layer), the Mohr-Coulomb model was kept and a hysteretic damping was added. The models were combine to provide suitable modelling of the site-response and bearing capacity. The site-response is sensitive to the shear stiffness and strain-based degradation of stiffness, and therefore was captured using the hysteretic damping option. The bearing capacity is sensitive to the soil strength capacity and therefore the Mohr-Coulomb constitutive model was used to achieve this. Using the MC model also had the added benefit that when the yield criterion is met than the hysteretic damping becomes inactive in those zones (page 83 Dynamic Analysis - FLAC Manual).

The hysteretic damping curves were based on research by Vardanega and Bolton (2013), however, the proposed shear modulus reduction curves from Vardanega and Bolton (2013) could not be directly implemented into FLAC as the exact functional form is currently not available. Therefore the model was fitted to the default functional form in FLAC (**Figure 2.79**). The Mohr-Coulomb failure criterion was set as 10% lower than the 'failure' point of the hysteretic model, defined as the stress that is required to reach the strain set by the L₂ parameter. The limit from hysteretic damping is required because the hysteretic damping option does not have suitable behaviour beyond the L₂ range. The model was initialised with the Mohr-Coulomb model with no hysteretic damping applied. This allowed for a quick convergence. However, it means that the static stresses from the foundation do not affect the nonlinearity from the hysteretic damping (page 83 Dynamic Analysis - FLAC Manual).



This project has received funding from the European Union's Horizon 2020 research and innovation programme under grant agreement No. 700748

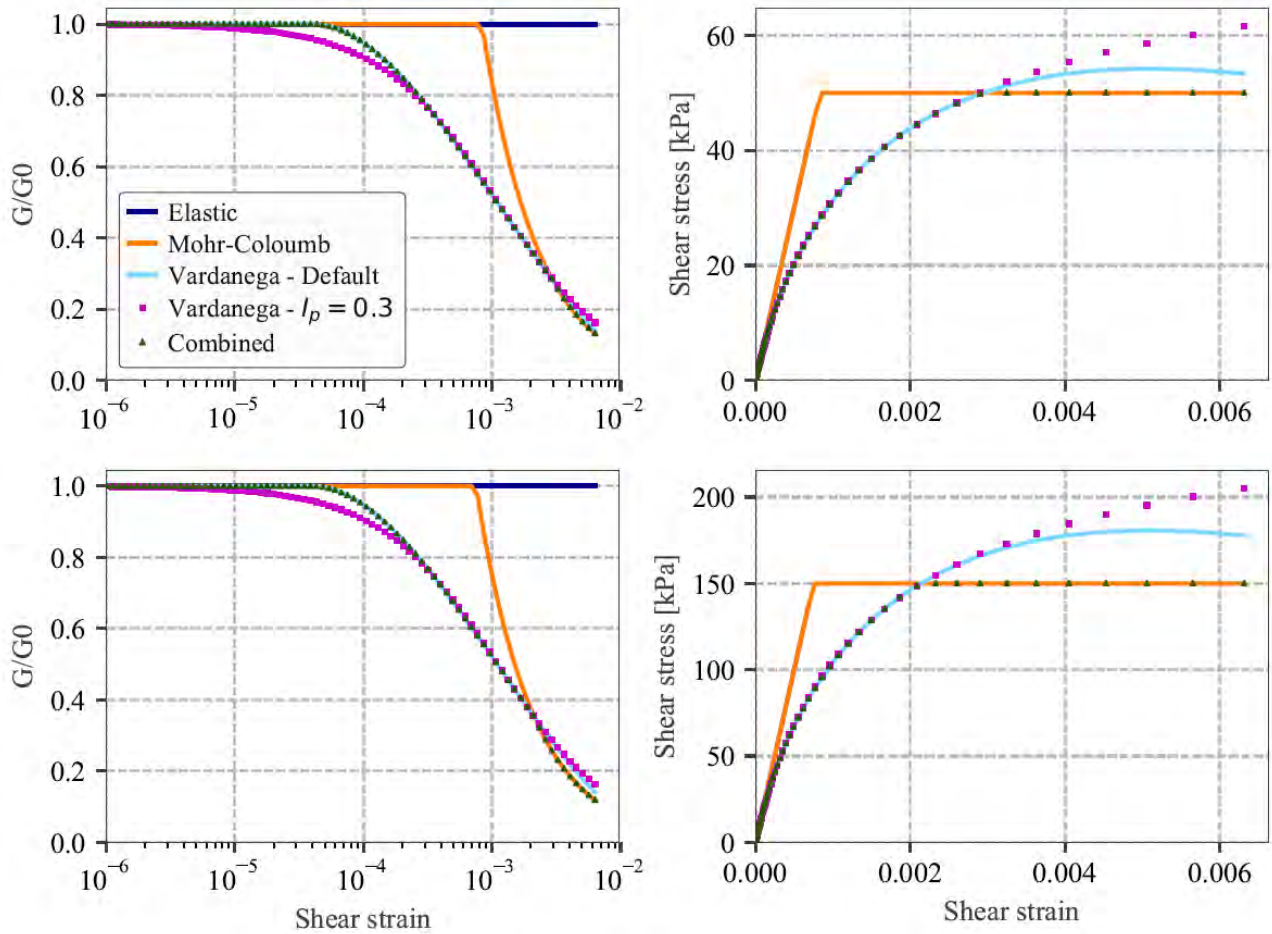


Figure 2.79: Clay theoretical tau gamma backbone

The PM4Sand constitutive model was adopted to simulate the behaviour of the second layer in the dynamic phase (See section 2.4). The shear modulus coefficient (G_0) was taken in PM4Sand Manual (Boulangier and Ziotopoulou, 2017) for the sand with $Dr=35\%$ as 476 and for the sand with $Dr=55\%$ as 677. The contraction rate parameter (hpo) was always assumed as 0.5. The secondary set of parameters were kept default.

Rayleigh damping

A small amount of Rayleigh damping was used in the numerical model to provide stability and simulate energy loss at small strain, consistent with other uses of the PM4Sand model (e.g. Luque (2017)). The parameters for the Rayleigh damping were input by setting the damping as both stiffness and mass proportional and then defining the ξ_{min} and f_{min} parameter using Equation (2.65) and (2.66), which correspond to the minimum point in the damping versus frequency relationship. f_1 and f_2 correspond to the lowest and highest frequencies of interest in the model, and $\xi_{1,2}$ is the ratio of critical damping set at those frequencies.

$$\xi_{min} = \sqrt{\alpha \cdot \beta} \tag{2.65}$$



This project has received funding from the European Union's Horizon 2020 research and innovation programme under grant agreement No. 700748

$$f_{min} = \frac{2 \cdot f_1 \cdot f_2}{\sqrt{4 \cdot f_1 \cdot f_2}} \quad (2.66)$$

$$\alpha = \frac{2 \cdot w_1 \cdot w_2}{w_2^2 - w_1^2} (w_2 \xi_{12} - w_1 \xi_{12}) \quad (2.67)$$

$$\beta = \frac{2}{w_2^2 - w_1^2} (w_2 \xi_{12} - w_1 \xi_{12}) \quad (2.68)$$

The lowest frequency of interest (f_1) is typically governed by the lowest natural frequency of the soil deposit or the lowest frequency of soil-structure system. The lowest frequency of the soil deposit corresponds to the first mode of the liquefied site, which was estimated by performing an elastic site response analysis $f_1=0.56$ [Hz] using the software Deepsoil (Hashash et al., 2016). The highest frequency of interest was governed by the 2nd mode frequency of the soil-structure system $f_2=5$ [Hz]. $\xi_{1,2}$ was set as 1%.

2.6.3. SETTLEMENTS OF BUILDINGS RESULTS

Figure 2.80 shows the settlements in the centre of the foundation obtained from numerical analyses (parametric study) compared with settlement values calculated from Karamitros et al. (2013a) and Bray and Macedo (2017) equations. Some discrepancies can be observed and an overestimation trend is observed in comparison to the latter empirical proposals, but in general these approaches provided reasonably consistent estimates of settlement compared to the results from FLAC.

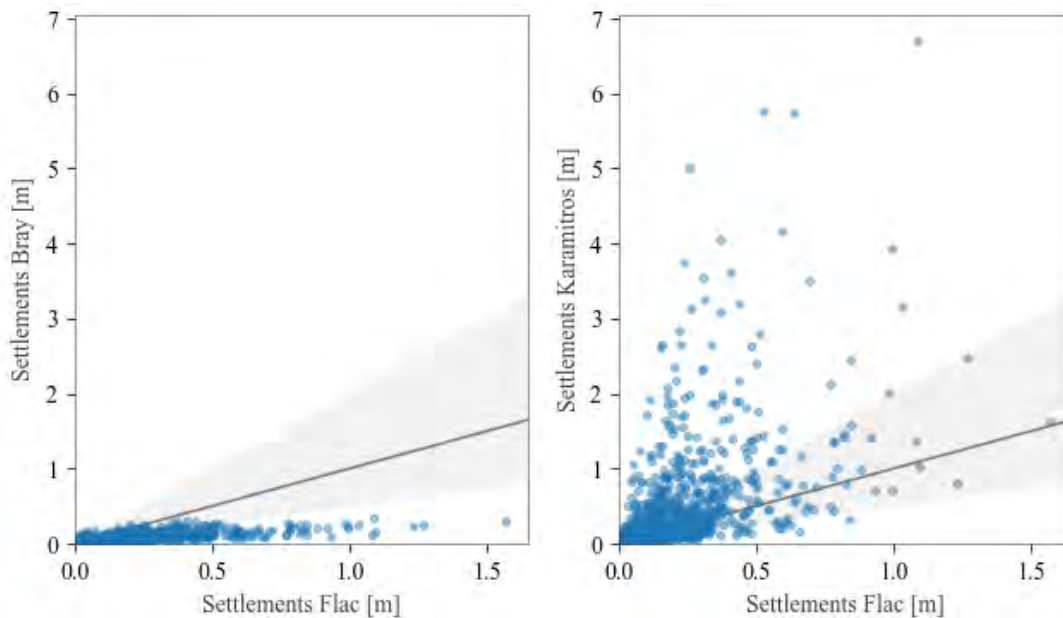


Figure 2.80: Comparison between numerical and analytical results of total settlements

The time history of foundation settlement from the numerical simulation is compared with the Karamitros et al. (2013a) and Bray and Macedo (2017) approaches in **Figure 2.81** for soil profile 8 and foundation 1 (B=10 and contact pressure=80kPa) using the ground motion #2 (Tabas, Mw=7.4) with scale factor of 0.25. Karamitros et al. (2013a) and Bray and Macedo (2017) can only be used to calculate the total seismic



This project has received funding from the European Union's Horizon 2020 research and innovation programme under grant agreement No. 700748

settlement of isolated buildings. A time series of the settlement was constructed using the integral of velocity for each dt in Karamitros et al. (2013a) and the cumulative CAVdp in Bray and Macedo (2017).

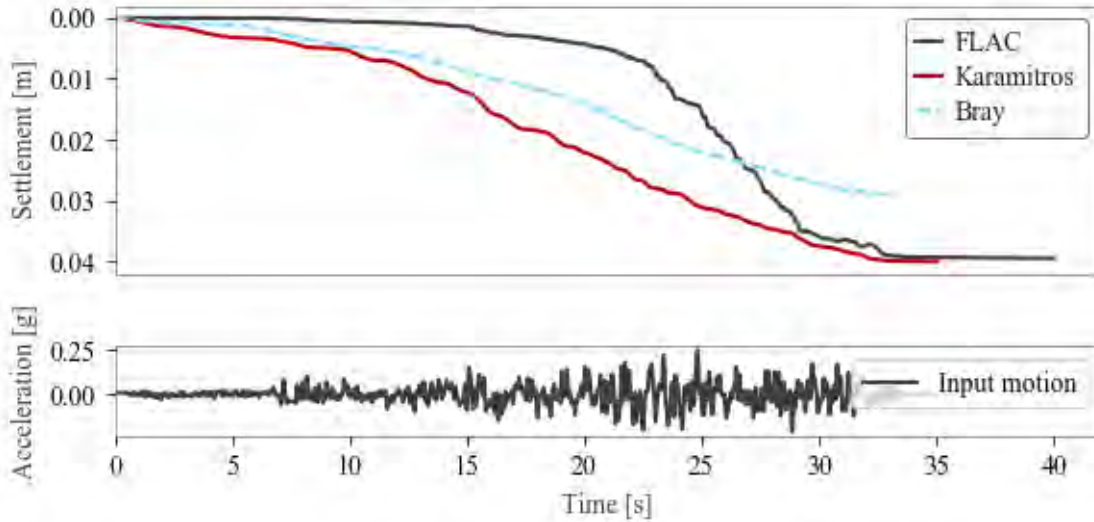


Figure 2.81: Comparison between numerical and analytical settlements for Soil Profile: 8 – Foundation: 1 – Ground motion: 2– Scale factor: 0.25

Based in Karamitros et al. (2013a) approach, another methodology (Karamitros modified) is proposed in this study to improve the time-series settlement results. The method consists in multiply the total settlement calculated from the original equation (See section 2.6.1) by a “weight” that depends on the Pore pressure ratio (R_u) time-series (See section 2.5). The time-series settlement can be calculated using the Equation (2.69) and **Figure 2.82** shows the comparison with the original Karamitros et al. (2013a) methodology.

$$\rho_{dyn,i} = c \cdot \pi^2 \cdot \int_{t=0}^{N \cdot T} |v(t)| dt \cdot \left(\frac{Z_{liq}}{B}\right)^{1.5} \cdot \left(\frac{1}{FS_{deg}}\right)^3 \cdot \frac{\sum_0^i |v_i| \cdot r_{u,i}}{\sum_0^{N \cdot T} |v_i| \cdot r_{u,i}} \quad (2.69)$$



This project has received funding from the European Union's Horizon 2020 research and innovation programme under grant agreement No. 700748

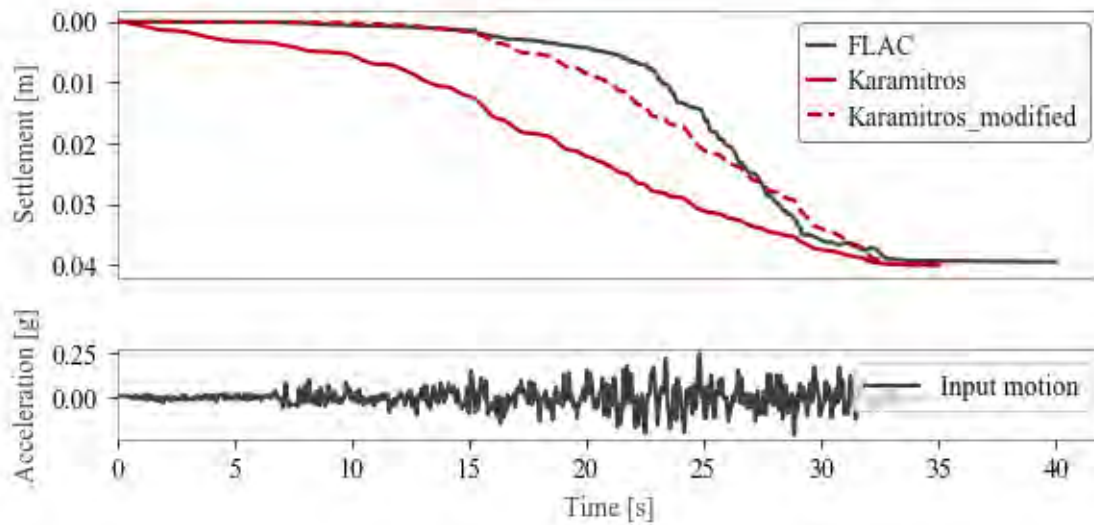


Figure 2.82: Comparison between numerical and analytical settlements for Soil Profile: 8 – Foundation: 1 – Ground motion: 2– Scale factor: 0.25

2.6.4. MODELLING RECOMMENDATIONS AND CONCLUSIONS

Karamitros et al. (2013a) and Bray and Macedo (2017) methodologies, provided viable options for efficiently assessing the total dynamic settlement of a building compared with nonlinear effective stress numerical calculations results.

The numerical model was validated against centrifuge experimental results in section 2.4 and a description about the construction of the model in Flac (Itasca, 2016) can be found in the same section. This method captures more of the response than the analytical methods as the shear demand, site response, water flow and soil-structure interaction are all directly modelled, but it requires a high computational effort (approximately 3 hours for a 40 second ground motion and a 2D foundation-only model) and therefore 2D modelling is not justifiable for vulnerability analysis unless the building is deemed critical and susceptible to liquefaction.

Karamitros et al. (2013a) results showed a good fit with Flac estimation when the excess pore pressure ratio was calculated with the energy based method in section 2.5. The pore pressure ratio time series can also be used to obtain the settlement time-series using the Karamitros modified method.

Bray and Macedo (2017) requires to perform a liquefaction triggering assessment, and calculate the safety factor against liquefaction triggering (FS_L) for each potentially liquefiable layer preferably using a CPT-based method. It showed an underestimation of the settlements when compared with Flac modelling. In this study a CSR for 15 cycles was obtain through element tests to calculate FS_L from Boulanger and Idriss (2014) method.



This project has received funding from the European Union's Horizon 2020 research and innovation programme under grant agreement No. 700748

2.7 SIMPLIFIED PROCEDURE TO ESTIMATE SURFACE GROUND MOTION

2.7.1 INTRODUCTION

The primary damage to buildings during earthquakes is shaking damage, therefore the modification to the ground shaking due to liquefaction is extremely important in the context of quantifying building performance.

Typically we can observe that ground motions from liquefied deposits have less high frequency content and can have larger displacement demands than their non-liquefied equivalents. Ishihara and Cubrinovski (2005) investigated the ground motions recorded at the Kobe Port Island Vertical Array site during the 1995 Kobe earthquake, illustrating that liquefaction caused a reduction in shaking amplitude, a loss of high frequency content and a shift to longer period motion in comparison to the adjacent Pack House site which experienced less liquefaction. In Adapazari, the heaviest concentrations of damage in the city generally coincided with surface soils that were less sensitive to liquefaction, whereas in areas with higher susceptibility to liquefaction, the building damage was relatively reduced (Bakir et al., 2002). These perceived beneficial effects have even prompted interest in deliberately using liquefaction to isolate buildings from strong shaking (e.g. Bouckovalas et al., 2017a; Mousavi et al., 2016).

However, liquefaction does not always result in less shaking. Bouckovalas et al. (2016) demonstrated that liquefaction of the soil can cause an amplification in the seismic shaking especially in lower frequencies which is highly dependent on the depth of the liquefied layer. Moreover, investigations by Wotherspoon et al. (2015) of the ground motion station NNBS during the 2011 Christchurch earthquake demonstrated post-liquefaction acceleration spikes that were double the size of pre-liquefaction acceleration values.

Our current understanding is that liquefaction causes a reduction in soil stiffness, increase in soil shear strain, and can amplify and reduce particular frequencies of the surface shaking.

Conceptually the reduction in stiffness can provide protection to buildings similar to base isolation techniques used within structural engineering and is often referred to as “natural seismic isolation” (**Figure 2.83**).

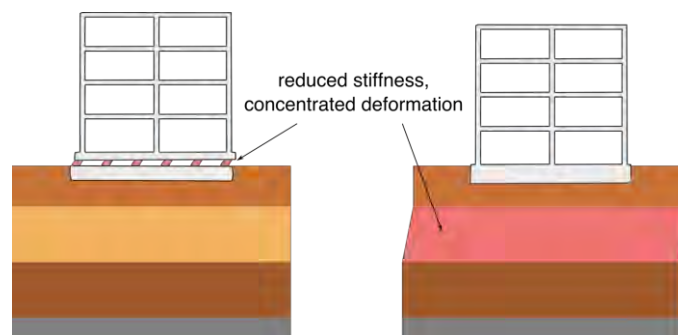


Figure 2.83: Natural seismic isolation due to liquefaction

The reduced stiffness lengthens the characteristic site period and means that shear waves dissipate more energy over the same distance because shear wave speeds have reduced, this is particularly evident for small cycle (high frequency) waves. The energy dissipation per cycle is also increased because the softer soil



This project has received funding from the European Union's Horizon 2020 research and innovation programme under grant agreement No. 700748

undergoes larger nonlinear strains and therefore the liquefied layer can act as a high-pass filter. However, not all frequencies are reduced. In some cases, particular frequencies can be amplified. The amplification of frequencies is dependent on the characteristic site period (fundamental frequency) of the soil deposit. When shaking frequencies are close to the fundamental frequency of the deposit the upward propagating wave reflects off the surface and superimposes forming standing wave that increases the surface shaking amplitude (**Figure 2.84**).

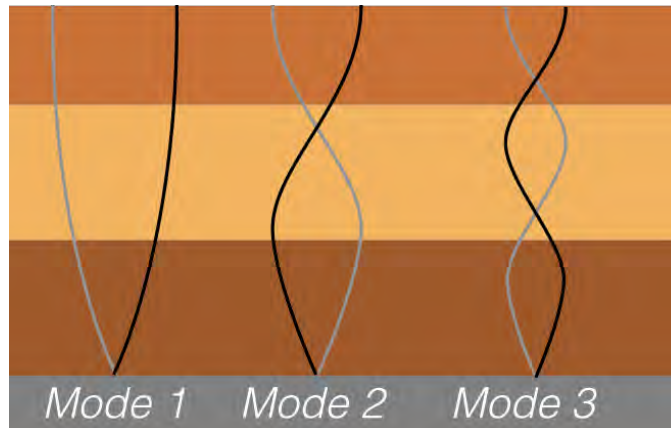


Figure 2.84: Standing wave modes that cause site amplification

The major parameters influencing the amplitude of amplification/de-amplification are the base soil stiffness contrast (i.e. how much wave energy is reflected back into the soil deposit) and the level of energy dissipation as the wave propagates through the soil. In terms of which frequencies are amplified, the major parameters are the shear wave velocity (V_s) and height of the deposit (H), as the natural modes of a site deposit can be approximated from Equation (2.70), where m is the wave number (Kramer, 1996).

$$T_m = \frac{4H}{(2m + 1)V_s} \quad (2.70)$$

When the soil deposit liquefies, the change in stiffness results in a change in the natural frequency of the soil deposit so different frequencies are superimposed. Kramer et al. (2011) investigated the ground motion recorded in the of Kawagishi-cho apartment building in 1964 Niigata earthquake and observed a shift in the dominant frequency of the motion from approximately 0.1s to 5 seconds once liquefaction occurred under the structure.

Additionally, the interface between liquefied and non-liquefied layers develops a stiffness contrast, which causes waves to reflect off the interface and can potentially cause superposition in the upper deposit (**Figure 2.85**).



This project has received funding from the European Union's Horizon 2020 research and innovation programme under grant agreement No. 700748

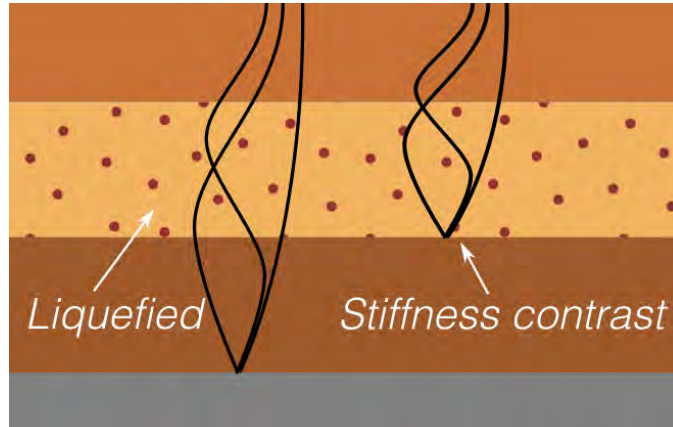


Figure 2.85: Site amplification in liquefied deposit

Bouckovalas et al. (2016) investigated the amplification of the shaking response of a two-layered visco-elastic soil deposit resting on a rigid bedrock. The top layer represented a non-liquefied crust and the lower layer represented a liquefied deposit, with a soil shear wave velocity ratio between the two layers ($V_{s,L}/V_{s,C}$) of 0.15, the densities were equal, the liquefied layer was three times thicker than the crust (H_L/H_C), and the viscous damping of the crust and lower deposit set to 10% and 15% respectively.

An analytical transfer function was developed between the bedrock acceleration and the top of the liquefied layer ($F(\omega)$) (Equation (2.71)).

$$F(\omega) = \frac{1}{\cos\left(2\pi\frac{H_L}{\lambda_L^*}\right) - a \tan\left(2\pi\frac{H_C}{\lambda_C^*}\right) \sin\left(2\pi\frac{H_L}{\lambda_L^*}\right)} \quad (2.71)$$

Where a is the impedance contrast between the crust and the liquefied layer, and λ^*L and λ^*C terms are the harmonic waves lengths in the liquefied layer and crust respectively.

This simple analytical model indicated that amplification of the excitation frequency would occur when the ratio of the height of the liquefied layer to the excitation wave length in the liquefied layer (H_L/λ^*L) was less than 0.25, while de-amplification would occur above this ratio.

Further work by Millen et al. (2019a) showed that for a soil profile with a single liquefiable layer, the change from de-amplification to amplification is dependent on the thickness of the liquefiable layer, and nonliquefying surface layer, as well as the reduction in stiffness of the liquefiable layer.

For the purpose of vulnerability analysis the surface shaking must be quantified to assess the dynamic performance of the building. One option is to perform nonlinear fully-coupled effective stress analysis using either finite element or finite difference formulations. The procedure depends on numerous input model parameters and ability of the constitutive model to reproduce the effects of excess pore pressure build-up. It has been successfully demonstrated on field recordings (e.g. Ishihara and Cubrinovski, 2005; Markham et al., 2016) and against centrifuge tests (e.g. Andrianopoulos et al., 2010; Karimi and Dashti, 2016). A more extensive review of constitutive models and effective stress analysis can be found in LIQUEFACT Deliverable 3.1 (Viana da Fonseca et al., 2017). The techniques to account for pore pressure build up vary significantly (e.g. based on number of cycles, cumulative elastic or inelastic shear strain), many of the most advanced



This project has received funding from the European Union's Horizon 2020 research and innovation programme under grant agreement No. 700748

models are discussed in Viana da Fonseca et al. (2017) Section 2.3 on soil constitutive models. Advanced constitutive models can capture the strength and stiffness degradation associated with the initiation of liquefaction, and can model the phase transformation of a soil changing from contractive to dilative, which is an important aspect in capturing acceleration spikes (Kramer et al., 2011). The majority of effective stress models are full constitutive models, however, there are also backbone curve-based effective stress models, which are simpler, in that the shape of the backbone response is modified based the level of pore pressure build up (e.g. Matasović and Vucetic, 1993).

There are other techniques for modelling site response, such as discrete particle methods and other mesh-less methods, however, these models have not matured enough to be used in practice or even widely within research circles (NASEM, 2016). There are also various advantages of using two-dimensional and three-dimensional models compared to the typical one-dimensional site response models, such as the ability to capture the influence of non-vertically oriented shear waves and capture basin effects. However, two-dimensional and three-dimensional models are considerably more computational demanding and will not be considered further here but further discussion can be found in Kramer (1996).

Alternative simplified analyses that decouple the build-up of pore pressure from the site response analysis have the advantage of exploring different assumptions about liquefaction triggering and being numerical efficient. Miwa and Ikeda (2006) proposed a method for assessing the site response of a liquefied deposit using equivalent linear analysis and reduced stiffness properties for the liquefied soil. The method was particularly developed for the assessment of piles where strains are typically the most damaging component. Bouckovalas et al. (2017b) reviewed this approach for obtaining the surface acceleration and demonstrated that it could provide reasonable estimates for the post-liquefaction section of the motion, but provided poor estimates of the pre-liquefaction section. Therefore Bouckovalas et al. (2017b) concluded that it should not be used for obtaining the surface acceleration when a soil has a reasonable resistance to liquefaction and the pre-liquefaction section may contain strong shaking.

Bouckovalas et al. (2017b) developed an adapted method called the "Spectral Envelope Method", where an equivalent linear analyses is preformed of the pre and post liquefaction segments of the ground motion, with the pre liquefaction segment using non-liquefied properties and the post-liquefaction segment using liquefied similar to Miwa and Ikeda (2006). Bouckovalas et al. (2017b) provided further guidance on the choice of post-liquefaction damping ratios and validated the proposed method against numerical analyses and recorded ground motions in the field. A recent method developed by Millen et al. (2019c) called the Stockwell transfer function (STF), is explored in detail in the following section. The STF extends the work by Bouckovalas et al. (2017b) and performs it in the time-frequency domain to obtain a surface acceleration time series. The STF is named because it creates a time-frequency transfer function between the upward propagating and surface motion to simulate liquefaction using the Stockwell transform. The upward propagating motion is first converted into the Stockwell transform in the time-frequency domain and then a series of excess pore pressure (time) dependent base-to-surface transfer functions are applied along the frequency axis before performing the inverse Stockwell transform to obtain the surface motion in the time domain.

There are many other mechanisms and phenomena that contribute to the response and ground shaking of a site. These phenomena have not been covered here as there are no specific interactions with liquefaction



This project has received funding from the European Union's Horizon 2020 research and innovation programme under grant agreement No. 700748

(i.e. they occur independently of whether liquefaction occurs). Several earthquake geotechnical engineering textbooks (e.g. Kramer, 1996) cover these effects which have been non-exhaustively listed below:

- Fault rupture mechanics
- Distance to fault
- Orientation incident shear waves
- Influence of surface waves
- Topographic amplification
- Basin effects

2.7.2 TIME-FREQUENCY FILTERING

The Stockwell transform or "S-transform" is an analytical more robust extension of the short-form Fourier transform, both of which present frequency content as a function of time (Stockwell et al., 1996).

A simple two frequency (0.5 and 5Hz) harmonic wave is shown in **Figure 2.86** and the Stockwell transform can be seen in **Figure 2.87**.

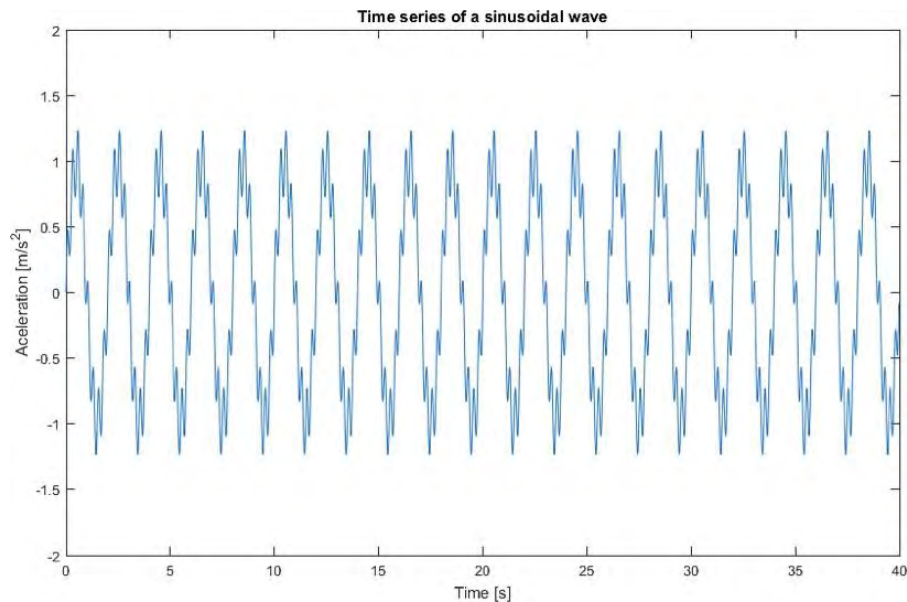


Figure 2.86: Two a frequency harmonic signal



This project has received funding from the European Union's Horizon 2020 research and innovation programme under grant agreement No. 700748

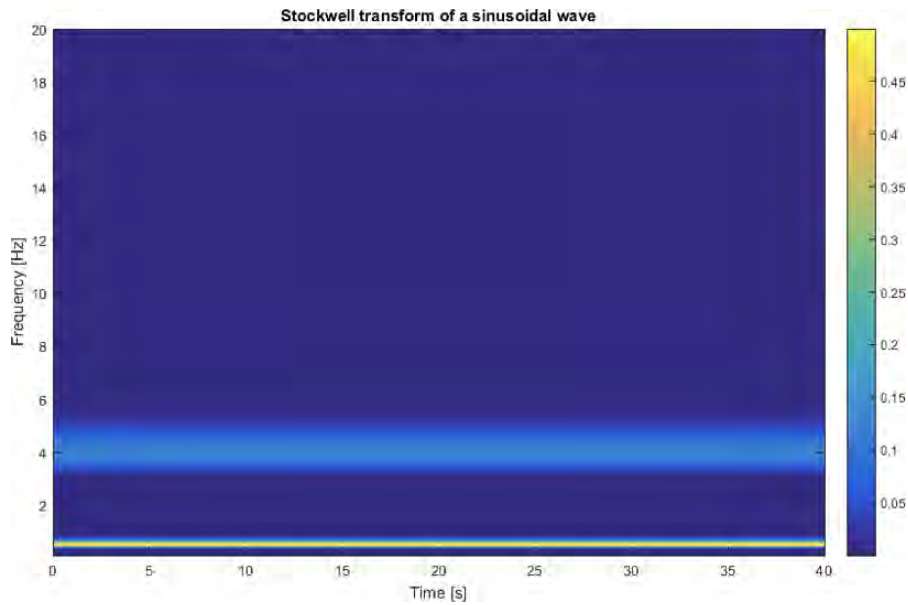


Figure 2.87: Stockwell transform of two a frequency harmonic signal

A Butterworth 4th order low-pass filter can be applied across the transform to filter out the 5Hz signal (Figure 2.88) and the inverse Stockwell transform can be applied to reproduce the signal in the time domain (Figure 2.89).

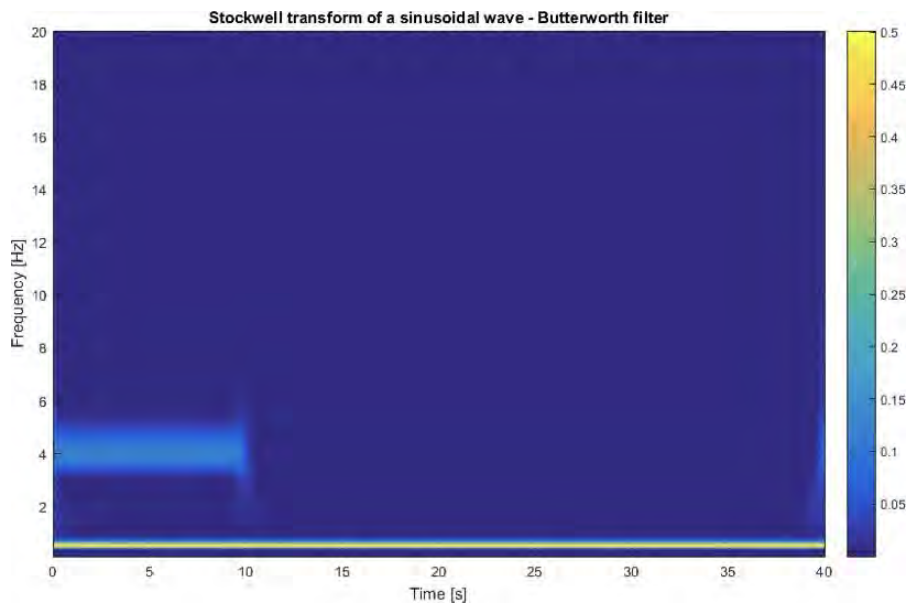


Figure 2.88: Stockwell transform of two a frequency harmonic signal



This project has received funding from the European Union's Horizon 2020 research and innovation programme under grant agreement No. 700748

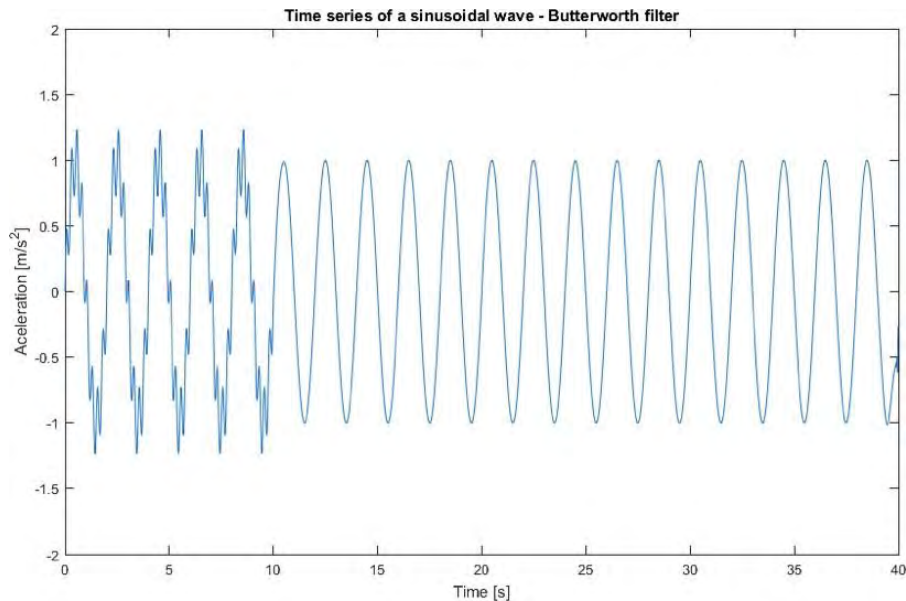


Figure 2.89: Two a frequency harmonic signal

2.7.3 THE STOCKWELL TRANSFER FUNCTION METHOD

The soil profile essential acts as a filter and converts the upward propagating wave to a surface motion. In the elastic soil domain a transfer function can exactly describe the filter in the frequency domain that converts the upward wave to the surface motion. While the solution is not exact for a nonlinear soil, the use of transfer functions is the basis for the majority of equivalent linear site response analysis tools.

In equivalent linear analysis the transfer function between the upward motion and surface is constant for the whole ground motion. However, in the event of liquefaction, the dramatic reduction in stiffness and increased energy dissipation makes the assumption of a constant transfer function invalid. Analysis number 26 from the 500 analyses presented in Millen et al. (2019b) and detailed in the pore pressure analysis section 2.5, can be used to illustrate the influence of liquefaction on the surface acceleration and transfer function. This analysis is a short record with liquefaction occurring in the middle of the strong shaking as seen in **Figure 2.90a - c**. The soil profile has a four metre non-liquefiable crust layer above a six metre liquefiable layer. The surface acceleration of the FLAC analysis with pore pressure build-up is shown in **Figure 2.90d** in comparison to the same analysis where excess pore pressure was prevented by setting the water bulk modulus to zero. The reduction in acceleration amplitude due to pore pressure build-up is dramatic. The Stockwell transform of surface acceleration of the liquefying motion is shown in **Figure 2.90e**, where the amplitude of high frequency content reduces immediately after liquefaction occurs. Finally **Figure 2.90e** shows in yellow the frequency content that was amplified with respect to the input motion, and purple the content that was de-amplified (i.e. **Figure 2.90e** divided by **Figure 2.90b**). The yellow block between 0-5 seconds and 1-5Hz is critical, the site response amplifies the ground motion at frequencies that are dangerous to short-to-mid-rise buildings. However, once liquefaction occurs at 4.7 seconds this block of yellow disappears, while a thin yellow line appears at very low frequencies. The yellow dashes at high frequencies throughout the record are due to numerical noise and the imperfect aliasing of the surface motion to the input motion time step, as in this can the surface motion exhibited not acceleration peaks due to soil dilation.



This project has received funding from the European Union's Horizon 2020 research and innovation programme under grant agreement No. 700748

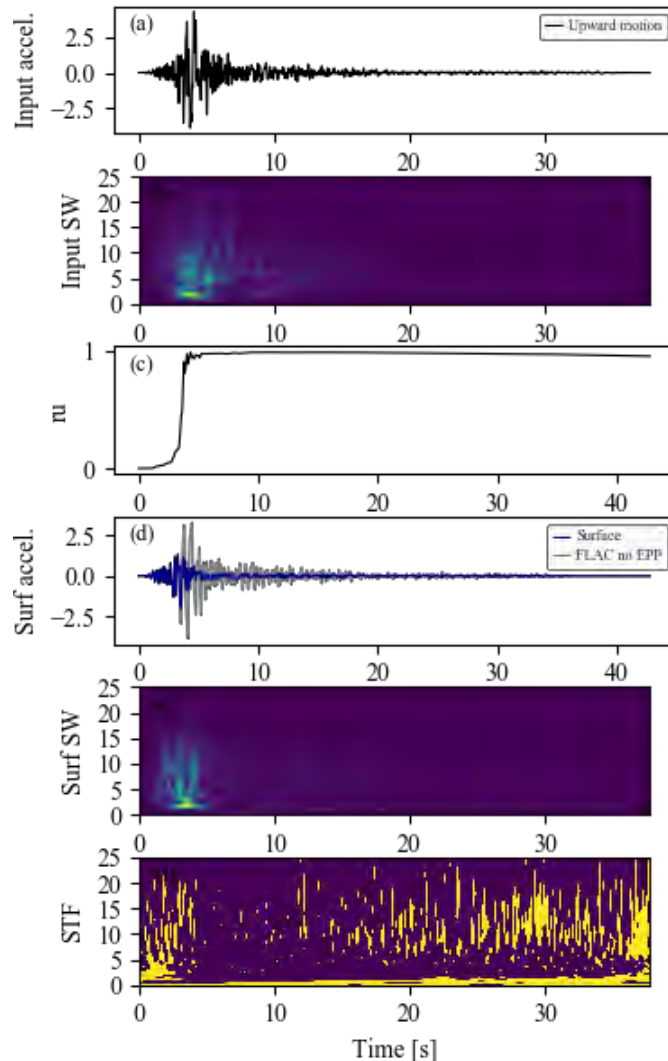


Figure 2.90: Influence of liquefaction on surface acceleration

The influence of liquefaction can be imitated by constructing transfer functions that represent the different parts of the ground motion (pre-liquefaction, liquefaction, post-liquefaction). To achieve this an equivalent linear site response analysis was conducted in the Open-source python package Pysra v0.3.0 Kottke (2018). The input to surface transfer function from this analysis was used for the pre-liquefaction segment, while the post-liquefaction segment used this transfer function but reduced the shear wave velocity by a factor of 10 and set the viscous damping to 20% for the liquefied layer. The liquefaction section was assumed to occur over three seconds from the point when the effective stress drops to below 5kPa in the centre of the liquefiable layer. During the liquefaction section the shear wave velocity was reduced and damping increased every 0.5 seconds by six equal incremental to match the post-liquefaction assumptions. The transfer functions are shown in **Figure 2.91**, where the pre-liquefaction section amplifies the acceleration signal at frequencies as high as 3.5Hz, while the post-liquefaction section only amplifies the motion at frequencies lower than 1Hz.



This project has received funding from the European Union's Horizon 2020 research and innovation programme under grant agreement No. 700748

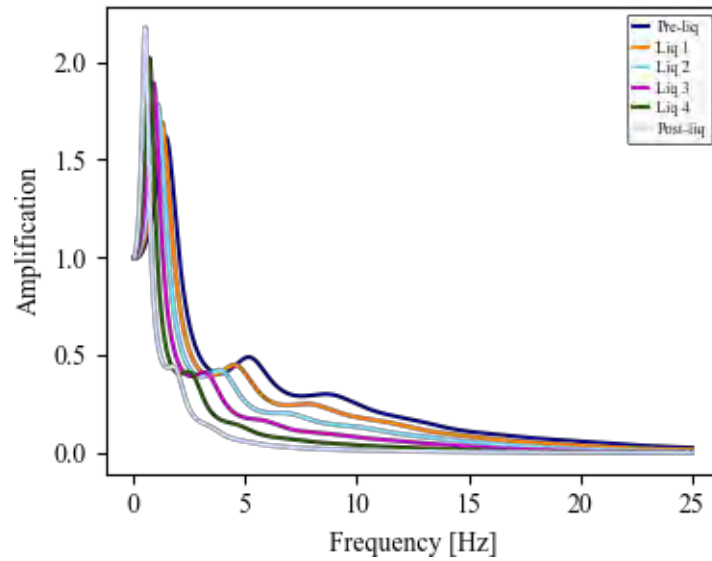


Figure 2.91: Transfer functions for Stockwell transfer function method

The same analysis (soil profile 26) has been simulated using the STF method in **Figure 2.92**, where the Stockwell transfer function is shown in **Figure 2.92d**. The yellow amplifying zone is clearly distinguished and follows the trends observed from the FLAC analysis. The transfer functions are applied to the input Stockwell transform and produce the surface Stockwell transform in **Figure 2.92e**, finally the inversion produces the surface time series **Figure 2.92f**.

Although the match is not perfect, it captures the key influential effects of liquefaction on the surface ground motion, particularly capturing the influence of the time of liquefaction and the changes in frequency content.



This project has received funding from the European Union's Horizon 2020 research and innovation programme under grant agreement No. 700748

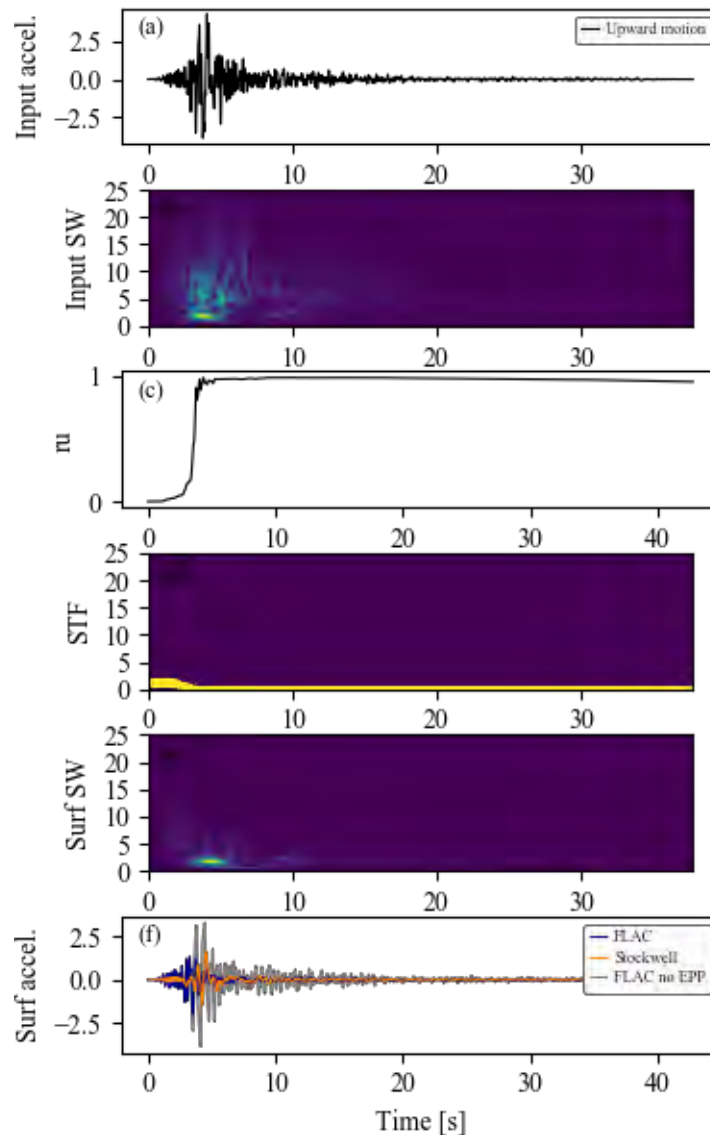


Figure 2.92: Stockwell explained example

2.7.4 COMPARISON OF METHODS

The Stockwell transfer function method is compared against two more analyses from the same set of 500 one-dimensional FLAC analyses presented in Millen et al. (2019b) and detailed in Section 2.5. The key attributes of the surface ground motion are typically the peak acceleration or velocity response spectra that governs the maximum deformation of the building, and the cumulative energy which gives an indication of the cumulative damage experienced by the building. The energy absorbed by a building is dependent on the frequency of the building and the frequency content of the ground motion. Since liquefaction strongly effects the frequency content (Kramer et al., 2011), a new spectrum is proposed here that is the cumulative absolute energy CAE of an SDOF. The CAE is calculated as the unit kinetic energy (Millen et al., 2019b) of a the response of a SDOF.



This project has received funding from the European Union's Horizon 2020 research and innovation programme under grant agreement No. 700748

Figure 2.93 presented the results of soil profile 26, showing the surface acceleration, pore pressure build-up, and input acceleration, as well as the displacement and CAE of two SDOFs, one with a period of 0.5s and one with a period of 3s.

Four different analyses are presented, FLAC with and without excess pore pressure, the equivalent linear analysis using Pysra, and the Stockwell transfer function method.

It can be seen that the FLAC analysis with excess pore pressure and Stockwell method are in close agreement, except for the additional high frequency content in the FLAC analysis prior to liquefaction. Meanwhile the FLAC with no excess pore pressure and the equivalent linear analyses are also in close agreement. This suggests that at least the Stockwell transfer function method correctly mimics the influence of liquefaction with respect to the response of the two SDOFs.

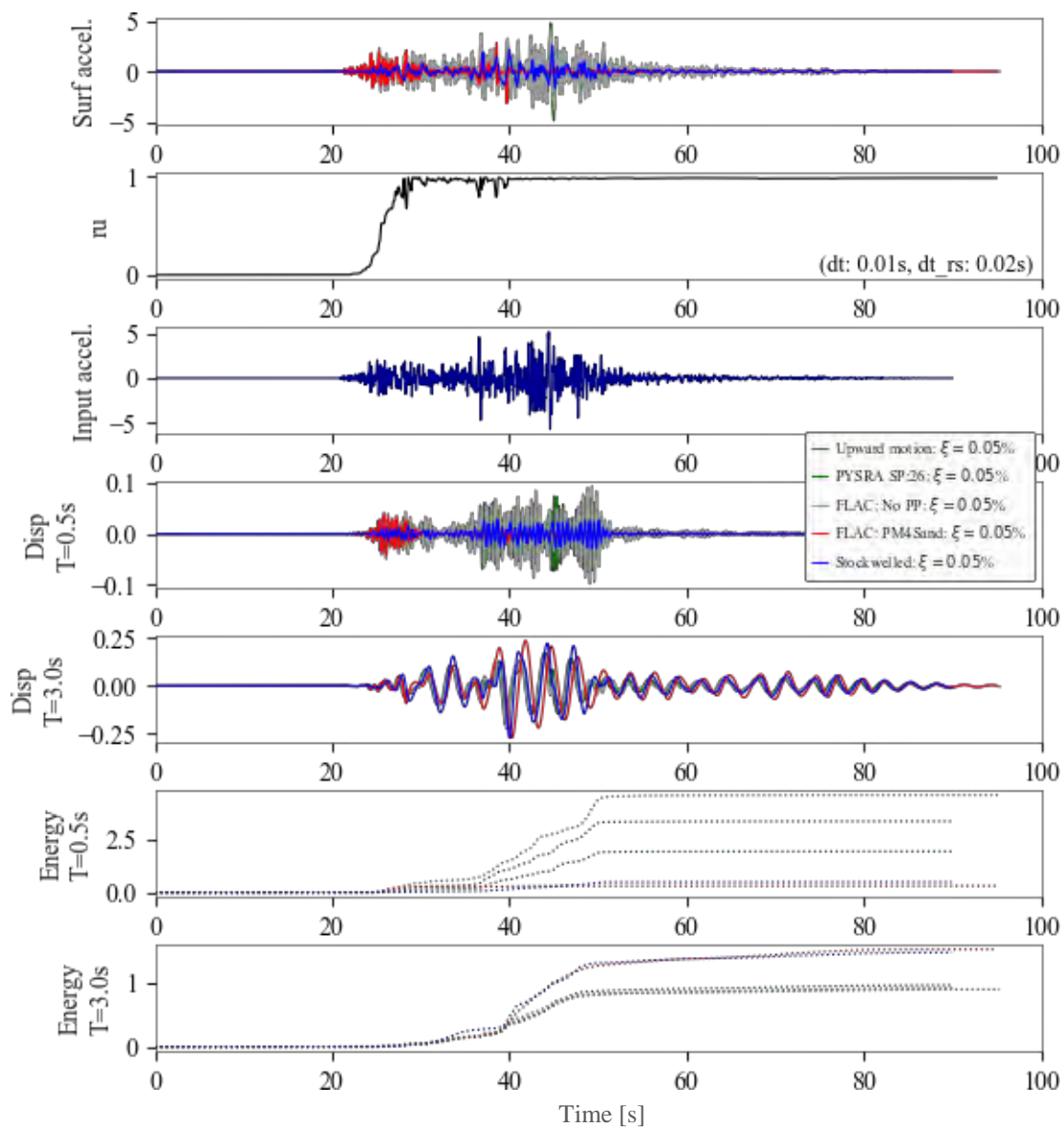


Figure 2.93: Comparison of time series for STF method



This project has received funding from the European Union's Horizon 2020 research and innovation programme under grant agreement No. 700748

In **Figure 2.94** the spectral velocity and the CAE spectrum are shown. Here the biases with the Stockwell method are more obvious, where the Stockwell method amplifies the peak response at about 1.7 seconds, whereas this amplification was not observed in the FLAC analyses. However, it does correctly reduce the high frequency and low frequency response. The same trend can be observed for the CAE spectrum where amplification was observed at about 1.7 seconds. This amplification appears to be because the FLAC analysis has almost zero surface motion after about 35 seconds, whereas the Stockwell method continues to amplify low frequency content. Further improvements to this method in terms of better calibration of the stiffness reduction and damping may yield improved results.

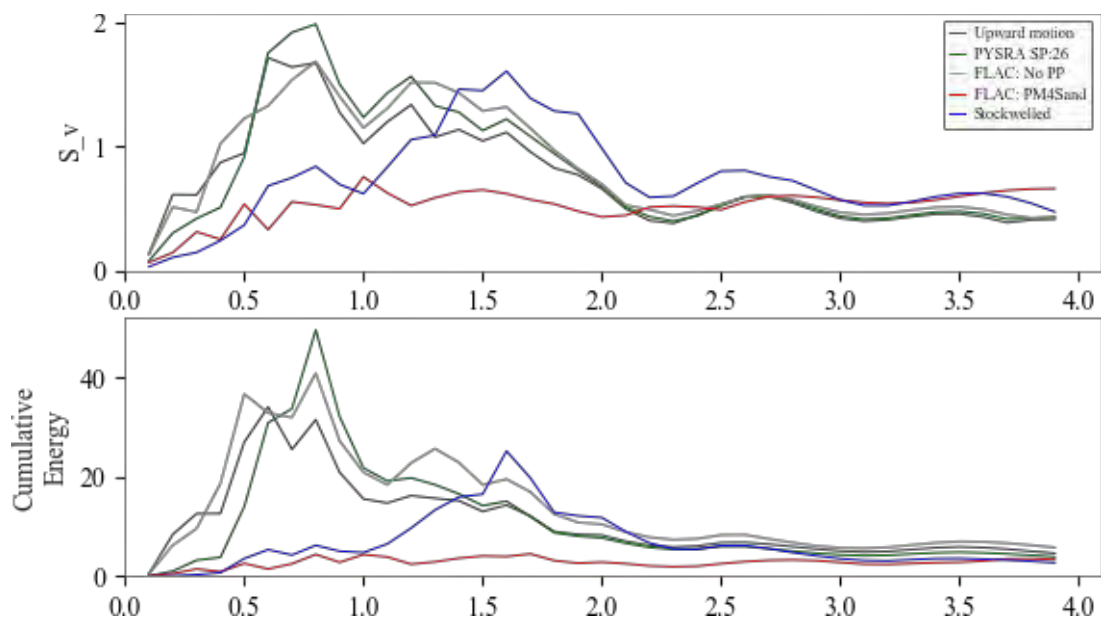


Figure 2.94: Comparison of spectral quantities for STF method

Figure 2.95 and **Figure 2.96** show a trivial case, where liquefaction occurs right at the end of the strong shaking. In this case all four of the analyses are congruent.



This project has received funding from the European Union's Horizon 2020 research and innovation programme under grant agreement No. 700748

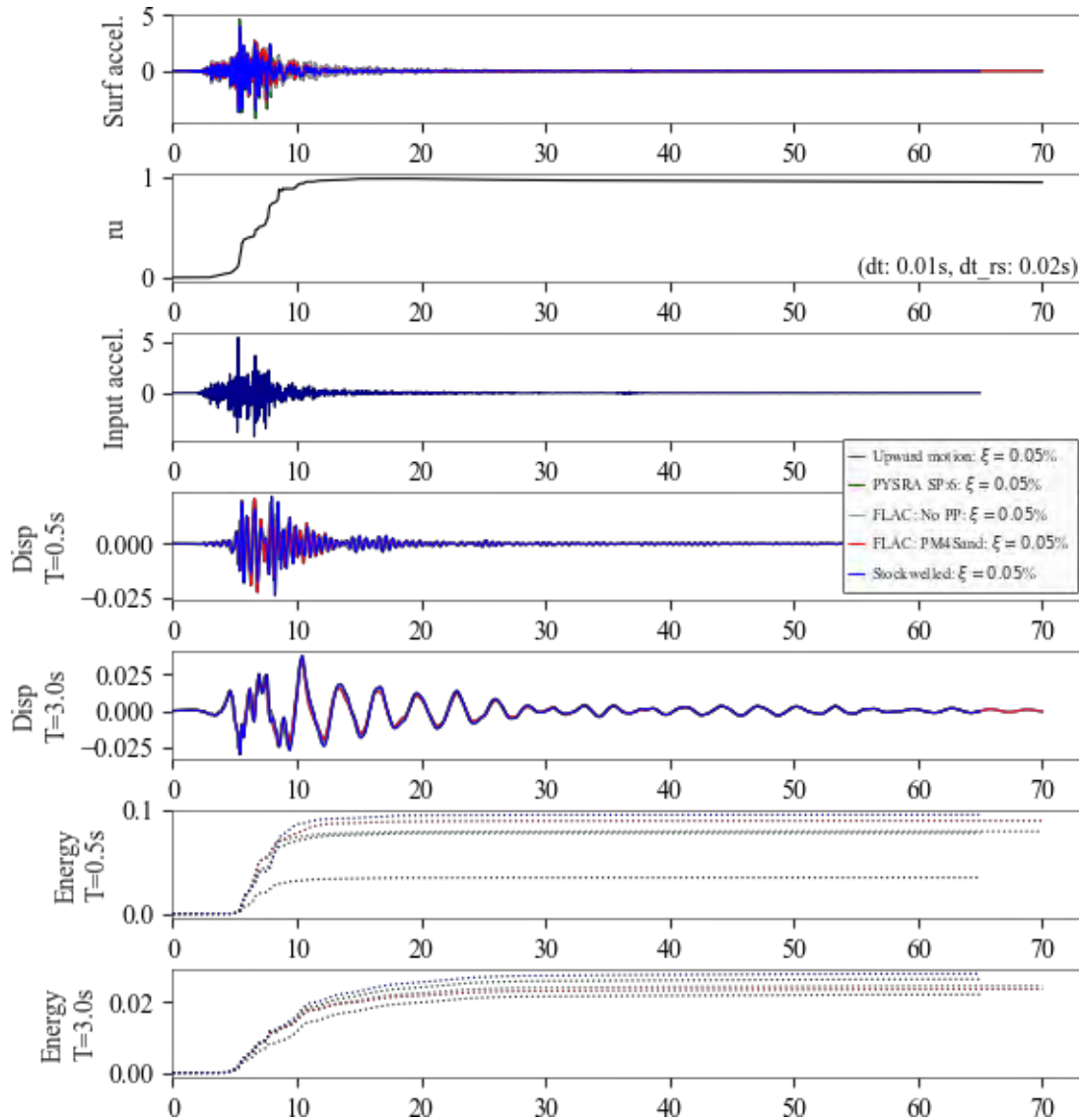


Figure 2.95: Comparison of time series for STF method - late liquefaction



This project has received funding from the European Union's Horizon 2020 research and innovation programme under grant agreement No. 700748

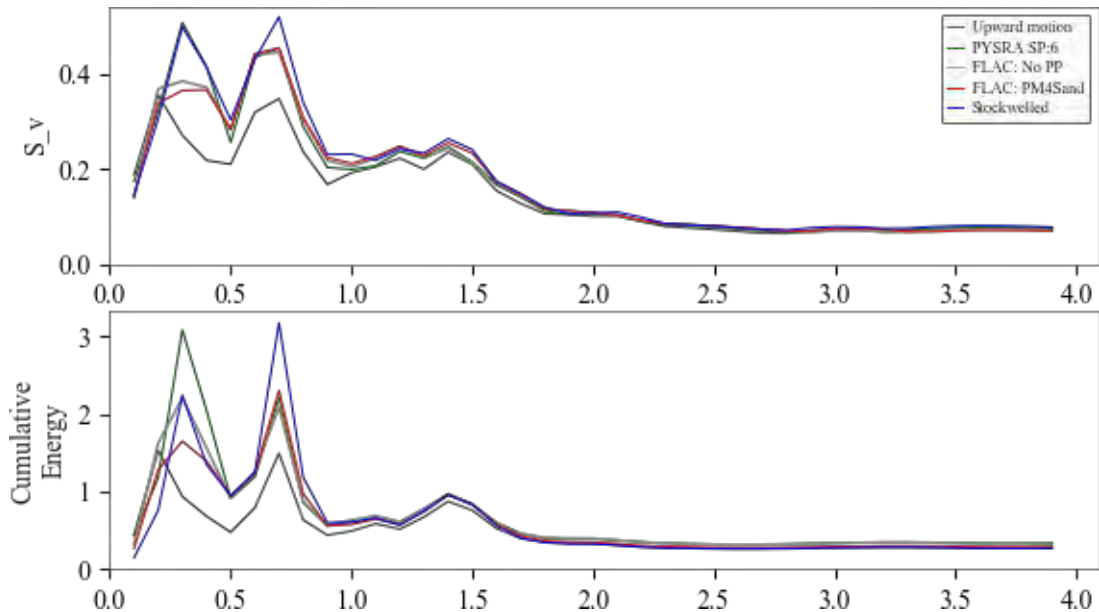


Figure 2.96: Comparison of spectral quantities for STF method - later liquefaction

2.7.5 MODELLING RECCOMENDATIONS AND CONCLUSIONS

This section has presented two viable options for obtaining the surface acceleration (effective stress analysis and Stockwell transfer function method). Although there are numerous other techniques available, the effective stress analysis option represents a rigorous approach while the Stockwell transfer function method represents the most simple and efficient approach. For the nonlinear effective stress analysis, it is recommended to use the PM4Sand with the default parameters, and set the contraction rate parameter (h_{p0}) using equation (2.48). The remaining aspects of the model should follow the procedure outlined in section 2.4. For the Stockwell transfer function method, it is recommended to use the python package Liquepy, that implements the Stockwell transform and performs the site response analysis using the python package Pysra v0.3.0 (Kottke, 2018). In the absence an equivalent linear analysis software and for preliminary studies the Eurocode 8 part 5 section 4.2.3 (CEN, 2004b) reccomendations for shear velocity and damping could be used for the estimation of the response for the pre-liquefied section of the ground motion. The damping and stiffness reduction for the post-liquefaction section should be set based on recommendations from Bouckovalas et al. (2017b).

Although the Stockwell transfer function method has some biases due to the linear nature of the transfer functions, It is numerical efficient and does not require a constitutive model and therefore is compatible with decoupled analyses that estimate the time of liquefaction triggering independent of dynamic site response. The ability to rapidly assess the impact of time of liquefaction and of strength and stiffness degradation is one of the major advantages of this method and is a useful benchmark for more advanced analyses.



This project has received funding from the European Union's Horizon 2020 research and innovation programme under grant agreement No. 700748

2.8 APPLICATION IN SPECIFIC CASE STUDY – PIEVE DI CENTO

2.8.1 LOCATION OF THE CASE STUDY SITE

The procedure described in this chapter called Macro Mechanism approach was applied to a specific case study in Pieve di Cento, Emilia Romana region, Italy (**Figure 2.97**).



Figure 2.97: Location of Pieve di Cento: a) within Italy map; b) geological map of the region (in blue is represented the fine-grained deposits and in yellow sand deposits from Appenninic rivers)

The stratigraphy of the site is available in Minarelli et al. (2016) which presents the geological information (Paolucci et al., 2015) supported by deep downhole investigations along a 35 km-long segment in the Po Plain, starting from Cento and ending in Occhiobello (**Figure 2.98**). The closest distances from the site to the investigation line and nearest deep downhole investigation are in the order of 2 and 5 kilometres, respectively.



This project has received funding from the European Union's Horizon 2020 research and innovation programme under grant agreement No. 700748

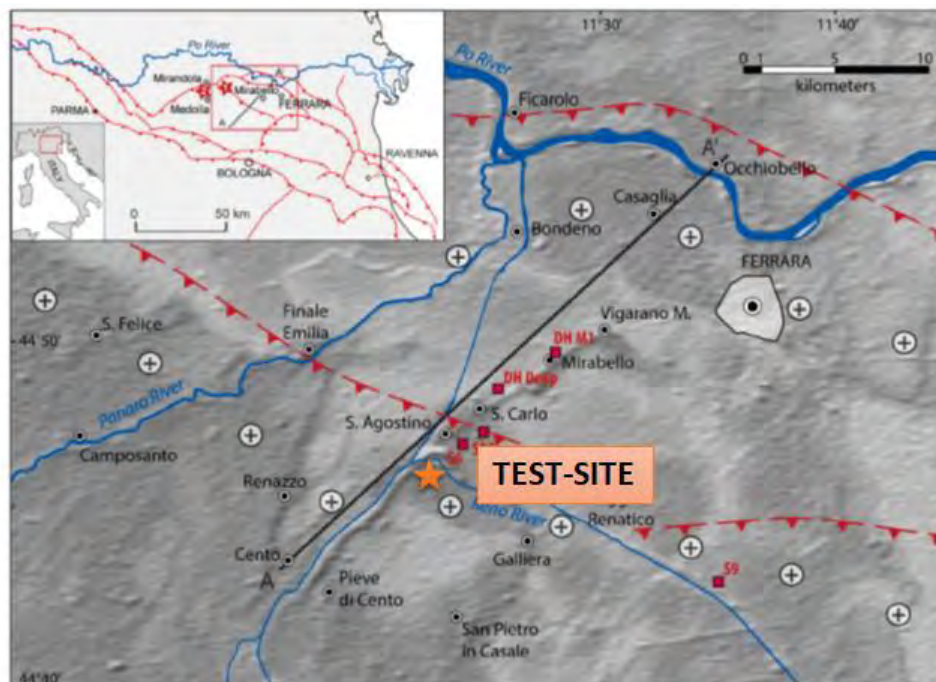


Figure 2.98: Location of Pieve di Cento (indicated by a star) and 35 km long segment in the Po Plain where deep downhole investigations were made (after Minarelli et al., 2016)

2.8.2 ANALYSIS PROCEDURE

500 analyses were performed to build fragility curves. Five different soil profiles, three methods to obtain the pore pressure in the middle of the liquefiable layer (described in section 2.5), two methods to obtain the surface acceleration (described in section 2.7), three methods to estimate the building settlements (described in section 2.6) and two methods to calculate the differential settlements (described in section 2.2) were considered. The major advantage of the macro-mechanism method over full modelling of the whole SLFSI problem is that numerous methods can be included at each step and the results can be de-aggregated to evaluate the influence of the different models. The deaggregation highlights inconsistencies where further field investigation or research is required to reduce uncertainty. 100 ground motions were uniform distributed in the 500 analysis. **Figure 2.99** shows the distribution of the methodologies in the 500 analyses, along with this the material properties for case study building were also varied within probably ranges.



This project has received funding from the European Union's Horizon 2020 research and innovation programme under grant agreement No. 700748

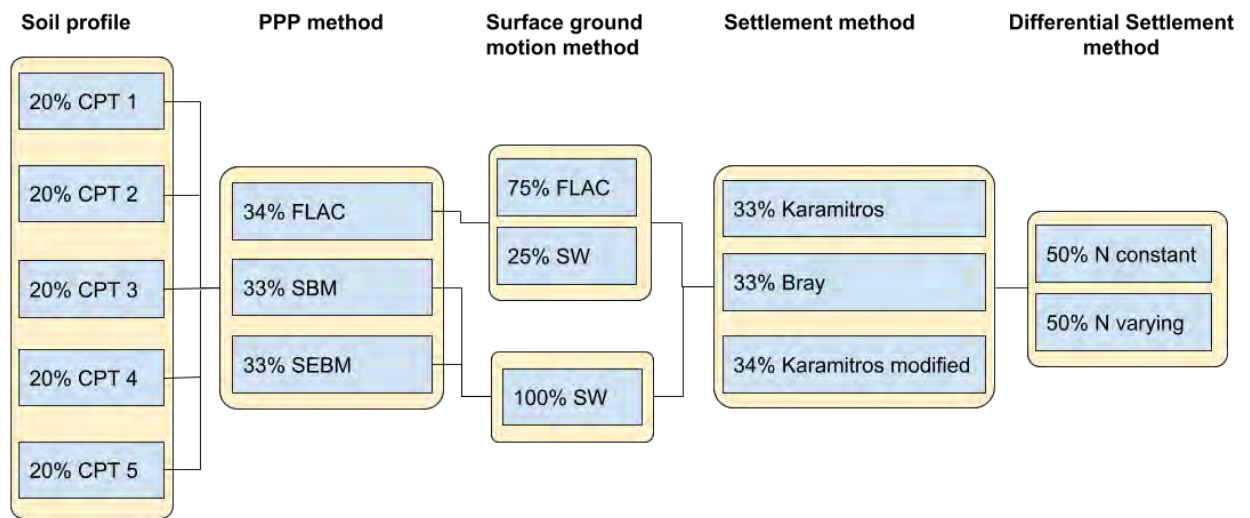


Figure 2.99: Logic tree of inputs and modelling decisions

2.8.3 SOIL PROFILES DESCRIPTION

The five different equivalent soil profiles (SP1 to SP5) were constructed automatically using the methodology showed in section 2.3 from the five CPTu results (Figure 2.100). Figure 2.101 to Figure 2.105 shows the equivalent soil profiles, their classification and the safety factor against liquefaction triggering (F_{SL}). Although being an automatic process and the CPTu profiles are similar, three equivalent soil profiles (SP1, SP4 and SP5) were generated without crust (only a liquefiable sand and a deeper clay) while the other two soil profiles were modelled with three layers (a clayey crust, a liquefiable sand and a deeper clay layer). For modelling settlement and surface accelerations using the Stockwell transfer function method, in the profiles without crust, the soil above the ground water level will be assumed to not liquefy, as a virtual crust.



This project has received funding from the European Union's Horizon 2020 research and innovation programme under grant agreement No. 700748

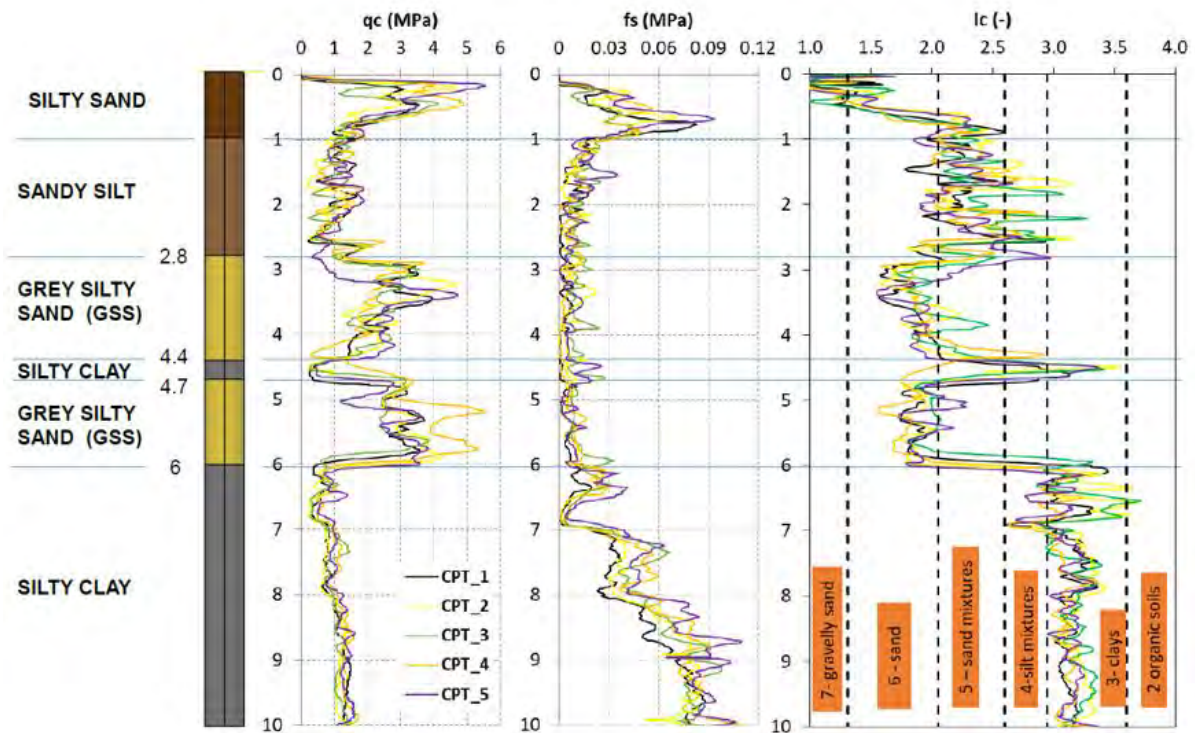


Figure 2.100: CPTu results.

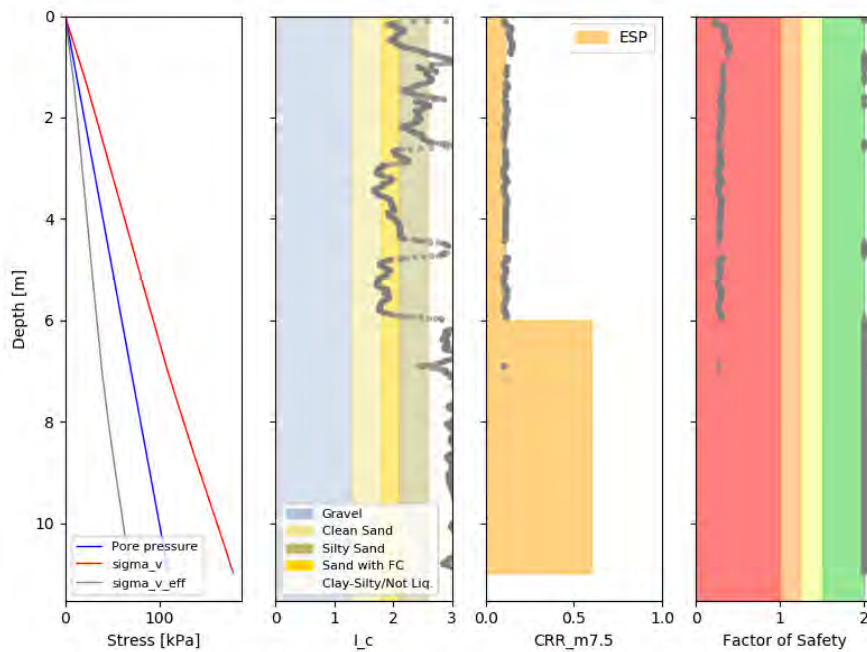


Figure 2.101: Soil profile 1 from CPT 1.



This project has received funding from the European Union's Horizon 2020 research and innovation programme under grant agreement No. 700748

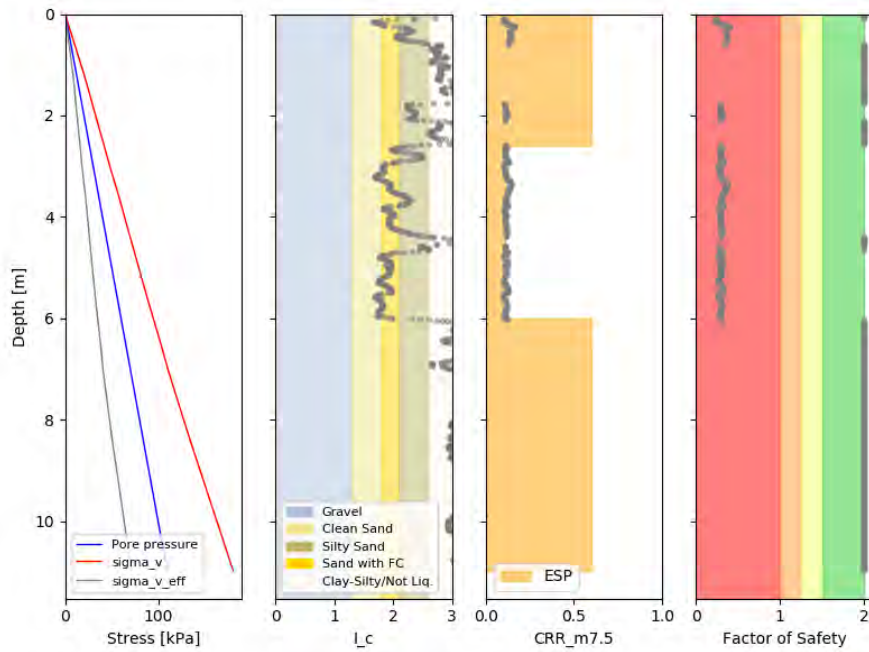


Figure 2.102: Soil profile 2 from CPTu 2.

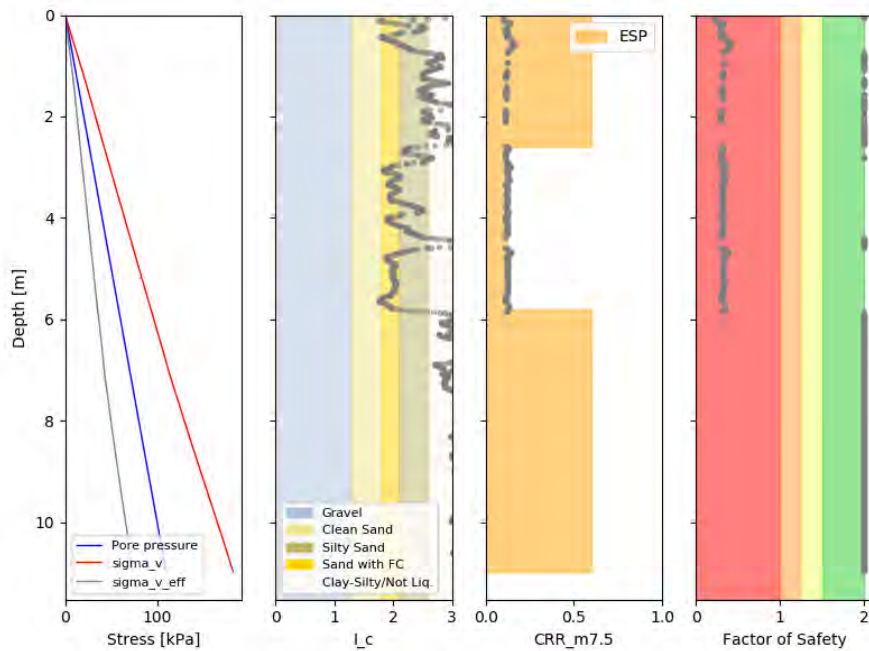


Figure 2.103: Soil profile 3 from CPTu 3.



This project has received funding from the European Union's Horizon 2020 research and innovation programme under grant agreement No. 700748

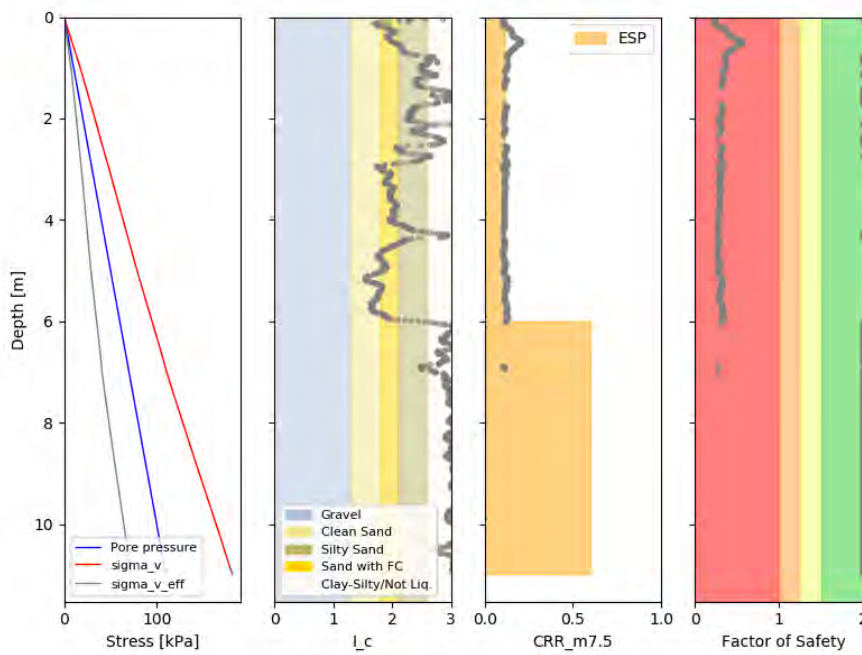


Figure 2.104: Soil profile 4 from CPTu 4.

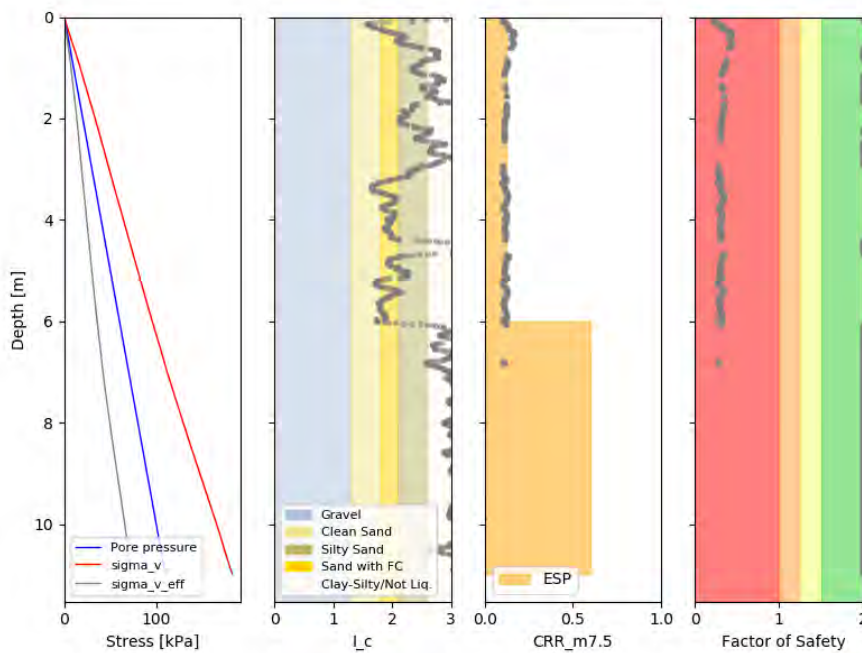


Figure 2.105: Soil profile 5 from CPTu 5.

The CPTu data was interpreted using CPeT-IT[®], a software package for the interpretation of Cone Penetration Test (CPT) data based on the Robertson (2009) methodology, to calculate some parameters of the soil. **Figure 2.109** to **Figure 2.110** shows the parameters taken from CPeT-IT software and **Table 2.15** and **Table 2.16** contain a summary with all the parameters. The ground water level was selected between 1.1 and 2.0 metres to reflect seasonal changes and uniform distributed in the 500 analysis.



This project has received funding from the European Union's Horizon 2020 research and innovation programme under grant agreement No. 700748

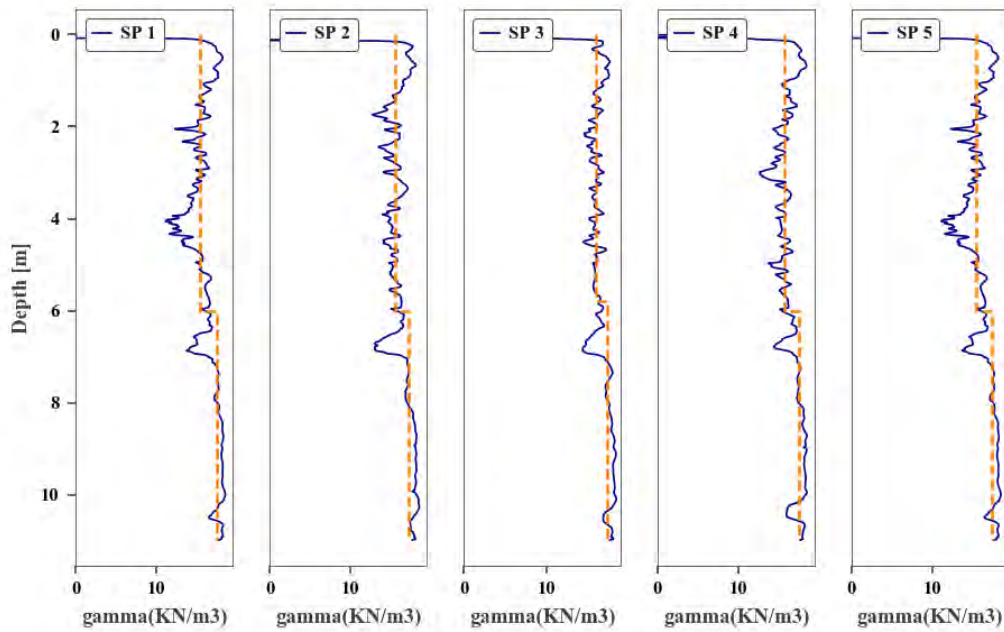


Figure 2.106: Unit weight (γ_{dry}) for the 5 soil profiles

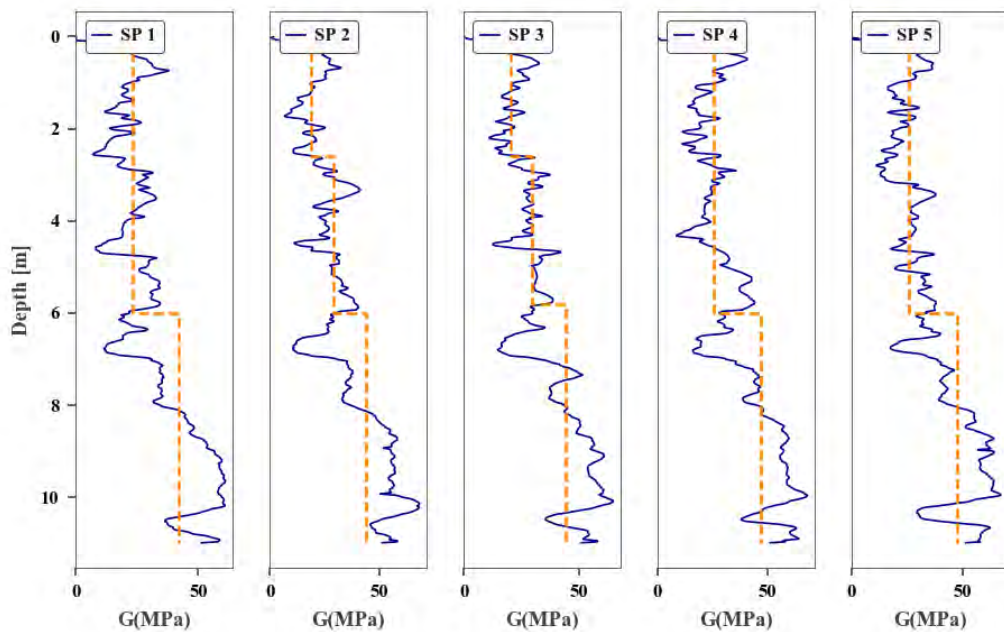


Figure 2.107: Maximum shear modulus ($G=G_{max}$) for the 5 soil profiles



This project has received funding from the European Union's Horizon 2020 research and innovation programme under grant agreement No. 700748

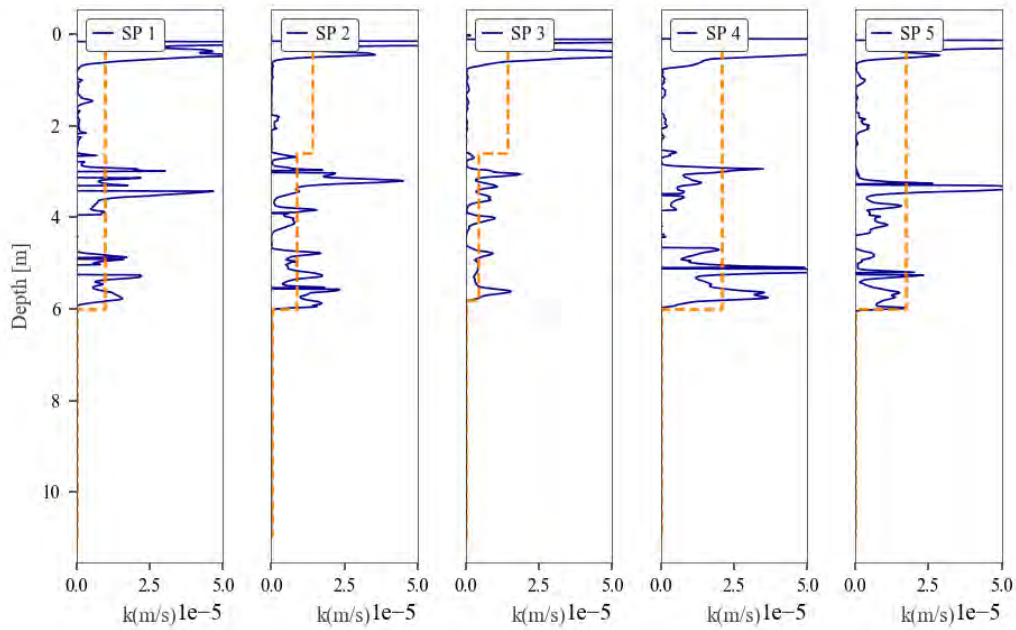


Figure 2.108: Permeability (k_H) for the 5 soil profiles

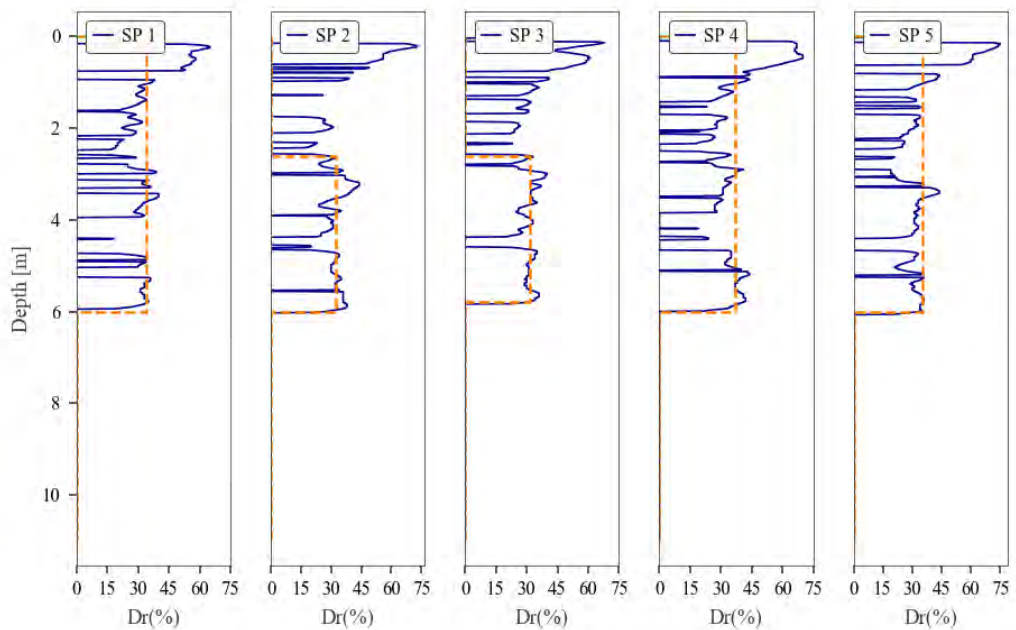


Figure 2.109: Relative density (D_r) for the 5 soil profiles



This project has received funding from the European Union's Horizon 2020 research and innovation programme under grant agreement No. 700748

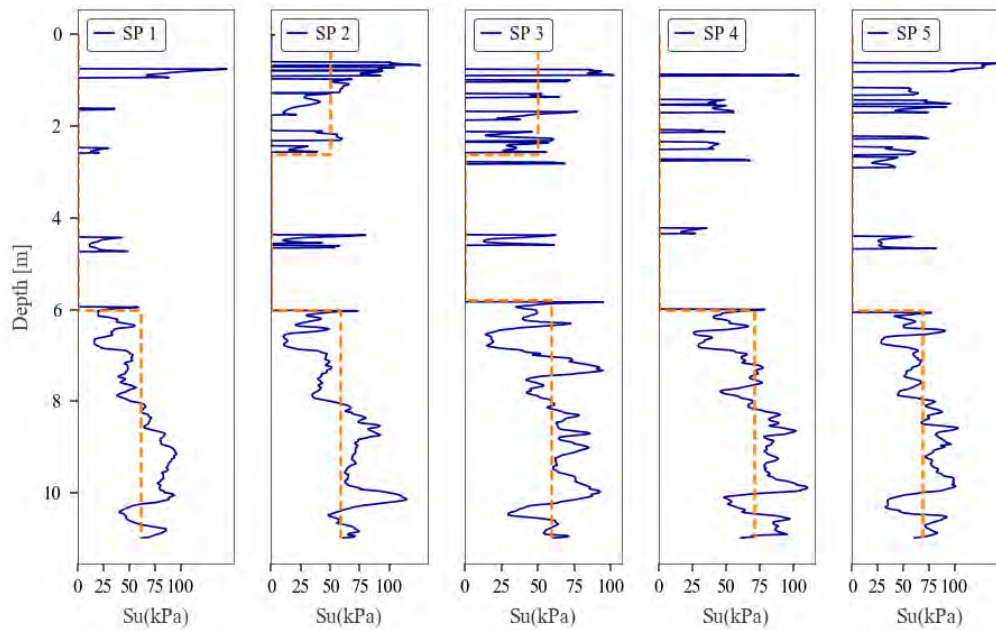


Figure 2.110: Undrained strength ($S_u=c_u$) for the 5 soil profiles.

Table 2.15: Parameters for the three soil profiles with 2 layers

Parameter	SP1	SP4	SP5
Properties of layer 1			
Height, H1 [m]	6.0	6.0	6.0
Unit weight, γ_{dry} [kN/m ³]	15.4	15.7	15.4
CSR _{n15}	0.111	0.116	0.120
Poisson ratio, ν	0.3	0.3	0.3
Relative density, D_r [%]	34.2	37.2	35.0
Constant volume friction angle, ϕ_{cv} [°]	33.0	33.0	33.0
Initial shear modulus, G_{max} [MPa]	23.0	25.7	25.8
Minimum void ratio, e_{min}	0.5	0.5	0.5
Maximum void ratio, e_{max}	0.8	0.8	0.8
PM4Sand hpo factor	Equation (2.48)	Equation (2.48)	Equation (2.48)
Normalised shear modulus, G_0	Equation (2.47)	Equation (2.47)	Equation (2.47)
Permeability, k_1 [m/s]	9.68e-06	2.07e-05	1.72e-05
Properties of layer 2			
Height, H2 [m]	14.0	14.0	14.0
Unit weight, γ_{dry} [kN/m ³]	17.4	17.4	17.4
Specific gravity, G_s	2.7	2.7	2.7
Poisson ratio, ν	0.35	0.35	0.35



This project has received funding from the European Union's Horizon 2020 research and innovation programme under grant agreement No. 700748

Initial shear modulus, G_{max} [MPa]	42.0	47.1	47.3
Undrained strength, S_u [kPa]	60.6	70.9	69.0
Permeability, k_2 [m/s]	3.60e-09	5.40e-09	3.63e-08

Table 2.16: Parameters for the two soil profiles with 3 layers

Parameter	SP2	SP3
Properties of layer 1		
Height, H_1 [m]	2.6	2.6
Unit weight, γ_{dry} [kN/m ³]	15.6	15.9
Specific gravity, G_s	2.7	2.7
Poisson ratio, ν	0.35	0.35
Initial shear modulus, G_{max} [MPa]	18.9	20.4
Undrained strength, S_u [kPa]	49.9	50.0
Permeability, k_1 [m/s]	1.39e-05	1.41e-05
Properties of layer 2		
Height, H_2 [m]	3.4	3.2
Unit weight, γ_{dry} [kN/m ³]	15.5	15.9
CSR _{n15}	0.111	0.120
Poisson ratio, ν	0.3	0.3
Relative density, D_r [%]	32.4	31.4
Constant volume friction angle, ϕ_{cv} [°]	33.0	33.0
Initial shear modulus, G_{max} [MPa]	29.0	29.6
Minimum void ratio, e_{min}	0.5	0.5
Maximum void ratio, e_{max}	0.8	0.8
PM4Sand hpo factor	Equation (2.48)	Equation (2.48)
Normalised shear modulus, G_0	Equation (2.47)	Equation (2.47)
Permeability, k_2 [m/s]	8.66e-06	4.34e-06
Properties of layer 3		
Height, H_3 [m]	14.0	14.2
Unit weight, γ_{dry} [kN/m ³]	17.2	17.3
Specific gravity, G_s	2.7	2.7
Poisson ratio, ν	0.35	0.35
Initial shear modulus, G_{max} [MPa]	44.0	44.3
Undrained strength, S_u [kPa]	58.3	58.9
Permeability, k_3 [m/s]	3.72e-09	6.49e-09



This project has received funding from the European Union's Horizon 2020 research and innovation programme under grant agreement No. 700748

2.8.4 GROUND MOTIONS DESCRIPTION

A total of 100 ground motions were selected from the NGAWest ground motion database (Ancheta et al., 2013). First 50 were selected to represent bedrock motions using the following criteria:

1. V_{s30} greater than: 600 m/s
2. Not a foreshock or aftershock event
3. From earthquake events with a magnitude larger than 5
4. Ground motion has a PGA higher than 0.10
5. Have a usable frequency less than or equal to 0.25 Hz
6. Are available from the PEER ground motion database
7. Have the start of the earthquake record
8. Did not suffer from excessive disturbance during recording that could be easily identified

From those, 50 motions were selected which were joined to the 49 motions recorded on soil that were presented in **Table 2.9**. Finally, another motion recorded on soil was added, so that the 100 ground motions are evenly distributed in terms of their type (rock or soil). **Table 2.17** summarises the information of the 51 ground motions that together with the ones presented in **Table 2.9** were considered in this case study. To reduce analysis time, for records longer than 60 seconds, only the strong shaking was considered, with the end of the record trimmed to remove any minor aftershocks.



This project has received funding from the European Union's Horizon 2020 research and innovation programme under grant agreement No. 700748

Table 2.17: Additional ground motions considered in the case study

ID	Record	E. dist [km]	Mw	Vs30	PGA	Earthquake	Year	Station
50	71	20.0	6.61	602	4.12	San Fernando	1971	Lake Hughes #12
51	150	4.4	5.74	663	3.61	Coyote Lake	1979	Gilroy Array #6
52	369	33.5	6.36	648	2.22	Coalinga-01	1983	Slack Canyon
53	763	29.0	6.93	730	2.54	Loma Prieta	1989	Gilroy - Gavilan Coll.
54	765	28.6	6.93	1428	3.59	Loma Prieta	1989	Gilroy Array #1
55	801	20.1	6.93	672	2.55	Loma Prieta	1989	San Jose - Santa Teresa Hills
56	809	16.5	6.93	714	2.84	Loma Prieta	1989	UCSC
57	810	16.3	6.93	714	4.07	Loma Prieta	1989	UCSC Lick Observatory
58	1012	14.4	6.69	706	3.54	Northridge-01	1994	LA 00
59	1020	40.7	6.69	602	3.04	Northridge-01	1994	Lake Hughes #12A
60	1023	44.8	6.69	671	2.95	Northridge-01	1994	Lake Hughes #9
61	1050	20.4	6.69	2016	4.07	Northridge-01	1994	Pacoima Dam (downstr)
62	1078	14.7	6.69	715	2.74	Northridge-01	1994	Santa Susana Ground
63	1102	61.9	6.9	609	1.42	Kobe, Japan	1995	Chihaya
64	1111	8.7	6.9	609	4.10	Kobe, Japan	1995	Nishi-Akashi
65	1161	47.0	7.51	792	3.05	Kocaeli, Turkey	1999	Gebze
66	1350	86.4	7.62	665	1.86	Chi-Chi, Taiwan	1999	ILA067
67	1511	16.0	7.62	615	4.03	Chi-Chi, Taiwan	1999	TCU076
68	1520	57.6	7.62	665	3.05	Chi-Chi, Taiwan	1999	TCU088
69	1521	7.0	7.62	672	2.61	Chi-Chi, Taiwan	1999	TCU089
70	2622	20.5	6.2	625	4.00	Chi-Chi, Taiwan-03	1999	TCU071
71	2627	20.8	6.2	615	4.75	Chi-Chi, Taiwan-03	1999	TCU076
72	3220	50.9	6.2	653	2.28	Chi-Chi, Taiwan-05	1999	TCU138
73	3932	45.5	6.61	710	3.54	Tottori, Japan	2000	OKYH14
74	3943	18.7	6.61	617	2.19	Tottori, Japan	2000	SMN015
75	4064	14.6	6	657	3.16	Parkfield-02, CA	2004	PARKFIELD - DONNA LEE
76	4097	31.5	6	648	3.85	Parkfield-02, CA	2004	Slack Canyon
77	4167	58.4	6.63	829	1.49	Niigata, Japan	2004	FKSH07
78	4213	36.5	6.63	655	3.91	Niigata, Japan	2004	NIG023
79	4481	4.5	6.3	685	3.12	L'Aquila, Italy	2009	L'Aquila - V. Aterno -Colle Grilli
80	4841	48.4	6.8	655	2.74	Chuetsu-oki	2007	Joetsu Yasuzukaku Yasuzuka
81	4842	45.7	6.8	655	4.27	Chuetsu-oki	2007	Joetsu Uragawaraku Kamabucchi
82	4846	55.3	6.8	606	3.63	Chuetsu-oki	2007	Joetsu Yanagishima paddocks
83	4858	47.7	6.8	640	2.90	Chuetsu-oki	2007	Tokamachi Chitosecho
84	4864	17.2	6.8	655	4.10	Chuetsu-oki	2007	Yoitamachi Yoita Nagaoka
85	4869	37.2	6.8	640	2.07	Chuetsu-oki	2007	Kawaguchi
86	4892	104.3	6.8	655	1.30	Chuetsu-oki	2007	Nagano Togakushi
87	5292	82.6	6.8	625	1.75	Chuetsu-oki	2007	NIGH19
88	5472	40.6	6.9	644	2.04	Iwate	2008	AKT017
89	5474	36.9	6.9	640	1.50	Iwate	2008	AKT019
90	5650	84.3	6.9	892	1.46	Iwate	2008	IWTH18
91	5655	86.3	6.9	923	1.20	Iwate	2008	IWTH23
92	5685	70.1	6.9	859	1.86	Iwate	2008	MYGH11
93	5686	65.5	6.9	748	1.04	Iwate	2008	MYGH12
94	5791	96.9	6.9	640	1.62	Iwate	2008	Maekawa Miyagi Kawasaki City
95	5819	30.7	6.9	640	3.31	Iwate	2008	Ichinoseki Maikawa
96	5820	75.9	6.9	640	2.53	Iwate	2008	Okura, Aobaku, Sendai
97	6928	54.3	7	650	3.06	Darfield, New Zealand	2010	LPCC
98	8110	15.7	6.2	650	1.84	Christchurch, New Zealand	2011	MQZ
99	8164	22.7	7.14	690	3.17	Duzce, Turkey	1999	IRIGM 487
100	4228	17.3	6.63	375	6.08	Niigata, Japan	2004	NIGH11



This project has received funding from the European Union's Horizon 2020 research and innovation programme under grant agreement No. 700748

2.8.5 FLAC 1-D NUMERICAL MODEL SETUP

170 analyses was performed in Flac (Itasca, 2016) to estimate the pore pressure time-series in the middle of the liquefiable layer. 130 of these analyses were also used to obtain the surface acceleration signal (see **Figure 2.99**).

Nonlinear effective stress 1-D analyses such as performed in section 2.5 were developed. The five soil profiles and 100 ground motions described above were used.

Since a compliant boundary was used in the base of the numerical model, a shear stress was calculated by converting the velocity time series (see section 2.6) using Equation (2.64) with *factor* value equal to 1.0. The calibration of this factor can be seen in **Figure 2.111**.

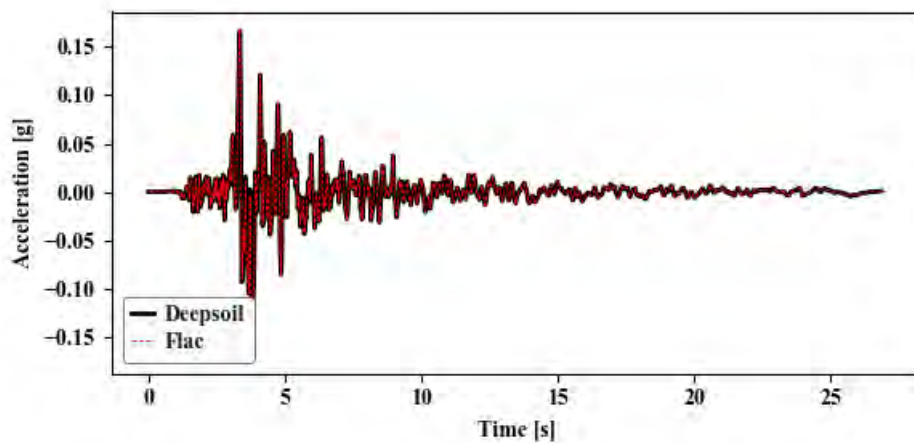


Figure 2.111: Calibration of factor value to calculate the input shear stress in numerical models

Hysteretic damping was used in the clay layers during the dynamic step. The model was fitted to the Sigmoidal model (sig4) functional form in FLAC (Flora et al., 2018). Sigmoidal curves are monotonic within the defined range, and have the appropriate asymptotic behaviour. Thus the functions are well-suited to the purpose of representing modulus degradation curves. The sig4 model is defined:

$$M_s = y_0 + \frac{a}{1 + \exp\left(-\frac{L - x_0}{b}\right)} \quad (2.72)$$

Where M_s is the strain-dependent normalized secant modulus and L is the logarithmic strain. For this model the 4 symbols, a , b , x_0 and y_0 are entered. **Table 2.18** gives the list of input parameters from Flora et al., (2018) of bottom clay and top clay when the soil profile have three layers.



This project has received funding from the European Union's Horizon 2020 research and innovation programme under grant agreement No. 700748

Table 2.18: Input parameters of the hysteretic damping model

Parameter	Crust	Bottom layer
a	0.95098	1.00023
b	-0.35966	-0.39049
x ₀	-1.53922	-0.89651
y ₀	0.04902	-0.00023

An additional 2% Rayleigh damping ($\xi_{1,2}$) was specified at f₁ and 5Hz to mitigate numerical instability. The lowest frequency (f₁) of the soil deposit corresponds to the first mode of the liquefied site, which was estimated by performing an elastic site response analysis using what software Deepsoil (Hashash et al., 2016).

Table 2.19 shows the lowest frequency for the 5 soil profiles considered.

Table 2.19: Natural frequency of the liquefied site

Soil profile	f ₁
1	0.3466
2	0.5136
3	0.5307
4	0.3636
5	0.3664

2.8.6 PORE PRESSURE ESTIMATION

The pore pressure estimate used three different methods SBM 33%, SEBM 33% and FLAC 34%, where the methods were implemented according to the modelling recommendations in section 2.5.6. From all 500 analyses 23.6% liquefied and the majority reached pore pressure ratios above 0.6 (see **Figure 2.112** showing the maximum pore pressure ratio obtained during each analysis). The liquefaction triggering was assumed when 5 kPa of effective stress was reached.



This project has received funding from the European Union's Horizon 2020 research and innovation programme under grant agreement No. 700748

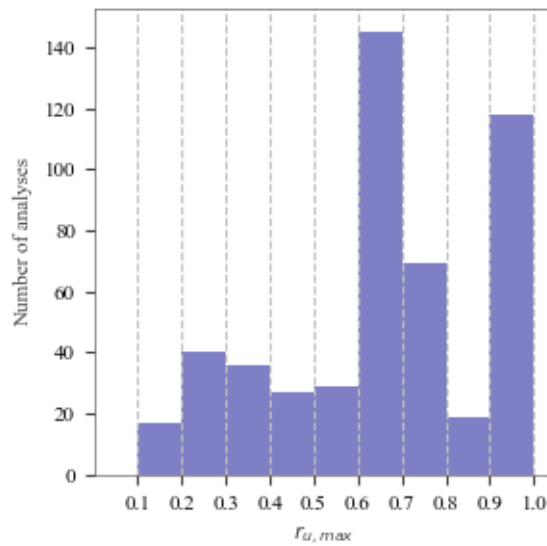


Figure 2.112: Histogram of the maximum pore pressure ratio

2.8.7 SETTLEMENTS ESTIMATION

The analytical methodologies showed in section 2.6 were used to estimate the settlement in the 500 analyses. Settlements were not estimated using numerical models because they require a high computational effort. The methods were implemented according to the modelling recommendations in section 2.6.

29.2% of foundations experienced settlements greater than 1m, which would make the building irreparable. The settlements of the remaining foundations can be seen in **Figure 2.113**. Most of the foundations experienced settlements either less than 10 centimetres (typically when no liquefaction occurred) or higher than 90 centimetres.

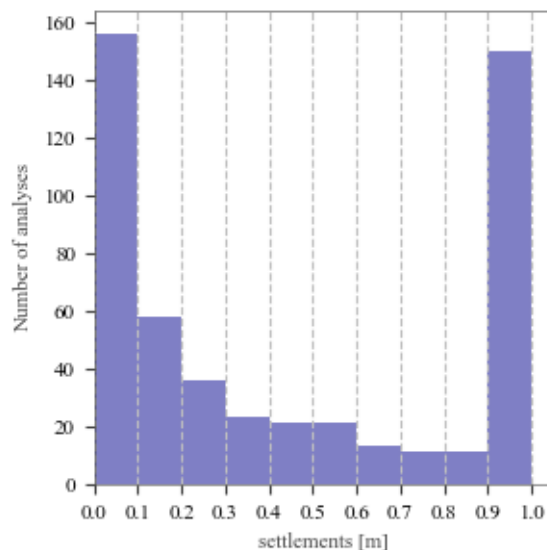


Figure 2.113: Settlement results



This project has received funding from the European Union's Horizon 2020 research and innovation programme under grant agreement No. 700748

2.8.8 BUILDINGS DESCRIPTION

Ten reinforced concrete (RC) frames with masonry infills and non-linear soil-foundation-structure interface were considered as reference structures for analysis. Each analysis considered a structure and a specific combination of soil profile and input motion, and calculation method for the pore pressure, surface motion, and imposed settlement. The ten RC frames have been designed by randomly assigning the material properties (concrete and steel stiffness and strength), and the values of the uniformly distributed gravitational loads in design and seismic combinations of actions, as described in section 2.2. The geometric properties were not selected through a random process and they were fixed a priori and assigned to all the structures, since this case study considers a single building, where only aspects of the design process and material properties would be unknown. The imposed values for the geometric properties correspond to the mean values of the probabilistic distributions reported in section 2.2. Thus, the ten structures have all the same geometric characteristics, shown in **Figure 2.11** and **Table 2.20**, and different reinforcement configurations of the structural elements, material resistances, and applied gravitational loads.

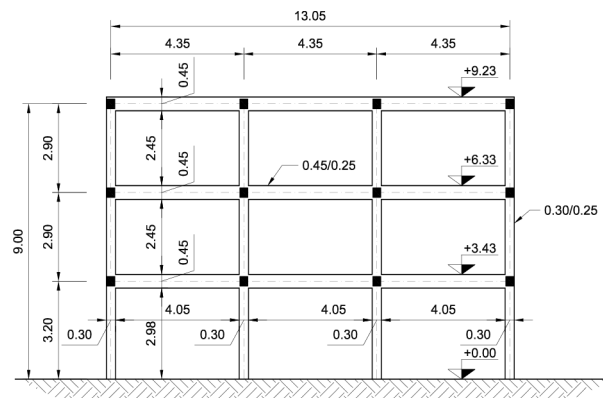


Figure 2.114: Physical model of the reference structure

Table 2.20: Geometric parameters for the reference model

Parameter	Measure
Number of storeys	3
Number of bays	3
Bay length	4.35 m
Height of ground floor	3.20 m
Height of upper floors	2.90 m
Beam height	0.45 m
Beam width	0.25 m
Column depth	0.30 m
Column width	0.25 m

2.8.9 RESULTS



This project has received funding from the European Union's Horizon 2020 research and innovation programme under grant agreement No. 700748

The results from the 500 analyses are analysed against six ground motion intensity measures in **Figure 2.115** and **Figure 2.116**. Three intensity measures capture peak energy, namely, peak ground acceleration (PGA), peak spectral acceleration at the effective period of 0.654 s ($Sa_{t,eff}$ between 0.26 and 17.15 m/s^2), and the average of the spectral acceleration (Sa_{av}) from the shortest possible first mode period of 0.248 s (which represent infills intact and no liquefaction) to the longest possible period of 1.060 s (which represent no infills yielding structure and liquefaction). The Sa_{av} values range between 0.365 and 11.48 m/s^2 . Note this is not average Sa from Kazanti and Vamvatsikos (2015). The other three intensity measures represent cumulative energy, Cumulative absolute velocity (CAV), Arias Intensity (I_a), and unit kinetic energy (UKE). The intensity measures are calculated for two times the upward propagating motion, and therefore compatible with ground motion prediction equations for surface quantities, except for in the case of soft soil on very shallow bedrock. The settlement values from the Bray method were included as it is, even in case of degraded bearing capacity factor of safety below one. The analyses that failed due to non-convergence or element failure are shown as triangles, the results that had a large residual inter-storey drift that exceeded the repairable limit of 0.005% (Sullivan et al. 2012) are shown as squares. There is clearly a lot of scatter with no intensity measure being an ideal candidate for quantifying performance. As expected, the peak intensity measures are slightly more correlated with the peak inter-storey drift of the superstructure ($\theta_{SS,p}$) since they are both measures of peak energy. Whereas, the cumulative intensity measures are more correlated to the tilt (β_f). The average spectral acceleration or PGA provide the best correlations for peak inter-storey drift and CAV provides the best correlation to tilt. The colours indicate the bins used for fitting the analytical fragility functions, where 10 bins were used in all cases.

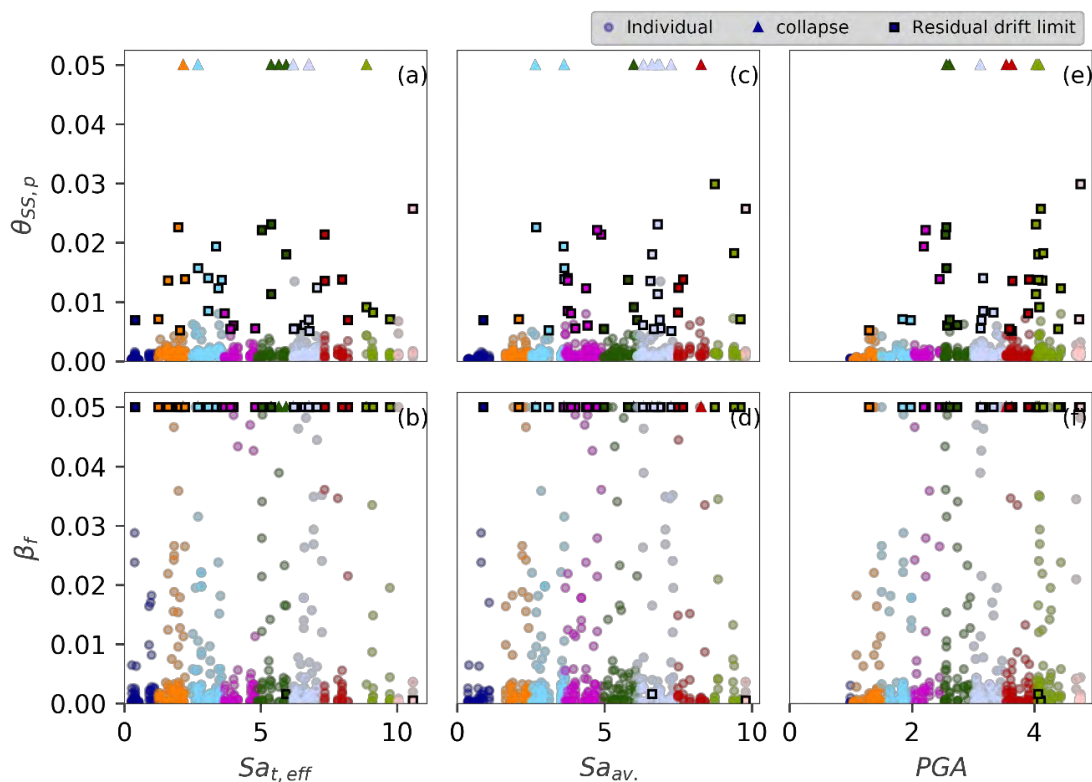


Figure 2.115: Performance measures versus peak intensity measures



This project has received funding from the European Union's Horizon 2020 research and innovation programme under grant agreement No. 700748

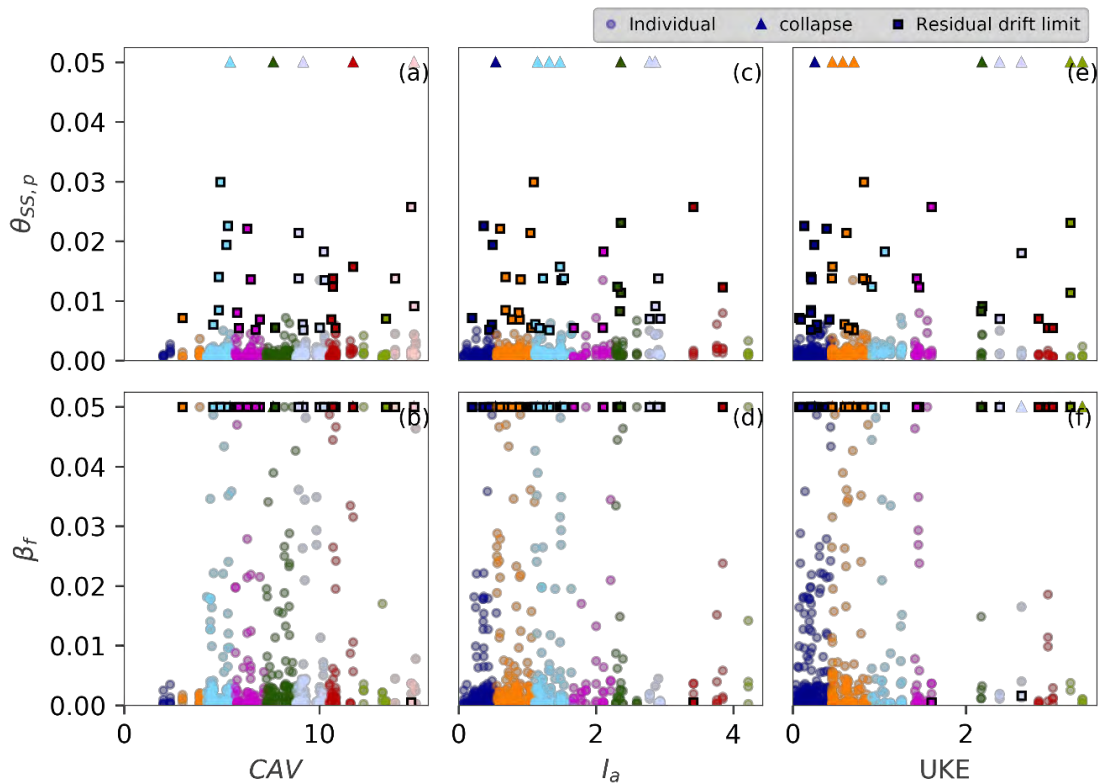


Figure 2.116: Performance measures versus cumulative intensity measures

Analytical fragility curves were obtained for all intensity measures (**Figure 2.117** and **Figure 2.118**) using the optimized function in the open-source python package Scipy (Jones et al., 2001). The Intensity Measures (IM) considered were the peak spectral acceleration at the effective period of 0.645 sec ($Sa_{t,eff}$), the average spectral acceleration (Sa_{av}) and the Peak Ground Acceleration (PGA). The probability of losses (LS) are represented in terms of (upper curves) inter-storey drifts (residual, $\theta_{SS,r}$; $\theta_{SS,i}$ for the limits of i – 0.005%, 0.01% and 0.02%). Collapse means non convergence or failure. In four cases ($Sa_{teff} - \theta_{SS>0.02}$, CAV - $\theta_{SS>0.05}$, CAV - $\theta_{SS>0.02}$, $I_a - \theta_{SS>0.01}$) a lack of data prevented an automated and the curve was fitted by eye.



This project has received funding from the European Union's Horizon 2020 research and innovation programme under grant agreement No. 700748

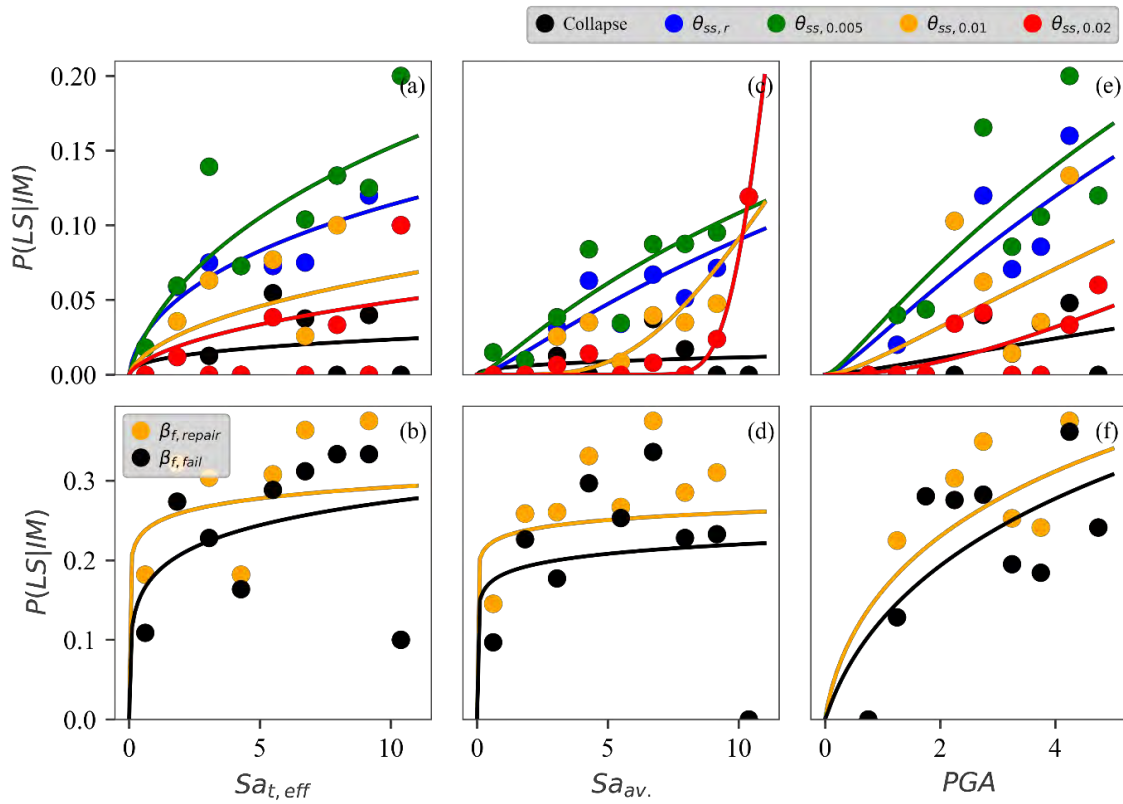


Figure 2.117: Fragility curves for peak intensity measures

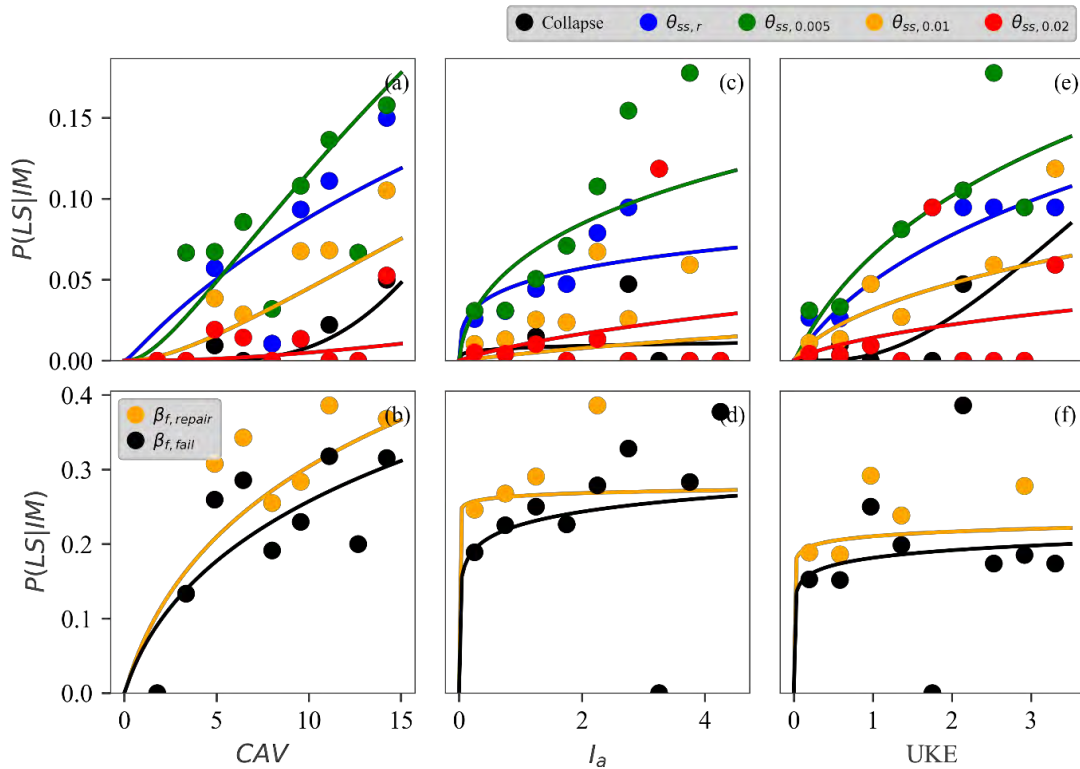


Figure 2.118: Fragility curves for cumulative intensity measures



This project has received funding from the European Union's Horizon 2020 research and innovation programme under grant agreement No. 700748

The median and standard deviation of each curve are shown in **Table 2.21**.

Table 2.21: Median and standar desviation of each intensity measure.

IM	EDP	median	std_dev
sa_teff	Collapse	3.53E+06	6.43
sa_teff	Residual	1067.23	3.87
sa_teff	$\Theta_{ss}>0.005$	233.35	3.07
sa_teff	$\Theta_{ss}>0.01$	3810.17	3.93
sa_teff	$\Theta_{ss}>0.02$	7620.00	4.00
sa_teff	$\beta f \leq f_{\text{repair}}$	1.02E+05	16.81
sa_teff	$\beta f \leq f_{\text{fail}}$	964.85	7.58
sa_av	Collapse	5.55E+06	6.39
sa_av	Residual	65.81	1.83
sa_av	$\Theta_{ss}>0.005$	58.33	1.94
sa_av	$\Theta_{ss}>0.01$	18.44	0.60
sa_av	$\Theta_{ss}>0.02$	11.66	0.14
sa_av	$\beta f \leq f_{\text{repair}}$	1.99E+07	23.42
sa_av	$\beta f \leq f_{\text{fail}}$	3.38E+06	16.97
pga	Collapse	404.26	2.25
pga	Residual	48.66	1.94
pga	$\Theta_{ss}>0.005$	43.64	2.00
pga	$\Theta_{ss}>0.01$	74.35	1.87
pga	$\Theta_{ss}>0.02$	55.61	1.36
pga	$\beta f \leq f_{\text{repair}}$	14.17	2.75
pga	$\beta f \leq f_{\text{fail}}$	15.98	2.47
CAV	Collapse	37.73	0.55
CAV	Residual	252.15	2.39
CAV	$\Theta_{ss}>0.005$	60.00	1.50
CAV	$\Theta_{ss}>0.01$	139.74	1.55
CAV	$\Theta_{ss}>0.02$	480.00	1.50
CAV	$\beta f \leq f_{\text{repair}}$	33.30	2.34
CAV	$\beta f \leq f_{\text{fail}}$	51.89	2.53
I_a	Collapse	2.00E+11	11.72
I_a	Residual	15535.79	6.87
I_a	$\Theta_{ss}>0.005$	101.34	3.68
I_a	$\Theta_{ss}>0.01$	1600.00	3.00



This project has received funding from the European Union's Horizon 2020 research and innovation programme under grant agreement No. 700748

I_a	$\Theta_{ss} > 0.02$	799.77	3.13
I_a	$\beta_f \leq f_{\text{repair}}$	2.90E+15	61.16
I_a	$\beta_f \leq f_{\text{fail}}$	4261.65	11.78
UKE	Collapse	7.65	0.85
UKE	Residual	21.66	2.43
UKE	$\Theta_{ss} > 0.005$	12.37	2.30
UKE	$\Theta_{ss} > 0.01$	102.72	3.08
UKE	$\Theta_{ss} > 0.02$	571.38	3.37
UKE	$\beta_f \leq f_{\text{repair}}$	1.35E+06	27.29
UKE	$\beta_f \leq f_{\text{fail}}$	21262.60	15.56

The influence of key assumptions can also be investigated by de-aggregating the results. The influence of the load redistribution model had the biggest influence on the results. **Figure 2.119** shows the interstorey-drift and foundation tilt versus the average spectral acceleration and CAV for the two different load redistribution models.

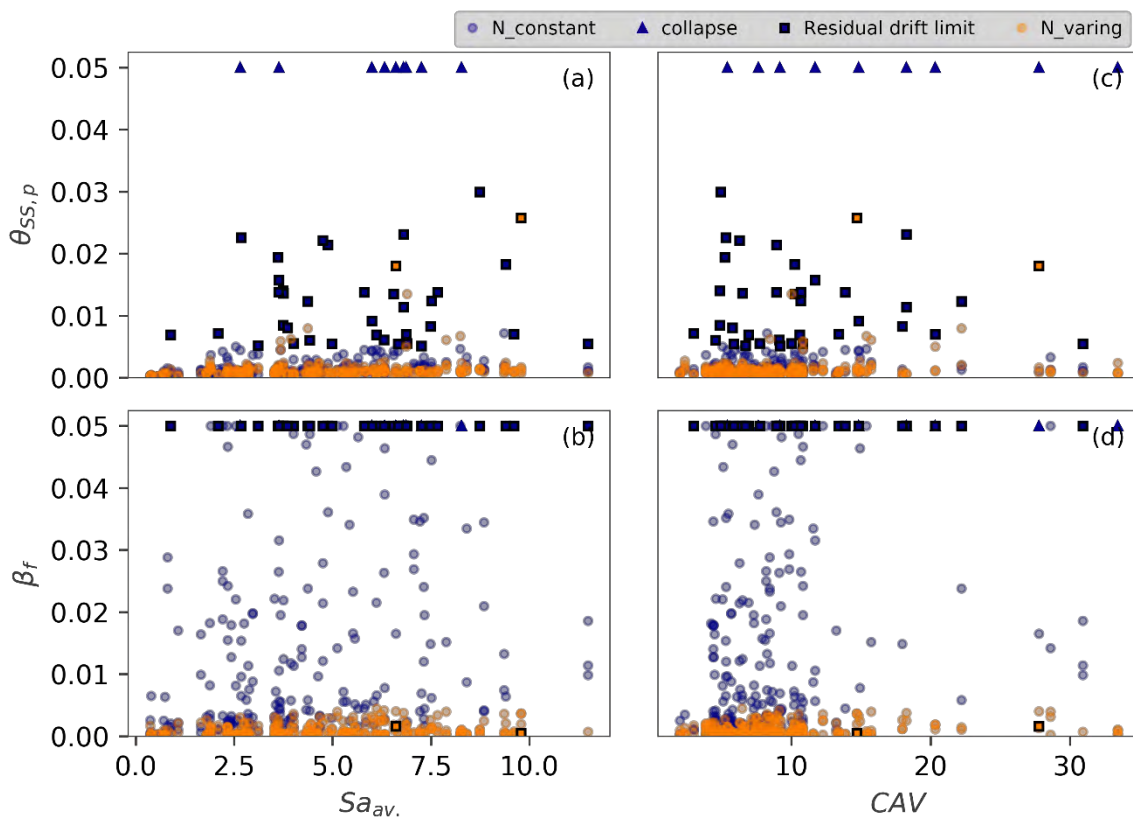


Figure 2.119: influence of load redistribution model



This project has received funding from the European Union's Horizon 2020 research and innovation programme under grant agreement No. 700748

Clearly the model that pre-calculates the settlement ($N_{constant}$) causes much larger drifts and foundation tilts. This model does not adjust the rate of settlement based on a change in vertical load and therefore two footings tend to take all of the vertical load which weakens the building resulting in larger drifts. The higher tilt reflects the random co-efficients that scale the settlement and a function of the ratio of the stiffness of the building and the stiffness of the supporting soil. There are numerous factors that cause settlement, (e.g. shear deformation, consolidation, soil ejecta) (See Section 2.6). Only settlement due to shear deformation during seismic action was modelled in these simulations. While shear deformation is dependent on the applied load, many of the other mechanisms of settlement are independent of the load, and therefore more similar in behaviour to the pre-calculated settlement time series method. As discussed in Section 2.2 the settlement rate is a key part of assessing the performance of buildings on liquefiable soil deposits and its influence further highlights that.

The influence of the choice of total settlement method is illustrated in **Figure 2.120**, however, only the $N_{varying}$ load redistribution method results are shown to remove the strong influence of this model choice. Clearly the Bray settlement model produces lower tilt than the Karamitros model (Karamitros et al., 2013a), this is because the Karamitros model tends to predict larger settlement than the Bray model as concluded in 2.6.3.

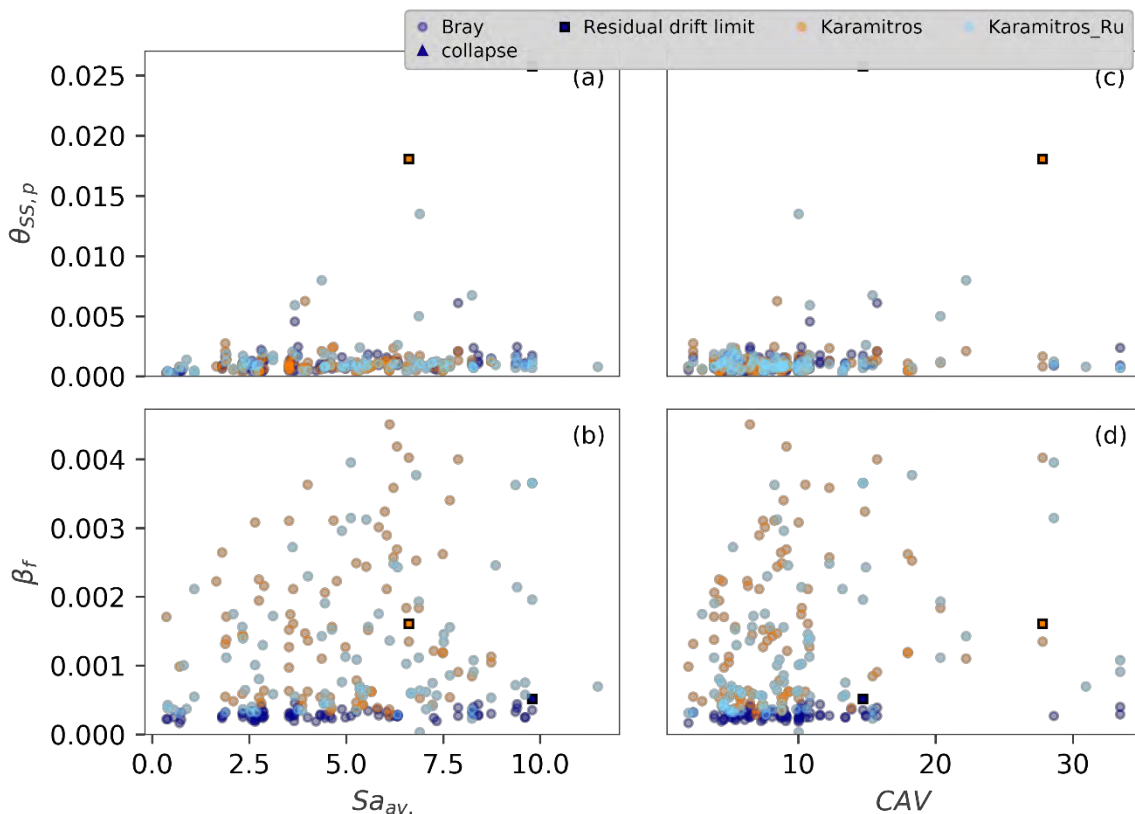


Figure 2.120: Influence of settlement model



This project has received funding from the European Union's Horizon 2020 research and innovation programme under grant agreement No. 700748

The influence of the pore pressure build-up model is illustrated in **Figure 2.121**. The choice of pore pressure build-up model has negligible bearing on the results. This is expected since there was very little difference in the predictions, with the stress-based method producing slightly high pore pressure build-up.

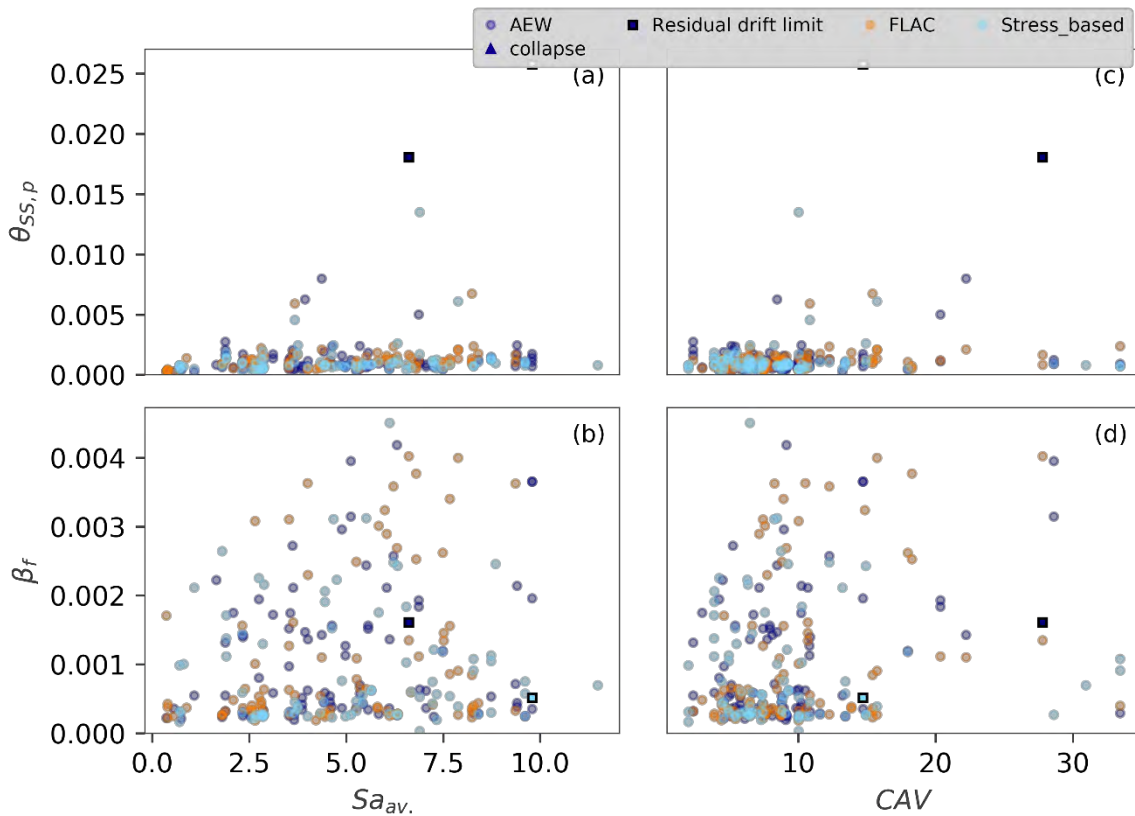


Figure 2.121: Influence of pore pressure build-up method

The influence of the surface ground motion model is investigated in the **Figure 2.122**. As expected the choice of surface motion method has negligible impact on the results as the two methods produced very similar peak and cumulative ground motion energy. Please take into account that this is referring to structural damage.

The influence of the choice of CPT record is shown in **Figure 2.123**. As expected the choice of CPT record has minimal impact on the results as the CPT records were very similar. However, a slightly lower tilt can be determined for CPTs 2 & 3, as these ESPs of these two CPTs were developed with a clay crust and therefore had more bearing capacity.

The influence of the ground water level (GWL) is shown in **Figure 2.124**. The GWL appears to have a negligible effect on the superstructure peak inter-storey drift and only slight increase in tilt for shallower water table depths.



This project has received funding from the European Union's Horizon 2020 research and innovation programme under grant agreement No. 700748

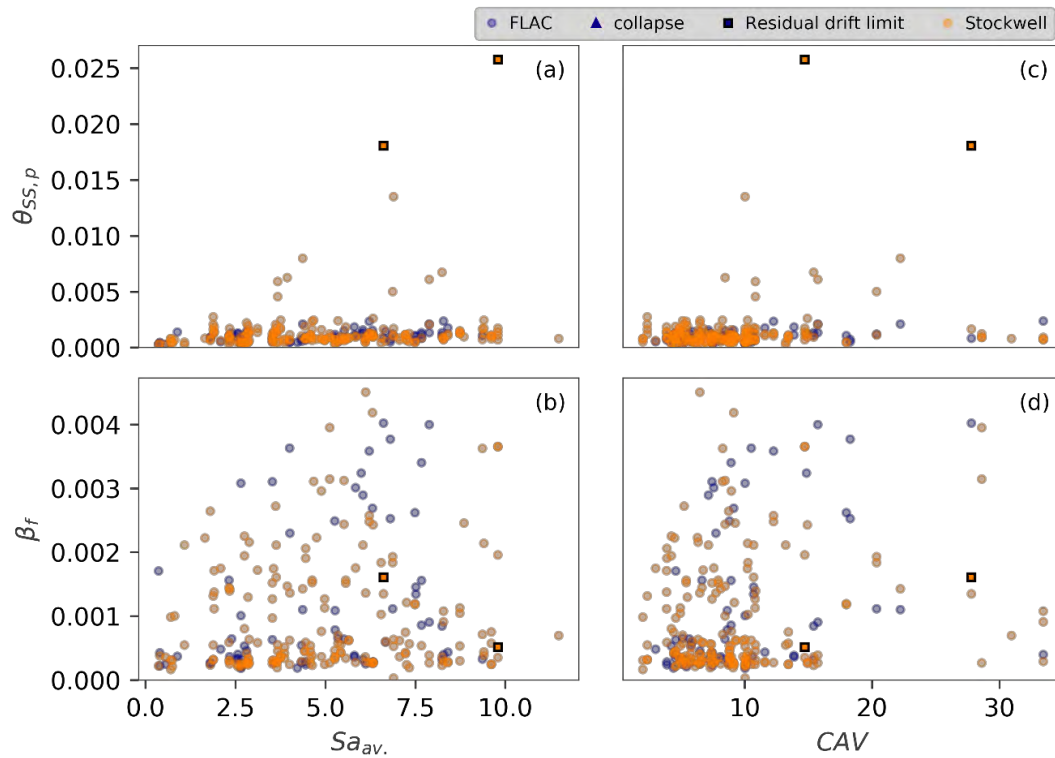


Figure 2.122: Influence of surface ground motion method

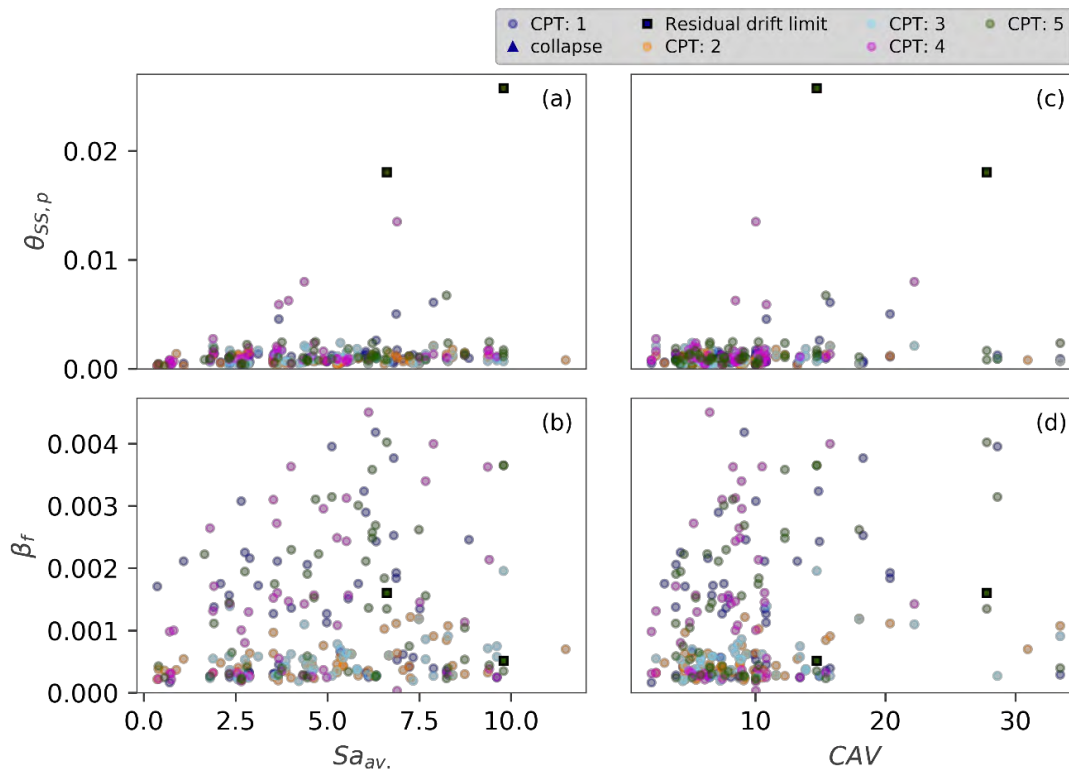


Figure 2.123: Influence of CPT



This project has received funding from the European Union's Horizon 2020 research and innovation programme under grant agreement No. 700748

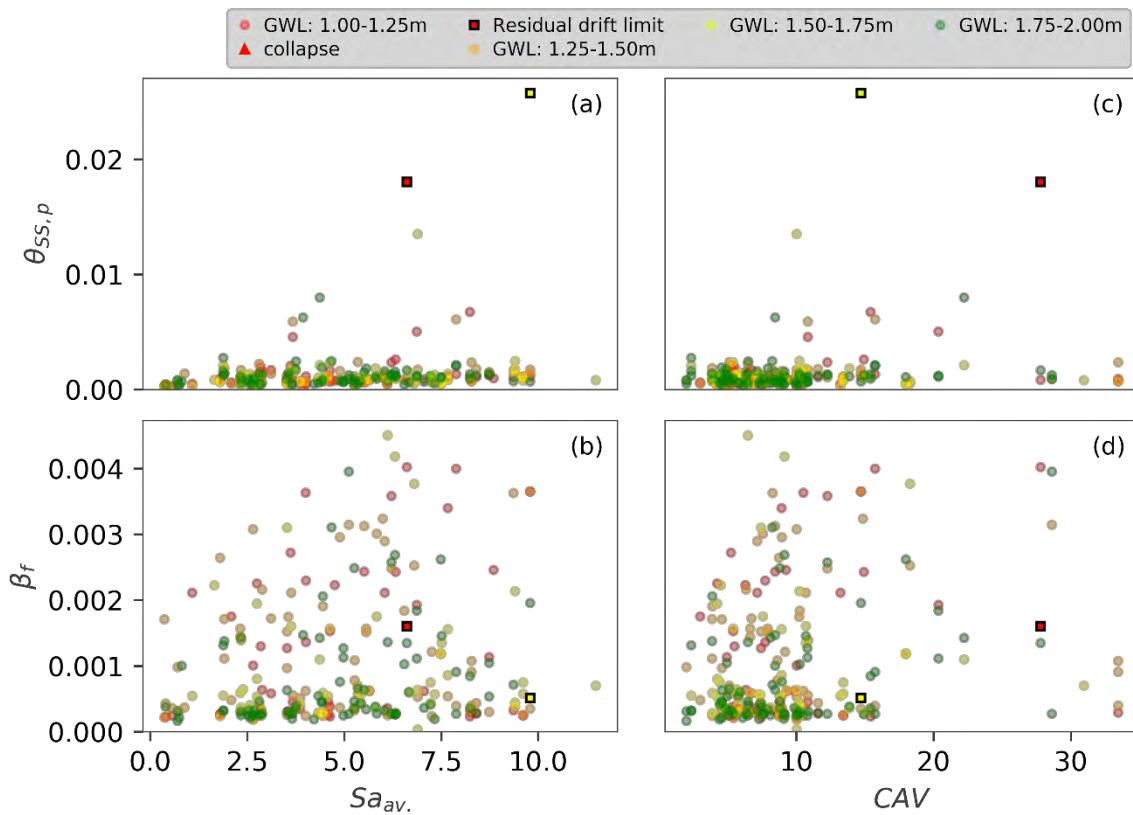


Figure 2.124: Influence of ground water level

2.9 RAPID RISK IDENTIFICATION OF SOIL LIQUEFACTION AND STRUCTURAL DAMAGE

2.9.1 INTRODUCTION AND MOTIVATION

Simulation of soil-structure interaction (SSI) with consideration of liquefaction using micro FEM (or FDM) models is complex and computationally extremely demanding. A single dynamic analysis of a liquefaction-related SSI models may require several days of uninterrupted computation before completing. In the case of risk and loss assessment methods, which are both based on results of fragility analysis, the computational time increases even more dramatically, since the seismic response has to be computed for a set of ground motions and different levels of seismic intensity. Despite continuous advances of computational power of modern computers and possibilities for parallel computing, fragility analysis of liquefaction-related SSI problems may still be infeasible in engineering practice, at least for structures of ordinary importance. Simplified fragility methods like the Macro-mechanism approach for buildings on shallow foundation can significantly reduce computational time and facilitate the implementation of risk and loss assessment methods in engineering practice, however, the 500 results produced for the case-study building still took 5 days across 10 computers.



This project has received funding from the European Union's Horizon 2020 research and innovation programme under grant agreement No. 700748

It should be noted that for many buildings located on liquefaction-susceptible soils, it can be still shown that the risk of liquefaction and liquefaction-induced damage is relatively low (e.g. buildings located on sites with low seismicity, moderate or high liquefaction resistance, sites with small thickness of liquefiable layer or sites with deep liquefiable layers). In such cases, detailed analyses of SSI with consideration of liquefaction may not be necessary, provided that an appropriate screening method is developed in order to identify the cases with low risk of unacceptable behaviour due to adverse effects of soil liquefaction. Such a screening method can be based on a simplified risk identification procedure, which enables decision-making about the necessity for more detailed analysis of SSI with consideration of liquefaction.

The objective of this section is to describe the method for Rapid Risk Identification (RRI) of soil liquefaction and structural damage, which was developed at University of Ljubljana in collaboration with University of Porto. The method is aimed at facilitating the decision regarding the need for detailed studies of soil liquefaction for an investigated building on shallow foundations. The decision about the need for detailed studies of soil liquefaction is based on risk assessment of a simplified SSI model. The aim of the simplified model is to allow for a rapid risk assessment without the need to perform time-consuming analyses. Based on such analysis it can be concluded if detailed studies of soil liquefaction are needed or not. Due to the employment of a simplified model, appropriate decision making is achieved provided that the obtained estimates of the mean (median) seismic response are slightly conservative. This is the basic assumption of the method for RRI, which is achieved on the basis of appropriate calibration of the simplified SSI model (see section 2.9.6.).

The methodology of the Rapid Risk Identification (RRI) methods is presented in Section 2.9.2, whereas the simplified model for SSI with consideration of liquefaction is described in Section 2.9.3. In Section 2.9.4, the application of the RRI method is demonstrated by means of an example considering a code-conforming building, located at two locations with different levels of seismic hazard. The conclusions of the study are presented in section 2.9.5. Details regarding the model calibration and validation of a simplified model for SSI are presented in sections 2.9.6, 2.9.7 and 2.9.8.

2.9.2 OVERVIEW OF PROCESSES OF THE METHOD FOR RAPID RISK IDENTIFICATION OF SOIL LIQUEFACTION AND STRUCTURAL DAMAGE

The processes of the method for Rapid Risk Identification of soil liquefaction and structural damage are presented in **Figure 2.125**. The first step is the definition of the required input data, i.e. data regarding the examined structure, soil profile, the seismic hazard at the location, the set of ground motions used for fragility analysis, the definition of the limit states and tolerable values of seismic risk related to liquefaction-induced damage. In the next, the data is used to develop the simplified model for SSI with consideration of liquefaction, which is described in section 2.9.3. The simplified SSI model is used for fragility analysis in order to obtain fragility curves for the designated limit states (LSs) which take into account, both, the damage of the building due to ground shaking, and also foundation settlements and rotations due to soil liquefaction. The fragility curves for defined LSs are then convoluted with the seismic hazard curve in order to calculate seismic risk, i.e. the probability of exceeding defined LSs. Finally, the risk of exceedance of a designated LS is compared with the corresponding tolerable risk. If the risk of exceedance of a designated LSs is lower than the tolerable risk, detailed studies of soil liquefaction are not necessary, since it is assumed that the risk of



This project has received funding from the European Union's Horizon 2020 research and innovation programme under grant agreement No. 700748

unacceptable behaviour due to adverse effects of soil liquefaction is sufficiently low. Appropriate level of confidence is introduced by careful (slightly conservative) calibration of the simplified SSI model. On the other hand, if the risk of exceedance of a designated LS is greater than the tolerable risk, the building is assumed to be susceptible to seismically-induced liquefaction damage (damage due to ground shaking or liquefaction) and detailed studies of soil liquefaction are necessary. In such cases, the Macro-mechanism approach for buildings on shallow foundation can be used to assess the seismic performance of the building (see previous sections).

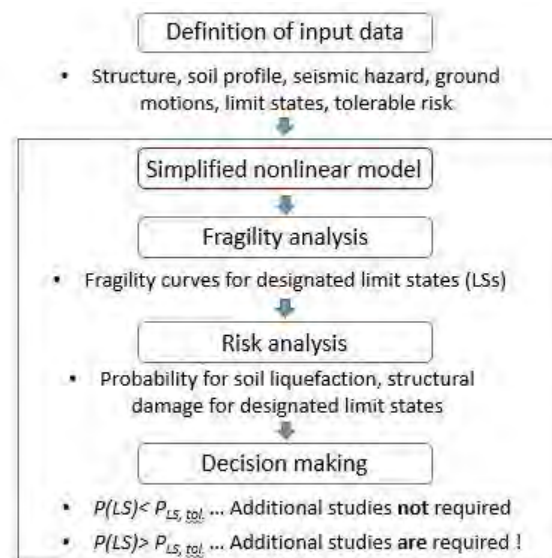


Figure 2.125: Processes of the method for Rapid Risk Identification (RRI) of soil liquefaction and structural damage.

2.9.3 SIMPLIFIED MODEL FOR SOIL-STRUCTURE INTERACTION WITH CONSIDERATION OF LIQUEFACTION

Overview

For the purpose of method for Rapid Risk Identification (RRI) of soil liquefaction and structural damage, a simplified model for soil-structure interaction (SSI) has been developed at University of Ljubljana in collaboration of University of Porto. A schematic representation of the simplified model for SSI with consideration of liquefaction is presented in Figure 2.126. The simplified model was developed in the open-source software OpenSees (2017). It consists of a simple inelastic single-degree-of-freedom (SDOF) structure attached to an inelastic rotational soil spring with time-dependent degradation of strength in case liquefaction is triggered during earthquake. The challenging part of the proposed method is the development of an appropriate model for the inelastic soil spring, which should approximately simulate the interaction between the structure and the liquefiable soil, including the related foundation settlements and rotations. In order to obtain sufficient amount of results for the calibration of the inelastic soil spring, parametric studies were performed in FLAC 2D (Itasca, 2017) by University of Porto. Parametric studies involved 2D seismic analyses of soil-structure interaction by varying characteristic of the structure, the soil profile and the ground motions. The results of calibration and validation of the simplified model are presented in Sections 2.9.6 to 2.9.8.



This project has received funding from the European Union's Horizon 2020 research and innovation programme under grant agreement No. 700748

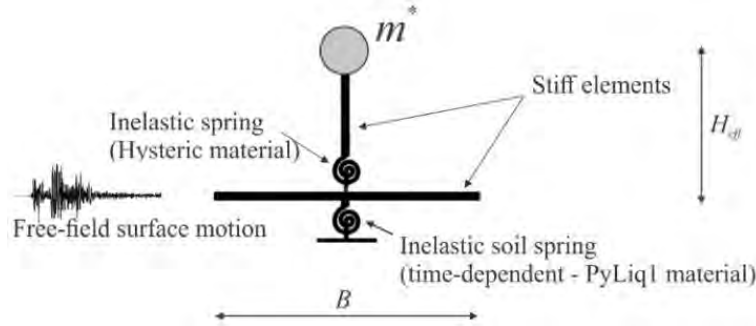


Figure 2.126: Schematic presentation of the simplified model for soil-structure interaction (SSI) with consideration of liquefaction.

The structure is modelled as an equivalent inelastic single-degree-of-freedom (SDOF) model. Such an approach is consistent with the new draft of Eurocode 8 - Annex E (CEN, 2018), which describes the estimation of target displacement based on dynamic analysis of an equivalent SDOF model. The force-displacement relationship of the structure can be estimated based on pushover analysis of the fixed-base model (e.g. Fajfar, 2000), simplified displacement-based approach (e.g. Sullivan et al. 2014) or based on engineering judgment. The idealized pushover curve and the corresponding force-displacement relationship of the equivalent (fixed-base) SDOF model are assumed to be elasto-plastic in the first part, followed by a linear strength degradation (see left part of **Figure 2.127**). The yield force F_y^* and the displacement D_y^* of the equivalent SDOF model, the displacement at the beginning of degradation D_m^* , the displacement at failure D_u^* , which corresponds to 80% strength in the post-capping region, the mass m^* , the period T^* , and the yield spectral acceleration of the equivalent SDOF model, are determined as follows (Fajfar, 2000):

$$F_y^* = \frac{F_y}{\Gamma}, D_y^* = \frac{D_y}{\Gamma}, D_m^* = \frac{D_m}{\Gamma}, D_u^* = \frac{D_u}{\Gamma}, \Gamma = \frac{m^*}{\sum_{i=1}^n m_i \phi_i^2}, m^* = \sum_{i=1}^n m_i \phi_i, T^* = 2\pi \sqrt{\frac{m^* D_y^*}{F_y}}, S_{ay} = \frac{F_y}{\Gamma m^*}, \quad (2.73)$$

where m_i is the mass of the i th storey, ϕ_i , is the component of the assumed shape vector in i th storey (typically the first mode shape), which is normalized to a roof displacement equal to 1, and Γ is the transformation factor which relates the displacement of an equivalent SDOF model to the roof displacement of the structure. The force F_y and the displacements D_y , D_m , D_u are based on the pushover analysis of the structure, and are obtained by idealizing the pushover curve using an equal-area concept (see left part of **Figure 2.127**). The mass of the equivalent SDOF model (m^*) is assumed to be located at the equivalent height of the SDOF model (H_{eq}), which is obtained under the assumption that the overturning moment at the base of the SDOF system is equal to the overturning moment of the structure:

$$H_{eq} = \Gamma H_{eq}^{MDOF} = \Gamma \cdot \frac{\sum_{i=1}^n m_i \phi_i h_i}{\sum_{i=1}^n m_i \phi_i} = \frac{\sum_{i=1}^n m_i \phi_i h_i}{\sum_{i=1}^n m_i \phi_i^2}, \quad (2.74)$$

where h_i is the elevation of i th mass, measured from the foundation level. Note that the equivalent height of the SDOF model (H_{eq}) has to be defined as product of transformation factor Γ and the equivalent height



This project has received funding from the European Union's Horizon 2020 research and innovation programme under grant agreement No. 700748

of the structure H_{eq}^{MDOF} . Only in such a way, the moment at the base of the SDOF model is equal to the global moment of the structure at the base. The mass of the SDOF model is attached to a stiff elastic element (column), which is at the bottom connected to the foundation with a zero length element. The zero-length element is assigned the OpenSees's uniaxial material "Hysteretic" and an appropriate moment-rotation relationship, which should be consistent with the force-displacement relationship of the equivalent SDOF model. Since $P-\Delta$ effect is considered in the analysis, the moment-rotation relationship of inelastic spring (see right part of **Figure 2.127**) is computed as follows:

$$\begin{aligned} M &= [M_y^*, M_m^*, M_u^*] = [F_y^*, F_y^*, 0.8F_y^*] \cdot H_{eq} + [D_y^*, D_m^*, D_u^*] \cdot m^* \cdot 9.81 \\ R &= [R_y^*, R_m^*, R_u^*] = [D_y^*, D_m^*, D_u^*] / H_{eq} \end{aligned} \quad (2.75)$$

The foundation is modelled with two rigid elastic elements and three node masses, which are used to simulate the foundation rotational inertia. The mid-point of the foundation is connected to an inelastic (rotational) soil spring which is restrained at the base of the model. The soil spring is modelled with a zero-length element and the OpenSees's uniaxial material "PyLiq1". The uniaxial material "PyLiq1" was originally developed for simulation of the hysteretic response of pile in liquefiable soils, but as it is shown in Sections 2.9.6 and 2.9.8, it can also be successfully employed for the simulation of the moment-rotation relationship of shallow foundations on liquefiable soils. The foundation moment-rotation relationship is defined based on the pre-liquefaction ultimate foundation moment capacity $M_{ult,1}$ and the rotation corresponding to 50% of ultimate moment capacity Θ_{50} (see **Figure 2.128**). The remaining parameters of the "PyLiq1" material were defined in order to best fit the results of FLAC 2D (see Section 2.9.6). The following parameters are suggested for simulation of moment-rotation response of shallow foundation on liquefiable soils:

$$soilType = 1, C_d = 1.0, c = 0, pRes = 0.05 M_{ult,1}, \quad (2.76)$$

where the parameters $soilType$ and C_d affect, respectively, the shape of the moment-rotation envelope and the shape of the hysteresis loops. The parameter c is the viscous damping term (set to 0) and $pRes$ is the value of residual strength below which the capacity never drops. Up to 35 % of the maximum moment, the behaviour of the model is linear-elastic (**Figure 2.128**). After this point, the material behaviour is inelastic. The material allows the simulation of the degradation of strength due to liquefaction based on predefined degradation function, which specified the drop of strength in relation to the initial value ($M_{ult,2} / M_{ult,1}$), where $M_{ult,2}$ is the post-liquefaction moment capacity. The degradation of stiffness is accounted for based on hysteretic rules implemented in the "PyLiq1" material. The expected degradation in strength has to be defined prior the analysis. Thus, an appropriate liquefaction triggering procedure has to be employed in order to assess when (and if) liquefaction is triggered for a given ground motion. The procedure used for simulation of the degradation of strength in the case that liquefaction is expected for a given ground motion is schematically presented in **Figure 2.129**. The simplified model for the soil spring is intended for simulation of the moment-rotation hysteretic response of shallow foundations and as such cannot directly simulate foundation settlement. Thus, the settlement of the building is estimated based on a predefined relationship between the foundation cumulative rotation and settlement. See following subsections for additional details, however, other simplified settlement prediction equations could be used (see section 2.6).



This project has received funding from the European Union's Horizon 2020 research and innovation programme under grant agreement No. 700748

It is important to note that due to the 2D implementation of the simplified model for SSI with consideration of liquefaction, the moment-rotation relationships (and mass) of the equivalent SDOF model and the inelastic soil spring should be computed for the same out-of-plane tributary width (usually computed per metre of length).

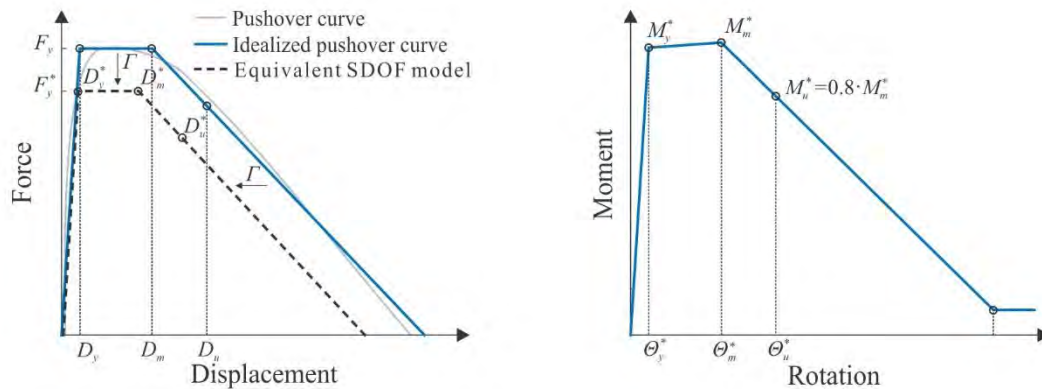


Figure 2.127: Pushover curve, idealized pushover curve and force-displacement relationship of the equivalent SDOF model of the structure (left), and (right) the corresponding moment-rotation relationship of the equivalent SDOF model of the structure.

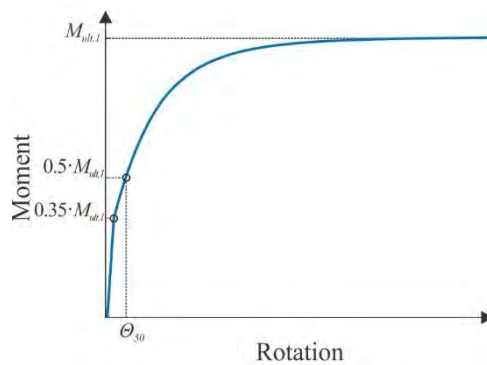


Figure 2.128: Moment-rotation relationship of the inelastic soil spring.

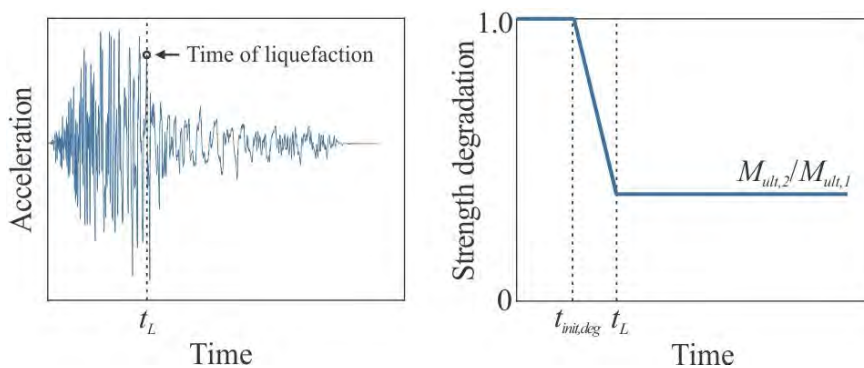


Figure 2.129: Schematic presentation of the procedure for simulation of the degradation of strength in case liquefaction is triggered for a given ground motion.

The seismic response of the system should be (in general) analysed by considering the free-field surface motions for the site under investigation, which can be obtained based on 1D site response analysis. However,



This project has received funding from the European Union's Horizon 2020 research and innovation programme under grant agreement No. 700748

in a simplified approach it is convenient to base the assessment on a code-base spectrum, which removes the need for site specific analysis. It is worth noting that EC8 (CEN, 2004) does not specify the elastic response spectrum to be used in case of liquefiable soils (class S2), but recommends to perform additional studies. The results of Section 2.9.7 (calibration of input motion for fragility analysis) indicate that the EC8 spectrum for soil type D produces a conservative estimate of the median (mean) horizontal response spectrum for all examined site. Thus, in a simplified approach it is suggested to base the assessment of the EC8 spectrum for soil type D, unless more accurate data is available.

In the following subsections, the simplified model for the inelastic soil spring is presented. The model is composed of six components: i) the model for pre-liquefaction foundation moment capacity, ii) the model for secant stiffness, (iii) the model for prediction of the time-dependent and ground-motion dependent triggering of liquefaction, (iv) the model for prediction of post-liquefaction foundation moment capacity, (v) the model for prediction of degradation of strength, and (vi) the model for prediction of settlements, which are not directly simulated in the analysis.

Model for prediction of pre-liquefaction foundation ultimate moment capacity

The pre-liquefaction foundation ultimate moment capacity $M_{ult,1}$ is computed considering the distribution of forces proposed by Meyerhof (1963) for foundations under eccentric inclined load (see **Figure 2.130**). The eccentricity of loading is accounted for considering a reduced foundation width

$$B' = B - 2e, \quad (2.77)$$

where B is the foundation width and e is the eccentricity of the resultant force R , i.e. vector sum of the horizontal and vertical force acting on the foundation (F_h and F_v). The eccentricity and inclination of the resultant force R to the vertical axis are computed as :

$$e = M / F_v = F_h H_{eq} / F_v, \quad \alpha = \text{atan}(F_h / F_v), \quad (2.78)$$

where M is the moment on the foundation due to the horizontal force F_h acting at the equivalent height of the SDOF model H_{eq} . The resultant force on the foundation R is resisted by the soil reaction Q , which is obtained as the product of the reduced foundation width B' and the vertical component of the foundation bearing capacity (q_{ult}). Note that q_{ult} accounts for the effect of the inclination of the resultant force R . In the described formulation, the foundation loading and ultimate capacity are couple. Consequently, the pre-liquefaction foundation ultimate moment capacity $M_{ult,1}$ is computed iteratively. The horizontal force F_h , which affects the eccentricity e and the foundation moment M , is gradually increased until the vertical component of the resultant force, i.e. $R \cos(\alpha) = F_v$, is in equilibrium with the soil reaction Q .



This project has received funding from the European Union's Horizon 2020 research and innovation programme under grant agreement No. 700748

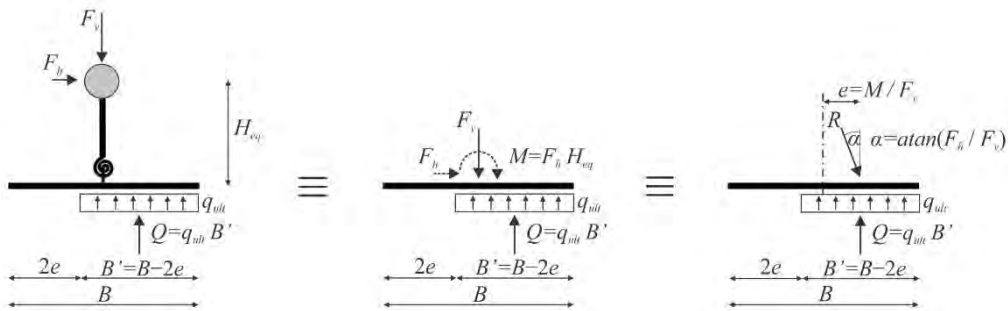


Figure 2.130: Assumed distribution of forces for computation of foundation ultimate moment capacity.

The vertical component of foundation bearing capacity q_{ult} is computed according to the Meyerhof and Hanna (1978) method for foundations on layered soils under inclined load. The soil profile is assumed to be an equivalent three-layered soil profile (i.e. a non-liquefiable crust, a potentially liquefiable layer and a third non-liquefiable layer) and can be determined using the procedures outlined in section 2.3. The Meyerhof and Hanna (1978) method is limited to the analysis of two-layer soil profiles. Consequently, it is further assumed that the mechanism of foundation bearing capacity is not significantly affected by the characteristic of third layer. The Meyerhof and Hanna (1978) approach accounts for two possible scenarios: i) a strong layer overlying a weak layer ($q_2 / q_1 \ll 1$), and ii) a weak layer overlying a strong layer ($q_2 / q_1 \gg 1$) (see Figure 2.131). The appropriate scenario is assessed based on the bearing capacity ratio q_2 / q_1 of the layers, where q_1 and q_2 , are the ultimate bearing capacities of strip foundations under vertical load on the surfaces of homogeneous thick beds of upper and lower soil, respectively:

$$\begin{aligned} q_1 &= c_1 N_{c1} + 0.5 \gamma_1 B N_{\gamma 1} \\ q_2 &= c_2 N_{c2} + 0.5 \gamma_2 B N_{\gamma 2} \end{aligned} \quad (2.79)$$

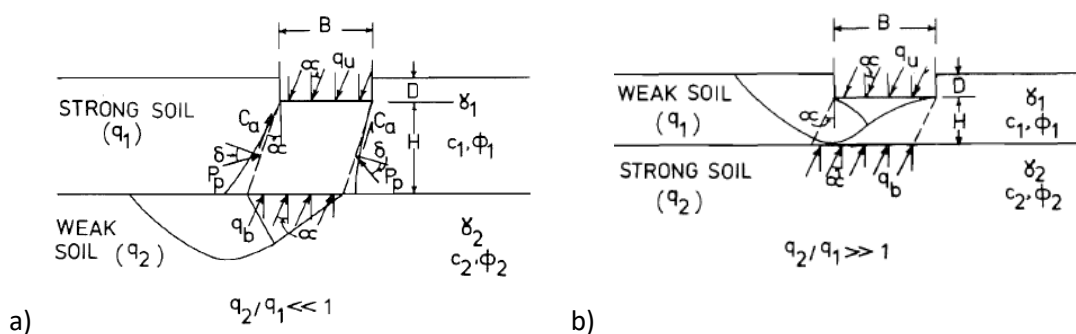


Figure 2.131: Mechanism of bearing capacity of two-layer soils according to Meyerhof and Hanna (1978): a) strong layer overlying a weak layer, and b) weak layer overlying a strong layer.

In the case of a strong layer overlying a weak layer ($q_2 / q_1 \ll 1$), the vertical component of foundation bearing capacity q_{ult} for a strip foundation of width B and depth D at a distance H above the surface of the weak layer is computed as



This project has received funding from the European Union's Horizon 2020 research and innovation programme under grant agreement No. 700748

$$q_{ult} = q_{bv} + 2c_a i_a H / B + \gamma_1 H^2 (1 + 2D \cos \alpha / H) (K_s i_s \tan \phi_1 / B) - \gamma_1 H \leq q_{tv}, \quad (2.80)$$

where q_{bv} and q_{tv} are vertical components of the ultimate bearing capacity under inclined loads on the lower and upper layer, respectively. c_a and K_s are the unit adhesion and coefficient of punching shear for vertical load, which are used in conjunction with inclination factors i_a and i_s , related to the inclination of load α . The characteristic of the upper and lower layer are defines with unit cohesions c_1 and c_2 , friction angles ϕ_1 and ϕ_2 , and unit weights γ_1 and γ_2 . The ultimate bearing capacities q_{bv} and q_{tv} are computed according to Meyerhof (1963) procedure:

$$\begin{aligned} q_{bv} &= c_2 N_{c2} i_{c2} s_{c2} + \gamma_1 (D + H) N_{q2} i_{q2} s_{q2} + 0.5 \gamma_2 B N_{\gamma 2} i_{\gamma 2} s_{\gamma 2} \\ q_{tv} &= c_1 N_{c1} i_{c1} s_{c1} + \gamma_1 D N_{q1} i_{q1} s_{q1} + 0.5 \gamma_1 B N_{\gamma 1} i_{\gamma 1} s_{\gamma 1} \end{aligned} \quad (2.81)$$

where N_c , N_q and N_γ are bearing capacity factors for strip foundation under vertical load, i and s are bearing capacity inclination and shape factors, respectively, and the subscripts 1 and 2 refer to the upper and lower soil, respectively.

In the case of a weak layer overlaying a strong layer ($q_2 / q_1 \gg 1$), the vertical component of foundation bearing capacity q_{ult} for a strip foundation is computed as

$$q_{ult} = q_{tv} + (q_{bv} - q_{tv}) (1 - H / H_f)^2 \geq q_{tv}, \quad (2.82)$$

where H_f is depth of failure surface beneath footing in thick bed of upper soil, and the bearing capacities q_{bv} and q_{tv} are defined in (2.81). As it can be observed from Equation (2.82), q_{ult} can be, in the case of a weak layer overlaying a strong layer, conservatively assumed to equal to the capacity of the upper layer, i.e. $q_{ult} = q_{tv}$. Additional details regarding the computation of q_{ult} can be found in (Meyerhof and Hanna, 1978).

Model for prediction of foundation secant stiffness at 50% of moment capacity

The foundation rotational secant stiffness ($K_{R,50}$), which corresponds to 50 % of foundation pre-liquefaction moment capacity and is used for definition of the moment-rotation relationship of the soil springs, is computed according to the procedure proposed by Gazetas et al. (2013). The secant stiffness is used to define the rotation at 50 % of moment capacity:

$$\Theta_{50} = 0.5 M_{ult,1} / K_{R,50}. \quad (2.83)$$

According to Gazetas et al. (2013), the foundation secant stiffness depends on the amplitude of rotation Θ and the foundation factor of safety under vertical loading F_s , i.e. $K_R(\Theta, F_s)$. The secant stiffness is estimated based on foundation elastic stiffness $K_{R,elastic}$ and predetermined relations between the elastic and nonlinear foundation stiffness, i.e. $CF(\Theta, F_s) \equiv K_R(\Theta, F_s) / K_{R,elastic}$, presented by Gazetas et al. (2013) (see **Figure 2.132**). The factor of safety under vertical load is estimated using the Meyerhor and Hanna (1978) method, presented in previous subsection. The elastic rotational stiffness of strip foundations is computed as



This project has received funding from the European Union's Horizon 2020 research and innovation programme under grant agreement No. 700748

$$K_{R,elastic} = \frac{\pi G (B/2)^2}{2(1-\nu)}, \quad (2.84)$$

where G and ν are the shear modulus and the Poisson's ratio of the soil, and B is the foundation width. In the case of a layered soil profile, the parameters G and ν of the uppermost layer can be used in Equation (2.84), if more accurate analysis is not performed (the mechanism of moment capacity is generally shallow). The foundation secant rotational stiffness $K_{R,50}$ is computed as

$$K_{R,50} = K_{R,elastic} CF(\Theta_{50}, F_s). \quad (2.85)$$

As it can be observed from Equations (2.85), the foundation secant stiffness depends on the amplitude of the foundation rotation. Thus, the secant rotation at 50% moment capacity Θ_{50} is estimated iteratively. In the first step, the initial estimate of Θ_{50} is obtained considering the elastic stiffness $K_{R,elastic}$ in Equation (2.83). Based on the obtained initial estimate of Θ_{50} , the factor $CF(\Theta_{50}, F_s)$ is obtained from **Figure 2.132** and it is used to compute $K_{R,50}$ using Equation (2.85). The estimated $K_{R,50}$ is then used in equation (2.83) to evaluate a new value of Θ_{50} . The iterative process is stopped when two consecutive values of Θ_{50} are within a selected tolerance. It should be noted that, in general, the convergence is fast and a sufficiently accurate estimates of Θ_{50} is obtained in few iterations.

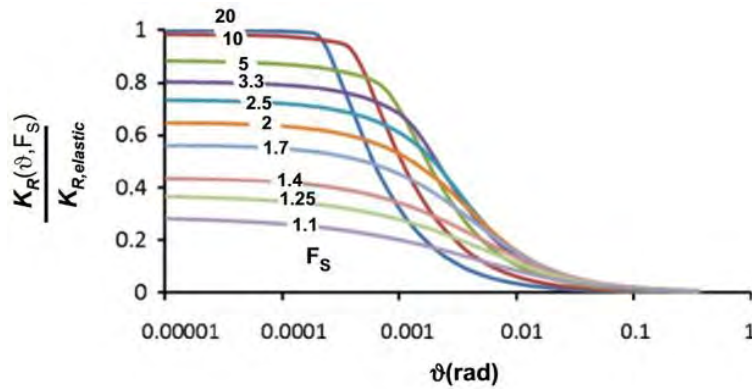


Figure 2.132: Relation between elastic and nonlinear rotational stiffness of strip foundations according to Gazetas et al. (2013).

Model for prediction of time-dependent and ground-motion dependent triggering of liquefaction

The time-dependent and ground-motion dependent triggering of liquefaction is assessed using the empirical triggering procedure proposed by Kramer et al. (2016). The procedure is based on the cyclic shear stress approach in which the demand is expressed in term of the cyclic stress ratio (CSR) and the capacity is expressed in term of the cyclic resistant ratio (CRR). The triggering of liquefaction is not only related to the amplitude of shear stress, but also to the equivalent number of loading cycles. Earthquake magnitude was historically used as a proxy for the number of loading cycles and the cyclic resistant ratio CRR was generally defined for an earthquake magnitude of 7.5. Because the excess pore pressure that produces liquefaction develops incrementally, CSR is modified by the magnitude scale factor MSF , which is intended to account



This project has received funding from the European Union's Horizon 2020 research and innovation programme under grant agreement No. 700748

for the number of loading cycles applied to the soil. The time of liquefaction can be estimated by realizing that the peak ground acceleration PGA and equivalent number of cycles N_{eq} of a ground motion increase over time (at least until the global maximum is reached). Thus, the conventional shear stress approach can be extended using a time-dependent formulation of the magnitude scale factor based on the equivalent number of cycles of a ground motion, i.e. $MSF(N_{eq}(t)) = MSF(t)$. As a consequence, the CSR become time-dependent and ground-motion dependent ($CSR \equiv CSR(t)$). It is assumed that liquefaction is triggered when $CSR(t)$ is equal to CRR (see **Figure 2.133**):

$$CSR(t) = 0.65 \frac{PGA(t)}{MSF(t)} \sigma_{vo} r_d / \sigma'_{vo} = CRR k_{\sigma}, \quad (2.86)$$

where σ_{vo} and σ'_{vo} are the total and effective vertical stresses in liquefiable layer under investigation, r_d is the stress reduction factor that depends on the depth of the liquefiable layer, and k_{σ} is the overburden normalization factor (see (Idriss and Boulanger, 2006) for details). The factor 0.65 is used to approximately convert a transient signal to an equivalent signal of uniform amplitude. The time at which liquefaction is triggered, is termed as t_L . It should be noted that the time of liquefaction can also be estimate using an alternative procedure, which was recently proposed at University of Porto (Millen et al. 2019).

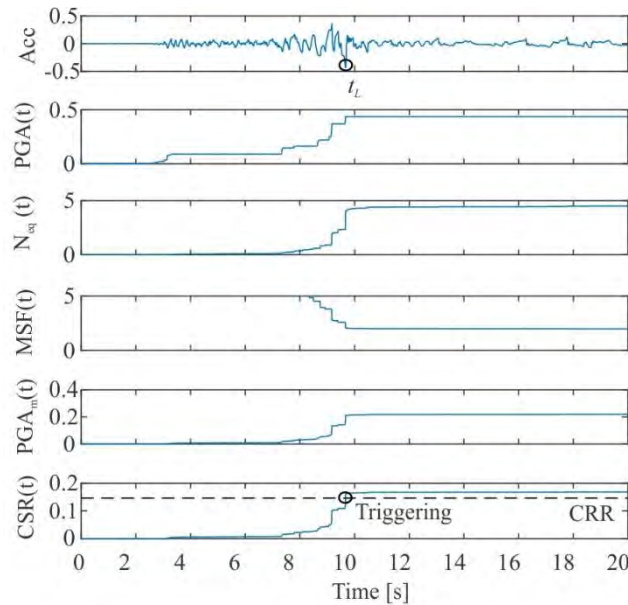


Figure 2.133: Schematic presentation of the Kramer's et al. (2016) procedure for time-dependent and ground-motion dependent triggering of liquefaction.

The cyclic resistant ratio CRR can be computed based on either SPT or CPT procedures, such as for example (Idriss and Boulanger, 2008) and (Boulanger and Idriss, 2016). In the current formulation of the procedure, the CRR is related to magnitude 7.5 and the effective vertical stress of 1 atm is computed using the SPT-based procedure by (Idriss and Boulanger, 2008):



This project has received funding from the European Union's Horizon 2020 research and innovation programme under grant agreement No. 700748

$$CRR_{M=7.5, \sigma_v=1atm} = \exp\left(\frac{(N_1)_{60cs}}{14.1} + \left(\frac{(N_1)_{60cs}}{126}\right)^2 - \left(\frac{(N_1)_{60cs}}{23.6}\right)^3 + \left(\frac{(N_1)_{60cs}}{25.4}\right)^4 - 2.8\right), \quad (2.87)$$

where $(N_1)_{60cs}$ is the corrected number of blow from SPT test, which account for loss of energy, overburden pressure and soil's fine content.

The magnitude scale factor is computed in relation the equivalent number of cycles according to the procedure proposed by Liu et al. (2001):

$$MSF(N_{eq}) = \exp\left(1.3 - 0.41 \cdot \left[\ln(N_{eq})\right]_{\mu} + \varepsilon\right), \quad (2.88)$$

where N_{eq} is the equivalent number of cycles and ε is the normally distributed standard error with mean zero and standard deviation of 0.19-0.24. The best estimated (median) value of the factor $MSF(N_{eq})$ is used in the computations.

The equivalent number of cycles of ground motion is computed using the peak counting method (Seed et al, 1975), which is describe in Appendix A of (Castiglia and Santucci de Magistris, 2018). The approach assumes that the ratio τ / τ_{max} between the shear stress induced by an earthquake in each load cycle and its maximum value is approximately equal to the ratio a_i / a_{max} . The ground motion is first normalized on its peak value so that the maximum acceleration equals to 1. The peaks of the signal are identified via the peak counting method, using a threshold value which depends on the selected normalization curve (see left part of **Figure 2.134**). The contribution of each peak, i.e. $|a_i / a_{max}|$, to the equivalent number of cycles is computed by taking into account the normalization curve, i.e. the liquefaction resistance curve CSR / CSR_1 , defined by Liu et al. (2001) (see right part of **Figure 2.134**). The mean of the DSS+ and DSS- normalization curves according to Liu et al. (2001) is used:

$$CSR / CSR_1 = mean\left(\left[R_1 N_{eq}^{m_1}, R_2 N_{eq}^{m_2} \right]\right), \quad (2.89)$$

where CSR_1 represents the amplitude of shear stress ratio that cause liquefaction in one cycles, R and m are the parameters that define the normalization curve, and the indexes 1 and 2 denote the DSS+ and DSS- normalization curves, respectively (according to Castiglia and Santucci de Magistris (2018): $R_1 = R_2 = 0.65$, $m_1 = 0.366$, $m_2 = 0.323$). The equivalent number of cycles of a signal up to the j -th peak ($N_{eq,j}$) is computed as a sum of the contributions of individual peaks using the following equation:

$$N_{eq,j} = \sum_{i=1}^j \frac{1}{2} N_{eq,i} = \sum_{i=1}^j \frac{1}{2} \left(\frac{a_i}{a_{max}} \frac{1}{R} \right)^{1/m}, \dots i \leq j \leq n \quad (2.90)$$

where i is the index of the i -th peak, j is the peak up to which the equivalent number of cycles is computed, and n is the total number of peaks above the selected threshold value, which is selected in such a way that the contribution of peaks below this amplitude is less than 1 % (0.01). Using such an approach the model for the estimation of equivalent number of cycles becomes time-dependent as well as ground-motion dependent.



This project has received funding from the European Union's Horizon 2020 research and innovation programme under grant agreement No. 700748

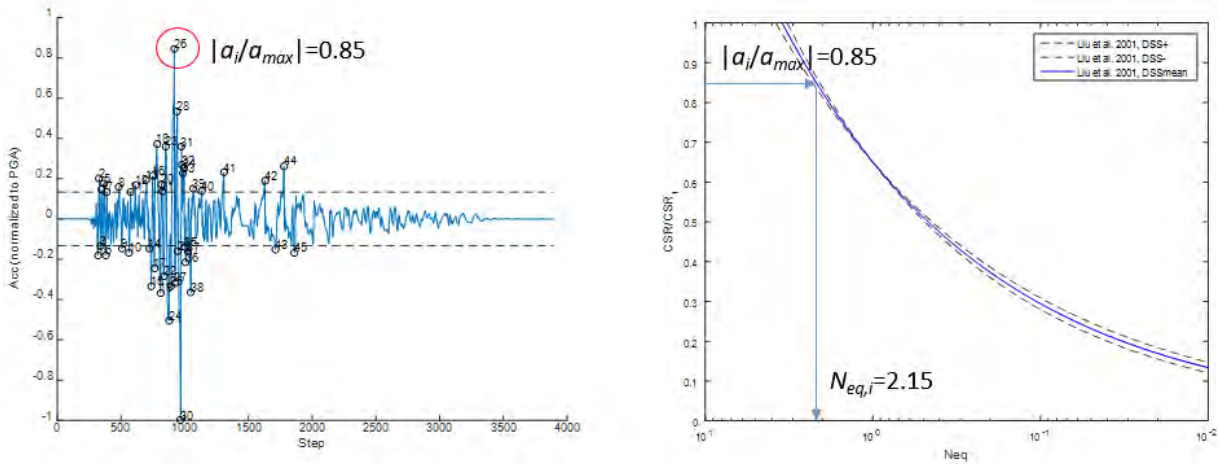


Figure 2.134: Estimation of the equivalent number of cycles of a signal using the peak counting method and the mean of the DSS+ and DSS- normalization curves according to Liu et al. (2001).

Model for prediction of post-liquefaction foundation moment capacity

The post-liquefaction moment capacity of foundation $M_{ult,2}$ is calculated iteratively under the condition that the vertical component of the resultant force that acts on the foundation, i.e. $R \cos(\alpha) = F_v$, is in equilibrium with the soil reaction (see **Figure 2.130**). The procedure for computation of the foundation moment capacity is practically the same as in the case of pre-liquefaction moment capacity. However, the shear strength of the liquefied layer is reduced, which can result in a significantly reduction of the foundation moment capacity. The post-liquefaction foundation bearing capacity is estimated using the simplified approach proposed by Karamitros et al. (2013b). The approach is based on the Meyerhof and Hanna (1978) punching shear failure mechanism for a strong layer overlaying a weak layer (see **Figure 2.131**), which was described in a previous subsection and which is representative of the case where a non-liquefiable crust overlies a liquefiable layer. The reduction in the shear strength of the liquefied layer is considered using a degraded friction angle, which depends on the average pore pressure ratio in the liquefiable layer. According to Karamitros et al. (2013b), the degraded friction angle of the liquefied layer can be computed as:

$$\phi_{2,deg} = \tan^{-1} \left[(1 - U_L) \tan(\phi_2) + U_L \tan(\phi_{2,res}) \right] \quad (2.91)$$

where U_L is the average pore pressure ratio in the liquefiable layer, and the index L denoted that the value correspond to the state of liquefaction ($U_L \equiv U(t_L)$). ϕ_2 and $\phi_{2,res}$ are the initial and the residual friction angle of the liquefiable layer. The residual friction angle $\phi_{2,res}$ is used to model the fact that a liquefied soil still retains a minimal value of shear strength (Idriss and Boulanger, 2007). An appropriate value of $\phi_{2,res}$ was assumed based on results of model calibration (Section 2.9.6), which indicate that a reasonable estimation of the foundation post-liquefaction moment capacity can be obtained using $\phi_{2,res} = 5^\circ$. In case of strip foundations, the average pore pressure ratio in the liquefied layer is computed as (Karamitros et al., 2013a):



This project has received funding from the European Union's Horizon 2020 research and innovation programme under grant agreement No. 700748

$$U_L = (U_{foot,L} + U_{ff,L}) / 2, \quad (2.92)$$

where $U_{foot,L}$ denotes the pore pressure ratio under the foundation, and $U_{ff,L}$ is the pore pressure ratio in the free-field. The index L denotes that both values correspond to the state at the time of free-field liquefaction (i.e. $U_{foot}(t_L) \equiv U_{foot,L}$ and $U_{ff}(t_L) \equiv U_{ff,L}$). At liquefaction, the pore pressure ratio in free-field reaches values close to 1.0. Results of FLAC 2D analyses (see Sections 2.9.6) indicate that the value 0.95 can be assumed for $U_{ff,L}$ at the triggering of liquefaction. The pore pressure ratio under the foundation is estimated using a slightly modified version of the Karamitros et al. (2013b) approach, in which the pore pressure ratio under the foundation is not estimated at the characteristic depth, but at the centre of the liquefiable layer. The modified approach was implemented because the original procedure was developed for a two-layer soil profile. The results of model calibration and validation (see sections 2.9.6 and 2.9.8) indicate that modified approach yields reasonable estimates of the pore pressure ratios under the foundation. The pore pressure ratio under the foundation is thus estimated as

$$U_{foot,L} = \frac{A}{(1 + \Delta\sigma_{v,c} / \sigma'_{vo,c})}, \quad (2.93)$$

where $\Delta\sigma_{v,c}$ is the additional vertical stress imposed by the foundation at centre of the liquefiable layer, $\Delta\sigma'_{vo,c}$ is the geostatic vertical effective stress, and A is a correction factor related to the dilative behaviour of the foundation subsoil, due to the accumulating seismic settlements and the associated shearing deformations at the end of shaking. For small settlement, the factor A has a value close to 1 and reduces with increasing dynamic settlements. For conservatism, the authors suggest to limit its minimal value to 0.8 (Karamitros et al. 2013b). Results of model calibration (see Sections 2.9.6) indicate that the value $A=0.90$ yields reasonable estimates of the pore pressure ratios under the foundation.

Model for prediction of strength degradation in case of liquefaction

The prediction of liquefaction-induced strength degradation in moment-rotation relationship of soil spring is based on a simplified model for the development of the average pore pressure ratio in the liquefiable layer ($U(t)$) (see blue line in left part of **Figure 2.135**), which is defined based on the distribution of pore pressure ratios $U_{ff}(t)$ and $U_{foot}(t)$ (see black and red lines in left part of **Figure 2.135**). Note that the degradation of stiffness is accounted for based on appropriate hysteretic rules. It is assumed that the development of pore pressure ratio $U(t)$ can be modelled using a trilinear model, which is composed of a pre-initiation phase (pore pressure ratio nearly zero), a linear build-up phase, and a post-liquefaction phase with nearly constant values of pore pressure ratio up to the end of shaking. The model for the development of $U(t)$ is defined using the following equation:



This project has received funding from the European Union's Horizon 2020 research and innovation programme under grant agreement No. 700748

$$U(t) = \begin{cases} 0 & \text{for } t \leq t_{init} \\ U_L(t - t_{init}) / (t_L - t_{init}) & \text{for } t_{init} < t \leq t_L, \text{ where } T_{init} = \frac{0.2 t_L}{U_{ff,L}} \\ U_L & \text{for } t > t_L \end{cases} \quad (2.94)$$

where t_{init} is the time of initiation of pore pressure build-up, t_L is the time of liquefaction, U_L is the average pore pressure ratio in the liquefiable layer (Equation (2.92)), and $U_{ff,L}$ is the pore pressure ratio in free field. An appropriate value for t_{init} was defined based on model calibration presented in Section 2.9.6. It should be noted that, in general, the development of pore pressure ratios varies significantly depending on the ground motion and foundation characteristics (e.g. bearing pressure). The simplified model is intended to simulate the “average” pore pressure development and as such cannot capture the change in the rate of build-up of pore pressure (see e.g. Polito et al. 2008) and significant fluctuations of pore pressure during ground shaking, which can result in sudden pinching and hardening effects in the hysteretic response of the foundation. Nevertheless, results of model validation presented in Section 2.9.8 suggest that the model is able to sufficiently accurately simulate the global response of foundation on liquefiable soils, at least to the level of accuracy necessary to allow decision making if more detailed analyses of soil liquefaction are needed.

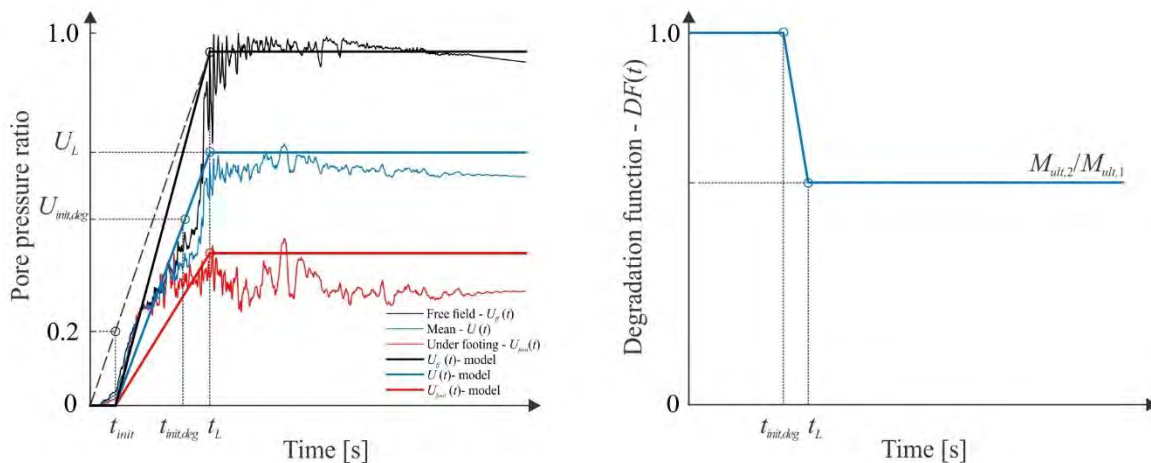


Figure 2.135: Proposed model for the degradation of strength due to liquefaction.

In the case if liquefaction is triggered, the strength degradation in the rotational spring representing SSI, is also modelled by a tri-linear time-dependent relationship (right part of **Figure 2.135**). The time-dependent strength degradation is composed of an initial part with constant value of moment capacity equal to the pre-liquefaction moment capacity, a linear softening branch, and a constant branch with post-liquefaction capacity. The degradation of strength is inputted in the OpenSees model by specifying the strength degradation function $DF(t)$, which represent the ratio between the post- and pre-liquefaction foundation moment capacity and is defined as follows:



This project has received funding from the European Union's Horizon 2020 research and innovation programme under grant agreement No. 700748

$$DF(t) = \begin{cases} 1.0 & \text{for } t \leq t_{init,deg} \\ 1.0 + \frac{(M_{ult,2} / M_{ult,1} - 1)}{(t_L - t_{init})} (t - t_{init}) & \text{for } t_{init,deg} < t \leq t_L \\ M_{ult,2} / M_{ult,1} & \text{for } t > t_L \end{cases} \quad (2.95)$$

where $t_{init,deg}$ is the time at the initiation of the strength degradation, t_L is the time of liquefaction, and $M_{ult,2} / M_{ult,1}$ is the ratio between pre- and post-liquefaction moment capacity. $t_{init,deg}$ is defined based on the average pore pressure ratio $U(t)$ at which the pore pressure is sufficiently high to influence the foundation moment capacity $U_{init,deg} \equiv U(t_{init,deg})$. It should be noted that $U_{init,deg}$ depend on the characteristics of the soil profile and the foundation system, such as depth of non-liquefiable crust (depth of the liquefiable layer), foundation dimensions and foundation bearing pressure. It is suggested to assess the appropriate value of $U_{init,deg}$ case-by-case by increasing subsequently the pore pressure ratio until the foundation moment capacity is starting to decrease due to pore pressure in the liquefiable layer (see **Figure 2.136**). The results of model calibration suggests that for the examined example, the values of $U_{init,deg}$ vary between 0.4 and 0.7. However, if more detailed analyses are not performed, a conservative estimate of $U_{init,deg} = 0.3$ can be assumed.

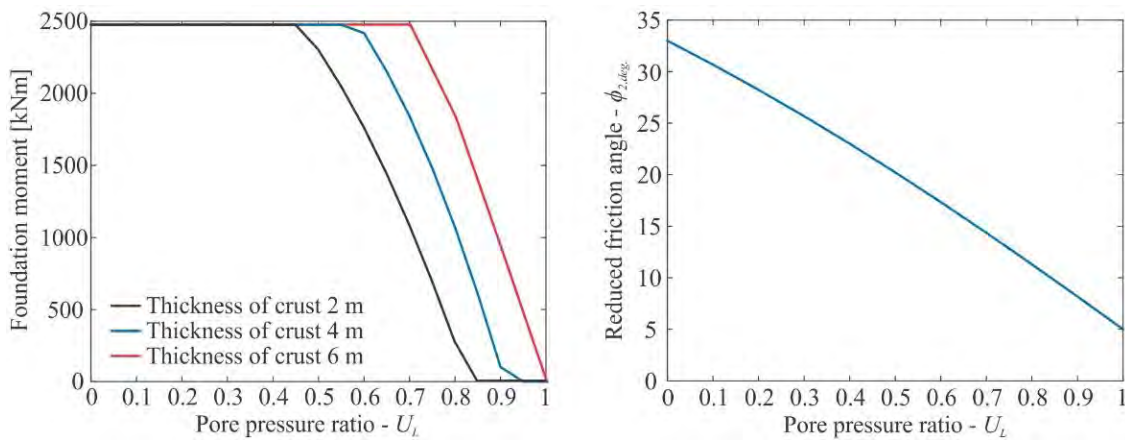


Figure 2.136: Example of (left) the relationship between the foundation moment capacity and the pore pressure ratio in the liquefiable layer for different thicknesses of the non-liquefiable crust and (right) the relationship between the pore pressure ratio and the degraded friction angle of the liquefiable layer.

Model for prediction of building settlement

The simplified model for SSI with consideration of liquefaction (**Figure 2.126**) is intended for simulation of foundation rotational hysteretic response and as such cannot be used directly for estimation of settlement. Thus, the settlement of the building can be estimated using the de-coupled settlement estimation methods in section 2.6 or estimated indirectly by calibrating results from simplified model to the results observed in the case of 2D analyses performed in FLAC. Based on such comparative studies, it was observed that correlation between foundation settlement and the cumulative rotation is high, which is consistent with the findings by Deng et al. (2012) for foundations on non-liquefiable soils. Thus, the simplified model assumes



This project has received funding from the European Union's Horizon 2020 research and innovation programme under grant agreement No. 700748

that the foundation settlement can be estimated based on a predetermined relationship between foundation cumulative rotation and settlement. Such an approach is consistent with the observation that liquefaction-induced settlement of buildings is mostly controlled by shear deformations resulting from soil-structure-induced foundation racking, partial bearing failure due to loss of strength, and localized volumetric strains (e.g. Dashti et al. 2010; Dashti and Bray 2013; Bray and Dashti 2014). Due to these effects, a major part of settlement happened during earthquake motion, however, post-liquefaction consolidation and soil ejecta can still represent a significant contribution, especially when the liquefaction occurs near the surface, and can be estimated using Bray and Macedo (2018) or Bullock et al. (2018) procedures. Furthermore, a simplified estimate of tilt from Bullock et al. (2019) can be used which accounts for dynamic and post-liquefaction settlement.

A model for the relationship between cumulative rotation and settlement was developed on the basis of results of 60 FLAC analyses, which are describe in Section 2.9.6. The obtained results are presented in **Figure 2.137**. In 12 out of 60 dynamic analyses liquefaction was not trigger (red lines), whereas in the remaining 48 cases liquefaction was triggered and resulted in larger foundation settlements (blue lines). The results obtained for liquefaction and non-liquefaction cases differ quite significantly. Consequently, separate relationships were proposed for these cases. A least-square fit of the data was used to obtain the mean (average) relationship between the cumulative rotation and settlement for liquefaction and non-liquefaction cases (see dashed lines in **Figure 2.137** and Equation (2.97)). For cases with liquefaction, the scatter of the data is significant. However, the fitted relationship can still provide a good estimate of the order of magnitude of the expected settlement.

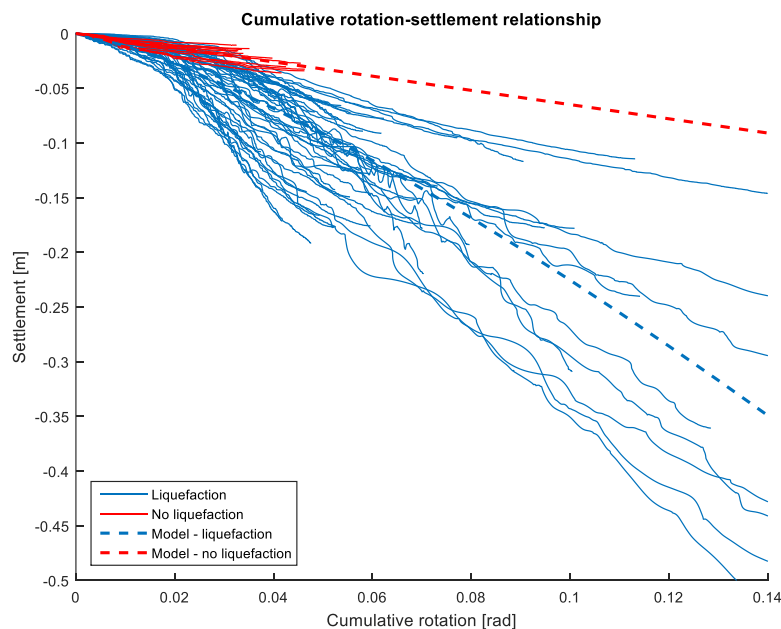


Figure 2.137: Cumulative rotation-settlement relationship based on FLAC analyses for liquefaction (blue color) and non-liquefaction cases (red color). The proposed settlement – cumulative rotation relationships are presented with dashed lines.



This project has received funding from the European Union's Horizon 2020 research and innovation programme under grant agreement No. 700748

The proposed settlement – cumulative relationships are used for estimation of building settlement. In the first step, the foundation rotations obtained from the dynamic analysis of the simplified SSI model are used to compute the cumulative rotation of the foundation at a given step of the analysis:

$$\Theta_{cum,j} = \sum_{i=2}^j |\Theta_i - \Theta_{i-1}|, \quad \Theta_{cum,1} = 0, \quad i \leq j \leq n, \quad (2.96)$$

where Θ_i and Θ_{i-1} are the foundation rotations at two consecutive steps of dynamic analysis, j is the steps of the analysis for which the cumulative rotation is computed, and n is the total number of steps. Next, the settlement of the foundation at a given step of analysis $U_{z,j}$ is computed based on the fitted relationships between the foundation cumulative rotation and settlement (dashed lines in **Figure 2.137**):

$$U_{z,j} = \begin{cases} -4.5 \Theta_{cum,j}^{1.3} & \text{if liquefaction is detected} \\ -0.65 \Theta_{cum,j} & \text{if liquefaction is not detected} \end{cases}. \quad (2.97)$$

Note that the proposed approach allows the estimation of the development of settlement during the analysis and not just the settlement at the end of the analysis.

2.9.4 CASE STUDY: APPLICATION OF RAPID RISK IDENTIFICATION METHOD TO A CODE-CONFORMING BUILDING WITH CONSIDERATION OF LIQUEFACTION AND DIFFERENT LEVELS OF SEISMIC HAZARD

The simplified model for SSI with consideration of liquefaction, presented in Section 2.9.3, is applied for Rapid Risk Identification (RRI) of a case study example. The example consists of code-conforming building located on potentially liquefiable soil. It is assumed that the investigated soil-structure configuration is located at two locations with different level of seismic hazard. The aim of RRI method is to assess the seismic risk of the investigated soil-structure configuration, which can be used to decide whether the detailed studies of soil liquefaction are necessary. In the following, the four steps required to apply RRI method to a case study are described (see **Figure 2.125**).

STEP 1: Definition of input data

The first step of the RRI method is the definition of data regarding the investigated structure, soil profile, the seismic hazard at the location, the set of ground motions used for fragility analysis, the definition of the limit states and tolerable values of seismic risk related to liquefaction-induced damage.

The geometry and characteristics of the case study example are presented in **Figure 2.138**. The example is a code-conforming mid-height building on shallow foundations, which is modelled as an equivalent SDOF system. The equivalent SDOF fixed-based model period T^* and yield spectral acceleration S_{ay} amount to 0.60 s and 0.6 g, respectively. The width B and the equivalent height H_{eq} of the building are 10 m and 20 m, respectively. The force-displacement relationship and the corresponding equivalent moment-rotation relationship of SDOF model are presented in **Figure 2.139**. The force-displacement relationship, which is obtained from pushover analysis, is transformed to moment-rotation relationship for the inelastic rotational



This project has received funding from the European Union's Horizon 2020 research and innovation programme under grant agreement No. 700748

spring of the building as presented in Equation (2.75). The mass of the equivalent SDOF model m^* and the foundation bearing pressure q_b amount to 106 t and 130 kPa, respectively. It should be noted that since a 2D analysis is performed, the mass m^* and the force-displacement (moment-rotation) relationship of the structure are computed for out-of-plane tributary width of 1 m. The model for the soil spring is defined as presented in Section 2.9.3. The moment-rotation relationship for the inelastic soil spring, which is obtained considering the pre-liquefaction foundation moment capacity $M_{ult,1}=2738$ kNm and rotation which corresponds to 50 % of moment capacity $\Theta_{50}=0.0005$, is presented in **Figure 2.140**. Note that the moment-rotation relationship is computed for out-of-plane tributary width of 1 m. With consideration of SSI the period of the building increases to 0.82 s (fixed-base period amounted to 0.6 s).

The soil profile is composed of three layers, i.e. a non-liquefiable clay crust of depth 2 m, a liquefiable layer of depth 4 m and a non-liquefiable layer of depth 26 m (see **Figure 2.138**). The upper layer consists of soft clay with undrained shear strength $c_u=50$ kPa, specific weight $\gamma=15.6$ kN/m³ and shear modulus $G=50$ MPa. The liquefiable layer consists of loose sand with relative density $D_r=0.55$, friction angle $\phi'=33^\circ$, cohesion $c'=0$, specific weight $\gamma=19.7$ kN/m³, shear modulus $G=60.5$ MPa and equivalent number of SPT blows $(N_1)_{60}=14$. The lower layer consists of stiff clay with undrained shear strength $c_u=200$ kPa, specific weight $\gamma=16.5$ kN/m³ and shear modulus $G=200$ MPa. The ground water is located 2 m below the surface. According to EC8 (CEN, 2004) the soil profile is characterized as S2, i.e. soil subjected to liquefaction.

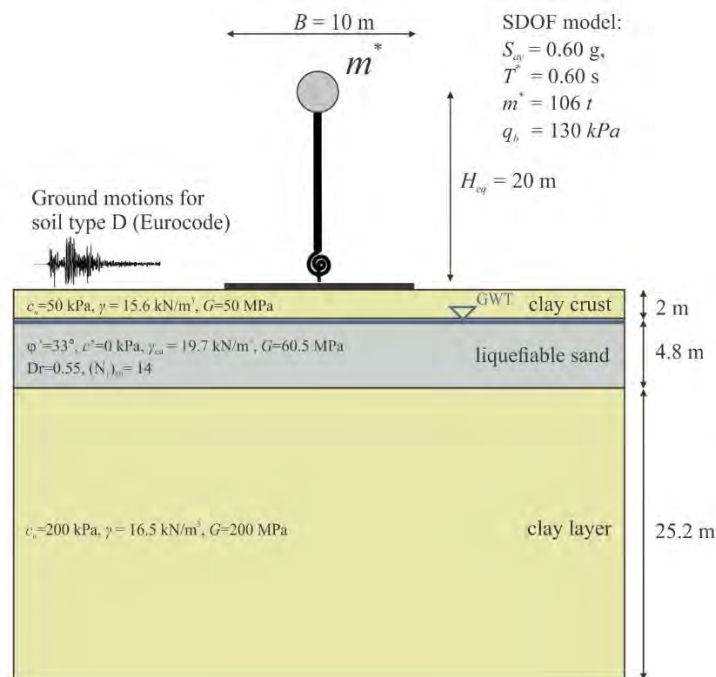


Figure 2.138: Geometry and characteristics of the investigated case study example.



This project has received funding from the European Union's Horizon 2020 research and innovation programme under grant agreement No. 700748

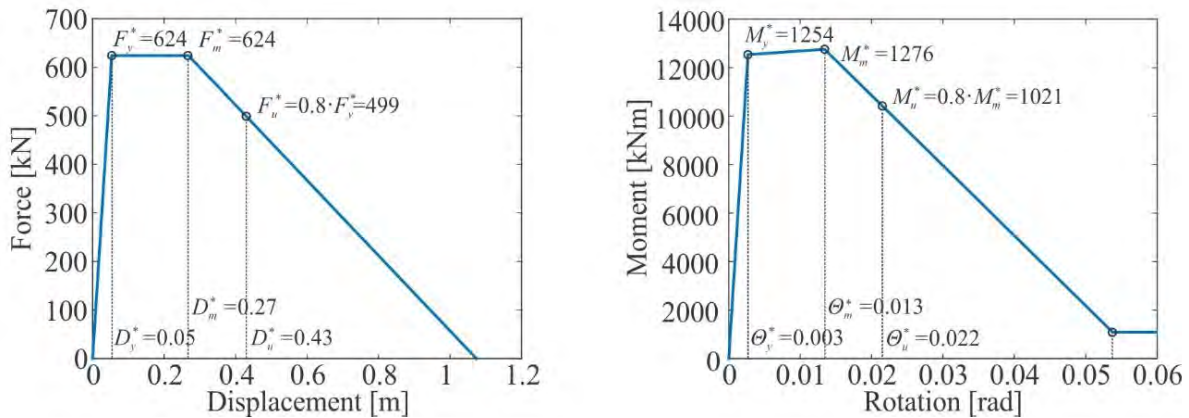


Figure 2.139: Force-displacement relationship and the corresponding equivalent moment rotation relationship of the SDOF model of the building.

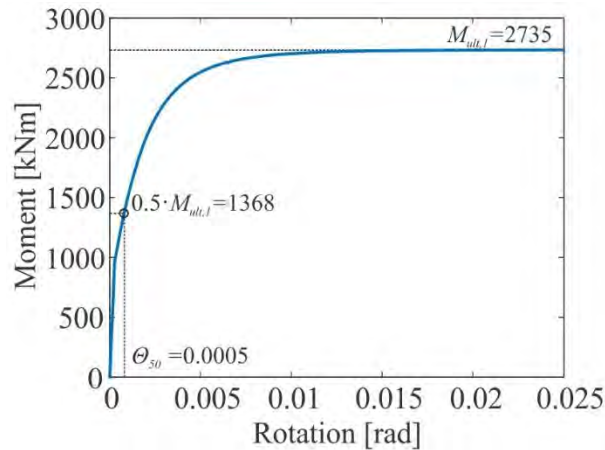


Figure 2.140: Moment-rotation relationship of the inelastic soil spring.

For comparison reasons, the soil-structure configuration is assumed to be located at two sites with different level of seismic hazard. The comparison of seismic hazard curve for the selected locations is presented in **Figure 2.141**. Note that the seismic hazard curves are expressed in term of peak ground acceleration (a_g), which is used as the intensity measure for fragility analysis. The hazard curves were obtained from SHARE hazard analysis results (Giardini et al., 2013), available from EFEHR web page (EFEHR, 2018). In the first case, the building is assumed to be located in a moderate seismic hazard region (Benavente (Lisbon), Portugal), whereas in the second case the building is assumed to be located in a low seismic hazard region (Düsseldorf, Germany). As it can be observed from the comparison of hazard curves in **Figure 2.141**, the seismic hazard curve for Düsseldorf is significantly lower than the hazard curve for Benavente. For example, the 475-years return period peak ground acceleration ($a_{g,475}$) for Benavente is 0.30 g, whereas for Düsseldorf $a_{g,475}$ is more than three times lower (0.08 g).



This project has received funding from the European Union's Horizon 2020 research and innovation programme under grant agreement No. 700748

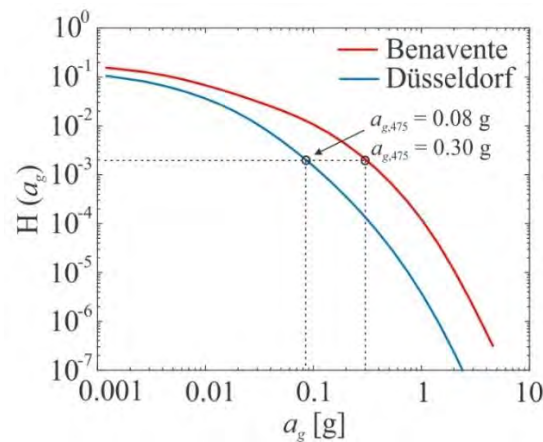


Figure 2.141: Comparison of seismic hazard curve from SHARE hazard data (Giardini et al., 2013) for the selected locations: Benavente (red) and Düsseldorf (blue).

The seismic response was computed for a set of 30 ground motions (see **Figure 2.142**). The set of ground motions was selected from the strong ground motion database which contains 9188 ground motion obtained from the NGA (Chiot et al. 2008) and the RESORCE (Akkar et al. 2014) database. The two databases were recently combined by the Institute of Structural Engineering, Earthquake Engineering and Construction IT (IKPIR) (Šebenik and Dolšek, 2016). The ground motions were selected in such a way that the mean of horizontal acceleration spectra matched the elastic spectrum according to EC8 (CEN, 2004) for soil type D by being conditioned to the peak ground acceleration (a_g) of 0.25g. The ground motion selection was performed according to the procedure proposed by Jayaram et al. (2011) considering the following constraints regarding the magnitude (M), source-to-site distance (R), and shear-wave velocity in the upper 30m of soil ($v_{s,30}$): $5.5 < M < 7.5$, $5 \text{ km} < R < 50 \text{ km}$ and $50 \text{ m/s} < v_{s,30} < 250 \text{ m/s}$. The ground motion selection could be further refined by additionally conditioning the selection based on Arias Intensity which is well correlated to the triggering of liquefaction (Dashti and Karimi, 2017). It is worth noting that EC8 (CEN, 2004) does not specify the elastic response spectrum to be used in case of liquefiable soils (class S2), but recommend to perform additional studies. The results of section 2.9.7 (calibration of input motion for fragility analysis) indicate that the EC8 spectrum for soil type D produces conservative estimates of the mean horizontal response spectrum for all examined soil profiles. Thus, in a simplified approach it is suggested to base the assessment on the EC8 spectrum for soil type D, unless more accurate data is available.

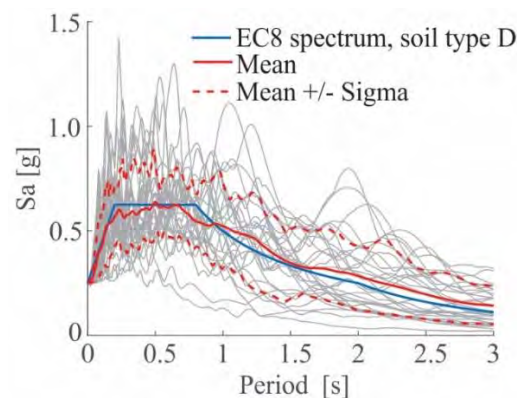


Figure 2.142: Acceleration response spectra (5% damping) of the selected set of ground motions (GMs) used for fragility analysis.



This project has received funding from the European Union's Horizon 2020 research and innovation programme under grant agreement No. 700748

The limit states of the building are based on structural damage, foundation rotations and settlements. In the example, four limit states are examined: i) slight damage (DL1), ii) moderate damage (DL2), iii) extensive damage (SD), and iv) complete damage (NC). Note that the complete damage state corresponds to the near collapse (NC) limit state according to EC8 (CEN, 2004) and not to the actual collapse of the building, which cannot be directly simulated with the simplified model. The limit states related to structural damage due to ground shaking are defined based on the peak rotations in the inelastic rotational spring at the base of the buildings, as presented in **Figure 2.143**. The limit states related to ground deformations, i.e. peak rigid body foundation rotations $\Theta_{peak,LS}$ and settlements $U_{z,LS}$, are defined according to the recommendations by Bird et al. (2006) (see **Table 2.22**). The authors do not provide the threshold value for slight damage (limit state DL1). Consequently, the threshold value for this limit state was assumed to be equal to half of the threshold value related to moderate damage (limit state DL2). The damage state of the building is defined considering all three criteria and it is assumed to be attained when the limit state is attained for the first of the examined criteria.

In addition to the fragility curves for the designated limit states, the so-called liquefaction fragility curve, which defines the probability of attaining liquefaction for a given value of peak ground acceleration (a_g), is also computed based on the results of the liquefaction triggering procedure (see Section 2.9.3).

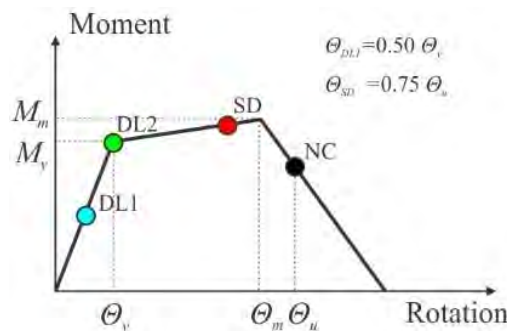


Figure 2.143: Schematic representation of the definition of limit states related to structural damage.

Table 2.22: Definition of limit state related to ground deformations, i.e. peak rigid-body foundation rotations and settlements. Adapted after Bird et al. (2006).

Limit state (LS):	$\Theta_{peak,LS}$ [rad]	$U_{z,LS}$ [m]
Slight - DL1	0.005	0.05
Moderate - DL2	0.01	0.10
Extensive - SD	0.04	0.30
Complete - NC	0.08	1.00

In order to make decision regarding the acceptable performance of the investigated soil-structure configuration, each of the investigated limit states should be assigned an appropriate threshold values of



This project has received funding from the European Union's Horizon 2020 research and innovation programme under grant agreement No. 700748

tolerable risk. The tolerable value of seismic risk should be selected depending on the potential consequences of the occurrence. In general, the decision making regarding the need for additional studies can be based on each of the selected limit states. However, in this example, the decision-making is based on the probability of exceeding the complete damage (NC limit state). The threshold value of tolerable seismic risk is set to 1 % in 50 years ($2 \cdot 10^{-4}$ /per year), which may be considered as a typical value for code-conforming buildings (Fajfar and Dolšek, 2012; Kosič et al. 2017).

STEP 2: Simplified fragility analysis of the soil-structure configuration with consideration of liquefaction

After the definition of input data, the next step of the RRI method involves evaluation of the fragility of the building, which is performed using the simplified SSI model with consideration of liquefaction (see **Figure 2.126** in Section 2.9.3). Note that in this example it is assumed that since the building and the geotechnical characteristics are the same at both locations, the same fragility curve applies for both locations. Consequently, only one fragility analysis was necessary for this example application. In reality, the fragility curves at the two locations would be slightly different due to different design seismic action (different hazard). However, different seismic design of the building is not expected to affect the results of this example since the limit state of building is mostly related to ground deformations (especially settlements).

The results of the fragility analysis are fragility functions $P(LS | IM)$, which define the conditional probability of exceeding a limit state for given a level of seismic intensity IM . The fragility functions depend of the measure used to represent the ground-motion intensity. In the presented study, the peak ground acceleration (a_g) is used as the intensity measure. The estimation of fragility curves involves nonlinear response history analyses, which are performed by scaling the ground-motion intensity until the limit state is reached. Assuming lognormal distribution of the fragility function, the fragility curve is fully defined by two fragility parameters, i.e. the median peak ground acceleration $\tilde{a}_{g,LS}$ and the corresponding logarithmic standard deviation β_{LS} . The fragility parameters are estimated using the maximum likelihood method, considering the sample of limit-state peak ground accelerations $a_{g,LS}(r)$ of size N_{gm} , which is the outcome of the performed nonlinear response history analyses:

$$\tilde{a}_{g,LS} = e^{\frac{1}{N_{gm}} \sum_{r=1}^{N_{gm}} \ln(a_{g,LS}(r))}, \quad \beta_{LS}^2 = \frac{1}{N_{gm}} \sum_{r=1}^{N_{gm}} (\ln(a_{g,LS}(r)) - \ln(\tilde{a}_{g,LS}))^2, \quad (2.98)$$

where N_{gm} is the number of ground motions used in the analysis, and r denote the r th ground motion. In case lognormal distribution of the fragility function is not assumed, the fragility function can be simply defined as the empirical cumulative distribution of limit-state peak ground accelerations.

Nonlinear response history analyses of the simplified SSI model were performed in OpenSees (2017). In total, 645 dynamic analyses were required for fragility analysis of the investigated example. However, due to computational efficiency of the simplified model, the fragility analysis was completed in less than one hour on a regular desktop computer (processor Inter(R) Core(TM) i7-2600 CPU @3.4 GHz, 16 GB RAM DDR3). Note that the computational time for the entire fragility analysis (in total 645 dynamic analyses) was significantly



This project has received funding from the European Union's Horizon 2020 research and innovation programme under grant agreement No. 700748

lower than the computational time of a singled dynamic analysis in FLAC 2D. Note also that the computational time can be decreased to few minutes, in case the fragility analysis is performed on a cluster of computers.

The result of the performed analysis are the fragility curves for designated limit states and the liquefaction fragility curve for the location of the building, which are presented in **Figure 2.144**. The fragility curves obtained based on the assumption of lognormal distribution of the fragility function are presented in thin lines, whereas the fragility function obtained based on the empirical CDF are presented in thick lines. Based on the results in **Figure 2.144**, it is interesting to observe that in case of a 475-years return period event (design earthquake for ordinary building according EC8 (CEN, 2004)), the expected damage of the building located in Benavente and Düsseldorf is significantly different. For example, the building located in Düsseldorf ($a_{g,475}=0.08$ g) is unlikely to experience any significant damage and the probability of observing soil liquefaction on the location is negligible. On the contrary, the building located in Benavente is likely to be non-operational and moderately damage during a 475-years return period event ($a_{g,475}=0.30$ g), i.e. the probability of exceeding limit states DL1, DL2, SD, and NC are 100 %, 86 %, 43 % and 23 %, respectively. The probability of observing soil liquefaction for the location in Benavente during a 475-years return period event is nearly 70 %. Note that the fragility curves can only provide the probability of exceeding the limit states for a given level of seismic intensity and does not incorporate the effects of seismic hazard at the location. Thus, in the next step of RRI, the fragility curves are combined with seismic hazard data to compute seismic risk.

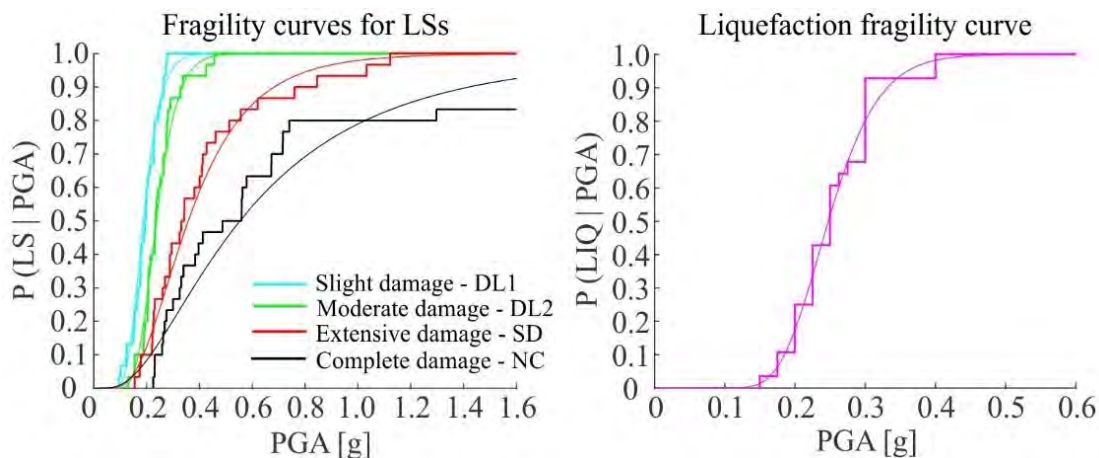


Figure 2.144: Fragility curves for designated limit states (left) and the liquefaction fragility curve (right) obtained based on the assumption of lognormal distribution of the fragility function (thin lines) and based on the empirical CDF (thick lines).

STEP 3: Risk assessment

The next step of the RRI method is risk assessment. The annual probability of exceeding designated limit states P_{LS} is computed by convolution of fragility functions from Step 2 (**Figure 2.144**) and the hazard functions for the two investigated locations (**Figure 2.141**). In this example, the probability of exceedance of designated limit states is compute using numerical integration:



This project has received funding from the European Union's Horizon 2020 research and innovation programme under grant agreement No. 700748

$$P_{LS} = \int_0^{\infty} P(LS | IM = im) \cdot \left| \frac{dH(im)}{d(im)} \right| \cdot d(im) \quad (2.99)$$

where $P(LS | IM = im)$ is the probability of exceeding the limit state if the intensity measure IM takes the value equal to im , and the hazard curve $H(im)$ is the annual rate of exceedance of im . In the computation of P_{LS} , the fragility function was defined based on the empirical cumulative distributions of limit-state peak ground accelerations (thick lines in **Figure 2.144**). An alternative approach to compute P_{LS} would be to use the Cornell's close-form solution (Cornell, 1996; Cornell et al., 2002) for estimation of seismic risk, as proposed by e.g. Fajfar and Dolšek (2012). However, such an approach would require additional assumptions (lognormal distribution of fragility; hazard curve is linear in logarithmic domain). The probability of exceeding designated limit states over a period of 50 years is computed as:

$$P_{LS,50} = 1 - (1 - P_{LS})^{50} \quad (2.100)$$

The fragility parameters $\tilde{a}_{g,LS}$ and β_{LS} , annual probabilities of exceeding designated limit states P_{LS} , and probabilities of exceeding designated limit states in 50 years ($P_{LS,50}$) obtained for the building located in Benavente (Portugal) and Düsseldorf (Germany) are presented in **Table 2.23**. It can be observed that despite the same fragility parameters of the building, the computed seismic risk at the two locations is significantly different. The seismic risk of the building located in Benavente is almost an order of magnitude larger than that of the building located in Düsseldorf, which is the consequence of the significantly larger seismic hazard (see **Figure 2.141**). For example, the probability of exceeding complete damage (NC limit state) over the life-time of the building in Benavente (50 years) is 6 %, whereas in the case of the building located in Düsseldorf is only 0.4 %. In addition, if the operability of the building is assumed to be related to the exceedance of DL2 limit state, the probability of non-operability in the life-time of the building in Benavente is 16 %, whereas it is only 1.4 % for the building in Düsseldorf. Very similar conclusions can be made also for the probability of observing liquefaction in the life-time of the building, i.e. 15 % for the site in Benavente and 1.2 % for the site in Düsseldorf. The computed probabilities of exceeding designated limit-state are used in the next section for risk-based decision-making.

STEP 4: Risk-based decision making regarding the need for detailed analysis of soil liquefaction

The final step of the RRI method is the risk-based decision making. If the computed probabilities of exceedance of designated limit states P_{LS} are smaller than the predefined tolerable probabilities $P_{LS,tol.}$, it is concluded that detailed studies of soil liquefaction are not necessary, since it is assumed that the risk of unacceptable behaviour due to adverse effects of soil liquefaction is sufficiently low. On the other hand, if the computed probabilities of exceedance of designated limit states P_{LS} are larger than the tolerable probabilities $P_{LS,tol.}$, the building is assumed to be susceptible to seismically-induced soil liquefaction damage and detailed studies of soil liquefaction are necessary.

In this example, the decision-making is based on the probability of exceeding the complete damage (NC limit state). The threshold value of tolerable seismic risk is set to 1 % in 50 years ($2 \cdot 10^{-4}$ /per year). As it can be observed from the result of **Table 2.23**, the probability of exceeding complete damage (NC limit state) is



This project has received funding from the European Union's Horizon 2020 research and innovation programme under grant agreement No. 700748

6 % in 50 years and is larger than the tolerable value of seismic risk. Consequently, the building is assumed to be susceptible to seismically-induced soil liquefaction damage and detailed studies of soil liquefaction are recommended. On the contrary, the probability of exceeding complete damage (NC limit state) for the building in Düsseldorf is only 0.4 % in 50 years and is smaller than the tolerable risk. In this case, detailed studies of soil liquefaction are not necessary and the issue of soil liquefaction can be disregarded from further seismic assessment of the building.

Table 2.23: Comparison of the fragility parameters $\tilde{a}_{g,LS}$ and β_{LS} , annual probabilities of exceeding designated limit states P_{LS} , and probabilities of exceeding designated limit states in 50 years ($P_{LS,50}$) obtained for the building located in Benavente (Portugal) and Düsseldorf (Germany), respectively.

Limit state (LS):	$\tilde{a}_{g,LS}$ [g]	β_{LS}	Benavente (Portugal)		Düsseldorf (Germany)	
			P_{LS} [10^{-4}]	$P_{LS,50}$ [%]	P_{LS} [10^{-4}]	$P_{LS,50}$ [%]
Slight - DL1	0,19	0,27	50,3	22	4,9	2,4
Moderate - DL2	0,24	0,27	35,0	16	2,8	1,4
Extensive – SD	0,36	0,50	21,0	10	1,5	0,8
Complete – NC	0,55	0,74	12,4	6	0,8	0,4
Liquefaction – LIQ	0,25	0,23	32,1	15	2,5	1,2

2.9.5 CONCLUSIONS

A method for Rapid Risk Identification (RRI) of soil liquefaction and structural damage is introduced. The objective of the method is to assess the seismic risk of soil-structure configuration with consideration of soil liquefaction, and to make risk-informed decision, if detailed studies of soil liquefaction are necessary or the issue of soil liquefaction can be disregarded for the investigated case. The method was developed at University of Ljubljana in collaboration of University of Porto. Its advantage is that it allows rapid risk identification on the basis of simulations, which are possible only by utilizing a simplified model for SSI with consideration of liquefaction. The decision about negligible impact of soil liquefaction is based on the evaluated seismic risk. In the case when the risk is smaller than a predefined tolerable risk, it can be concluded that risk for liquefaction-induced damage is negligible and that detailed studies of soil liquefaction are not necessary. On the other hand, if the evaluated seismic risk is greater than a predefined tolerable risk, the building is assumed to be susceptible to seismically-induced soil liquefaction damage and that detailed studies of soil liquefaction are necessary. In the latter case, the Macro-mechanism approach for buildings on shallow foundation can be used to assess the seismic performance of the building (see section 2.2).

The major novelty of the proposed method is the simplified model for simulation of SSI with consideration of liquefaction, which can be used for rapid evaluation of fragility functions for a specific soil-structure configuration (e.g. buildings on shallow foundations), which may be located at a site susceptible to soil liquefaction. The key element of the simplified SSI model is the model for the inelastic soil spring, which is used to simulate the interaction between the foundation and the liquefiable soil, including softening effects



This project has received funding from the European Union's Horizon 2020 research and innovation programme under grant agreement No. 700748

and ground deformations in the case of liquefaction being triggered during an earthquake. The simplified SSI model consists of an inelastic soil spring with time-dependent degradation of strength in case liquefaction is detected for a given ground motion, based on an empirical triggering procedure. The degradation of stiffness is accounted for based on appropriate hysteretic rules. Appropriate confidence in the decision making is achieved by adequate calibration of the simplified SSI model so that it does not lead to underestimation of the mean (median) seismic response (see section 2.9.6 and 2.9.8).

The proposed method was demonstrated by means of an example of a soil-structure configuration, which was considered located at sites with different seismic hazard. Rapid risk identification was made possible by the employment of the simplified SSI model, which reduced the computational time required for fragility analysis to less than one hour on a regular desktop computer (i.e. few minutes on cluster of computers). Note that the computational time for the entire fragility analysis (in total 645 dynamic analyses) was significantly less than the computational time of one dynamic analysis in FLAC 2D. The results of the case study indicated that the seismic risk of the building located in moderate seismic region (Benavente, Portugal) was significantly larger than the seismic risk of building located in a low seismic region (Düsseldorf, Germany), which was mainly attributed to larger risk of soil liquefaction for the site in Benavente. Based on Rapid Risk Identification (RRI) method, additional studies of soil liquefaction were recommended for the building located in Benavente, whereas for the building located in Düsseldorf the issue of soil liquefaction could be disregarded from further seismic assessment. By the presented examples it was demonstrated how the RRI method can be used to screen out of from the further examination only the cases for which the risk of unacceptable behaviour due to adverse effects of soil liquefaction was observed to be sufficiently low.

It should be noted that the simplified SSI model, which is used within the RRI method, was defined on the basis of several assumptions and has, like any other simplified model, several limitations. The assumptions and limitations of the simplified SSI model are:

- The structure is modelled as an equivalent SDOF model. Thus, the simplified model can be applied only to first-mode predominant structure (low- to mid-rise buildings). It should be noted, however, that such a simplification is consistent with the new draft of Eurocode 8 – Annex E (CEN, 2018).
- The input motion used for dynamic analysis does not consider the effects of soil liquefaction, which are only accounted for by appropriate degradation of the strength and stiffness of the soil spring. In addition to this, the input motion for fragility analysis was based on the EC8 (CEN, 2004) elastic spectrum for soil type D. Such an assumption is considered acceptable for a simplified approach since, according to results of Section 2.9.7, yields conservative estimate of the mean (median) horizontal spectrum for the investigated soil profiles but liquefaction based site effects could be simulated through the application of the Stockwell transform method (see section 2.7).
- The investigated profiles are composed of three layers, i.e. a non-liquefiable clay layer, a liquefiable sand layer, and an underlying non-liquefiable stiff clay layer and engineering judgement must be applied to assess the critical liquefiable layer to account for site system response effects such as seismic isolation and pore water flow (Cubrinovski et al., 2018). For application of the method to produce a three-layered profile (see section 2.3).
- The foundation is considered to be rigid compared to the soil, which means that the effects of differential settlements on the building damage cannot be directly simulated. However, the effects



This project has received funding from the European Union's Horizon 2020 research and innovation programme under grant agreement No. 700748

of foundation rotation (tilt) and settlement on the limit state of the building are implicitly accounted based on empirical relations between the rigid body movements and the limit state of building (e.g. Bird et al. 2006).

- The simplified model is intended to simulate the “average” pore pressure development and as such cannot capture pinching and hardening effects in the hysteretic response of the foundation due to significant fluctuations of pore pressure during ground shaking. Additional studies are required to better understand the background of such phenomena and to improve the predictive capacity of the simplified model. The results of model calibration and validation indicate that the simplified model for the soil spring slightly underestimates the foundation moment capacity. This may produce slight underestimation of the seismic demand of the structure, and an overestimation of ground deformations (foundation rotations and settlements). Note that ground deformations are often the decisive parameter for the risk assessment of buildings located on liquefiable soils.
- In the development of the model, it is assumed that the results of FLAC 2D analyses yield the best estimate of the seismic response of soil-structure interacting system on liquefiable soil, although the comprehensive numerical analyses (e.g. FLAC 2D) are subject to several modelling limitations and can also provide biased results in some cases. For example, the model for the prediction of foundation settlement is based entirely on the results of FLAC 2D analyses. On the other hand, the remaining components of the model (e.g. estimation of pre- and post-liquefaction foundation moment capacity, foundation secant stiffness, triggering on liquefaction, degradation of strength in case of liquefaction) are based on semi-analytical models from existing literature and only few input parameters of the models were calibrate based on results of FLAC 2D analyses.
- The model for the soil spring was developed and calibrated based on limited number of results of FLAC 2D analyses (60 dynamic analyses responses, see Section 2.9.6.). Thus, the calibration of the model can be improved if additional results are used.

Additional studies are required to further calibrate the model and to test the employed assumption for different soil profiles (e.g. thicknesses of the crust and liquefiable layer, soil characteristic etc.), and different characteristics of the structure (e.g. ratios between the width and the height of the building, foundation bearing pressures etc.). Nevertheless, the results of model validation presented in Section 2.9.8 suggest that the model is able to sufficiently accurately simulate the global response of buildings on liquefiable soils, at least to make risk-informed decision, if detailed studies of soil liquefaction are necessary or the issue of soil liquefaction can be disregarded for the investigated case.



This project has received funding from the European Union's Horizon 2020 research and innovation programme under grant agreement No. 700748

REFERENCES

- Acacio A. A., Kobayashi Y., Towhata I., Bautista R.T. and Ishihara K. (2001). "Subsidence of building foundation resting upon liquefied subsoil case studies and assessment". *Soils and Foundations*, 41(6):111–28.
- Akkar, S., Sandikkaya, M.A., Şenyurt, M., Azari Sisi, A., Ay B.O., Traversa, P., Douglas, J., Cotton, F., Luzi, L., Hernandez, B., Godey, S. (2014). Reference database for seismic ground-motion in Europe (RESORCE). *Bulletin of Earthquake Engineering*, 12(1):311–39.
- Ancheta, T. D., Darragh, R., Stewart, J. P., Emel, S., Silva, W., Chiou, B., Wooddell, K. E., Graves, R. W., Kottke, A. R., Boore, D. M., Kishida, T., and Donahue, J. (2013). PEER NGA-West2 Database PEER Report No. 2013/03. *Pacific Earthquake Engineering Research Center, University of California, Berkeley, 03*, 134.
- Argeri, M. 2018. Moment-Rotation behaviour of shallow foundations on liquefiable soils. MSc Thesis. Politecnico di Torino
- Arias, A. (1970). A measure of earthquake intensity. *Seismic Design for Nuclear Power Plants*.
- Baradaran Shoraka, M. and Elwood, K. J. (2013). Mechanical Model for Non Ductile Reinforced Concrete Columns. *Journal of Earthquake Engineering*, 17:7, 937-957.
- Berril, J., & Davis, R. (1985). Energy dissipation and seismic liquefaction of sands: a revised model. *Soil Dynamics and Earthquake Engineering*, 25(2), 106–118.
- Bertalot, D. & Brennan, A. J. (2015). Influence of initial stress distribution on liquefaction-induced settlement of shallow foundations. *Géotechnique*, 65 (5), 418–428. DOI: 10.1680/geot.SIP.15.P.002.
- Bird, J.F., Bommer, J.J., Crowley, H. and Pinho, R. (2006). Modelling liquefaction-induced building damage in earthquake loss estimation. *Soil Dynamics and Earthquake Engineering* 26(1):15–30, DOI: 10.1016/j.soildyn.2005.10.002.
- Booker, J. R., Rahman, M. S., & Seed, H. B. (1976). "GADFLEA— A computer program for the analysis of pore pressure generation and dissipation during cyclic or earthquake loading." *Rep. No. EERC 76-24*.
- Bouckovalas, G. D., Tsiapas, Y. Z., Theocharis, A. I., and Chaloulos, Y. K. (2016). Ground response at liquefied sites: seismic isolation or amplification? *Soil Dyn and Earthq Eng*, DOI: 10.1016/j.soildyn.2016.09.028.
- Bouckovalas, G. D., Tsiapas, Y. Z., Zontanou, V. A., and Kalogeraki, C. G. (2017). Equivalent Linear Computation of Response Spectra for Liquefiable Sites: The Spectral Envelope Method. *Journal of Geotechnical and Geoenvironmental Engineering*, 143(4):04016115–12, DOI: 10.1061/(ASCE)GT.1943-5606.0001625.
- Boulanger, R. (2010). A sand plasticity model for earthquake engineering applications, Report No. UCD/CGM- 10-01. Technical report, Center for Geotechnical Modeling, Department of Civil and Environmental Engineering, University of California.
- Boulanger, R. W., & Idriss, I. M. (2006). Liquefaction Susceptibility Criteria for Silts and Clays. *Journal of Geotechnical and Geoenvironmental Engineering*, 132(11), 1413–1426. [https://doi.org/10.1061/\(ASCE\)1090-0241\(2006\)132:11\(1413\)](https://doi.org/10.1061/(ASCE)1090-0241(2006)132:11(1413))
- Boulanger, R.W. & Idriss, I.M. (2014). CPT and SPT based liquefaction triggering procedures. Report No. UCD/CGM-14/01. Center for Geotechnical Modeling, University of California, Davis. 134 pp. Retrieved from http://nees.ucdavis.edu/publications/Boulanger_Idriss_CPT_and_SPT_Liq_triggering_CGM-14-01_2014.pdf
- Boulanger, R. W., & Idriss, I. M. (2016). CPT-Based Liquefaction Triggering Procedure. *Journal of Geotechnical and Geoenvironmental Engineering*, 142(2), 04015065. [https://doi.org/10.1061/\(ASCE\)GT.1943-5606.0001388](https://doi.org/10.1061/(ASCE)GT.1943-5606.0001388)
- Boulanger, R. and Ziotopoulou, K. (2012). PM4Sand (Version 2): A sand plasticity model for earthquake engineering applications, Report No. UCD/CGM-12/01. Technical report, Center for Geotechnical Modeling, Department of Civil and Environmental Engineering College of Engineering, University of California at Davis.



This project has received funding from the European Union's Horizon 2020 research and innovation programme under grant agreement No. 700748

- Boulanger, R. and Ziotopoulou, K. (2015). PM4Sand (Version 3): A sand plasticity model for earthquake engineering applications, Report No. UCD/CGM-15/01. Technical report, Center for Geotechnical Modeling, Department of Civil and Environmental Engineering College of Engineering, University of California at Davis.
- Boulanger, R. and Ziotopoulou, K. (2017). PM4Sand (Version 3.1): A sand plasticity model for earthquake engineering applications, Report No. UCD/CGM-17/01. Technical report, Center for Geotechnical Modeling, Department of Civil and Environmental Engineering College of Engineering, University of California at Davis.
- Boulanger, R. W., Curras, C. J., Kutter, B. L., Wilson, D. W., and Abghari, A. (1999). Seismic soil-pile-structure interaction experiments and analyses. *Journal of Geotechnical and Geoenvironmental Engineering*, 125(9):750–759.
- Bray, J. and J. Macedo (2017). 6th Ishihara lecture: Simplified procedure for estimating liquefaction induced building settlement. *Soil Dynamics and Earthquake Engineering* 102, 215–231.
- Bray, J. D., Markham, C. S., & Cubrinovski, M. (2017). Liquefaction assessments at shallow foundation building sites in the Central Business District of Christchurch, New Zealand. *Soil Dynamics and Earthquake Engineering*, 92(10), 153–164. <https://doi.org/10.1016/j.soildyn.2016.09.049>
- Bray, J.D., Dashti, S. (2014). Liquefaction-induced building movements. *Bulletin of Earthquake Engineering*, 12:1129-1156.
- Bullock, Z., Dashti, S., Karimi, Z., Liel, A., Porter, K. & Franke, K. (2018). A physics-informed semi-empirical probabilistic model for the settlement of shallow-founded structures on liquefiable ground. *Géotechnique*, 1-14. doi:10.1680/jgeot.17.P.174.
- Bullock, Z., Dashti, S., Karimi, Z., Liel, A., Porter, K., Franke, K. (2019). Probabilistic Models for the Residual and Peak Transient Tilt of Mat-Founded Structures on Liquefiable Soils. *ASCE Journal of Geotechnical and GeoEnvironmental Engineering*, 145(2).
- Campbell, K. W. and Y. Bozorgnia (2012). A Comparison of Ground Motion Prediction Equations for Arias Intensity and Cumulative Absolute Velocity Developed Using a Consistent Database and Functional Form. *Earthquake Spectra* 28 (3), 931–941.
- Campbell, K.W. and Bozorgnia, Y. (2011). Prediction equations for the standardized version of cumulative absolute velocity as adapted for use in the shutdown of US nuclear power plants. *Nuclear Engineering and Design*, 241(7):2558-2569.
- Carraro, J. A. H., Bandini, P., & Salgado, R. (2003). Liquefaction Resistance of Clean and Nonplastic Silty Sands Based on Cone Penetration Resistance. *Journal of Geotechnical and Geoenvironmental Engineering*, 129(11), 965–976. [https://doi.org/10.1061/\(ASCE\)1090-0241\(2003\)129:11\(965\)](https://doi.org/10.1061/(ASCE)1090-0241(2003)129:11(965))
- Castiglia, M., Santucci de Magistris, F. (2018). Prediction of the number of equivalent cycles for earthquake motion. *Bulletin of Earthquake Engineering*, 16(9):3571-3603.
- CEN (2005). Eurocode 8: Design of structures for earthquake resistance-Part 3: Assessment and retrofitting of buildings. European Committee for Standardization, Brussels
- CEN (2004a). European standard EN 1998-1:2004. Eurocode 8: Design of structures for earthquake resistance. Part 1: General rules, seismic action and rules for buildings. European Committee for Standardization, Brussels
- CEN (2004b). European standard EN 1998-5:2004. Eurocode 8: Design of structures for earthquake resistance Part 5: Foundations, retaining structures and geotechnical aspects. European Committee for Standardization, Brussels
- CEN (2018). Final document EN 1998-1 NEN SC8 PT1 (Working draft). Eurocode 8: Design of structures for earthquake resistance. Part 1: General rules, seismic action and rules for buildings. European Committee for Standardization, Brussels
- Chiaradonna, A., Tropeano, G., d’Onofrio, A., & Silvestri, F. (2018). Development of a simplified model for pore water pressure build-up induced by cyclic loading. *Bulletin of Earthquake Engineering*, 16(9), 3627–3652. <https://doi.org/10.1007/s10518-018-0354-4>



This project has received funding from the European Union's Horizon 2020 research and innovation programme under grant agreement No. 700748

- Chiou, B., Darragh R., Gregor, N., Silva W. (2008). NGA project strong-motion database. *Earthquake Spectra*, 24(1):23-44.
- Cornell, C.A. (1996). Calculating building seismic performance reliability: a basis for multi-level design norms. Eleventh World Conference on Earthquake Engineering, Mexico City, Mexico, Paper No.2122.
- Cornell, C.A., Jalayar, F., Hamburger, R.O., Foutch, D.A. (2002). Probabilistic basis for 2000 SAC Federal Emergency Management Agency Steel Moment Frame Guidelines. *Journal of Structural Engineering ASCE*, 128 (4):526-533.
- Cubrinovski M. & Robinson K. (2016). Lateral spreading: Evidence and interpretation from the 2010–2011 Christchurch earthquakes, *Soil Dyn. Earthq. Eng.*, 91: 187–201. doi: 10.1016/j.soildyn.2016.09.045.
- Cubrinovski, M., Bray, J., Taylor, M., Giorgini, S., Bradley, B., Wotherspoon, L. & Zupan, J. (2011). Soil Liquefaction Effects in the Central Business District during the February 2011 Christchurch Earthquake. *Seismological Research Letters*, 82, 893-904. doi: 10.1785/gssrl.82.6.893.
- Cubrinovski, M., Rhodes, A. Ntritsos, N. & van Ballegooy, S. (2017). System response of liquefiable deposits. In 3rd International Conference on Performance-based Design in Earthquake Geotechnical Engineering, pp. 1–18.
- Cubrinovski, M., Rhodes, A., Ntritsos, N., & van Ballegooy, S. (2018). System response of liquefiable deposits. *Soil Dynamics and Earthquake Engineering*, 1–18. <http://doi.org/10.1016/j.soildyn.2018.05.013>
- Dafalias, Y. and Manzari, M. (2004). Simple plasticity sand model accounting for fabric change effects. *Journal of Engineering Mechanics* 130 (6), 622–634.
- Dashti S., Bray J.D. (2013). Numerical Simulation of Building Response on Liquefiable Sand. *Journal of Geotechnical and Geoenvironmental Engineering*, 139 (8): 1235-1249.
- Dashti, S. and Montgomery, J. (2013). Numerical Simulation of Building Response on Liquefiable Sand. *Journal of geotechnical and geoenvironmental engineering* (139(8)), 1235–1249.
- Dashti, S., Karimi, Z. (2017). Ground Motion Intensity Measures to Evaluate I: The Liquefaction Hazard in the Vicinity of Shallow-Founded Structures. *Earthquake Spectra*, 33(1):241-276.
- Dashti S., Bray J.D., Pestana, J.M., Riemer, M., Wilson, D. (2010). Mechanisms of Seismically Induced Settlement of Buildings with Shallow Foundations on Liquefiable Soil. *Journal of Geotechnical and Geoenvironmental Engineering*, 136(1):151-164. DOI: 10.1061/ ASCE GT.1943-5606.0000179.
- Dashti, S., Bray, J. D., Riemer, M., and Wilson, D. (2007). NEESR-II Project: “Towards Developing an Engineering Procedure for Evaluating Building Performance on Softened Ground” Centrifuge Test Plan for Test Series SHD02. pages 1–38.
- Dashti, S., Bray, J.D., Pestana, J.M., Riemer, M.R. and Wilson, D. (2010). Mechanisms of seismically-induced settlement of buildings with shallow foundations on liquefiable soil. *Journal of geotechnical and geoenvironmental engineering* (136(1)), 151–164.
- Davis, R., & Berril, J. (1982). Energy dissipation and seismic liquefaction in sands. *Earthquake Engineering & Structural Dynamics*, 10(1), 59–68. <https://doi.org/10.1002/eqe.4290100105>
- Davis, R., & Berril, J. (2001). Pore Pressure and Dissipated Energy in Earthquakes—Field Verification. *Journal of Geotechnical and Geoenvironmental Engineering*, 127(March), 269–274.
- Deng, L., Kutter, B.L., Kunnath, S.K. (2012). Centrifuge Modeling of Bridge Systems Designed for Rocking Foundations. *Journal of Geotechnical and Geoenvironmental Engineering*, 138(3):335-344.
- Diaz, D. (2016). *Vulnerabilidad de construcciones debido a licuación inducida por sismo*. National Autonomous University of Mexico. Mexico City.
- Dobry, R. and Liu, L. (1994). Centrifuge modeling of soil liquefaction. In *10th World Conference of Earthquake Engineering*.
- Dobry, R., Pierce, W., Dyvik, R., Thomas, G., & Ladd, R. (1985). Pore pressure model for cyclic straining of sand. *Civil*



This project has received funding from the European Union's Horizon 2020 research and innovation programme under grant agreement No. 700748

Engineering Department, Rensselaer Polytechnic Insti-Tute, Troy.

- Dolsek, M. and Fajfar, P. (2008). The effect of masonry infills on the seismic response of a four-storey reinforced concrete frame—a deterministic assessment. *Engineering Structures*, 30(7):1991–2001.
- EFEHR. (2018). European Facilities for Earthquake Hazard and Risk (EFEHR). (<http://www.efehr.org/en/home/>)
- Elwood, K. J. (2004). Modelling failures in existing reinforced concrete columns. *Canadian Journal of Civil Engineering*, 31(5), 846–859.
- Fajfar P. (2000). A nonlinear analysis method for performance-based seismic design. *Earthquake Spectra*, 16(3):573-592.
- Fajfar, P., Dolšek, M. (2012). A practice-oriented estimation of the failure probability of building structures. *Earthquake Engineering and Structural Dynamics*, 41 (3):531-547.
- Finn, W., & Bhatia, S. (1982). Prediction of seismic porewater pressures. In *Proceedings of the 10th international conference on soil mechanics and foundation engineering* (pp. 201–206).
- Flora, A., Bilotta, E., Nappa, V., Chiaradonna, A., Fasano, G., Lirer, S., Quintero, J., Millen, M.D.L., Viana da Fonseca, A., Lai, C.G., Andreotti, G., Özcebe, A.G., Bozzoni, F. and Zuccolo E. (2018). Database of calibrated numerical modelling results DELIVERABLE 4.4 of LIQUEFACT project “Assessment and mitigation of liquefaction potential across Europe: a holistic approach to protect structures / infrastructures for improved resilience to earthquake-induced liquefaction disasters” (www.liquefact.eu)
- Fotopoulou, S., Karafagka, S. and Pitilakis, K. (2018). Vulnerability assessment of low-code reinforced concrete frame buildings subjected to liquefaction-induced differential displacements. *Soil Dynamics and Earthquake Engineering*, 110, pp.173-184.
- Gazetas, G. (1991). Foundation vibrations. In *Foundation engineering handbook*, pages 553–593. Springer.
- Gazetas, G., Anastasopoulos, I., Adamidis, O., Kontopouri, Th.(2013). Nonlinear rocking stiffness of foundations. *Soil Dynamics and Earthquake Engineering*, 47: 83–91. <https://doi.org/10.1016/j.soildyn.2012.12.011>
- Gazetas, G. (2012). Should Elastic Response Spectra be the Basis of Seismic Design of Strongly Inelastic and Soft-Soil–Structure Systems? In *Proceedings of the 3rd International Symposium on Advances in Urban Safety*, pages 1–12, Nadjing.
- Gerace, A. (2018). Equivalent simplified soil profiles for liquefaction assessment. MSc Thesis, University of Porto (FEUP).
- Giardini, D., et al., (2013). Seismic Hazard Harmonization in Europe (SHARE): Online Data Resource, doi: 10.12686/SED-00000001-SHARE, 2013.
- Gomez, F., Millen, M. D. L., Romão, X., Costa, P. A., and Viana da Fonseca, A. (2018). Potential relevance of differential settlements in earthquake-induced liquefaction damage assessment. In *16th European Conference on Earthquake Engineering*, Thessaloniki.
- Green, R. a., Mitchell, J. K., & Polito, C. P. (2000). 【LR other models P6】 An Energy-Based Excess Pore Pressure Generation Model for Cohesionless Soils. *Proceeding of the John Booker Memorial Symposium*, 1–9.
- Habibullah, A. and Pyle, S. (1998). Practical three dimensional nonlinear static pushover analysis. *Structure magazine*, Winter.
- Hak, S., Morandi, P., Magenes, G., and Sullivan, T. J. (2012). Damage control for clay masonry infills in the design of RC frame structures. *Journal of Earthquake Engineering*, 16(sup1):1–35.
- Haselton, CB., Liel A B., Taylor Lange, S., and Deierlein, G.G. (2016). Calibration of Reinforced Concrete Beam-Columns for Simulating Seismic Response to Collapse. *ACI Structural Journal*, 113(6): 1141-1152.
- Hashash, Y., M. Musgrove, J. Harmon, D. Groholski, C. Phillips, and D. Park (2016). DEEPSOIL 6.1, UserManual.
- Hsu, H. L. (1995). Study on the relationship between shear work and porewater pressure for saturated sand in undrained test. In K. Ishihara (Ed.), *Proceedings of the 1st international conference on earthquake geotechnical engineering*. (pp. 301–307). A Balkema Publishers, Rotterdam, Netherlands.



This project has received funding from the European Union's Horizon 2020 research and innovation programme under grant agreement No. 700748

- Ibarra, L.F., Medina, R., and Krawinkler, H. (2005). Hysteretic Models that Incorporate Strength and Stiffness Deterioration. *Earthquake Engineering & Structural Dynamics*, 34. 1489 - 1511. 10.1002/eqe.495.
- Idriss, I. M. (1999). An update to the Seed-Idriss simplified procedure for evaluating liquefaction potential. In *TRB Workshop on New Approaches to Liquefaction Publication No. FHWARD- 99-165*. Federal Highway Administration.
- Idriss, I.M., Boulanger, R.W. (2006). Semi-empirical procedures for evaluating liquefaction potential during earthquakes. *Soil Dynamics and Earthquake Engineering*, 26:115-130.
- Idriss, I.M., Boulanger, R.W. (2007). SPT- and CPT-based relationships for the residual shear strength of liquefiable soils. In: Pitilakis K.D. (eds) *Earthquake Geotechnical Engineering. Geotechnical, Geological and Earthquake Engineering*, vol 6. Springer, Dordrecht. (https://doi.org/10.1007/978-1-4020-5893-6_1).
- Idriss I.M., Boulanger R.W. (2008). Soil liquefaction during earthquakes. Monograph MNO-12, Earthquake Engineering Research Institute, Oakland, CA, 261 pp.
- Ishihara, K. (1985). Stability of natural deposits during earthquakes, *Proceedings of the 11th International Conference on Soil Mechanics and Foundation Engineering*, Vol. 1, pp. 321-376.
- Ishihara, K., Yasuda, S. & Yoshida, Y. (1990). Liquefaction- induced flow failure of embankments and residual strength of silty sands, *Soils and Foundations*, 30 (3), 69-80.
- Itasca (2016). FLAC, Fast Lagrangian Analysis of Continua v8.0.438. Additional information available on: www.itascacg.com: Itasca Consulting Group, Inc.
- Itasca (2017). FLAC, Fast Lagrangian Analysis of Continua, Itasca Consulting Group, Inc. Additional information available on: www.itascacg.com/flac.
- Ivšić, T. (2006). A model for presentation of seismic pore water pressures. *Soil Dynamics and Earthquake Engineering*, 26(2–4), 191–199. <https://doi.org/10.1016/j.soildyn.2004.11.025>
- Jafarian, Y., Mehrzad, B., Lee, C. J., & Haddad, A. H. (2017). Centrifuge modeling of seismic foundation-soil-foundation interaction on liquefiable sand. *Soil Dynamics and Earthquake Engineering*, 97(3), 184–204. <https://doi.org/10.1016/j.soildyn.2017.03.019>
- Jayaram, N., Lin, T., Baker, J.W. (2011). A computationally efficient ground-motion selection algorithm for matching a target response spectrum mean and variance. *Earthquake Spectra*, 27 (3):797-815.
- Jeon, J.S., Lowes, L.N., DesRoches, R., and Brilakis, I. (2015). Fragility curves for non-ductile reinforced concrete frames that exhibit different component response mechanisms. *Engineering Structures*, 85: 127-143.
- Jones E, Oliphant E, Peterson P, et al. SciPy: Open Source Scientific Tools for Python, 2001- , <http://www.scipy.org/>[Online; accessed 2018-12-20].
- Karamitros, D. K., Bouckovalas, G. D., and Chaloulos, Y. K. (2013a). Seismic settlements of shallow foundations on liquefiable soil with a clay crust. *Soil Dynamics and Earthquake Engineering*, 46, 64-76.
- Karamitros, D.K., Bouckovalas, G.D. and Chaloulos, Y.K. (2013b). Numerical analysis of liquefaction-induced bearing capacity degradation of shallow foundations on a two-layered soil profile. *Soil Dynamics and Earthquake Engineering*, 44:90-101.
- Karamitros, D. K., Bouckovalas, G. D., and Chaloulos, Y. K. (2013c). Insight into the Seismic Liquefaction Performance of Shallow Foundations. 139(4):599–607, DOI: 10.1061/(ASCE)GT.1943-5606.0000797.
- Karatzia, X., Mylonakis, G., and Bouckovalas, G. (2017). Equivalent-linear dynamic stiffness of surface footings on liquefiable soil. In *COMPDYN 2017 - Proceedings of the 6th International Conference on Computational Methods in Structural Dynamics and Earthquake Engineering*, 1388–1402. National Technical University of Athens.
- Kazantzi, A. K. and Vamvatsikos, D. (2015) Intensity measure selection for vulnerability studies of building classes. *Earthquake Engineering & Structural Dynamics*, 44(15), 2677-2694.



This project has received funding from the European Union's Horizon 2020 research and innovation programme under grant agreement No. 700748

- Keino, C. and Kohiyama, M. (2012). Health disturbance of residents in a house with liquefaction damage in Mihama Ward, Chiba City. *Proceedings of the International Symposium on Engineering Lessons Learned from the 2011 Great East Japan Earthquake*.
- Kishida, T., & Tsai, C.-C. (2014). Seismic Demand of the Liquefaction Potential with Equivalent Number of Cycles for Probabilistic Seismic Hazard Analysis. *Journal of Geotechnical and Geoenvironmental Engineering*, 140(3), 04013023. [https://doi.org/10.1061/\(ASCE\)GT.1943-5606.0001033](https://doi.org/10.1061/(ASCE)GT.1943-5606.0001033)
- Kokusho, T. (2013). Liquefaction potential evaluations: energy-based method versus stress-based method. *Canadian Geotechnical Journal*, 50(10), 1088–1099. <https://doi.org/10.1139/cgj-2012-0456>
- Kosič, M., Dolšek, M., Fajfar, P. (2017). Pushover-based risk assessment method: a practical tool for risk assessment of building structures. Proceedings of the 16th World Conference on Earthquake Engineering, Santiago, Chile, 9-13 January 2017.
- Kottke, A. (2018). Pysra v0.2.1. Pypi - Python package repository. <https://doi.org/10.5281/zenodo.1400588>
- Kramer, S., & Mitchell, R. A. (2006). Ground motion intensity measures for liquefaction hazard evaluation. *Earthquake Spectra*, 22(2), 413–438. <https://doi.org/10.1193/1.2194970>
- Kramer, S., Hartvigsen, A. J., Sideras, S. S., & Ozener, P. T. (2011). Site response modelling in liquefiable soil deposits. In *4th IASPEI - Effects of surface geology on seismic motion* (pp. 1–12).
- Kramer, S.L., Sideras, S.S. & Greenfield, M.W. (2016). The timing of liquefaction and its utility in liquefaction hazard evaluation, *Soil Dynamics and Earthquake Engineering*, 91, 133-146, doi: 10.1016/j.soildyn.2016.07.025.
- Krawinkler, H. and Seneviratna, G. (1998). Pros and cons of a pushover analysis of seismic performance evaluation. *Engineering structures*, 20(4-6):452–464.
- Liang, L., Figueroa, J. L., & Saada, A. S. (1995). Liquefaction under random loading: unit energy approach. *Journal of Geotechnical Engineering*, 121(11), 776–781. [https://doi.org/10.1061/\(ASCE\)0733-9410\(1995\)121:11\(776\)](https://doi.org/10.1061/(ASCE)0733-9410(1995)121:11(776))
- Lignos D, Krawinkler H (2011). Deterioration Modeling of Steel Components in Support of Collapse Prediction of Steel Moment Frames under Earthquake Loading. *Journal of Structural Engineering*, 137(11): 1291-1302.
- Lignos, D. G. and Krawinkler, H. (2012). Development and utilization of structural component databases for performance-based earthquake engineering. *Journal of Structural Engineering*, 139(8):1382–1394.
- Liu, A. H., Stewart, J. P., Abrahamson, N. A., & Moriwaki, Y. (2001). Equivalent Number of Uniform Stress Cycles for Soil Liquefaction Analysis. *Journal of Geotechnical and Geoenvironmental Engineering*, 127(12), 1017–1026. [https://doi.org/10.1061/\(ASCE\)1090-0241\(2001\)127:12\(1017\)](https://doi.org/10.1061/(ASCE)1090-0241(2001)127:12(1017))
- Liu, L. & Dobry, R. (1997). Seismic Response of Shallow Foundation on Liquefiable Sand. *Journal of Geotechnical and Geoenvironmental Engineering* 123(6), 557–567.
- Lu, C. W. (2017). A Simplified Calculation Method for Liquefaction- Induced Settlement of Shallow Foundation. *Journal of Earthquake Engineering* 21 (8), 1385-1405.
- Luque, R. (2017). Numerical Analyses of Liquefaction-Induced Building Settlement. Ph. D. thesis.
- Maurer, B.W., Green, R.A, Taylor, O. (2015). Moving towards an improved index for assessing liquefaction hazard: Lessons from historical data. *Soils and Foundations*, 55 (4), 778-787. doi: 10.1016/j.sandf.2015.06.010.
- Mazzoni, S., McKenna, F., Scott, M. H., and Fenves, G. L. (2006). OpenSees command language manual. *Pacific Earthquake Engineering Research (PEER) Center*, 264.
- MBIE (2016). Module 3: Identification, assessment and mitigation of liquefaction hazards. pages 1–44.
- Mejia, L. H. and Dawson, E.M. (2006). Earthquake deconvolution for FLAC. 4th International FLAC Symposium on Numerical Modeling in Geomechanics (04(10)), 1–9.



This project has received funding from the European Union's Horizon 2020 research and innovation programme under grant agreement No. 700748

Methodology for the liquefaction fragility analysis of critical structures and infrastructures: description and case studies

v. 1.0

- Meyerhof, G. G. & Hanna, A. M. (1978). Ultimate bearing capacity of foundations on layered soils under inclined load. *Canadian Geotechnical Journal* 15(4), 565–572.
- Meyerhof, G. G. (1963). Some recent research on the bearing capacity of foundations. *Canadian Geotechnical Journal*, 1(1):16–26.
- Millen, M. D. L. (2016). *Integrated Performance-based Design of Building-foundation Systems*. PhD thesis. University of Canterbury.
- Millen, M. D. L., Pampanin, S., Cubrinovski, M., and Carr, A. J. (2016). A performance assessment procedure for existing buildings considering foundation deformations. In *2016 NZSEE Conference*, pages 1–8.
- Millen, M., Rios, S., Quintero, J., & Viana da Fonseca, A. (2019). Prediction of time of liquefaction using kinetic and strain energy. *Soil Dynamics and Earthquake Engineering*, submitted.
- Minarelli L, Amoroso S, Tarabusi G, Stefani M, Pulelli G (2016). Down-hole geophysical characterization of middle-upper Quaternary sequences in the Apennine Foredeep, Mirabello, Italy. *Annals of Geophysics*, 59(5), doi: 10.4401/ag-7114.
- Miwa, S. and Ikeda, T. (2006). Shear modulus and strain of liquefied ground and their application to evaluation of the response of foundation structures. *Structural engineering / earthquake engineering*, 23(1):167s–179s, DOI: 10.2208/jscesee.23.167s.
- Negulescu, C. and Foerster, E. (2010). Parametric studies and quantitative assessment of the vulnerability of a RC frame building exposed to differential settlements. *Natural Hazards and Earth System Sciences*, 10(9):1781-1792.
- Nemat-Nasser, S., & Shokoh, A. (1979). A unified approach to densification and liquefaction of cohesionless sand in cyclic shearing. *Canadian Geotechnical Journal*, 16(4), 659–678. <https://doi.org/10.1139/t79-076>
- Noh, N. M., Liberatore, L., Mollaioli, F., and Tesfamariam, S. (2017). Modelling of masonry infilled RC frames subjected to cyclic loads: State of the art review and modelling with OpenSees. *Engineering Structures*, 150:599 – 621.
- NTC (2018). *Norme tecniche per le costruzioni (NTC 2018)*. Standard, Ministero Infrastrutture e Trasporti, Rome, IT.
- Okamura, M., Ishihara, M., & Oshita, T. (2003). LIQUEFACTION RESISTANCE OF SAND DEPOSIT IMPROVED WITH SAND COMPACTION PILES. *Soil Mech Found Div ASCE*, 43(5), 175–187. https://doi.org/10.3208/sandf.43.5_175
- Open system for earthquake engineering simulation (OpenSees) (2017). Pacific Earthquake Engineering Research Center, University of California, Berkeley, CA. Available from: <http://opensees.berkeley.edu>.
- Park, T., Park, D., & Ahn, J. K. (2015). Pore pressure model based on accumulated stress. *Bulletin of Earthquake Engineering*, 13(7), 1913–1926. <https://doi.org/10.1007/s10518-014-9702-1>
- Polito, C. P., Green, R. A., & Lee, J. (2008). Pore Pressure Generation Models for Sands and Silty Soils Subjected to Cyclic Loading. *Journal of Geotechnical and Geoenvironmental Engineering*, 134(10), 1490–1500. [https://doi.org/10.1061/\(ASCE\)1090-0241\(2008\)134:10\(1490\)](https://doi.org/10.1061/(ASCE)1090-0241(2008)134:10(1490))
- Priestley, M., Calvi, G., and Kowalsky, M. (2007). Direct displacement-based seismic design. In *2005 NZSEE Conference*, pages 33–43.
- Robertson, P. K. (2009). “Interpretation of Cone Penetration Tests – a unified approach”. *Can. Geotech. J.* 27(1): 151-158.
- Šebenik, Ž., Dolšek, M. (2016). Strong ground motion database. Ljubljana, University of Ljubljana, Faculty of Civil and Geodetic Engineering, IKPIR.
- Seed, H. ., Idriss, I., Makdidi, F., & Nanerjee, N. (1975). Representation of irregular stress time histories by equivalent uniform stress series in liquefaction analyses Report No. EERC 75–29. *Earthquake Engineering Research Center, University of California Berkeley*.



This project has received funding from the European Union's Horizon 2020 research and innovation programme under grant agreement No. 700748

- Shahir, H. & Pak, A. (2010). Estimating liquefaction-induced settlement of shallow foundations by numerical approach. *Computers and Geotechnics* 37(3), 267–279.
- Silver, N. L., Wilson, J. H., Valera, J. E., Townsend, F. C., Tiedemann, D. A., Lee, K. L., ... Chan, C. K. (1976). Cyclic Triaxial Strength of Standard Test Sand. *Journal of the Geotechnical Engineering Division*, 102(5), 511–523.
- Sullivan, T. J., Priestley, M. J. N., and Calvi, M. G. (2012). *DBD12: A model code for the displacement-based seismic design of structures*. IUSS Press, Italy.
- Sullivan, T.J., Welch, D.P., Calvi, G.M. (2014). Simplified seismic performance assessment and implications for seismic design. *Earthquake Engineering and Engineering Vibration*, 13(S1), 95-122.
- Tasnimi, A.A. and Mohebkhah, A., 2011. Investigation on the behavior of brick-infilled steel frames with openings, experimental and analytical approaches. *Engineering Structures*, 33(3): 968-980.
- Tokimatsu, K., and Seed, H. B. (1987). "Evaluation of Settlement in Sands Due to Earthquake Shaking." *Journal of Geotechnical Engineering*, 113 (8), 861-878.
- Tonkin & Taylor Ltd. (2013). Liquefaction vulnerability study - Report to Earthquake Commission. NZ Earthquake Commission, Report 52020.0200, 1–59.
- Trifunac, M. D. and Brady, A. G. (1975). A study on the duration of strong earthquake ground motion. *Bulletin of the Seismological Society of America*, 65(3):581–626.
- Vardanega, Paul and Bolton, Malcolm (2013). "Stiffness of Clays and Silts: Normalizing Shear Modulus and Shear Strain". *Journal of Geotechnical and Geoenvironmental Engineering*, 139: 1575-1589.
- Viana da Fonseca et al (2018). Methodology for the liquefaction fragility analysis of critical structures and infrastructures: description and case studies, LIQUEFACT Proj. Deliverable D3.1, Horizon 2020 European Union funding for Research & Innovation Project ID: 700748 (www.liquefact.eu).
- Yoshimi, Y. and Tokimatsu, K. (1977). "Settlement of Buildings of Saturated Sand during Earthquakes". *Soil and Foundations*, 17(1): 23-38.
- Youd, T. L., I. M. Idriss, R. D. Andrus, I. Arango, G. Castro, J. T. Christian, R. Dobry, L. Finn, L. F. J. Harder, M. E. Hynes, K. Ishihara, J. K. Mitchell, Y. Moriwaki, M. S. Power, P. K. Robertson, R. B. Seed, & K. H. Stokoe (2001). Liquefaction Resistance of Soils: Summary Report from the 1996 NCEER and 1998 NCEER/NSF Workshops on Evaluation of Liquefaction Resistance of Soils. *Journal of Geotechnical and Geoenvironmental Engineering*, 1–17.
- Zarnic, R. and Gostic, S. (1997). Masonry infilled frames as an effective structural sub-assembly. In *Proceedings of the international workshop on seismic design methodologies for the next generation of codes*.
- Zarnic, R. and Gostic, S. (1998). Non-linear modelling of masonry infilled frames. In *11th ECEE*, Paris, France. A.A. Balkema, Rotterdam.
- Zhang, G., P. Robertson, and R. Brachman (2004). Estimating Liquefaction induced Lateral Deformations from SPT and CPT. *ASCE, Journal of Geotechnical and Geoenvironmental Engineering* 130 (8), 861–871.
- Ziotopoulou, K. and Montgomery, J. (2017). Numerical modeling of earthquake-induced liquefaction effects on shallow foundations. In *Proceedings of the 16th World Conference on Earthquake Engineering*.



This project has received funding from the European Union's Horizon 2020 research and innovation programme under grant agreement No. 700748

3. VULNERABILITY ASSESSMENT OF EMBANKMENTS USING FINITE ELEMENT MODELING

3.1 MODELING OF EMBANKMENTS ON LIQUEFIABLE DEPOSITS

This chapter is divided into the following parts – theoretical background, presentation of numerical work and subsequent evaluation of sample fragility curves for traffic embankments, feasibility study on the possible use of artificial neural networks for interpolation / extrapolation of numerical results to different geometrical situations. Finally, the produced fragility curves were validated against two well documented case histories from Turkey.

The study begins with a brief literature review. Next, a description of the methodology for deriving fragility curves is presented. Among various options for the assessment of fragility curves (empirical, analytical, numerical, expert judgement and hybrid approach), numerical approach was selected. There were not enough data from the literature in order to rely on empirical data or expert judgement. Rare well documented case histories available in the literature were used for the validation purpose.

3.1.1 INTRODUCTION

The study begins with a brief literature review. Next, a description of the methodology for deriving fragility curves is presented. Among various options for the assessment of fragility curves (empirical, analytical, numerical, expert judgement and hybrid approach), numerical approach was selected. There were not enough data from the literature in order to rely on empirical data or expert judgement. Rare well documented case histories available in the literature were used for the validation purpose.

In order to produce the fragility curves, the criteria for damage states have to be defined. Available similar works used the permanent embankment settlement at its centre as damage parameter. Criteria for minor, moderate and severe damage for highways and railways were taken from the SYNER-G project (2011).

Numerical analyses of the behaviour of traffic embankments built on liquefiable ground during dynamic loading were performed by numerical software package FLAC and PM4Sand material model (Boulanger and Ziotopoulou, 2015). The main goal was to obtain a suitable number of results for a number of different seismic excitation and different intensity measures so that the fragility curves could be developed. It is obvious that the fragility curves can only be obtained for a finite number of possible variations of ground and embankment geometries and material properties. Variations of relative density of liquefiable layer, its thickness, presence of clayey crust layer and embankment height and width enabled the analysis of the influence of these factors on the probability of exceedance of selected damage state.

The numerical effort to obtain the results presented in this study was huge. For each combination of geometrical and material properties, 240 numerical analyses were made. Therefore, the artificial neural networks were tested for their ability to interpolate/extrapolate the results to new situations based on the cases, which were covered by our numerical analyses.



This project has received funding from the European Union's Horizon 2020 research and innovation programme under grant agreement No. 700748

3.1.2 LITERATURE REVIEW

In seismically active areas, where a soil profile is predominantly composed of a sandy to silty sandy layers and saturated with groundwater, a liquefaction can occur during seismic event. The occurrence of this phenomenon can cause serious damage to the traffic infrastructure, such as road and railway embankments, due to the increase of pore water pressure and consequent decrease of a shear strength in a soil medium. Traffic embankments and overall transport infrastructure are of vital importance, since they represent links between affected areas and hospitals or other assistant institutions. Besides human and physical losses during earthquake shaking, any interruption of traffic serviceability can cause further significant socio-economic losses.

Some earthquake events around the world in the last decade (Emilia Romagna, Italy – 2012; Christchurch, New Zealand – 2010 & 2011; Wenchuan, China – 2008; Kumamoto, Japan – 2016, Palu, Indonesia – 2018; etc.) caused minor to serious earthquake-liquefaction-induced deformations to transportation infrastructure. Additional cases of recorded damages on the traffic infrastructure due to soil liquefaction at historical earthquake events are listed in Bird et al (2004).

Under this study, the attention will be given to the road and railway embankments, which are most common earthfill structures among transportation infrastructure to maintain desired level of the pavement or railway track elevation. Due to the complexity of soil liquefaction and its interaction with traffic embankment, various failure mechanisms at the surface of embankment can be found – crest settlements, slope instability, lateral spreading of the toe of the embankment, piping failure through cracks, water ponding on the road surface etc. (NIBS 2004, Sasaki et al 2007, Maruyama et al 2010, Oka et al 2012, Tsukamoto et al (2012), Rapti et al (2018) and Argyroudis et al 2018). According to above mentioned failure mechanisms, different engineering damage state parameter can be used for a vulnerability assessment of the traffic embankment under consideration through fragility functions by which the probability of exceedance of a certain limit state can be estimated. Lagaros et al (2009) constructed fragility curve based on a factor of safety, while Maruyama et al (2010) used actual number of damage incidents per kilometre of expressway embankment. Nevertheless, crest settlements are still widely held as damage level, due to simple comparison with in-situ measurements from affected sites (Argyroudis and Kaynia, 2015, Khalil et al 2017 and Argyroudis et al 2018). In general, four approaches for derivation of fragility curves are presented in the literature: (1) empirical, (2) analytical, (3) expert judgement and (4) hybrid method. Each method has its advantages and disadvantages, but nowadays the fragility curves are mostly derived using analytical (numerical) results due to the availability of powerful software packages, which include advanced material models capable of capturing various soil response phenomena. Among above mentioned references, empirical approach was used by Maruyama et al only, while no reference was found on fragility curves for traffic embankments based on expert judgement.

Since complex geotechnical problems are very computationally demanding and time consuming when using finite difference (or finite element) methods, different soft computing techniques (e.g. artificial neural networks – ANN) can be applied in the analysis. Georgopoulos et al (2006) and Lagaros et al (2009) used in their computations ANN technique to simulate seismic response of an embankment. The accuracy and reliability of these techniques decrease with problem nonlinearity.



This project has received funding from the European Union's Horizon 2020 research and innovation programme under grant agreement No. 700748

Even though effects of mitigation measures on the traffic embankment were not considered in this study, several alternatives can be found in the literature. Lopez-Caballero et al (2016) described the impact of the embankment preloading on seismic resistance increase. Bhatnagar et al (2016) studied the impact of densification by sand compaction and sheet pile enclosure on dynamic behaviour of the embankment. Furthermore, the influence of stone column reinforced composite foundation under highway was numerically simulated by Jiang et al (2012). In general, different remediation methods for reducing soil liquefaction potential beneath all kind of structures can be applied to the ground: densification, in-situ stress increase, desaturation, cementation, reinforcement, drainage, etc.

In addition, Pando et al (2001) studied the liquefaction potential of railway embankments due to train induced vibrations.

3.1.3 METHODOLOGY FOR THE VULNERABILITY ASSESSMENT OF EMBANKMENTS

The vulnerability assessment of the traffic embankment is the process of identifying threats and risks to seismic hazards. It is related to sensitivity of the embankments and occurrence of such conditions, which would lead to the exceedance of a certain limit state. One of widely used tools in engineering practice for those analyses is fragility curve.

The probability of exceedance of selected damage state (ds) for a given earthquake intensity measure (IM) is described through fragility functions. Two main parameters: median threshold value of IM , θ and total lognormal standard deviation, β are needed to define the fragility curve. Usually, it is described by a lognormal cumulative distribution function, given by equation (3.1).

$$P_f(ds \geq ds_i|S) = \Phi \left[\frac{1}{\beta_{tot}} \ln \left(\frac{IM}{IM_{mi}} \right) \right] \quad (3.1)$$

where P_f is the probability that certain damage state for a given earthquake intensity measure is exceeded, Φ stands for standard cumulative probability function, IM_{mi} is the median threshold of intensity measure to cause i th damage state, and β_{tot} is the total lognormal standard deviation (Argyroudis et al 2015).

In the following subchapters different approaches for the derivation of fragility curves, selection of damage states for traffic embankments, intensity measure options and key uncertainties are presented. The contents of those subchapters are mostly summarized from the SYNER-G project.

3.1.3.1 Methods for deriving fragility curve

Empirical method

Most straightforward approach for derivation of fragility curve can be achieved empirically, due to direct consideration of soil-structure interaction, site conditions before and after shaking and seismic loading source characteristics at site. However, empirical fragility curves are normally based on very few observed damage surveys, due to a lack of earthquake events at the same site with the same embankment under observation, especially at its initial state. The decrease of uncertainties related to diverse seismic motions (different intensity levels, durations, etc.) and the increase of usefulness of empirical curves can be achieved



This project has received funding from the European Union's Horizon 2020 research and innovation programme under grant agreement No. 700748

combining a wide range of ground motions together with similar ground types and structure properties from other sites.

Typically, the empirical fragility curves are useful only for structures built at specific areas and are not suitable for widespread conditions.

An example of empirically obtained fragility curves was performed by Maruyama et al (2010), where they derive curves for expressway embankments in Japan based on number of damage incidents per km and peak ground velocity, PGV, as intensity measure.

Analytical method

In recent years (decades), most common approach to develop the fragility curve is based on analytical procedure through the results from numerical analyses. Constantly improving computer capabilities and the availability of software packages with advanced material models, capable of simulating complex soil-structure interaction during seismic loading, enable a comprehensive analysis of a same structure (e.g. traffic embankment) subjected to diverse earthquake loads. By applying various acceleration time histories to the numerical model in conjunction with gradually increased intensity levels, the results of damage distribution can be further analysed with statistical tools. In addition, analytical fragility curve reflects a more reliable representation of the probability of exceeding a certain limit state, due to the decrease of some uncertainties, especially those related to input ground motions.

However, the analytical fragility curve is not directly related to exact real case, but to its approximation through numerical model, which is constructed with various assumptions. Besides numerical restrictions (related to boundary conditions, material models, dynamic loading, etc.), a wide dispersion of material characteristics and soil deposit stratigraphy at real site influence the difference between reality and numerical simulations.

General procedure to generate analytical fragility curve for specific/single road elements is summarized by SYNER-G project and presented in **Figure 3.1**.



This project has received funding from the European Union's Horizon 2020 research and innovation programme under grant agreement No. 700748

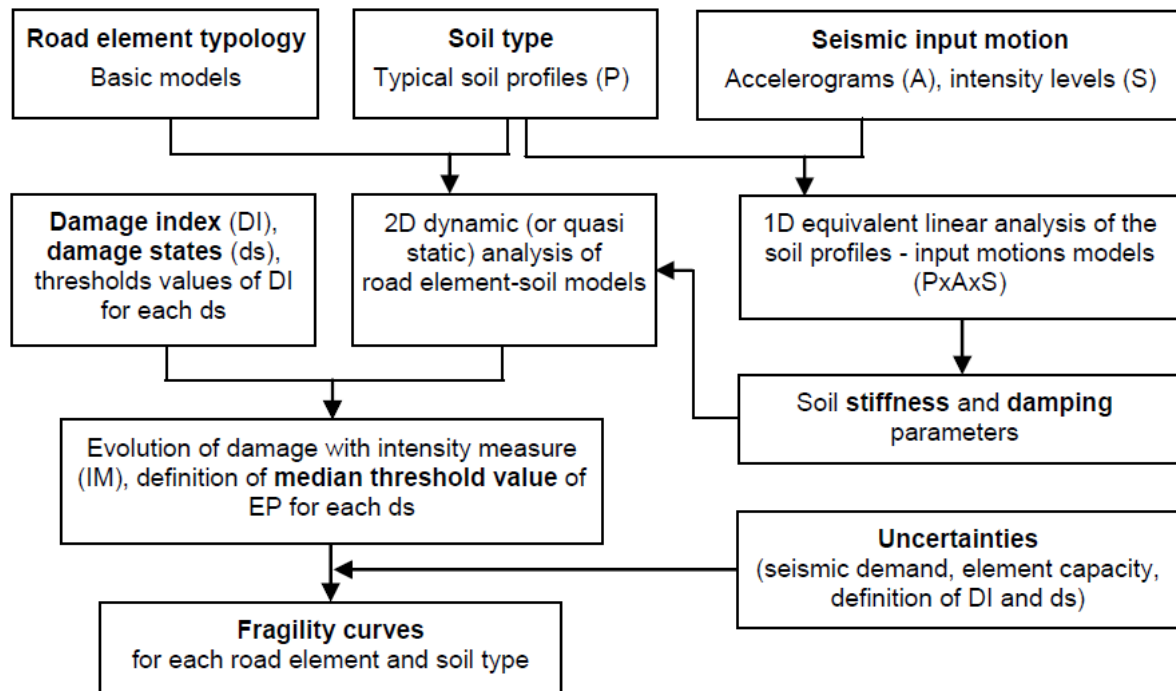


Figure 3.1: General procedure for deriving numerical fragility curves for road elements (SYNER-G, 2011).

Some examples of analytical fragility curves for embankments were proposed by the following authors: Lagaros et al (2009), Argyroudis and Kaynia (2015), Khalil et al (2017), Yin et al (2017) and Argyroudis et al (2018).

Expert judgement

One of the approaches to derive fragility curves is based on expertise – experts` judgement. This approach/procedure is quick, but it allows a huge deviation with high level of uncertainties between fragility curves derived by various experienced experts. It is very unscientific method, where the input data and final results are not statistically considered. However, the curves serve satisfactorily for a quick assessment of the embankments` condition.

Hybrid approach

The hybrid approach involves a combination of the aforementioned methods for derivation of fragility curves. Hybrid method is useful when with a single method it is not possible to capture the entire fragility curve range, due to a lack of damage data for particular intensity levels.

3.1.3.2 Damage states

Every single change in the stress state in the soil profile or embankment leads to deformations. These are even greater when the object under observation is subjected to dynamic loads (e.g. earthquake), and



This project has received funding from the European Union's Horizon 2020 research and innovation programme under grant agreement No. 700748

underlain by saturated loose sandy layers susceptible to soil liquefaction. Typical consequences on the embankment due to this phenomenon are crest settlements, lateral spreading and slope instability.

In the following section a brief review of damage states for embankments is proposed as gathered from the literature:

Maruyama et al (2010) used in their study a serviceability-damage classification table presented in **Table 3.1**. Observed damages on expressway were classified into five damage levels from very minor to severe. Although the damage states are defined primarily for other elements of transport infrastructure (bridges, tunnels, pavement, ...), there are links between mentioned damage states and embankments – cracks/gaps in roadway and slope instability.

Other authors (Argyroudis et al, 2003; Argyroudis et al, 2018 and Werner et al, 2006 – summarized from SYNER-G, 2011) defined limit states based on permanent ground displacement (PGD) or ground settlements. Thresholds values of PGD are presented in **Table 3.2**, **Table 3.3** and **Table 3.4**.

Table 3.1: Damage state criteria by Maruyama et al (2010).

Damage	Severe (As)	Major (A)	Moderate (B)	Minor (C)	Very minor (D)
Bridge superstructure	Collapse	Large lateral displacement, but no collapse Rupture of steel girder	Deformation or buckling of steel girder	Deformation of bridge joint	
Bridge substructure	Failure of bridge pier	Rupture of reinforcement	Large detachment or crack in cover concrete Exposure of reinforcement	Small detachment or crack in cover concrete Small detachment or crack in cover concrete	
Bearing structure		Rupture of bearing Rupture of anchor bolt	Large detachment or crack in cover concrete Shear deformation of bearing Rupture of concrete	Partial damage to bearing Crack in concrete or anchor bolt Breakaway of anchor bolt	Loose anchor bolt
Tunnel		Rupture of lining	Large detachment or crack in lining	Small detachment or crack in lining	
Side slope		Total collapse	Partial collapse	Deformation	
Gap in roadway			Traffic lane: more than 3 cm Shoulder: more than 20 cm	Traffic lane: 1–3 cm Shoulder: 1–20 cm	Less than 1 cm
Crack in roadway			More than 5 cm	3–5 cm	Less than 3 cm

Table 3.2: Damage state criteria by RISK-UE approach (SYNER-G, 2011).



This project has received funding from the European Union's Horizon 2020 research and innovation programme under grant agreement No. 700748

Serviceability	Damage States	Direct damages	Indirect damages
Fully closed due to temporary repairs for few days to few weeks. Partially closed to traffic due to permanent repairs for few weeks to few months.	Extensive	Major settlement or offset of the ground (>60 cm).	Considerable debris of collapsed structures.
Fully closed due to temporary repairs for few days. Partially closed to traffic due to permanent repairs for few weeks.	Moderate	Moderate settlement or offset of the ground (30 to 60cm).	Moderate amount of debris of collapsed structures.
Open to traffic. Reduced speed during repairs.	Minor	Slight settlement (<30cm) or offset of the ground.	Minor amount of debris of collapsed structures.
Fully open.	None	/	No damage/ Clean road.

* The duration of closure depends on the length of damaged roadway

For the purpose of the LIQUEFACT project and task related to preparation of sample fragility curves for traffic embankments built on liquefiable ground within this report, mean values of damage states defined by researchers of SYNER-G project and collected for both road and railways, were chosen (**Table 3.3**).

Table 3.3: Damage state criteria by Argyroudis et al (2018).

Typology	Damage State	Permanent vertical ground displacement [m]			Serviceability
		Min	Max	Mean	
Highways	Minor	0.02	0.08	0.05	Open, reduced speeds or partially closed during repair
	Moderate	0.08	0.22	0.15	Closed or partially closed during repair works
	Extensive/Complete	0.22	0.58	0.40	Closed during repair works
Railways	Minor	0.01	0.05	0.03	Open, reduced speeds
	Moderate	0.05	0.10	0.08	Closed during repair works
	Extensive/Complete	0.10	0.30	0.20	Closed during reconstruction works

Table 3.4: Damage state criteria by Werner (2006) (summarized by SYNER-G, 2011).



This project has received funding from the European Union's Horizon 2020 research and innovation programme under grant agreement No. 700748

Damage State				Traffic State		Repair Costs (per lane-mile)
REDARS™ Designation	Perm. Ground Displacement, inches.	Description (see Figures 1 through 4)	Repair Procedure	Days after EQ (incl. mobilization time)	Lanes Available (% of Pre-EQ lanes)	
1 (None)	< 1 in.	No repairs needed	None	0	100%	\$0
2 (Slight)	≤ 1 in and <3 in.	Slight cracking/ movement. No interruption of traffic.	Horizontal Displacement: crack/seal. Vertical Displace: mill and patch.	0	100%	\$50,000 (=0.083*RC)
3 (Moderate)	≤ 3 in and <6 in.	Localized moderate cracking/ movement. Reduced structural integrity of pavement surface.	No repair needed for subbase. If asphalt pavement, or if damage to concrete pavement extends over long length, use AC overlay. If damage to concrete pavement is localized, replace concrete slab.	0-3 days ≥ 4 days	0% 100%	\$100,000 (=0.167*RC)
4 (Extensive)	≤ 6 in and <12 in.	Failure of pavement structure, requiring replacement. Movement but not failure of subsurface soils.	Rebuild pavement structure and subbase. Provide soil improvement for subsurface materials.	0-7 days ≥ 8 days	0% 100%	\$300,000 (=0.500*RC)
5 (Irreparable)	≥ 12 in.	Failure of pavement structure and subsurface soils.	Remove and replace existing pavement structure and subsurface materials.	0 – 49 days ≥ 50 days	0% 100%	\$600,000 (=RC)

Lagaros et al (2009) in their work dealt with large geostuctures (also with highway embankments), where they used limit states defined in terms of slope stability safety factor (**Table 3.5**).

Table 3.5: Damage state criteria by Lagaros et al (2009).

Vulnerability state	Safety margins	Range of damage index
Optimal	Very high	FoS > 2.0
Sufficient	High	1.4 < FoS < 2.0
Moderate	Moderate	1.25 < FoS < 1.4
Minor	Low	1.0 < FoS < 1.25
Unacceptable	None	FoS < 1.0

3.1.3.3 Intensity measures

A selection of suitable intensity measure (IM) that will cover the complete impact of the earthquake load and site conditions on traffic embankments is a very challenging task. Several measures that characterise ground motion or soil profile composition with its susceptibility to liquefaction have been developed by various researchers. Consequently, a wide range of intensity measures can be found in the literature and used for the derivation of fragility curves. Some of them are summarized in the following list:

- peak ground acceleration (PGA),
- peak ground velocity (PGV),
- peak ground displacement (PGD),
- Arias intensity (I_a),
- spectral acceleration (S_a), velocity (S_v) or displacement (S_d)
- transient ground strain,
- equivalent number of uniform cycles (N_{eq}),



This project has received funding from the European Union's Horizon 2020 research and innovation programme under grant agreement No. 700748

- liquefaction potential index (LPI),
- liquefaction severity number (LSN),
- ...

Due to its practicality and direct correlation with many engineering quantities, PGA is still most commonly used IM, besides others such as PGV or PGD, and I_a .

3.1.3.4 *Uncertainties*

In general, geoscience engineers deal with high dispersion of input data, due to the non-homogeneity of the ground composition and complex non-linear soil behaviour. This relates to a several uncertainties that affect the trustworthiness of developed fragility curves. Earthquake input motion, response of the element under observation and definition of the damage state are three main sources of uncertainties (NIBS, 2004 and SYNER-G, 2013).

The effect of uncertainties can be reduced by increasing the number of performed analyses.



This project has received funding from the European Union's Horizon 2020 research and innovation programme under grant agreement No. 700748

3.1.4 NUMERICAL PROCEDURE TO DEVELOP FRAGILITY CURVES FOR EMBANKMENTS

In the following chapters, the methodology and an example of deriving fragility curves for traffic embankments by numerical approach using 2D finite difference program FLAC is shown. The FLAC software was selected since it was the only available software at the beginning of the project that enabled to take into account the dissipation of pore pressures during earthquake excitation and at the same time contained a suitable material model. The behaviour of liquefiable soil layer was modelled by PM4Sand material model (Boulanger and Ziotopoulou, 2015). In the meantime, other codes became available with same features and can be used for the same task.

Based on the literature review for traffic embankments built on liquefiable ground and subjected to seismic load, peak ground acceleration was selected for the intensity measure. One of the reasons for choosing PGA as intensity measure is its wide application in practice. Alternatively, Arias intensity was also used. For the damage state, the vertical displacement (at the middle point of the embankment crest) was chosen, since it is simply comparable to the field measurements from the affected sites. Threshold values of vertical displacement were selected from SYNER-G project (**Table 3.3**).

After validating the PM4Sand material model and FLAC software on the example of embankment built on liquefiable ground (3.1.4.1), more detailed description of numerical model (geometry, soil properties, input motions, etc.) is introduced. After that, few examples of derived fragility curves are presented. An attempt has also been made to employ artificial neural networks in the procedures for development of fragility curves for traffic embankments in order to reduce numerical efforts needed for demanding nonlinear numerical calculations.

3.1.4.1 Validation procedure

Introduction

In order to assess the performance of the numerical model to simulate behaviour of traffic embankments built on liquefiable layers and further development of fragility curves, a validation procedure was carried out. For this purpose, Naruse river levees analysis was selected and analysed with 2D FLAC software.

Although the selected case history for validation procedure does not include traffic embankment, the case was chosen due to the availability of the in-situ measurements of excess pore water pressure within the levee during earthquake event and numerical results performed with different software package than FLAC (Cubrinovski, 2011 and Takahashi et al, 2009).

Brief description of the case history

A section of Naruse river levees, considered under this study, is located near the mouth of Naruse river, NW of Ishinomaki Bay on the east side of Japan coast. On July 26th 2003 a sequence of several earthquakes occurred in the area and caused damage to levees and other infrastructure. The magnitude of the main shock was 6.2 by JMA magnitude scale, while foreshocks and aftershocks reached 5.5 and 5.3, respectively. The locations of the damaged levees and epicentres are represented in **Figure 3.2**.



This project has received funding from the European Union's Horizon 2020 research and innovation programme under grant agreement No. 700748

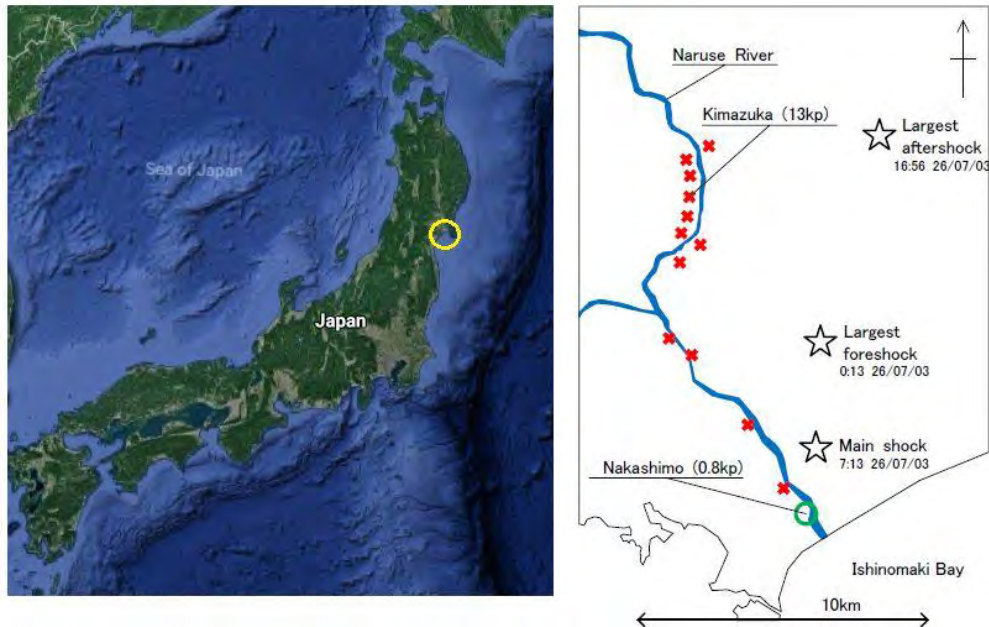


Figure 3.2: Naruse River Levee site location with damaged levees and epicentre marks (Takahashi and Sugita, 2009 - modified).

The most affected levees were constructed along the old river channels, which were underlain by clayey silts (A_{c1} , A_{c2}) and sandy layers (A_{cs} , A_s). These sands are susceptible to excess pore water pressure (EPWP) build up and consequently liquefaction. A typical cross section of Naruse river levees with micro locations of accelerometers and pore water pressure transducers is shown in **Figure 3.3**. From the figure it can be seen that sensors are arranged in two almost vertical lines. The first one runs under the embankment crest through an unimproved zone, while the other one runs under the right berm, where the material is improved by installing Sand Compaction Piles (SCP) with diameter of 70 cm. The SCP spacing in the direction of levee axis is 2.2 m, while in perpendicular direction is 1.7 m. In addition to five seismic sensors, three pore water pressure transducers were installed, one in the unimproved zone and two between the sand compaction piles in the SCP zone. During the Miyagi-Hokubu earthquake event, pore pressure ratio R_u rose to 0.8 in the unimproved zone under the embankment crest and up to 0.4 in the SCP zone, respectively. Despite nearly liquefied sandy layers, Matsuo (2004) indicated in his report embankment settlements ranging merely between a few centimetres and 0.2 m. (Cubrinovski, 2011)



This project has received funding from the European Union's Horizon 2020 research and innovation programme under grant agreement No. 700748

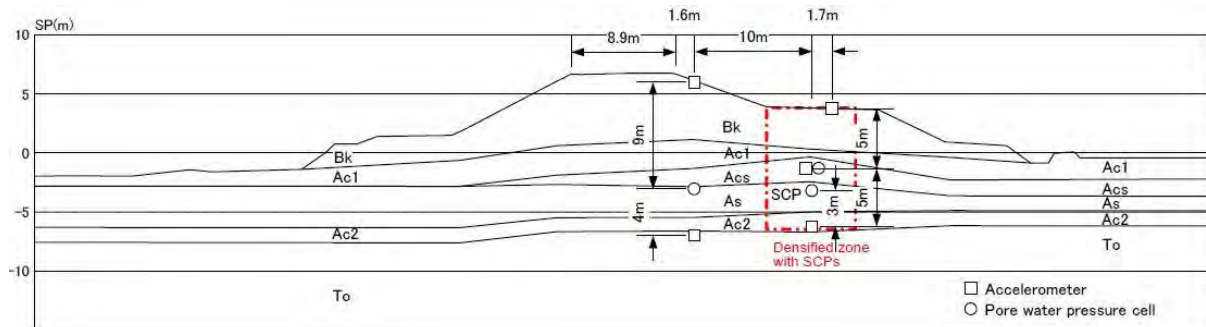


Figure 3.3: Cross section of Naruse river levee and locations of sensors (Takahashi and Sugita, 2009).

At the site, several SPT tests and borehole drilling were performed. Moreover, relevant soil properties were obtained in the laboratory. The results from in-situ and laboratory investigations are summarised in **Table 3.6** and **Figure 3.4**.

Cubrinovski (2011) numerically analysed the Naruse river levee using finite element method, where he used an elastic-plastic constitutive model, Stress-Density Model (Cubrinovski, 1993; Cubrinovski and Ishihara, 1998a; 1998b), for liquefiable layers. Results of his seismic effective stress analysis, measurements from the test site and numerical results, conducted with finite difference method in FLAC are compared and presented below.

Table 3.6: Soil properties – Naruse river levee (Takahashi and Sugita, 2009).

	Soil type	Specific gravity ^{*1}	Natural water content ^{*1*2}	Grading (%) ^{*1}			Plasticity index ^{*4}	q_u (kPa) ^{*5}	R_{L20} ^{*6}
				Gravel	Sand	Fines			
Bk	Fill	2.69	20% ^{*3}	0–2	60–82	16–40			
Ac1	Sandy silt	2.56	51% 46%	0–1	12–38	62–87	29–48	60	
Acs	Sand with fines	2.65	36%	8–10	70–88	4–22			0.19
As			27%						0.23
Ac2	Sandy silt	2.63	72% 57%	0–21	20–31	59–89	48–67	120	
To	Soft rock (siltstone or arenite)	–	–	–	–	–	–	–	–

*1 All data were obtained from boreholes for instrumentation.

*2 Except Bk, the upper value is for the boreholes near the crest, while the lower is for those at the berm.

*3 $\gamma_s=16.6 \text{ kN/m}^3$

*4 At H7-2-1, H7-2-1-A and H7-2-1-C

*5 At H7-2-1

*6 At H7-2-1-A (0.19) and H7-2-1-C (0.23) using tube samples



This project has received funding from the European Union's Horizon 2020 research and innovation programme under grant agreement No. 700748

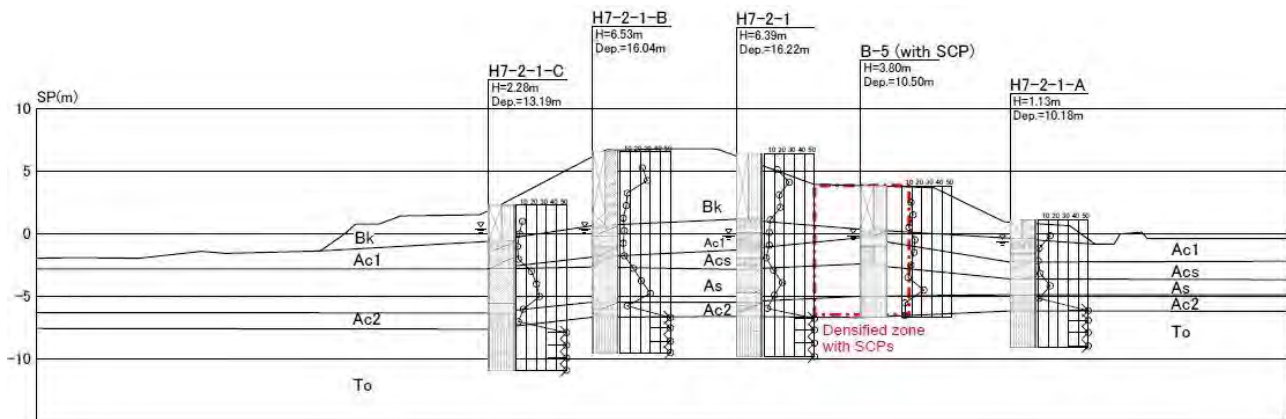


Figure 3.4: Borehole data and SPT-N value distribution – Naruse river levee (Takahashi and Sugita, 2009).

Numerical model

The case history of Naruse river levee was modelled numerically with 2D FLAC software, which is based on a finite difference method and an explicit integration scheme. In connection with the advanced constitutive material model, this software is capable of calculating pore water pressure build up and its dissipation due to densification of the material at the same time. For the purpose of simulating the liquefaction phenomenon under embankments, PM4Sand (Boulanger and Ziotopoulou, 2015) material model was chosen for the sandy layers.

Numerical model of Naruse river levee is shown in **Figure 3.5**.

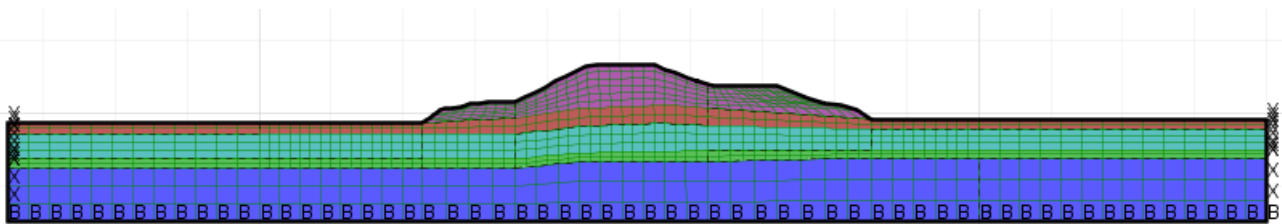


Figure 3.5: Numerical model of Naruse river levees.

Material parameters for each layer in the model were obtained from data documented by Takahashi and Sugita (2009), while missing parameters were estimated on published correlations between SPT-N values and requested soil property (Kumar et al, 2016; Anbazhagan et al, 2012; Logar, 2011). Basic parameters used in effective stress analyses are collected in **Table 3.7**. Moreover, the water level was assumed using borehole data (**Figure 3.4**).



This project has received funding from the European Union's Horizon 2020 research and innovation programme under grant agreement No. 700748

Table 3.7: Material parameters used in numerical analyses – Naruse river Levee.

Soil ID	Dry density [kg/m ³]	Permeability [m/s]	Friction angle [°]	Cohesion [kPa]	Bulk modulus [MPa]	Shear modulus [MPa]	PM4Sand		
							G ₀	D _r	h _{po}
Bk	1750	1.0E-6	31.0	5	20.8	9.6	720	0.6	0.5
Ac1	1150	1.0E-8	28.0	20	10.0	2.1			
As	1450	1.0E-4	30.0	0	16.7	10.0	550	0.35	0.55
Ac2	1000	1.0E-8	26.0	20	10.0	2.1			
To	2000	1.0E-10	0.0	150	27.8	20.8			
DZ_Ac1	1150	1.0E-6	30.8	0	20.0	4.3			
DZ_As (*)		1.0E-2					720	0.8	0.5
	1450		30.5	0	15.0	6.9			
DZ_As (**)		1.0E-3					720	0.75	0.5

Notes: DZ – densified zone by Sand Compaction Piles

* FLAC m1

** FLAC m2

Material parameters for densified zone (SCP zone) were similar to that in the unimproved region. Higher relative density and permeability (in FLAC expressed with mobility coefficient) were applied in SCP zone due to the installation of sand piles.

Validation procedure was carried out on two similar models, FLAC m1 and FLAC m2. Due to lack of material data for SCP zone, two models were analysed in order to get better matching between measured and calculated excess pore water pressure. Difference between them is in the permeability and relative density of As material in densified zone, where in first case permeability and relative density is slightly higher (**Table 3.7**).

A seismic load was applied to the bottom boundary in the numerical model as a shear stress history, converted from acceleration time history recorded at the top of soft rock layer during Miyagiken-Hokubu earthquake event (**Figure 3.6**).



This project has received funding from the European Union's Horizon 2020 research and innovation programme under grant agreement No. 700748

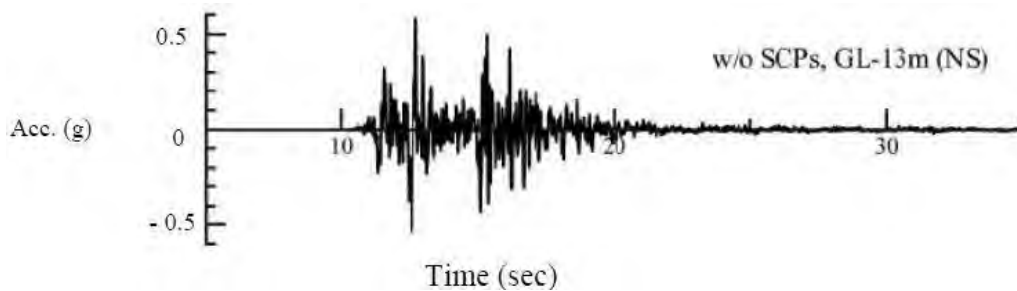


Figure 3.6: Recorded acceleration time history at the top of base layer – Naruse river levee (Cubrinovski, 2011).

Results

In the next figures (**Figure 3.7** to **Figure 3.10**) comparisons between recorded and numerically computed excess pore water pressures within Naruse river levee are presented. In addition, **Figure 3.11** shows embankment crest settlement during strong part of ground motion. Two sets of numerical results are presented: from Cubrinovski (2011) and from this study (results are denoted by FLAC m1 and FLAC m2).

Development of excess pore water pressure in the unimproved and SCP zone was generally similar in all three cases (recorded, Cubrinovski model, FLAC m1 or FLAC m2) with small differences from case to case. An acceptable match was found between the increase of pore water pressure in all numerical analyses and the recorded data, during the time of strong part of the ground motion. Although, it is slightly faster in case of numerical simulations compared to measured values. However, there is a minor difference in the maximum value between the two variants of FLAC analyses (approximately 10-15 kPa in the unimproved zone and consequent dissipation of the EPWP, as a result of minor changes in permeability between both FLAC models).

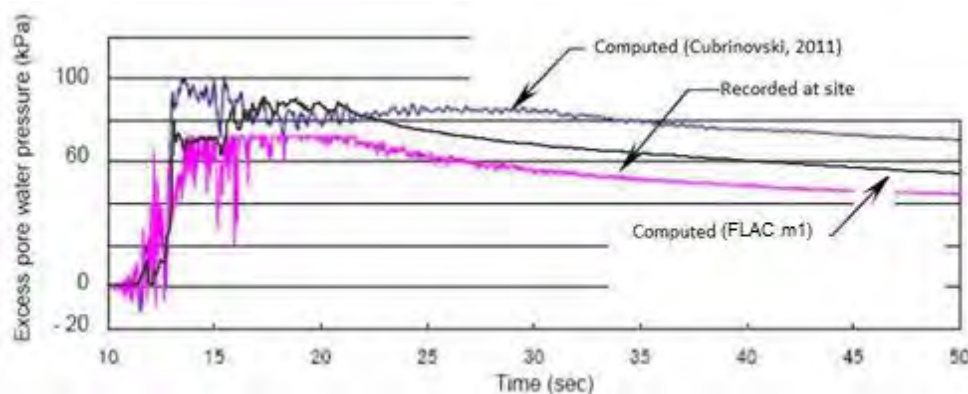


Figure 3.7: EPWP in the unimproved zone: recorded and calculated values by Cubrinovski (2011) and from FLAC analysis (model: FLAC m1).



This project has received funding from the European Union's Horizon 2020 research and innovation programme under grant agreement No. 700748

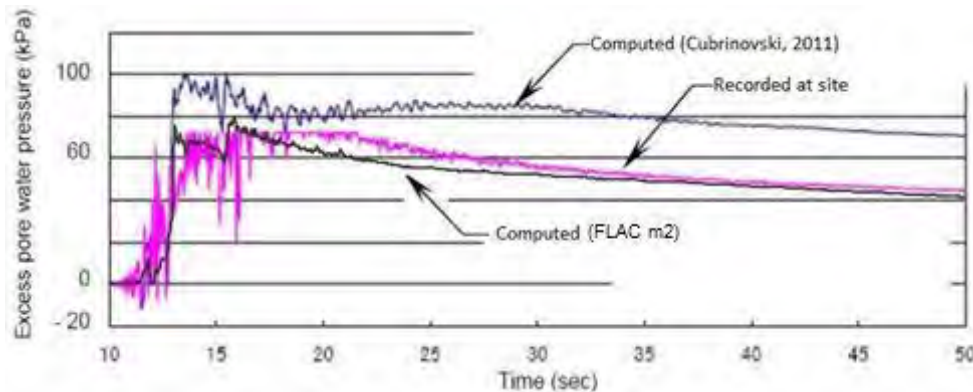


Figure 3.8: EPWP in the unimproved zone: recorded and calculated values by Cubrinovski (2011) and from FLAC analysis (model: FLAC m2).

Considerably slower dissipation of the EPWP from FLAC analyses (especially after 21 seconds of the ground motion) in the SCP zone can be seen in **Figure 3.9** and **Figure 3.10**. The majority of this mismatching with field measurements is a consequence of a number of simplifications used in modelling of densified zone, due to the lack of sand compaction piles data. The simplifications were summarized after Cubrinovski (2011).

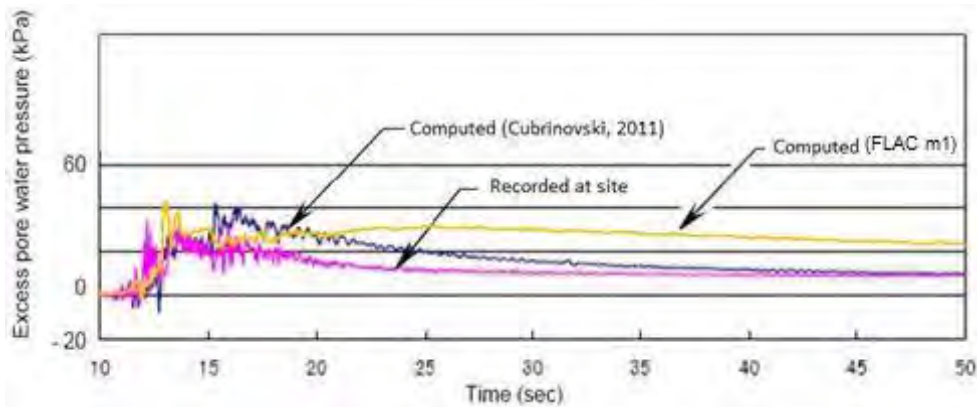


Figure 3.9: EPWP in the SCP zone: recorded and calculated values by Cubrinovski (2011) and from FLAC analysis (model: FLAC m1).

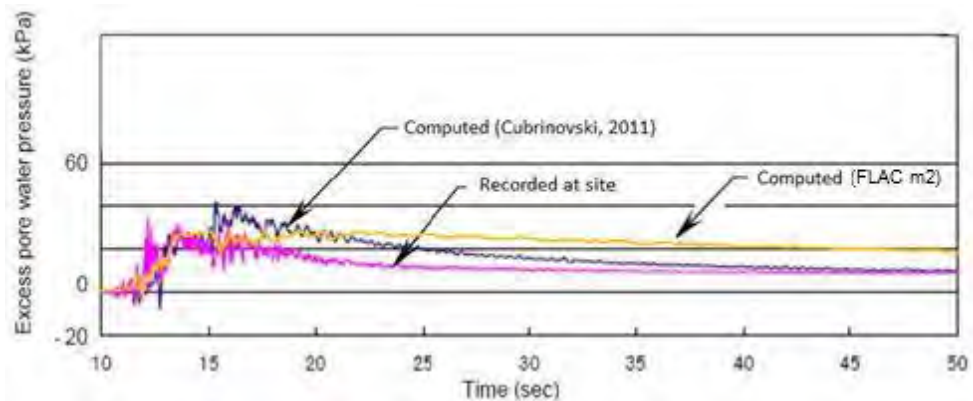


Figure 3.10: EPWP in the SCP zone: recorded and calculated values by Cubrinovski (2011) and from FLAC analysis (model: FLAC m2).



This project has received funding from the European Union's Horizon 2020 research and innovation programme under grant agreement No. 700748

Computed crest settlement for the embankment was between 12 and 14 centimetres, which is consistent with a visual observation from the site. A slightly larger horizontal displacement (lateral spreading) of around 0.3 m was calculated and observed on the site at the toe of the embankment.

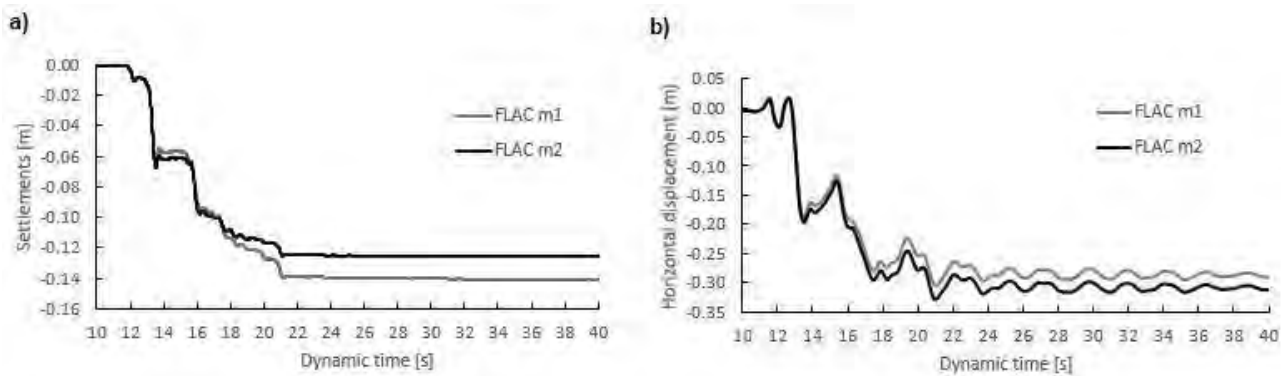


Figure 3.11: a) Crest settlement and b) horizontal displacement at left toe – Naruse river levee (FLAC models).

On the basis of the above results from validation procedure of the Naruse river levee, it can be seen that response of the levee/embankment structure built on liquefiable soils can be reasonably well captured by numerical approach with FLAC software using the advanced material model PM4Sand, specifically developed for modelling the behaviour of liquefiable soils.

3.1.4.2 Description of the numerical model used for the derivation of fragility curves

Model geometry

General layout of the model geometry is presented in **Figure 3.12**, consisting of a traffic embankment underlain by three horizontal soil layers. Under upper clayey crust layer, a sandy layer susceptible to liquefaction is placed, while lower layer represents base of stiff clay.

The earthquake-liquefaction-induced response of the traffic embankments was comprehensively captured through parametric study by varying thickness of liquefiable layer, embankment height, crest width, presence of crust layer and material properties for liquefiable sandy layer.

Four different soil profiles – S1, S2, S4 and S5 (**Table 3.8**), four embankment heights (2, 4, 6 and 8 m) and three crest widths (6, 12 and 24 m) were considered. Soil profiles S1 and S2 contain 7 m thick liquefiable layer with 1 m thick crust layer and without it, respectively. Soil profiles S4 and S5 have both 1 m thick crust layer with 2 and 4 m thick liquefiable layer, respectively.

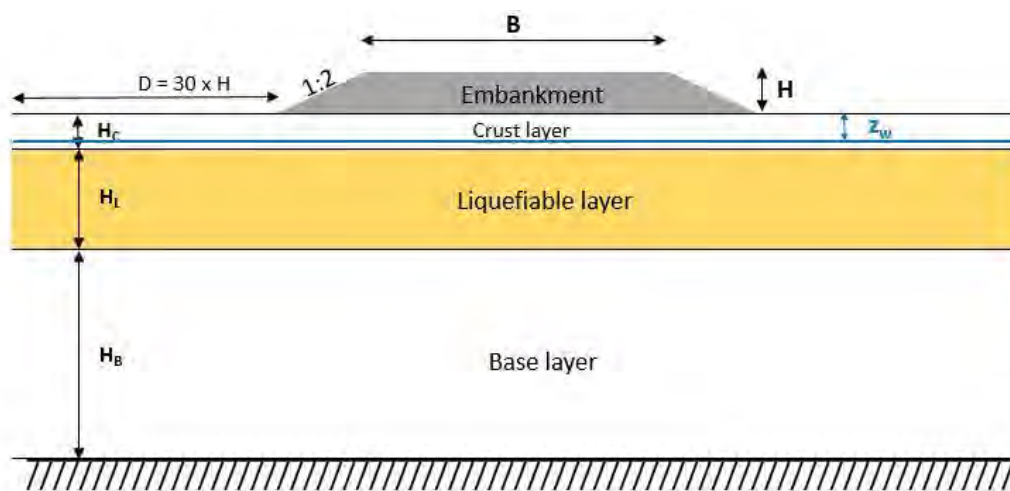
Ground water level was set one meter below the ground surface and was kept constant through all analyses. Additionally, the embankment slope inclination equal to 1:2 (vertical:horizontal) remained unchanged.



This project has received funding from the European Union's Horizon 2020 research and innovation programme under grant agreement No. 700748

Table 3.8: Soil profiles used in numerical calculations.

Soil ID	C – thickness of crust [m]	L – thickness of liquefiable layer [m]	B – thickness of base layer [m]
S1	1	7	24
S2	0	7	24
S4	1	2	24
S5	1	4	24



Embankment geometry variations

H [m]	B [m]	D	Slope inclination
2, 4, 6, 8	6, 12, 24	D = 30xH	(Ver : Hor) = 1 : 2

Soil profile geometry variations

H _c [m]	H _l [m]	H _b [m]	z _w [m]
0, 1	2, 4, 7	24	1

Figure 3.12: Geometry variations for parametric study of embankment.

Material properties

For the purpose of this research, a simplified soil profiles with horizontal layers and assumed material properties were taken. Upper layer represents clayey crust layer, resistant to instantaneous pore pressure build up during seismic loading. Beneath crust layer a sandy layer prone to liquefaction is located. Two sets of material characteristics, regarding relative density of liquefiable layer were considered – medium dense sand ($D_r = 0.6$) and loose sand ($D_r = 0.35$). Bottom layer is described as stiff clay layer with undrained shear strength equal to 150 kPa.



This project has received funding from the European Union's Horizon 2020 research and innovation programme under grant agreement No. 700748

The material properties of the soil layers and embankment used in numerical analyses are given in **Table 3.9** and **Table 3.10**.

Table 3.9: Material properties for numerical simulations – general parameters.

Layer	Dry density (kg/m ³)	Bulk modulus (MPa)	Shear modulus (MPa)	Friction angle (°)	Cohesion (kPa)	Porosity (/)	Permeability («isotropic») (m/s)
Crust	1784	64	30	0	80	0.45	8.0E-8
Liquefiable “medium dense”	1486	77	77	30	0	0.43	1.60E-5
Liquefiable “loose”	1486	57.3	43	30	0	0.41	1.65E-5
Base	1436	227	105	0	150	0.45	1.00E-9
Embankment	1800	83.3	38.5	35	5	0.30	1.18E-5

In order to simulate liquefaction phenomenon, the advanced PM4Sand material model was applied to sandy layer after initial stress state was calculated. Three main input parameters (D_r , G_0 and h_{po}) of PM4Sand material model were assigned to the liquefiable material, while others were kept at their default values. D_r parameter stands for sand's relative density and is expressed as a ratio. Furthermore, small strain shear modulus is controlled by constant shear modulus coefficient G_0 and the third one is the contraction rate parameter h_{po} which, according to the authors of the material model, is used for calibration of the model to specific values of cyclic resistance ratio (CRR) (Boulanger and Ziotopoulou, 2015). Assigned values of primary parameters for PM4Sand material models are highlighted in **Table 3.10**.

Table 3.10: Material properties for numerical simulations – PM4 parameters.

Layer	Dry density (kg/m ³)	Bulk modulus (MPa)	Shear modulus (MPa)	Friction angle (°)	Cohesion (kPa)	PM4Sand		
						D_r (/)	G_0 (/)	h_{po} (/)
Crust	1784	64	30	0	80	-	-	-
Liquefiable “medium”	1486	77	77	30	0	0.60	760	0.55
Liquefiable “loose”	1486	57.3	43	30	0	0.35	476	0.5
Base	1436	227	105	0	150	-	-	-
Embankment	1800	83.3	38.5	35	5	-	-	-

Input motions

A set of 30 ground motions (GM) recorded on rock outcrop were selected from the Strong ground motion database which contains 9188 ground motions obtained from the NGA (Chiou et al, 2008) and the RESORCE (Akkar et al, 2014) database. The two databases were recently combined by the Institute of Structural



This project has received funding from the European Union's Horizon 2020 research and innovation programme under grant agreement No. 700748

Engineering, Earthquake Engineering and Construction IT (IKPIR) (Šebenik and Dolšek, 2016). The selected ground motions correspond to events with magnitudes between 5 and 7.5, and source-to-site distances of between 5 and 50 km. Due to a lack of records from sites where shear wave velocity in upper 30 meters of soil ($v_{s,30}$) exceeds 800 meters per second (representing soil class A in Eurocodes), less strict criteria was chosen ($v_{s,30} > 500$ m/s) in selecting procedure. Average $v_{s,30}$ of all 30 GMs is equal to 680 m/s. The mean spectrum obtained from selected acceleration time histories coincides well with EC8 spectrum for soil class A related to peak ground acceleration $a_g = 0.25$ g (Figure 3.13). The largest considered scale factor was 1.99. The duration of ground motions and Arias Intensity varies from 7.4 to 61.0 seconds (in average 17.4 seconds per ground motion) and 0.26 to 3.4, respectively.

More detailed information for all used ground motions is given in Table 3.11.

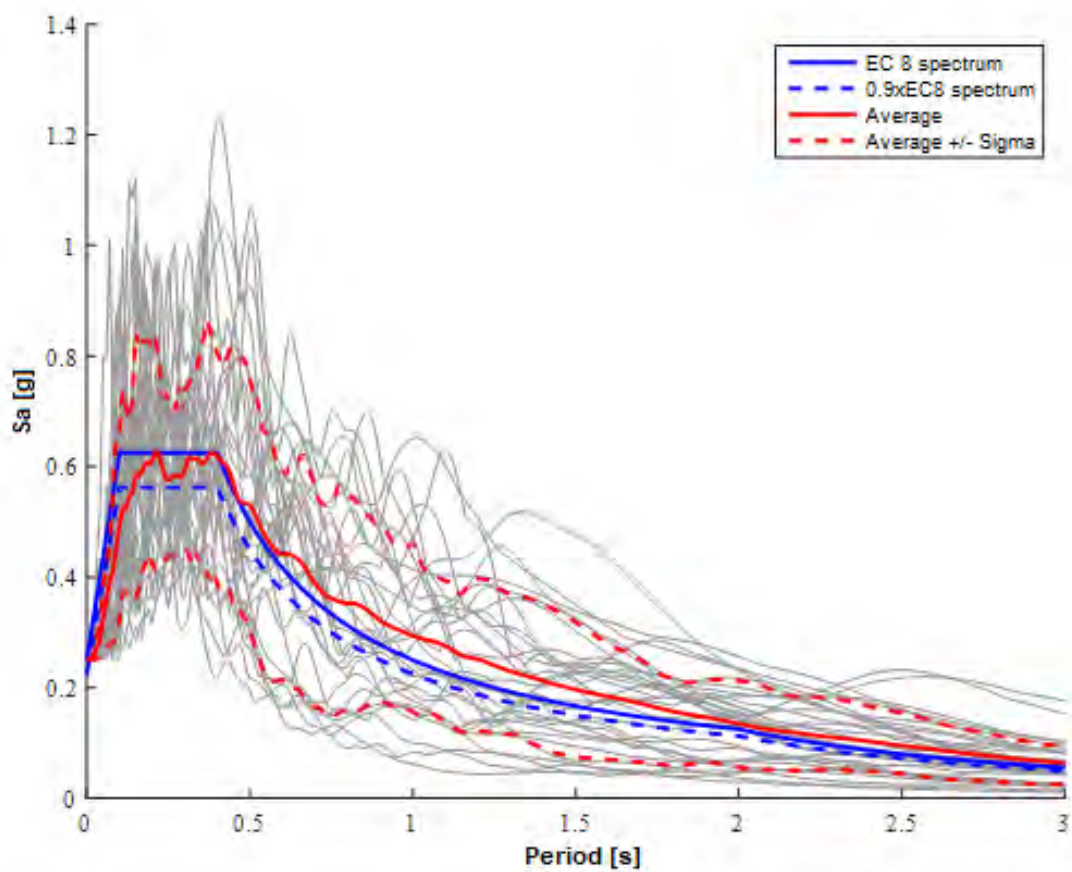


Figure 3.13: Spectra of used ground motions.

The procedure for selecting ground motions followed the proposal by Jayaram et al (2011).



This project has received funding from the European Union's Horizon 2020 research and innovation programme under grant agreement No. 700748

Table 3.11: Set of used ground motions

Record Number	id	Earthquake location	Station location	Date	M	Closest distance	Soil_v _{s,30}
1	983	Northridge-01	Jensen Filter Plant Generator	1994-01-17	6.7	5	526
2	2734	Chi-Chi, Taiwan-04	CHY074	1999-09-20	6.2	6	553
3	3548	Loma Prieta	Los Gatos - Lexington Dam	1989-10-18	6.9	5	1070
4	164	Imperial Valley-06	Cerro Prieto	1979-10-15	6.5	15	660
5	2734	Chi-Chi, Taiwan-04	CHY074	1999-09-20	6.2	6	553
6	2661	Chi-Chi, Taiwan-03	TCU138	1999-09-20	6.2	22	653
7	1078	Northridge-01	Santa Susana Ground	1994-01-17	6.7	17	715
8	1787	Hector Mine	Hector	1999-10-16	7.1	12	685
9	1013	Northridge-01	LA Dam	1994-01-17	6.7	6	629
10	361	Coalinga-01	Parkfield - Vineyard Cany 2E	1983-05-02	6.4	24	713
11	755	Loma Prieta	Coyote Lake Dam (SW Abut)	1989-10-18	6.9	20	597
12	3220	Chi-Chi, Taiwan-05	TCU138	1999-09-22	6.2	48	653
13	164	Imperial Valley-06	Cerro Prieto	1979-10-15	6.5	15	660
14	1012	Northridge-01	LA 00	1994-01-17	6.7	19	706
15	3269	Chi-Chi, Taiwan-06	CHY029	1999-09-25	6.3	41	545
16	769	Loma Prieta	Gilroy Array #6	1989-10-18	6.9	18	663
17	6006	Montenegro (Aftershock)	Petrovac-Hotel Rivijera	1979-05-24	6.2	13	713
18	1078	Northridge-01	Santa Susana Ground	1994-01-17	6.7	17	715
19	994	Northridge-01	LA - Griffith Park Observatory	1994-01-17	6.7	24	1016
20	2461	Chi-Chi, Taiwan-03	CHY028	1999-09-20	6.2	24	543
21	2661	Chi-Chi, Taiwan-03	TCU138	1999-09-20	6.2	22	653
22	3268	Chi-Chi, Taiwan-06	CHY028	1999-09-25	6.3	34	543
23	2703	Chi-Chi, Taiwan-04	CHY028	1999-09-20	6.2	18	543
24	3549	Northridge-01	Monte Nido Fire Station	1994-01-17	6.7	26	660
25	3268	Chi-Chi, Taiwan-06	CHY028	1999-09-25	6.3	34	543
26	3703	Irpinia, Italy-02	Calitri	1980-11-23	6.2	7	524
27	765	Loma Prieta	Gilroy Array #1	1989-10-18	6.9	10	1428
28	801	Loma Prieta	San Jose - Santa Teresa Hills	1989-10-18	6.9	15	672
29	1013	Northridge-01	LA Dam	1994-01-17	6.7	6	629
30	1020	Northridge-01	Lake Hughes #12A	1994-01-17	6.7	21	602



This project has received funding from the European Union's Horizon 2020 research and innovation programme under grant agreement No. 700748

2D finite difference numerical analyses

The numerical analyses were performed using software package FLAC 2D v8.0 (Itasca, 2016). It is an explicit finite difference program capable of simulating liquefaction phenomenon as it is shown in validation procedure.

The numerical model was set up in several phases. At first, the geometry of the soil profiles, material characteristics and boundary conditions for static calculations were assigned to the model. Bottom boundary was fixed in both vertical and horizontal direction, while lateral boundaries of the model were constrained in horizontal direction only. Initial hydrostatic pore pressure distribution was assigned to the model and no discharge at lateral sides was allowed. The degree of saturation at the surface was set equal to 0. With that restrictions ground water drainage was assumed through model surface only. After initial stress state of the free field ground was calculated, the embankment was constructed. In the next phase material model for liquefiable sandy layer was changed from Mohr-Coulomb (MC) model to advanced user defined PM4Sand material model. However, MC model was kept assigned to crust and base layer as well as for embankment. Following the definition of some extra variables and time histories a dynamic phase was modelled.

In order to satisfy accurate wave propagation through soil profile, the mesh density of finite difference model fulfilled the condition of spatial element size related to highest frequency component of input motion (FLAC, 2016). In addition, element size rises from embankment toe to lateral edges with a small gradient to decrease a number of all elements and preserve quality results within the area of particular interest around embankment structure. However, the distance to the lateral boundary of the models also increases by increasing the height of the embankment. Since a free field boundary condition in software packages cannot absorb all outward propagating waves, a sufficient width of the model ensures small enough influence on the behaviour of the embankment. At the bottom of the model, compliant base boundary condition was applied. All displacements were set to zero before the application of seismic loading. Selected acceleration time histories were transformed to shear stress history and applied to the compliant base of each model.

Figure 3.14 presents basic numerical model in FLAC.

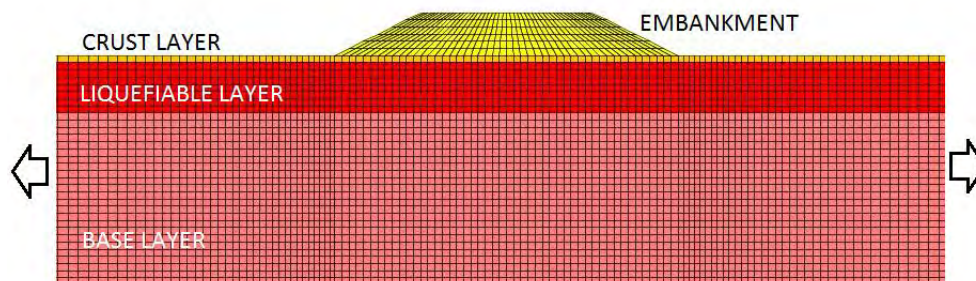


Figure 3.14: Numerical model in FLAC.



This project has received funding from the European Union's Horizon 2020 research and innovation programme under grant agreement No. 700748

Not all possible combinations of above mentioned geometrical variations were numerically simulated in FLAC. **Table 3.12** summarises the performed analyses. Two geometrically same sets of analyses were repeated for two different material properties for the sandy layer (medium dense and loose state).

Table 3.12: Matrices with all performed analyses in FLAC.

Soil profile ID		Layer thickness [m]	Embankment height [m] (crest width: 24 m)				Soil profile ID		Layer thickness [m]	Embankment height [m] (crest width: 24 m)			
			2	4	6	8				2	4	6	8
S1	Crust	1	✓	✓	✓	✓	S1 Loose	Crust	1	✓	✓	✓	✓
	Liq.	7						Liq.	7				
	Base	24						Base	24				
S2	Crust	0	✓	✓	✓	✓	S2 Loose	Crust	0	✓	✓	✓	✓
	Liq.	7						Liq.	7				
	Base	24						Base	24				
S4	Crust	1	✓	✓	✓	✓	S4 Loose	Crust	1	✓	✓	✓	✓
	Liq.	2						Liq.	2				
	Base	24						Base	24				
S5	Crust	1	✓	✓	✓	✓	S5 Loose	Crust	1	✓	✓	✓	✓
	Liq.	4						Liq.	4				
	Base	24						Base	24				

Initially, the models with different crest width (6, 12 and 24 m) with four meters high embankment underlain by soil profile S1 were analysed – those analyses are not included in the above matrices. Subsequently, the various embankment heights (2, 4, 6 and 8 m) were applied to all above soil profiles, while the crest width of the embankment remained constant and equal to 24 m.

Technical information

All analyses were performed on a desktop computer with Intel® Core™ i7-6700K processor (4 cores; 8 logical processors) and 16 GB of installed memory (RAM). Two parallel instances of FLAC calculations were running on 2 cores each.

For the derivation of a single fragility curve of the embankment built on liquefiable ground through numerical approach a various time duration is needed, depending on the size of the model, duration of the ground motions, material characteristics, etc. While the lateral distance to the model boundary was increased with embankment height, it took approximately three weeks to calculate 240 analyses with 8 m high embankment (30 ground motions multiplied by 8 intensity levels). It was less time consuming to calculate models with lower embankment height – for H = 6 m (a little less than two weeks), H = 4 m (a week) and for H = 2 m (few days).



This project has received funding from the European Union's Horizon 2020 research and innovation programme under grant agreement No. 700748

3.1.4.3 Results of numerical analyses

Only selected results of all 7200 cases were saved for later analyses:

- final calculated state of entire model (displacements, strain and stress state including pore water pressures),
- time history of vertical displacements in selected 6 points of embankment (**Figure 3.15**),
- time history of horizontal displacements in selected 4 points of embankment (**Figure 3.15**),
- time history of pore pressure ratio R_u in selected 6 points within liquefiable layer (**Figure 3.15**).

Figure 3.16 and **Figure 3.17** show typical calculation results at the end of calculation in terms of total displacements and pore pressure ratio.

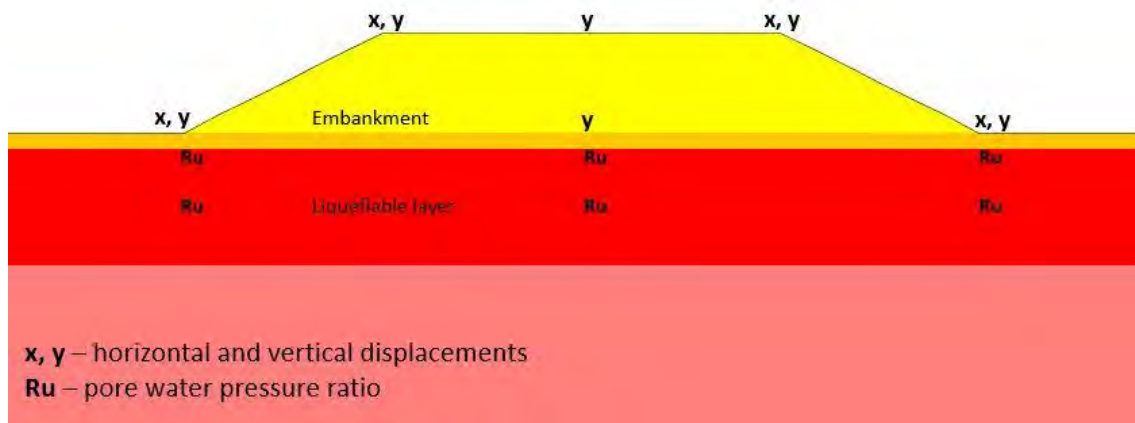


Figure 3.15: Locations of time history points.

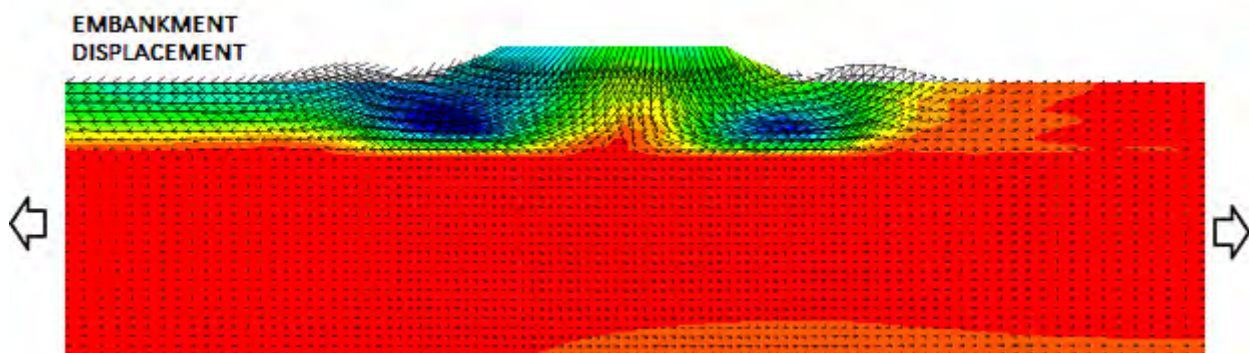


Figure 3.16: Typical embankment displacements.



This project has received funding from the European Union's Horizon 2020 research and innovation programme under grant agreement No. 700748

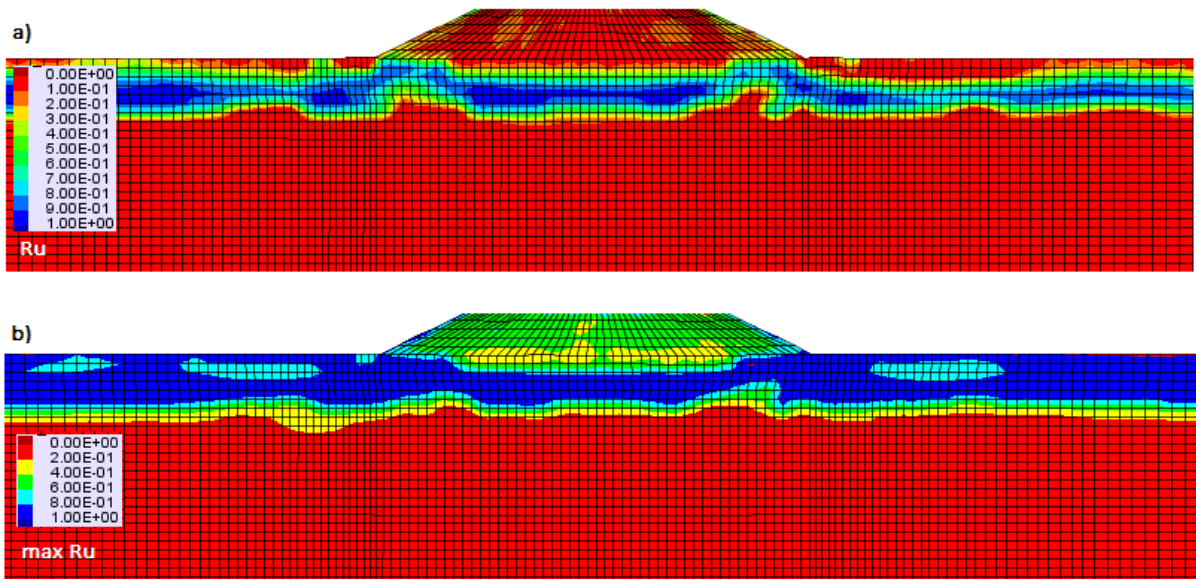


Figure 3.17: a) Pore water pressure ratio (R_u) at final calculated state and b) maximum R_u during analysis.

A proper damage state parameter has to be selected in order to obtain fragility curves from the performed numerical calculations. Vertical settlement of the central point of the crest of embankment is proposed in the literature (Argyroudis, Kaynia, 2015). However, some other damage indicators might better represent observed damage in an embankment cross section after strong earthquakes (Sasaki and Tamura, 2007), eg. differential settlements, differential horizontal displacements, displacement at the side of embankment. In cases of lateral spreading, horizontal displacements could better represent a state of embankment damage than vertical displacements. In order to justify the selection of a damage state parameter, we plotted all 7200 results of some possible alternative damage state parameters vs. vertical settlement at the central top of embankment (see **Figure 3.18**). From this figure we can see that vertical and horizontal displacements at crest edges of embankment are well correlated to the settlement of top midpoint. The same is valid for difference of horizontal displacements at both top edge points (Δx). However, for cases where differential settlements at both edges of embankment according to the central top point (Δy) may be important for assessing damage, settlement of top midpoint is not a representative parameter. Based on this analysis we decided to keep vertical displacement at top midpoint of embankment as a damage state parameter. Nevertheless, we will show also examples of fragility curves developed for difference of horizontal displacements at both top edge points (Δx).

The last graph in **Figure 3.18** shows the relationship between pore pressure parameter R_u and settlement of top midpoint of embankment. One can observe that considerable settlements start to develop at $R_u > 0.6$ but even the value $R_u = 1$ does not lead to large settlements in all cases.



This project has received funding from the European Union's Horizon 2020 research and innovation programme under grant agreement No. 700748

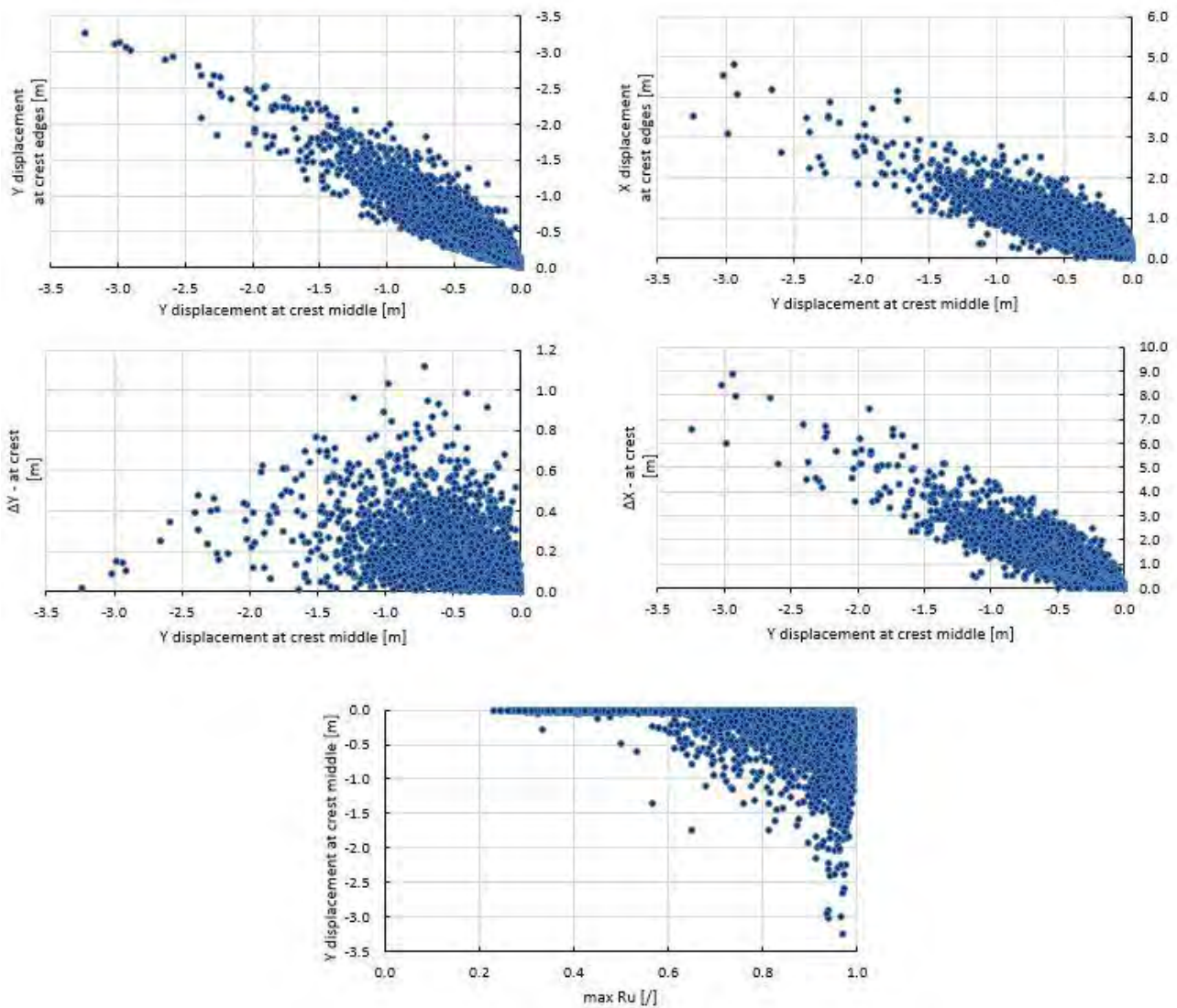


Figure 3.18: Correlations with vertical displacement at central top point of embankment.

3.1.4.4 Multiple Stripe Analysis and few examples of fragility curves

Numerical analyses in FLAC were performed considering a multiple stripe analysis method, which means that numerical calculations were carried out at discrete IM levels (8 PGA levels were used), and a series of different GMs, 30 in this particular case. According to Baker (2015), there is no need to perform the analysis up to such IM level that the limit state is exceeded for all ground motions. Besides, number of collapses may not strictly increase with increasing IM level. Figure 3.19 briefly describes the derivation of fragility curves based on calculated data from numerical analyses in FLAC, using multiple stripe analysis method, for case with 4 m high embankment and 24 m wide embankment crest, underlain by the soil profile S5 (4 m thick liquefiable layer). Number of exceeded cases and corresponding fragility curve is assessed for damage state 2 (ds2), only. The fitting procedure, considering multiple IM levels was achieved using the maximum of likelihood function.



This project has received funding from the European Union's Horizon 2020 research and innovation programme under grant agreement No. 700748

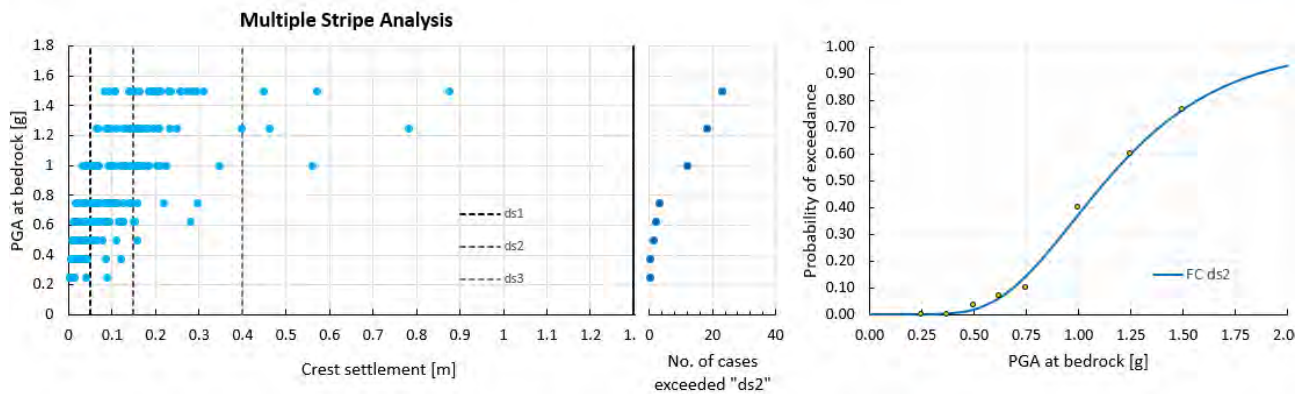


Figure 3.19: Multiple stripe analysis procedure for derivation of »ds2« fragility curve – case H4B24-S5.

For more detailed description of the multiple stripe analysis method and others (incremental dynamic analysis (IDA)) see Baker (2015).

Within this research, a probabilistic analysis was performed to find the probability of exceedance of a selected damage states for road and railway embankments based on a numerical parametric study of an embankment built on a liquefiable ground. The influence of variation of some model parameters (crest width, embankment height, thickness of liquefiable layer, presence of crust layer and relative density of sandy layer) was examined through fragility curves. Fragility curves are based on correlation between damage states in terms of permanent vertical ground displacement in the middle of the embankment crest and PGA at bedrock as intensity measure. Some typical results presented as fragility curves for traffic embankments by varying aforementioned model parameters are presented in figures bellow (**Figure 3.20** to **Figure 3.27**).

The definitions of the limit states for traffic embankments were taken from literature and are presented in **Table 3.3**. For the evaluation of fragility curves, mean values of vertical displacement given in **Table 3.3** were used as threshold values for each damage state.

Moreover, **Table 3.13** to **Table 3.22** summarize values of main two parameters (μ , σ) for the derivation of the fragility curves for all performed analyses. Red numbers present less reliable results, due to selection of damage criteria in combination with intensity levels, which led to poor distribution of data points along particular fragility curve. Due to the same reasons, it was impossible to determine fragility curves for some cases (empty gray cells in tables below).



This project has received funding from the European Union's Horizon 2020 research and innovation programme under grant agreement No. 700748

Table 3.13: Fragility curve parameters in terms of PGA – medium dense soil (road embankments).

Medium dense soil (Dr = 0.6)	Soil ID	Fragility parameters	embankment height (crest width B = 24m)											
			2			4			6			8		
			ds1	ds2	ds3	ds1	ds2	ds3	ds1	ds2	ds3	ds1	ds2	ds3
S1	μ	0.503	0.945	2.808	0.412	0.735	1.490	0.415	0.681	1.202	0.274	0.480	1.030	
	σ	0.381	0.427	0.572	0.395	0.321	0.394	0.423	0.400	0.338	0.565	0.565	0.427	
S2	μ	0.424	0.773	2.808	0.390	0.623	1.367	0.469	0.591	1.078				
	σ	0.370	0.370	0.572	0.337	0.390	0.488	0.270	0.409	0.411				
S4	μ				0.832	1.754	2.400	0.499	0.718	1.491	0.522	0.760	1.202	
	σ				0.418	0.409	0.325	0.366	0.386	0.527	0.314	0.366	0.405	
S5	μ	1.014			0.600	1.132	2.721	0.455	0.804	1.460	0.445	0.619	1.007	
	σ	0.486			0.369	0.388	0.495	0.362	0.395	0.365	0.425	0.373	0.378	

Table 3.14: Fragility curve parameters in terms of PGA – loose soil (road embankments).

Loose soil (Dr = 0.35)	Soil ID	Fragility parameters	embankment height (crest width B = 24m)											
			2			4			6			8		
			ds1	ds2	ds3	ds1	ds2	ds3	ds1	ds2	ds3	ds1	ds2	ds3
S1	μ	0.208	0.363	1.033	0.207	0.325	0.680	0.207	0.310	0.605	0.091	0.120	0.386	
	σ	0.393	0.379	0.429	0.310	0.373	0.388	0.310	0.306	0.378	0.516	0.654	0.588	
S2	μ	0.231	0.319	0.863	0.231	0.241	0.563	0.175	0.224	0.504				
	σ	0.095	0.351	0.422	0.095	0.441	0.408	0.400	0.486	0.415				
S4	μ	0.842			0.226	0.542		0.235	0.382	0.878		0.291	0.814	
	σ	1.068			0.310	0.521		0.087	0.471	0.434		0.377	0.692	
S5	μ	0.350	1.160		0.226	0.509	1.262	0.201	0.413	0.807	0.201	0.263	0.558	
	σ	0.316	0.633		0.310	0.304	0.417	0.371	0.313	0.397	0.371	0.386	0.412	

Table 3.15: Fragility curve parameters in terms of PGA – medium dense soil and crest width variations (road embankments).

Medium dense soil (Dr = 0.6)	Soil ID	Fragility parameters	Crest width (embankment height H = 4m)					
			6			12		
			ds1	ds2	ds3	ds1	ds2	ds3
S1	μ	0.348	0.557	1.133	0.378	0.582	1.205	
	σ	0.310	0.402	0.429	0.327	0.444	0.466	

Table 3.16: Fragility curve parameters in terms of PGA – medium dense soil (railway embankments).

Medium dense soil (Dr = 0.6)	Soil ID	Fragility parameters	embankment height (crest width B = 24m)											
			2			4			6			8		
			ds1	ds2	ds3	ds1	ds2	ds3	ds1	ds2	ds3	ds1	ds2	ds3
S1	μ	0.442	0.632	1.226	0.373	0.507	0.855	0.358	0.493	0.820	0.219	0.327	0.616	
	σ	0.402	0.325	0.535	0.326	0.372	0.346	0.317	0.407	0.371	0.420	0.607	0.513	
S2	μ	0.375	0.525	1.086	0.338	0.431	0.767	0.336	0.450	0.687				
	σ	0.310	0.378	0.452	0.296	0.362	0.373	0.296	0.411	0.387				
S4	μ				0.655	1.164	2.801	0.418	0.573	0.858	0.446	0.598	0.856	
	σ				0.368	0.447	0.623	0.368	0.327	0.442	0.363	0.328	0.402	
S5	μ	0.668	1.521	3.269	0.460	0.739	1.546	0.417	0.610	0.958	0.428	0.500	0.733	
	σ	0.374	0.539	0.580	0.333	0.398	0.447	0.382	0.345	0.367	0.390	0.357	0.416	



This project has received funding from the European Union's Horizon 2020 research and innovation programme under grant agreement No. 700748

Table 3.17: Fragility curve parameters in terms of PGA – loose soil (railway embankments).

Soil ID	Fragility parameters	embankment height (crest width B = 24m)											
		2			4			6			8		
		ds1	ds2	ds3	ds1	ds2	ds3	ds1	ds2	ds3	ds1	ds2	ds3
S1	μ	0.232	0.223	0.468	0.230	0.200	0.385	0.227	0.199	0.370	0.108	0.086	0.166
	σ	0.100	0.440	0.438	0.099	0.461	0.328	0.102	0.411	0.334	0.171	0.716	0.647
S2	μ	0.224	0.198	0.395	0.221	0.207	0.335	0.223	0.207	0.298			
	σ	0.100	0.444	0.398	0.096	0.310	0.320	0.101	0.310	0.369			
S4	μ				0.156	0.310	0.777	0.227	0.214	0.453	0.172	0.217	0.361
	σ				0.436	0.341	0.455	0.087	0.467	0.462	0.394	0.395	0.435
S5	μ	0.288	0.494	1.866	0.231	0.322	0.617	0.230	0.257	0.491	0.234	0.199	0.338
	σ	0.220	0.371	0.654	0.095	0.279	0.353	0.097	0.269	0.333	0.093	0.411	0.375

Table 3.18: Fragility curve parameters in terms of PGA – medium dense soil and crest width variations (railway embankments).

Soil ID	Fragility parameters	Crest width (embankment height H = 4m)					
		6			12		
		ds1	ds2	ds3	ds1	ds2	ds3
S1	μ	0.306	0.423	0.705	0.373	0.507	0.855
	σ	0.305	0.417	0.452	0.326	0.372	0.346

Table 3.19: Fragility curve parameters in terms of Arias intensity – medium dense soil (road embankments).

Soil ID	Fragility parameters	embankment height (crest width B = 24m)											
		2			4			6			8		
		ds1	ds2	ds3	ds1	ds2	ds3	ds1	ds2	ds3	ds1	ds2	ds3
S1	μ	9.762	25.050		4.935	12.787		4.688	11.846	29.385	3.666	9.266	21.238
	σ	0.676	0.593		0.587	0.704		0.558	0.509	0.433	0.535	0.501	0.341
S2	μ	7.069	19.785		5.022	12.241	32.250	4.139	11.047	23.492			
	σ	0.610	0.474		0.501	0.588	0.421	0.538	0.558	0.408			
S4	μ				16.384			6.727	13.980	54.491	5.495	12.016	28.086
	σ				0.549			0.525	0.516	0.657	0.500	0.450	0.594
S5	μ				10.418	25.600		6.106	14.315	72.088	4.666	10.242	20.822
	σ				0.566	0.314		0.538	0.401	0.900	0.525	0.528	0.456

Table 3.20: Fragility curve parameters in terms of Arias intensity – loose soil (road embankments).

Soil ID	Fragility parameters	embankment height (crest width B = 24m)											
		2			4			6			8		
		ds1	ds2	ds3	ds1	ds2	ds3	ds1	ds2	ds3	ds1	ds2	ds3
S1	μ	2.464	8.351	52.310	1.518	4.446	15.473	1.335	3.531	11.862	1.196	2.771	9.544
	σ	0.775	0.813	0.880	0.727	0.695	0.541	0.708	0.664	0.539	0.693	0.670	0.569
S2	μ	1.711	5.785	23.429	1.254	3.405	12.721	1.181	2.900	10.889			
	σ	0.697	0.725	0.615	0.752	0.688	0.536	0.740	0.725	0.581			
S4	μ				4.618	22.253		2.406	8.749	42.149	1.243	3.108	7.815
	σ				0.829	0.739		0.789	0.765	0.896	0.550	0.571	0.385
S5	μ	7.963	46.563		2.735	9.559	51.736	1.913	6.168	20.994	1.460	3.820	11.901
	σ	0.779	0.934		0.680	0.601	0.727	0.682	0.633	0.490	0.722	0.683	0.592



This project has received funding from the European Union's Horizon 2020 research and innovation programme under grant agreement No. 700748

Table 3.21: Fragility curve parameters in terms of Arias intensity – medium dense soil (railway embankments).

Medium dense soil (Dr = 0.6)	Soil ID	Fragility parameters	embankment height (crest width B = 24m)											
			2			4			6			8		
			ds1	ds2	ds3	ds1	ds2	ds3	ds1	ds2	ds3	ds1	ds2	ds3
S1	μ	6.443	13.620	52.310	3.186	7.305	17.175	2.994	6.582	14.479	2.243	5.600	11.501	
	σ	0.617	0.599	0.880	0.627	0.647	0.696	0.589	0.560	0.403	0.532	0.516	0.451	
S2	μ	4.939	11.573	26.979	3.208	7.402	15.665	2.633	6.150	12.712				
	σ	0.605	0.677	0.501	0.653	0.596	0.414	0.619	0.550	0.456				
S4	μ				9.795	23.132		4.807	9.502	17.103	4.129	7.537	15.028	
	σ				0.513	0.482		0.495	0.560	0.471	0.449	0.466	0.456	
S5	μ	14.352	38.343		6.277	13.806	38.343	4.286	9.166	18.454	3.556	6.611	12.791	
	σ	0.495	0.497		0.547	0.413	0.497	0.520	0.526	0.447	0.516	0.531	0.516	

Table 3.22: Fragility curve parameters in terms of Arias intensity – loose soil (railway embankments).

Loose soil (Dr = 0.35)	Soil ID	Fragility parameters	embankment height (crest width B = 24m)											
			2			4			6			8		
			ds1	ds2	ds3	ds1	ds2	ds3	ds1	ds2	ds3	ds1	ds2	ds3
S1	μ	1.710	4.020	12.402	1.064	2.271	6.229	0.924	1.900	5.020	0.870	1.632	3.799	
	σ	0.728	0.814	0.792	0.750	0.705	0.664	0.690	0.661	0.603	0.672	0.676	0.674	
S2	μ	1.173	2.571	8.609	0.865	1.790	5.053	0.833	1.637	4.256				
	σ	0.790	0.755	0.756	0.800	0.687	0.659	0.730	0.735	0.667				
S4	μ				2.564	9.197	44.771	1.582	4.105	13.301	0.935	1.728	4.013	
	σ				0.866	0.846	1.019	0.747	0.795	0.710	0.611	0.536	0.476	
S5	μ	4.497	14.448	78.546	1.728	4.634	13.196	1.245	2.963	8.984	1.065	2.049	5.166	
	σ	0.747	0.721	0.824	0.703	0.629	0.542	0.754	0.642	0.596	0.710	0.731	0.660	

All generated fragility curves for traffic embankments are gathered in appendices.

In **Figure 3.20** to **Figure 3.27**, the light green colour depicts fragility curves for minor damage (ds1), the blue colour for moderate damage (ds2) and the red colour for extensive damage (ds3). Variation of crest width, embankment height, soil profiles and relative soil density of liquefiable layer (L=loose and M=medium dense) are denoted by different line types.

In terms of serviceability, damage state “ds1” presents still useful road/railway with required speed reduction, while traffic is partially blocked for “ds2”, and totally disabled during repair works for “ds3”.

3.1.4.4.1 Road embankments

Effect of crest width

Comparison was done on a case with soil profile S1 and for 4 m high embankment. Fragility curves presented in **Figure 3.20** move to the right (vulnerability decreases) with increasing crest width for the studied range of crest widths (6, 12 and 24 m).



This project has received funding from the European Union's Horizon 2020 research and innovation programme under grant agreement No. 700748

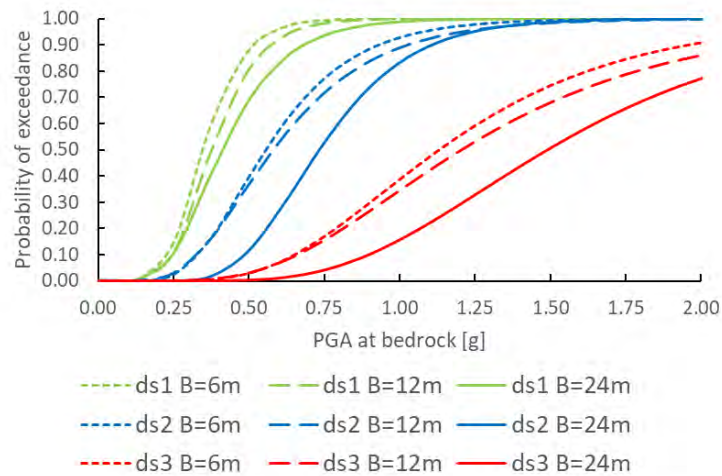


Figure 3.20: Fragility curves for different crest widths (road embankments).

Effect of embankment height

For this comparison, embankment with 24 m wide crest and built on soil profile S1 was analysed. Figure 3.21 expresses higher influence of embankment height on fragility curves than crest width, especially for extensive damage state (ds3). The higher the embankment, the higher are crest settlements.

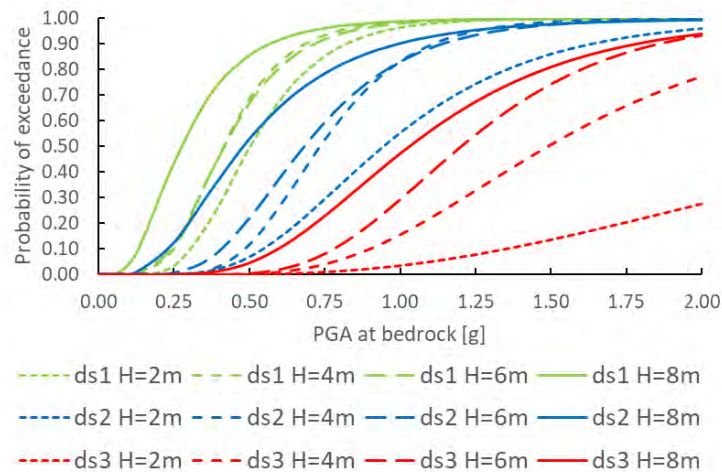


Figure 3.21: Fragility curves for different embankment height (road embankments).

Effect of thickness of liquefiable layer

Fragility curves in Figure 3.22 are based on results of numerical analyses, where embankment height was 4 m and crest width 24 m. Expectedly, thickness of liquefiable layer has great impact on soil/embankment response. Crest settlements increase and consequently fragility curves move to the left with increasing thickness of liquefiable layer (L = 2, 4 and 7 m). Even larger settlements were calculated in case without crust layer and 7 m thick liquefiable layer. Reliability of fragility curves for soil profile S5 and S4 for extensive



This project has received funding from the European Union's Horizon 2020 research and innovation programme under grant agreement No. 700748

damage state is very low, due to the lack of calculations where the embankment is subjected to more intense ground motions.

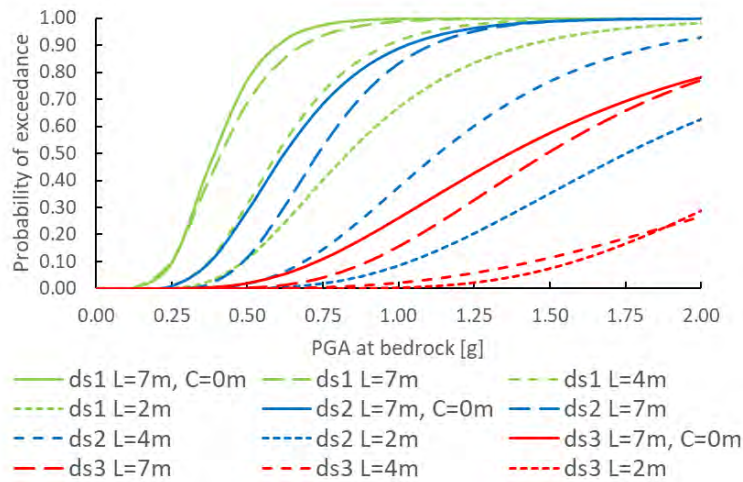


Figure 3.22: Fragility curves for different soil profiles (road embankments).

Comparison between “loose” and “medium dense” soil

Effect of soil density of the liquefiable layer is captured through fragility curves in **Figure 3.23**. The results of the models with S1 soil profile, 4 m high embankment and 24 m wide crest were examined. A greater potential for liquefaction and larger deformations of the embankment are expected for ground profile with loose sand, which is also confirmed by fragility curves in **Figure 3.23**.

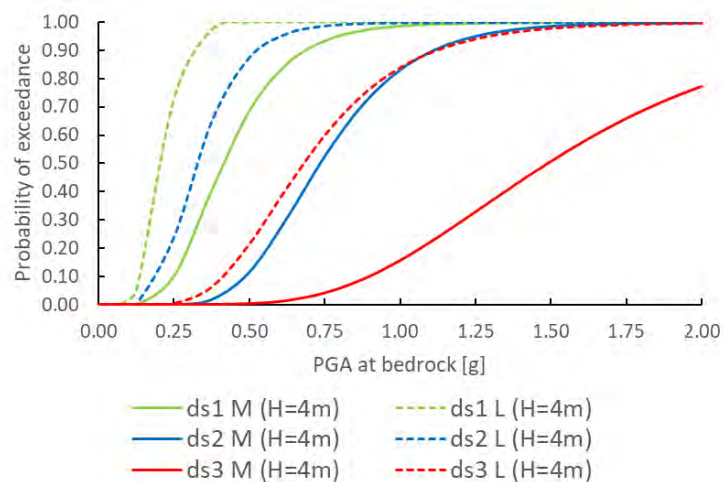


Figure 3.23: Fragility curves for different relative density of liquefiable sandy layer (road embankments).



This project has received funding from the European Union's Horizon 2020 research and innovation programme under grant agreement No. 700748

3.1.4.4.2 Railway embankments

Similar trends were obtained considering damage state criteria for railway embankments. However, all fragility curves for railway embankments are shifted to the left in relation to fragility curves for road embankments, due to more strict damage state criteria.

The effects of variations of the model geometry and material properties for liquefiable layer, expressed through fragility curves related to limit states for railway embankments, are gathered in **Figure 3.24** to **Figure 3.27**.

Effect of crest width

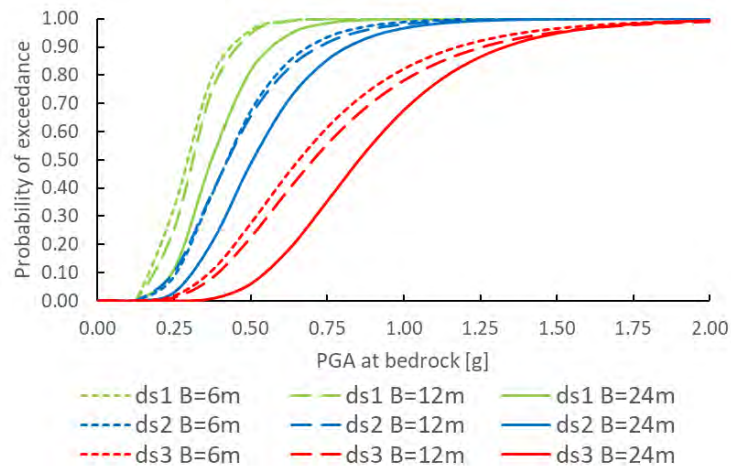


Figure 3.24: Fragility curves for different crest width (railway embankments).

Effect of embankment height

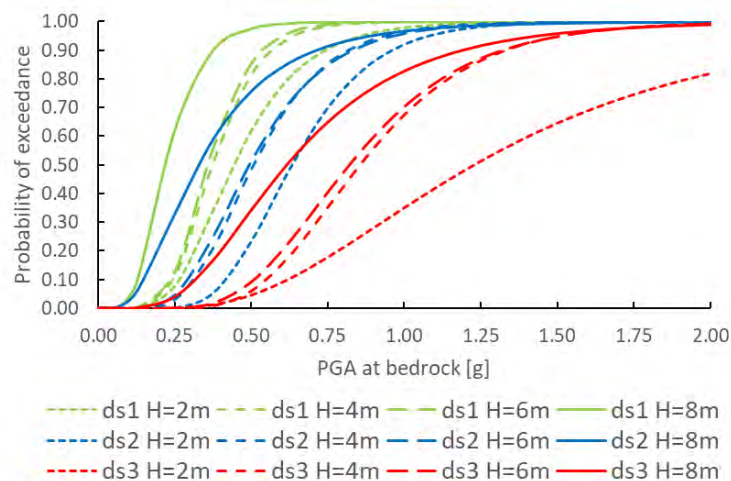


Figure 3.25: Fragility curves for different embankment height (railway embankments).



This project has received funding from the European Union's Horizon 2020 research and innovation programme under grant agreement No. 700748

Effect of thickness of liquefiable layer

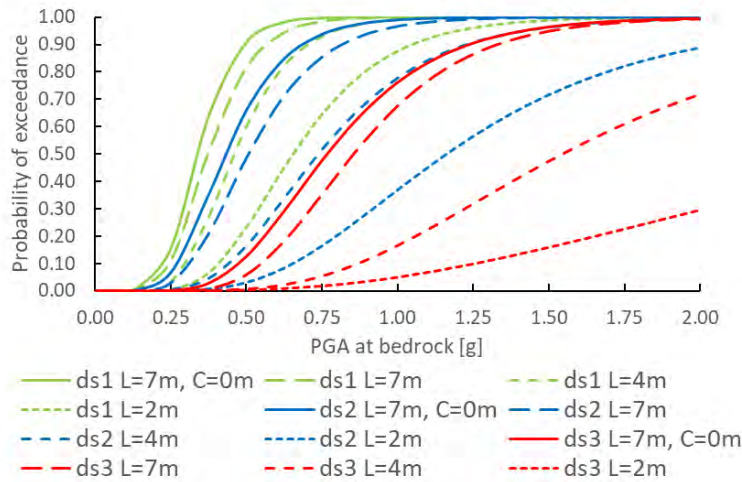


Figure 3.26: Fragility curves for different soil profiles (railway embankments).

Comparison between “loose” and “medium dense” soil

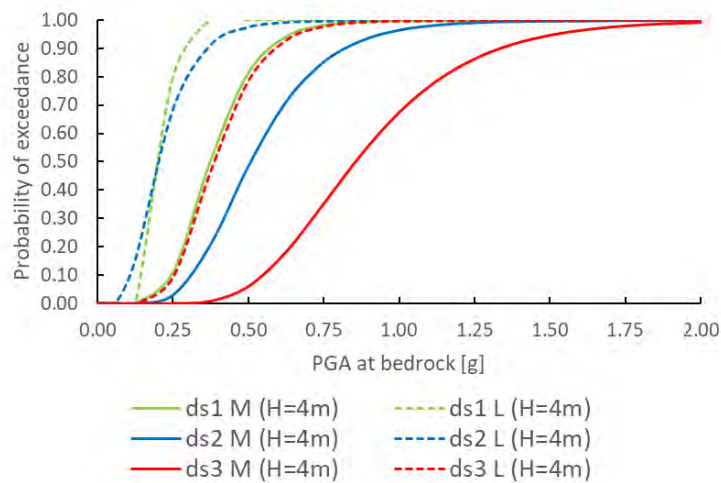


Figure 3.27: Fragility curves for different relative density in sandy layer (railway embankments).

3.1.4.4.3 Further considerations

Uncertainties of crest deformation shape

Although a set of 30 ground motions for each analysis were used to take account of variability of earthquake input data, a large amount of uncertainties remains due to the definition of damage states.

Besides threshold values of the limit states, the location of the observed point(s) is also important. From **Figure 3.28**, representing a deformed shapes of the embankment crest, it is evident that middle point is representative for the case B=6 m, while for B=24 m the choice of a representative point is a matter of



This project has received funding from the European Union's Horizon 2020 research and innovation programme under grant agreement No. 700748

discussion for a selected case. Both curves were obtained with same input data, except crest width. In most literature, it is not very clear what kind of a value (average, maximum, ...) is used in the analyses for describing the damage level (e.g. vertical displacement) and where exactly the value was taken. Argyroudis and Kaynia (2015) used the average crest settlements, measured at the edge and middle of the embankment surface. Nonetheless, according to the **Figure 3.28** this does not significantly (if in anyway) improve the problem exposed here.

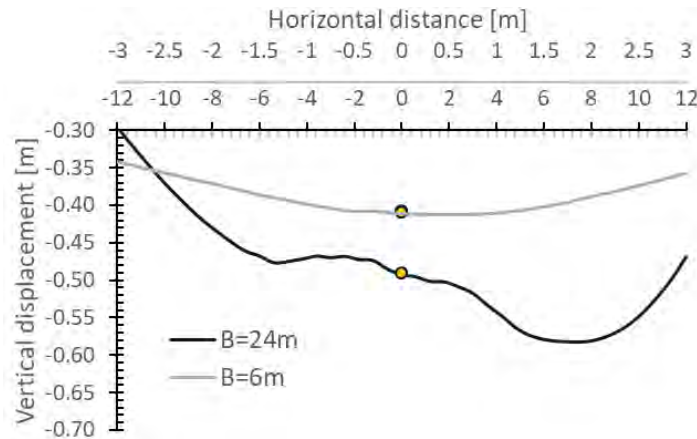


Figure 3.28: Crest deformation shapes for crest width $B = 6$ m and $B = 24$ m.

Fragility curves based on damages induced by lateral spreading

All the fragility curves presented in this report (except in this subsection) are based on the damage states defined by vertical displacement. Therefore, one of several possible alternatives for defining damage state criteria and derivation of respective fragility curve is briefly presented here. In many cases, lateral spreading is the main failure mechanism during liquefaction, where minor to significant horizontal movements are observed. Vertical displacement of the embankment crest in this situation can be very large or negligible.

Figure 3.29 to **Figure 3.32** present the fragility curves, where damage state is defined in terms of the difference between horizontal displacements of the left and the right edge point at crest and foundation level. Similar threshold values for damage states were used for the derivation of fragility curves – $ds1 = 10$ cm, $ds2 = 20$ cm and $ds3 = 40$ cm. Curves were prepared for the case with 2 m high embankment, underlain by 1 m crust and 2 m thick liquefiable layer at both density states (MD – $D_r=0.6$ and L – $D_r=0.35$).



This project has received funding from the European Union's Horizon 2020 research and innovation programme under grant agreement No. 700748

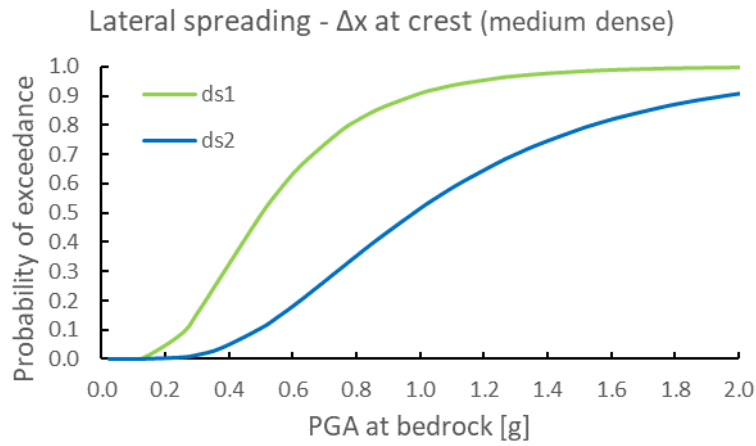


Figure 3.29: Fragility curves based on horizontal displacements - at crest and medium dense soil.

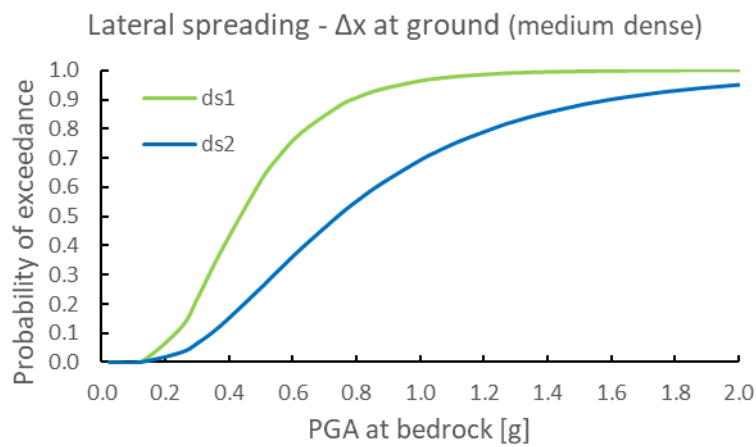


Figure 3.30: Fragility curves based on horizontal displacements - at ground level and medium dense soil.

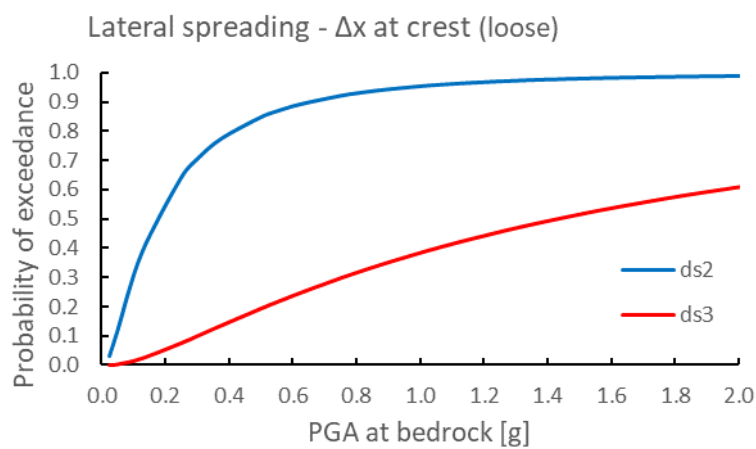


Figure 3.31: Fragility curves based on horizontal displacements - at crest and loose soil.



This project has received funding from the European Union's Horizon 2020 research and innovation programme under grant agreement No. 700748

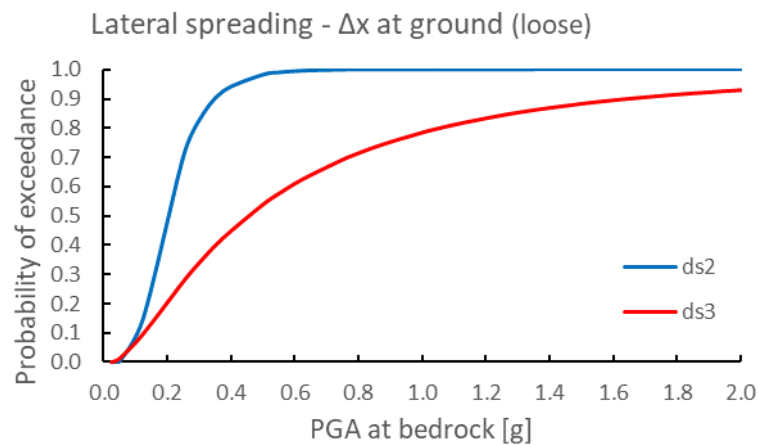


Figure 3.32: Fragility curves based on horizontal displacements - at ground level and loose soil.

3.1.4.5 The use of Artificial Neural Networks for the assessment of fragility curves

7200 numerical analyses were required to obtain fragility curves for just 30 combinations of embankment and ground geometry and 2 variations of material properties of liquefiable soil (**Table 3.12**). In order to check whether interpolation between analysed cases is possible by artificial neural networks (ANN), a study was made using the results of all available computations by FLAC. This additional study was carried out mainly for the following two reasons:

- Numerical analyses are very time consuming. Only a small part of countless possible variations of geometry and soil parameters were simulated using FLAC software. Moreover, for the derivation of fragility curve a set of analyses with different ground motions is needed on the same ground-embankment model, which considerably increases the duration of numerical analyses. Artificial neural networks as universal approximation functions could be used either (i) for the decrease of number of calculations for single geometry by interpolating for additional seismic excitations or (ii) for the derivation of parameters of fragility functions for an unknown geometry based on numerical results for known geometries.
- Within the framework of the LIQUEFACT project, a software package is being developed by NORSAR to allow the user to obtain a preliminary vulnerability assessment, including fragility curves. Since this serves mainly for a preliminary assessment of the response of the observed structure (e.g. traffic embankment) without detailed knowledge on ground properties, the use of less accurate methods (eg. ANN) can still be used for an estimation of fragility curve parameters.

Here we only present the methodology and results of the feasibility study on the performance of ANN for the above purpose. Should the approach yield satisfactory and promising results, further development will be made within WP 6.

For the purpose of ANN simulations Python programming language was used with its module Scikit – learn (Python machine learning library).



This project has received funding from the European Union's Horizon 2020 research and innovation programme under grant agreement No. 700748

3.1.4.5.1 Training data and pre-processing

Initially, results from all performed analyses in FLAC were gathered in a single table and used as a training set in ANN study. 15 distinct model geometries for 2 different material parameters and 30 ground motions with 8 intensity levels give us total of 7200 examples (**Table 3.12**). Since the initial trials have shown that 7200 cases are hardly enough for satisfactory ANN predictions, training set was enlarged with intermediate results at selected values of Arias intensity (0.1, 0.2, 0.4, 0.8, 1.6, 3.2, 6.4, 12.8 and 25.6), which gave a total of 51915 input-output sets of data. This can be justified by the observation that vertical displacement at top middle point of embankment ceases to increase as soon as the seismic excitation is stopped (see **Figure 3.11 a**) as an example). Hence, any current settlement of embankment may be considered as a good estimate of permanent settlement if the seismic excitation stops at that moment. This initial set of data with 51915 input-output pairs is referred to as data set 1.

Embankment height (2, 4, 6 and 8 m), crest width (6, 12, 24 m), thickness of crust layer (0 and 1 m), thickness (2, 4 and 7 m) and relative density (0.35 and 0.6) of liquefiable layer were all used as input parameters as well as PGA at bedrock, ground motion duration and Arias intensity. Permanent vertical displacement at the top middle point of the embankment was chosen as output parameter in ANN study.

All the data used in ANN procedure were standardized by the following equation $z = \frac{x - \hat{x}}{\sigma}$ (where \hat{x} represents the mean value of every input parameter x and σ its variance), due to the neural network scale dependency.

In the following, two different ANN techniques were examined: regression and classification. Based on the guidelines from the literature (Heaton, 2008), 10 and 7 hidden neurons within one hidden layer for regression and classification technique, respectively, were used according to the recommendations below:

- the number of hidden neurons should be between the size of the input and output layer,
- the number of hidden neurons should be $2/3$ of the size of input layer, plus the size of the output layer,
- the number of hidden neurons should be less than twice the size of the input layer.

The following notation and parameters are used for the evaluation of ANN model performance:

ANN Regression:

- X^{in}, X^{out} – input and output training set,
- Y^{in}, Y^{out} – input and output test set (set for predicted values for Y^{in} is denoted as Y^{pred}),
- I – number of input parameters,
- O – number of output parameters,
- N – number of train examples,
- M – number of test examples.
- Coefficient of determination for all parameters at once:



This project has received funding from the European Union's Horizon 2020 research and innovation programme under grant agreement No. 700748

$R^2 = 1 - \frac{u}{v}$, where $u = \sum_{i=0}^M \sum_{j=0}^O (Y_{ij}^{out} - Y_{ij}^{pred})^2$ and $v = \sum_{i=0}^M \sum_{j=0}^O (Y_{ij}^{out} - \hat{Y}^{out})^2$. With \hat{Y}^{out} the average value of Y^{out} is denoted, so $\hat{Y}^{out} = \sum_{i=0}^M \sum_{j=0}^O \frac{Y_{ij}^{out}}{MO}$. It can be easily seen that $R^2 \in (-\infty, 1)$, which means that 1 is the highest possible score obtained when a prediction of single value of every parameter is exactly correct. Score 0 implies, that our model is as good as the model that constantly predicts average value \hat{Y}^{out} and negative values mean that prediction is even worse.

- Coefficient of determination for single output parameter:

$R_j^2 = 1 - \frac{u_j}{v_j}$, where $u_j = \sum_{i=0}^M (Y_{ij}^{out} - Y_{ij}^{pred})^2$, $v_j = \sum_{i=0}^M (Y_{ij}^{out} - \hat{Y}^{out})^2$ and $\hat{Y}^{out} = \sum_{i=0}^M \frac{Y_{ij}^{out}}{M}$ is the average value of j th parameter.

- Average distance from true value for every parameter:

$$\Delta \hat{Y}_j^{out} = \frac{1}{M} \sum_{i=0}^M |Y_{ij}^{out} - Y_{ij}^{pred}|.$$

- Maximum distance from true value for every parameter:

$$\max_i (\Delta Y_{ij}^{out}) = \max_i |Y_{ij}^{out} - Y_{ij}^{pred}|.$$

- Percentage of examples for which $|Y_{ij}^{out} - Y_{ij}^{pred}| > c$, where c represents selected threshold for the parameter. Under this work $c \in \{0.03, 0.05, 0.1, 0.15, 0.2, 0.5 \text{ and } 1 \text{ meter}\}$. The percentage for the lower threshold value should always be bigger or equal to the percentage of higher threshold, since we are always counting all examples.

ANN Classification:

- M_i – number of correct classification for class i ,
- N_i – number of all examples that would have to be classified in class i .
- $A_i = \frac{M_i}{N_i}$ – accuracy of classification for each class,
- $A = \frac{M_0 + M_1}{N_0 + N_1}$ – total accuracy of the model.

After first training and testing of ANN with initial data set described above, two further data sets with different geometries were prepared by FLAC software with 957 and 775 new examples. Input parameters for additional numerical analyses are summarized in **Table 3.23** and **Table 3.24**.

The reason for using these additional data sets comes from the intended use of ANN within LRG software. Most likely scenario for the user of LRG software will be that fragility curves for the specific ground conditions and embankment geometry for the actual case will not be available. Therefore, ANN will be employed to predict the fragility curves for unseen combination of data. The more the actual data differ from the data, for which the fragility curves are available, the larger errors in ANN predictions are expected. Hence, the question is, how much can we improve such ANN prediction by including just few calculations (2 to 5) on real geometry in ANN training set. Based on this reasoning, the data sets 2 and 3 (**Table 3.23** and **Table 3.24**) contain geometries that are different from those in original data set 1. However, data sets 2 and 3 contain same geometries and material properties with different seismic records and different PGA as can be seen by comparing **Table 3.23** and **Table 3.24**. The procedure will be as follows:



This project has received funding from the European Union's Horizon 2020 research and innovation programme under grant agreement No. 700748

1. Train the ANN with data set 1
2. Test the ANN on cases from data set 2 and 3
3. Include data set 2 into training data set
4. Test the ANN on cases from data set 3

Table 3.23: Additional numerical analyses data set 2.

Embankment height	Crest width	Thickness of crust	Thickness of liquefiable layer	Relative density of liq. layer	Intensity level (max PGA of input GM)	Ground motions
(m)	(m)	(m)	(m)	Dr (%)	(g)	
2	6	1	7	0.6	0.25 & 0.75	1, 2, 13, 20, 27
2	6	1	7	0.35	0.25 & 0.75	1, 2, 13, 20, 27
2	12	1	7	0.6	0.25 & 0.75	1, 2, 13, 20, 27
2	12	1	7	0.35	0.25 & 0.75	1, 2, 13, 20, 27
4	6	4	7	0.6	0.375 & 0.625	8, 13, 27
4	6	8	7	0.6	0.375 & 0.625	8, 13, 27
4	12	4	7	0.6	0.375 & 0.625	8, 13, 27
4	12	8	7	0.6	0.375 & 0.625	8, 13, 27
4	12	1	15	0.6	0.25, 0.625 & 0.75	5, 13
4	24	1	15	0.6	0.25, 0.625 & 0.75	5, 13
6	6	1	7	0.6	0.25 & 0.625	5, 8, 13, 22, 27
6	6	1	7	0.35	0.25 & 0.625	5, 8, 13, 22, 27
6	12	1	7	0.6	0.25 & 0.625	5, 8, 13, 22, 27
6	12	1	7	0.35	0.25 & 0.625	5, 8, 13, 22, 27
6	12	4	7	0.6	0.375 & 0.75	13, 18, 27
6	12	8	7	0.6	0.375 & 0.75	13, 18, 27
6	24	4	7	0.6	0.375, 0.75 & 1.5	13, 18, 27
6	24	8	7	0.6	0.375, 0.75 & 1.25	13, 18, 27



This project has received funding from the European Union's Horizon 2020 research and innovation programme under grant agreement No. 700748

Table 3.24: Additional numerical analyses data set 3.

Embankment height	Crest width	Thickness of crust	Thickness of liquefiable layer	Relative density of liq. layer	Intensity level (max PGA of input GM)	Ground motions
(m)	(m)	(m)	(m)	Dr (/)	(g)	
2	6	1	7	0.6	0.375 & 1.0	3, 20, 21
2	6	1	7	0.35	0.375 & 1.0	3, 20, 21
2	12	1	7	0.6	0.375 & 1.0	3, 20, 21
2	12	1	7	0.35	0.375 & 1.0	3, 20, 21
4	6	4	7	0.6	0.25 & 0.75	8, 13, 22
4	6	8	7	0.6	0.25 & 0.75	8, 13, 22
4	12	4	7	0.6	0.25 & 0.75	8, 13, 22
4	12	8	7	0.6	0.25 & 0.75	8, 13, 22
4	12	1	15	0.6	0.375, 0.5 & 1.25	3, 5, 12
4	24	1	15	0.6	0.375, 0.5 & 1.25	3, 5, 12
6	6	1	7	0.6	0.375 & 1.0	16, 23, 27
6	6	1	7	0.35	0.375 & 1.0	16, 23, 27
6	12	1	7	0.6	0.375 & 1.0	16, 23, 27
6	12	1	7	0.35	0.375 & 1.0	16, 23, 27
6	12	4	7	0.6	0.25, 0.625 & 1.0	12, 18
6	12	8	7	0.6	0.25, 0.625 & 1.0	12, 18
6	24	4	7	0.6	0.25, 0.625 & 1.0	12, 18
6	24	8	7	0.6	0.25, 0.625 & 1.0	12, 18

3.1.4.5.2 ANN simulations: Regression and Classification technique

In general, neural network for regression and classification are very similar. Using the regression technique, we will predict the value of e.g. embankment settlement for a given set of material and geometrical data. By using ANN for classification, the output will only say whether the result is below or above a given threshold parameter. However, this is precisely what we need for the development of fragility curves.

Main difference between both approaches is the choice of loss function and activation function for the output layer. Squared loss function and linear activation function were used in regression technique, while logarithmic loss function and logistic activation function were selected for classification. The logic in the background is to predict the result as a real number for regression and as a value between 0 and 1 for classification which will determine the class of input according to whether the value is bigger or smaller than a certain threshold value. As an upgrade to the classification technique, the classification results (p) were interpreted as probabilities for input being in a class 1 and consequently, $(1-p)$ probabilities for input being in class 0.



This project has received funding from the European Union's Horizon 2020 research and innovation programme under grant agreement No. 700748

3.1.4.5.2.1 ANN regression technique

Performance on random unseen sample

As a first attempt, a comparison was made between the true and predicted vertical displacement at embankment crest, using 80 % of randomly selected examples out of all 52000 cases from data set 1 for training set and 20 % for the test set. **Figure 3.33** shows a satisfactory match between the predicted values and results from numerical analyses. Note however, that in this case the training set included data points from all geometries and all seismic records.

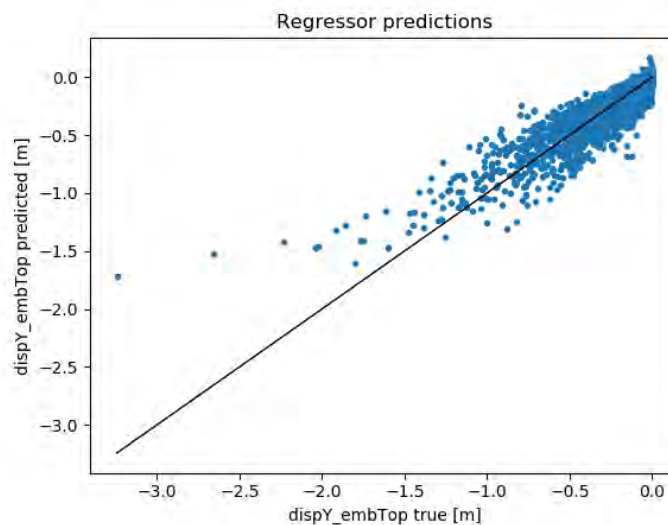


Figure 3.33: Predicted versus true results on the 20 % of the data as test set.

In the next phase, the impact of the data set size was analysed. For this purpose evaluation diagram was prepared (**Figure 3.34**), where top left graph shows R^2 , top right graph average miss of the parameter, bottom left graph maximum error of parameter and bottom right graph percentage of exceedance the true value for more than the selected threshold value (c). All graphs are shown with respect to the size of the training set expressed as a ratio between training set and full size of the data set – $\left| \frac{D_t}{D} \right|$.

Figure 3.35 shows similar graphs for the case where training and testing data sets were formed in such a way that all the results of single FLAC analyses were always either in training or testing set. One can observe that the results are not much different from those in **Figure 3.34**.



This project has received funding from the European Union's Horizon 2020 research and innovation programme under grant agreement No. 700748

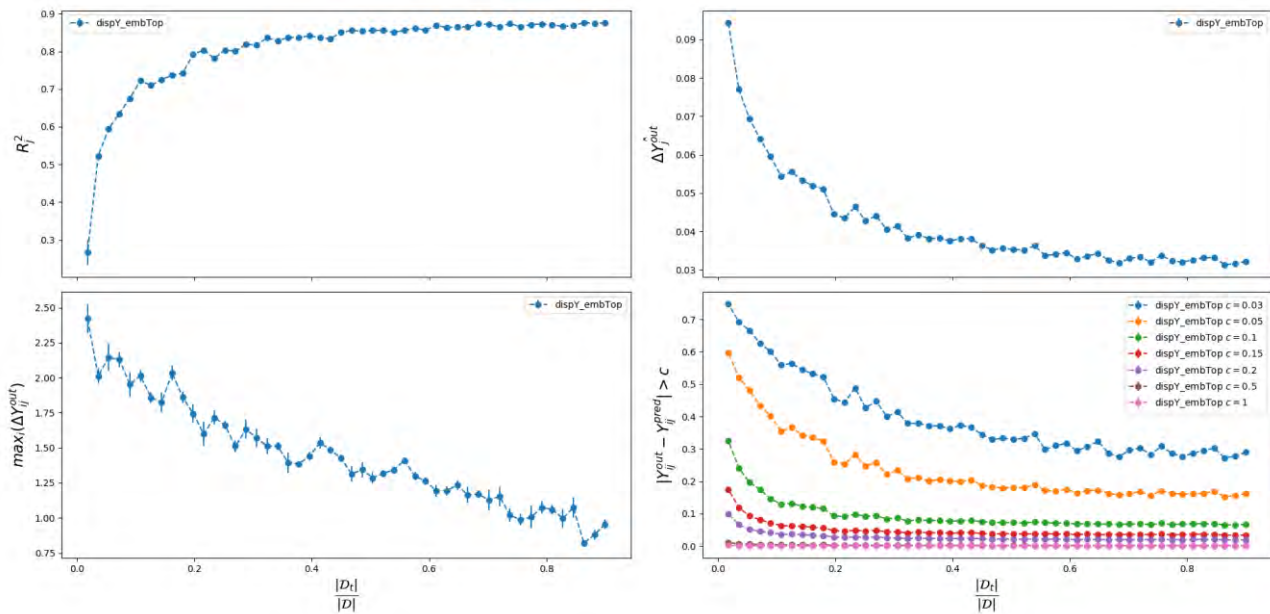


Figure 3.34: Evaluation diagram for data set 1. Graphs show the performance of ANN with respect to the percentage of data included in training set (D_t/D). Subdivision into training and testing data set is made randomly.

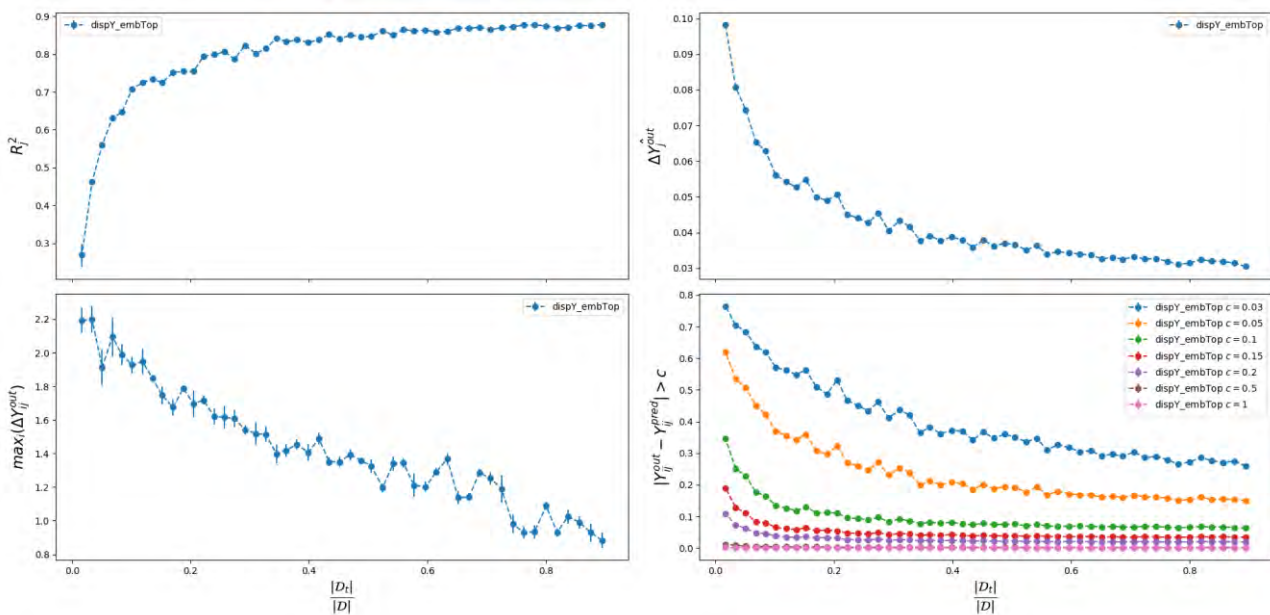


Figure 3.35: Evaluation diagram for data set 1. Graphs show the performance of ANN with respect to the percentage of data included in training set (D_t/D). Subdivision into training and testing data set is made randomly under condition that all data points from single FLAC analysis are included either in training or in testing data set.

From the evaluation diagrams shown in **Figure 3.35** it can be seen that saturation happened approximately at $\frac{|D_t|}{|D|} = 0.65$. This result means that similarly good results for fragility curves can be obtained by performing just 65% of FLAC analyses for certain geometry. The additional 35% of results can be obtained by trained



This project has received funding from the European Union's Horizon 2020 research and innovation programme under grant agreement No. 700748

ANN. From the bottom right graph in **Figure 3.35** one can observe that 70% of predictions miss the true value by less than 3 cm and 80 % by less than 5 cm. On the basis of the above findings, further analyses were performed taking into account 65 % and 35 % of available data for the training and testing set, respectively.

Performance on unseen geometry

The next more demanding task for the ANN was the prediction of embankment settlements and subsequent derivation of fragility curves for the ground and/or embankment geometry that was not previously seen by ANN. The subdivision into training and testing data set was made in such a way that one entire geometry of the analysed cross section with all 240 seismic excitations (30 records by 8 PGA values) was only considered for testing the ANN performance and was not included in the training data set. The results are presented in **Figure 3.36** as parameters of all 30 fragility curves and in **Figure 3.37** as examples of fragility curves for four selected geometries (two sets of fragility curves with poor and two with satisfactory performance). The detailed description of the model geometry in each graph can be deduced from the title of each particular graph, where: H – embankment height, B – crest width, C – thickness of crust layer, L – thickness of liquefiable layer, D_R – relative density of liquefiable layer, and S1, S2 or S3 represents damage states for highway (H) or railway (R) embankment. The same notation is used on similar graphs below.

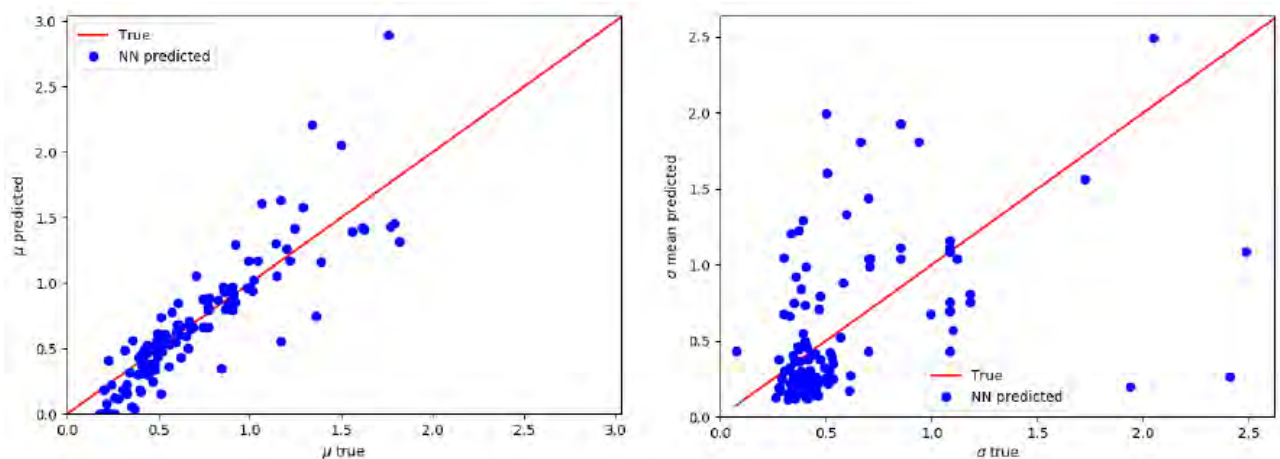


Figure 3.36: Fragility curve fitting parameters μ and σ for unseen geometry and regression technique.



This project has received funding from the European Union's Horizon 2020 research and innovation programme under grant agreement No. 700748

Methodology for the liquefaction fragility analysis of critical structures and infrastructures: description and case studies

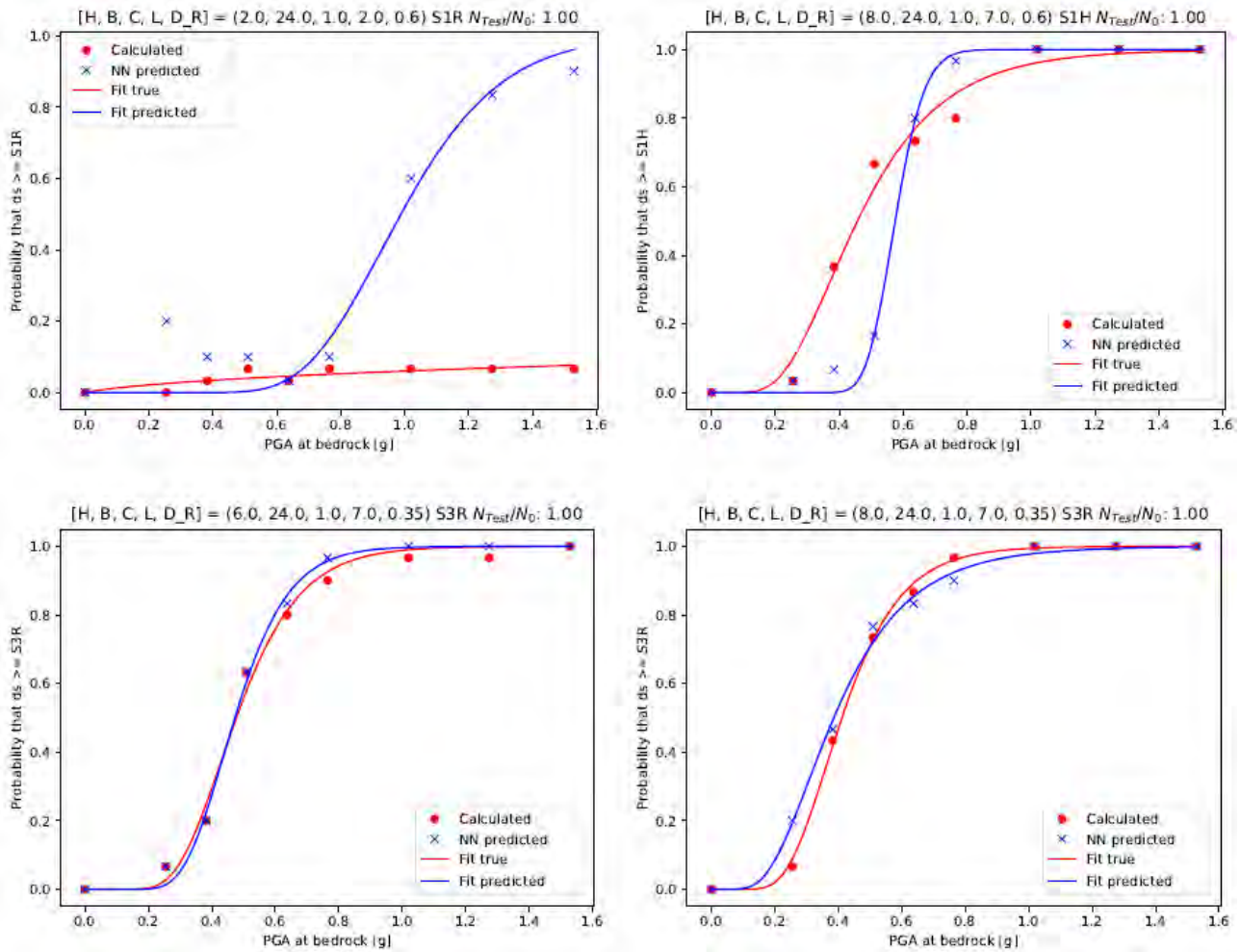


Figure 3.37: Examples of fragility curves for unseen geometry and regression technique.

Figure 3.38 presents the ANN predictions by regression technique in terms of embankment settlements for another four selected cases of geometries from the data set 1.

Finally, let us test the ANN performance on unseen geometry by data sets 2 and 3. Initial ANN training is performed on entire data set 1 and both additional data sets 2 and 3 are used for testing. The result is shown in Figure 3.39 and the performance is poor. Considerable improvement of ANN performance is obtained if only few (2 to 5) numerical results with different seismic records are included in training data set for unseen geometry (Figure 3.40). We can suppose that with larger data base of numerical results including a larger variety of geometrical situations and material properties ANN performance will further improve.



This project has received funding from the European Union's Horizon 2020 research and innovation programme under grant agreement No. 700748

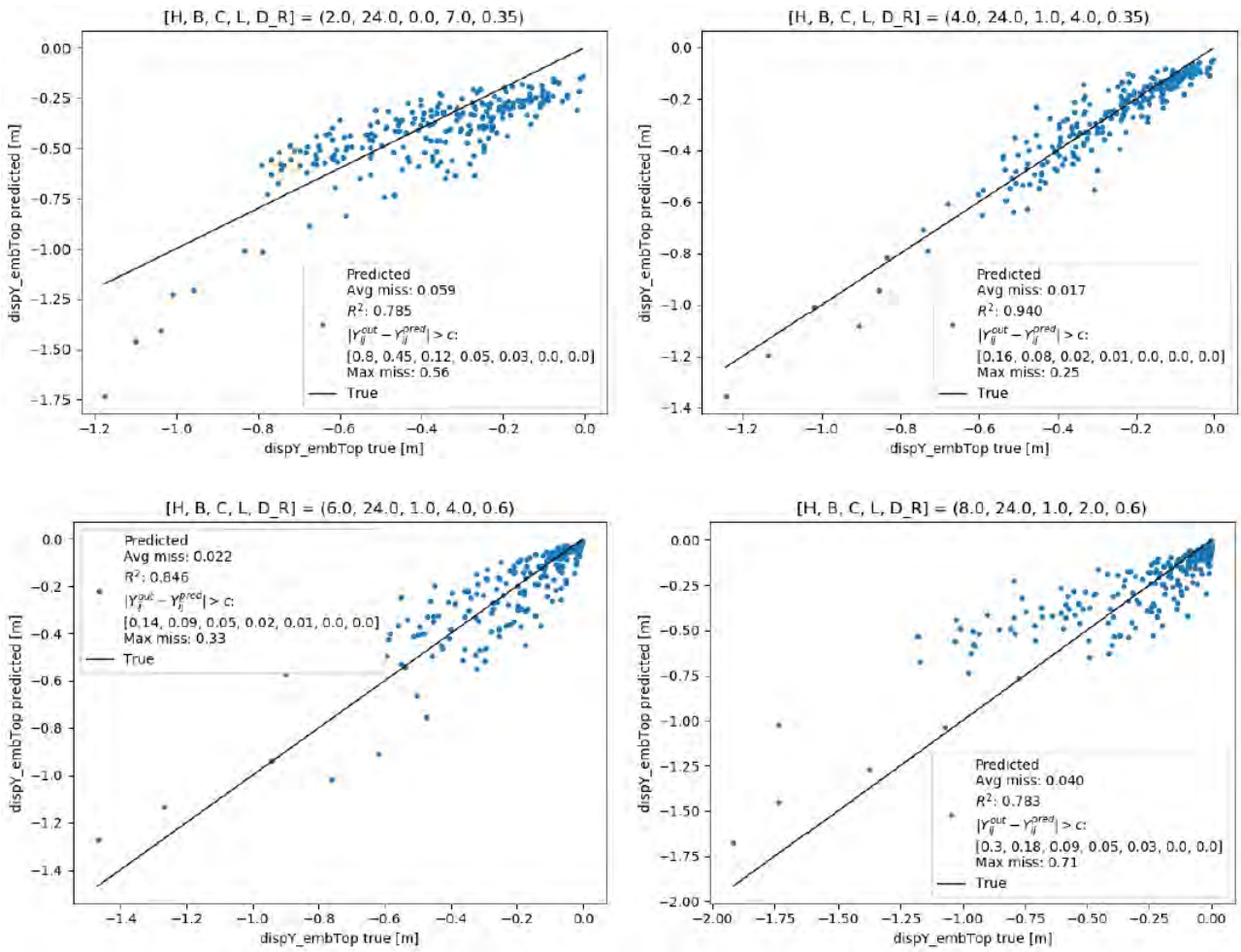


Figure 3.38: Examples of ANN predictions of embankment settlement by regression technique for unseen geometry.

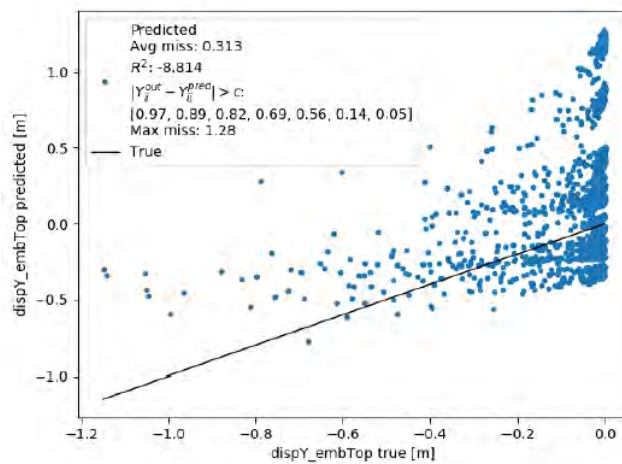


Figure 3.39: ANN predictions of embankment settlement by regression technique for data sets 2 and 3 based on training with data set 1.



This project has received funding from the European Union's Horizon 2020 research and innovation programme under grant agreement No. 700748

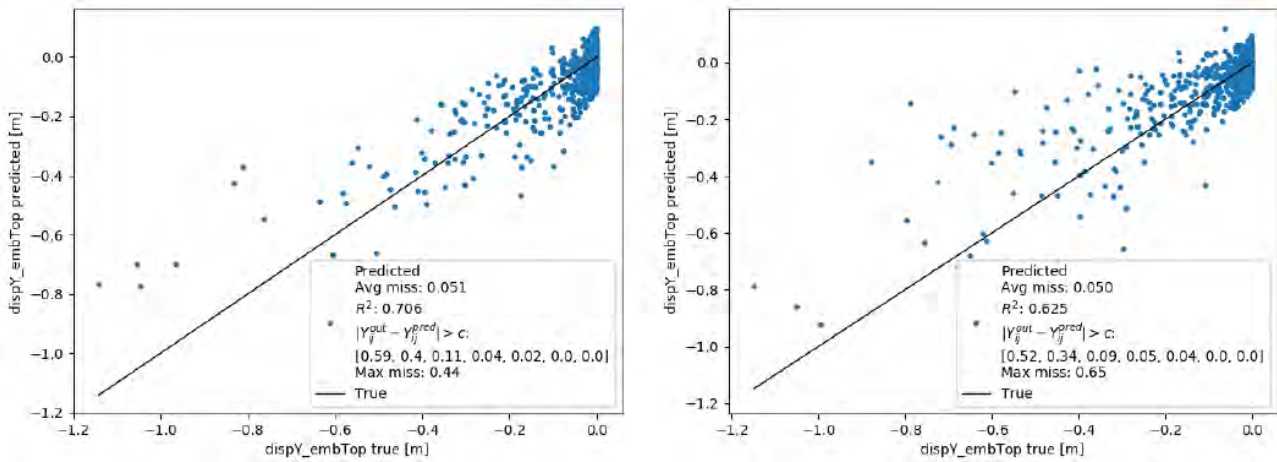


Figure 3.40: ANN predictions of embankment settlement by regression technique for unseen geometry. Left: prediction for data set 3 based on training with data sets 1 and 2. Right: prediction for data set 2 based on training with data sets 1 and 3.

3.1.4.5.2.2 ANN classification technique

The second approach was with neural networks as classifiers. The main differences from the regression technique is the use of logistic activation function for the output layer instead of linear one and logarithmic loss function. In such a way, output values will always be in between 0 and 1, therefore we can interpret them as probability for falling in certain class. This approach is usually more stable on small training set as in our case and generalizes better.

We will apply the classification technique as follows. For fragility curve, we need to know probability that permanent vertical displacement at the top middle of the embankment will be larger or smaller than some pre-set threshold value. We will label each dataset according to the threshold value. Those datasets that have vertical displacement larger than threshold value will go to class 1 and the ones below the threshold value to class 0. At the end, we can get the points for fragility curves by assessing the probability based on counting datasets in each class. On the graphs below, these results are referred to as “NN predicted”.

In interpretation of the ANN classification results we have used also an alternative approach. The output from ANN for certain dataset will rarely be exactly 0 or 1. We can interpret the output result as a probability that dataset belongs to a certain class. With such definition, we will develop fragility curves in alternative – “probabilistic” way. Instead of just checking the label (0 or 1) we will check the probability p that input falls in the class 1. Then, we will put the example in class 1 with probability p and in class 0 with probability $(1-p)$. On the graphs below, these results are referred to as “probabilistic”.

An important difference from regression technique is, that now we always need to label the data. To do that, we have to choose the damage state with its threshold value in advance.

We used the recommended number of hidden layers (1) and number of neurons in hidden layer (7), since we have 9 input variables and just one output parameter.



This project has received funding from the European Union's Horizon 2020 research and innovation programme under grant agreement No. 700748

For the evaluation of ANN performance, two parameters A and A_i were used, which are defined in paragraph 3.1.4.5.1.

Performance on random unseen sample

We have tested the classification technique by excluding 35 % of complete FLAC analyses from training data set. These 35 % of results formed the testing data set.

The results are presented in **Figure 3.41** as a comparison of true and ANN predicted fitting parameters for fragility curves and in **Figure 3.42** in terms of fragility curves for some selected typical cases. Four different types of interpretation of results are shown for comparison:

- Red line: true results from FLAC analyses using 100% of datasets. Shown for comparison.
- Green dots: true results from FLAC analyses using just the training set (65% of datasets). Shows the deterioration of results if we reduce number of calculations by 35 %.
- Blue dots: fragility curves are generated from the data of training set plus the results of ANN predictions on testing data set. This case simulates the methodology where number of FLAC analyses is reduced and the “missing” results are provided by trained ANN.
- Magenta dots: as in previous case, only that the output of ANN classification is considered as probability that input belongs to class 1.

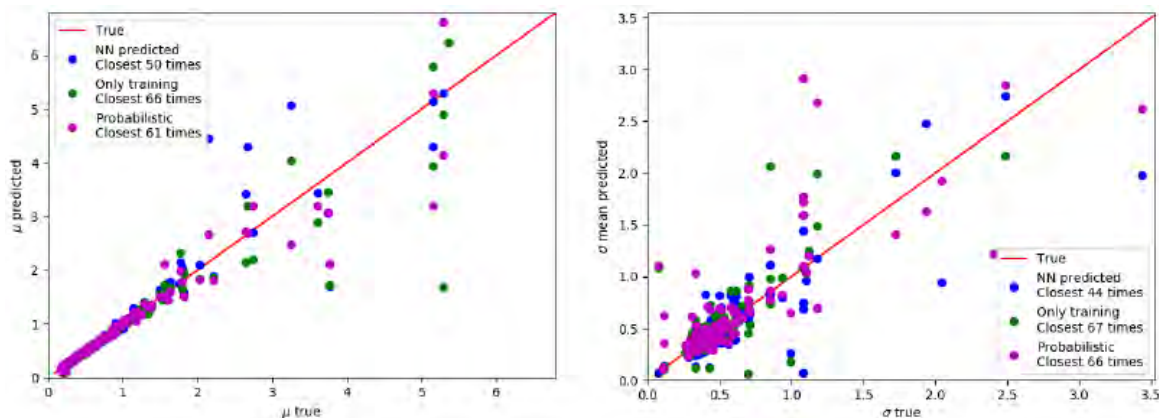


Figure 3.41: Fragility curve fitting parameters μ and σ – unseen random samples and classification technique.



This project has received funding from the European Union's Horizon 2020 research and innovation programme under grant agreement No. 700748

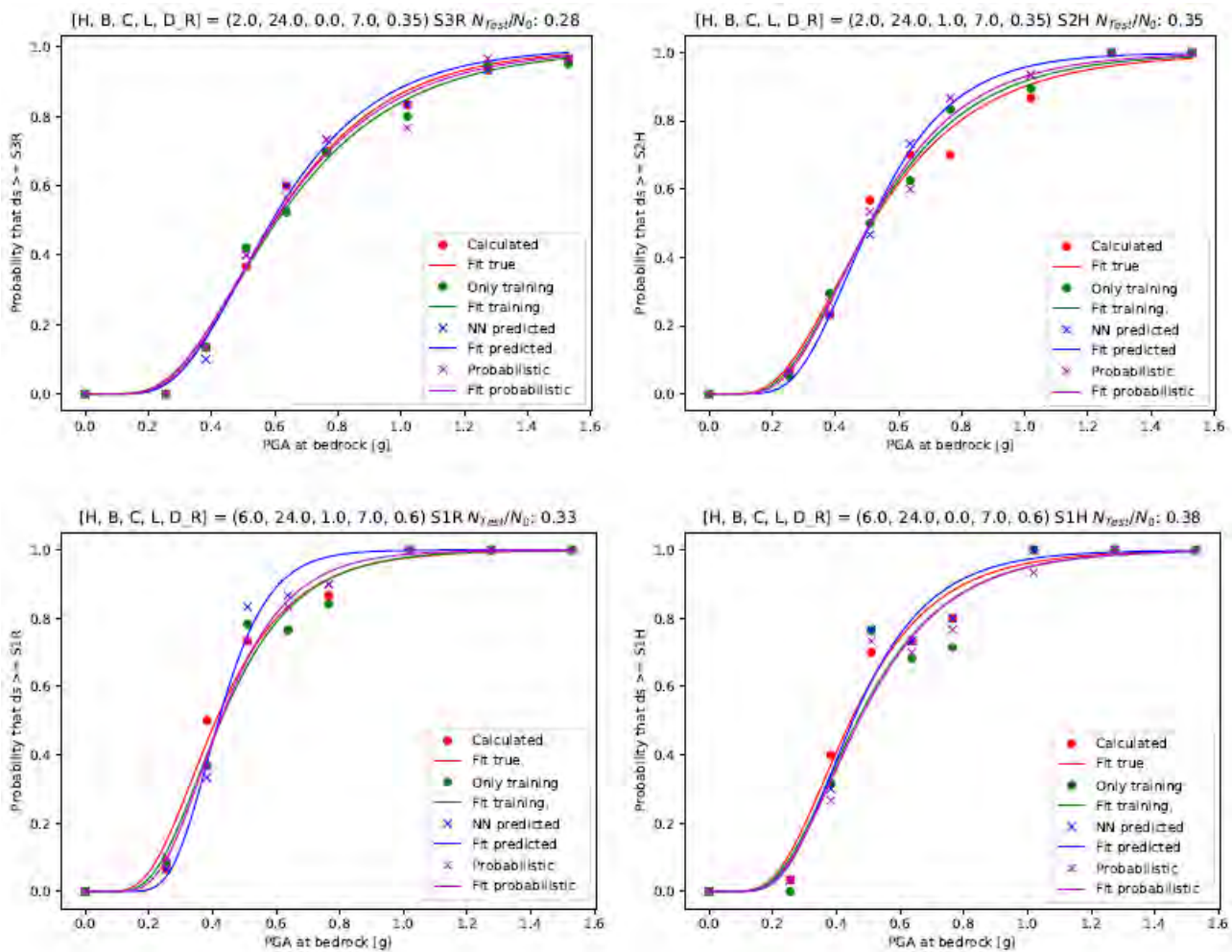


Figure 3.42: Examples of fragility curves μ and σ – unseen random samples and classification technique.

After these promising results, we can test the ANN for the performance on random unseen geometry.

Performance on random unseen geometry

In previous chapter, the ANN was asked to predict the result for cases not directly included in training set although the training set included the same geometry with different earthquake excitations and same earthquake loading with different geometries. Here, we are going to test the ANN performance for cases that were completely excluded from training data set. This situation is closer to the intended use of ANN – the prediction of fragility curves for new geometrical situations based on database of existing results obtained by numerical analyses.

The performance of ANN in this case was tested in such a way that one complete geometry with all 240 numerical calculations is removed from training set and is only used for testing. The results are presented in **Figure 3.43** in terms of fitting parameters for fragility curves. For some combination of geometry, seismic loading and threshold value for selected damage state we don't have enough points for fragility curves along



This project has received funding from the European Union's Horizon 2020 research and innovation programme under grant agreement No. 700748

the entire range of probabilities. Therefore, **Figure 3.43** only presents those cases for which the difference between maximum and minimum probability of exceedance of given damage state is >0.6 . From this figure we can also note that the alternative “probabilistic” approach performs better.

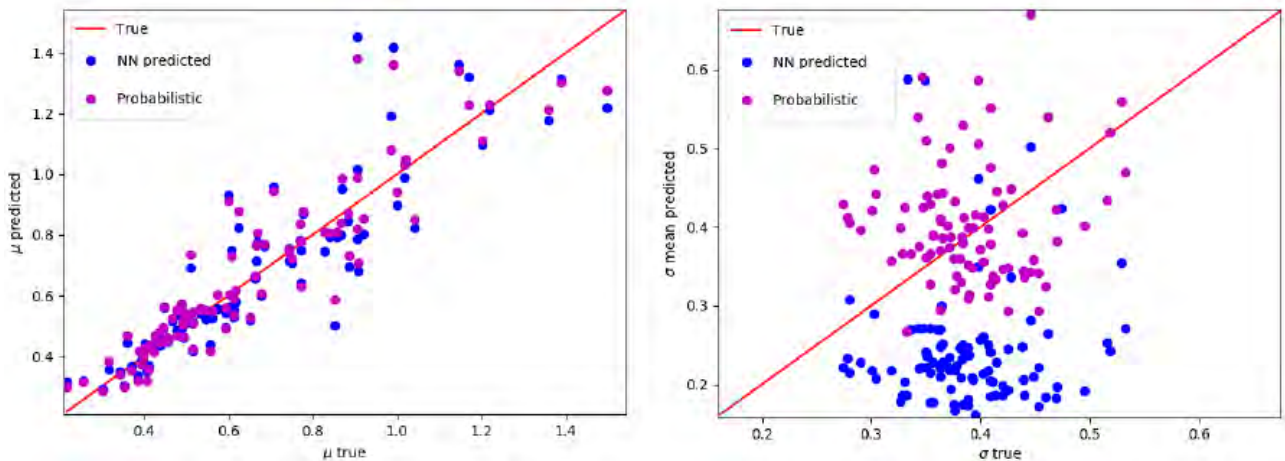


Figure 3.43: Fragility curve fitting parameters μ and σ – unseen geometry and classification technique.

The final test for the classification technique was to predict the results for data sets 2 and 3 based on training with data set 1. Obviously, for cases from data sets 2 and 3 we cannot produce fragility curves since only 5 to 8 different seismic records were used on individual ground and embankment geometry. It was only possible to check whether the individual result has been classified correctly with respect to selected threshold value.

With two prediction classes we have 4 possible outcomes:

- True class 1, predicted class 1
- True class 0, predicted class 1
- True class 1, predicted class 0
- True class 0, predicted class 0

For the graphical representation of results, the confusion matrix was used. In order to allow the comparison with regression technique, confusion matrices are produced for both techniques and are presented in parallel in **Figure 3.44** for highway embankments and in **Figure 3.45** for damage state criteria for railways. From both figures it can be observed that the classification technique produces much better results than regression. Out of 1730 cases, classifier wrongly predicted maximum 195 cases or 11 %. The regression method made wrong prediction in 17 % of cases when it performed best. On average, classification method was successful in 92% of cases while the regression only in 56% of cases with previously unseen geometry.



This project has received funding from the European Union's Horizon 2020 research and innovation programme under grant agreement No. 700748

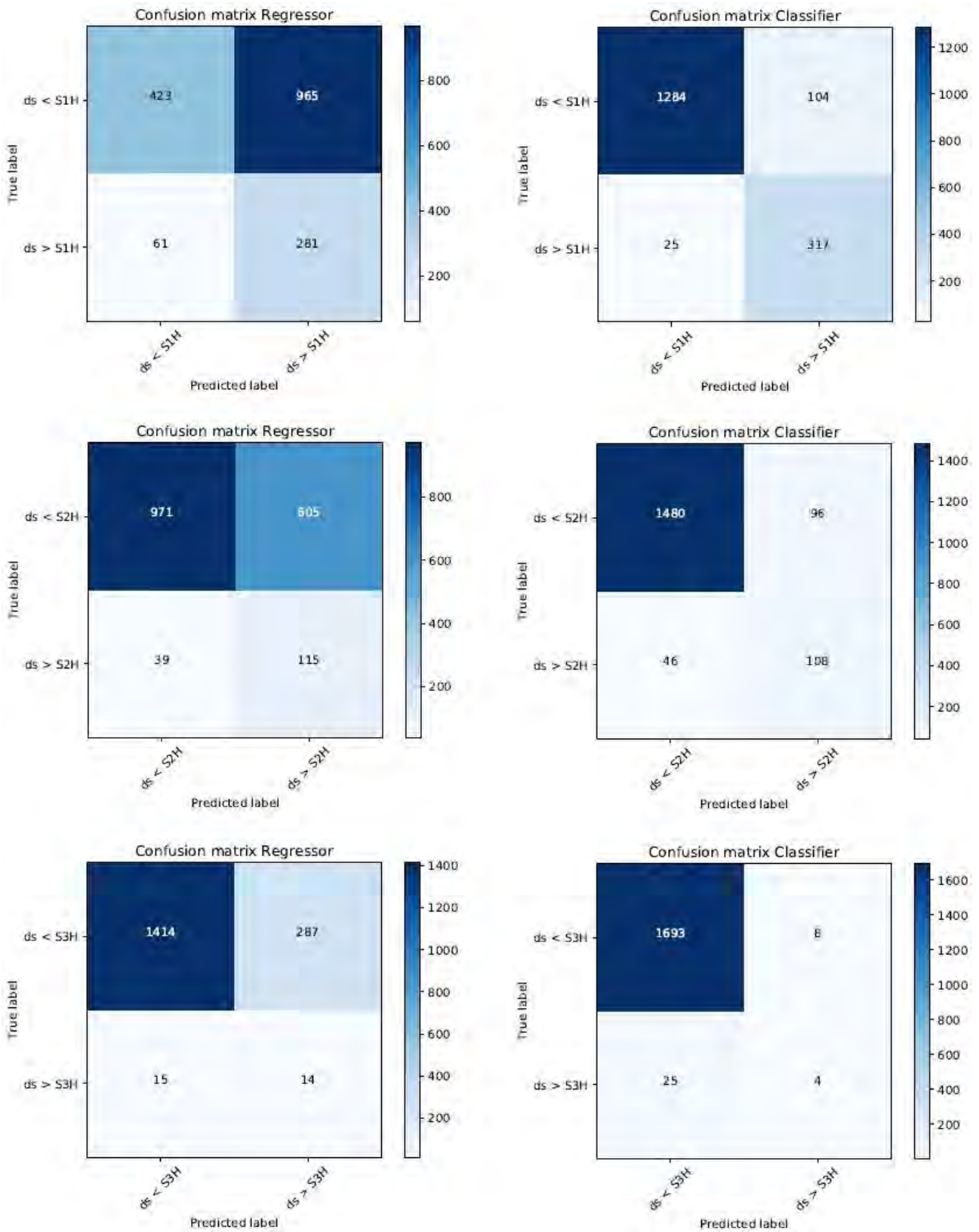


Figure 3.44: Confusion matrices for highway embankment damage states - predicting both new data sets (Logar, 2018).



This project has received funding from the European Union's Horizon 2020 research and innovation programme under grant agreement No. 700748

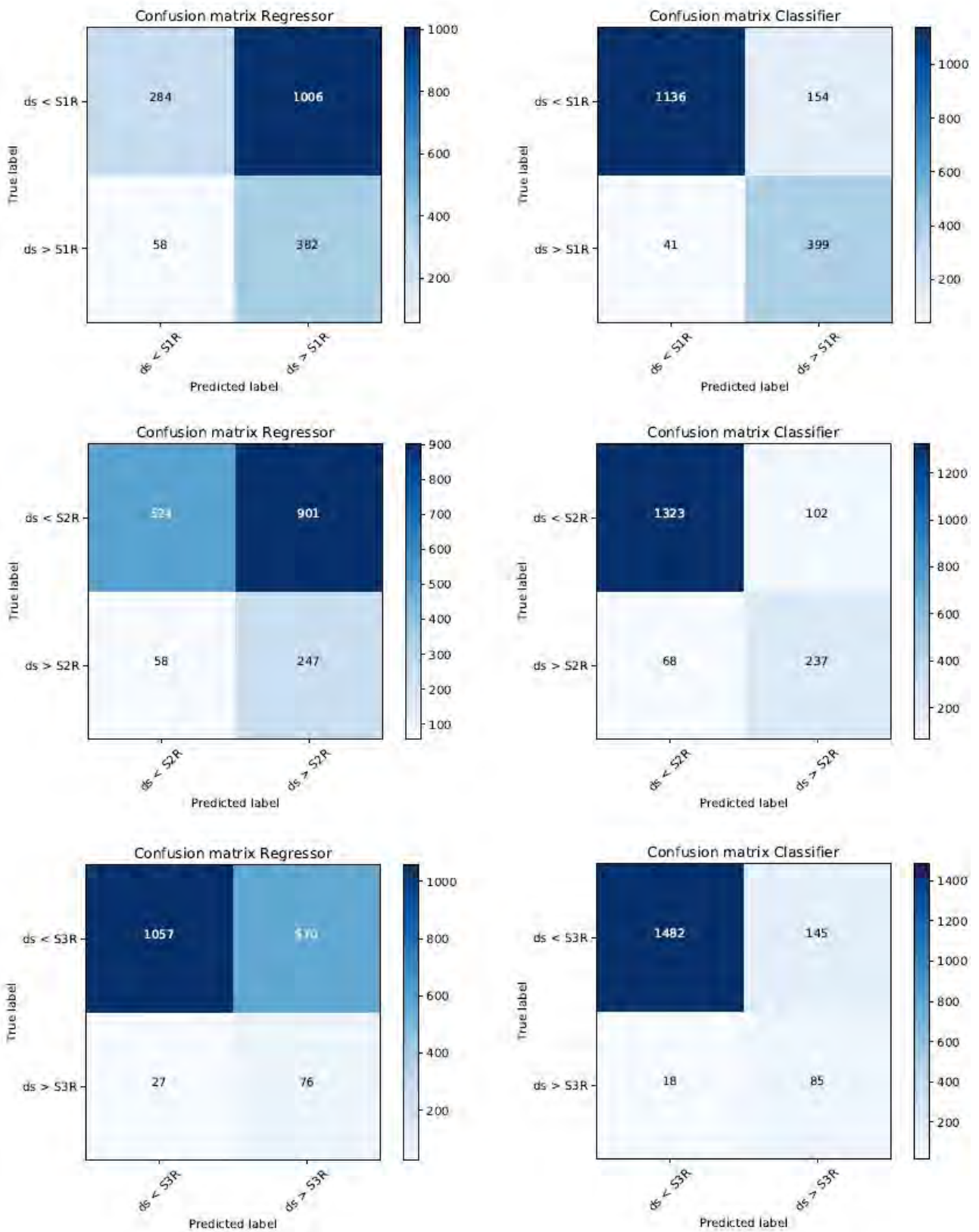


Figure 3.45: Confusion matrices for railway embankment damage states - predicting both new data sets (Logar, 2018).



This project has received funding from the European Union's Horizon 2020 research and innovation programme under grant agreement No. 700748

3.1.4.5.3 Conclusions on ANN study

The effectiveness of artificial neural networks for predicting the response of the traffic embankments built on liquefiable ground and subjected to seismic loading cannot be assessed to its full potential within this study, due to a relatively small number of data variations especially with respect to geometry and material properties. The below conclusions have to be taken as preliminary.

Better results were achieved, when intermediate numerical results were included in the training set and when just few individual samples with similar conditions (similar geometry) to the predictive examples were included in the training data set.

Compared to the regression technique, better matching between predicted and true values was found for the more stable classification method. An additional step forward was the so-called “probabilistic way”, which took into account the probability that the data fell into a certain class, and consequently the deviation from the true values was slightly lower.

Although the main goal is to predict the results on a completely unknown geometry, the prediction accuracy can be rapidly improved with few additional numerical calculations for this new situation. However, due to high soil non-linearity during liquefaction phenomenon, the high accuracy of predicted vertical displacement or any other parameter with ANN methods is doubtful. Nevertheless, by suitable strategy (optimal selection of input and output data, and optimal type of ANN) a large number of predictions can be made in short time. High precision of each individual prediction is not absolutely necessary, as long as the prediction errors are distributed evenly and do not affect significantly the predicted fragility curve.

From this study, we can understand that ANN predictions can be used for preliminary assessment of fragility curves for analyses at regional scale where a large number of numerical analyses cannot be made. For studies on smaller areas, at least few additional numerical calculations are recommended and their results have to be included in training data set.



This project has received funding from the European Union's Horizon 2020 research and innovation programme under grant agreement No. 700748

3.1.5 CONCLUSION

An extensive study of the earthquake-liquefaction-induced deformations of the traffic embankments was conducted within this work. Numerical analyses were carried out with 2D finite difference code FLAC, using PM4Sand material model to simulate liquefiable soil behaviour during seismic event. The suitability of this choice was first demonstrated by comparison of numerical prediction to the in-situ measurements of the embankment displacements and excess pore water pressure build up inside liquefiable layer at the site of Naruse river levee.

First part of the chapter 3 summarizes the methodology for the derivation of fragility curves. Among few possible approaches, numerical method seemed the only possible for the case of embankments on liquefiable ground and was conducted within this study. One of the main advantages using this approach is the repeatability of the analyses with same embankment geometry, same soil properties and various input ground motions. With a larger set of GMs, the influence of some uncertainties, especially those related to the input motions, is reduced. On the other hand, many assumptions are inevitable in numerical modelling (boundary conditions in dynamic analysis, material characteristics, etc.). Nevertheless, a good match between the results of numerical calculations and field measurements can be achieved.

The influence of variation of some model parameters (crest width, embankment height, thickness of liquefiable layer, presence of crust layer and relative density of sandy layer) on the developed fragility curves was examined. The presented fragility curves were mostly developed for permanent vertical ground displacement in the middle point of embankment crest as damage parameter and PGA at bedrock (alternatively Arias intensity) for intensity measure. Based on the results, the following was found:

- With increasing embankment height (2, 4, 6 and 8 m) or thickness of liquefiable layer (2, 4, and 7 m) crest settlements increase and fragility curves move to the left. In the absence of crust layer, even higher probability of exceedance of the set damage state was observed.
- The increase of crest width (6, 12 and 24 m) decreases vertical displacement in the centre of the embankment crest. Fragility curves move to the right with larger crest width.
- Denser liquefiable layer produces smaller deformations at the crest in comparison with loose material. Consequently, fragility curves move to the left for cases with loose sand.

Fragility curves were prepared for road and railway embankments based on SYNER-G criteria (SYNER-G, 2013). Brief discussion on the problem of uncertainties regarding the damage states for traffic embankments, and geotechnical structures in general, as well as few examples of fragility curves based on horizontal movements were presented.

Finally, a feasibility study on the prediction of vertical displacement and fragility curves using artificial neural network was performed. Two different techniques were tested, where classification method gave better results compared to regression method. Further improvements seem possible and additional research is needed to make final conclusions. Larger data base of numerically analysed cases would definitely improve the ANN predictions.



This project has received funding from the European Union's Horizon 2020 research and innovation programme under grant agreement No. 700748

3.2 APPLICATION TO A CASE STUDY OF EMBANKMENTS - TURKEY

In order to validate the proposed method, two well-documented case histories from the literature were used. The first case is the Cark Canal which is located in Adapazari and underlain by fine grained sediments, whereas the Police Station case is adjacent to Golcuk and underlain by medium dense silty sands (**Figure 3.46**). Both sites were strongly influenced by the 1999 Kocaeli Earthquake. Detailed land surveys and subsurface investigations were performed to reveal the liquefaction-related ground failure.

- Cark Canal case will be used for the validation of embankment fragility curves for vertical displacement
- Police Station case will be used for validating the embankment fragility curves produced for lateral spreading

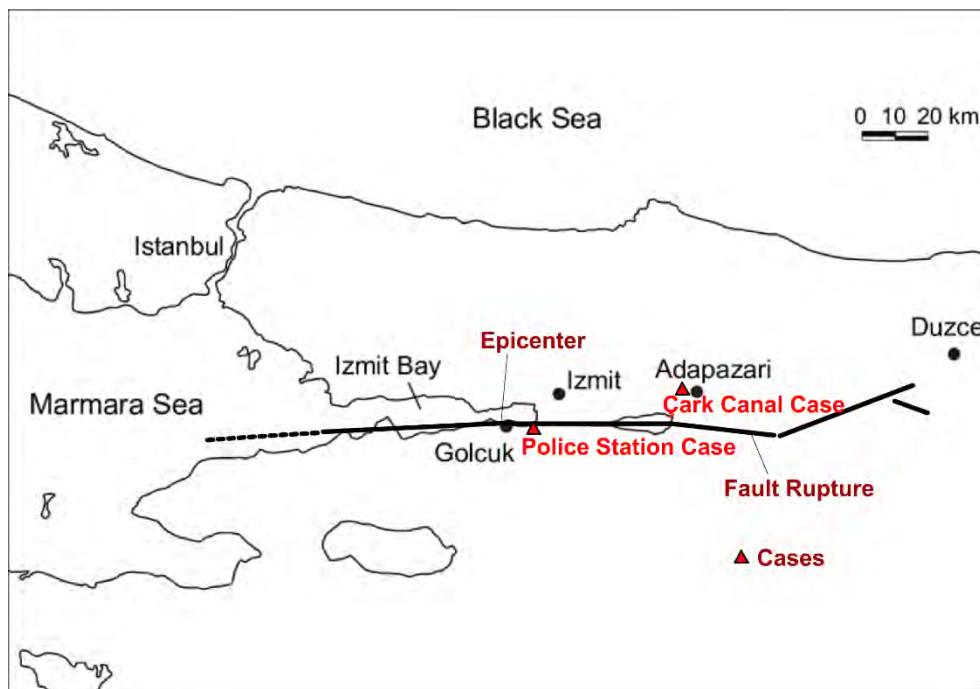


Figure 3.46: The location of the sites.

3.2.1 CARK CANAL SITE

Cark Canal is located on Cark River in Adapazari where the city is founded on Holocene alluvial deposits, bounded by the Sakarya River on the east and Cark River on the west (**Figure 3.47**). Over geological ages both rivers deposited heterogeneous layers of clay, silt and sand so that the subsurface conditions of the city demonstrate large variations in both vertical and horizontal directions (Bay and Cox 2001, Youd et al. 2009).

Detailed information about the Cark Canal geometry is provided by Youd et al. (2009) based on the land surveys performed sometime after the 1999 Kocaeli Earthquake. The Cark Canal was described as a channelized segment of trapezoidal cross section with a 6.5 m depth, 20 m width at the surface and 6 m



This project has received funding from the European Union's Horizon 2020 research and innovation programme under grant agreement No. 700748

width at the base. The canal has 1H:1V steep slopes on each sides, where both surfaces were covered with stone and mortar (**Figure 3.48**). The groundwater level was at 2.5 meters depth below the crest of the Çark Canal embankment. The shear wave velocity profile provided by Bay and Cox (2001) showed a deep and very soft soil profile starting from a depth of 1 meter through the entire profile.

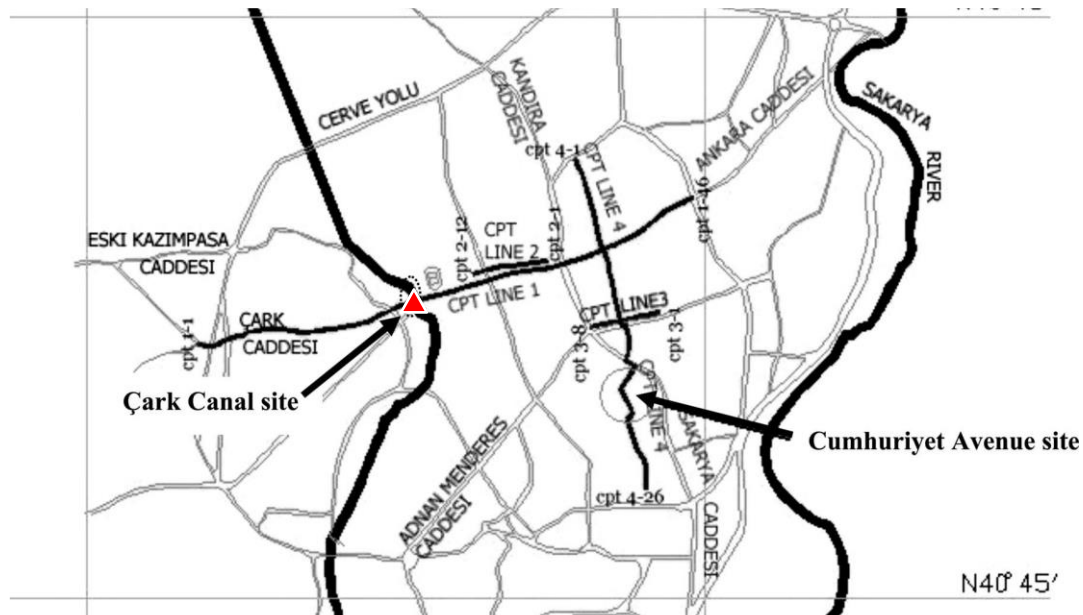


Figure 3.47: Map of Adapazari showing the location of Çark and Sakarya Rivers, Çark Canal site and CPT Line 1 (Bray et al. 2001, Youd et al. 2009).

The Çark Canal site provides a good opportunity to validate vulnerability assessment of embankment since the CPT Line 1 and Line 2 of the Pacific Earthquake Engineering Research Center's building damage inventory (Bray et al. 2001, Youd et al. 2009) intersect almost at the canal location (**Figure 3.47**). Along the Çark River four CPT tests and two SPT boreholes were installed. As seen on **Figure 3.48**; CPT 1-22, 1-23, SCPTU 1-24 and SPT 1-24 are located on the west whereas CPT 1-25 and SPT 1-25 are located to the east side of the canal. Cone resistance q_c and the soil behavior type index I_c measured from the SCPTU 1-24 are given in **Figure 3.49**.



This project has received funding from the European Union's Horizon 2020 research and innovation programme under grant agreement No. 700748

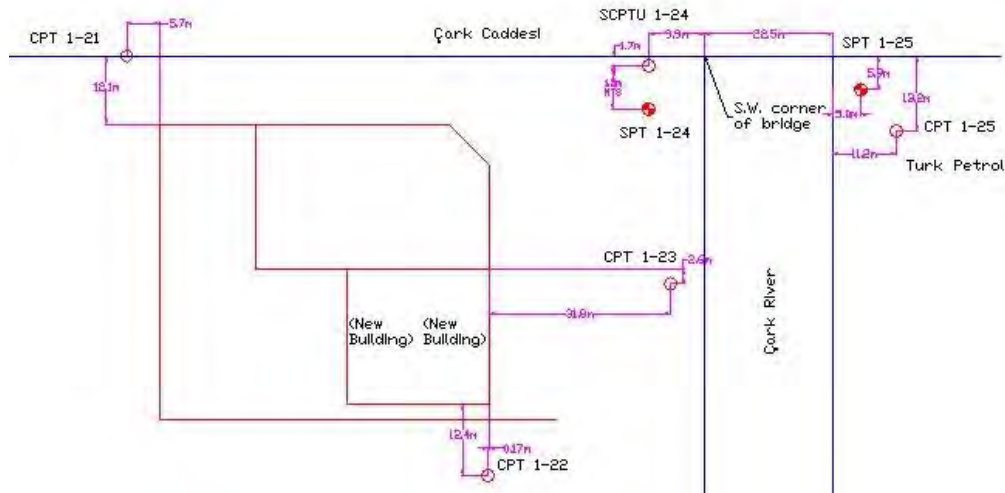


Figure 3.48: Plan view of the CPT tests and the boreholes (Bray et al. 2001).

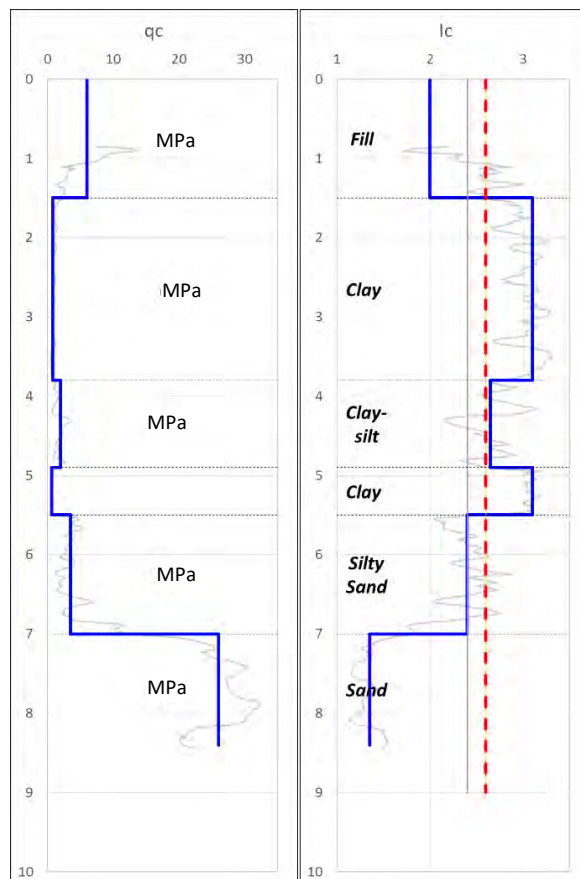


Figure 3.49: q_c and I_c profile of SCPTU 1-24.

Using the data gathered both from the site surveys and the subsurface investigation by SPT and CPT tests, Youd et al. (2009) prepared a schematic cross-section view of the topography and also the sediment stratigraphy as given in **Figure 3.50**. According to their measurements, the groundwater depth was 2.6 m at



This project has received funding from the European Union's Horizon 2020 research and innovation programme under grant agreement No. 700748

the west of the canal in CPT 1-24, on June 28, 2000. Two years later a depth of 3.3 m was measured at the east of the canal in Borehole SPT 1-25, in August 2002. As Youd et al. (2009) stated, the 2.6 m depth was measured during a wet season as the depth of the water flowing in the canal was only 1 m. The 3.3 m depth was measured during a dry period with only little water in the canal. In addition to **Figure 3.50**, Bray et al. (2001) also provided the generalized cross section of the Cark Canal where the soil stratification, soil type and the location of the groundwater level is clearly stated (**Figure 3.51**).

The photo of the Cark Canal Bridge and Cark Canal taken by Bay and Cox (2001) is given in **Figure 3.52** whereas the current view of the Canal is presented in **Figure 3.53**.

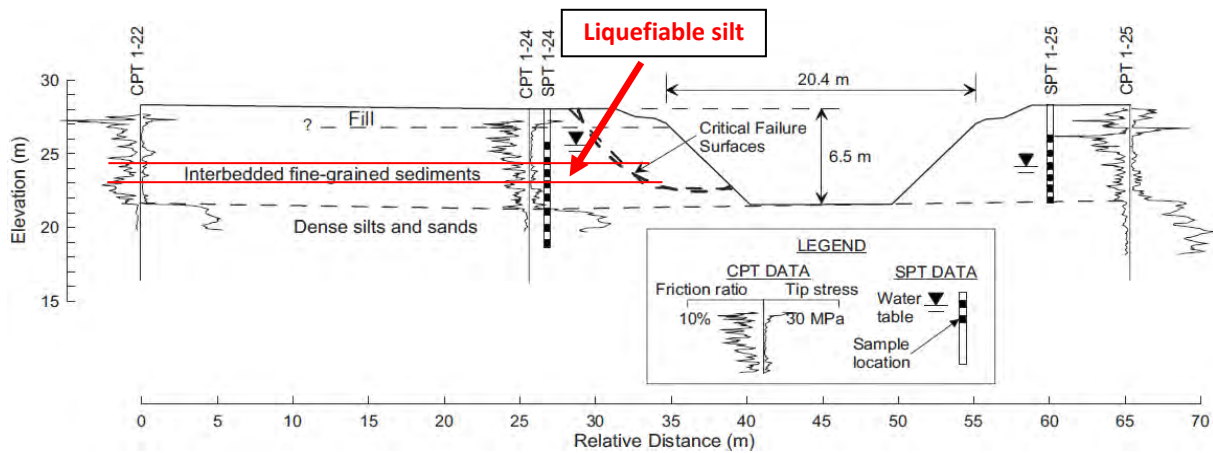


Figure 3.50: Section view of the river embankment and soil profile (Youd et al. 2009).

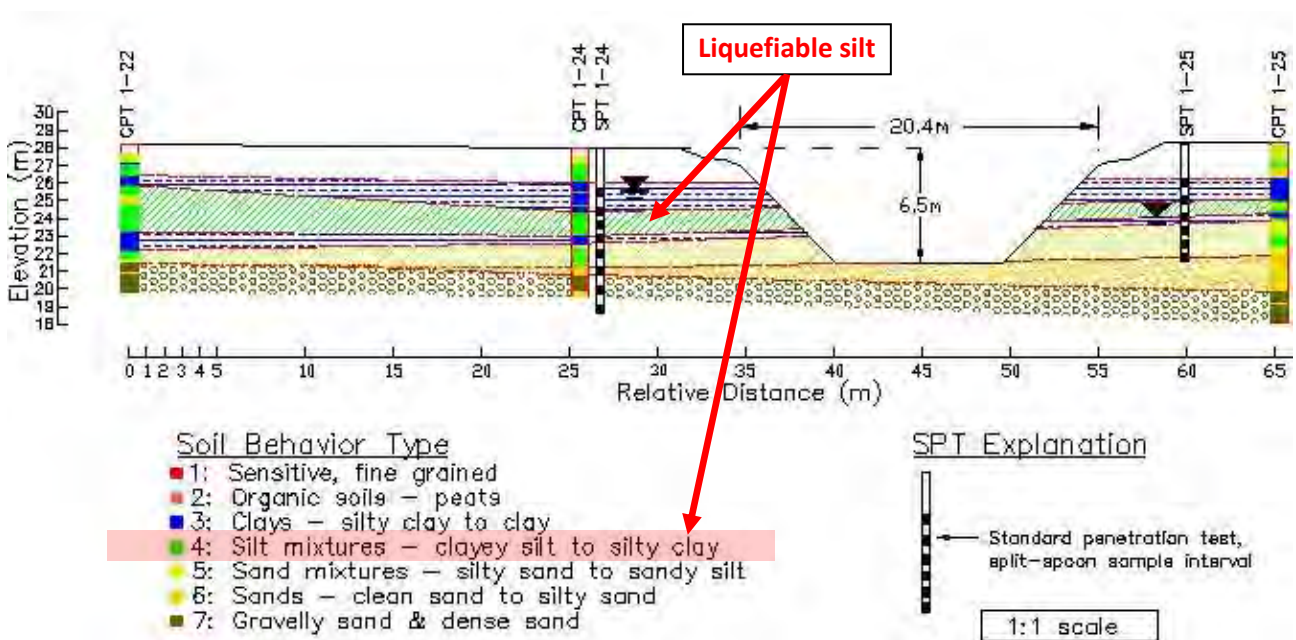


Figure 3.51: General cross section view with; soil stratification, soil type and the groundwater level (Bray et al. 2001).



This project has received funding from the European Union's Horizon 2020 research and innovation programme under grant agreement No. 700748



Figure 3.52: A north to south view of the canalized river (Bay and Cox 2001, Photo by Brady Cox).



Figure 3.53: Current (November 2018) view of canal from the bridge.



This project has received funding from the European Union's Horizon 2020 research and innovation programme under grant agreement No. 700748

Bay and Cox (2001) observed no sign of lateral spreading along the Canal site through their land surveys, although the conditions were ideal to trigger a lateral spreading. Youd et al. (2009) also confirmed the similar observations and restated the below findings for the Canal site;

- (i) there was no surface evidence of ground displacement near the canal,
- (ii) there was an absence of ground fissures and pavement cracks near the banks of the canal;
- (iii) a lack of deformation or damage to the bridge, exposed pipes, and other structures crossing the canal,
- (iv) a lack of detectable deformation or cracking of the canal lining.

However, Youd et al. (2009) also pointed out that some displacements not exceeding more than 100 mm into underlying fine-grained sediment were observed for some of the buildings near the Cark Canal. They claimed that these were the indications of liquefaction or cyclic ground softening occurred during the 1999 Kocaeli Earthquake.

Validation by Vulnerability Curves

As discussed in Section 3.1, a methodology is proposed to assess the vulnerability of embankments by using fragility curves for a set of ground conditions and different embankment heights and widths. Cark Canal geometry and its soil properties were used to compare the results of the proposed methodology with the observed behavior of the Canal during the 1999 Kocaeli Earthquake. The idealized cross section of the canal geometry, soil layers and groundwater table are given in **Figure 3.54**. The probability of exceedance for Cark Canal case were estimated for the conditions, such as:

- Embankment height of 4 meters
- Liquefiable layer thickness of 1 meter as medium dense sand
- The slope of the embankment is 1V:1H
- Using the relevant attenuation relationships, the bedrock acceleration at the Cark Canal site was calculated as 0.40g

The fragility curve used for the Cark Canal case is given in **Figure 3.55**, by using the proposed methodology in Section 3.1. The probability of damage due to liquefaction for a bedrock acceleration of 0.4g corresponds to probability of exceedance of approximately 5-8 % for minor damage state, which is in good agreement with the field evidences where no sign of ground movement was observed throughout the canal area (Bay and Cox 2001, Youd et al. 2009).



This project has received funding from the European Union's Horizon 2020 research and innovation programme under grant agreement No. 700748

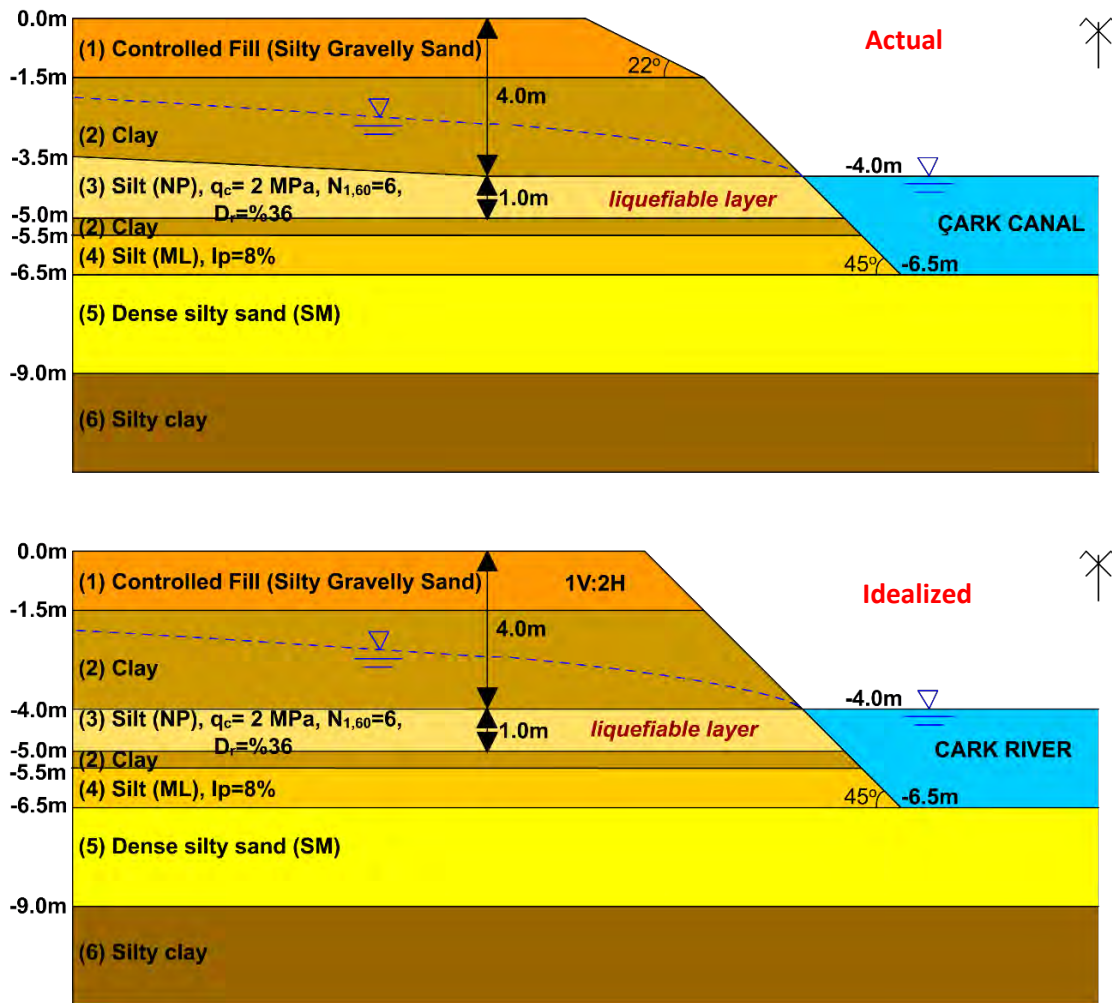


Figure 3.54: Actual and idealized section and soil profile of the canal case.

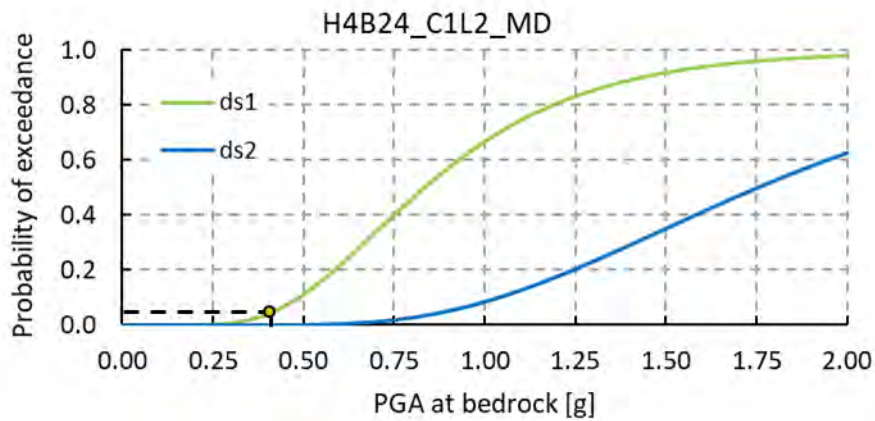


Figure 3.55: Fragility curve used for the Cark Canal case.



This project has received funding from the European Union's Horizon 2020 research and innovation programme under grant agreement No. 700748

Validation by FE Analyses

The proposed methodology in Section 3.1. was developed for embankments with a slope of 1V:2H. However, for the Cark Canal case the embankment slope is 1V:1H as defined by Bray et al. (2001). In order to justify the difference at geometrical conditions, a series of numerical analyses were carried out specifically for 1V:1H slope of Cark Canal river. The numerical model is given in **Figure 3.56**.

The layer (3) Silt (NP) given in **Figure 3.54** has the potential for liquefaction. PM4Sand was used to model the liquefaction behavior of this layer. The cyclic behavior of the (3) Silt (NP) layer is numerically modelled with cyclic DSS test and compared with the experimental data given by Sancio (2003) from the same silt layer at Site A, which is not so far from the Cark Canal site. The calibrated PM4Sand parameters are given in **Table 3.25** whereas numerical and experimental results are compared in **Figure 3.57**.

The ru profile given in **Figure 3.58** clearly showed that the liquefiable layer (3) Silt (NP) has reached zero effective stress and thus fully liquefied. The vertical displacement profile given in **Figure 3.59** also clearly showed that the displacements are very limited as it should be. Only 2-3 cm of vertical displacement was calculated at the crest of the embankment and once more this finding complies well with the field surveys where no sign of ground movement was observed throughout the canal area (Bay and Cox 2001, Youd et al. 2009). The effect of embankment slope was also evaluated by using the same results of the numerical model. As given in **Figure 3.60** the embankments with 1V:1H and 1V:2H slope deformed almost similarly, indicating the minor influence of the slope angle.

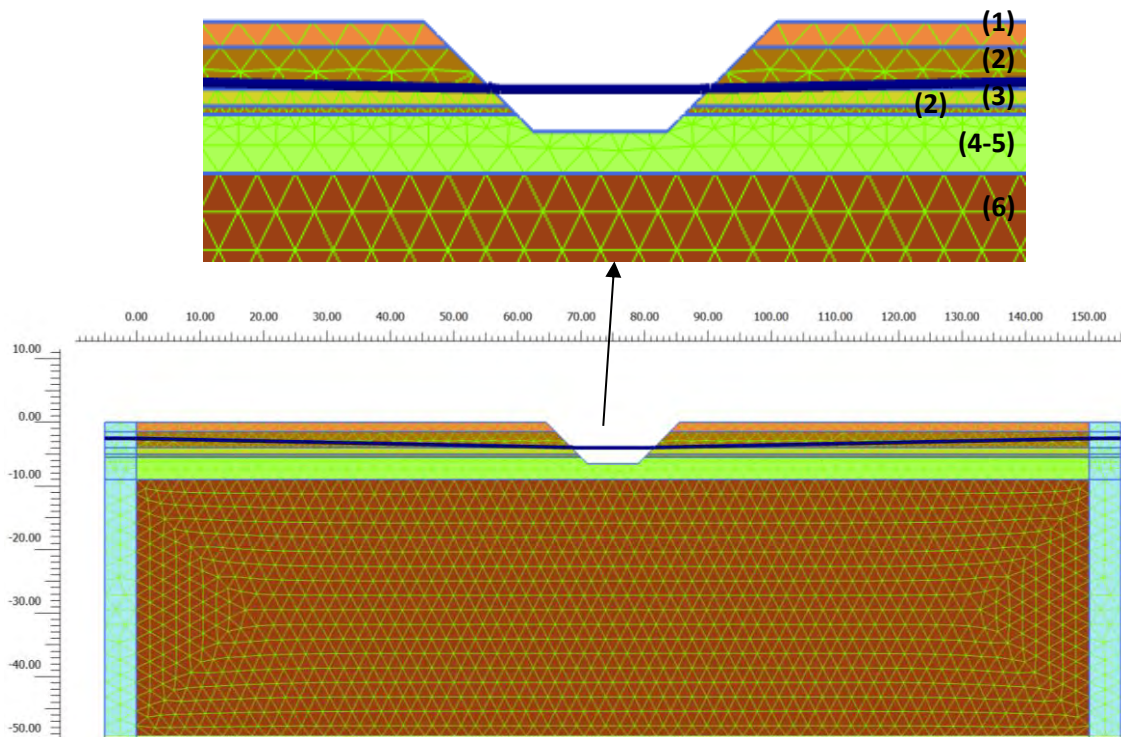


Figure 3.56: Numerical model of the Cark Canal site.



This project has received funding from the European Union's Horizon 2020 research and innovation programme under grant agreement No. 700748

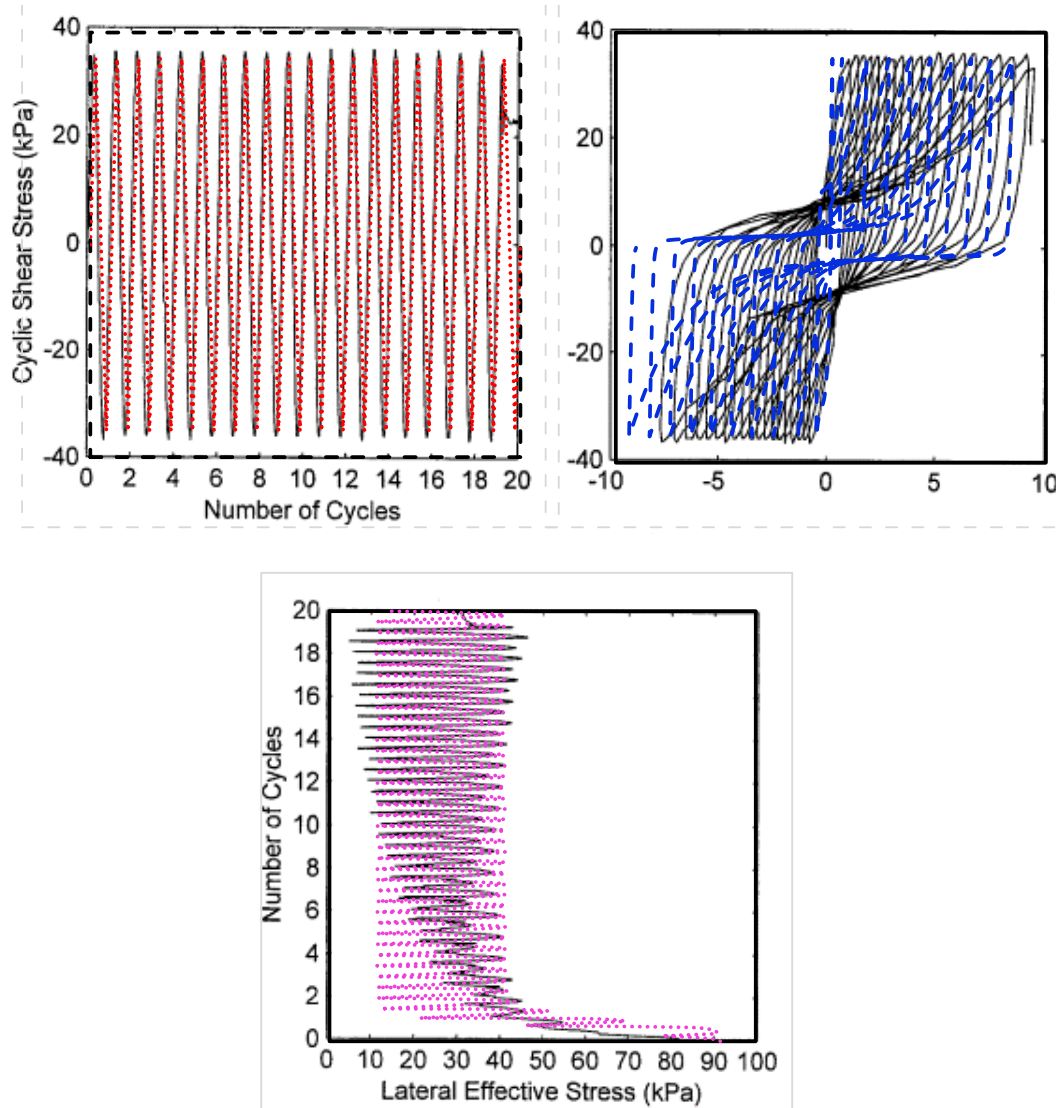


Figure 3.57: PM4Sand model results with the parameters given in Table 3.25.

Table 3.25: Calibrate PM4Sand parameters for the liquefiable (3) Silt (NP) layer at the Cark Canal site.

(3)_Silt (NP)_dyn_pm4	
DR0	0.3600
G0	1171
hp0	0.7500
emax	1.2
emin	0.692
phicv	28.0



This project has received funding from the European Union's Horizon 2020 research and innovation programme under grant agreement No. 700748

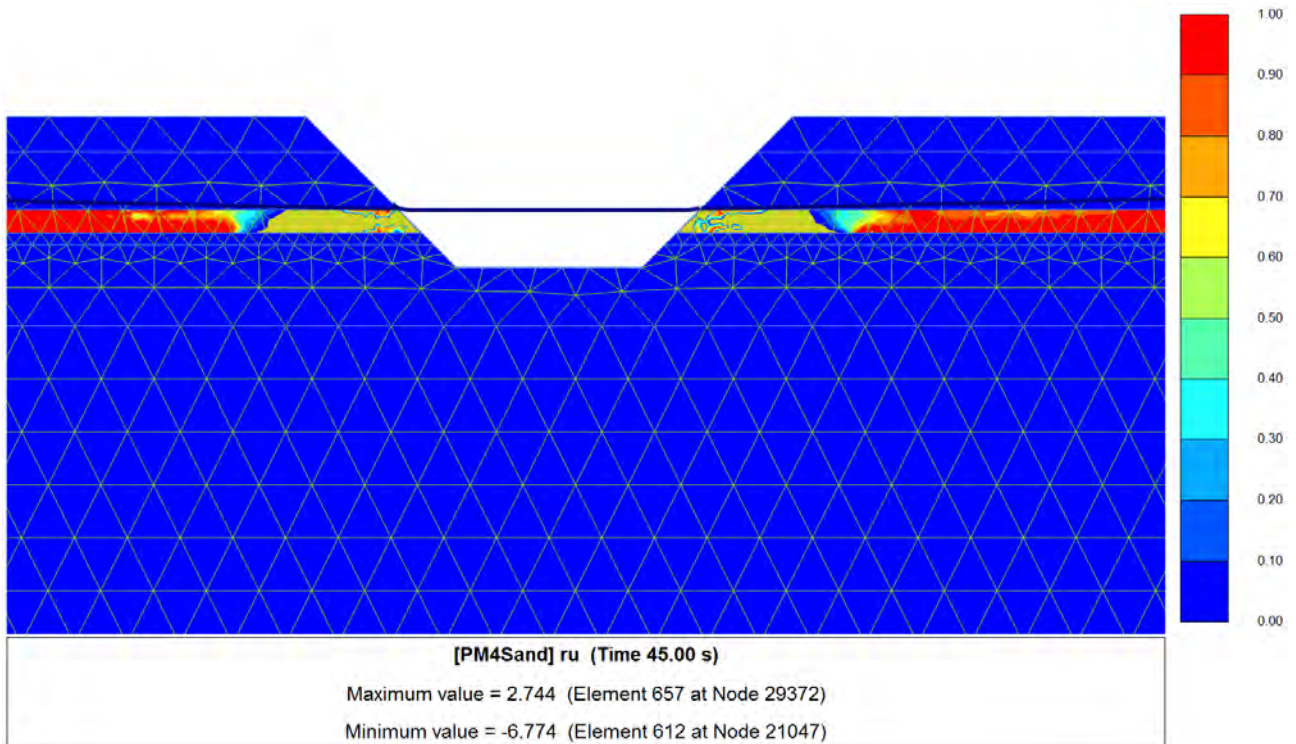


Figure 3.58: ru values at the end of the dynamic model.

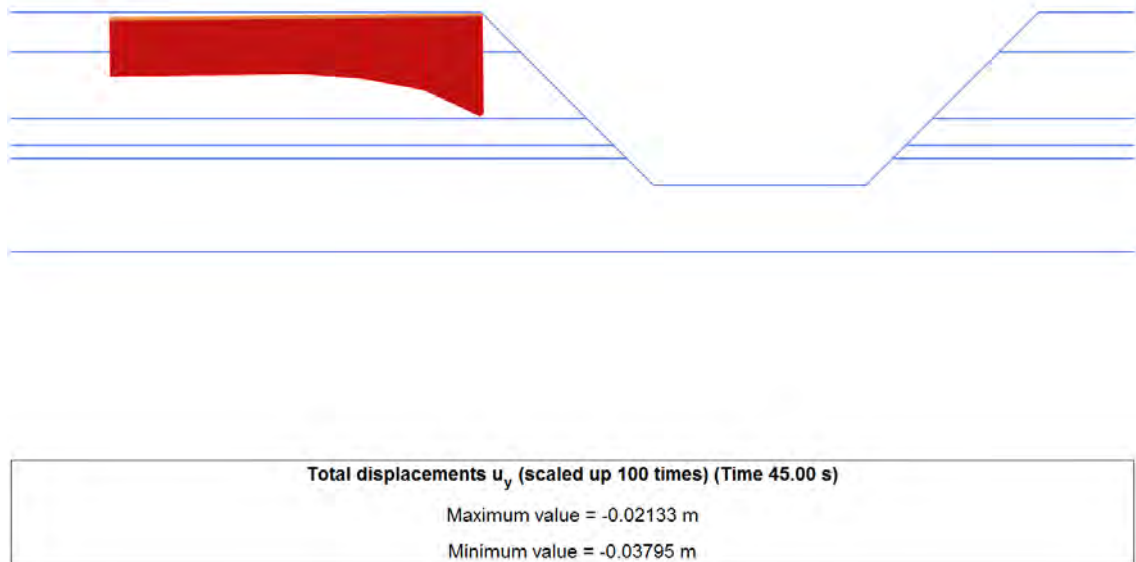


Figure 3.59: Vertical displacement profile at the embankment crest.



This project has received funding from the European Union's Horizon 2020 research and innovation programme under grant agreement No. 700748

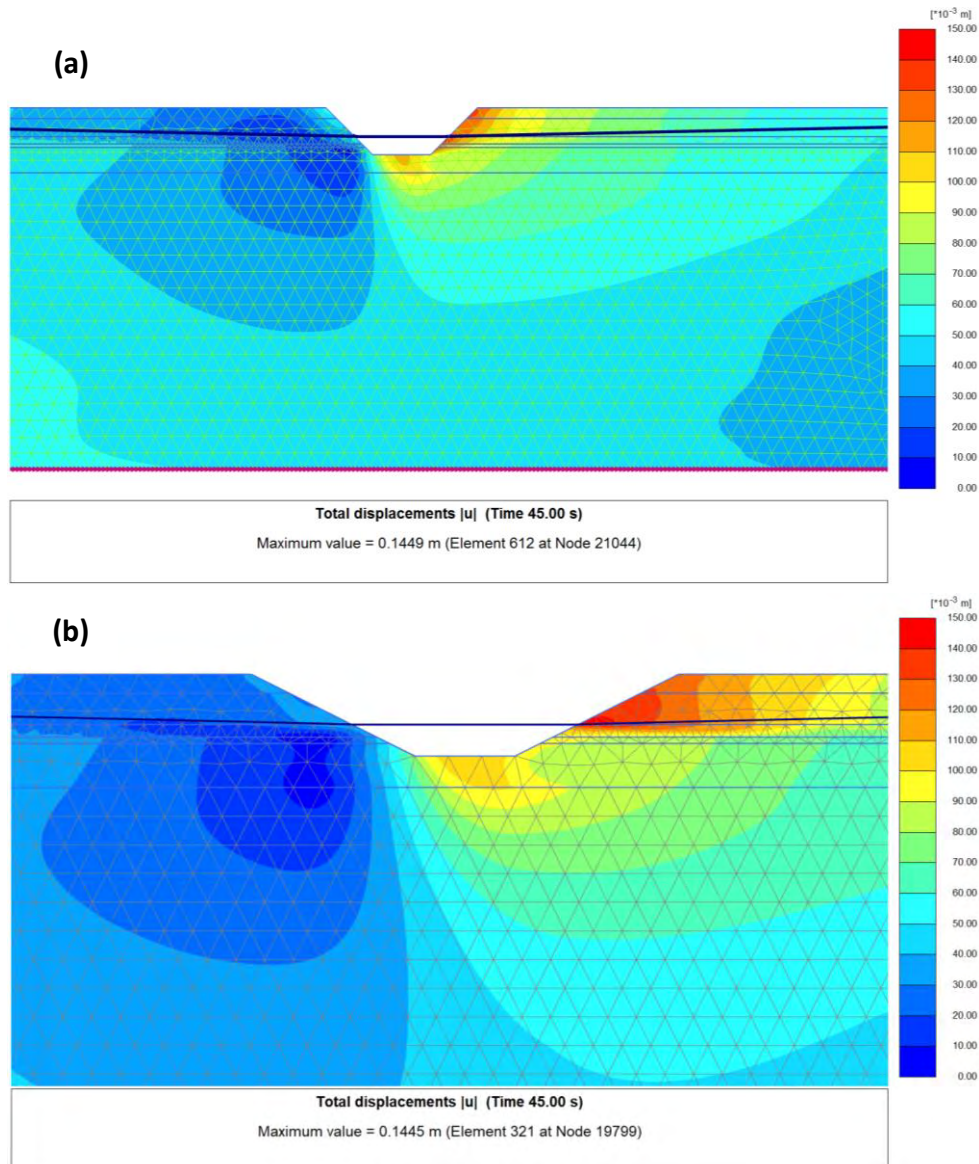


Figure 3.60: The effect of embankment slope (a) 1V:1H and (b) 1V:2H in terms of total displacements.

3.2.2 POLICE STATION SITE

The police station site is located in the town of Golcuk close to the eastern shore of Izmit Bay, as shown in **Figure 3.2**. The case of Police Station has specific importance since lateral spreading ground displacements were observed behind 2-storey structures located approximately 100 m inboard from the shoreline. Cetin et al. (2004) mapped ground cracks induced by the lateral spreading. As shown in **Figure 3.61** the magnitude of ground displacement due to lateral spreading reaches up to 2.4 m at the shore of sections I, II and III. Ground displacements are reduced with the distance away from the shorelines of Izmit Bay. Along the Section II, at the vicinity of CPT-PS-2 and SPT-PS-2, the ground cracks due to lateral spreading were found to be close to 10 cm and 35 cm respectively.



This project has received funding from the European Union's Horizon 2020 research and innovation programme under grant agreement No. 700748

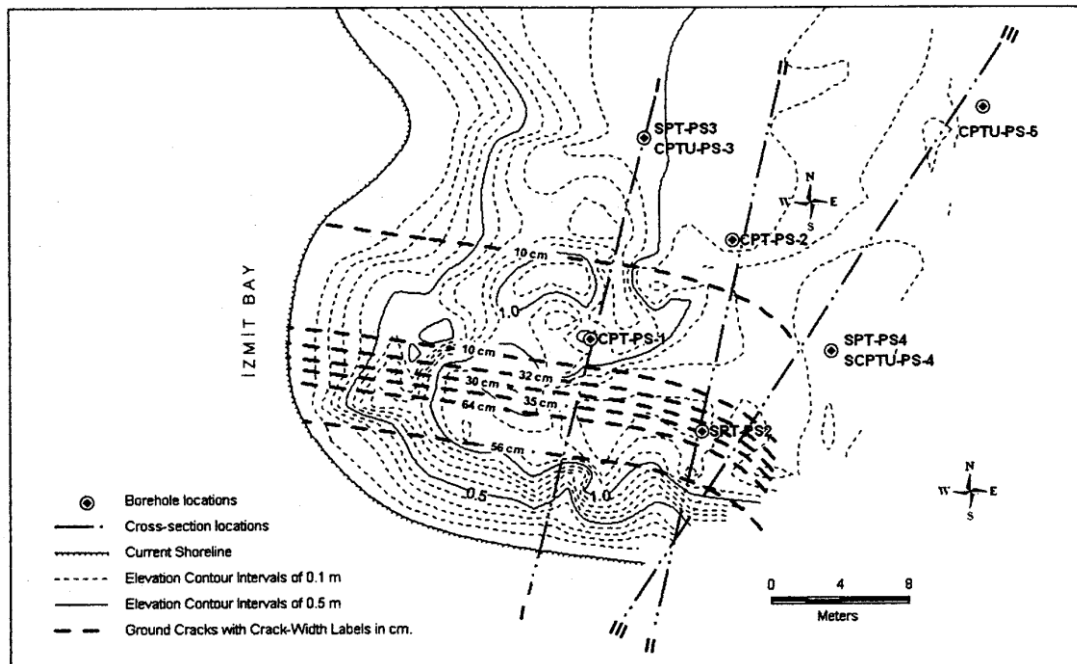


Figure 3.61: Ground displacement map observed at the Police Station site (Cetin et al. 2004).



Figure 3.62: Ground displacements in the will (embankment) (Cetin et al. 2004).

The soil profile given in **Figure 3.62** is defined by CPT-PS-2 and SPT-PS-2. Typical soil profile consists of artificial fill ranging from 1.5 to 2.0 m. Fill layer is underlain by a 1.5–2.0 m thick loose gray silty sand layer. Energy corrected SPT blow counts $(N)_{60}$ are as low as 3 blows/ft in this silty sand layer. At about 4 m depth, a soft and low plasticity silty clay layer about 3.5–4 m in thickness is present. Liquid limits (LLs) and plasticity indices (PIs) of the layer are 40–45 and 18–23, respectively. This silty clay layer is underlain by a 1.5 m thick very loose to loose silty sand layer. Below this layer there lies a soft and low plasticity silty clay layer with LL and PI values of 37 and 17 (Cetin et al. 2004). The soil profile from SPT-PS-2 borehole is given in **Figure 3.63**.



This project has received funding from the European Union's Horizon 2020 research and innovation programme under grant agreement No. 700748

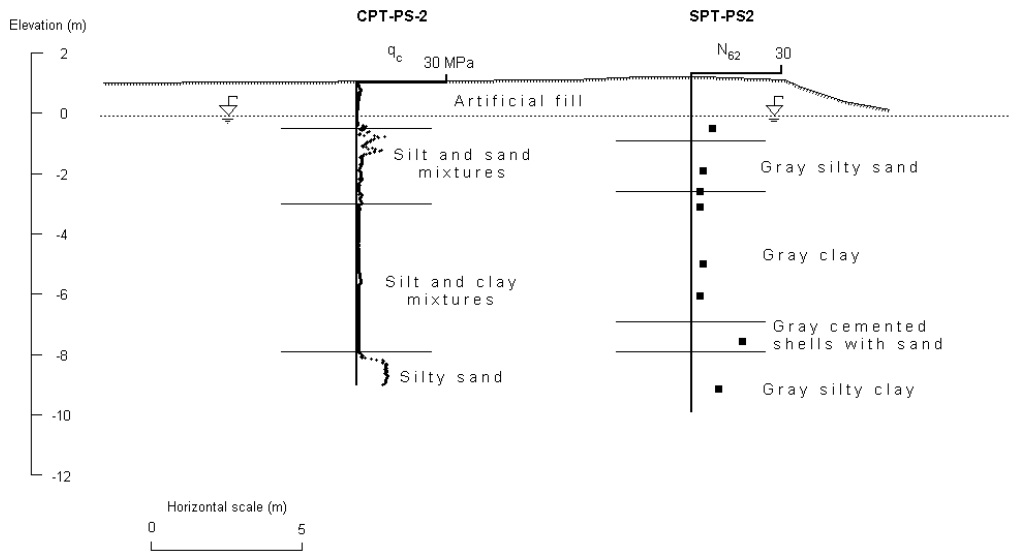


Figure 3.63: Soil profile is presented by CPT-PS-2 and SPT-PS-2 (Cetin et al. 2004).

Depth Scale (m)	Lithology	USCS	Sample Type and No.	Recovery/Length (cm)	SPT Blows/15 cm	Casing Depth (m)	Rod Length (m)	Energy Ratio (%)	Description
0									FILL: Dessicated brown clay fill.
1									FILL: Brown to gray gravelly sandy silt.
2		SP-SM	S-PS2-1	8/45	3-4-4	1.70	5.20	55*	SM: Gray silty sand
3			S-PS2-2	0/45	1-2-2	3.10	6.72	60*	
4		CL	S-PS2-3	40/45	1-1-2	3.80	8.24	65*	CL: Low plasticity gray clay.
5			SH-PS2-4	50/50		5.70			
6		CL	S-PS2-5	35/45	1-2-2	5.70	9.77	65*	
7		CL	S-PS2-6	44/45	1-1-2	7.30	11.29	65*	
8									SAND: Gray cemented shells with sand
9		SW-SM	S-PS2-7	30/45	7-8-9	8.70	12.82	65*	
10		CL	S-PS2-8	25/45	3-4-5	10.20	12.82	65*	CL: Gray silty clay

Figure 3.64: SPT-PS-2 borehole data (Cetin et al. 2004).



This project has received funding from the European Union's Horizon 2020 research and innovation programme under grant agreement No. 700748

Validation by Vulnerability Curves

From **Figure 3.63** and **Figure 3.64** the thickness of the fill (embankment) layer is around 2.0m and also the liquefied silty sand thickness is around 2.0m. Bedrock acceleration 0.4g is given for the Police Station case. The closest fragility curve that fits for this soil profile is with 1 m crust between 2 m thick liquefiable soil and 2 m high embankment. For this particular case, the calculated settlements are very low and so the conclusion would be; probability of any significant settlement in the center of embankment is low. However, as mentioned by Cetin et al. (2004) actually lateral spreading was observed at this site. Hence, fragility curves are developed specifically for this case, based on results of same numerical analyses but for lateral movements. As a damage parameter, Δx (the difference between horizontal displacements at both edges of embankment) is selected. The fragility curves below are generated for $\Delta x = 0.1$ m, 0.2 m and 0.4 m and denoted as damage states ds1, ds2 and ds3, respectively.

The fragility curves for crest (top surface of embankment) and the bottom (line in contact with the ground) of embankment are given in **Figure 3.65** and **Figure 3.66**. These curves are valid for loose ($D_r=0.35$) type of liquefiable soil which is the case here.

From below figures we can see that for PGA = 0.4 g and loose liquefiable layer the probability of exceeding 20 cm differential lateral movements is very likely but very unlikely to exceed 40 cm differential lateral displacements.

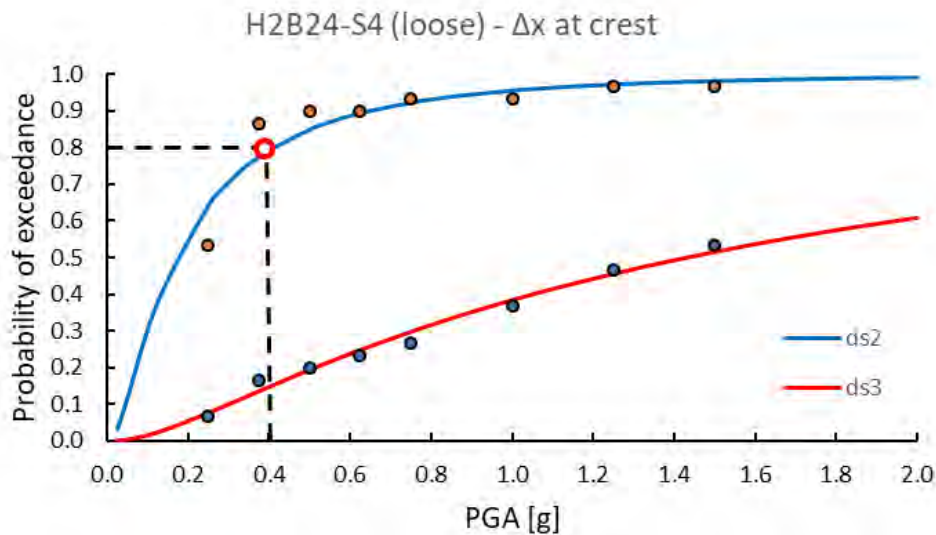


Figure 3.65: Fragility curve for crest of the embankment at loose sand.



This project has received funding from the European Union's Horizon 2020 research and innovation programme under grant agreement No. 700748

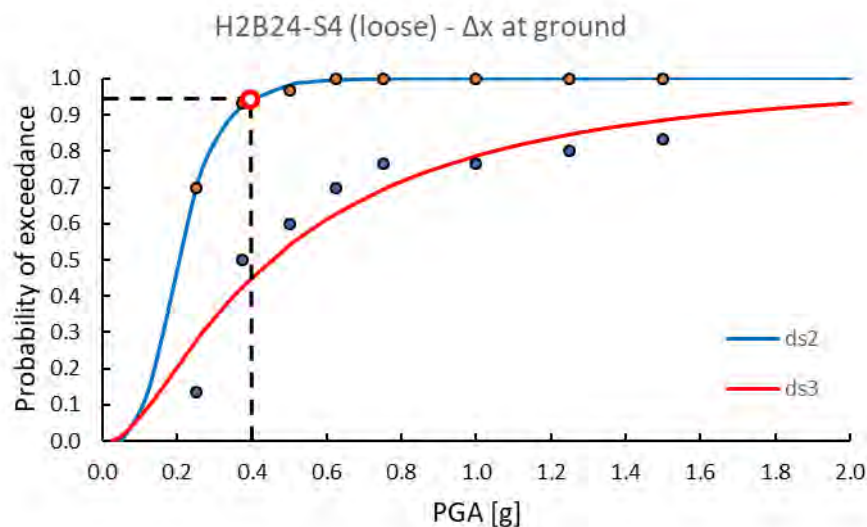


Figure 3.66: Fragility curve for the bottom of the embankment at loose sand.

3.2.3 CONCLUSION

Although the fragility curves from section 3.1 were developed using simplified soil profiles with assumed ground properties, the comparison with two well-documented case histories showed reasonably good agreement with observed behavior. This validation promises that the developed fragility curves for traffic embankments can be used for vulnerability assessment of traffic infrastructure on liquefiable ground as long as the actual soil profiles do not differ too much from the soil profiles assumed in our numerical models. Otherwise, further numerical analyses shall be made following the procedure from section 3.1 and site-specific fragility curves shall be developed. For rough preliminary estimations, ANN can be used to adapt existing fragility curves to new but similar geometrical situations.

REFERENCES

- adali, K., Elgamal, A.W., Martin, G.R. (1998). Foundation Liquefaction Countermeasures for Earth Embankments. *Journal of Geotechnical and Geoenvironmental Engineering* 124(6): 500-517.
- Akbar, S., Sandikkaya, M.A., Şenyurt, M., Azari Sisi, A., Ay, B.O., Traversa, P., et al (2014). Reference database for seismic ground-motion in Europe (RESORCE). *Bull Earthquake Engineering* 12:311–39.
- Anbazhagan, P., Parihar, A. and Rashmi, H.N. (2012). Review of correlations between SPT N and shear modulus: A new correlation applicable to any region, *Soil Dynamics and Earthquake Engineering* 36:52-69.
- Argyroudis, S., Monge, O., Finazzi, D. and Pessina, V. (2003). Vulnerability assessment of lifelines and essential facilities (WP06): Methodological Handbook – Appendix 1: Roadway Transportation System, Risk-UE Final Report. Report n° GTR-RSK 0101-152av7.
- Argyroudis, S., Kaynia, A.M. (2015). Analytical seismic fragility functions for highway and railway embankments and cuts. *Earthquake Engineering & Structural Dynamics* 44: 1863-1879.



This project has received funding from the European Union's Horizon 2020 research and innovation programme under grant agreement No. 700748

- Argyroudis, S., Mitoulis, S., Kaynia, A.M., Winter, M.G. (2018). Fragility Assessment of Transportation Infrastructure Systems Subjected to Earthquakes. *Geotechnical Earthquake Engineering and Soil Dynamics V GSP 292*: 174-183.
- Baker, J.W. (2015). Efficient analytical fragility function fitting using dynamic structural analysis. Technical note. Stanford University.
- Bay J.A. and Cox B.R. (2001). Shear Wave Velocity Profiling and Liquefaction Assessment of Sites Shaken by the 1999 Kocaeli, Turkey Earthquake. PEER Project SA3017-18336.
- Bhatnagar, S., Kumari, S., Sawant, V.A. (2016). Numerical Analysis of Earth Embankment Resting on Liquefiable Soil and Remedial Measures. *International Journal of Geomechanics* 16(1).
- Bird, J.F., Bommer, J.J. (2004). Evaluating Earthquake Losses Due to Ground Failure and Identifying Their Relative Contribution. 13th World Conference on Earthquake Engineering, Vancouver, B.C., Canada. Paper No. 3156.
- Boulanger, R.W. and Ziotopoulou, K. (2015). PM4Sand (Version 3): A Sand Plasticity Model for Earthquake Engineering Applications. Center for Geotechnical Modeling, Department of Civil and Environmental Engineering, University of California, Davis, California, Report no. UCD/CGM-15/01, pp. 70-76.
- Bray, J.D., Youd T.L., Cetin K.O., Seed R.B., Durgunoglu T., Onalp A. (2001). Documenting incidents of ground failure resulting from the August 17, 1999 Kocaeli, Turkey Earthquake." Pacific Earthquake Engineering Research Center, <https://apps.peer.berkeley.edu/publications/turkey/adapazari/index.html> (April 28, 2003).
- Cetin K.O., Youd T.L., Seed R.B., Bray J.D., Stewart J.P., Durgunoglu T., Lettis W. and Yilmaz M.T. (2004). Liquefaction-Induced Lateral Spreading at Izmit Bay During the Kocaeli (Izmit)-Turkey Earthquake. *Journal of Geotechnical and Geoenvironmental Engineering*, Volume 130. Issue 12.
- Chiou, B.S.J., Darragh, R.B., Gregor, N.J., Silva, W.J. (2008). NGA project strong-motion database. *Earthquake Spectra* 24:23–44.
- Cubrinovski, M. (1993). A constitutive model for sandy soils based on a stress-dependent density parameter. Dr. Eng. Thesis, University of Tokyo, Japan.
- Cubrinovski, M. and Ishihara, K. (1998a). Modelling of sand behaviour based on state concept. *Soils and Foundations* 38(3):115-127.
- Cubrinovski, M. and Ishihara, K. (1998b). State concept and modified elastoplasticity for sand modelling. *Soils and Foundations* 38(4):213-225.
- Cubrinovski, M. (2011). Seismic Effective Stress Analysis: Modelling and Application. 5th International Conference on Earthquake Geotechnical Engineering, Santiago, Chile.
- Georgopoulos, E.C., Tsompanakis, Y., Lagaros, N.D., Psarropoulos, P.N. (2006). Simulating the seismic response of an embankment using soft computing techniques. Proceeding on 6th European Conference on Numerical Methods in Geotechnical Engineering.
- Heaton, J. (2008). Introduction to neural networks with Java. Heaton Research, Inc.
- Itasca Consulting Group Inc. (2016). Fast Lagrangian Analysis of Continua. FLAC manuals – Sixth Edition (FLAC Version 8.0). Minneapolis, Minnesota, USA.



This project has received funding from the European Union's Horizon 2020 research and innovation programme under grant agreement No. 700748

- Jayaram, N., Lin, T., Baker, J.W. (2011). A computationally efficient ground-motion selection algorithm for matching a target response spectrum mean and variance. *Earthquake Spectra* 27(3):797–815.
- Jiang, M., Han, S., Li, H. (2012). Numerical Study of Stone Column Reinforced Composite Foundation of Highway under Static and Seismic Load. *Advanced Materials Research* (602-604): 1526-1531.
- Khalil, C., Rapti, I., Lopez-Caballero, F. (2017). Numerical Evaluation of Fragility Curves for Earthquake-Liquefaction-Induced Settlements of an Embankment. *Geo-Risk 2017 GSP* 283: 21-30.
- Kohavi, R. (1995). A study of cross-validation and bootstrap for accuracy estimation and model selection. *Ijcai* 14(2).
- Kumar, R., Bhargava, K. and Choudhury, D. (2016). Estimation of Engineering Properties of Soils from Field SPT Using Random Number Generation. *Indian National Academy of Engineering* 1:77-84.
- Lagaros, N.D., Tsompanakis, Y., Psarropoulos, P.N., Georgopoulos, E.C. (2009). Computationally efficient seismic fragility analysis of geostructures. *Computers and Structures* 87: 1195-1203.
- Logar, J. (2011). Geotehnični podatki – script/lecture notes (<http://fgg-web.fgg.uni-lj.si/kmtal-gradiva/Gradiva%20za%20vec%20predmetov/Skripta%20Janko%20Logar/TERENSKE%20PREISKAVE.pdf>).
- Logar, M. (2018). On estimating fragility curves with Feed Forward Neural Networks. Internal report.
- Lopez-Caballero, F., Modaresi-Farahmad-Razavi, A., Stamatopoulos, C.A. (2016). Numerical Evaluation of Earthquake Settlements of Road Embankments and Mitigation by Preloading. *International Journal of Geomechanics* 16(5).
- Maruyama, Y., Yamazaki, F., Mizuno, K., Tsuchiya, Y., Yogai, H. (2010). Fragility curves for expressway embankments based on damage datasets after recent earthquakes in Japan. *Soil Dynamics and Earthquake Engineering* 30: 1158-1167.
- National Institute of Building Sciences (NIBS). (2004). HAZUS-MH: Users's Manual and Technical Manuals. Federal Emergency Management Agency, Washington, D.C.
- Oka, F., Tsai, P., Kimoto, S., Kato, R. (2012). Damage patterns of river embankments due to the 2011 off the Pacific Coast of Tohoku Earthquake and a numerical modelling off the deformation of river embankments with a clayey subsoil layer. *Soils and Foundations* 52(5) 890-909.
- Pando, M.A., Guney Olgun, C., Martin, II J.R. (2001). Liquefaction Potential of Railway Emabnkments. 4th International Conferences on Recent Advances in Geotechnical Earthquake Engineering and Soil Dynamics, Missouri University of Science and Technology, Paper no. 2.29.
- Rapti, I., Lopez-Caballero, F., Modaresi-Farahmad-Razavi, A., Foucault, A., Voldoire, F. (2018). Liquefaction analysis and damage evaluation of embankment-type structures. *Acta Geotechnica* 13(5): pp 1041-1059.
- Sancio, R. B. (2003). Ground Failure and Building Performance in Adapazari Turkey. PhD Thesis, Univ. of California.
- Sancio, R., Bray, J. D., Durgunoglu, T. & Onalp, A. (2004). Performance of buildings over liquefiable ground in Adapazari, Turkey. *Proceedings of the 13th world conference on earthquake engineering, 13WCEE, Ottawa, ON, Canada.*
- Sasaki, Y. and Tamura, K. (2007). Failure mode of embankments due to recent earthquakes in Japan. 4th International Conference on Earthquake Geotechnical Engineering, Thessaloniki, Greece, 1479.



This project has received funding from the European Union's Horizon 2020 research and innovation programme under grant agreement No. 700748

- SYNER-G Fragility functions for roadway system elements (2011). Systemic Seismic Vulnerability and Risk Analysis for Buildings, Lifeline Networks and Infrastructures Safety Gain. Project N°: 244061, Call N°: FP7-ENV-2009-1.
- SYNER-G Guidelines for deriving seismic fragility functions of elements at risk: Buildings, lifelines, transportation networks and critical facilities (2013). Kaynia AM (ed.) Systemic Seismic Vulnerability and Risk Analysis for Buildings, Lifeline Networks and Infrastructures Safety Gain. Project N°: 244061, Call N°: FP7-ENV-2009-1.
- Šebenik, Ž., Dolšek, M. (2016). Strong ground motion database. Ljubljana, University of Ljubljana, Faculty of Civil and Geodetic Engineering, IKPIR.
- Takahashi, A. and Sugita, H. (2009). Behaviour of SCP-improved levee during 2003 Miyagiken-Hokubu Earthquake. Proc. IS-Tokyo2009, Earthquake Geotechnical Case Histories for Performance-Based Design, Kokusho, (ed) 2009 Taylor & Francis, pp. 177-184.
- Tsukamoto, Y., Ishihara, K., Kawabe, S., Kanemitsu, S. (2012). Liquefaction-induced road embankment failures. Forensic Engineering 166(FE2): 64-71.
- Yasuda, S., Towhata, I., Ishii, I., Sato, S., Uchimura, T. (2013). Liquefaction-Induced Damage to Structures during the 2011 Great East Japan Earthquake. Journal of JSCE (1): 181-193.
- Youd T.L., DeDen D.W., Bray J.D., Sancio R., Cetin K.O. and Gerber T.M. (2009). Zero-Displacement Lateral Spreads, 1999 Kocaeli, Turkey, Earthquake. Journal of Geotechnical and Geoenvironmental Engineering Vol. 135, Issue 1, [https://doi.org/10.1061/\(ASCE\)1090-0241\(2009\)135:1\(46\)](https://doi.org/10.1061/(ASCE)1090-0241(2009)135:1(46))
- Yin, C., Shi, J., Liu, F-F., Tian, W. (2017). Embankment seismic fragility assessment based on IDA-PSDA. China J. Highway Transp. 30(5): 28-37.
- Werner, S.D., Taylor, C.E., Cho, S., Lavoie, J-P., Huyck, C., Eitzel, C., Chung, H., Eguchi, R.T. (2006). REDARS 2: Methodology and Software for Seismic Risk Analysis of Highway Systems MCEER-06-SP08.



This project has received funding from the European Union's Horizon 2020 research and innovation programme under grant agreement No. 700748

4. VULNERABILITY ASSESSMENT OF MASONRY BUILDINGS USING HISTORICAL DATA

4.1 INTRODUCTION

Severe structural damage induced by liquefaction has occurred over time during the earthquakes in Anchorage (USA, 1964), Niigata (Japan, 1964), Kobe (Japan, 1995), Kocaeli (Turkey, 1999), Christchurch (New Zealand, 2012), Emilia-Romagna (Italy, 2012) and, more recently, Hualien (Taiwan, 2018) and Palu (Indonesia, 2018). The effects of liquefaction on the buildings in these areas were catastrophic, with rotations of entire structural complexes leading to a loss of functionality and operative state (Tokimatsu et al. 1996; Yoshida et al. 2001; Cubrinovski 2013; Fioravante et al. 2013; Chiaradonna et al. 2018b). Consequently, a great effort was made to understand building movements on shallow foundations using centrifuge testing and numerical modeling (Karamitros et al. 2013; Bray and Dashti 2014). In detail, Dashti and Bray 2013 individualized possible liquefaction-induced displacement mechanisms in three different typologies: (a) volumetric strains caused by water flow in response to transient gradients; (b) partial bearing failure due to soil softening; and (c) soil-structure-interaction-induced building ratcheting during earthquake loading. Nevertheless, most of the research was devoted to soil-structure-interaction studies on individual buildings, and these are strictly dependent on the specific case under study, e.g. the type of structure and foundation system (Luque & Bray 2017). Very little research has been conducted on fragility curves related to soil liquefaction. Zhang et al. (2008), however, derived fragility functions for different classes of typical bridges in California when subjected to seismic shaking or liquefaction-induced lateral spreading. Lopez-Caballero and Khalil (2018) assessed numerically the effect on a levee of the liquefaction-induced settlement of the soil foundation in terms of analytical fragility curves constructed on the basis of a nonlinear dynamic analysis. Furthermore, using a database of buildings affected by liquefaction during the 2010 Mexicali, 2010 New Zealand and 2011 Japan earthquakes, and with reference to building damage, Cazares et al. (2012) proposed vulnerability functions that are obtained as a result of a combination of the functions defined as empirical and those obtained through damage statistics.

Several approaches have been developed in the literature for correlating types of damage with seismic intensity parameters through a fragility curve. There are methods based on simplified mechanism-based procedures (Cosenza et al. 2005; Borzi et al. 2008), capacity spectrum methods (Iervolino et al. 2007; Del Gaudio et al. 2015), and displacement-based methods (Calvi 1999; Crowley et al. 2004; Borzi et al. 2008). There is, however, also a group of methods based on empirical observations of the expected damage suffered during seismic events (Rota et al. 2008, Del Gaudio et al. 2017).

In the current study, the structural and non-structural damage caused to masonry buildings is analyzed and empirical fragility curves are produced using observational damage data collected after the 2012 Emilia earthquake (see section 4.2.2). Starting from an analysis of the structural damage described in AeDES forms (Baggio et al. 2007), it has been possible to carry out both a qualitative and quantitative analysis of the



This project has received funding from the European Union's Horizon 2020 research and innovation programme under grant agreement No. 700748

observed damage (see section 4.2.3). In this way, the damage has been subsequently correlated with a new parameter characterizing the liquefaction phenomenon. Different methodologies for estimating fragility functions from data on damage grades and the parameters of potential liquefaction are illustrated, discussed and applied to the database, leading to the derivation of EMS-98-based fragility curves (see section 4.2.4).

4.2 EMILIA EARTHQUAKE

4.2.1 RECONSTRUCTION PROCESS

Reconstruction processes and data collected after the 2012 Emilia-Romagna earthquake are presented in this section. At the beginning, reconstruction process ordinances were issued for private buildings: Ordinance n. 29, 2012 for buildings temporarily or partially unusable for residential use; Ordinance n. 51, 2012 for buildings that have suffered severe damage and were assessed as unusable; and Ordinance n. 86, 2012 for buildings that were severely damaged and needed a seismic strengthening intervention or demolition and reconstruction. However, for the first time in Italy, it was also possible to obtain grants for the consolidation of soil foundation. An increased economic contribution for reconstruction up to 15% of the total grant was provided in the areas affected by liquefaction. It should be highlighted that a specific documentation, aiming at certify liquefaction effects, was required to obtain such extra funding. Moreover, microzonation studies were carried out in the areas struck by the seismic events in order to identify and delimit areas with homogeneous seismic behavior, distinguishing the areas susceptible to the amplification of seismic motion and those susceptible to liquefaction.

4.2.2 DATA COLLECTION ON DAMAGED BUILDINGS

Several municipalities were affected by liquefaction, including: Cavezzo; Bondeno; Cento; Pieve di Cento; the hamlet of San Carlo in Sant'Agostino; and Mirabello (Gruppo di lavoro RER, 2012).

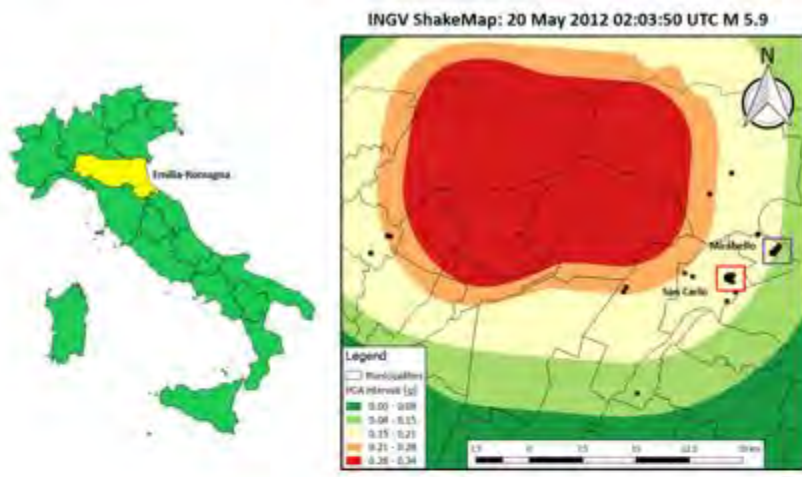
The data related to liquefaction sites were collected and subsequently georeferenced in the GIS environment. **Figure 4.1a** shows the spatial distribution of cases affected by liquefaction (black squares), with a ShakeMap superimposition related to the event of May 20, 2012.

The distribution of the sites affected by liquefaction is concentrated in the areas related to the municipalities of San Carlo and Mirabello. **Figure 4.1b** and **Figure 4.1c** show a comparison between the distributions of liquefaction evidences and the geological maps of the two considered municipalities. It can be observed that the most of the liquefaction manifestations occurred along paleo-river beds and paleo-channel systems originating from the depositional activity of the Reno river (Facciorusso et al. 2012). In order to investigate the effects of liquefaction on the behavior of structures, data related to masonry residential buildings located in San Carlo and Mirabello were collected. In detail, two sets of samples were identified and divided into two classes: a) a sample of structures whose soil foundation was not affected to liquefaction phenomena (unliquefied soil – US); and b) a sample affected by liquefaction (liquefied soil – LS). The evaluation of building usability were made by AeDES forms after the earthquake, (Baggio et al. 2007), a tool for the evaluation of earthquake-induced damage.

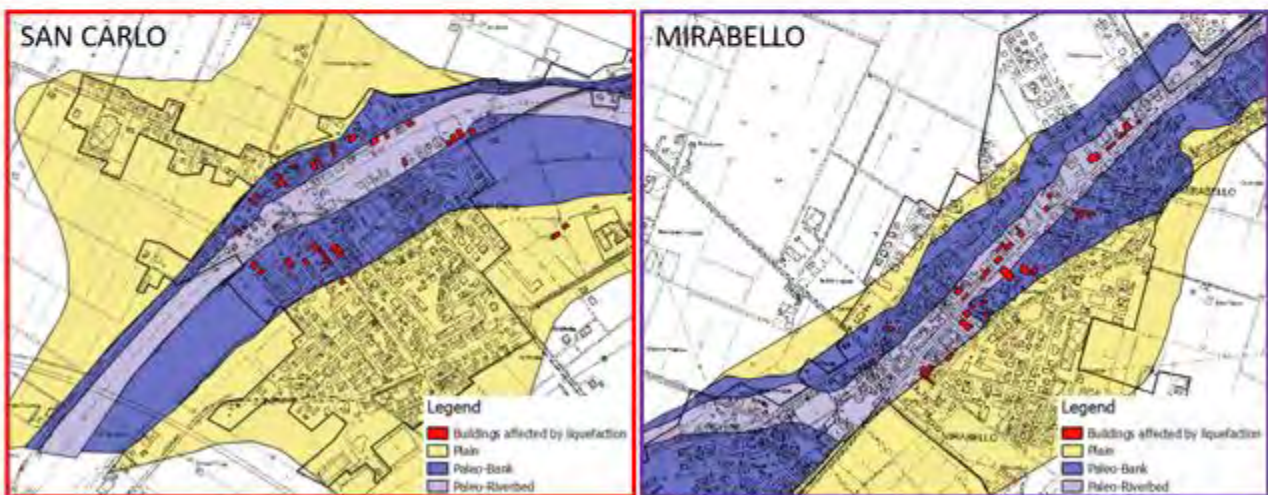


This project has received funding from the European Union's Horizon 2020 research and innovation programme under grant agreement No. 700748

Methodology for the liquefaction fragility analysis of critical structures and infrastructures: description and case studies



(a)



(b)

(c)

Figure 4.1: ShakeMap (<http://shakemap.rm.ingv.it/shake/index.html>) representing the spatial distribution of peak ground acceleration (PGA) and the buildings affected by liquefaction (a); San Carlo (b) and Mirabello (c) dataset with geological maps.

The data contained in the AeDES forms were used to make an initial comparison between the US and LS buildings, in terms of construction age, number of floors, average story surface area, and masonry quality. These macro-parameters may greatly affect building behavior in case of seismic events and were thus analyzed to verify if they play a crucial role in defining the different empirical damage detected in the US and LS buildings.

Figure 4.2 reports the frequency and cumulative percentage of the two classes of structure, i.e. US and LG as a function of the construction age, number of stories and average story surface area. The construction age was classified according to eight periods (before 1919, between 1919 and 1945, 1946-1961, 1962-1971, 1972-1981, 1982-1991, 1991-2001, and after 2001), as commonly adopted in the census data (and the AeDES



This project has received funding from the European Union's Horizon 2020 research and innovation programme under grant agreement No. 700748

forms). The trend of the cumulative percentage was similar. **Figure 4.2a** shows that 82.6% of the US building dataset (corresponding to 455 buildings) and 73.3% of the LS building dataset (corresponding to 92 buildings) were built before 1971. The graph in **Figure 4.2b** shows that about 98% of the buildings in the datasets (corresponding to 635 buildings for the US class and 99 buildings for the LS class) had between one and three stories. Finally, **Figure 4.2c** highlights that about 40% of the buildings (corresponding to 365 buildings for the US and 63 buildings for the LS classes) had an average story surface area between 70-100 and 170-230 m².

Consequently, it was possible to assume that the two classes are comparable in terms of the macro-parameters affecting the structural vulnerability to seismic action. Moreover, the data related to the quality of the masonry revealed a percentage of buildings of good quality and with regular texture masonry (77% and 61% for the US and LS classes, respectively).

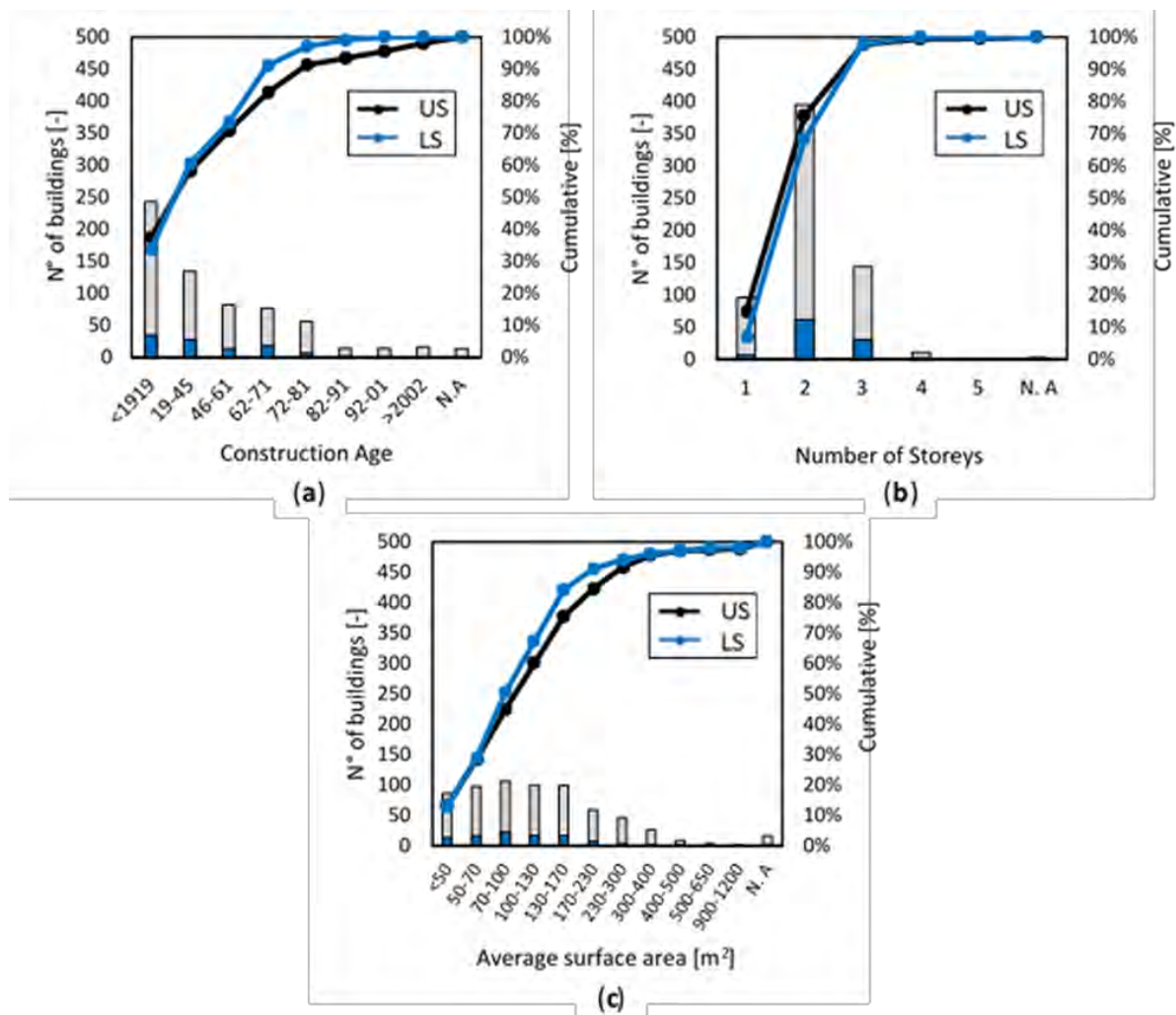


Figure 4.2: Distribution and cumulative percentage of the buildings as a function of the construction age (a), number of stories (b) and average story surface area (c).



This project has received funding from the European Union's Horizon 2020 research and innovation programme under grant agreement No. 700748

4.2.3 LIQUEFACTION INDUCED DAMAGE

The liquefaction phenomenon caused the loss of bearing capacity of the foundation soil. The consequence of this phenomenon has been the formation of differential or absolute failures that have caused a variable damage to the structures, but such as to reach the inaccessibility in some cases. In particular, it was possible to observe, where the phenomenon affected the entire foundation ground, absolute failure of more than 30 cm which led the entire building to undergo rotating mechanisms (**Figure 4.3a**). In other cases, there has been a widespread presence of differential failure which has caused the opening of diagonal lesions on both vertical structures (**Figure 4.3b**) and on the horizontal ones with widespread damage to external paving (**Figure 4.3c**) or inside (**Figure 4.3d** and **Figure 4.3e**).



Figure 4.3: Damage induced by liquefaction

Finally, they were observed in some buildings, in addition to the presence of damage induced by liquefaction, inertial damage (**Figure 4.3f** and **Figure 4.3g**). In fact, the activation of the phenomenon of liquefaction of-hangs from the acceleration of site. It is therefore possible that the liquefaction may have occurred after the initial phase for which it was possible to observe a combined damage.

4.2.4 EMPIRICAL DAMAGE: US vs. LS BUILDINGS

A comparative analysis of damage to the US and LS buildings is carried out herein using data from Section 4 of AeDES forms, see **Figure 4.4**. In particular, the data refer to the severity and extent of the damage detected in: vertical structures (VS); floors (F); stairs (S); roofs (R); and infill-partitions (IP). The AeDES forms identify four damage levels for each structural or non-structural component: no damage, D0; slight damage, D1; medium-severe damage, D2-D3; and very heavy damage or collapse, D4-D5. The damage extent is reported



This project has received funding from the European Union's Horizon 2020 research and innovation programme under grant agreement No. 700748

as follows: damage extent less than 1/3; between 1/3 and 2/3; and greater than 2/3 of the storey components.

Level - extension Structural component Pre-existing damage		DAMAGE									
		D4-D5 Very heavy			D2-D3 Medium-severe			D1 Slight			Null
		> 2/3	1/3 - 2/3	< 1/3	> 2/3	1/3 - 2/3	< 1/3	> 2/3	1/3 - 2/3	< 1/3	
		A	B	C	D	E	F	G	H	I	L
1	Vertical structures	☐	☐	☐	☐	☐	☐	☐	☐	☐	○
2	Floors	☐	☐	☐	☐	☐	☐	☐	☐	☐	○
3	Stairs	☐	☐	☐	☐	☐	☐	☐	☐	☐	○
4	Roof	☐	☐	☐	☐	☐	☐	☐	☐	☐	○
5	Infills-partitions	☐	☐	☐	☐	☐	☐	☐	☐	☐	○
6	Pre-existing damage	☐	☐	☐	☐	☐	☐	☐	☐	☐	○

Figure 4.4: Section 4- AeDES form: Damage to structural elements and existing short term countermeasures

Figure 4.5 shows a comparison between the LS and US buildings in terms of cumulative damage probability matrices (C-DPMs) that represent the percentage of buildings that reaches or exceeds the j-th level of damage in VSs. The figure clearly shows that the LS-class buildings suffered damage to the VSs that was more severe than that observed in the US sample. The data related to other structural or non-structural components are not represented because they essentially confirm that the severity and extent of the damage detected in the LS buildings was greater than that in the US buildings, especially with reference to stairs.

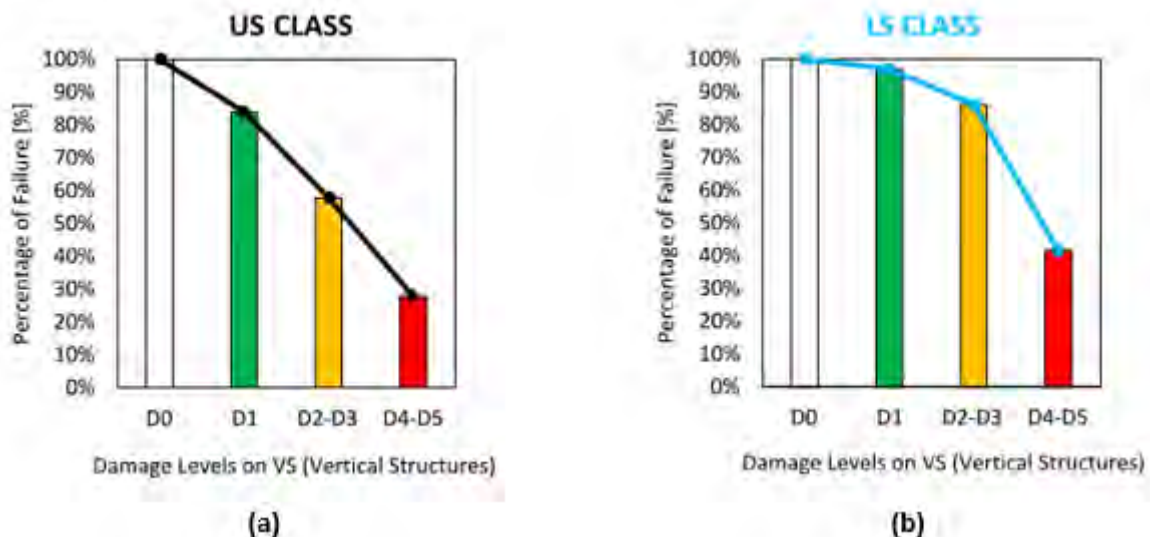


Figure 4.5: Vertical structure C-DPMs: US class (a); LS class (b).



This project has received funding from the European Union's Horizon 2020 research and innovation programme under grant agreement No. 700748

4.2.5 EFFECTS OF STRUCTURAL VULNERABILITY ON EMPIRICAL DAMAGE

In order to analyze the effects of structural vulnerability on the empirical damage detected in the US and LS buildings, different subsets of buildings for each class are defined in this section according to data related to vertical and horizontal structure types. In particular, Section 3 of the AeDES forms (Baggio et al. 2007) identifies five vertical structure types: a) unknown; b) masonry with an irregular layout or bad quality without ties; c) masonry with an irregular layout or bad quality with ties; d) masonry with a regular layout or good quality without ties; and e) masonry with a regular layout or good quality with ties. Furthermore, six horizontal structure types are reported: a) unknown; b) vaults with no ties; c) vaults with ties; d) beams with flexible slabs; e) beams with semi-rigid slabs; and f) beams with rigid slabs. Neglecting unknown structural types, the combination of vertical and horizontal structures leads to 20 masonry subsets of buildings, representing different vulnerability categories. A mean empirical global damage factor, μ_D , has been computed for each subset as the mean value of the global damage related to each building, $\mu_{D,i}$, defined as:

$$\mu_{D,i} = \sum_j D_j \gamma_j \quad (4.1)$$

where D_j is the damage level and extent related to the j^{th} component ($j=VS, F, S, R$ and IP), and γ_j is a coefficient, ranging between 0 and 1, accounting for the weight of the damage on the j^{th} component. D_j is computed as:

$$D_j = \frac{\sum_{D=D_0}^{D_5} D \cdot e_{k,D}}{5} \quad (4.2)$$

where D is the damage level ($D_0=0, D_1=1, D_2-D_3=2.5, D_4-D_5=4.5$) and $e_{k,D}$ is a coefficient accounting for the damage extent of the damage level D ; $e_{k,D}$ can assume three values depending on the percentage of the building affected by damage, k : $k < 1/3, e_{k,D} = 0.17$; k between $1/3$ and $2/3, e_{k,D} = 0.5$; and $k > 2/3, e_{k,D} = 0.83$) (Dolce et al. 2001).

Figure 4.6 reports an overall comparison between the mean damage, μ_D , suffered by the different subsets of data for the US (**Figure 4.6a**) and LS (**Figure 4.6b**) buildings, respectively. The number of buildings required to compute the mean global damage of each subset is also reported in **Figure 4.6**.

Figure 4.6a shows a very similar μ_D value (i.e. In the range 0.10 -0.20) for masonry buildings with vaults with or without tie rods or with flexible slabs. As expected, the mean empirical global damage decreases in the case of buildings with a horizontal structure characterized by semi-rigid or rigid slabs, with values lower than 0.10 for each building subset. This result is consistent with the favourable role of such structural components in the global behavior against seismic action due to the transfer of action on VSs and the relevant attainment of the so-called “box-type” building behavior. Furthermore, there is clear evidence of the benefits provided by a regular layout and good quality masonry compared to an irregular layout and bad quality stonework. Accordingly, a clear trend can be observed between the parameters influencing structural vulnerability to



This project has received funding from the European Union's Horizon 2020 research and innovation programme under grant agreement No. 700748

lateral actions and the mean empirical global damage. In contrast, **Figure 4.6b** clearly shows that the trend between the mean empirical global damage and the vertical/horizontal structural types is less evident than in the US building class. This is probably because the liquefaction may induce localized effects or the global rotation of the buildings that are less affected by those structural characteristics. Furthermore, the mean empirical global damage peak value is greater in the LS class buildings than in the US subsets: $\mu_D = 0.07 - 0.27$ versus $\mu_D = 0.20$. However, it should be noted that the number of buildings in each data subset for the LS class is significantly lower than in the US subsets and this may influence the results.

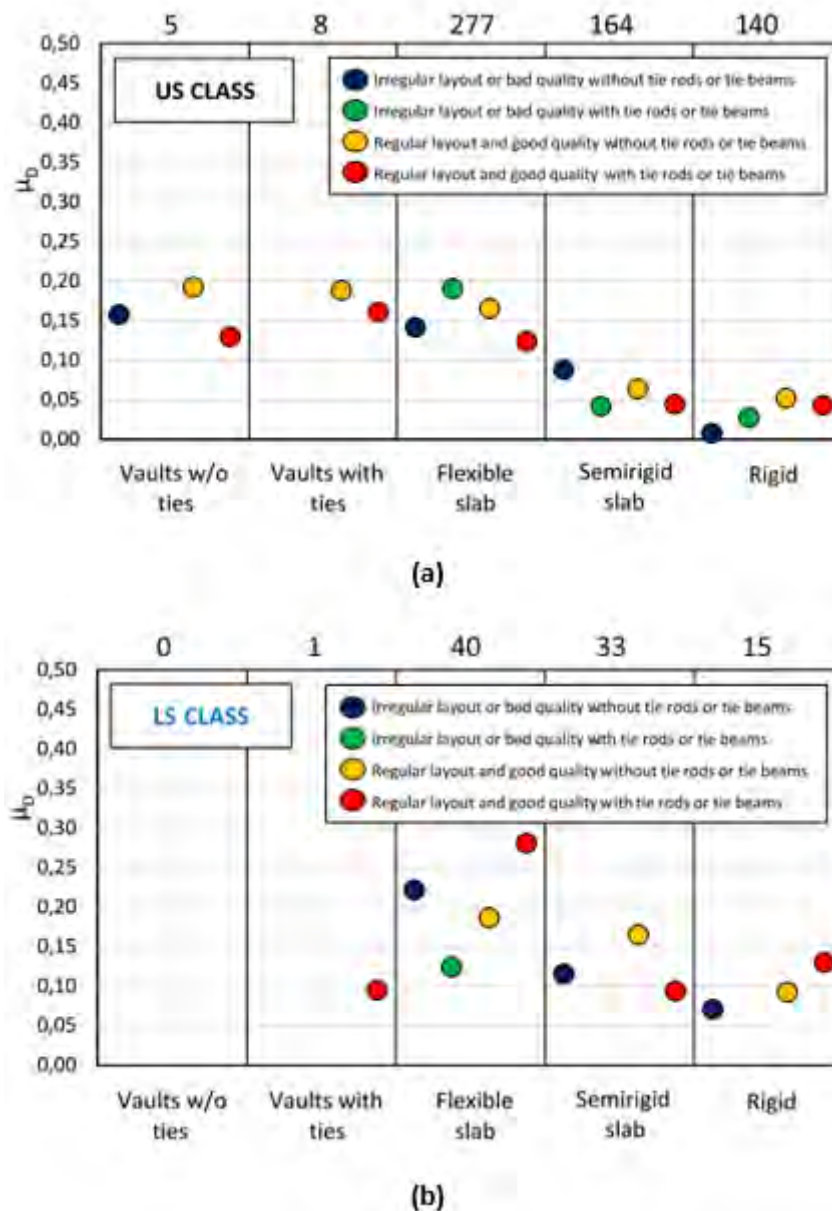


Figure 4.6: Mean empirical damage as a function of the vulnerability categories of buildings.



This project has received funding from the European Union's Horizon 2020 research and innovation programme under grant agreement No. 700748

4.2.6 PREDICTION OF REPAIR COSTS

The mean empirical damage is a measure of the global damage detected in a building, but may not be an adequate measure when it comes to making a prediction of losses, because it does not correlate the damage caused to each building component with its economic value. Consequently, in this section, in order to focus on the impact of liquefaction in terms of economic losses, a different parameter is used to compute these losses, in particular a measure that is related to the aftermath of the L'Aquila event (De Martino G. et al. 2017). This parameter, named as the damage factor (DF), has been calibrated on data costs related to the reconstruction process and directly accounts for the real losses computed by practitioners involved in the estimation of repair costs (Di Ludovico et al. 2016a and b). The DF is directly computed using the data reported in Section 3 of the AeDES forms, but depends on the D_j and γ_j values specifically calibrated for loss analyses. Furthermore, a relationship between the DF and actual repair costs (ARC) induced by damage (or between the DF and an a-dimensional cost ratio obtained as a ratio between the ARC related to the building and the average building demolition and reconstruction cost - building repair cost ratio, C_r) is reported in De Martino et al. 2017 and recalled as follows:

$$ARC = 143 + 849 DF - 277 DF^2 \quad (4.3)$$

$$C_r = 0.12 + 0.71 DF - 0.23 DF^2 \quad (4.4)$$

The median DFs are 0.052 and 0.124, corresponding to a median C_r of 0.156 and 0.204 for the US and LS classes, respectively. Accordingly, the effects of liquefaction may lead, based on the predictions of such a model, to an increase in the repair costs of about 30% in cases where liquefaction was not observed.

4.3 EMPIRICAL FRAGILITY CURVES

Fragility curves related to seismic events define the exceeding probability of a given damage grade (DG) as a function of a ground motion intensity measure (IM). The IM may be a macroseismic parameter or, as commonly adopted in recent studies, is represented by a ground motion intensity record in terms of various peak ground parameters: acceleration (PGA); velocity (PGV); and displacement (PGD). A commonly used functional form and regression technique to produce fragility curves is the lognormal cumulative distribution function:

$$P[DG \geq dg|IM] = \Phi\left(\frac{\ln(IM) - \mu}{\sigma}\right) \quad (4.5)$$

where $\Phi(\cdot)$ is the standard normal cumulative distribution function (CDF), μ is the logarithmic mean and σ is the logarithmic standard deviation defining the lognormal distribution. This returns values between 0 and 1 and is particularly suitable for fitting data clustered around low values, as is commonly the case in fragility analyses (Rossetto et al. 2013). The parameters μ and σ can be determined according to the nonlinear least squares estimation (LSE) methodology, which aims to derive the most accurate description of data, or by



This project has received funding from the European Union's Horizon 2020 research and innovation programme under grant agreement No. 700748

means of the maximum likelihood estimation (MLE) approach (e.g. Baker 2015), which is an iterative method to determine the parameters maximizing the likelihood function:

$$Likelihood = \prod_{j=1}^m \binom{N_j}{n_j} p_j^{n_j} (1 - p_j)^{N_j - n_j} \quad (4.6)$$

where p_j is the probability that n_j number of buildings over N_j shows damage that is greater than or equal to a threshold DG_i in the j^{th} bin of the IM.

Another available functional form used in the literature is the exponential model (Rossetto and Elnashai 2003, Amiri et al. 2007).

$$P[DG \geq dg|IM] = 1 - e^{-\alpha IM^\beta} \quad (4.7)$$

The parameters α and β can be determined according to the LSE or MLE methodology. In the following, both functional forms (i.e. lognormal and exponential) are used, along with the nonlinear LSE and MLE methodologies. In order to produce fragility curves that take into account the liquefaction phenomenon, it is necessary to define suitable DGs and IMs.

4.3.1 DAMAGE GRADES

The empirical data collected in Section 4 of the AeDES forms (Baggio et al. 2007) were used to define the buildings' DGs. In particular, the DG of each building was determined by accounting for the level and extent of the damage to the VS component, and five damage grades were assumed based on the European Macroseismic Scale, EMS-98 (Grüenthal 1998). The criterion used to convert the empirical damage to DGs was that reported in Dolce et al. 2017 and is summarized in **Table 4.1**.

The table shows the corresponding DGs assumed for the building for each damage level and its relevant extent. Note that the AeDES forms allow multiple choices in the selection of the damage level and extent and so different combinations are possible.

4.3.2 LIQUEFACTION INDICES

In this study, a synthetic liquefaction potential index was adopted as an IM, in order to correlate the observed building damage due to the occurrence of liquefaction.



This project has received funding from the European Union's Horizon 2020 research and innovation programme under grant agreement No. 700748

Table 4.1: DG (EMS-98) and corresponding damage levels to VSs according to the AEDES survey forms (Baggio et al. 2007).

Vertical structures			
EMS-98 damage		AeDES damage	
Damage grade	Damage description	Damage level	Extent
DG1	<i>Fine cracks in plaster over frame members or in walls at the base.</i>	D1	<1/3 1/3-2/3 >2/3
		D2-D3	<1/3
DG2	<i>Cracks in the columns and beams of frames and in structural walls.</i>	D2-D3 and D1	<1/3 <1/3 and 1/3-2/3 <1/3 and >2/3
		D2-D3 and D1	1/3-2/3 and <1/3
DG3	<i>Cracks in the columns and beam-column joints of frames at the base and at the joints of coupled walls.</i>	D2-D3	1/3-2/3 >2/3
		D4-D5	<1/3
		D4-D5 and D1	<1/3 and <1/3 <1/3 and 1/3-2/3
		D4-D5 and D2-D3	<1/3 and <1/3
		D4-D5 and D2-D3 and D1	<1/3
DG4	<i>Large cracks in structural elements, with a compression failure of the concrete and a fracture of rebars; [...] collapse of a few columns or a single upper floor.</i>	D4-D5 and D2-D3	<1/3 and 1/3-2/3 <1/3 and >2/3
		D4-D5	1/3-2/3
		D4-D5 and D1	1/3-2/3 and 1/3-2/3
		D4-D5 and D2-D3	1/3-2/3 and <1/3
DG5	<i>Collapse of ground floor or parts of buildings.</i>	D4-D5 and D2-D3	1/3-2/3 and 1/3-2/3
		D4-D5	>2/3
		D4-D5 and D1	>2/3 and <1/3
		D4-D5 and D2-D3	>2/3 and <1/3

The assessment of potential liquefaction is still one of the most debated topics in earthquake geotechnical engineering. In common engineering practice, it is usually based on simplified methods which propose empirical relationships between liquefaction evidence observed after strong seismic events and soil liquefaction resistance, as measured with traditional in-situ tests, such as CPTs and SPTs (Boulanger & Idriss 2016). Within this framework, it is possible to calculate a safety factor, F_L , for each of the investigated layers as the ratio between the soil liquefaction capacity, CRR, and the expected seismic demand, CSR. The increased attention paid to the effects on the built environment induced by liquefaction has led over time to



This project has received funding from the European Union's Horizon 2020 research and innovation programme under grant agreement No. 700748

the introduction of indices which synthetize the liquefaction susceptibility of soil. The earliest index was proposed by Iwasaki et al. 1984 as a function of the safety factor F_L against liquefaction and is as follows:

$$LPI = \int_0^{20} F(z) \cdot W(z) dz \quad (4.8)$$

where z is the depth of the midpoint of the soil layer in meters and $F(z)$ and $W(z)$ are:

$$F(z) = \begin{cases} 1 - F_L & \text{for } F_L < 1 \\ 0 & \text{for } F_L \geq 1 \end{cases} \quad (4.9)$$

$$W(z) = 10 - 0.5z \quad (4.10)$$

Although it has gained wide popularity worldwide, the LPI only accounts for conditions of full liquefaction ($F_L \leq 1$), while excess pore pressure build-up can induce a significant reduction in stiffness and strength of soil also when liquefaction condition has not been attained. Such excess pore pressure build-up induces settlement, while the reduction of shear strength reduces the bearing capacity safety margins, possibly leading to building collapse prior to liquefaction triggering. Furthermore, even in these non-liquefied conditions, the post-seismic consolidation process (possible if the stratigraphic conditions allow for drainage) leads to settlement at ground level (Chiaradonna et al. 2018a). Over the years, modifications to the LPI have been proposed by several authors (Sonmez 2003; Sonmez & Gokceoglu 2005; Rashidian & Gillins 2018). Sonmez & Gokceoglu (2005), for instance, introduced a liquefaction probability in the original formulation. However, the threshold value of the safety factor that they introduce in the analysis is still a debated issue.

Recently, Van Ballegooy et al. 2014 introduced a new synthetic parameter, named liquefaction severity number (LSN). This parameter is calculated by considering soil volumetric deformation, and has the advantage of allowing the contribution of unliquefied ($F_L \geq 1$) soil strata to be taken into account, thus removing one of the shortcomings of LPI. Nevertheless, the assessment of volumetric deformation is purely empirical, being based on the use of charts in which it is related to relative density (D_r) and to F_L for a specific clean Japanese sand (Zhang et al. 2002). Even though these correlations are easy to use, they have the major drawback of being based on laboratory test results obtained on specific sand (Fuji River sand). Therefore, there is really no reason why they should correctly interpret the behavior of sand with different grades and mineralogy.

Despite the limitations of the synthetic parameters previously discussed, they have the great advantage of allowing the estimation of an order of magnitude of the effect of liquefaction. Whatever the choice, the synthetic parameter to be used as IM for the construction of fragility curves needs to be clearly related to the effects of pore pressure build-up at ground level that cause the damage of structures. Therefore, there should be a rational link between this IM and the induced ground settlement. As the effects of sand ejecta (if any) are difficult to quantify, post-consolidation settlement was specifically considered in this case to propose a simple but sound integral indicator. In free-field conditions, such a settlement can be expressed as:



This project has received funding from the European Union's Horizon 2020 research and innovation programme under grant agreement No. 700748

Methodology for the liquefaction fragility analysis of critical structures and infrastructures: description and case studies

$$w = \int_{z_{min}}^{z_{max}} \frac{\Delta\sigma'_v(z)}{E_{oed}(z)} dz \quad (4.11)$$

where z_{min} and z_{max} are, respectively, the minimum and maximum depths of the uppermost saturated, potentially liquefiable, soil layer (**Figure 4.7**); $\Delta\sigma'_v$ is the increase of effective vertical stress induced by the dissipation of the excess pore pressure, Δu ; and E_{oed} is the constrained (oedometric) modulus.

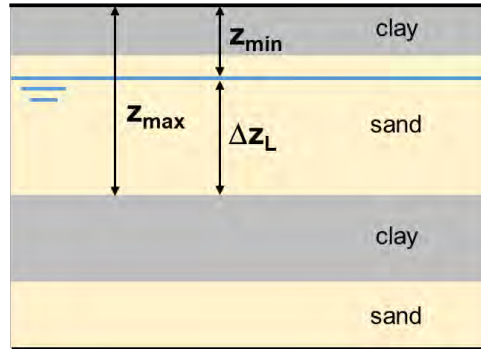


Figure 4.7: Minimum, z_{min} , and maximum, z_{max} , depths of the uppermost saturated, potentially liquefiable, soil layer.

A new liquefaction potential index is proposed in this work as follows:

$$I_{AM} = \frac{1}{1 + z_{min}} \cdot \int_{z_{min}}^{z_{max}} r_u \cdot dz \quad (4.12)$$

in which r_u is the excess pore pressure ratio (defined as the ratio between the excess pore pressure induced by the seismic event, Δu , and the initial effective vertical stress in free-field conditions, σ'_{v0}). This index was adopted because it is strictly related to the volumetric settlement of ground level induced by liquefaction, as will be shortly discussed in the following. Using the parameter r_u , Equation (4.11) can be written as:

$$w = \int_{z_{min}}^{z_{max}} \frac{r_u \cdot \sigma'_{v0}(z)}{E_{oed}(z)} dz \quad (4.13)$$

Assuming for $\sigma'_{v0}(z)$ and $E_{oed}(z)$ the mean values $\sigma'_{v0,m}(z = (z_{min} + z_{max})/2)$ and $E_{oed,m}(z = (z_{min} + z_{max})/2)$, Equation (4.13) can be rearranged as:

$$\frac{w \cdot E_{oed,m}}{\sigma'_{v0,m}} = \int_{z_{min}}^{z_{max}} r_u dz \quad (4.14)$$

Therefore, in a fully liquefied layer ($r_u=1$):



This project has received funding from the European Union's Horizon 2020 research and innovation programme under grant agreement No. 700748

$$\frac{w \cdot E_{oed,m}}{\sigma'_{v0,m}} = \int_{z_{min}}^{z_{max}} dz = z_{max} - z_{min} = \Delta z_L \quad (4.15)$$

Equation (4.15) allows to easily calculate the effect of liquefaction in terms of potential post-liquefaction consolidation settlement, normalized to the average values of the vertical effective stress and the constrained modulus in the uppermost liquefiable layer. This can be done simply by considering such a normalized settlement as the thickness of the uppermost liquefiable layer. In order to make this normalized settlement non-dimensional, and considering that the potential post-liquefaction settlement is more likely to take place as this layer gets closer to ground level, the desired (and physically based) synthetic parameter I_{AM} is finally obtained and defined as:

$$I_{AM} = \frac{w \cdot E_{oed,m}}{\sigma'_{v0,m} \cdot (1 + z_{min})} = \frac{\Delta z_L}{1 + z_{min}} \quad (4.16)$$

I_{AM} can then be simply calculated on the basis of stratigraphic evidence. The proposed potential index has been computed for both study areas based on the field investigation database produced by the Emilia Romagna region, which is composed of 166 CPTs and 170 CPTUs. The calculation has been carried out by assuming that the 20th May 2012 seismic event induced the full liquefaction of the potentially liquefiable deposits, according to Equation (4.16). This simplified assumption is realistic, since there was widespread evidence of liquefaction in the study area (Fioravante et al. 2013; Lai et al. 2015; Papathanassiou et al. 2015).

Figure 4.8 shows the minimum depth isolines of the first potentially liquefiable soil layer under the surface, z_{min} (in meters), superimposed on the geological map. The figure highlights that the liquefiable soil deposits are shallowest along the paleochannel and paleobank (depth of 2-3 m on average), while higher depths are observed in the surrounding plain.

Figure 4.9 reports the spatial distribution of the proposed index, according to Equation (4.16), which is consistent with the geological setting and the observed damage. As a matter of fact, higher I_{AM} values are calculated along the paleo-channel of the Reno River in both municipalities, where most of the LS buildings are also located.

Since the I_{AM} distribution reflects the geological map of the area (**Figure 4.9**), a mean I_{AM} value has been assigned to any geological unit, as reported in **Figure 4.10**.



This project has received funding from the European Union's Horizon 2020 research and innovation programme under grant agreement No. 700748

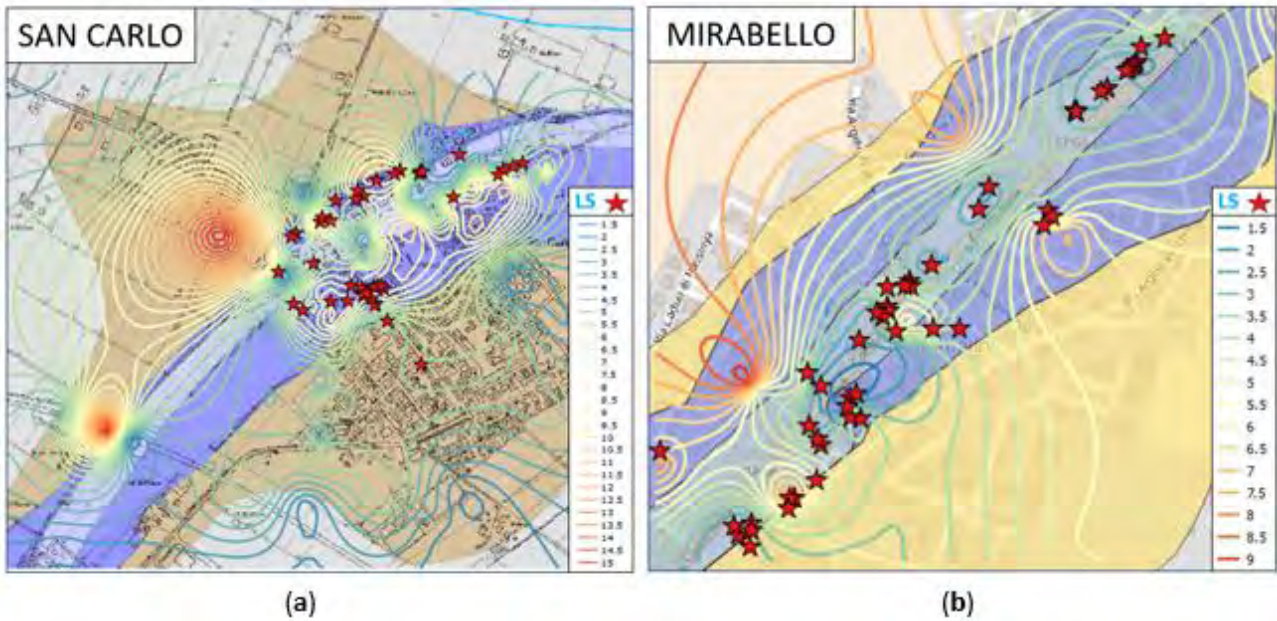


Figure 4.8: Minimum depth isolines of the first potentially liquefiable soil layer under the surface, z_{min} (in meters), superimposed on the geological map, vs. the observed building damage induced by liquefaction (red symbols) in the municipalities of S. Carlo (a) and Mirabello (b).

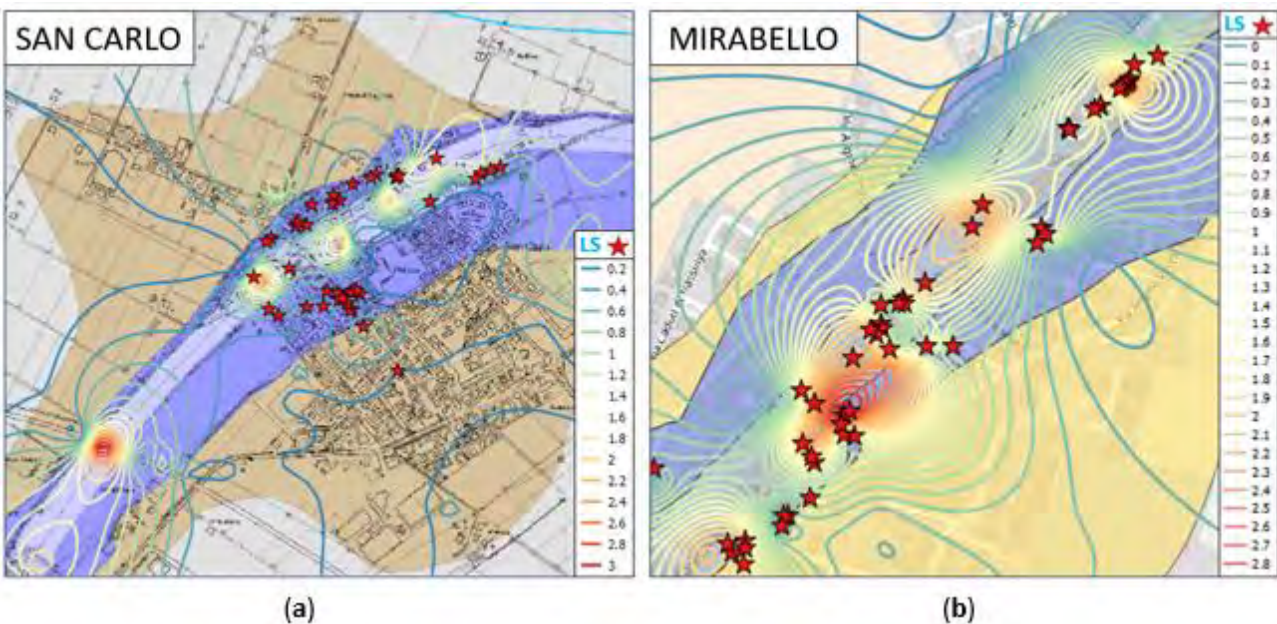


Figure 4.9: I_{AM} index isolines superimposed on the geological map, vs. the observed building damage induced by liquefaction (red symbols) in the municipalities of S. Carlo (a) and Mirabello (b).



This project has received funding from the European Union's Horizon 2020 research and innovation programme under grant agreement No. 700748

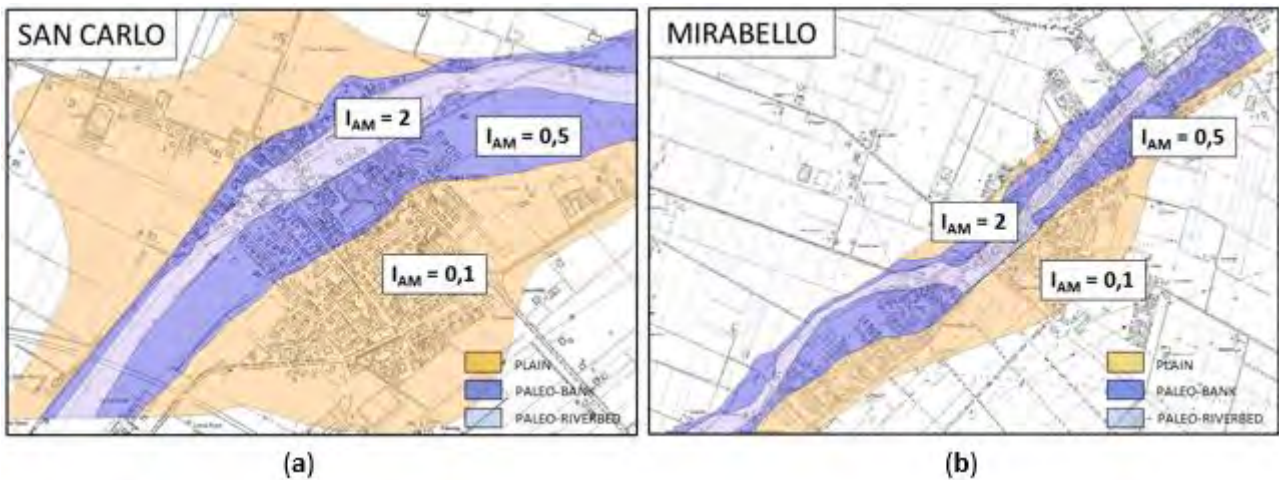


Figure 4.10: Geological map with I_{AM} values adopted for the municipalities of S. Carlo (a) and Mirabello (b).

4.3.3 LIQUEFACTION FRAGILITY CURVES

In this section, preliminary liquefaction fragility curves are derived according to the methodologies described above for the entire dataset of buildings (i.e. about 750 in the US and LS classes and about 350 with no damage). **Figure 4.11** reports the fragility curves for the assumed functional forms and fitting methodologies. Due to the reduced amount of data, no reliable estimation of the fragility curves at DG4 and DG5 can be provided. **Figure 4.11** shows that no significant difference is observed in the lognormal or exponential models. Strictly speaking, the advantages of using a functional form can be evaluated by comparing the values of: a) the weighted sum of the square of the errors in the LSE methodology; and b) the likelihood in the MLE methodology, obtained by adopting the lognormal and exponential models. In both cases, the use of the lognormal model yields slightly better results, i.e. a lower weighted sum of the square of the errors (with the LSE methodology) and a higher likelihood (with the MLE methodology).



This project has received funding from the European Union's Horizon 2020 research and innovation programme under grant agreement No. 700748

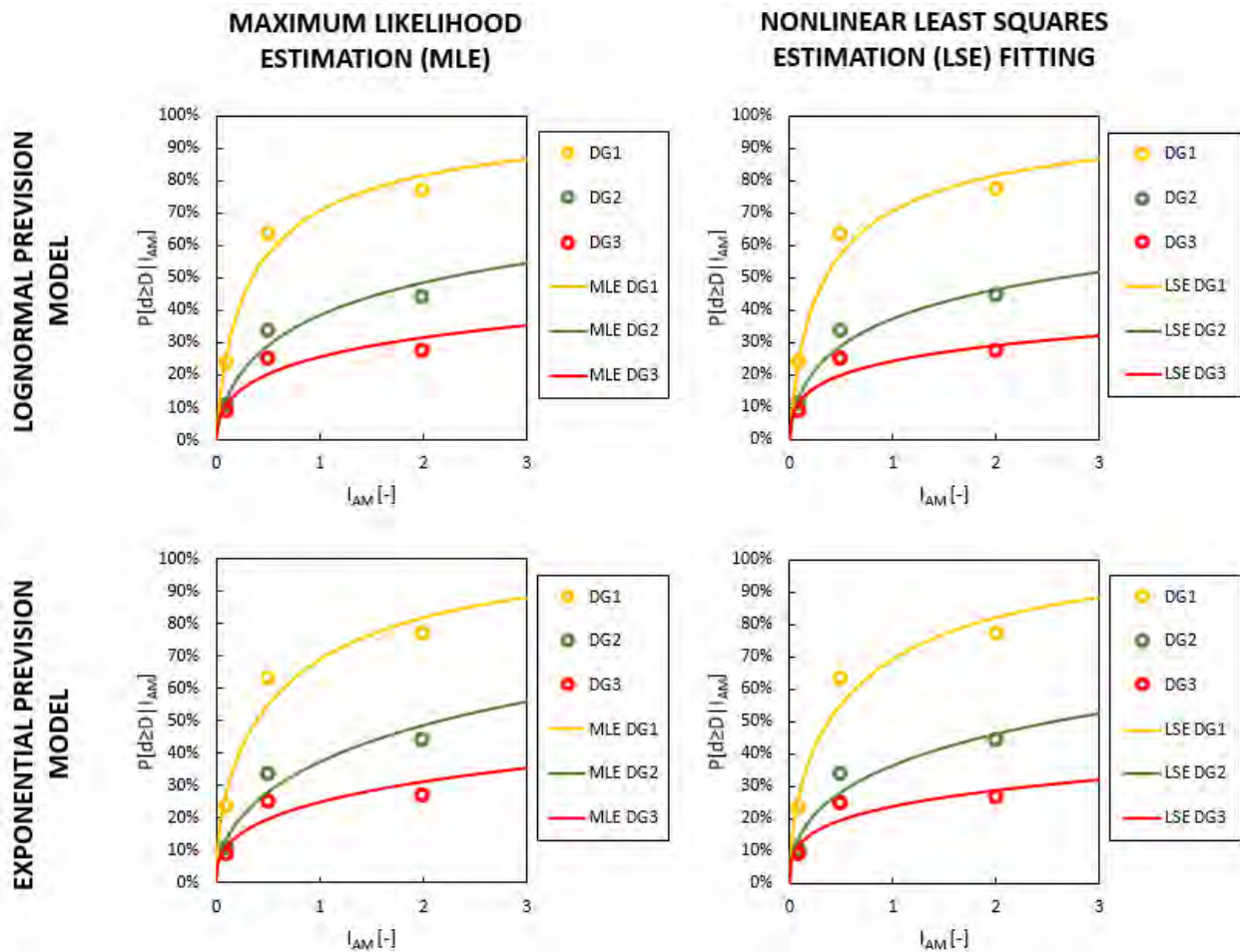


Figure 4.11: Lognormal and exponential fragility curves (solid lines) fitting observed fragility data (circles) for all the buildings and the adopted regression techniques (MLE and LSE).

4.4 CONCLUSIONS

The 2012 Emilia earthquake highlighted the large extent of the damage caused to structures and infrastructures due to soil liquefaction. The study presented herein investigated the effects of liquefaction on private residential masonry buildings using data on about 1,000 such structures located in several municipalities hit by the earthquake. According to empirical data collected immediately after the seismic event, it was possible to compare the behavior of structures whose soil foundation was not subjected to the liquefaction phenomena (the US class of buildings) with that of buildings that were (the LS class of buildings). The analysis of the damage in the LS class of buildings confirmed that, if immediately activated, liquefaction works as a natural isolation system against the transmission of inertial seismic actions on a superstructure; in these cases, the damage is mainly governed by the rigid rotation of buildings or settlements. However, liquefaction is often not immediately activated and this leads to a damage pattern that is characterized by both typical inertial damage (i.e. masonry walls overturning or in-plane cracks) and localized settlements (i.e. rigid rotation or one-way diagonal cracks).



This project has received funding from the European Union's Horizon 2020 research and innovation programme under grant agreement No. 700748

The comparative analysis of the damage observed to the US and LS building classes has revealed evidence of the impact of soil liquefaction on structures. In particular, the empirical damage detected to the LS class of buildings was generally more severe than that sustained by the US class. The macro-parameters influencing the structural vulnerability of masonry buildings to inertial actions was less decisive in the evaluation of the global building damage caused by liquefaction. However, rigid horizontal structures confirmed their crucial role in limiting damage for both building classes. By using a model calibrated empirically to compute losses, the predicted repair costs were about 30% higher in the LS than the US buildings.

The correlation between structural damage and soil liquefaction allowed to derive empirical fragility curves, and a suitable synthetic and new parameter to define liquefaction effects has also been defined and presented. Such a new liquefaction index can be calculated in a very straightforward way and is clearly related to the effects that damage structures at ground level, and so to the calculation of ground settlement. This allowed us to produce suitable fragility curves to determine the probability of exceeding the damage grades defined according to EMS-98 as a function of a parameter that specifically accounts for the potential liquefaction of the shallower liquefiable soil layer. Although the curves presented herein depend on the local context where the seismic event occurred and further data from other events are required, they certainly represent a preliminary tool to predict losses in liquefaction-prone areas and to establish priorities and reconstruction policies for use in the aftermath of future earthquakes.

REFERENCES

- Amiri GG, Jalalian M, Amrei SAR (2007) Derivation of vulnerability functions based on observational data for Iran. In: Proceedings of international symposium on innovation and sustainability of structures in civil engineering, Tongji University, China
- Baggio C, Bernardini A, Colozza R, Coppari S, Corazza L, Della Bella M, Di Pasquale G, Dolce M, Goretti A, Martinelli A, Orsini G, Papa F, Zuccaro G (2007) Field manual for post-earthquake damage and safety assessment and short-term countermeasures (Pinto A, Taucer Feds), Translation from Italian: Goretti A, Rota M, JRC Scientific and technical reports, EUR 22868 EN-2007
- Baker JW (2015) Efficient analytical fragility function fitting using dynamic structural analysis. *Earthq Spectra* 31(1):579–599
- Borzi B, Pinho R, Crowley H (2008) Simplified pushover-based vulnerability analysis for large scale assessment of RC buildings. *Eng Struct* 30(3):804–820
- Boulangier RW, Idriss IM (2016) CPT-Based Liquefaction Triggering Procedure. *Journal of Geotechnical and Geoenvironmental Engineering*, 142(2):04015065.
- Bray JD Dashti S (2014) Liquefaction-induced building movements. *Bulletin of Earthquake Engineering*, 12: 1129-1156.
- Calvi GM (1999) A displacement-based approach for vulnerability evaluation of classes of buildings. *J Earthq Eng* 3(3):411–438
- Cazares U, Nino M, Reinoso E (2012) Vulnerability functions for buildings due to liquefaction. Proceedings of the 15th World Conference on Earthquake Engineering (15WCEE), Lisboa, Portugal.
- Chiaradonna A, Bilotta E, d’Onofrio A, Flora A, Silvestri F (2018a) A simplified procedure for evaluating post-seismic settlements in liquefiable soils. Proceedings of the 5th Conference on Geotechnical Earthquake Engineering and Soil Dynamics (GEESDV), Austin (TX), GSP 290:51-59. DOI: 10.1061/9780784481455.005



This project has received funding from the European Union's Horizon 2020 research and innovation programme under grant agreement No. 700748

- Chiaradonna A, Tropeano G, d'Onofrio A, Silvestri F (2018b) Interpreting the deformation phenomena of a levee damaged during the 2012 Emilia Earthquake. Special Issue of Soil Dynamic and Earthquake Engineering, SDEE, <https://doi.org/10.1016/j.soildyn.2018.04.039>
- Cosenza E, Manfredi G, Polese M, Verderame GM (2005) A multi-level approach to the capacity assessment of existing RC buildings. *J Earthq Eng* 9(1):1–22
- Crowley H, Pinho R, Bommer JJ (2004) A probabilistic displacement-based vulnerability assessment procedure for earthquake loss estimation. *Bull Earthq Eng* 2(2):173–219
- Cubrinovski M (2013) Liquefaction-Induced Damage in The 2010-2011 Christchurch (New Zealand) Earthquakes, Seventh International Conference on Case Histories in Geotechnical Engineering.
- Dashti S, Bray JD (2013) Numerical Simulation of Building Response on Liquefiable Sand. *Journal of Geotechnical and Geoenvironmental Engineering*, 139(8): 1235-1249.
- Del Gaudio C, Ricci P, Verderame GM, Manfredi G (2015) Development and urban-scale application of a simplified method for seismic fragility assessment of RC buildings. *Eng Struct* 91:40–57. doi: 10.1016/j.engstruct.2015.01.031
- Del Gaudio C., De Martino G., Di Ludovico M., Manfredi G., Prota A, Ricci P., Verderame G.M. (2017) “Empirical fragility curves from damage data on RC buildings after the 2009 L’Aquila earthquake”, *Bulletin of Earthquake Engineering*, Volume 15, Issue 4, 2017, Pages 1425-1450,, DOI 10.1007/s10518-016-0026-1
- De Martino G., Di Ludovico M., Prota A., Moroni C., Manfredi G., Dolce M. (2017) Estimation of Repair Costs for RC and Masonry Residential Buildings Based on Damaged Data Collected by Post-Earthquake Visual Inspection, *Bulletin of Earthquake Engineering*, Volume 15, Issue 4, 2017, Pages 1681-1706, DOI 10.1007/s10518-016-0039-9.
- Di Ludovico M, Prota A, Moroni C, Manfredi G, Dolce M (2017a) “Reconstruction process of damaged residential buildings outside the historical centres after L’Aquila earthquake—part I: “light damage” reconstruction. *Bull Earthq Eng*. doi:10.1007/s10518-016-9877-8
- Di Ludovico M, Prota A, Moroni C, Manfredi G, Dolce M (2017b) Reconstruction process of damaged residential buildings outside historical centres after the L’Aquila earthquake—part II: “heavy damage” reconstruction. *Bull Earthq Eng*. doi:10.1007/s10518-016-9979-3
- Dolce M., Moroni C., Samela C., Marino M., Masi A., Vona M. (2001) Una Procedura di Normalizzazione del Danno per la Valutazione degli Effetti di Amplificazione Locale, *Proceedings of the X National conference of seismic engineering in Italy*, Potenza-Matera, 9-13 September (in Italian)
- Dolce M, Speranza E, Giordano F, Borzi B, Bocchi F, Conte C, Di Meo A, Faravelli M, Pascale V (2017) Da.D.O - Uno strumento per la consultazione e la comparazione del danno osservato relativo ai più significativi eventi sismici in Italia dal 1976, ANIDIS 2017 - XVII Convegno Pistoia 17 settembre 2017 – 21 settembre 2017.
- Facciorusso J, Madiari C, Vannucchi G (2012) Rapporto sulla risposta sismica locale e pericolosità di liquefazione a S. Carlo e Mirabello. <http://ambiente.regione.emilia-romagna.it/geologia/temi/sismica/liquefazione-gruppo-di-lavoro>
- Fioravante V, et al. (2013) Earthquake Geotechnical engineering aspects of the 2012 Emilia-Romagna earthquake (Italy). *Proceedings of the 7th International Conference on case Histories in Geotechnical Engineering*. pp. 1–34.
- Grüenthal G (1998) *Cahiers du Centre Européen de Géodynamique et de Séismologie: volume 15—European Macroseismic Scale 1998*. European Center for Geodynamics and Seismology, Luxembourg
- Gruppo di lavoro per la valutazione degli effetti di liquefazione a seguito dei terremoti del 20 e 29 maggio 2012 (Regione Emilia-Romagna, PG.2012.0134978 del 31/5/2012), Rapporto sugli effetti della liquefazione osservati a Mirabello (Provincia di Ferrara), Dipartimento Protezione Civile e Regione Emilia Romagna. <http://ambiente.regione.emilia-romagna.it/geologia/temi/sismica/speciale-terremoto/interventi-per-la-ricostruzione-e-la-ripresa>
- Iervolino I, Manfredi G, Polese M, Verderame GM, Fabbrocino G (2007) Seismic risk of R.C. building classes. *Eng Struct* 29(5):813–820



This project has received funding from the European Union's Horizon 2020 research and innovation programme under grant agreement No. 700748

- Iwasaki T, Arakawa T, Tokida K (1984) Simplified Procedures for Assessing Soil Liquefaction During Earthquakes. *Soil Dynamics and Earthquake Engineering*, 3(1):49–58.
- ISTAT (2011) 15° Censimento della popolazione e delle abitazioni 2011. Istituto Nazionale di Statistica. <http://www.istat.it/it/censimento-popolazione/censimento-popolazione-2011>
- Karamitros DK, Bouckovalas GD, Chaloulos YK (2013) Seismic settlements of shallow foundations on liquefiable soil with a clay crust. *Soil Dynamics and Earthquake Engineering*, 46, pp.64–76. Available at: <http://dx.doi.org/10.1016/j.soildyn.2012.11.012>.
- Lai CG, et al. (2015) Soil liquefaction during the 20 May 2012 M5.9 Emilia earthquake, Northern Italy: Field reconnaissance and post-event assessment. *Earthquake Spectra*, 31(4):2351–2373.
- Lopez-Caballero F, Khalil C (2018) Vulnerability Assessment for Earthquake Liquefaction–Induced Settlements of an Embankment Using Gaussian Processes. *ASCE-ASME Journal of Risk and Uncertainty in Engineering Systems, Part A: Civil Engineering*, 4(2):04018010. Available at: <http://ascelibrary.org/doi/10.1061/AJRU6.0000957>.
- Luque R, Bray JD (2017) Dynamic Analyses of Two Buildings Founded on Liquefiable Soils during the Canterbury Earthquake Sequence. *Journal of Geotechnical and Geoenvironmental Engineering*, 143(9):04017067. Available at: <http://ascelibrary.org/doi/10.1061/%28ASCE%29GT.1943-5606.0001736>.
- Ordinanza n. 29 del 28 agosto 2012 Regione Emilia-Romagna, Criteri e modalità di assegnazione di contributi per la riparazione e il ripristino immediato di edifici e unità immobiliari ad uso abitativo danneggiati dagli eventi sismici del 20 e 29 maggio 2012 e temporaneamente o parzialmente inagibili. Ordinanza Commissario Delega Regione Emilia-Romagna n.29 del 28/08/2012. <http://ambiente.regione.emilia-romagna.it/geologiatemi/sismica/speciale-terremoto>
- Ordinanza n. 51 del 5 ottobre 2012 Regione Emilia-Romagna, Criteri e modalità di assegnazione di contributi per la riparazione e il ripristino con miglioramento sismico di edifici e unità immobiliari ad uso abitativo che hanno subito danni significativi dagli eventi sismici del 20 e 29 maggio 2012 e che sono stati dichiarati inagibili. (ESITO E0). Ordinanza Commissario Delega Regione Emilia-Romagna n. 51 del 5/10/2012. <http://ambiente.regione.emilia-romagna.it/geologia/temi/sismica/speciale-terremoto>
- Ordinanza n. 86 del 6 dicembre 2012 Regione Emilia-Romagna, Criteri e modalità di assegnazione di contributi per la riparazione, il ripristino con miglioramento sismico o la demolizione e ricostruzione di edifici e unità immobiliari ad uso abitativo che hanno subito danni gravi a seguito degli eventi sismici del 20 e 29 maggio 2012 e che sono stati dichiarati inagibili (ESITO E1, E2 o E3). Ordinanza Commissario Delega Regione Emilia-Romagna n.86 del 6/12/2012. <http://ambiente.regione.emilia-romagna.it/geologia/temi/sismica/speciale-terremoto>
- Papathanassiou G et al. (2015) Assessment of liquefaction potential for two liquefaction prone areas considering the May 20, 2012 Emilia (Italy) earthquake. *Engineering Geology*, 189:1–16. <http://dx.doi.org/10.1016/j.enggeo.2015.02.002>.
- Rashidian V, Gillins DT (2018) Modification of the liquefaction potential index to consider the topography in Christchurch, New Zealand. *Engineering Geology*, 232:68–81. Available at: <https://doi.org/10.1016/j.enggeo.2017.11.010>.
- Rossetto T, Elnashai A (2003) Derivation of vulnerability functions for European-type RC structures based on observational data. *Eng Struct* 25(10):1241–1263
- Rossetto T, Ioannou I, Grant DN (2013) Existing empirical fragility and vulnerability functions: compendium and guide for selection. GEM technical report 2013-X, GEM Foundation, Pavia
- Rota M, Penna A, Strobbia CL (2008) Processing Italian damage data to derive typological fragility curves. *Soil Dyn Earthq Eng* 28(10):933–947
- Sonmez H (2003) Modification of the liquefaction potential index and liquefaction susceptibility mapping for a liquefaction-prone area (Inegol, Turkey). *Environmental Geology*, 44(7):862–871.



This project has received funding from the European Union's Horizon 2020 research and innovation programme under grant agreement No. 700748

- Sonmez H, Gokceoglu C (2005) A liquefaction severity index suggested for engineering practice. *Environmental Geology*, 48(1):81–91.
- Tokimatsu K, Mizuno H, Kakurai M (1996). Building damage associated with geotechnical problems. *Special Issue of Soils and Foundations*, 219-234.
- Van Ballegooy S et al. (2014) Assessment of liquefaction-induced land damage for residential Christchurch. *Earthquake Spectra*, 30(1):31–55.
- Yoshida N, Tokimatsu K, Yasuda S, Kokusho T, Okimura T (2001) Geotechnical aspects of damage in Adapazari city during 1999 Kocaeli, Turkey earthquake. *Soils and Foundations*, 41(4):25-45.
- Zhang G, Robertson PK, Brachman RW (2002) Estimating liquefaction-induced ground settlements from CPT for level ground. *Canadian Geotechnical Journal*, 39(5):1168–1180. Available at: <http://www.nrcresearchpress.com/doi/abs/10.1139/t02-047>.
- Zhang J, Huo Y, Brandenberg SJ, Kashighandi P (2008) Effects of Structural Characterizations on Fragility Functions of Bridges Subject to Seismic Shaking and Lateral Spreading. *Earthquake Engineering and Engineering Vibrations*. 7(4):369-382



This project has received funding from the European Union's Horizon 2020 research and innovation programme under grant agreement No. 700748

5. VULNERABILITY ASSESSMENT OF PIPELINES USING HISTORICAL DATA

5.1 INTRODUCTION

Lifelines are like veins of the human body, they are vital for a community life. The development and growth of a society is reflected in the quality and efficiency of its lifeline system. Lifeline system includes a set of components, including pipelines, water treatment plants, wastewater treatment plants etc. Nature of pipelines is complex with a variation in its pipe materials, pipe diameters, pipe lengths, pipeline laying years and depths, and most importantly its spatial variation. Pipelines carry these variable attributes all across a city, which makes study of pipelines much more complex in nature. Occurrence of an earthquake can cause extensive damage to pipelines. Damage rates vary with pipeline depths, materials, diameters, and age. The burial and connected nature of pipelines, makes it very vulnerable to earthquakes and its hazards. Pipeline damage is given as Repair Rate (RR) or individual pipeline damage (a binary term, damage or no damage). Earthquake hazards of liquefaction causes severe damage to pipelines, due to eventual ground deformations, sand boils, lateral spreading. Pipeline damage prediction is not a simple process or a spatially similar process. Several past studies have developed correlations between Repair Rates (RR) of pipelines and various intensity measures. Intensity measures like Peak Ground Velocity (PGV), which represents transient ground deformations (Toprak et al., 2017), Permanent Ground Deformation (PGD), angular distortion, lateral strain, Liquefaction Severity Number (LSN), Settlement have been used in developing fragility curves for pipeline damage (Eguchi, 1991; Eidinger, 1998; Isoyama et al., 2000; O'Rourke et al., 2012; Toprak et al., 2017; Bagriacik et al., 2018). Most commonly used are PGV and PGD. Eguchi et al., 1991 was the first to develop relationship between RR and PGD for different pipe materials (Eguchi et al., 1991). Angular distortion and Lateral strain were used by O'Rourke et al., 2012, which have a good correlation with pipeline damage, but they are typically difficult to measure and their predictions are variable due to their dependency on surveying instruments (Toprak et al., 2017).

To find the most appropriate IM representing the damage measure of the structure, Luco & Cornell (2002) recommended two parameters namely, efficiency and sufficiency. Shakib et al., 2016, applied the Luco & Cornell (2002) method to find the most appropriate IM for buried pipelines. Shakib et al., did not consider liquefaction during the analysis (Shakib et al., 2016).

City of Christchurch suffered a series of earthquake and aftershocks during the period of Sept 2010 – December 2011. The phenomenon of liquefaction was seen in the central and eastern regions of Christchurch. Liquefaction caused ground deformations, lateral spreading around the Avon river, sand boils, differential settlements, etc. These earthquakes and aftershocks caused extensive damage to infrastructures and lifelines. An extensive pipeline damage was seen during the CES, with approx. 3800 repairs seen only for the Feb 2011 earthquake. Extensive data collection was followed by the CES. This data was utilised for our study.



This project has received funding from the European Union's Horizon 2020 research and innovation programme under grant agreement No. 700748

The following study utilises the CES pipeline repair dataset and the liquefaction severity dataset calculated for liquefaction parameters of LPI, LSN, Settlement and LPIsh. In our study these parameters are collectively called as Liquefaction Demand Parameters (LDP). LDPs are a synonym to Intensity Measures (IM). The study aims develop correlations between RR (Mains) pipeline network of Christchurch City and Liquefaction Severity Indicators (mentioned in our study as Liquefaction Demand Parameters (LDP)) for the 22nd February 2011 earthquake. The LDPs utilized in this study are settlement, LSN, Liquefaction Potential Index(LPI) and Liquefaction Potential Index as given by Ishihara (LPIsh). The Luco & Cornell (2002) criteria of efficiency and sufficiency are adopted to identify the most appropriate LDP.

5.2 LITERATURE REVIEW

This section discusses various fragility functions developed over the years for pipeline damage due to liquefaction hazard. Fragility functions for pipelines are mostly given as RR/km (i.e. repairs / Km) (NIBS, 2004) or damage rate. Fragility functions are developed empirically, analytically or as a hybrid (combination of empirical and analytical). Most fragility functions listed in **Table 5.1** are calculated empirically, using pipeline damage data observed in liquefaction areas. Three functions from the given list are calculated analytically for continuous and segmented pipelines separately. They clearly highlight the shortcomings of an analytical process in replicating the damage caused by liquefaction on pipelines. Liquefaction hazard is typically quantified using permanent ground deformation (PGD), and therefore it is common to express fragility functions in terms of PGD. In 1980's the number of repairs observed due to liquefaction compared to wave propagation was very low, therefore, to develop a fragility curve, the damage data of liquefaction and wave propagation was combined. However, in the recent years, the data observed is higher in number and accurate due to increase/improvements in Geological Survey methods. This has helped engineers tremendously in developing fragility functions not only in terms of PGD but also lateral strain, angular distortion and Liquefaction Severity Number (LSN). O'Rourke et al. (1998, 2014) & Toprak et al. (2014, 2015) describe an alternate representation of pipeline damage using lateral strain and angular distortion. **Table 5.1** presents fragility functions for pipeline damage due to liquefaction. In addition, a summary of each fragility function is given.

5.2.1 EGUCHI ET AL., 1991

This paper is a follow up to Eguchi (1983). Eguchi (1983) developed fragility functions for damages due to fault movements. Also, Eguchi (1991) mainly concentrates on repair rates due to fault movement but includes a separate vulnerability model for liquefaction. The current paper only uses the damage data from 1971 San Fernando earthquake which are also used in Eguchi (1983). Failure models for fault rupture, landslides and liquefaction are presented separately (Eguchi, 1991). This paper concluded that AC and concrete pipes are more vulnerable than PVC pipes; PVC and welded steel pipes with caulked joints suffered almost equal damage; Ductile Iron (DI) pipes experienced on average about 8 times fewer repairs per unit length than the worst performing pipes; and finally, the repair rate of X grade steel pipes with arc-welded joints was half of DI pipes.



This project has received funding from the European Union's Horizon 2020 research and innovation programme under grant agreement No. 700748

Table 5.1: List of Fragility Functions

Study	Type of Material	IM or Methodology	EDP/ Earthquake/ Location	Proposed severity-impact relationship
Eguchi et al., 1991	AC, CI (welded-steel gas welded joints, welded-steel arc welded joints, welded-steel caulked joints)	PGD/ Empirical	1971 San Fernando EQ/ U.S.A	See Figure 5.1
Honnegar et al., 1992 NIBS, 2004	Ductile (steel, DI, PVC,) or brittle (AC, Concrete, CI)	PGD/ Empirical	U.S.A	$RR \cong Prob [liq] \times PGD^{(0.56)}$ where, RR = Repair Rate (Repairs/km) PGD = Permanent ground deformation in inches
Eidinger, 1998	CI	PGD/ Empirical	1989 Loma Prieta EQ/ East Bay, USA	$n = 1.04 \times PGD^{0.53}$ where, n = Repairs /1000 ft) PGD = Permanent ground deformation in inches
O'Rourke et al., 1998	CI, Steel	Ground Strain/ Empirical	1994 Northridge EQ/ Los Angeles, California, USA	See Figure 5.4
Isoyama et al., 2000	DIP, CIP, VP, SP, Unidentified	PGV/ Empirical	1995 Hyogoken-nanbu (Kobe) EQ/ Ashiya & Nishinomiya Japan	$R_m(IM) = C_1 C_2 \dots C_n R(IM)$ where, Rm(IM) = modified damage rate (failures/km) Ci = correction factors (i =1 to n) R(IM) = standard damage rate (failures/km) IM = maximum acceleration of seismic ground motion (cm/sec ²)



This project has received funding from the European Union's Horizon 2020 research and innovation programme under grant agreement No. 700748

LIQUEFACT
Deliverable D3.1

State of the art review of numerical modelling strategies to simulate
liquefaction-induced structural damage and of uncertain/random factors on the
behaviour of liquefiable soils
v. 1.0

ALA, 2001	CI, WS, AC, Concrete w/s cyl, PVC, DI	PGD/ Empirical	1989 Loma Preta, 1983 Nihonkai, 1971 San Fernando, 1906 San Francisco EQ's/ U.S.A	$RR = K_2(1.06)PGD^{0.319}$ where, RR = repairs per 1000 of main pipe PGD = Permanent ground deformation in inches K_2=Fragility Curve modification factor
Terzi et al., 2006	Continuous Pipes (Amiantocement)	PGD/ Analytical	2003 Lefkas EQ/ Greece	$y = 11.76x^{0.7875}$ (x = PGD in m, y = RR/Km)
Terzi et al., 2007	Segmented Pipes (PVC)	PGD/ Analytical	2003 Lefkas EQ/ Greece	$y = 3.2103x^{0.4103}$ (x = PGD in m, y = RR/Km)
O'Rourke et al., 2012	AC, CI, PVC, MPVC, other	Angular Distortion & Lateral Strain/ Empirical	7.1Mw Sept 4 2010 Darfield , 6.2 Mw Feb 22 2011 Christchurch, 6.0 Mw 13 June 2011 EQ/ New Zealand	Angular Distortion:- AC pipe: $y = 0.48x + 2.22$ CI Pipe: $y = 0.12x + 1.48$ PVC pipe: $y = 0.41x + 0.59$ where, $y = RR$ i. e. repairs/Km , $x = Angular\ distortion, \beta (\times 10^{-3})$ Lateral Strain:- AC pipe: $RR = 2.1408 + 7.8302x$ CI pipe: $RR = 0.2022 + 8.7199x$ PVC pipe: $RR = -0.5956 + 10.175x$ where, $RR = RR$ i. e. repairs/Km ,



This project has received funding from the European Union's Horizon 2020 research and innovation programme under grant agreement No. 700748

LIQUEFACT
Deliverable D3.1

State of the art review of numerical modelling strategies to simulate
liquefaction-induced structural damage and of uncertain/random factors on the
behaviour of liquefiable soils
v. 1.0

$x = \text{Lateral strain}, \epsilon (\%)$

Angular Distortion:-

(Yamazaki, 2010)

Lateral Strain:-

AC pipe: $RR = 8.04x + 2.12x$

CI pipe: $RR = 8.38x + 0.41$

PVC pipe: $RR = 6.37x + 0.01$

EW pipe: $y = 5.77x + 1.19$

UPVC & PVC Pipe: $y = 6.41x + 0.01$

where,

$RR = RR \text{ i. e. repairs/Km}$,

$x = \text{Lateral strain}, \epsilon (\%)$

See **Figure 5.22**

$BR[km^{-1}] = a \times MMI^b$

where,

BR = break rate (breaks per kilometre) a and b = curve fitting constants

Angular Distortion:-

AC pipe: $RR = 0.386\beta + 7.193$

CI Pipe: $RR = 0.425\beta + 3.018$

where,

$RR = RR \text{ i. e. repairs/Km}$,

$\beta = \text{Angular distortion}, \beta (\times 10^{-3})$

Lateral Strain:-

O'Rourke et al., 2014	AC, CI, PVC, EW, RCRR, Conc, UPVC	Angular Distortion & Lateral Strain/ Empirical	6.2 Mw 22 February 2011 EQ/ New Zealand	
Toprak et al., 2014	AC	Lateral Ground Strain/ Empirical	6.2 Mw 22 February 2011 EQ/ New Zealand	
Sherson et al., 2015	See Table ... & Table	MMI/ Empirical	Feb and June EQ's/ New Zealand	
Toprak et al., 2015	CI, AC	Angular Distortion & Lateral Strain/ Empirical	6.2 Mw, 22 February 2011 EQ/ New Zealand	



This project has received funding from the European Union's Horizon 2020 research and innovation programme under grant agreement No. 700748

LIQUEFACT
Deliverable D3.1

State of the art review of numerical modelling strategies to simulate
liquefaction-induced structural damage and of uncertain/random factors on the
behaviour of liquefiable soils
v. 1.0

LiDAR 56m
AC pipe: $RR = 9.75\epsilon + 3.46$
CI pipe: $RR = 10.98\epsilon + 1.90$
LiDAR 4m
AC pipe: $RR = 9.40\epsilon + 3.86$
CI pipe: $RR = 8.55\epsilon + 2.28$
Air Photo
AC pipe: $RR = 8.37\epsilon + 4.70$
CI pipe: $RR = 11.78\epsilon + 1.28$
where,
 $RR = RR$ i.e. repairs/Km ,
 $\epsilon =$ Lateral strain, ϵ (%)

CI: $RR = 0.0949 \times LSN + 0.42$
PVC: $RR = 0.0839 \times LSN - 0.7898$
AC pipe: $RR = 0.03 \times LSN + 2.33$
where,
 $RR=RR$ i.e. repairs/Km ,
LSN=Liquefaction Severity Number

Angular Distortion:-
AC pipe: $Y = 0.61x + 1.61$
CI Pipe: $Y = 0.27x + 1.11$
PVC Pipe: $Y = 0.55x - 0.93$
where,
 $Y = RR$ i.e. repairs/Km ,
 $x =$ Angular distortion, $\beta (\times 10^{-3})$

Toprak et al., 2017 CI, PVC, AC LSN/
Empirical 6.2 Mw, 22 February 2011 EQ/
New Zealand

D. Bouziou et al., 2017 AC, CI, PVC Angular Distortion &
Lateral Ground Strain/
Empirical 6.2 Mw, 22 February 2011 EQ/
New Zealand



This project has received funding from the European Union's Horizon 2020 research and innovation programme under grant agreement No. 700748

LIQUEFACT
Deliverable D3.1

State of the art review of numerical modelling strategies to simulate liquefaction-induced structural damage and of uncertain/random factors on the behaviour of liquefiable soils
v. 1.0

				Lateral Strain: See Figure 5.31
O'Rourke et al., 2018	CI	Ground Strain/Analytical		See Figure 5.33
				Lateral Strain:- LiDAR 56m AC pipe: $RR = 12.93\epsilon + 2.96$ CI pipe: $RR = 15.86\epsilon + 1.36$ LiDAR 4m AC pipe: $RR = 13.21\epsilon + 2.12$ CI pipe: $RR = 12.64\epsilon + 1.75$ Air Photo AC pipe: $RR = 5.7\epsilon + 3.96$ CI pipe: $RR = 17.22\epsilon + 0.39$ Satellite AC pipe: $RR = 3.85\epsilon + 4.57$ where, $RR = RR$ i. e. repairs/Km , $\epsilon =$ Lateral strain, ϵ (%)
Toprak et al., 2018	AC, CI	Lateral Ground Strain/ Empirical	6.2 Mw, 22 February 2011 EQ/ New Zealand	



This project has received funding from the European Union's Horizon 2020 research and innovation programme under grant agreement No. 700748

The vulnerability relationship due to liquefaction of repairs per 1000 ft for different pipe material is shown below in terms of pipe material vs Repair rate: **Figure 5.1**

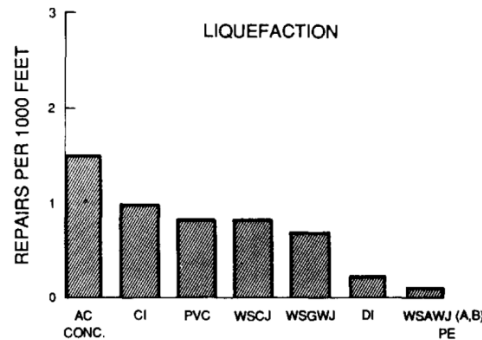


Figure 5.1: Earthquake vulnerability relationships for underground pipelines in liquefaction areas (Eguchi, 1991)

5.2.2 HONEGGAR ET AL., 1992

For ground failure the damage relation is given as shown below with permanent ground deformation in m.

$$Repair\ Rate\ \left[\frac{Repairs}{Km} \right] \cong Prob\ [liq] \times PGD^{(0.56)} \quad (5.1)$$

The corrective factor K is equal to 1 for brittle pipes (CI, AC, RCC) and 0.3 for ductile pipes (DI, S, PVC). It is assumed that damage due to ground failure will consist of 20 % leaks and 80 % breaks.

5.2.3 NIBS, 2004

The fragility function discussed by Honeggar and Eguchi (1992) is adopted by NIBS in their Multi-hazard Loss Estimation Methodology i.e. the HAZUS model. The damage algorithm for buried pipelines due to ground failure is for the San Diego County Water Authority (SDCWA). With PGD expressed in inches.

Table 5.2: Damage algorithms for water pipelines (NIBS, 2004)

	PGD Algorithm	
	$Repair\ Rate\ [Repairs/Km] \cong Prob\ [liq] \times PGD^{(0.56)}$	
Pipe Type	Multiplier	Example of Pipe
Brittle Pipes	1	CI, AC, RCC
Ductile Pipes	0.3	DI, S, PVC



This project has received funding from the European Union's Horizon 2020 research and innovation programme under grant agreement No. 700748

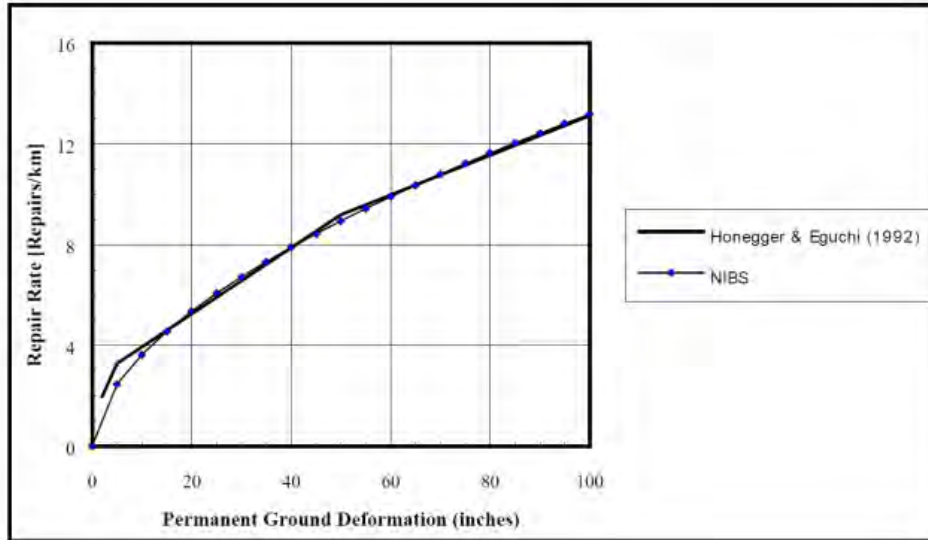


Figure 5.2: Ground Deformation Damage Model for Cast Iron Pipes by HAZUS (NIBS, 2004)

For Oil pipelines mild steel pipelines with submerged arc welded joints are classified as ductile pipes, while the older gas welded steel pipelines, if any, are classified as brittle pipes.

Table 5.3: Damage algorithms for Oil pipelines (NIBS, 2004)

PGD Algorithm		
$Repair\ Rate\ [Repairs/Km] \cong Prob\ [liq] \times PGD^{(0.56)}$		
Pipe Type	Multiplier	Example of Pipe
Brittle Oil Pipelines	1	Steel Pipe w/ Gas WJ
Ductile Oil Pipelines	0.3	Steel Pipe w/ Arc WJ

5.2.4 EIDINGER, 1998

Eidinger (1998) investigated the repair rates for the East Bay Municipal District (EBMUD) for the 1989 Loma Prieta earthquake. Liquefaction induced damage was separated from ground shaking by comparison of liquefied soil zones with the actual locations of the damaged pipelines. Liquefaction damage was quantified by permanent ground deformation (PGD). PGD includes both lateral spreading and vertical settlement. In young alluvial soils PGD is primarily from vertical settlement. For bay mud and bay soil, lateral PGD depended on PGA, distance from shoreline and duration of ground shaking and vertical settlement depends on the duration of ground shaking. PGD movement direction was towards the shoreline. PGD in this case is taken as



This project has received funding from the European Union's Horizon 2020 research and innovation programme under grant agreement No. 700748

the vector sum of lateral and vertical components (Eidinger, 1998). The corresponding pipeline fragility function is given by:

$$n = 1.03 (PGD)^{0.53} \tag{5.2}$$

Where n is the repair rate per 1000 ft of pipe and PGD is in inches. The fragility curve is given for cast iron pipeline, as shown in the **Figure 5.3** and **Table 5.4** also shows the number of repairs observed due to each type of hazard:-

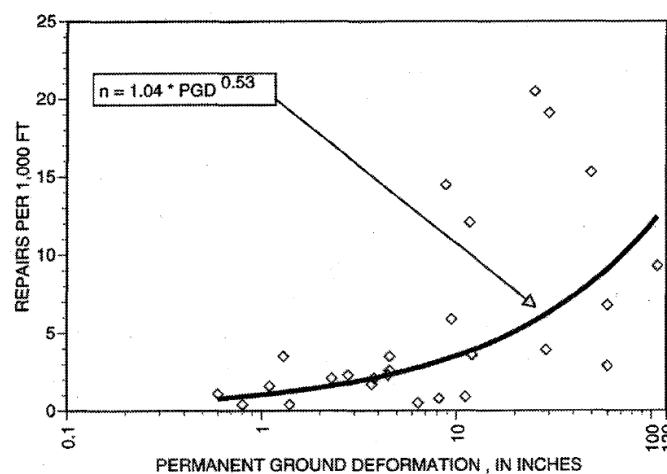


Figure 5.3: Pipe repair-rate fragility curve versus permanent ground deformation (Eidinger, 1998)

Table 5.4: Number of repairs for type of hazard (Eidinger, 1998)

	Number of repairs		
	High	Low	Mean
Total -----	161	108	138
Ground shaking -----	79	63	72
Liquefaction -----	86	41	66
Landslide -----	0	0	0
Fault crossing -----	0	0	0

5.2.5 O'ROURKE ET AL., 1998

The Los Angeles Department of Water and Power water delivery system was investigated for the 1994 Northridge earthquake. In the balboa Blvd and Rinaldi st. liquefaction was observed. The ground strain was calculated by superimposing the air photo measurements of the horizontal displacements taken over the regularly spaced grids using GIS, and calculating the mean displacement. Grid dimensions of 100m x 100m were found to provide best results. GIS was also used to prepare repair rate contours by combining ground



This project has received funding from the European Union's Horizon 2020 research and innovation programme under grant agreement No. 700748

strain contours, pipeline networks and pipeline repair locations. Further, repair rates corresponding to the areas delineated by a particular contour interval were calculated. Fig 2.3.4 shows CI mains superimposed on areal distribution of ground strains. For repair rate correlation the ground strain interval was 0.1% and repair rate was 5 repairs/Km. 34 repairs were observed for CI pipes and two for steel.

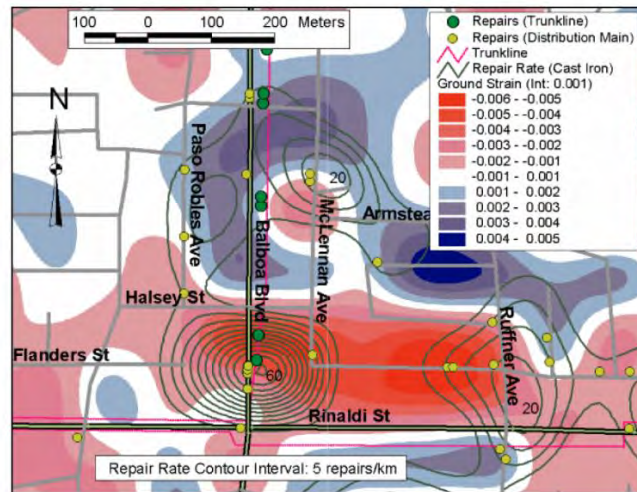


Figure 5.4: Distribution of CI Repair Rate and Ground strain (T. O'Rourke S. T.-S., 1998)

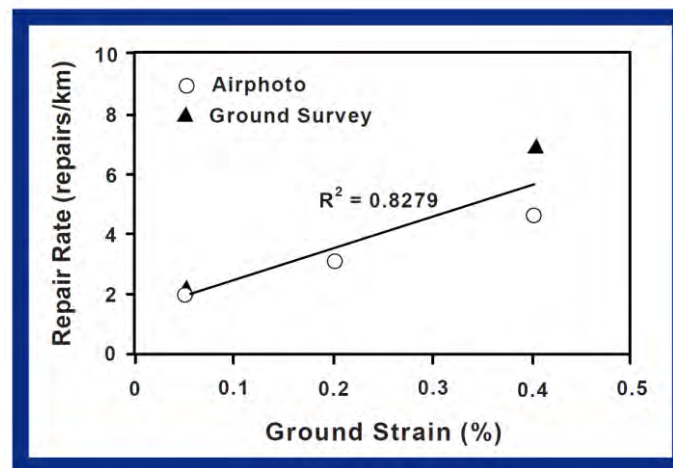


Figure 5.5: Correlation between Ground Strain and CI Repair Rate (T. O'Rourke S. T.-S., 199)

5.2.6 ISOYAMA ET AL., 2000

The work of Isoyama et al. (2000) is based on earlier studies of the 1995 Kobe earthquake, for the Ashiya and Nishinomiya cities. The pipeline fragility relationships were derived using the following functional forms:

$$R_m(IM) = C_1 \times C_2 \times C_3 \times C_4 \dots C_n \times R(IM) \tag{5.3}$$



This project has received funding from the European Union's Horizon 2020 research and innovation programme under grant agreement No. 700748

where, $R_m(IM)$ is a modified damage rate (failures/km), C_i represents various correction factors ($i = 1$ to n), $R(IM)$ is a standard damage rate (failures/km), and IM is the maximum acceleration of seismic ground motion (cm/sec²). The correction factors varies with pipe material, pipe diameter, soil condition, the degree of liquefaction, and etc. The standard damage rate $R(IM)$ is assumed to be the rate of damage to cast-iron water supply pipes of diameter 100 to 200 mm buried in alluvial soil at a shallow depth of about 1 m, shown as follows:

$$R(IM) = c(IM - A)^b \tag{5.4}$$

Parameters a , b and A are regression coefficients calculated on the basis of damage dataset for a particular earthquake. Using GIS the cities were divided topographically in 50m grid cells including the degree of liquefaction for each division. A multivariate analysis was carried out to compute empirical correction factors to account for pipe material, pipe diameter, ground topography, and liquefaction in the fragility relation. Damage rate using above functions were calculated for the Hanshin district as a case study.

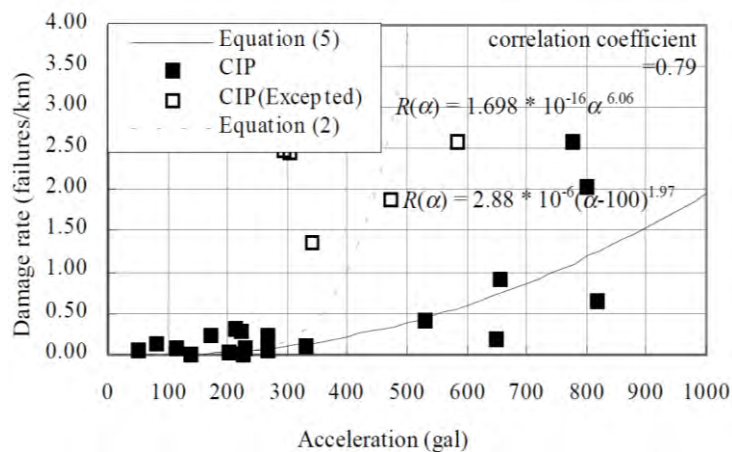


Figure 5.6: Relation between PGA and damage rate of CIP (R. Isoyama, 2000)

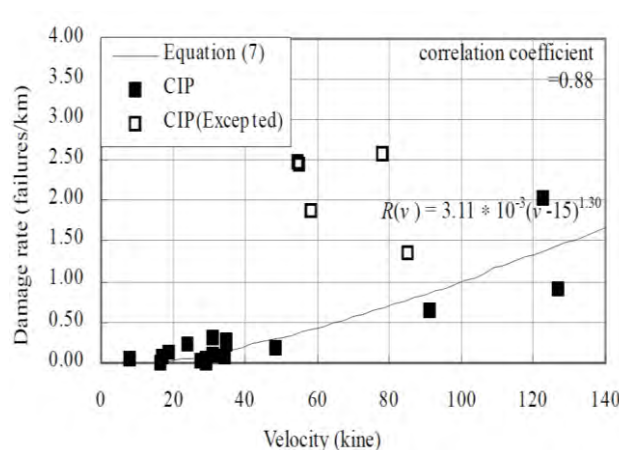


Figure 5.7: Relation between PGV and damage rate of CIPb (R. Isoyama, 2000)



This project has received funding from the European Union's Horizon 2020 research and innovation programme under grant agreement No. 700748

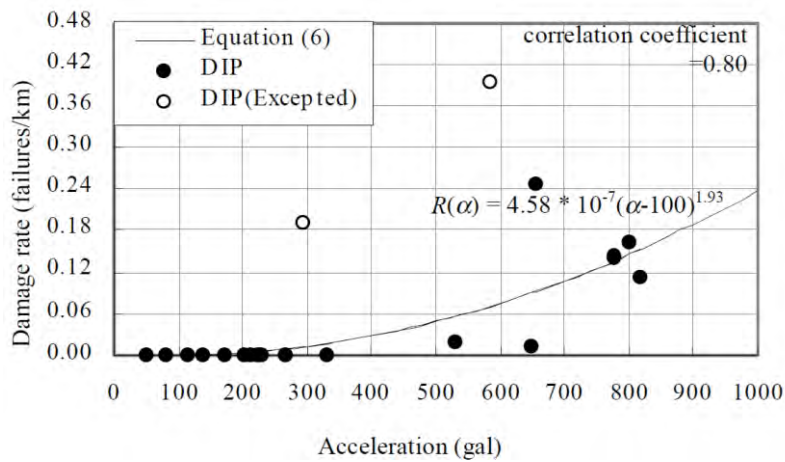


Figure 5.8: Relation between PGA and damage rate of DIP (R. Isoyama, 2000)

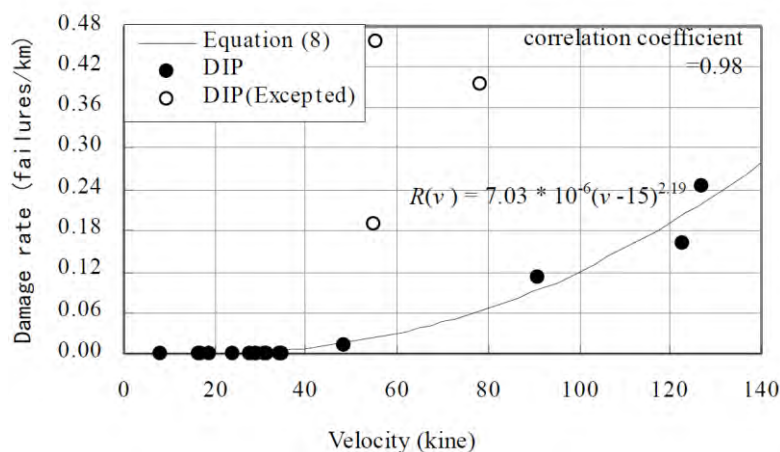


Figure 5.9: Relation between PGV and damage rate of DIP (R. Isoyama, 2000)

5.2.7 ALA, 2001

ALA (2001) presented backbone curves using database of the earthquakes and data points given in **Table 5.5**. The backbone curve was for use when there was no knowledge of pipe materials, joinery, diameter, corrosion status, etc. of the pipeline inventory. This curve represents the average performance of the pipelines for all kinds of pipes in earthquakes. The backbone curve is given in **Table 5.6**.



This project has received funding from the European Union's Horizon 2020 research and innovation programme under grant agreement No. 700748

Table 5.5: Earthquake and Number of Points in PGD Database (Alliance, 2001)

Earthquake	Number of Data Points	Percentage	Ground Failure Type
1989 Loma Prieta	12	28 %	Liquefaction vertical settlement
1983 Nihonkai-Chubu	20 (note 1)	48 %	Liquefaction lateral spread
1971 San Fernando	5	12 %	Local tectonic uplift
1906 San Francisco	5	12 %	Liquefaction lateral spread
Totals	42	100 %	

Note 1. Excludes 14 data points for gas pipes which are listed in database but not used in statistical analysis.

Table 5.6: Buried Pipe Vulnerability Functions (Alliance, 2001)

Hazard	Vulnerability Function	Comment
Permanent Ground Deformation	$RR = 1.06 \times PGD^{0.319}$	Based on 42 data points of which largest percentage (48%) was AC pipe.

Notes:

RR = repairs per 1000 of main pipe

PGD = Permanent ground deformation in inches

Ground failure mechanisms used in PGD formulation: Liquefaction (88%); Local tectonic uplift (12%)

The fragility curve modification factors (K_2), is calculated by combination of various pipe materials, diameters, soil types, etc, as shown in **Table 5.7**. By diameter, small means 4-inch to 12 inch diameter, large means 16 inch diameter and larger.

$$RR = K_2(1.06)PGD^{0.319} \quad (5.5)$$

5.2.8 TERZI ET AL., 2006

Fragility function of repair rate/Km was calculated using the analytical approach and compared with the empirical approach. A fragility model was developed for Lefkas Potable water system, Greece using the damage data obtained for the Lefkas Earthquake of 2003, primarily for continuous pipelines. The empirical approach for amianto cement pipes obtained a failure rate of 0.245 RR/Km. Also, average failure rate was calculated using Honnegger & Eguchi (1992), Eidinger & Avila (1999), ALA (2001) which was found to be 0.137, 0.893, 0.756, respectively. Hence the observed failure rate of 0.245 RR/Km lied between Honnegger & Eguchi (1992) and ALA (2001). As for the analytical analysis, a part (400m in length) of the pipeline system was modelled, which suffered liquefaction induced damage. The pipe modelled was of amianto cement material, 500mm in dia and 1 m buried deep. The pipeline consists of 6m length interconnected pipelines. By using ADINA, a finite element computer program, a finite element model of the pipeline was developed utilizing



This project has received funding from the European Union's Horizon 2020 research and innovation programme under grant agreement No. 700748

large deformation theory, pipe-soil interaction forces (soil springs) and plastic stress-strain relations for the pipe material. Vertical and transverse displacements that were imposed on the pipeline, corresponded to the observed settlements and lateral spreading of the area where this pipe was located. The failure in the analytical analysis referred to the pipe material non linearity included. Pipeline was modelled to calculate the fragility curves, in accordance with the physical model of pipeline and soil deformation considered by T. O'Rourke (8). For the loading, different PGD widths and distribution pattern were considered. For simplicity the uniform distribution scheme proposed by Suzuki et al. (1988) was initially followed. Different values of the failure index for the same of PGD correspond to different PGD zone width. Therefore, the resulting pairs of PGD versus RR/km are scattered around a trend line whose type can be described as a power of the PGD. The damage state depends on the value of the displacement imposed as well as on the width of the PGD zone.

Table 5.7: Constants for fragility curve (Alliance, 2001)

Pipe Material	Joint Type	K_2	Reference Sections
Cast iron	Cement	1.0	4.4.2
Cast iron	Rubber gasket	0.8	4.4.2
Cast iron	Mechanical restrained	0.7	4.4.2
Welded steel	Arc welded, lap welds (large diameter, non corrosive)	0.15	4.4.4
Welded steel	Rubber gasket	0.7	4.4.3
Asbestos cement	Rubber gasket	0.8	4.4.3
Asbestos cement	Cement	1.0	4.4.6
Concrete w/Stl Cyl.	Welded	0.6	4.4.6
Concrete w/Stl Cyl.	Cement	1.0	4.4.6
Concrete w/Stl Cyl.	Rubber Gasket	0.7	4.4.6
PVC	Rubber gasket	0.8	4.4.6
Ductile iron	Rubber gasket	0.5	4.4.6

The analytical analysis held some limitations. It overestimated the RR/Km even if they lay between the empirical's. This is due to the fact that a symmetrical model as well as a symmetrical loading was used in the fragility curves calculation whereas in a real case the distribution of displacement may be random. Although in the real case, there may be parts of the network that have no damage at all, the estimation of the RR/km is then brought up to the total length of the entire network whereas in the analytical calculation the length of the pipeline model is constant and the RR/km is expressed proportionally to a network of one kilometre length. The only failure criterion in the analytical study is attributed to the pipeline material whereas in the real case the RR index takes into account the failure of the network connections as well. The analytical calculation refers to a new pipeline however, in the real case failures of already weakened pipeline material or connections may worsen due to the earthquake events and consequently are taken into account into the RR estimation.



This project has received funding from the European Union's Horizon 2020 research and innovation programme under grant agreement No. 700748

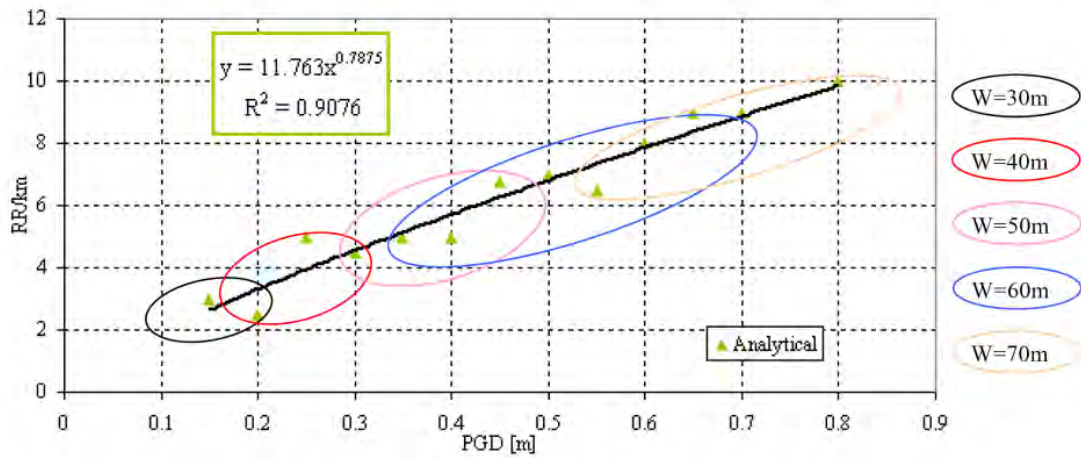


Figure 5.10: Analytical fragility curve for different width of liquefied zone (V. Terzi M. A., 2006)

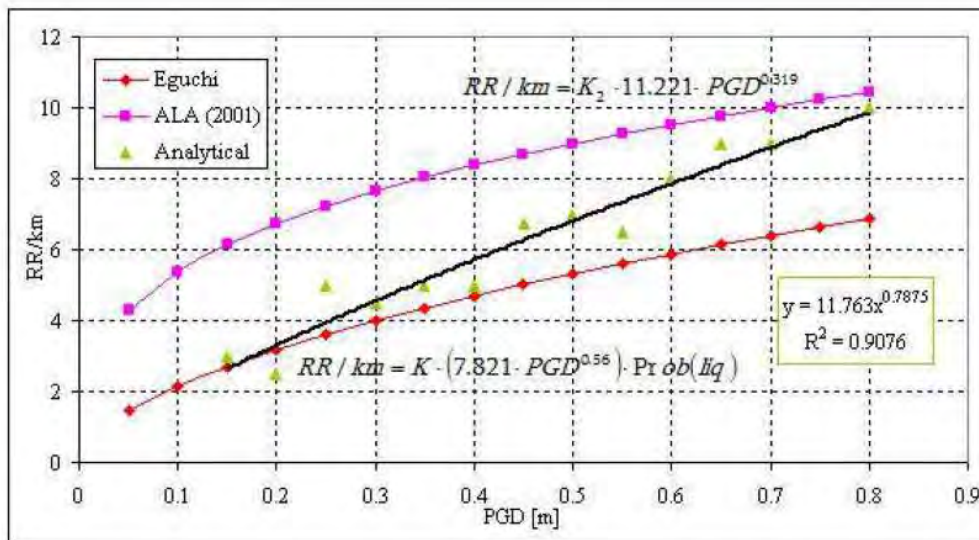


Figure 5.11: Comparison of empirical and analytical fragility curves (V. Terzi M. A., 2006)

5.2.9 TERZI ET AL., 2007

This paper follows the similar method of analysis that of Terzi 2006, but it has been done for segmented PVC pipes. PVC pipeline of 250.87m length, was analysed for damage caused by permanent ground deformation and Dia. 110 mm and 1m deep buried. Estimation of fragility curves is a combination of numerical results and definition of damage states criterion. The empirical results of the fragility curves were compared with that of the numerical analysis and it was found to be closer to ALA, 2001. This model proved more satisfactory than the Terzi 2006.



This project has received funding from the European Union's Horizon 2020 research and innovation programme under grant agreement No. 700748

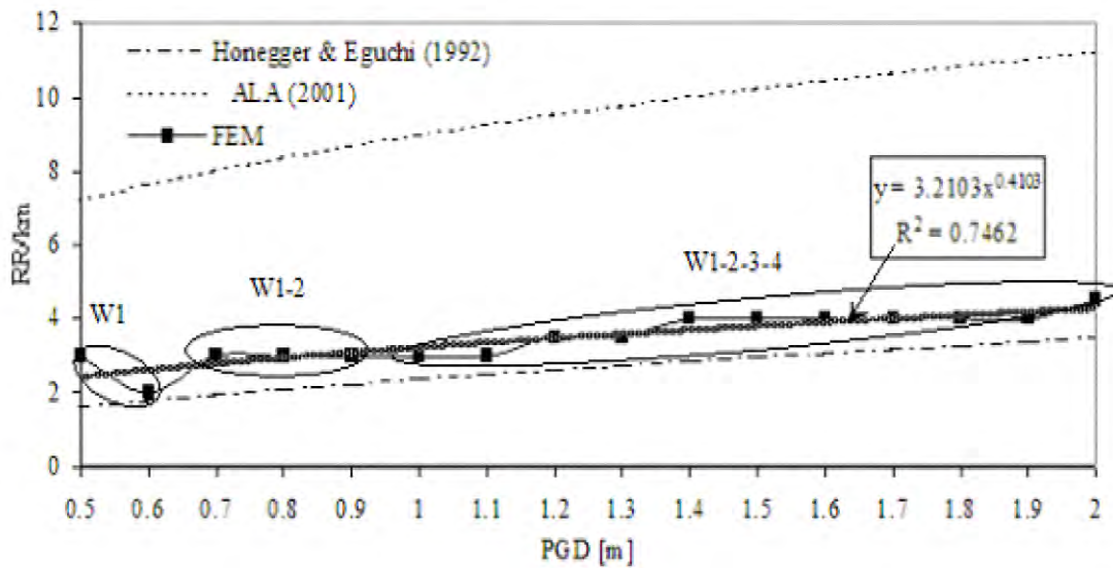


Figure 5.12: Comparison of empirical and analytical fragility curve (V. Terzi M. A., 2007)

5.2.10 O'ROURKE, 2012

O'Rourke gives a co-relation between pipeline repair rate and Lateral strain/Angular Distortion calculated using LiDAR for the 7.1Mw Sept 4th 2010, Darfield, 6.2Mw Feb 22nd 2011 Christchurch, 6.0Mw 13 JUNE 2011 earthquakes. The pipeline inventory before each earthquake and repair database associated with each earthquake was provided by the Christchurch City Council (CCC) and the stronger Christchurch Rebuild Team (SCRIT). 1700km of water distribution pipelines data was included. The repair database included all daily repairs conducted between February 23, 2011 and May 14, 2012 during which 13 June 2011 and 23 December earthquakes and numerous aftershocks were encountered.

The vertical and lateral ground movement data observed in high liquefaction area with high resolution Lidar data used in calculation of angular distortion was available through Canterbury Earthquake Recovery Authority (CERA) (2012). The angular distortion was calculated by subtracting the vertical settlement between two points and divided by the horizontal distance separating them. This gives the differential vertical movement on pipeline damage. The advantages of angular distortion as said by O'Rourke, is that it's a dimensionless and it can be scaled to appropriate dimensions for future applications and by subtracting the vertical movements of two adjacent points, the systematic errors associated with the LiDAR elevation surfaces is eliminated. Angular distortion was calculated for 5m cells. Then repair rate was given by the number of repairs and pipeline lengths of each pipe type in the 5m cell. The RR vs angular distortion for intervals of 1×10^{-3} was calculated.

For the Lateral movements, the LiDAR measurements available through CERA (2012), as displacements in E-W and N-S directions at 56m intervals. Displacement in E-W and N-S directions and shear strains were calculated by computing spatial derivatives of displacements using linear interpolation. Further, horizontal strains were calculated at the centre of the 56x56m cell following the method described by Cook (1995). The regression results of lateral strain vs RR showed strong co-relation with pipeline damage and lateral strain as



This project has received funding from the European Union's Horizon 2020 research and innovation programme under grant agreement No. 700748

indicated by relatively high R square values. AC pipes showed highest RR, twice as high at strains exceeding 0.05% as that for PVC pipes. Linear regression from O'Rourke (1998) for Northridge Earthquake for CI pipes plotted against the regression analysis of O'Rourke (2012) follows a trend consistent with AC and CI pipes from O'Rourke(2012), It plots higher than CI and very close to AC. Correlation of RR vs combined effect of angular distortion and Lateral strain was also calculated and shown in the **Figure 5.13**. The AC and CI pipes are brittle hence showed a low threshold for angular distortion and lateral movement or a combination of both. The repair rate was 4 to 5 times larger than PVC pipes. PVC pipes RR was 2 to 4 times higher than MPVC pipelines. Damage during Darfield and Christchurch earthquakes was generally 10 to 30 times larger in liquefaction areas as compared to areas with no liquefaction.

Angular Distortion:

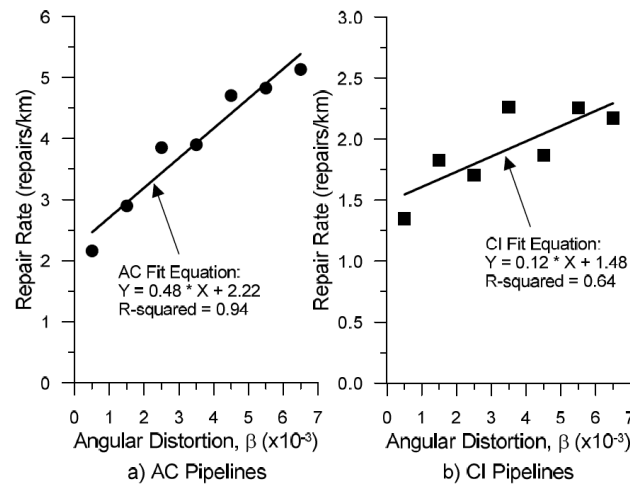


Figure 5.13: Repair Rate vs. angular distortion of AC, CI and PVC pipelines for Christchurch earthquake (T. O'Rourke S.-S. J., 2012)



This project has received funding from the European Union's Horizon 2020 research and innovation programme under grant agreement No. 700748

Lateral Strain:

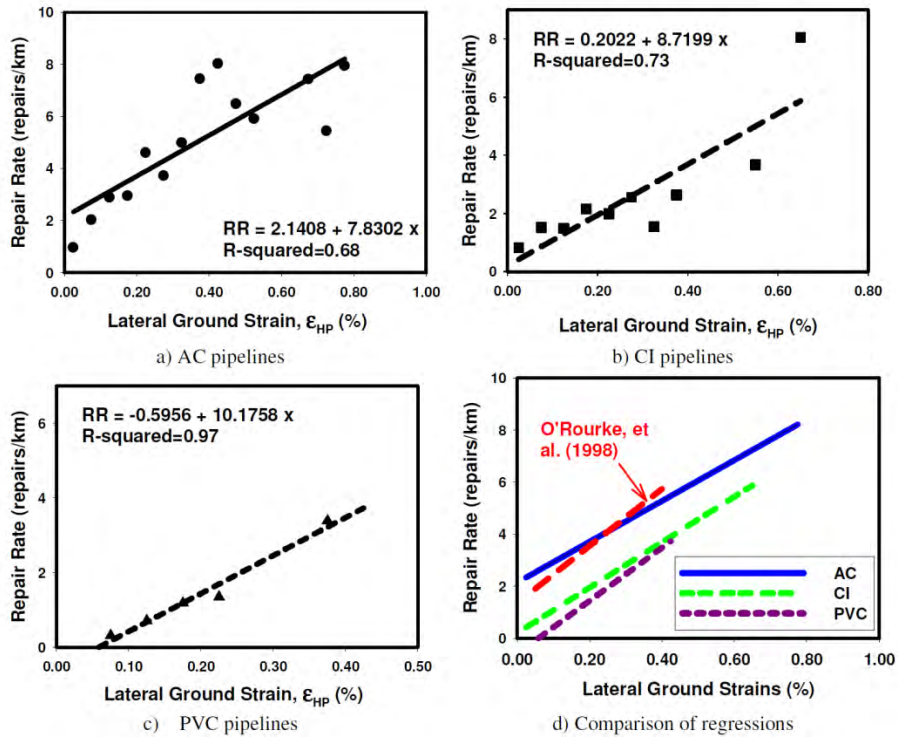


Figure 5.14: Repair Rate vs. lateral ground strain correlations for different pipe materials (T. O'Rourke S.-S. J., 2012)

Combined effect of lateral strain and angular distortion:

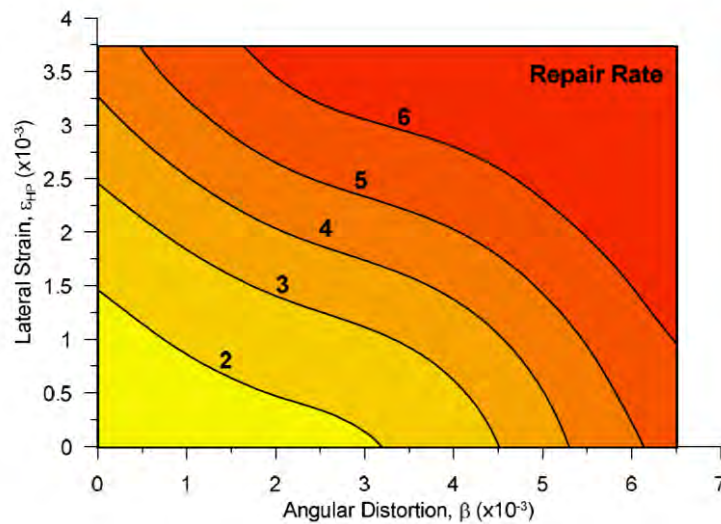


Figure 5.15: Repair Rate vs. lateral ground strain and Angular distortion of AC pipelines for Christchurch earthquake (T. O'Rourke S.-S. J., 2012)



This project has received funding from the European Union's Horizon 2020 research and innovation programme under grant agreement No. 700748

5.2.11 O'ROURKE ET AL., 2014

The analysis was similar to the one carried out in O'Rourke (2012), except the earthquakes here considered were only 22nd Feb 2011 and 13th June 2011. The RR's were calculated for water supply pipelines and also wastewater pipelines. The linear correlation calculated was slightly different than the one for O'Rourke et al (2012).

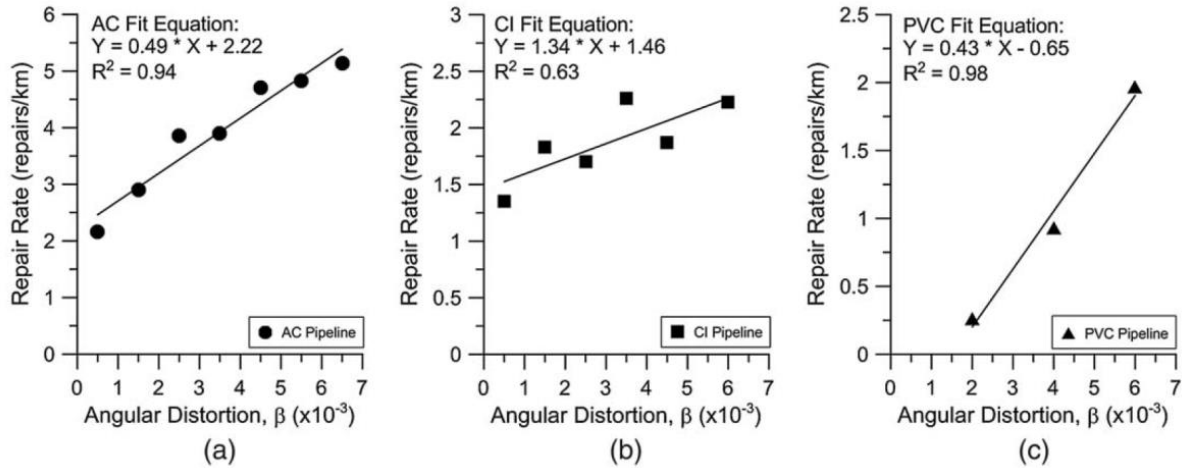


Figure 5.16: Repair rate vs angular distortion of (a) AC, (b) CI, (c) PVC water pipelines for the 22nd February earthquake (T. O'Rourke S.-S. J., 2014)

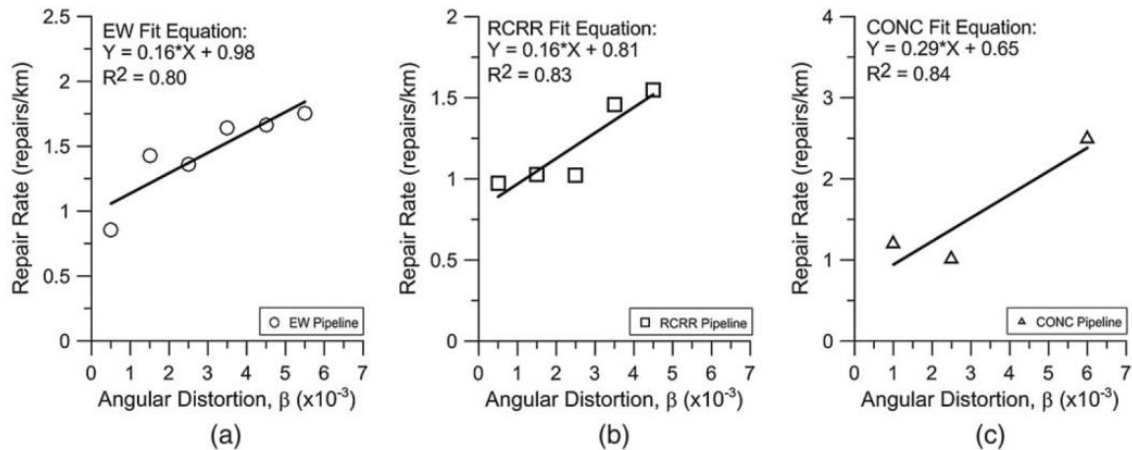


Figure 5.17: Repair rate vs angular distortion of (a) earthenware(EW), (b) reinforced concrete rubber ring(RCRR), (c) concrete(CONC) wastewater pipelines for the 22nd February earthquake (T. O'Rourke S.-S. J., 2014)



This project has received funding from the European Union's Horizon 2020 research and innovation programme under grant agreement No. 700748

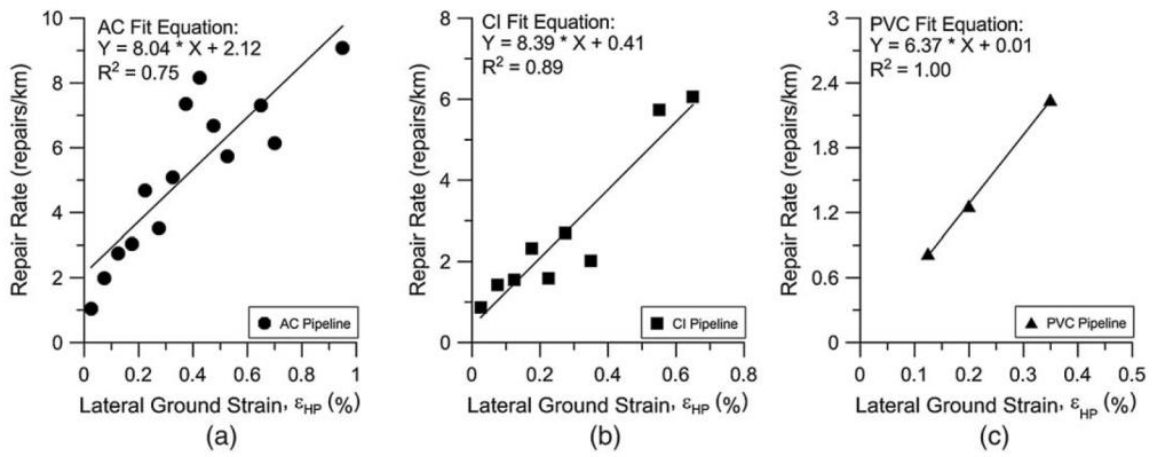


Figure 5.18: Repair rate vs lateral ground strain of (a) AC, (b) CI, (c) PVC water pipelines for the 22nd February earthquake (T. O'Rourke S.-S. J., 2014)

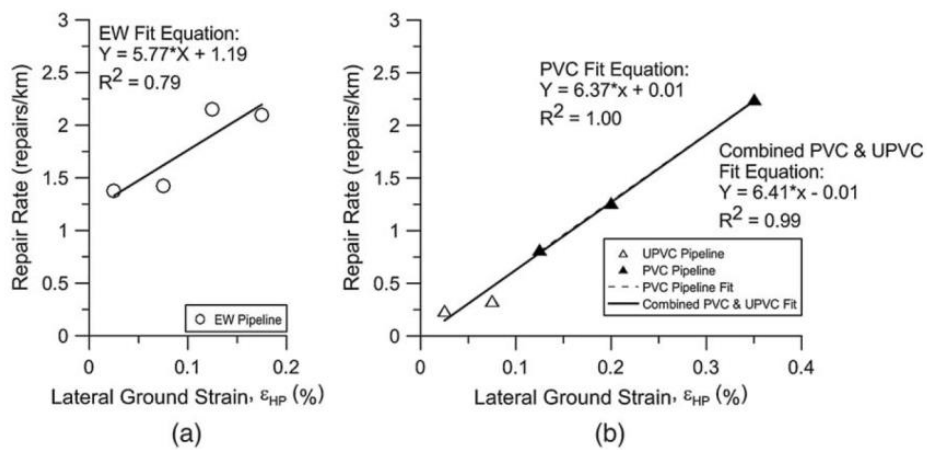


Figure 5.19: Repair rate vs Lateral Ground Strain of (a) earthenware(EW), (b) PVC and UPVC wastewater pipelines for the 22nd February earthquake (T. O'Rourke S.-S. J., 2014)



This project has received funding from the European Union's Horizon 2020 research and innovation programme under grant agreement No. 700748

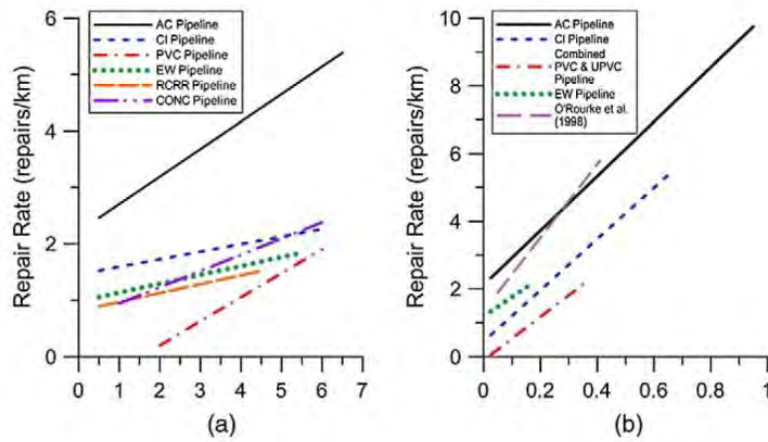


Figure 5.20: Comparison of repair rate vs angular distortion and lateral ground strain UPVC wastewater pipelines for the 22nd February earthquake (T. O'Rourke S.-S. J., 2014)

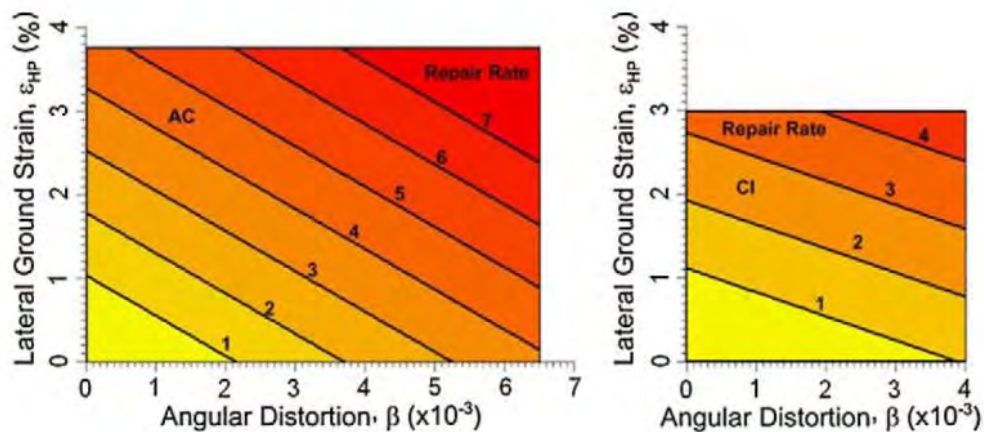


Figure 5.21: Repair rate vs. lateral strain, and angular distortion for AC and CI pipelines (T. O'Rourke S.-S. J., 2014)

5.2.12 TOPRAK ET AL., 2014

Air photos and high resolution Light detection and ranging (LiDAR) survey data acquired before and after the 6.2 Mw 22 February 2011 earthquake were utilised in calculating the lateral displacements for the Avonside area, Christchurch, New Zealand. Repair rate were developed for AC pipes, in correlation with the lateral ground strains. The calculation of ground strain was similar to that of O'Rourke 2014. The paper mainly compares the displacements calculated by air photos and LiDAR, but also provides a repair rate for the Avonside area as shown in the fig below.



This project has received funding from the European Union's Horizon 2020 research and innovation programme under grant agreement No. 700748

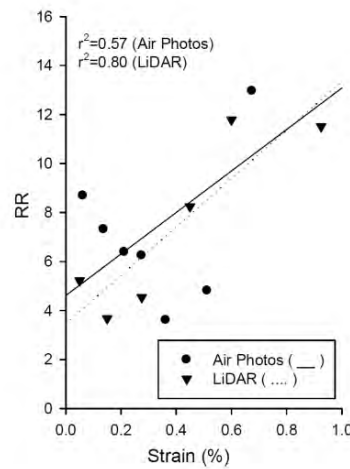


Figure 5.22: Repair Rate values obtained from LiDAR and air photo measurements (S. Toprak E. N.-S., 2014)

5.2.13 SHERSON ET AL., 2015

Modified Mercalli Intensity maps of Christchurch superimposed with repair rates superimposed with liquefaction map, were used to develop fragility function for pipelines and break rates. The empirical analysis was done for February and June 2011 earthquakes. This damage data was combined with the data that was used by Cousins (2013) to derive the fragility functions. In **Table 5.9** each point represents the performance of a particular class of pipe (combination of material type and size) during the earthquakes for different soil conditions (liquefied or non-liquefied). The empirical fragility models inherit the subjective-ness of the macro-seismic scale due to the use of MMI. The fragility model is given as follows:

$$BR[km^{-1}] = a \times MMI^b \tag{5.6}$$

Where, BR is the break rate in breaks per kilometre and, a and b, are curve fitting constants for the pipe class as shown in **Table 5.9**. The r-squared values are quite low for some classes, which show that variations in the break rates for some classes are not adequately captured by varying intensity. Hence, it was suggested to use the fragility models with some caution.



This project has received funding from the European Union's Horizon 2020 research and innovation programme under grant agreement No. 700748

Table 5.8: Wastewater pipes break rates for the combined and averaged data (Both Feb and June) (A.K. Sherson, 2015)

Pipe Material	Combined Pipe Length (km)	Combined Length %	Combined No of Breaks	Overall Average Break rate	Breaks in Liquefied Areas	Breaks in Non Liquefied Areas	Pipeline Length in Liquefied Areas (km)	Length in Non Liq Areas (km)	Ave Break Rate in Liq Areas	Ave Break Rate In Non Liq Areas	Ratio Liq/Non-Liq
RCRR	1,366.6	0.3	356	0.26	255	101	408.3	958.3	0.62	0.11	5.9
EW	783.8	0.2	345	0.44	255	90	342.6	441.1	0.74	0.20	3.6
UPVC	722.6	0.2	39	0.05	25	14	118.9	603.7	0.21	0.02	9.1
AC	370.6	0.1	81	0.22	50	31	92.0	278.6	0.54	0.11	4.9
CONC	281.8	0.1	64	0.23	48	16	146.8	134.9	0.33	0.12	2.8
PVC	104.7	0.0	5	0.05	1	4	18.9	85.8	0.05	0.05	1.1
CI	60.1	0.0	19	0.32	14	5	29.5	30.6	0.47	0.16	2.9
HDPE	46.4	0.0	10	0.22	7	3	12.3	34.1	0.57	0.09	6.5
Other	297.0	0.1	6	0.02	5.0	1.0	96.9	200.2	0.05	0.00	10.3
Total	4,033		925		660	265	1,266	2767			

Table 5.9: Break rates for water pipes in the February and June earthquakes (A.K. Sherson, 2015)

Pipe Material	Pipe Length (km)	Length %	No. of Breaks	Overall Average Break Rate	Breaks in Liquefied Areas	Breaks in Non Liquefied Areas	Pipeline length in Liquefied Areas (km)	length in non Liq Areas (km)	Ave. Break Rate in Liq. Areas	Ave. Break Rate in Non Liq. Areas	Ratio (Liq/Non-Liq)	
Feb.	HDPE	923.2	26.4%	456	0.5	286	170	337.3	585.9	0.8	0.3	2.9
	AC	902.9	25.8%	1022	1.1	732	290	236.0	666.9	3.1	0.4	7.1
	MDPE 80	461.8	13.2%	98	0.2	71	27	132.8	328.9	0.5	0.1	6.5
	PVC	272.4	7.8%	78	0.3	56	22	80.9	191.5	0.7	0.1	6.0
	CI	227.1	6.5%	252	1.1	191	61	98.0	129.1	1.9	0.5	4.1
	GI	212.0	6.1%	962	4.5	649	313	88.5	123.6	7.3	2.5	2.9
	Other	499.8	14.3%	154	0.3	119	35	135.3	364.5	0.9	0.1	8.5
	TOTAL	3,499.3		3,022		2,104	918	1,108.8	2,390.4			
June	HDPE	923.3	26.7%	126	0.1	70	56	329.9	593.4	0.2	0.1	2.2
	AC	901.8	26.1%	248	0.3	162	86	223.8	678.1	0.7	0.1	5.7
	MDPE 80	465.2	13.5%	21	0.0	13	8	144.7	320.5	0.1	0.02	3.6
	PVC	271.5	7.9%	20	0.1	15	5	78.6	192.9	0.2	0.03	7.4
	CI	225.9	6.5%	71	0.3	37	34	86.2	139.6	0.4	0.2	1.8
	GI	211.9	6.1%	201	0.9	139	62	78.9	133.0	1.8	0.5	3.8
	Other	454.9	13.2%	52	0.1	41	11	121.1	333.7	0.3	0.03	10.3
	TOTAL	3,454.5		739		477	262	1,063.2	2,391.3			



This project has received funding from the European Union's Horizon 2020 research and innovation programme under grant agreement No. 700748

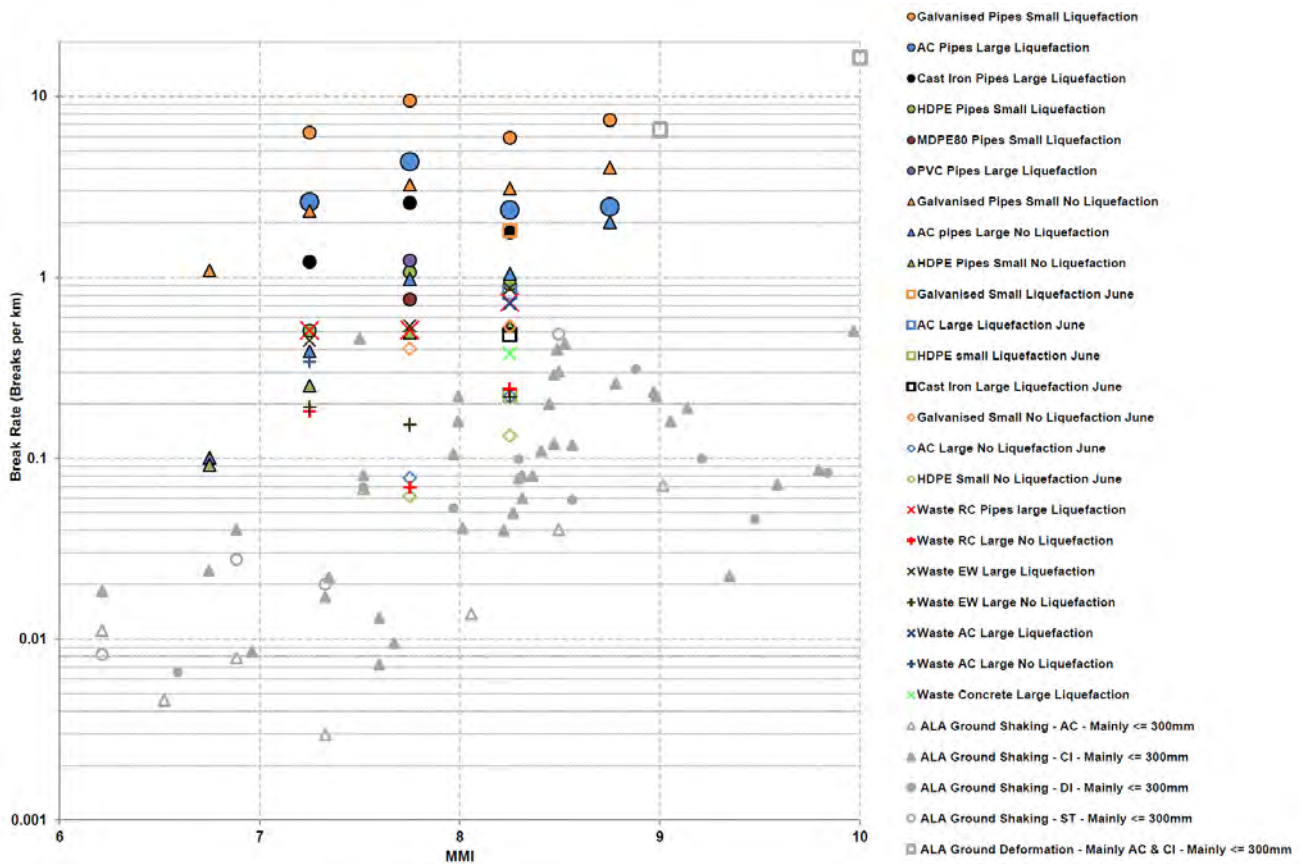


Figure 5.23: Christchurch water and wastewater pipes break rates for the different combinations of pipe material and size, calculated for different shaking intensity levels and ground liquefaction susceptibilities. Small wastewater pipes are smaller than 150mm and small water supply pipes are smaller than 100mm (A.K. Sherson, 2015)

5.2.14 TOPRAK ET AL., 2015

This paper is a follow up to Toprak 2014, with the inclusion of angular distortion and also LiDAR cells are divided into 4m and 56m. This paper calculated the repair rate in correlation with lateral strain and angular distortion. The data used is taken from Toprak 2014 for the Avonside area, Christchurch. The fragility functions developed for AC and CI pipes. Lateral strain is calculated as per Toprak2014 and Angular distortion as per O'Rourke 2014. Comparisons of damage correlations of 56m and 4m LiDAR and air photo displacements is given with difference between them not so significant for AC and CI pipelines. The fragility curves obtained are shown in the fig below.



This project has received funding from the European Union's Horizon 2020 research and innovation programme under grant agreement No. 700748

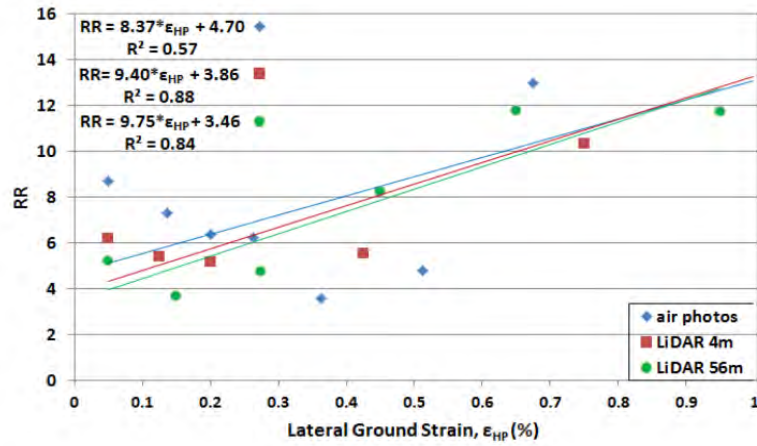


Figure 5.24: Repair Rate vs Lateral Strain relationships for AC pipes (S. Toprak E. N.-S., 2014)

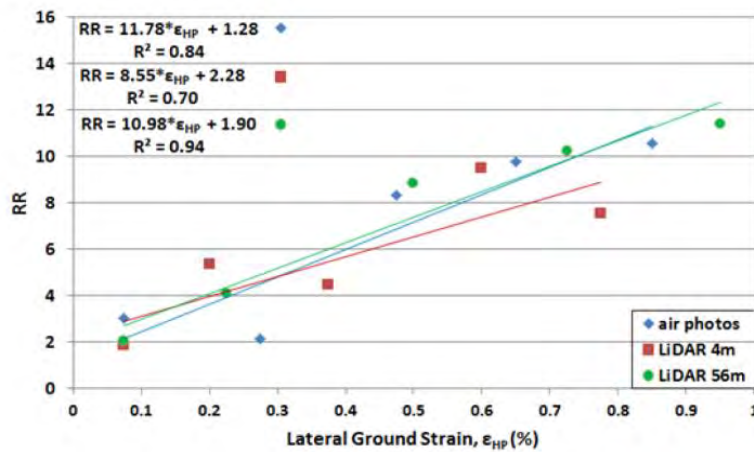


Figure 5.25: Repair Rate vs Lateral Strain relationships for CI pipes (S. Toprak E. N.-S., 2014)

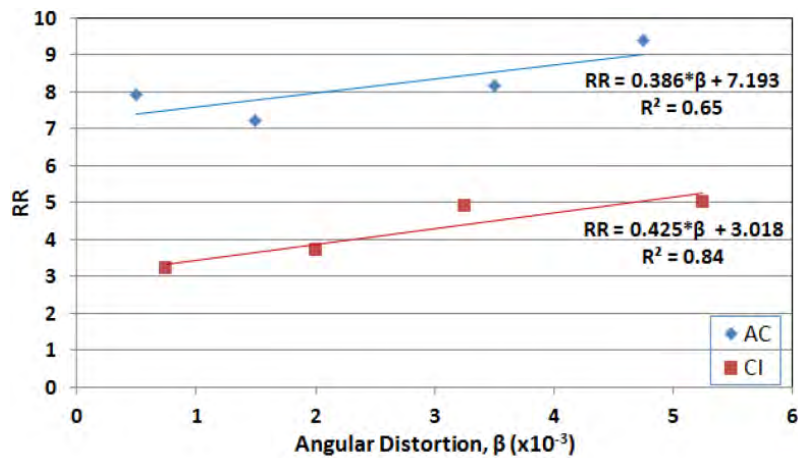


Figure 5.26: Repair Rate vs Angular Distortion for AC and CI pipes (S. Toprak E. N.-S., 2014)



This project has received funding from the European Union's Horizon 2020 research and innovation programme under grant agreement No. 700748

5.2.15 TOPRAK ET AL., 2017

Toprak presented a correlation between pipeline repair rate and Liquefaction Severity Number (LSN) for the 22nd February 2011 earthquake in Christchurch New Zealand. LSN was calculated using the CPT data which was obtained from the numerous CPT tests conducted up to March 2015. It was indicated LSN correlated well with the land and residential house foundation liquefaction induced damage observations recorded in Canterbury, as per previous studies (Tonkin and Taylor (2013); van Ballegooy et al 2014). For his study LSN was calculated from Zhang et al (Ref). He also indicated that one other aspect of LSN is that strains converge on a limiting value that depends on the initial relative density and LSN tends to converge on a maximum value for a given soil profile as the PGA increases. The RR values were calculated for AC, CI and PVC pipes. Toprak (2017) superimposed the LSN area with the repairs conducted for each type of pipeline. Using the above map, he calculated the repair rate by counting number of repairs and pipeline lengths for each type of pipe in each LSN interval of 10. 90% confidence and $\alpha = 50\%$ were applied to develop the regressions between RR and LSN. Pipeline damage ratios were also calculated by dividing the sum of pipe lengths needing repairs to the sum of all pipe lengths in the LSN interval. A strong co-relation was observed between pipeline damage for AC, CI, PVC pipelines and LSN, given by relatively high r-squared values. The studies only included the areas where liquefaction damage was observed, hence the repair rate for lower LSN values was high, particularly for AC pipes. Toprak suggested that if this bias was allowed, the correlation would be strengthened since the repairs in the low LSN zones (i.e. no liquefaction damage zones) was very low. In addition, the correlation presented are specific to Boulanger and Idris (2012) liquefaction triggering assessment methodology using the 15th percentile CRR curves. The RR rates are as follows:-

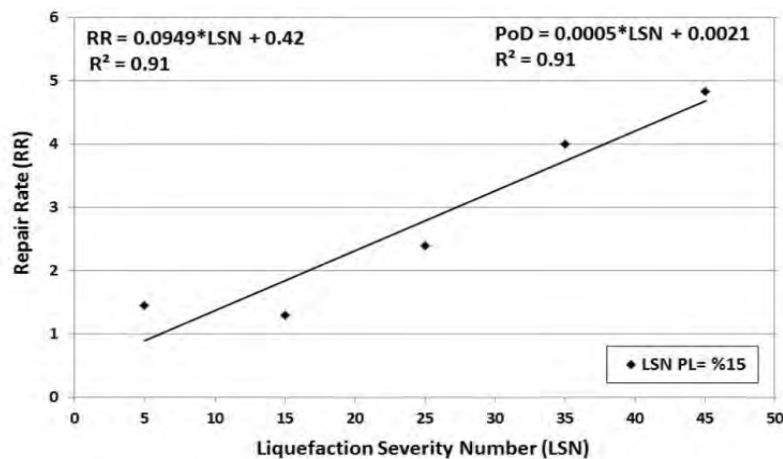


Figure 5.27: Repair Rate vs LSN for CI pipes (S. Toprak E. N., 2017)



This project has received funding from the European Union's Horizon 2020 research and innovation programme under grant agreement No. 700748

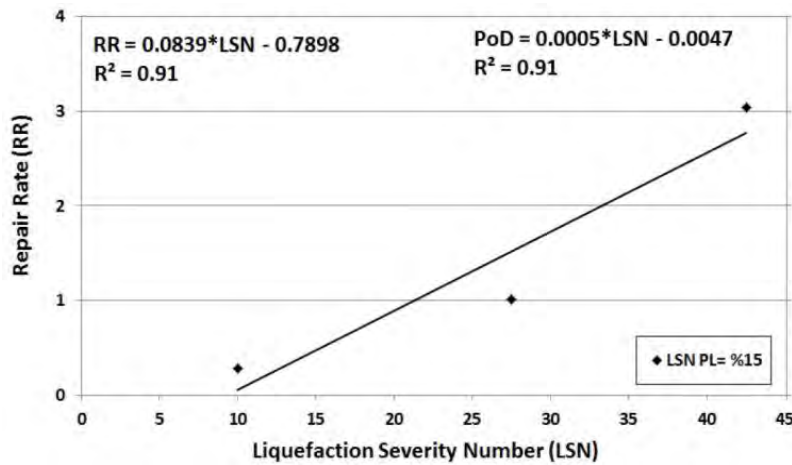


Figure 5.28: Repair Rate vs LSN for PVC pipes (S. Toprak E. N., 2017)

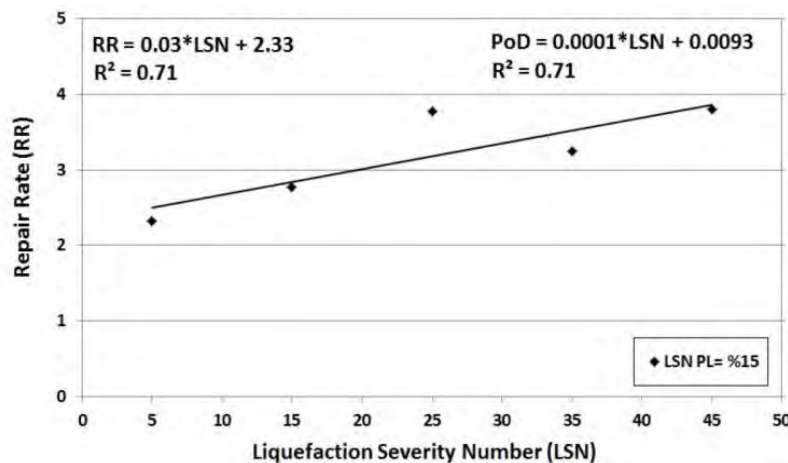


Figure 5.29: Repair Rate vs LSN for AC pipes (S. Toprak E. N., 2017)

5.2.16 D. BOUZIOU ET AL., 2017

The study was conducted for Christchurch city, New Zealand, for 22nd Feb 2011 Earthquake. This paper follows on work by O'Rourke et al. 2014 by using the most recent and complete repair records, using high resolution Light Detection and Ranging (LiDAR) measurements of lateral movements on 4-m spacing, using the higher resolution data and improved screening criteria to provide better correlations among pipeline damage and liquefaction-induced lateral ground strains and differential vertical ground movements. The regressions between RR and ground angular distortion, β in the current paper show a slightly lower level of damage for AC pipelines at small β compared to the regressions obtained by O'Rourke et al. (2014), but for AC, CI, and PVC pipelines compare well with the earlier work. In the present study, RRs vs β for AC pipelines plot approximately two times higher than those for CI pipelines, and 5–10 times higher than those for PVC pipelines. The regressions between RR and lateral ground strain, ϵ_{HP} , using the 4-m LiDAR measurement spacing are significantly different for AC and PVC pipelines than those previously reported for LiDAR



This project has received funding from the European Union's Horizon 2020 research and innovation programme under grant agreement No. 700748

measurements on 56-m spacing. The RR vs ϵ_{HP} regressions for CI pipelines compare favourably because the pipelines were located in relatively uniform strain fields for which there is no significant difference between 4-m and 56-m resolution. RRs vs ϵ_{HP} for AC pipelines are approximately 50–100% higher than those for CI pipelines, and approximately 3 to 11 times higher than those for PVC pipelines. The correlations among RR, ϵ_{HP} , and β for AC and CI pipelines in this work are a significant improvement over those previously presented by O'Rourke et al. (2014). These correlations provide the means to predict RR with respect to the combined effects of lateral ground strain and differential vertical ground movement. Correlations among pipeline repair rates (RR), lateral ground strains, and differential vertical ground surface movements provide the means to predict pipeline damage on the basis of the combined effects of lateral ground strain and differential vertical ground movement.

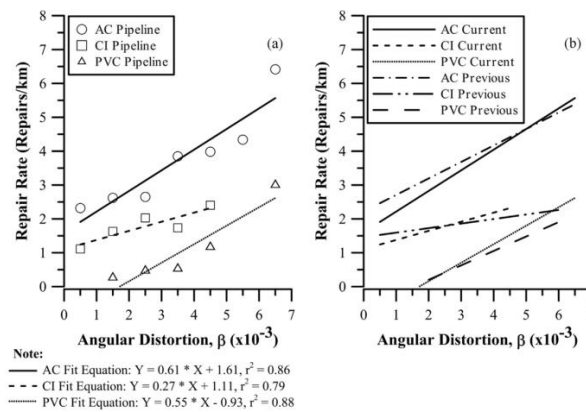
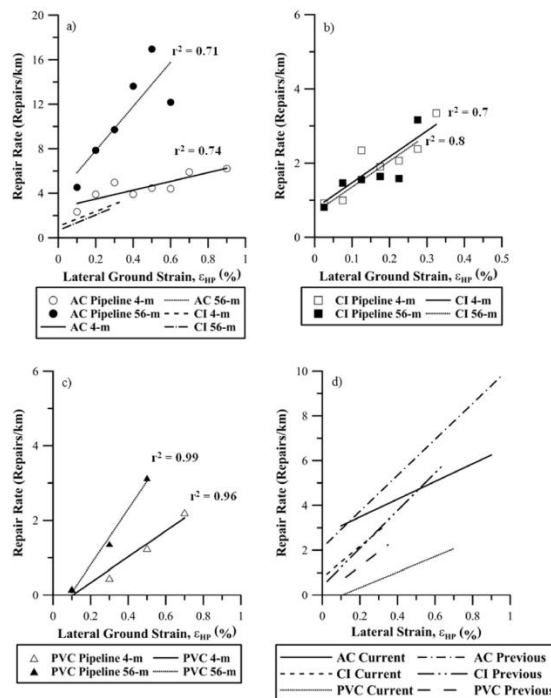


Figure 5.30: Repair rate vs. angular distortion for AC, CI and PVC pipelines: a) Results with updated measurements, b) Comparison of current and previous results (D. Bouziou, 2017)





This project has received funding from the European Union's Horizon 2020 research and innovation programme under grant agreement No. 700748

Figure 5.31: Correlations of repair rate with lateral ground strain at 4-m and 56-m spacing for a) AC, b) CI and c) PVC pie materials for the 22nd Feb. 2011 earthquake and d) comparison of repair rate with lateral ground strain at 4-m spacing with previous work by O'Rourke et al. (2014) (D. Bouziou, 2017)

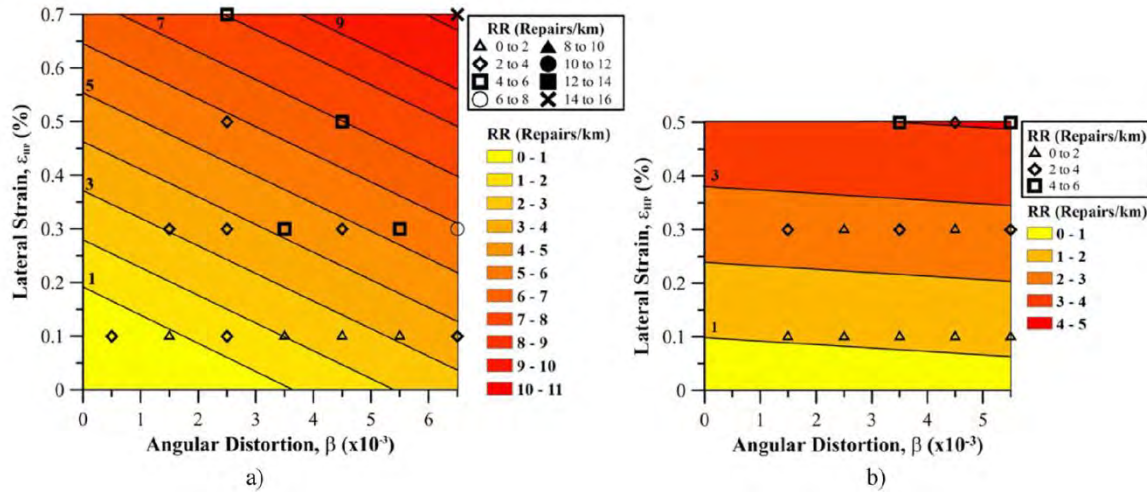


Figure 5.32: Repair rate vs. lateral ground strain and ground angular distortion for a) AC and b) CI pipelines (D. Bouziou, 2017)

5.2.17 O'ROURKE ET AL., 2018

O'Rourke & Vargas-Londono constructed an analytical model of segmented pipelines, subjected to ground strain resulting from PGD (i.e. $\epsilon > 0.002$). The analytical model is based upon mechanics principles of equilibrium and compatibility and accounts for probabilistic variability associated with leakage at the cast iron joints. The seismic hazard is uniform tensile ground strain along the pipes longitudinal axis due to permanent ground deformation. This paper does not exactly specify liquefaction induced ground strain, but assumes a generalised ground strain for $\epsilon > 0.002$. Seismic performance for pipelines with increasing diameters and increasing ground strain, is calculated. It was observed that with increase in diameter the repair rates decrease. Damage rates of 2.0 repairs/km were observed for ground strains of 0.005 and larger. The diameter effects exclusively from PGD were more complex than the ones for wave propagation, For smaller strains and larger dia. the repair rate increases with dia. and as for higher strains the diameter effects disappear, and minimum damage is observed in pipe damage. The repair rate vs ground strain for different diameter of cast iron pipelines is given in **Figure 5.33**, also including a comparison with empirical repair rates.



This project has received funding from the European Union's Horizon 2020 research and innovation programme under grant agreement No. 700748

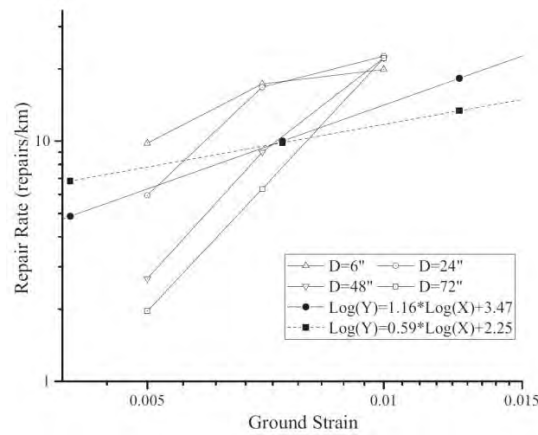


Figure 5.33: Comparison Between Empirical and Analytical Fragility Relations for Various Cast Iron Pipe Diameters. High Ground Strain Model (T. O'Rourke T. V.-L., 2018)

5.2.18 TOPRAK ET AL., 2018

Toprak 2018 follows the similar methodology as of Toprak et al., (2015), with an addition of satellite imagery calculated displacements with LiDAR and Air Photo displacements. The study was conducted for 22nd Feb. 2011 earthquake, for study area of Avonside, Christchurch, New Zealand. Fragility functions were obtained for AC and CI pipes as repair rate vs lateral strain. The methodology of calculating lateral strain is similar to Toprak 2015. Repair rate for AC pipes was much higher for CI pipes for lower lateral strain.

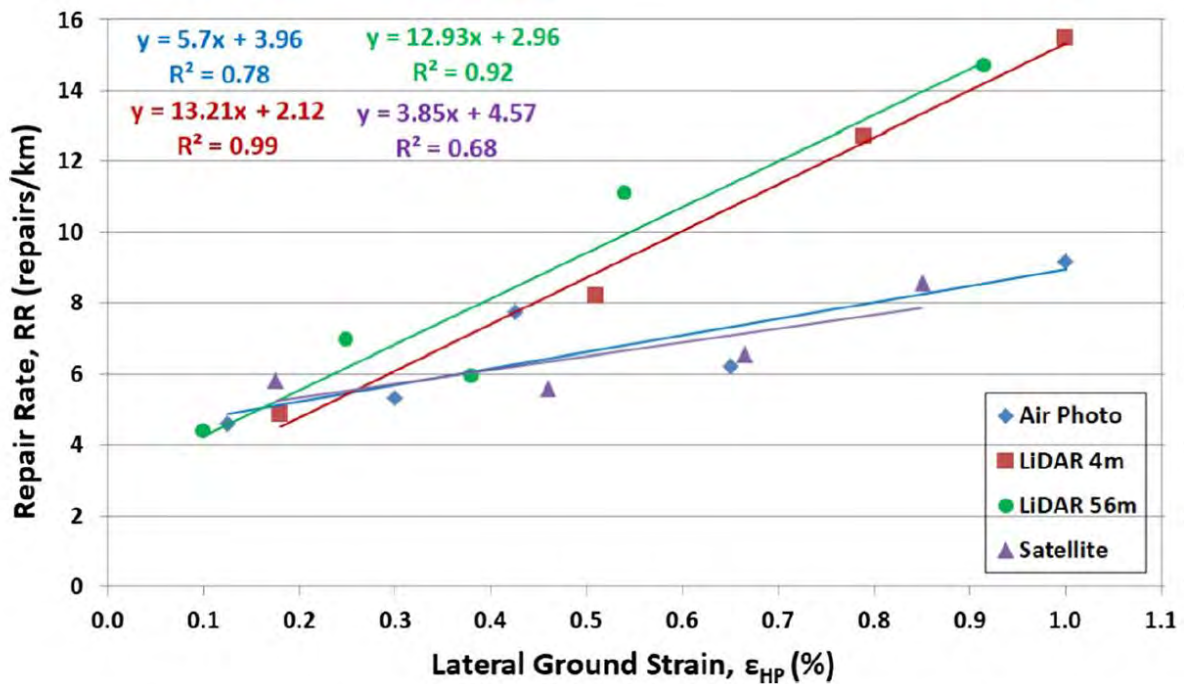


Figure 5.34: RR vs. lateral ground strain for AC pipes (S. Toprak E. N., 2018)



This project has received funding from the European Union's Horizon 2020 research and innovation programme under grant agreement No. 700748

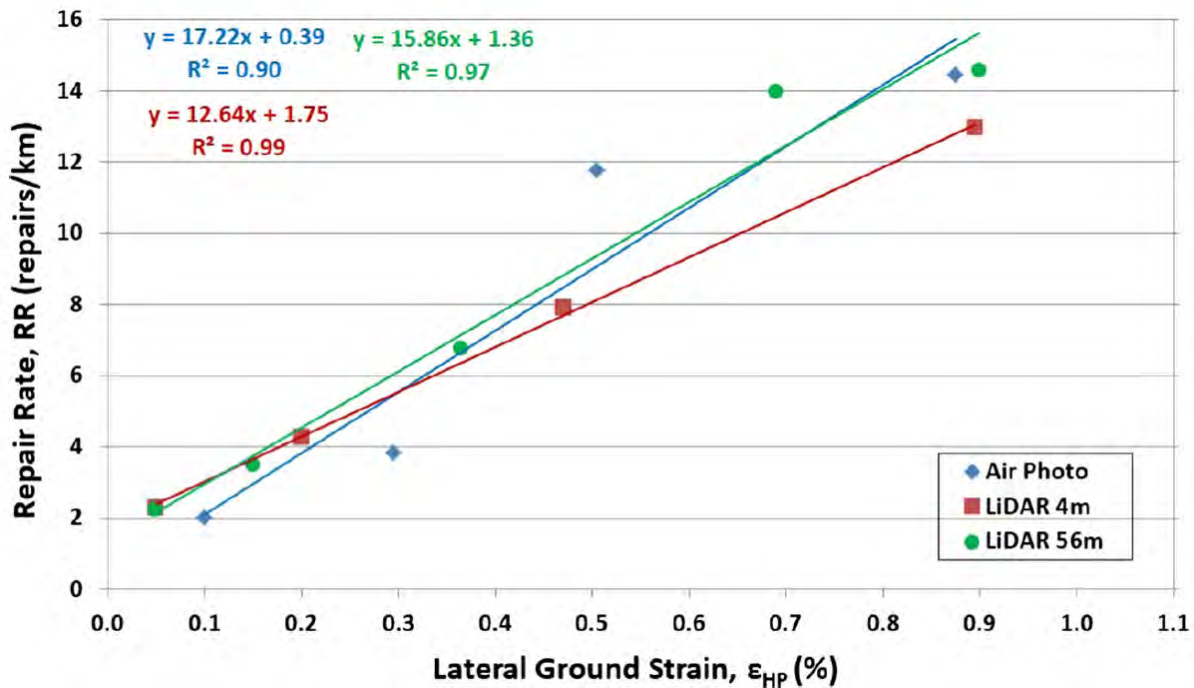


Figure 5.35: RR vs. lateral ground strain for CI pipes (S. Toprak E. N., 2018)

5.3 CHRISTCHURCH CITY CASE STUDY

This chapter gives an overview of the Canterbury earthquake sequence (CES), water supply pipeline network, hazards caused due to the CES and water supply pipeline damages of Christchurch city, New Zealand.

5.3.1 THE 2010-2011 CANTERBURY EARTHQUAKE SEQUENCE CES

The city of Christchurch (population = 350,000 , area = 450 km²), New Zealand suffered a series of earthquakes and aftershocks, named as the Canterbury Earthquake Sequence (CES), between Sept 2010 to December 2011. It had 6 main events (See **Figure 5.1**), 4th September 2010 (Mw = 7.1), 22nd February 2011 (Mw = 6.2), 13th June 2011 (2 earthquakes; Mw = 5.3 at 1 pm; Mw = 6.0 at 2:20 pm) , 23rd December 2011 (2 Earthquakes; Mw = 5.8 at 1:58 pm, Mw = 5.9 at 3:18 pm) (See **Figure 5.36**). The 22nd February 2011 event was the most damaging earthquake causing 185 casualties. Earthquake hazards such as liquefaction phenomenon was seen throughout central and eastern area of Christchurch, with thousands of residential properties, infrastructures and lifelines damaged. The Central Business District (CBD) of Christchurch lost 3000 buildings being damaged beyond repair. The total economic loss caused by 2010-2011 CES is estimated approx. 30 billion NZ dollars (15% of NZ GDP), cost of rebuild at approx. 40 billion NZ billion dollars (Curbrinovski et al., 2011,2014, 2015).

For the Sept 2010 earthquake, the principal Greendale fault rupture reached approximately 12 km west edge of the city and 18 km from its CBD. It produced moderate to strong ground shaking with the ground motions reaching up to 475-design level in some period ranges (Curbrinovski et al., 2011,2014, 2015).



This project has received funding from the European Union's Horizon 2020 research and innovation programme under grant agreement No. 700748

Feb 2011 earthquake, was caused by a local fault just beneath the Port Hills to the south of Christchurch. The fault was approx. 5 km to the south-east of CBD. The fault produced strong to very strong ground shaking, with ground motions well above the 475-design level in south, south-east and east suburbs of Christchurch and CBD. Proximity of the fault to the city, rupture and wave propagation characteristics and basin and site effects contributed to the very high ground motions (Curbrinovski et al., 2011,2014, 2015).

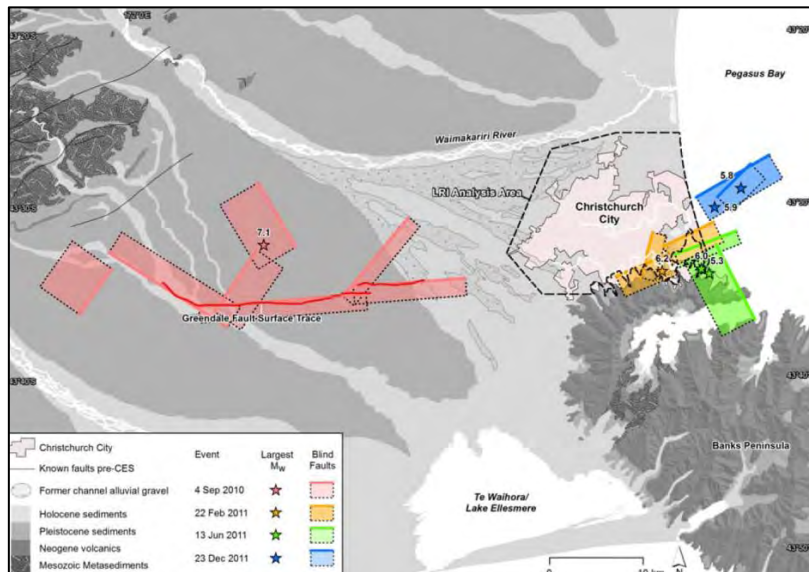


Figure 5.36. Map showing CES events (Cubrinovski et al., 2015)

Table 5.10: Table showing CES events with their magnitudes and epicentral depths (Callaghan 2014; Cubrinovski et al., 2015)

Earthquake Event Name / Site Name	Magnitude (Richter Scale)	Date	Epicentre Depth
Darfield	7.1	September 2010	10 Km
Christchurch City	6.2	February 2011	5 Km
Christchurch City	5.3 & 6.0	June 2011	10 Km
Lyttelton / Christchurch	5.8 & 5.9	December 2011	6 Km

5.3.2 WIDESPREAD LIQUEFACTION MANIFESTATIONS DURING CES

CES caused extensive liquefaction in eastern and central region of Christchurch. Liquefaction at the ground surface was observed for PGA as low as 0.057 (Quigley et al., 2013). After the 22nd February 2011 earthquake, Cubrinovski & Taylor, 2011 produced a liquefaction map (See Figure 5.37) after conducting a drive-through parts of Christchurch, documenting the surface evidence and severity of liquefaction. The map produced as shown in Figure 5.2. quantified the liquefaction severity as follows: (a) moderate to severe liquefaction (red zone, with very large areas covered by sand ejecta, mud and water, large distortion of ground and pavement surfaces, large fissures in the ground, and significant liquefaction-induced impacts on buildings and infrastructure), (b) low to moderate liquefaction (yellow zone, with generally similar features as for the



This project has received funding from the European Union's Horizon 2020 research and innovation programme under grant agreement No. 700748

Methodology for the liquefaction fragility analysis of critical structures and infrastructures: description and case studies

v. 1.0

severe liquefaction, but of lesser intensity and extent), (c) liquefaction predominantly on roads with some on properties (magenta zone, where heavy effects of liquefaction were seen predominantly on roads, with large sinkholes and 'vents' for pore pressure dissipation, and limited damage to properties/houses), and (d) traces of liquefaction (red circular symbols, with clear signs of liquefaction, but limited in extent and deemed not damaging for structures). The solid blue line indicates roads where no liquefaction was observed (Cubrinovski & Taylor, 2011). The map does not cover all of Christchurch, but shows the severity of observed liquefaction. The map also shows severe liquefaction occurred near and around the Avon river.

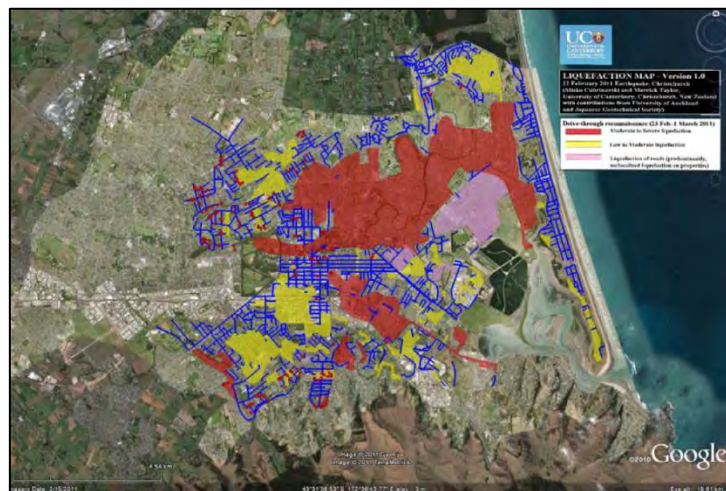


Figure 5.37. Liquefaction Map of Christchurch as produced by Curbrinovski and Taylor , 2011 (Reproduced from Cubrinovski et al., 2014)

Soil Liquefaction is a process most often observed in saturated, loose sandy soils. It's a process when the sandy soil loses strength and stiffness and transforms into a liquid state from a normal solid state in response to an applied stress such as shaking during an earthquake. During such excessive shaking the pore water pressure increases and triggering the flow of water towards the ground surface, the water carries with itself a significant amount of soil and thus leading to creation of sink holes or vents for pore pressure dissipation. Liquefaction also causes ground deformation, heavy structures to sink and light structures to float. Ground deformations can be associated with large permanent vertical displacement (settlement) and lateral displacements resulting in large cracks and fissures in the ground and sand/silt/water ejecta (Cubrinovski and McCahon, 2011).

Liquefaction was observed in Christchurch's due to its soil formation, high water table levels, excessive ground shaking, etc. Christchurch, central and eastern, is mostly formed of gravels, non-plastic sand deposits, drained peat swamps, estuaries, lagoonal, dune and coastal swamp deposits (Quigley et al., 2013; Cubrinovski et al., 2015, 2011). High water tables are a result, due to presence of aquifers and natural springs in the area and nearby coastline. The soil is also relatively young due to its Holocene nature of sand deposits, and the artesian pressure and upward water flow reduce the effective stress in the subsurface soils and reduce the possibility for soils to get stiffer and stronger due to ageing effects. Widespread liquefaction was seen due to 22nd February earthquake, due to its close proximity to the city, lower depth of the epicenter and high ground shaking. After repeated earthquakes, the soil fabric of the re-solidified deposits post-



This project has received funding from the European Union's Horizon 2020 research and innovation programme under grant agreement No. 700748

liquefaction, is very weak, with low liquefaction resistance. A map (**Figure 5.40**) showing liquefaction occurrence from different earthquakes of CES was also produced, indicating that liquefaction repeatedly occurred during multiple earthquakes especially 4th September 2010, 22nd February 2011, 13th June 2011.



Figure 5.38: Liquefaction map showing the areas of liquefaction and severity observed from different earthquakes. 4th Sept 2010 (white contours), 22nd February 2011 (red, yellow, magenta areas; Cubrinovski and Taylor, 2011) and 13th June 2011 (black contours; Cubrinovski and Hughes, 2011).

Liquefaction land damage map (See **Figure 5.41**) was produced by Bradley & Hughes (2012) which shows the ground surface damage observations throughout Christchurch. It shows that approximately more than 87% of land damage was seen due to severe subsidence, throughout eastern and central Christchurch (van Ballegooy et al., 2014). The severe subsidence is seen as a result of topographic re-levelling, volume loss due to water, sand ejecta to the ground surface, post liquefaction volumetric densification and differential ground settlements (Cubrinovski, et al., 2015; van Ballegooy, et al., 2014).



This project has received funding from the European Union's Horizon 2020 research and innovation programme under grant agreement No. 700748

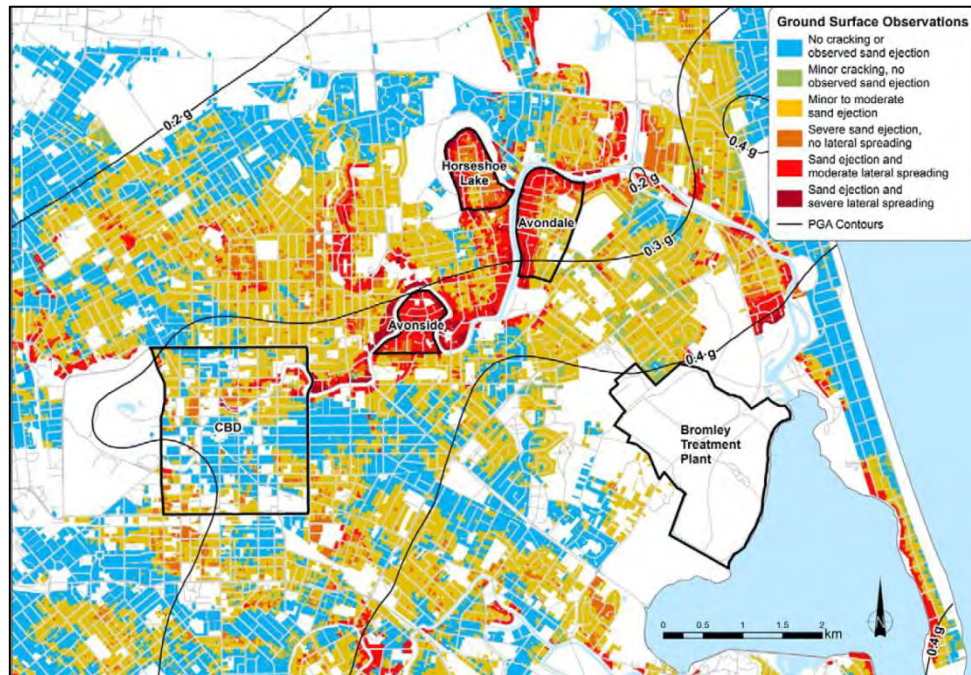


Figure 5.39: Liquefaction induced Land Damage observations across Christchurch after the February 2011 earthquake, with Feb 2011 magnitude-weighted equivalent $M_w = 7.5$ PGA contours overlaid based on Bradley & Hughes (2012) (Reproduced from Van Ballegooy et al., 2014)

The mapping recorded the incremental effects of each earthquake, since the ejected liquefied material was removed and major cracks filled but not repaired, which would mean lower integrity of non-liquefied soil (Van Ballegooy et al., 2013). Similar damage conditions (**Figure 5.43**) can be observed in the pictures taken after the 22nd February 2011 earthquake. Quigley et al., 2013 showed the effect of earthquake (shaking) in series on liquefaction, this clearly justifies that the soil densifies after liquefaction but loses its strength and hence its liquefaction resistance (See **Figure 5.42**).



Figure 5.40: Field Photographs of sand blows at study site following (A) Darfield ML = 7.1 earthquake, (B) 22nd February 2011 ML 6.3, 5.8 and 5.9 earthquakes, (C) 16 April 2011 ML 5.5 earthquake, (D) 13 June 2011-a ML 5.6 earthquake, (E) 13 June 2011-b ML 6.4 earthquake and (F) 23 December 2011 ML 5.8 and 6.0 earthquakes. All images were taken within 3 hours of the last inducing earthquake (Reproduced from Quigley et al., (2013))



This project has received funding from the European Union's Horizon 2020 research and innovation programme under grant agreement No. 700748



(a)



(b)



(c)



(d)



(e)



(f)

Figure 5.41: Observed liquefaction-induced land damage and dwelling foundation damage due to Christchurch earthquakes: (a) Extensive liquefaction in low-lying Christchurch suburbs (23rd February 2011), (b) Suburban Christchurch street covered with liquefaction ejecta (23 February 2011), (c) Pavement completely buried by liquefaction ejecta and ponded water after liquefaction (24th February 2011), (d) Surface water flowing over liquefaction ejecta with collapsed concrete block wall (22 February 2011), (e) Liquefaction ejecta next to brick house that subsided (25 May 2011), and (f) Uplift of concrete floor inside house with liquefaction ejecta and water mark around base of walls (01 March 2011). (Reproduced from Van Ballegooy et al., 2014)



This project has received funding from the European Union's Horizon 2020 research and innovation programme under grant agreement No. 700748

5.3.3 INDICATORS OF LIQUEFACTION SEVERITY

Various liquefaction severity indicators including settlement, LSN, LPI are used. These are useful in assessing land damage and liquefaction susceptibility caused due to liquefaction. They are explained as below:

Liquefaction Potential Index (LPI)

Iwasaki's Liquefaction Potential Index (LPI) is a measure of the vulnerability of sites to liquefaction effects. The LPI is the summation of liquefaction severity in each soil layer, which in turn is a function of the Factor of Safety for liquefaction triggering (FS), weighted by a depth factor that decreases linearly from 10 to 0 over the top 20 m. The LPI value is between 0 (representing no liquefaction vulnerability) and 100 (representing extreme liquefaction vulnerability). By weighting soils to have an increasing influence on LPI as depth decreases, this parameter is able to represent the beneficial effects of an increasing non-liquefied surface layer thickness, or crust. Juang et al. (2005a and 2005b) report that sites with an LPI of more than 5 have a high liquefaction risk, and sites with LPI greater than 15 indicate very high risk (Iwasaki et al. 1982). Toprak and Holtzer (2003) indicated similar LPI values based on observations from the 1989 Loma Prieta earthquake. Potentially liquefiable layers only contribute to the LPI when their calculated FS falls below 1.0. As FS decreases, it provides a higher contribution of the calculated LPI. LPI is given as follows (Iwasaki et al. 1982):

$$LPI = \int_0^{20} F_1 W(z) dz \quad (5.7)$$

Where $W(z) = 10 - 0.5z$, $F_1 = 1 - \text{FoS}$ for $\text{FoS} < 1.0$, $F_1 = 0$ for $\text{FoS} > 1.0$ and z is the depth below the ground surface in metres. The LPI presented here is based on the I&B triggering method.

Liquefaction Severity Number (LSN)

The Liquefaction Severity Number LSN is a new calculated parameter developed by Tonkin & Taylor to reflect the more damaging effects of shallow liquefaction on residential land and foundations. The equation used to calculate LSN is presented below. LSN considers depth weighted calculated volumetric densification strain within soil layers as a proxy for the severity of liquefaction land damage likely at the ground surface. The published strain calculation techniques consider strains that occur where materials have a calculated triggering FoS that reduces below 2.0. This means that the LSN begins to increase smoothly as factors of safety drop, rather than when the FoS reaches 1.0. One other aspect of LSN to note is that strains self-limit based on the initial relative density as the factor of safety drops, so a given soil profile has a maximum LSN that it tends towards as the PGA increases (Tonkin & Taylor 2013; Van Ballegooy et al., 2014).

$$LSN = 1000 \int \frac{\epsilon_v}{z} dz \quad (5.8)$$

where ϵ_v is the calculated post-liquefaction volumetric reconsolidation strain in the subject layer from Zhang et al., (2002) entered as a decimal and z is the depth below the ground surface in meters for depths greater than 0.0. LSN is calculated as the summation of the post-liquefaction volumetric reconsolidation strains calculated for each soil layer divided by the depth to the midpoint of that layer. The value of LSN is



This project has received funding from the European Union's Horizon 2020 research and innovation programme under grant agreement No. 700748

theoretically between 0 (representing no liquefaction vulnerability) to a very large number (representing extreme liquefaction vulnerability).

Settlement (S)

The calculated settlement indicator is based on published methods to estimate volumetric shear strains. These strains are integrated to calculate ground settlement. The MBIE(2012) documents recommend using the I&B triggering method with the Zhang et al. (2002) volumetric densification calculation, which uses a normalised tip resistance and factor of safety to estimate settlements. The Zhang et al. (2002) method predicts strain in layers where the liquefaction factor of safety is less than 2.0. The calculated settlement indicator increases as the factor of safety drops and the material approaches a liquefied state. Therefore, some settlement is calculated when FoS is more than 1 even though liquefaction triggering has not occurred (Tonkin and Taylor 2013).

5.3.4 DAMAGE TO WATER SUPPLY NETWORK IN CHRISTCHURCH DURING CES

The water supply pipeline network is divided into pipe types of mains, submains, trunk mains and crossovers. Mains are approx. 1700 Km in length laid on the carriageway, 2-2.5m from the kerb and submains are approx. 2000 Km laid beneath the footpaths, 150mm from boundaries. Mains have pipe diameters from 100mm to 600mm, while submains have diameters of 50 mm and 63mm. Crossovers are 50 mm in diameter, serve to submains located at the fire hydrants. Watermains are laid in trenches 200-300 mm wider than the pipe diameter, at shallow depths (see **Figure 5.42**). The cover thickness depends on the pipe size, location and material, but is usually about 800mm (at least 750mm, but no more than 1.5m for the standard watermains diameters). Typical thickness of cover for submains is 300-500 mm. The trenches are backfilled with native soils and are compacted to 95%, 90% and 70% of the material's maximum dry density (NZS 4402.4.1.1) for trafficked, pedestrian and landscape areas, respectively. The year of laying these pipes varies from 1890's to present. **Figure 5.43** shows a typical illustration of a pipe laying and backfill (Cubrinovski et al., 2011, 2014).

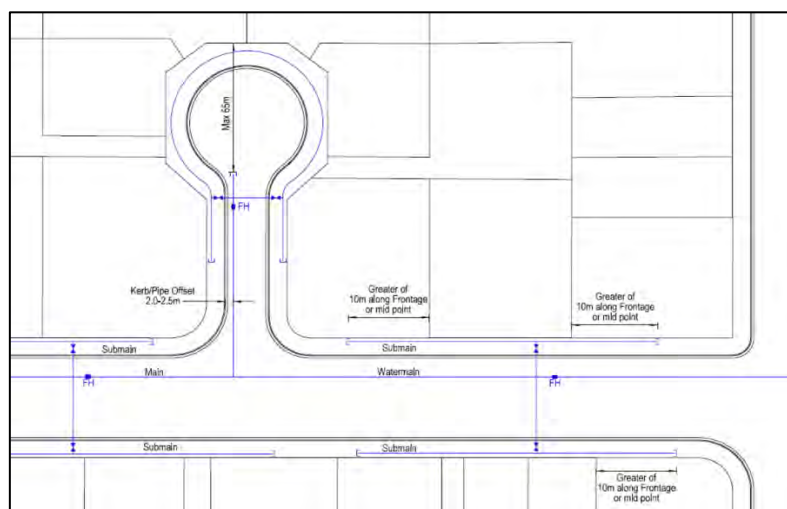


Figure 5.42: Typical layout of watermains and submains in the carriageways and footpaths of Christchurch (reproduced from Cubrinovski et al., 2011). Typical layout of watermains and submains in the carriageways and footpaths of Christchurch (reproduced from Cubrinovski et al., 2011).



This project has received funding from the European Union's Horizon 2020 research and innovation programme under grant agreement No. 700748

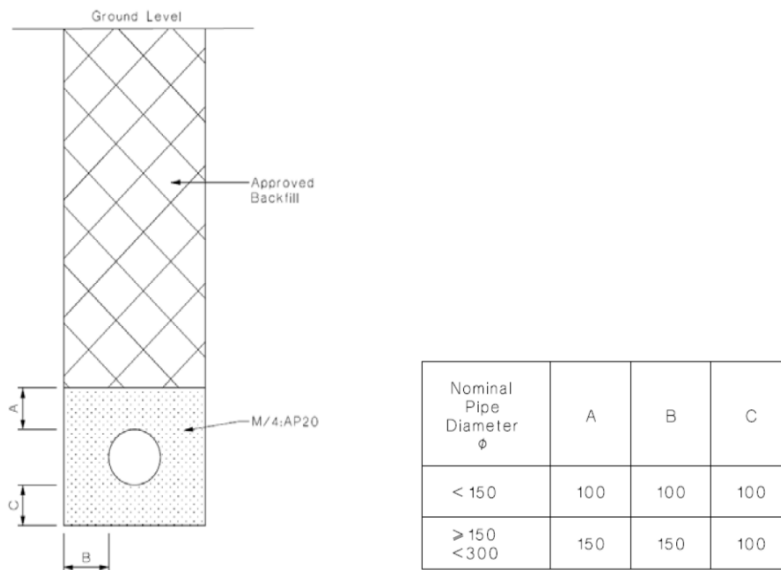


Figure 5.43: Illustration of backfill and pipe-laying details (units in mm) (Reproduced from Cubrinovski et., 2011)

The damage observed to the water supply pipeline was due to three factors namely, earthquake, soil and pipe parameters. Earthquake factors like closeness of the epicentre, magnitude and depth affect the damage to the pipelines. Higher damage was seen for long duration of ground shaking and shallow events, closely associated with occurrence of liquefaction.

Pipe parameters like pipeline direction, pipe age, pipe material, pipeline joints, pipeline diameter affect the damage of the pipelines. Pipeline direction if vertical or almost vertical to the fault causes higher damage. Also, brittle pipe material were observed to be more vulnerable to earthquake shaking. Flexible pipes like PE and PVC suffered 3-5 times less damage than AC, steel and GI pipelines. Older pipelines suffer corrosion, hence vulnerable to damage. The Repair rates are observed to be higher for pipe dia (less than 12 inches) than in large diameter pipelines. Large diameter pipelines suffer less damage due it higher wall thickness. Pipelines in general with less connections, fittings and irregularity suffer less damage. AC pipelines suffered damage to the pipe body itself (62%), commonly circumferential & longitudinal splits type damage. The damage to pipe fittings was observed to be 38%. The pipes which suffered damage to pipe fittings, property connections, coupler, gibaults were HDPE (82%), MDPE80 (90%), PVC (80%), CI (79%), GI (58%). **Table 5.11** shows the different types of pipes with its modes of failure.



This project has received funding from the European Union's Horizon 2020 research and innovation programme under grant agreement No. 700748

Table 5.11: Types of Pipe Materials and its mode of failure

Type of Pipe Material	Total damage (in percentage, %)	Mode of Failure	Physical Failure Mechanism
AC	62	Pipe Body	Longitudinal and circumferential split
AC	38	Pipe Fittings	Property Connection, Coupler Connection, Gibualts
HDPE	82	Pipe Fittings	
MDPE80	90	Pipe Fittings	
PVC	80	Pipe Fittings	
CI	79	Pipe Fittings	Longitudinal and circumferential split
GI	58	Pipe Fittings	Pinhole repairs

Table 5.12: Repair Count for different Pipe Materials

Pipe Material	Repair Count	% of Repair Count	Pipe Material	Repair Count	% of Repair Count
ABS	0	0	HDPE	1592	28.2
AC	1491	26.4	LDPE	0	0
AL	0	0	MDPE100	0	0
API	0	0	MDPE80	337	5.96
CI	495	8.76	MLDI	1	0.02
CLDI	1	0.02	MPVC	31	0.55
CLS	151	2.67	PE	0	0
DI	45	0.8	PE100	0	0
GALV	1214	21.5	PVC	185	3.27
Unknown	0	0	RCRR	0	0
UPVC	27	0.48	STEEL	82	1.45



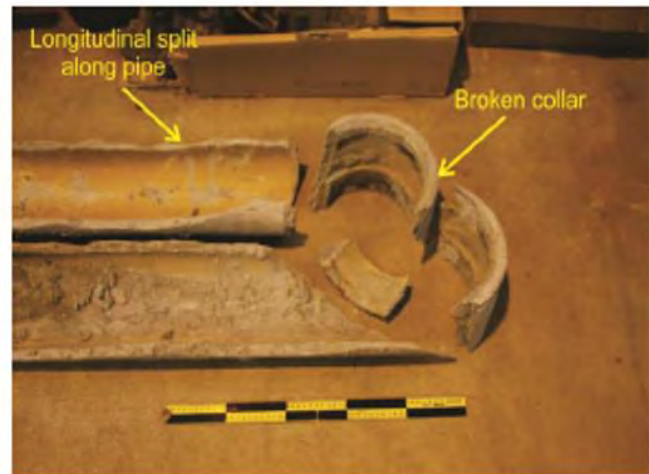
This project has received funding from the European Union's Horizon 2020 research and innovation programme under grant agreement No. 700748

Table 5.13: Repair Count for different Pipe Diameters

Pipe Diameter	Repair Count	% of Repair Count	Pipe Diameter	Repair Count	% of Repair Count
13	1	0.02	100	1499	26.5
15	3	0.05	125	0	0
20	774	13.7	150	528	9.34
25	623	11	175	0	0
32	32	0.57	180	0	0
38	13	0.23	200	272	4.81
40	773	13.7	225	17	0.3
50	830	14.7	250	17	0.3
63	147	2.6	300	88	1.56
65	0	0	350	0	0
75	12	0.21	375	17	0.3
80	0	0	400	0	0
550	0	0	425	0	0
600	4	0.07	450	2	0.04



(a)



(b)

Figure 5.44: (a) Circumferential split on AC main, Rowan Avenue (Picture reproduced from Cubrinovski et al., 2015), (b) AC main broken collar and longitudinal split (Reproduced form Cubrinovski et al., 2015)



This project has received funding from the European Union's Horizon 2020 research and innovation programme under grant agreement No. 700748



(a)



(b)

Figure 5.45: (a) Longitudinal split on AC main, (b) Broken CI main (Reproduced from Curbrinovski et al., 2014)



(a)



(b)

Figure 5.46: (a) bursts in the wall (indicated) of a CLS, (b) PVC mains (Reproduced from Cubrinovski et al., 2014)



This project has received funding from the European Union's Horizon 2020 research and innovation programme under grant agreement No. 700748



Figure 5.47: (a) Compression effects in AC pipe joint, Sewell Street Kaiapoi, (b) Tension effects in AC pipe joint, Sewell Street Kaiapoi (Reproduced from Toprak et., 2017)

5.4 METHODOLOGY TO DEVELOP EMPIRICAL FRAGILITY CURVES FOR PIPELINES

In this chapter a series of steps are followed to understand the process of developing a fragility functions, identifying the dataset available, examining the dataset and further applying the Luco & Cornell Method (2002) and Machine learning techniques to develop fragility function.

A conceptual fragility model framework is shown in **Figure 5.48**, this framework describes the relationship between pipeline damage and LDPs and is also a guide in developing fragility functions for pipelines. The development of the fragility model framework was guided by the literature review as conducted in chapter - - and data availability of the water supply pipelines and earthquake hazard. Pitilakis 2011, defines fragility functions as deterministic, probabilistic or statistical relationships relating the pipeline damage with an appropriate measure of intensity of an earthquake hazard (Pitilakis et al., 2011). The framework given in fig – is built upon framework provided by Bagriacik et al., (2018) which says pipeline damage is an interaction of earthquake hazard, pipeline exposure and pipeline vulnerability. In our study earthquake hazard includes Liquefaction demand Parameters (LDP, synonym for intensity measure for our study). LDPs are permanent ground deformations (PGD) or measures of liquefaction severity given by settlement, LSN, LPI, LPIish, which require ground motion, liquefaction susceptibility and groundwater depth data for its computation (Bagriacik et al., 2018). Pipeline vulnerability includes pipe material, pipe type, pipe diameter and year pipe was laid (Bagriacik et al., 2018). Pipeline length gives the pipe exposure, by incorporating the spatial differential behaviour of interaction of pipelines and liquefaction severity. Pipe exposure and vulnerability collectively fall under pipeline data, forming our total pipeline dataset. The measure of pipeline damage is given by pipe damage (a binary term, pipe is damaged or not). Different variables are assigned to different factors influencing pipeline damage as shown in **Figure 5.48**.



This project has received funding from the European Union's Horizon 2020 research and innovation programme under grant agreement No. 700748

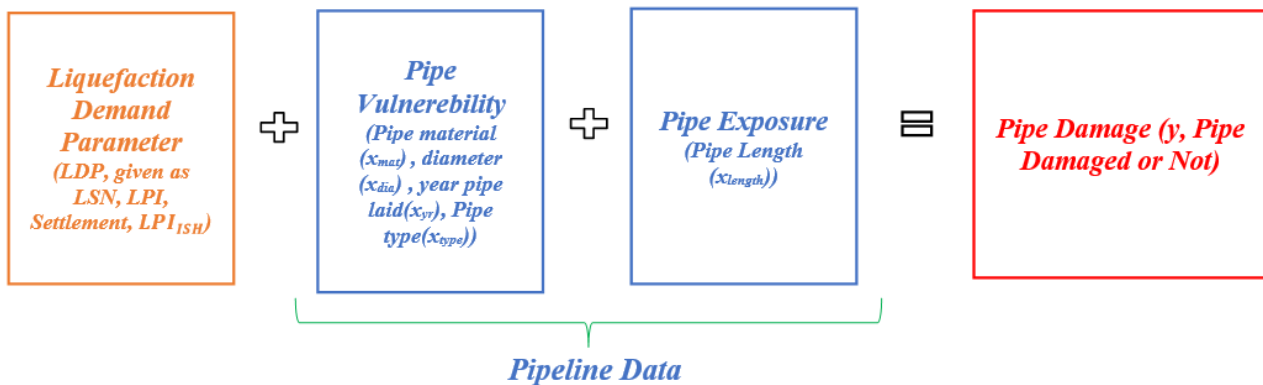


Figure 5.48: framework for development of the fragility model

Utilising the above framework, the following steps are followed to develop pipeline fragility function:

Step 1: Christchurch Water Supply Network Database

This section aims to identify the available water supply pipeline and water supply repair dataset to be further used for our analysis.

Step 1.1: Water Supply Pipeline Network Data

GIS (Geographical Information System) database of Christchurch water supply pipeline network and pipeline repair data during CES, was prepared by Christchurch City Council (CCC) and Stronger Christchurch Infrastructure Rebuild Team (SCRIT). Pipeline network data, available as polylines in GIS format, included data regarding pipe diameter, pipe length, pipe material, pipe types and year the pipes were laid. The pipeline repair database also available as polylines in GIS format, included data regarding number of repairs conducted during CES for each pipeline, repair dates, description of the damage and number of days required for repair. The number of repairs for each earthquake is given in **Table 5.14**. February 2011 earthquake shows the highest number of repairs, this is due to its close proximity (4-10 Km within city boundary) to the Christchurch City. The total number of pipelines in the database is 146772 nos. The total statistics of the available pipeline data is shown in **Table 5.14**.



This project has received funding from the European Union's Horizon 2020 research and innovation programme under grant agreement No. 700748

Table 5.14: Table showing (a) Lengths of different pipe types (b) Repairs conducted after each event of CES (c) Lengths of different Pipe Materials.

Pipe Type	Length (Km)			
Main	1700	Pipe Material	Pipe Length(Km)	Pipe Material
Submains	1522	ABS	0.0699	HDPE
Cross Overs	143	AC	872.0984	LDPE
Trunk Mains	291	AL	0.0712	MDPE100
		API	0.2346	MDPE80
		CI	208.2447	MLDI
		CLDI	8.8321	MPVC
		CLS	53.6754	PE
		CONC	0.1501	PE100
		DI	51.2643	PVC
		GALV	173.7273	RCRR
		Unknown	0.0558	STEEL
		UPVC	130.3438	WI

(a)

CES Event	Number of Repairs
Sept 2010	Approx. 98
Feb 2011	Approx. 3800
June 2011	Approx. 1500

(b)

(c)

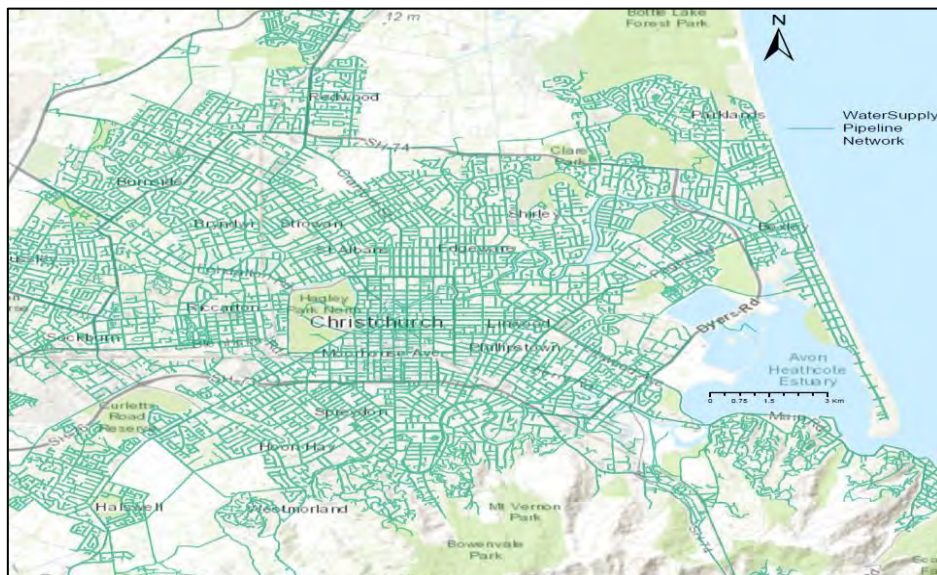


Figure 5.49: Water Supply Network of Christchurch



This project has received funding from the European Union's Horizon 2020 research and innovation programme under grant agreement No. 700748

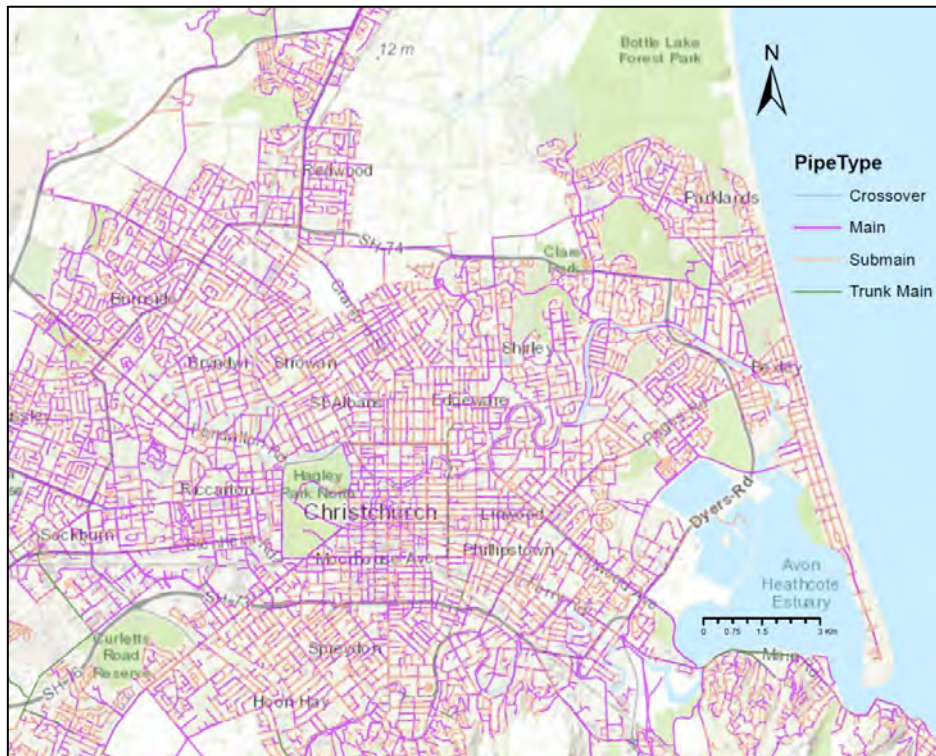


Figure 5.50: Water Supply Network of Christchurch with different pipe types

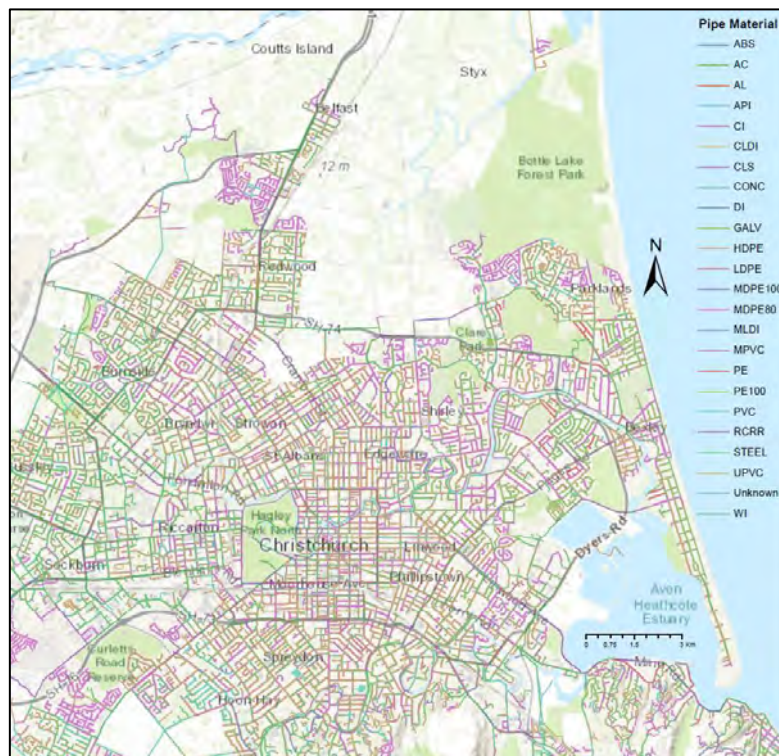


Figure 5.51: Water Supply Network of Christchurch with different pipe materials



This project has received funding from the European Union's Horizon 2020 research and innovation programme under grant agreement No. 700748

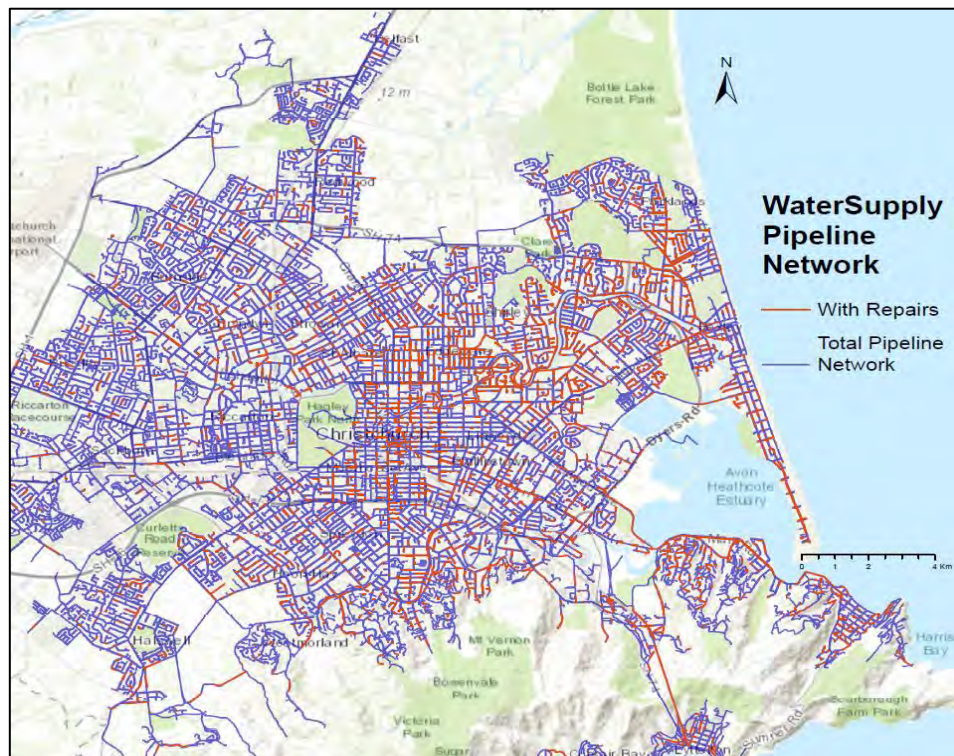


Figure 5.52: Water Supply Pipeline Network of Christchurch with repairs

Step 1.2: Liquefaction Demand Parameter (LDP) Data

A large scale geotechnical investigation program was undertaken after each earthquake during CES, this included 15649 Cone Penetration Tests (CPT) between Sept 2010 and March 2013. The database is available in Canterbury Geotechnical database at <https://nzgd.org.nz>. Christchurch City Council (CCC) and Tonkin and Taylor (2013) developed an analysis tool, based on Boulanger and Idriss (2014) liquefaction triggering method to develop independent regional-scale maps of different liquefaction vulnerability indicators, hereinafter called Liquefaction Demand Parameters (LDP), for a range of earthquake scenario's, groundwater table surfaces and soil properties (Tonkin & Taylor, 2013).

The LDPs are as follows (Taylor & Taylor, 2013):

- Settlement (S) - Based on Zhang, Robertson and Brachman (2002)
- Liquefaction Severity Number (LSN) - As defined in Tonkin & Taylor (2013)
- Liquefaction Potential Index (LPI) - As defined by Iwasaki et al. (1978)
- Liquefaction Potential Index (LPI_{ISH}) - Using the Ishihara inspired LPI method developed by Maurer et al. (2014a)



This project has received funding from the European Union's Horizon 2020 research and innovation programme under grant agreement No. 700748

For each earthquake scenario these indicators were mapped with a selection of liquefaction triggering input parameters (Tonkin & Taylor, 2013):

1. Probability of Liquefaction, PL (PL = 15%, PL = 50% and $P_L = 85\%$).
2. Fines content versus I_c relationship calibration parameter, C_{FC} ($C_{FC} = 0$ and $C_{FC} = 0.2$).
3. PGA distribution given by Cornell and Bradley (Taylor, 2013; Bradley et al., 2012b; Bradley et al., 2012c), separately.

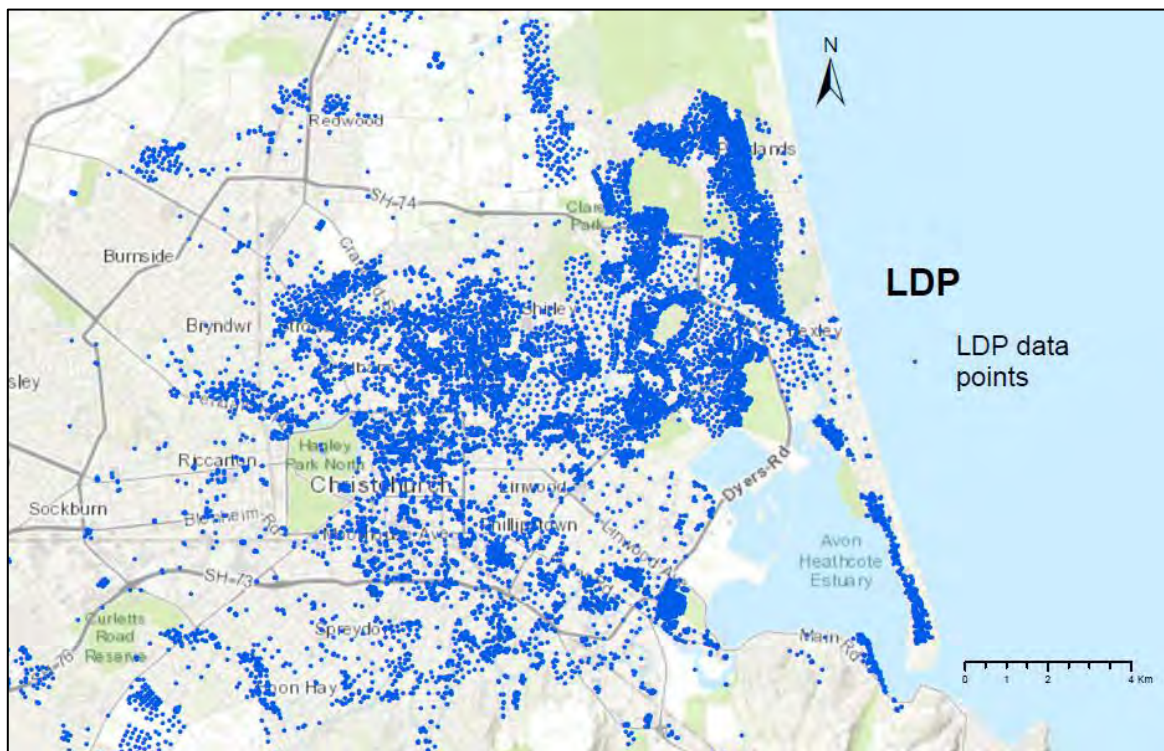


Figure 5.53: Sample LDP Map showing the data points where CPT tests were conducted.

Step 2: Earthquake and LDP Map Selection

This section aims to identify and select the most damaging earthquake from CES and also identify the most suitable LDP map from the given range of input parameters.

Following the 22nd February 2011 event, Christchurch city water pipelines suffered the highest number of repairs as shown in the **Table 5.13**. A series of aftershocks and main events (13th June 2011 and 2- December 2011) occurred after 22nd February 2011 earthquake, which led to continuous number of pipeline repairs being conducted. Such conditions does not make it easy to identify cause of repairs after June 2011 and Dec 2011 are not due to Feb 2011. Hence, the available repair dataset between 22nd February 2011 and 13th June 2011 is considered the complete pipeline repair dataset, for our study. This includes 2964 number of pipeline repairs. The pipeline dataset was reduced from the total number of pipelines (146772 nos.) to 127354 nos.



This project has received funding from the European Union's Horizon 2020 research and innovation programme under grant agreement No. 700748

of pipes, by considering only pipelines In-service, removed or abandoned upto 22nd February 2011 and removing any unknown or blank values.

As per Lacrose et al., 2015, observed land damage in eastern Christchurch generally correlates with $P_L = 15\%$ whereas western Christchurch correlates more closely with $P_L = 85\%$. The spatial division for each probability of liquefaction was not complete and available, due to which the LDP maps developed with $P_L = 50\%$ were further used as a representation for the city of Christchurch in our study.

Step 3: Analysis of data under a GIS environment

The water supply pipeline network data map, water supply pipeline repair data map and LDP data map were compiled into a single master file, giving a clarity of the available data.

Step 3.1: Selection of LDP points

The LDP dataset includes large number of points (15649 nos.), which may misguide the analysis. This data was reduced by removing LDPs calculated for CPT's taken after March 2013. To further reduce the dataset, a 20m buffer was created around each pipeline (See **Figure 5.54**), and intersecting LDPs (**Figure 5.55**) were separated to be used for our analysis.



20m Buffer Area Water Supply Pipeline Network LDP points

Figure 5.54: Sample 20m buffer superimposed with water supply pipelines.



This project has received funding from the European Union's Horizon 2020 research and innovation programme under grant agreement No. 700748

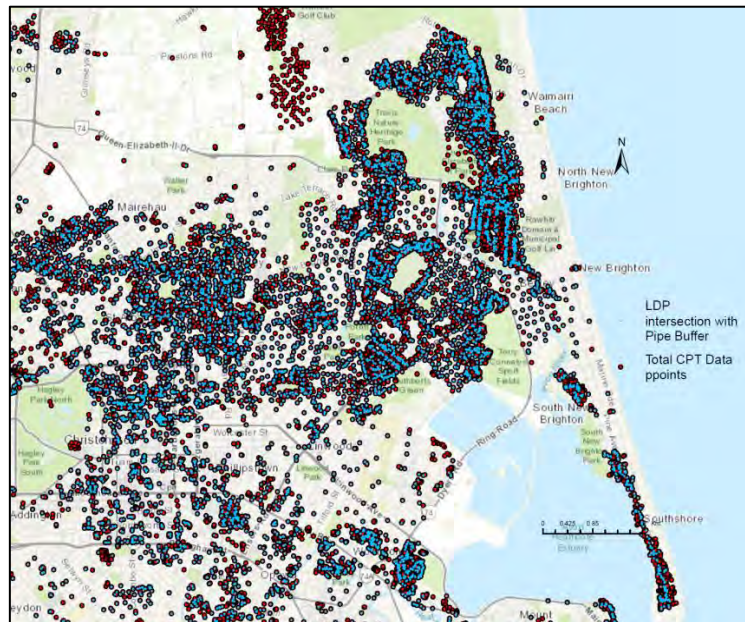


Figure 5.55: Intersected LDP points with buffer superimposed with Total LDP data points

Step 3.2 LDP Mapping

The final intersected LDP points (approx. 8000) were mapped for the city of Christchurch by the use of Kriging interpolation in ArcGIS. The LDP were biased for a certain region of Christchurch where CPT dataset was available. This LDP mapping interpolation also lead to losing high ranged values of LDPs.

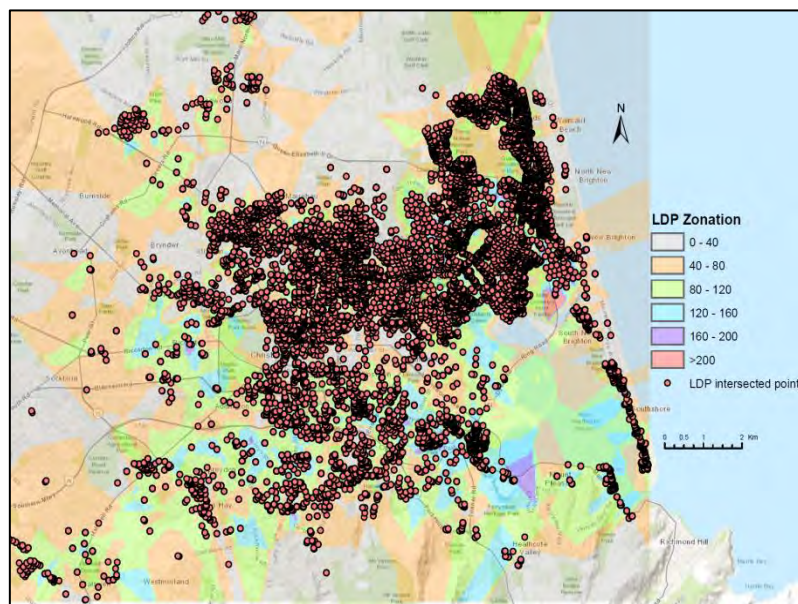


Figure 5.56: LDP points showing superimposed with LDP zonation



This project has received funding from the European Union's Horizon 2020 research and innovation programme under grant agreement No. 700748

Step 3.3 Conversion of Water Supply Polylines to Points at midpoint.

LDP values could not be extracted on the pipelines due to its polyline shape in GIS, hence the pipelines were converted to points, assigning the point at the mid of the polyline. These points contained all attributes of the pipelines but created an uncertainty when LDP values were extracted for pipelines.

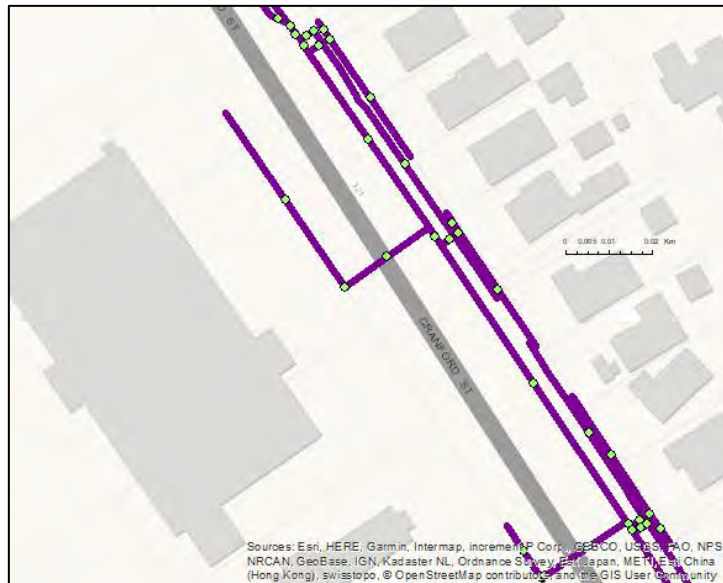


Figure 5.57: Figure showing conversion of pipelines to points

Step 3.4 Extraction of LDP values on Pipelines.

LDP values from LDP maps were extracted on to the pipeline points. After removing the pipelines which did not have any intersecting LDP data the final number of pipelines remaining was 113109.

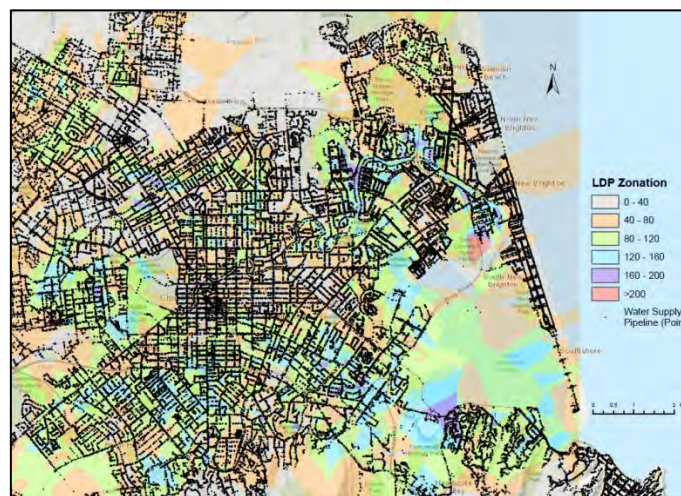


Figure 5.58: Sample Pipeline points superimposed with LDP zonation map



This project has received funding from the European Union's Horizon 2020 research and innovation programme under grant agreement No. 700748

Step 4: Application of the Luco and Cornell method to identify the optimal LDP

Step 4.1 General Approach

Probabilistic seismic demand analysis tool is utilised in evaluating the exceedance of an engineering demand parameter or damage parameter for a given structure (Hamzeh Shakib, 2016). The exceedance of an engineering demand parameter correlates with the intensity measure taken into consideration. The correlation of exceedance of the EDP and IM depends on the ability of the IM to represent the earthquake intensity. Luco et al. (2007) developed an analytical method to find the most appropriate intensity measure. Two parameters, efficiency and sufficiency of the IM, were put forth in finding the most appropriate IM. The efficiency of the intensity measure results in a small variability of the structural demand measure. And sufficiency of an IM leads to an engineering demand parameter or damage parameter which is independent of earthquake magnitude (M) and the source to the site distance (R). In our study, the Intensity measure was taken as the LDP's and the damage parameter or engineering demand parameter was taken as the Repair Rate (RR, repairs per Km length of the pipeline). The damage parameter defined as RR is only considered in Luco and Cornell method for the ease of the analysis in identifying the appropriate LDP. Efficiency and sufficiency approach was applied empirically for our study.

The probability of a structure exceeding a given limit state is given by the annual frequency of the exceedance of the given limit state $\lambda[LS]$ as shown in Equation (5.9).

$$\lambda[LS] = \iint_0^{DM,IM} G[LS|DM]dG[DM|IM]d\lambda[IM] \quad (5.9)$$

Where $G[LS|DM]$ indicates the probability of exceedance of limit state given a demand measure. $G[DM|IM]$ is the conditional probability of the DM given an IM. $\lambda[IM]$ gives the probability of exceedance of a given IM. The selection of the optimal intensity measure is based on efficiency and sufficiency (Hamzeh Shakib, 2016). The seismic demand can be assumed in the power form (Hamzeh Shakib, 2016).

$$EDP = a(IM)^b \quad (5.10)$$

Which transforms into

$$LN(EDP) = Ln(a) + b * Ln(IM) \quad (5.11)$$

The constants a and b can be found by linear regression on EDP and IM. Thus, efficiency is determined using regression analyses of the natural logarithm of Repair Rates (LnRR) on the natural logarithm of corresponding values of the LDP (LnLDP). It is characterized in terms of the dispersion of the residuals, which is calculated by the standard deviation of the residuals **Invalid source specified**.. Sufficiency is determined by the statistical significance of the trend of the residuals from regression between the LDP and magnitude or distance, given by the highest p-value. Residuals are given by the residuals of the predicted RR values and



This project has received funding from the European Union's Horizon 2020 research and innovation programme under grant agreement No. 700748

the observed. In our case, since we use single earthquake and pipeline locations are same for all LDP's, no difference in P-value is observed for the regression between magnitude and RR. As for distance, the distance to the magnitude is averaged for each zone of LDP and plotted against the residuals of the RR's, due to the large number of pipelines present. The RR interval is also checked against the screening criteria given by O'Rourke et al., 2014 to obtain strong correlations between RR and LDP.

Step 4.2 Results

The following table shows the results for efficiency and sufficiency for Luco and Cornell (2002) for different LDPs considered in our study.

Table 5.15: Results of Luco & Cornell Method (2002)

LDP	R2 (RR vs LDP)	Efficiency	Sufficiency (p-value)	
	R2	Standard Deviation	Magnitude	Distance
Bradley PGA, CFC = 0.0, PL = 50%				
Settlement	0.96	0.16	1	0.86
LSN	0.016	0.63	1	0.329
LPlish	0.072	0.599	1	0.36
LPI	0.89	0.12	1	0.94
Bradley PGA, CFC = 0.2, PL = 50%				
Settlement	0.898	0.13	1	0.936
LSN	0.23	0.17	1	0.8
LPlish	0.12	0.495	1	0.42
LPI	0.94	0.11	1	0.99
Cornell PGA, CFC = 0.0, PL = 50%				
Settlement	0.916	0.156	1	0.938
LSN	0.08	0.58	1	0.2
LPlish	0.7	0.085	1	0.738
LPI	0.86	0.126	1	0.98
Cornell PGA, CFC = 0.2, PL = 50%				
Settlement	0.98	0.14	1	0.8
LSN	0.042	0.15	1	0.69
LPlish	0.1	0.22	1	0.73
LPI	0.85	0.98	1	0.75



This project has received funding from the European Union's Horizon 2020 research and innovation programme under grant agreement No. 700748

Standard deviation values for LPlish (Cornell PGA, CFC=0.0, PL=50%) are the lowest but the corresponding p-values for distance are not the lowest amongst all LDPs. LPI (Bradley PGA, CFC=0.2, PL=50%) shows low standard deviation value and p-value for sufficiency.

Step 4.2.1: RR vs LDP

For Bradley PGA, CFC= 0.0, PL= 50%

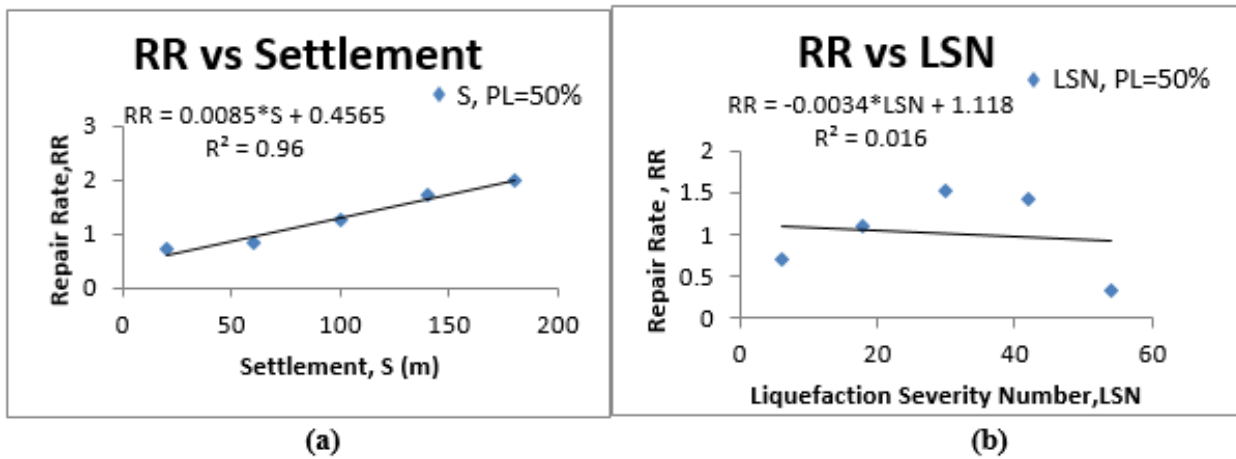


Figure 5.59: (a) RR vs Settlement, (b) RR vs LSN

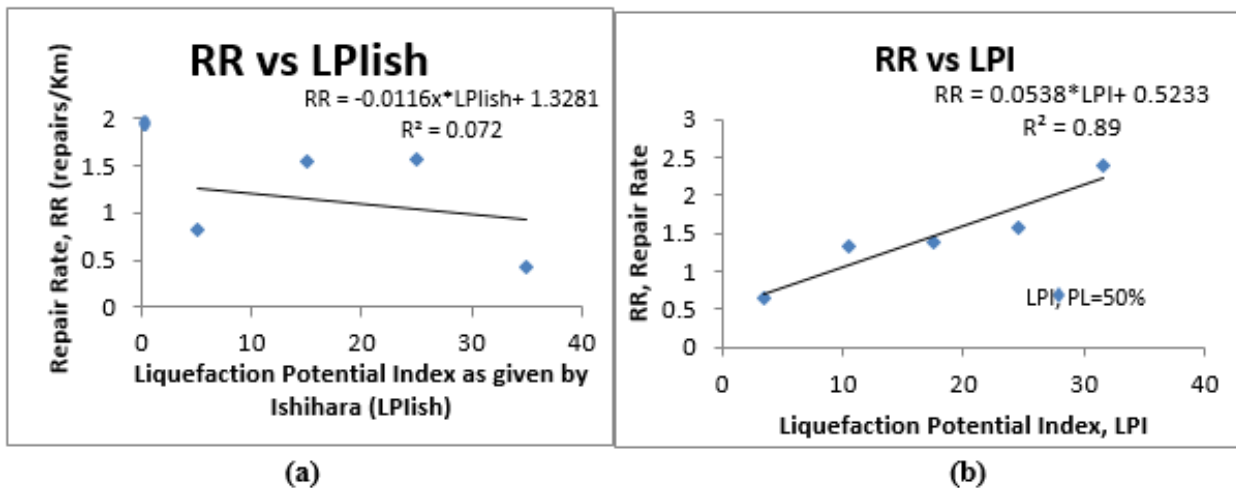


Figure 5.60: (a) RR vs LPlish, (b) RR vs LPI



This project has received funding from the European Union's Horizon 2020 research and innovation programme under grant agreement No. 700748

Bradley PGA, CFC= 0.2, PL= 50%

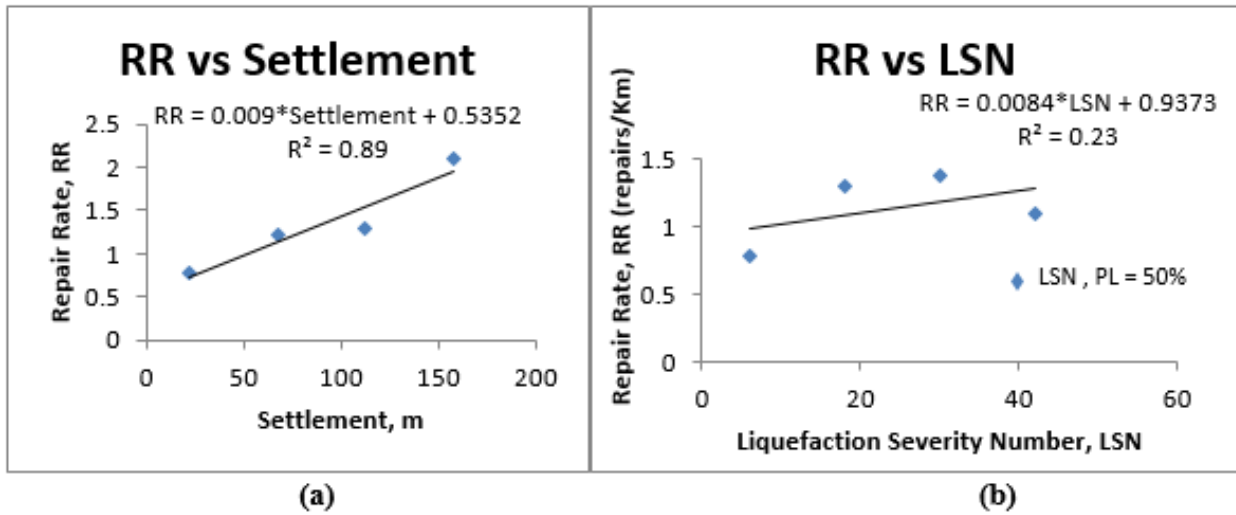


Figure 5.61: (a) RR vs Settlement, (b) RR vs LSN

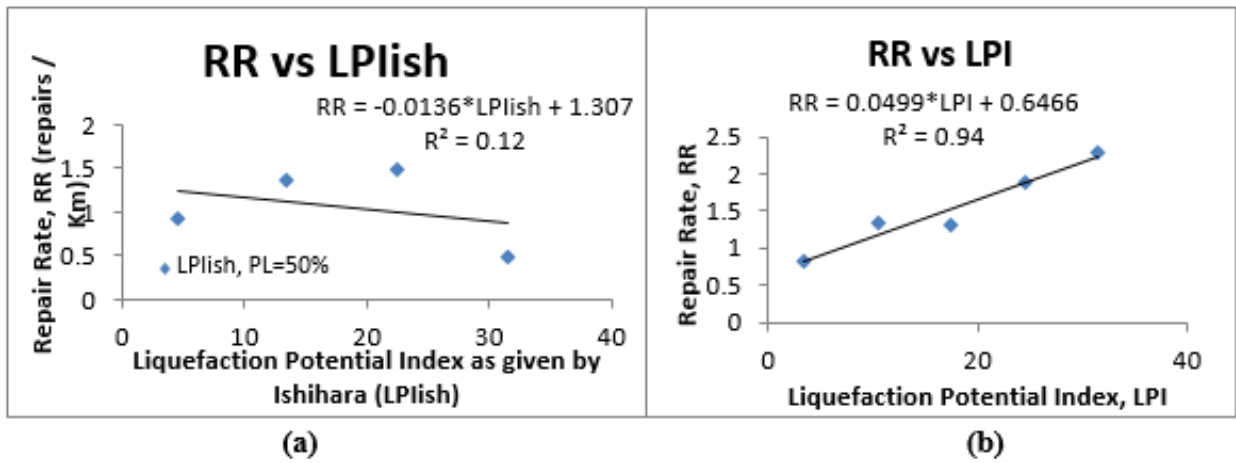


Figure 5.62: (a) RR vs LPIsh, (b) RR vs LPI



This project has received funding from the European Union's Horizon 2020 research and innovation programme under grant agreement No. 700748

Cornell PGA, CFC= 0.0, PL= 50%

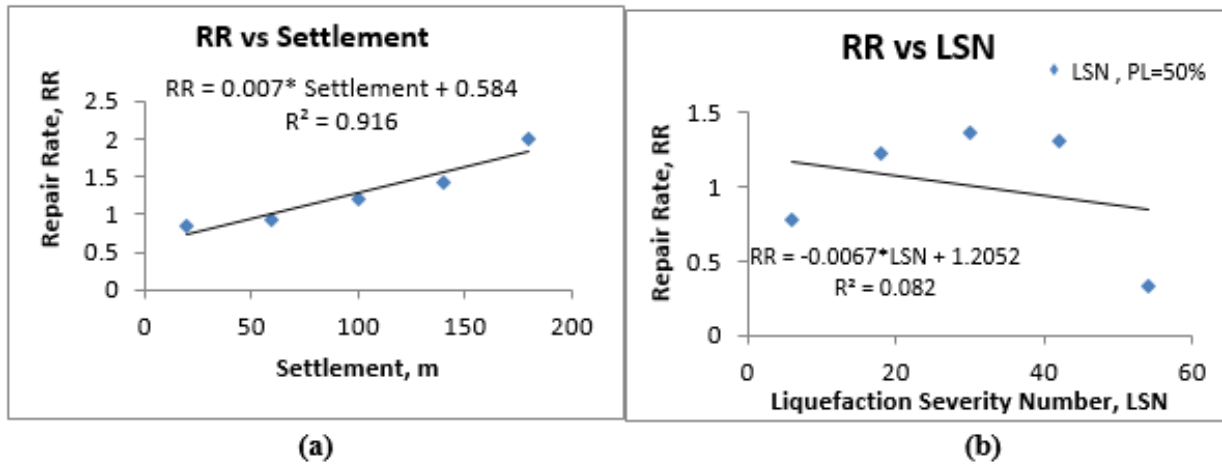


Figure 5.63: (a) RR vs Settlement, (b) RR vs LSN

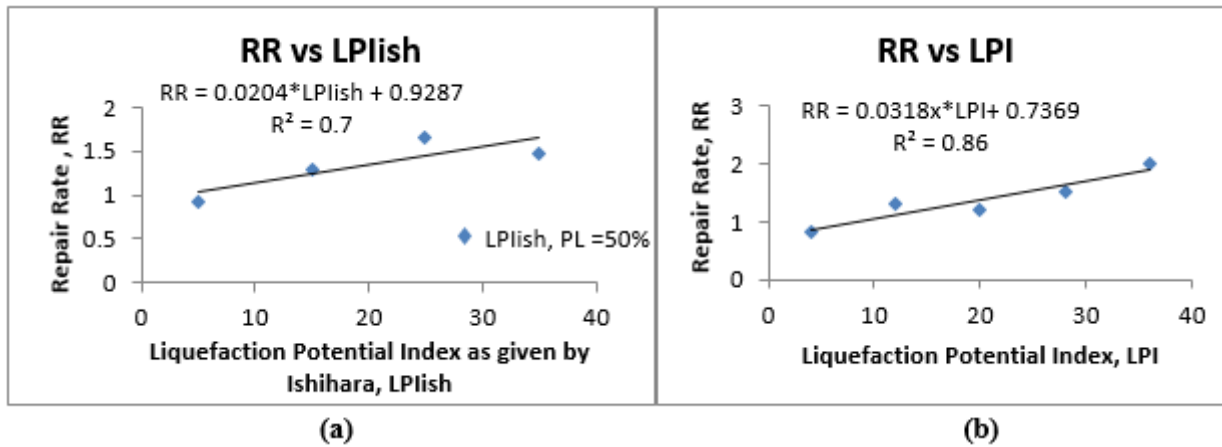


Figure 5.64: (a) RR vs LPIish, (b) RR vs LPI



This project has received funding from the European Union's Horizon 2020 research and innovation programme under grant agreement No. 700748

Cornell PGA, CFC= 0.2, PL= 50%

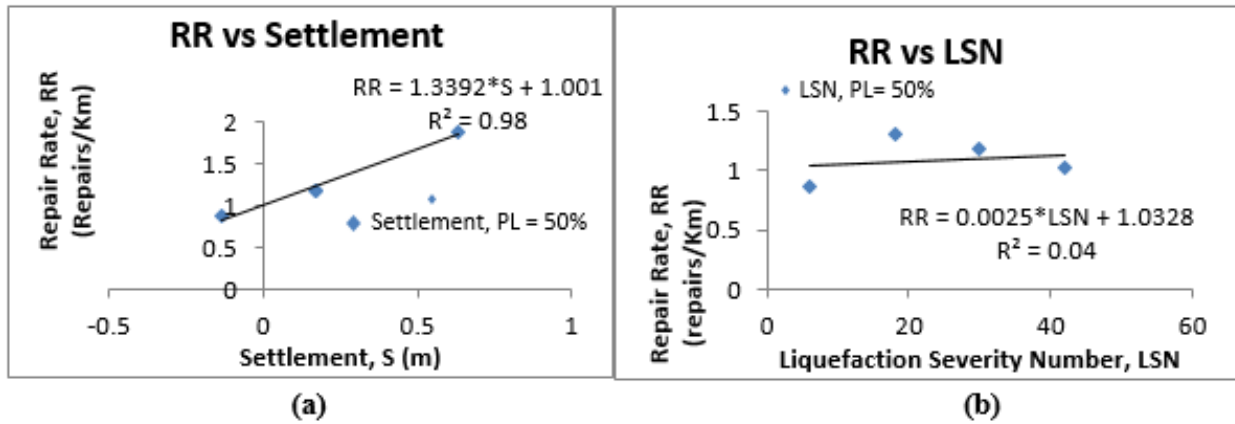


Figure 5.65: (a) RR vs Settlement, (b) RR vs LSN

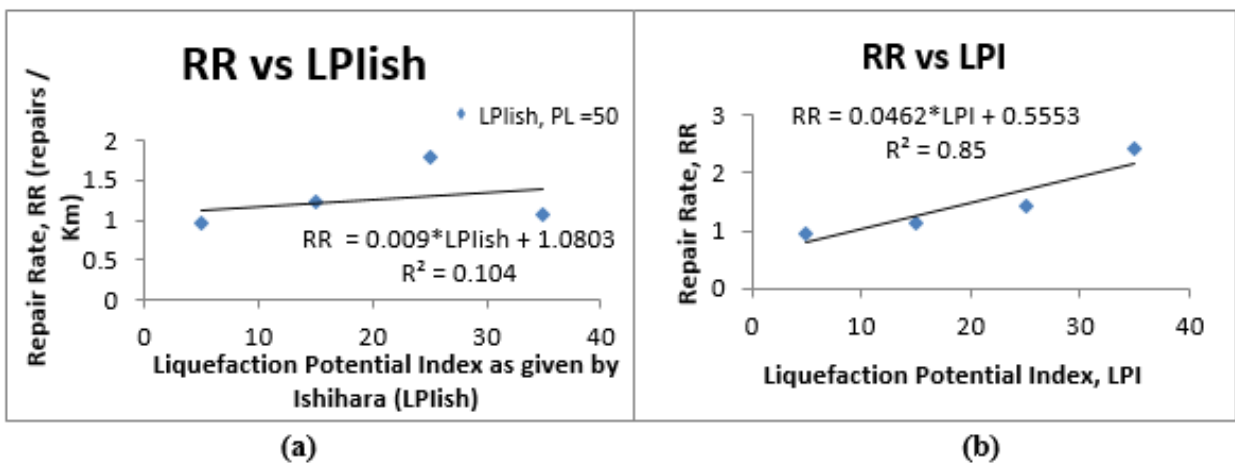


Figure 5.66: (a) RR vs LPIish, (b) RR vs LPI



This project has received funding from the European Union's Horizon 2020 research and innovation programme under grant agreement No. 700748

Step 4.2.2: Efficiency

Bradley PGA, CFC= 0.0, PL= 50%

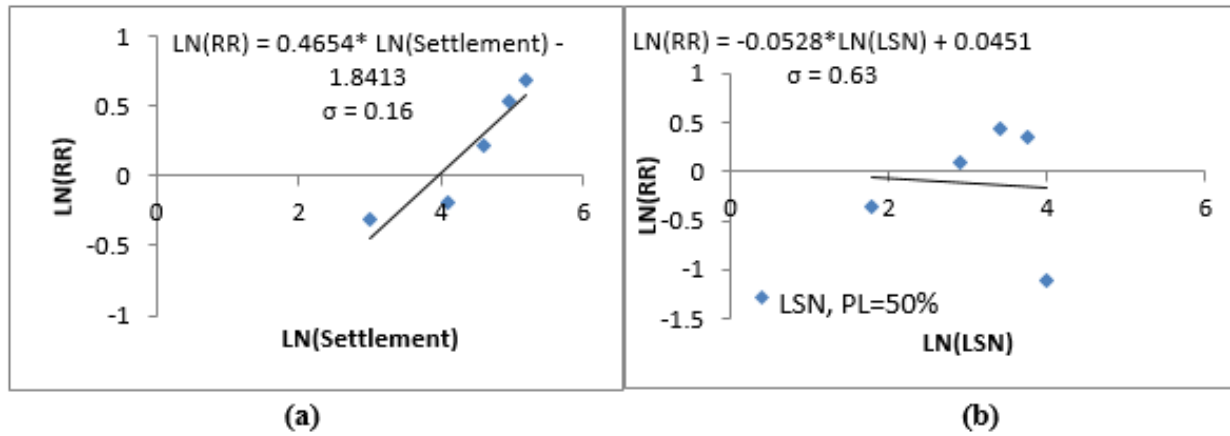


Figure 5.67: Efficiency results for (a) Settlement, (b) LSN

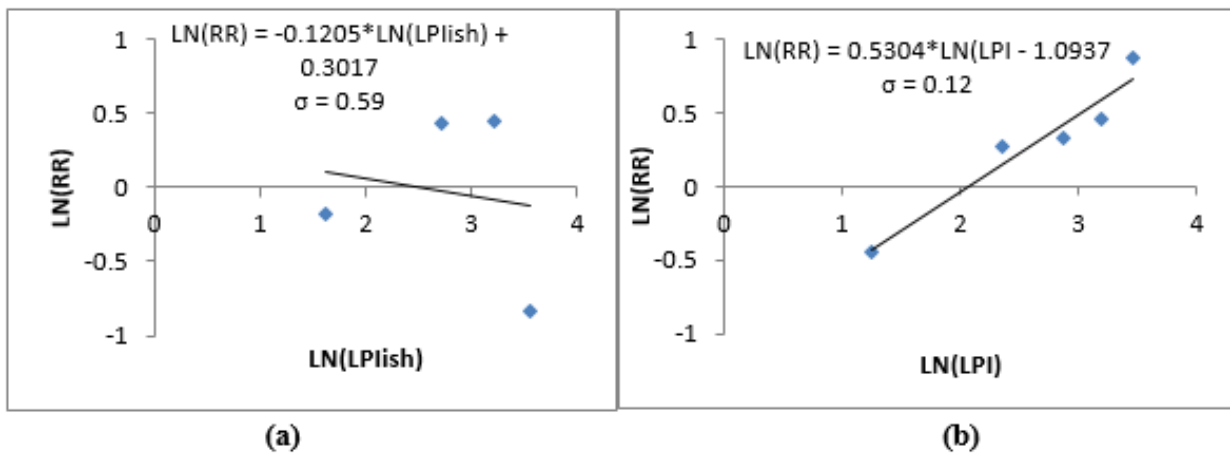


Figure 5.68: Efficiency results for (a) LPIish, (b) LPI



This project has received funding from the European Union's Horizon 2020 research and innovation programme under grant agreement No. 700748

Bradley PGA, CFC= 0.2, PL= 50%

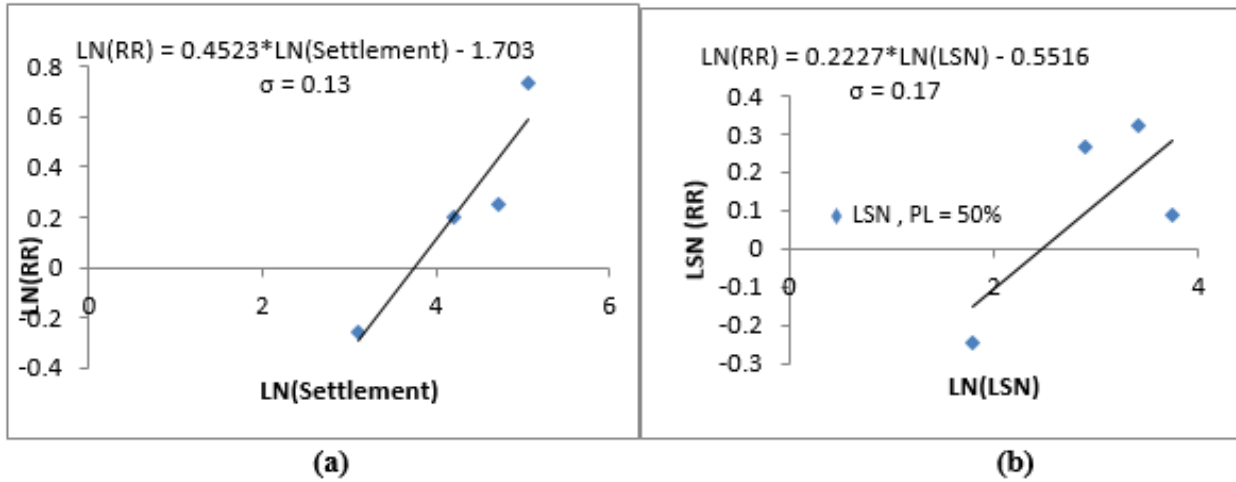


Figure 5.69: Efficiency results for (a) Settlement, (b) LSN

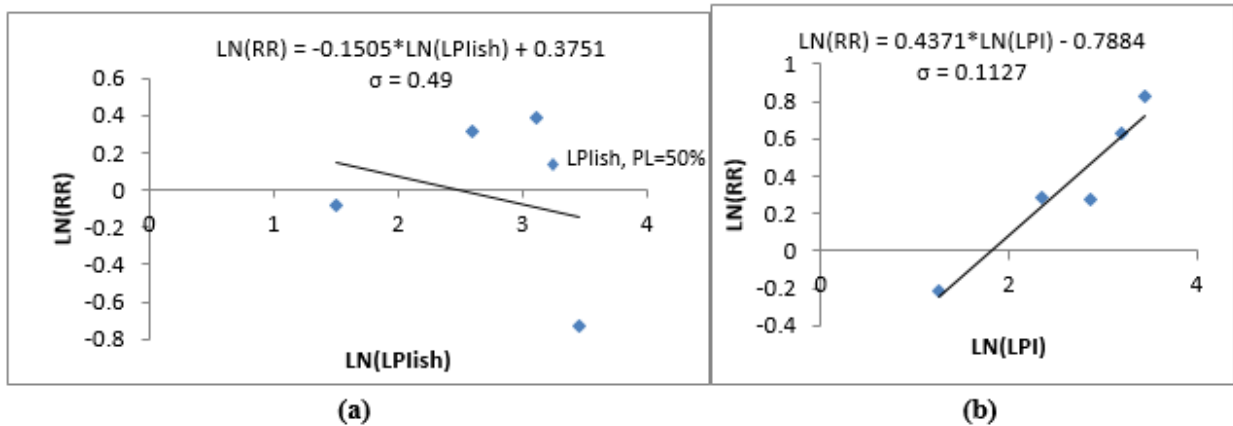


Figure 5.70: Efficiency results for (a) LPIish, (b) LPI



This project has received funding from the European Union's Horizon 2020 research and innovation programme under grant agreement No. 700748

Cornell PGA, CFC= 0.0, PL= 50%

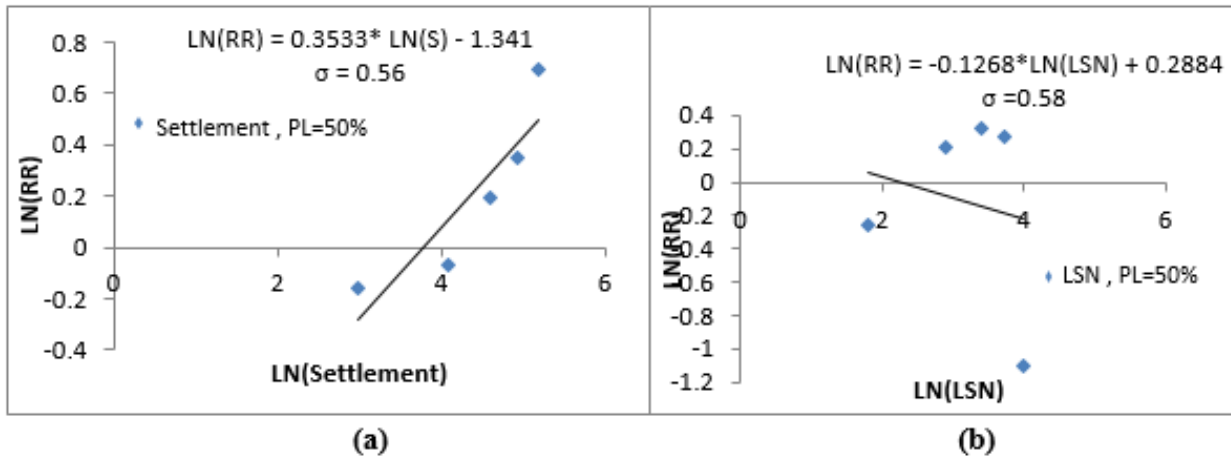


Figure 5.71: Efficiency results for (a) Settlement, (b) LSN

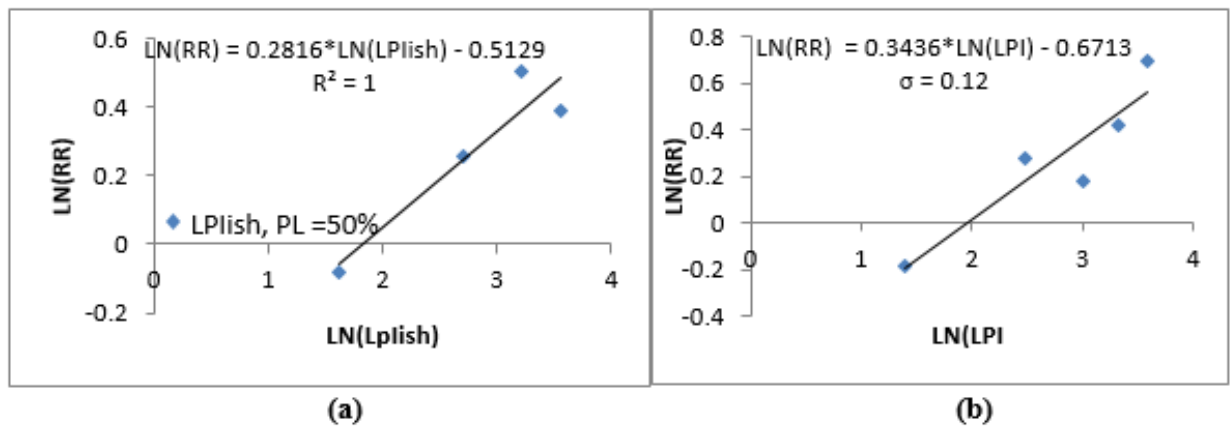


Figure 5.72: Efficiency results for (a) LPlish, (b) LPI



This project has received funding from the European Union's Horizon 2020 research and innovation programme under grant agreement No. 700748

Cornell PGA, CFC= 0.2, PL= 50%

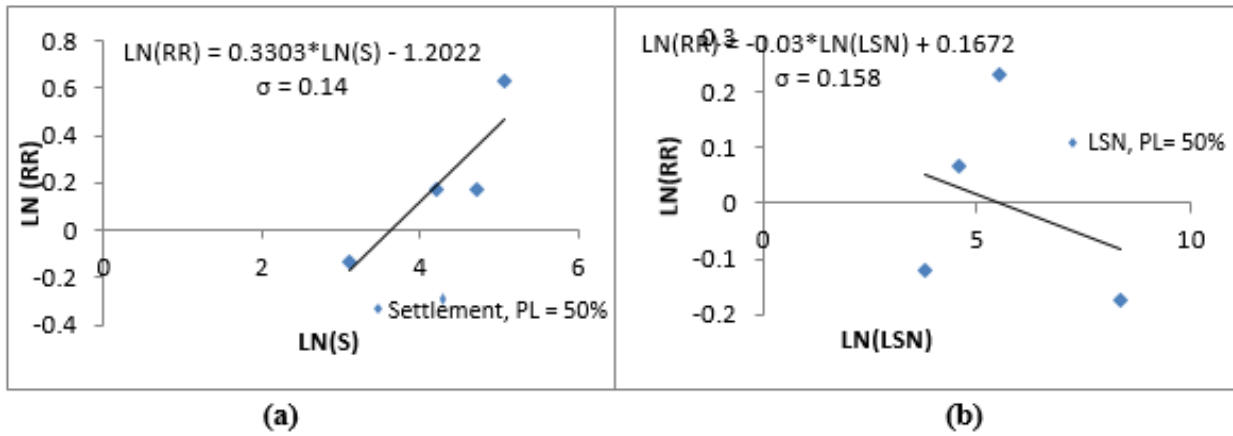


Figure 5.73: Efficiency results for (a) Settlement, (b) LSN

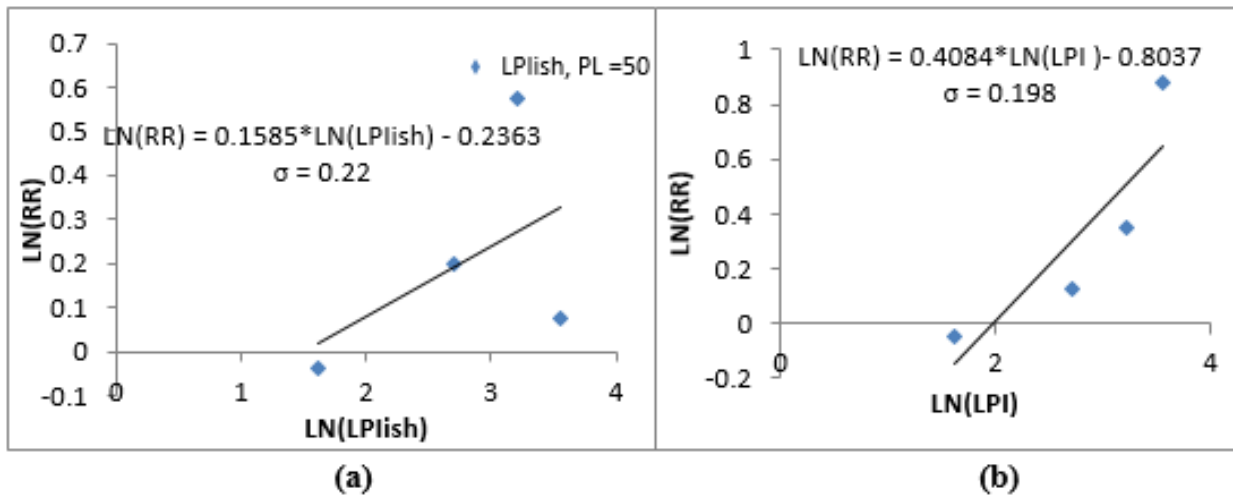


Figure 5.74: Efficiency results for (a) LPlish, (b) LPI



This project has received funding from the European Union's Horizon 2020 research and innovation programme under grant agreement No. 700748

Step 4.2.3: Sufficiency

Step 4.2.3.1: Magnitude

Bradley PGA, CFC= 0.0, PL= 50%

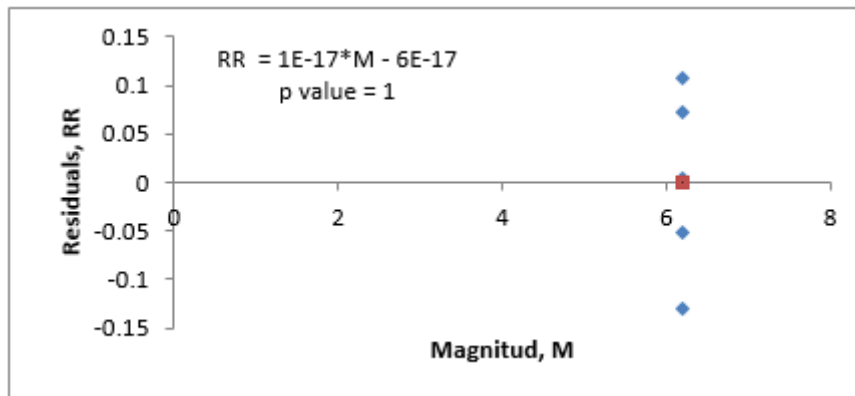


Figure 5.75: Sample Magnitude Sufficiency results for Settlement

Bradley PGA, CFC= 0.2, PL= 50%

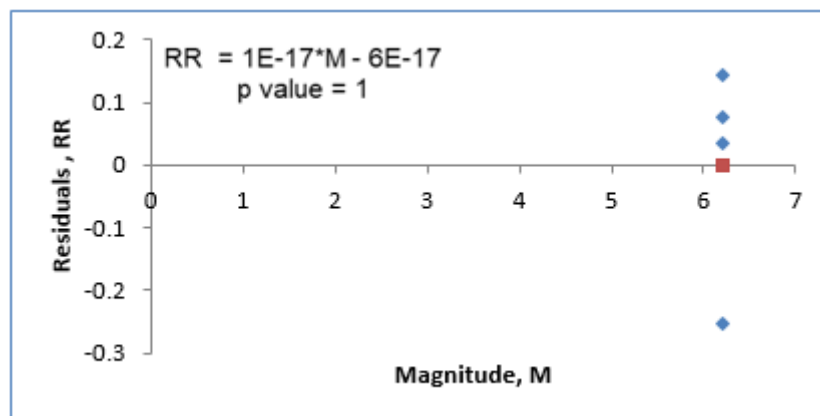


Figure 5.76: Sample Magnitude Sufficiency results for Settlement



This project has received funding from the European Union's Horizon 2020 research and innovation programme under grant agreement No. 700748

Cornell PGA, CFC= 0.0, PL= 50%

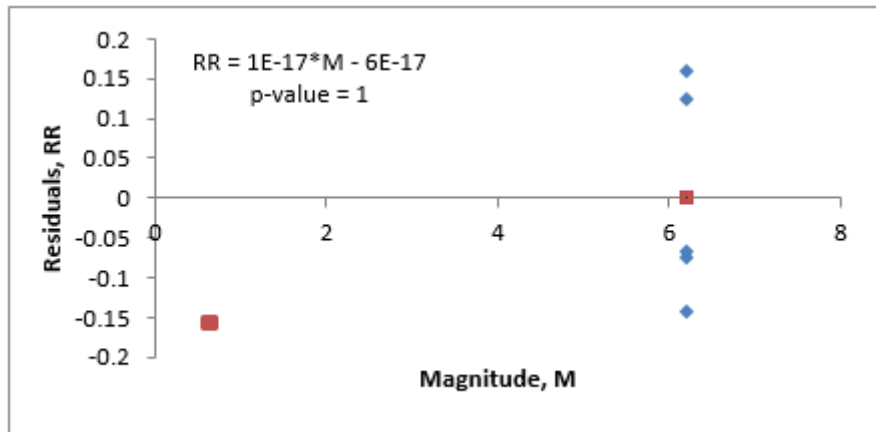


Figure 5.77: Sample Magnitude Sufficiency results for Settlement

Cornell PGA, CFC= 0.2, PL= 50%

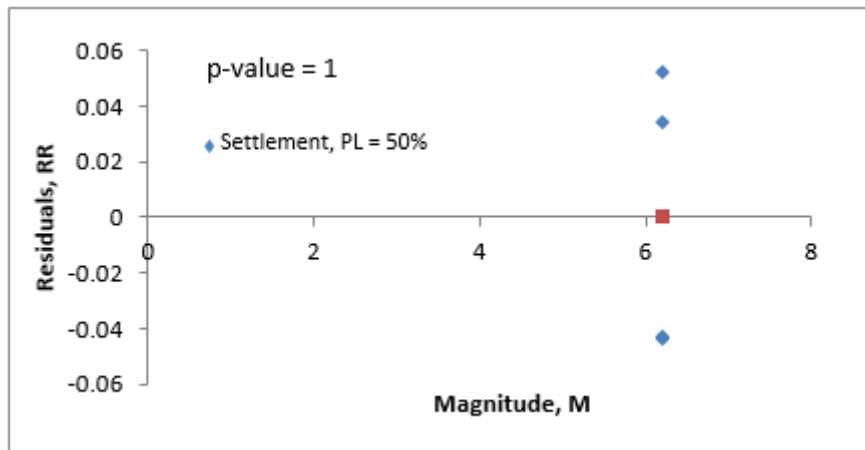


Figure 5.78: Sample Magnitude Sufficiency results for Settlement



This project has received funding from the European Union's Horizon 2020 research and innovation programme under grant agreement No. 700748

Step 4.2.3.2: Distance

Bradley PGA, CFC= 0.0, PL= 50%

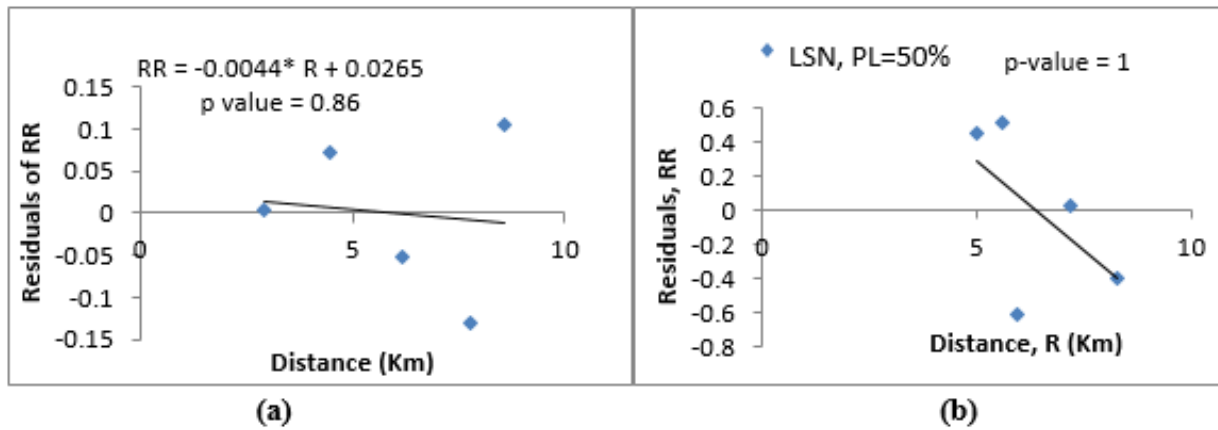


Figure 5.79: Distance Sufficiency results for (a) Settlement, (b) LSN

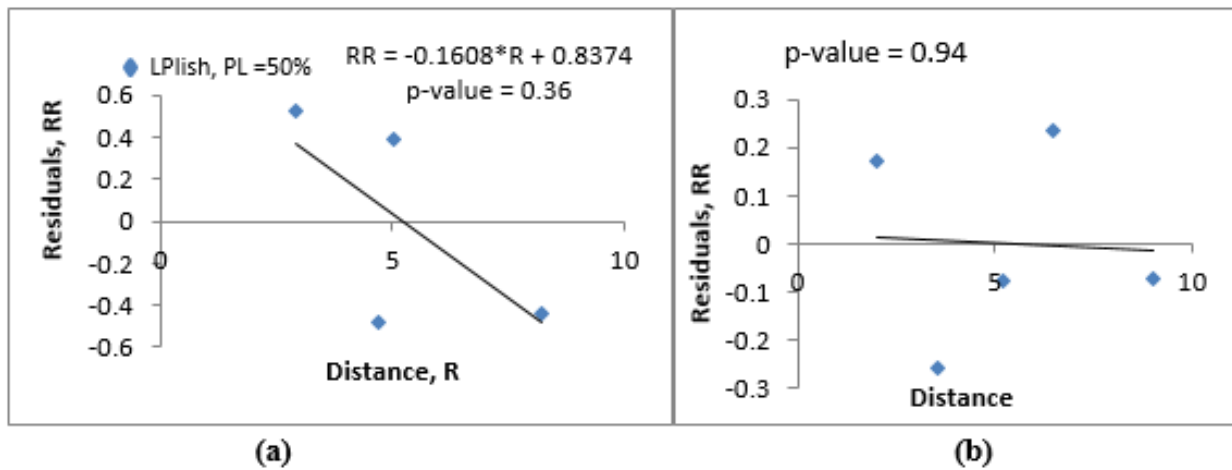


Figure 5.80: Distance Sufficiency results for (a) LPlish, (b) LPI



This project has received funding from the European Union's Horizon 2020 research and innovation programme under grant agreement No. 700748

Bradley PGA, CFC= 0.2, PL= 50%

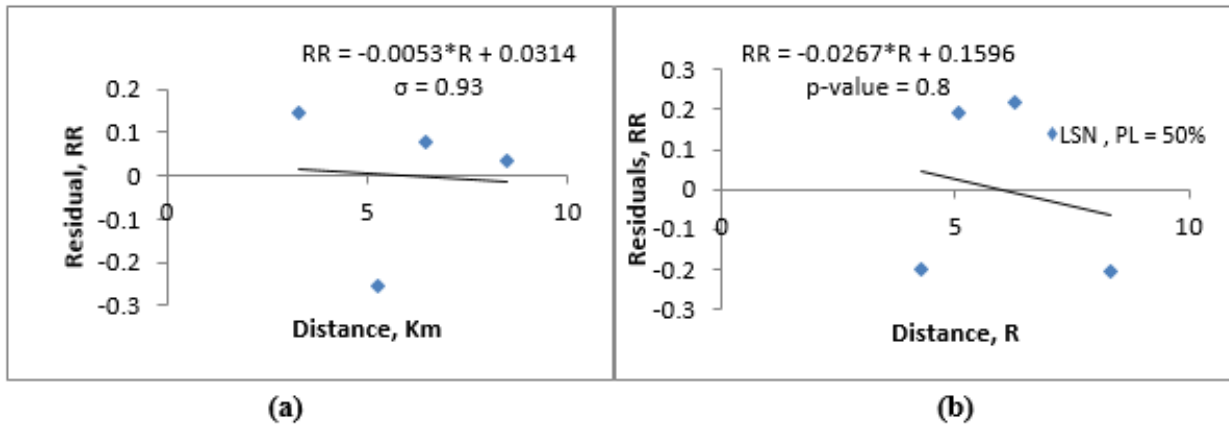


Figure 5.81: Distance Sufficiency results for (a) Settlement, (b) LSN

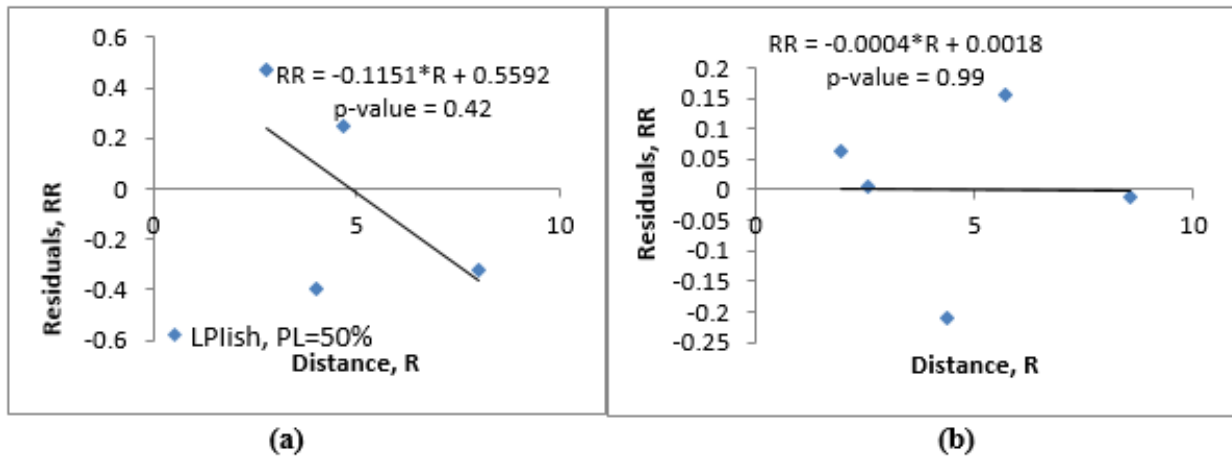


Figure 5.82: Distance Sufficiency results for (a) LPIish, (b) LPI



This project has received funding from the European Union's Horizon 2020 research and innovation programme under grant agreement No. 700748

Cornell PGA, CFC= 0.0, PL= 50%

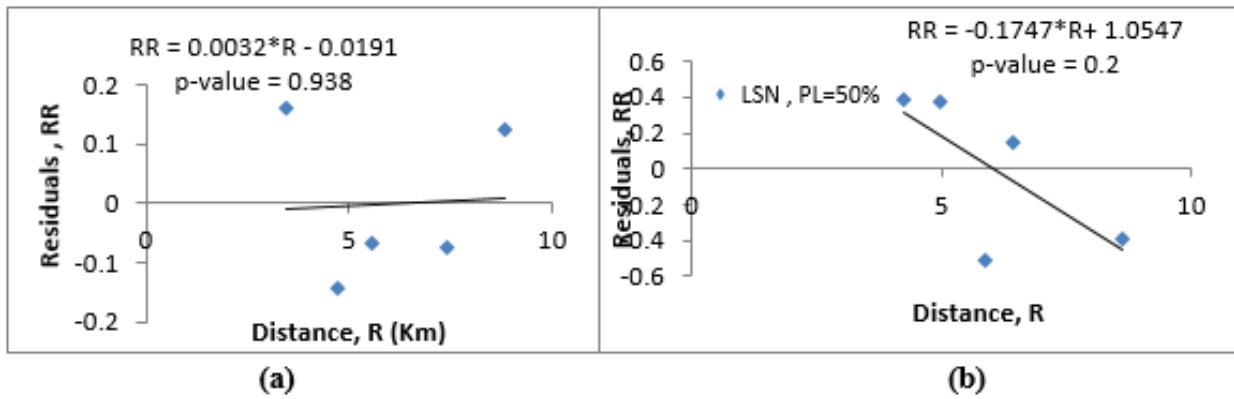


Figure 5.83: Distance Sufficiency results for (a) Settlement, (b) LSN

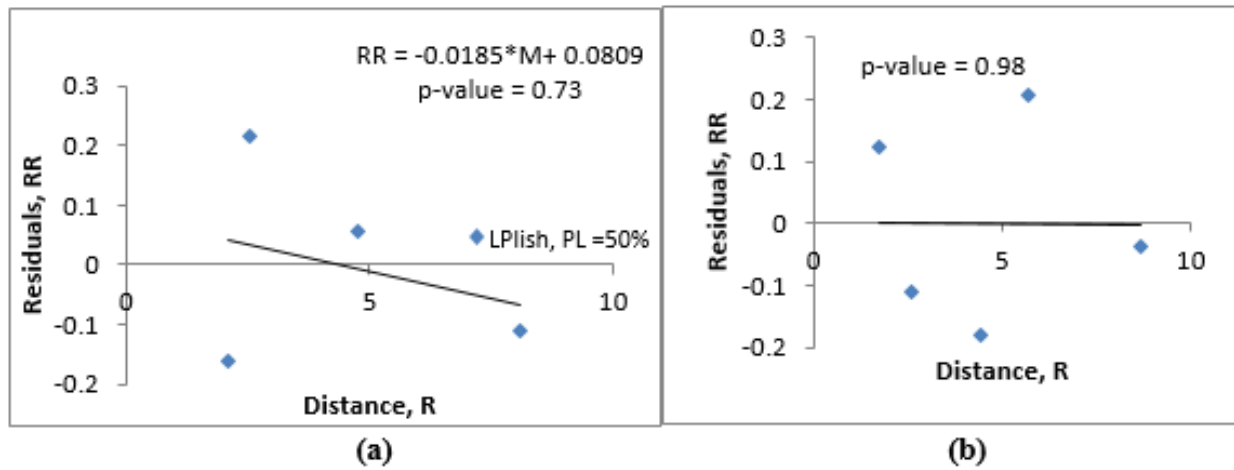


Figure 5.84: Distance Sufficiency results for (a) LPlish, (b) LPI



This project has received funding from the European Union's Horizon 2020 research and innovation programme under grant agreement No. 700748

Cornell PGA, CFC= 0.2, PL= 50%

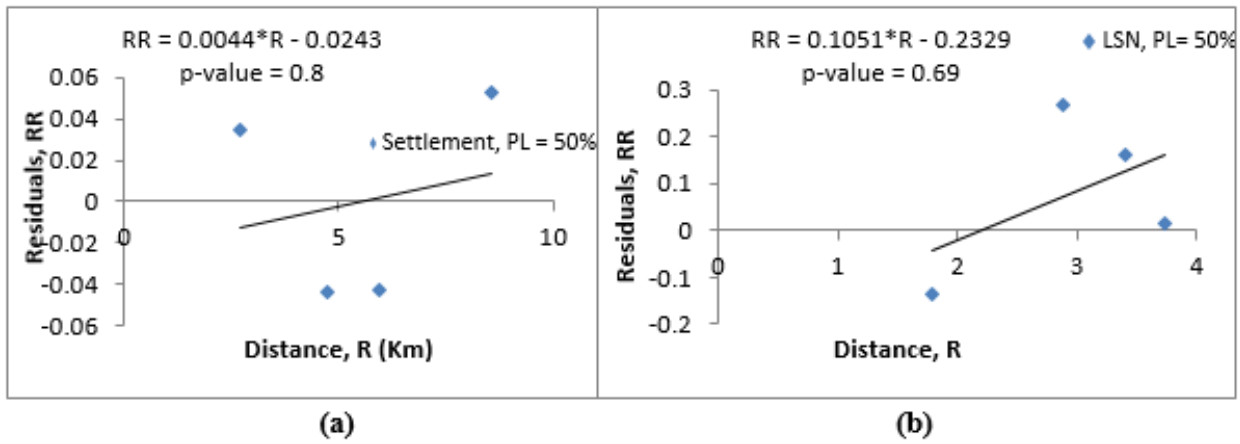


Figure 5.85: Distance Sufficiency results for (a) Settlement, (b) LSN

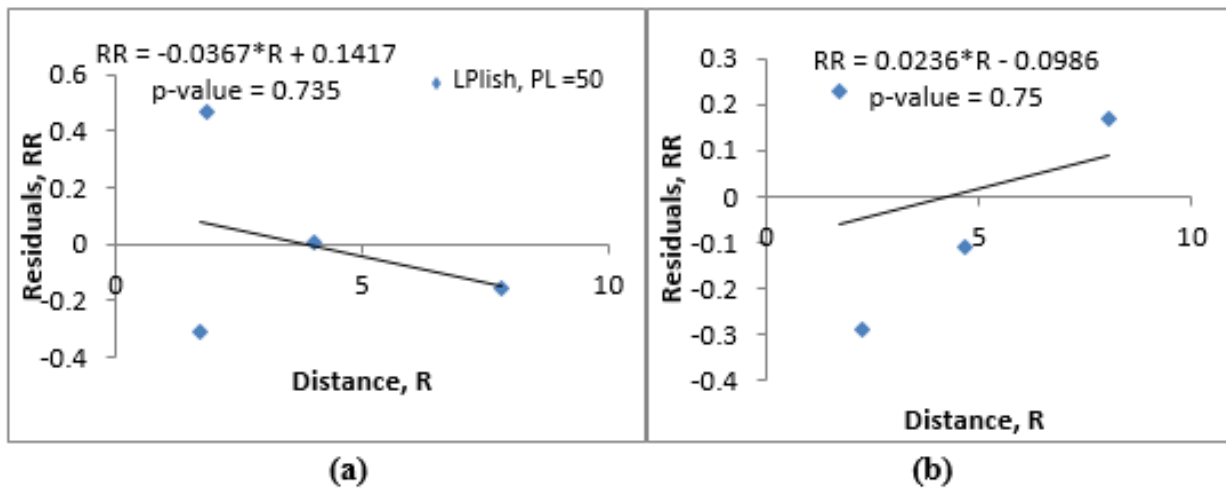


Figure 5.86: Distance Sufficiency results for (a) LPlish, (b) LPI

Step 5: Approach to derive fragility functions using by using Artificial Neural Network (ANN)

Step 5.1: Final Dataset

The LPI (Bradley PGA, $C_{FC} = 0.2$, $P_L = 50\%$) is the dataset chosen to go ahead with the statistical analysis to develop the fragility functions. Statistics of this data is shown in **Table 5.16**. The number of pipelines utilised



This project has received funding from the European Union's Horizon 2020 research and innovation programme under grant agreement No. 700748

is 113106, excluding the unknown values from the pipeline material dataset. The pipelines with 1 or more number of repairs are attributed as damaged and pipelines with no repairs as not damaged. The machine learning technique of Artificial Neural Network is correlating LPI and Damage probability.

Table 5.16: Table showing pipeline attributes.

Pipe attribute		Mean	Median	Maximum	Minimum
Pipe Length	X_{length}	26.06131	9.6	1082.5	0.1
Pipe Diameter	X_{dia}	86.50862	63	600	13
Year Pipe Laid	X_{yr}	1982.672	1988	2011	1900

Step 5.2 Artificial Neural Network

An Artificial Neural Network (ANN) can be described as a parallel, interconnected network of basic computing elements that demonstrate information processing characteristics similar to several hypothesized models of the functioning of the brain. The ANN comprises a number of connected computational elements referred to as artificial neurons, similar to that of brain neurons. The theoretical research behind neural networks can be traced back to early 1940s. Their application in civil engineering problems is illustrated in the comprehensive literature review by Adeli [26], who dates the first journal article on civil engineering applications back to 1989 [27]. Authors have also used ANNs for geotechnical engineering and earthquake engineering applications which included several references in the fields of pile capacity studies, settlement of foundations, soil properties and behavior, liquefaction, site characterization, earth retaining structures, slope stability, tunnels and underground openings (Calabrese et al., 2013).

The Neural Network Matlab tool is utilised here, with pattern recognition method. The network type used in this work is the feed-forward backpropagation model, with two layers, and its topology is depicted in Fig. 83(Calabrese et al., 2013). The hidden layer is characterized by Tan-sigmoid transfer functions, while the output layer is characterized by linear transfer functions, Fig. 9. There are 6 input nodes as follows: (i) Pipe Material, (ii) Pipe Diameter, (iii) Pipe Length, (iv) Year Pipe was laid, (v) Pipe Type, (vi) LPI values, with one output node for Pipe Damage, which is taken as a binary term, damage or no damage. The total number of pipes with damage is 1932 and pipes with no damage is 111173 nos.

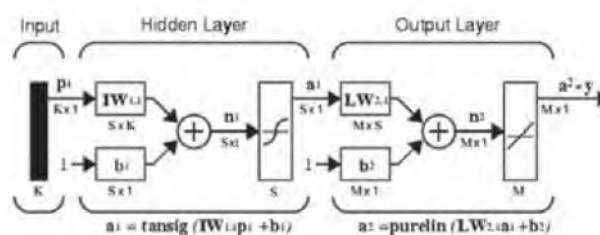


Figure 5.87: Architecture of the ANN network (Calabrese et al., 2013)



This project has received funding from the European Union's Horizon 2020 research and innovation programme under grant agreement No. 700748

To avoid overfitting, and to improve generalization, the early stopping method implemented in the MATLAB neural network toolbox was also adopted. The available data was randomly divided into three subsets. The data is divided into the training set validation set and test set. The training set is used for computing the gradient and updating the network weights and biases. The second subset is the validation set, and the prediction error on this array is monitored during the training process. The validation error normally decreases during the initial phase of training, as does the training set error. However, when the network begins overfitting the data, the error in the validation set begins to rise. The training is stopped when such validation error increases for a specific number of iterations. Consequently, the weights and biases at the minimum of the validation error are used to characterize the network. The test set error is helpful in comparing different ANNs models. It is also practical to plot the test set error during the training process. If the error in the test set reaches a minimum at a significantly different iteration number than the validation set error, this may indicate a poor division of the data set.

The LPI (Bradley PGA, $C_{FC} = 0.2$, $P_L = 50\%$) dataset is divided in the following manner, 70% of the data was used for training, 15% of the data for validation and 15% for testing. Figure – depicts the convergence of the developed network during the corresponding training cycles (also called the epochs). It is assessed by looking at the average sum squared error, whose target value is set to a relatively low value of $10E-4$. Starting from some trial values, the training process is therefore repeated from the newly updated weights and biases until the specified threshold is reached. The results for ANN are plotted in Fig. 5.88.



Figure 5.88: Confusion Matrix of the ANN model



This project has received funding from the European Union's Horizon 2020 research and innovation programme under grant agreement No. 700748

The confusion matrix does show that the results obtained for prediction of no damage in the case of validation, train or test data is exact, the same does not apply for the test data. It has predicted 2 damages correctly for the train data set and 1 each for the validation and test data. Hence, ANN model is unable to predict the damage of the pipelines very well.

5.5 CONCLUDING REMARKS

Based on the results of the analyses the following conclusions can be drawn:

1. There is a visible bias in the locations of the CPT tests and hence in the location of LDP values. The CPT's were conducted where liquefaction was observed. This bias is also visible in the RR vs LDP relationships developed, with many pipelines (with repairs) not being represented by any value of LDP.
2. The higher values of the LDPs are not repeatedly observed, which is a result of them being lost during interpolation of LDP over an area.
3. If CPT dataset was available for the areas where liquefaction was not observed on the ground surface it would reduce the bias observed and help develop stronger RR vs LDP relationships, since the repairs would not be high and LDP values would be low.
4. The trend or the correlation of the RR and LDP is highly dependent on the LDP zonation taken into consideration.
5. The bias of the CPT dataset is also represented in the standard deviation results of efficiency.
6. LPI was observed to be the most appropriate LDP for the given dataset of pipeline repairs and Liquefaction Demand Parameters (LDP).
7. Sufficiency parameter for magnitude does not have any input, hence weakening the efficiency and sufficiency approach in identifying the most appropriate LDP.
8. Sufficiency calculated with distance includes a large uncertainty, since distance was averaged over each zone of LDP and not truly reflecting reality.
9. The application of Luco & Cornell (2002, 2007) approach for empirical and large pipeline dataset is not trivial and does include large number of uncertainties.
10. Due to low number of damage data compared to the no damage data, the ANN model very well predicts the no damage, but does not do well in predicting the damage in the pipelines.
11. ANN input requires numerical values, which complicates our data, since it includes pipe material and pipe type. Other machine learning algorithms such as Boosted Regression trees, logistic regression and random forest consider text value. This may have also lead to the ANN model not predicting the damage well.



This project has received funding from the European Union's Horizon 2020 research and innovation programme under grant agreement No. 700748

12. For our analysis during Luco and Cornell (2002), it was necessary to use the repair rates to fit our empirical data to the framework of the Luco and Cornell method. And as for the machine learning analysis, the required damage parameter was suppose to be a binary, which was incorporated as 1 or more repairs as damaged pipeline and 0 repairs as no damage.
13. The CPT's were all taken at similar locations due to which the number of CPT's still remains very high after its intersection with pipeline buffer.
14. This dataset is further to be utilised in developing fragility functions with different machine learning algorithms.
15. The fragility curve developed will be validated using the September 2010 repair dataset.

Acknowledgments

The authors would like to express their deepest gratitude to Prof. Matthew Hughes and Prof. Misko Cubrinovski from the University of Canterbury (Christchurch, New Zealand) for providing the water supply pipeline data of the Christchurch Case Study.

REFERENCES

- A.K. Sherson, M. N. (2015). Seismic Performance of Underground Pipes during the Canterbury Earthquake Sequence. Sydney : Proceedings of the Tenth Pacific Conference on Earthquake Engineering Building an Earthquake Resilient Pacific 6-8 November 2015 .
- Agilent Technologies . (2000). The Fundamentals of Signal Analysis . USA: Agilent Technologies .
- Alliance, A. L. (2001). Seismic Fragility Formulations for Water Systems . Federal Emergency Management Agency (FEMA) and American Society of Civil Engineers (ASCE).
- Armando Calabrese, C. L. (2013). Fragility functions of blockwork wharves using artificial neural networks . Soil Dynamics and Earthquake Engineering , 88-102.
- Bagriacik, A., Davidson , R., Hughes, M., Bradley , B., & Cubrinovski, M. (2018). Comparison of statistical and machine learning approaches to modeling earthquake damage to water pipelines. Soil Dynamics and Earthquake Engineering , 76-88.
- Boulanger, R. W., & Idriss, I. M. (April 2014). CPT and SPT based liquefaction triggering procedures. California: Center for Geotechnical Modeling, Department of Civil Engineering and Environmental Engineering University of California Davis.
- Bradley , B., & Hughes, M. (2012b). Conditional Peak Ground Accelerations in the Canterbury Earthquakes for Conventional Liquefaction Assessment. Ministry of Business, Innovation and Employment.
- Bradley, B., & Hughes, M. (2012c). Conditional Peak Ground Accelerations in the Canterbury Earthquakes for Conventional Liquefaction Assessment: Part 2. Ministry of Business, Innovation and Employment.
- Cubrinovski, M., Hughes, M., Bradley, B., McCahon, I., McDonald, Y., Simpson, H., . . . O'Rourke, T. (December 2011). Liquefaction Impacts on Pipe Networks, Short Term Recovery Project No.6. Christchurch: University of Canterbury.
- Cubrinovski, M., Hughes, M., Bradley, B., Noonan, J., McNeill, S., English, G., & Gracia Sampedro, I. (2015). Horizontal Infrastructure Performance and Application of the Liquefaction Resistance Index Methodology in Christchurch City through the 2010-2011 Canterbury Earthquake Sequence. Christchurch: Civil & Natural Resources Engineering, University of Canterbury.



This project has received funding from the European Union's Horizon 2020 research and innovation programme under grant agreement No. 700748

Methodology for the liquefaction fragility analysis of critical structures and infrastructures: description and case studies

v. 1.0

- Cubrinovski, M., Hughes, M., Bradley, B., Noonan, J., McNeill, S., English, G., & Gracia Sampedro, I. (September 2015). Horizontal Infrastructure Performance and Application of the Liquefaction Resistance Index Methodology in Christchurch City through the 2010-2011 Canterbury Earthquake Sequence. Christchurch: Civil & Natural Resources Engineering, University of Canterbury.
- Cubrinovski, M., Hughes, M., Bradley, B., Noonan, J., McNeill, S., English, G., & Hopkins, R. (March 2014). Performance of Horizontal Infrastructure in Christchurch City through the 2010-2011 Canterbury Earthquake Sequence. Christchurch: Civil & Natural Resources Engineering, University of Canterbury.
- D. Bouziou, T. O. (2017). Response of the Christchurch water distribution system to the 22nd Feb 2011 earthquake. 97. Earthquake Commission, C. C. (2018, November). <https://www.nzgd.org.nz/>. Retrieved from <https://www.nzgd.org.nz/>: <https://www.nzgd.org.nz/>
- Eguchi, R. T. (1991). Seismic Hazard Input for Lifeline Systems. 10.
- Eidinger, J. (1998). Water Distribution System .
- Esposito, S. (2011). Systemic Seismic Risk Analysis of Gas Distribution Networks . Naples.
- G. Lanzano, E. S. (2013). Seismic vulnerability of gas and liquid buried pipelines.
- Giovanni Lanzano, E. S. (2013). Seismic Vulnerability of natural gas pipelines . Reliability Engineering and System Safety , 73-80.
- Hamzeh Shakib, V. J. (2016). Intensity measures for the assessment of the seismic response of buried steel pipelines. 14(4).
- Iwasaki, T., Tatsuoka, F., & Yasyda, S. (1978). A practical method for assessing soil liquefaction potential based on case studies at various sites in Japan. 2nd Int. Conf. on Microzonation, (pp. 885-896). San Francisco .
- K. Pitilakis, H. C. (2014). SYNER-G: Typology Definition and Fragility Functions for Physical Elements at Seismic Risk . Springer .
- Kameda, H. (2000). Engineering Management of Lifeline Systems under Earthquake Risk . 12WCEE .
- Lacrosse, V., Ballegooy van, S., & Bradley, B. A. (2015). Effect of Liquefaction Triggering Uncertainty on Liquefaction Consequence. 6th International Conference on Earthquake Geotechnical Engineering . Christchurch.
- Liu, T. O. (1999). Response of buried pipelines subject to earthquake effects. Multidisciplinary Centre for Earthquake Engineering Research .
- Luco, N., Mai, P. M., Cornell, C. A., & Beroza, G. C. (2002). Probabilistic Seismic Demand Analysis at a Near-Fault Site using ground motion simulations based on stochastic-kinematic earthquake source model. 7th U.S National Conference on Earthquake Engineering .
- Luco, N., & Cornell, A. (2007). Structure-Specific Scalar Intensity Measures for Near Source and Ordinary Earthquake Ground Motions. Earthquake Spectra, 23(2), 357-392.
- Milashuk, M. (2012). Acceleration records from selected aftershocks, pers.comm.
- NIBS. (2004). HAZUS-MH. Washington, D.C.: Federal Emergency Management Agency .
- Omar Pineda-Porras, M. N. (2010). Seismic Damage Estimation for Buried Pipelines: Challenges after Three Decades of Progress. 1(1).
- Paultre, P. (2011). Dynamics Of Structures . USA: John Wiley & Sons, Inc.
- Pitilakis, K., & Argyroudis, S. (2014). Seismic Vulnerability Assessment: Lifelines. Encyclopedia of Earthquake Engineering .
- Quigley, M. C., Bastin, S., & Bradley, B. (2013). Recurrent liquefaction in Christchurch, New Zealand, during the Canterbury Earthquake Sequence. Geology, 41, 419-422. doi:10.1130/G33944.1



This project has received funding from the European Union's Horizon 2020 research and innovation programme under grant agreement No. 700748

- R. Ioyama, E. I. (2000). Seismic Damage Estimation Procedures for Water Supply Pipelines. 12WCEE.
- Roberta Piccinelli, E. K. (2013). Analysis of natech risk for pipelines: A review. JRC Scientific and Policy Reports.
- S. Toprak, E. N. (2015). Seismic Damage Probabilities for Segmented Buried Pipelines in Liquefied Soils. Christchurch: 6th International Conference on Earthquake Geotechnical Engineering .
- S. Toprak, E. N. (2017). Pipeline Damage Predictions in Liquefaction Zones using LSN . Santiago, Chile : 16th World Conference on Earthquake, 16WCEE 2017 .
- S. Toprak, E. N. (2018). Comparison of Horizontal ground displacements in Avonside area, Christchurch from air photo, LiDAR and satellite measurements regarding pipeline damage assessment.
- S. Toprak, E. N.-S. (2014). Pipeline Damage Assessment using Horizontal Displacements from Air Photo and LiDAR Measurements in Avonside Area, Christchurch, NZ. Istanbul : Second European Conference on Earthquake Engineering and Seismology, Aug 25-29, 2014 .
- Simona Esposito, I. I. (2015). Simulation-Based Seismic Risk Assessment of Gas Distribution Networks. Computer-Aided Civil and Infrastructure Engineering, 508-523.
- SYNER-G. (2011). D2.4 - Definition of system components and the formulation of system functions to evaluate the performance of gas and oil pipeline . AMRA.
- SYNER-G. (2013). D8.10 - Guidelines for deriving seismic fragility functions of elements at risk: Buildings, lifelines, transportation networks and critical facilities. Joint Research Centre.
- T. O'Rourke, S. T.-S. (1998). GIS Characterization of the Los Angeles Water Supply, Earthquake Effects, and Pipeline Damage . New York: Research Progress and accomplishments:1997-1999.
- T. O'Rourke, S.-S. J. (2012). Underground Lifelines System Performance during the Canterbury Earthquake Sequence . Lisbon: 15WCEE.
- T. O'Rourke, S.-S. J. (2014). Earthquake Response of Underground Pipeline Networks in Christchurch, NZ . 30(1).
- T. O'Rourke, T. V.-L. (2018). Influence of diameter on seismic response of buried segmented pipelines . (107).
- Taylor, T. &. (2013). Liquefaction Vulnerability Study. Christchurch: Tonkin & Taylor Ltd.
- V. Terzi, M. A. (2006). Vulnerability Assessment for pipelines under Permanent Ground Deformations. Comparison between analytical and empirical approach. . Lisbon: III European Conference on Computational Mechanics Solids, Structures and Coupled Problems in Engineering.
- V. Terzi, M. A. (2007). Numerical Assessment of Damage State of Segmented Pipelines due to Permanent Ground Deformation.
- van Ballegooy, S., Malan, P., Lacrosse, V., Jacka, M. E., Cubrinovski, M., Bray, J. D., . . . Cowan, H. (2014). Assessment of Liquefaction-Induced Land Damage for Residential Christchurch. Earthquake Spectra, 30, 31-55.
- Yamazaki, Y. M. (2010). Construction of fragility curve for water distribution pipes based on damage datasets from recent earthquakes in Japan. Toronto: Proceedings of the 9th U.S National and 10th Canadian Conference on Earthquake Engineering .



This project has received funding from the European Union's Horizon 2020 research and innovation programme under grant agreement No. 700748

6. FINAL REMARKS

This report provided an overview of an efficient probabilistic numerical procedure for the simulation of liquefaction-induced damage and fragility analysis of some critical structures and infrastructures. Improved numerical modelling strategies were proposed to simulate liquefaction-induced structural damage and uncertain/random factors with relevant effects on the behaviour of liquefiable soils and of interacting structure-soil systems.

Essential aspects related to the definition of exposure models in a situation where liquefaction effects may be relevant were discussed and a new hazard independent liquefaction susceptibility classification system was developed using equivalent soil profiles. A methodology for obtaining a simplified equivalent three-layered soil profile based on the liquefaction assessment of a soil profile from CPT data was developed. The equivalent soil profile (ESP) is defined as a soil profile classification tool for the purpose of the seismic response of shallow-founded buildings in liquefied soils. This methodology uses three governing parameters: the depth of the crust (D_{liq}), the thickness of the liquefied layer (H_{liq}) and its shear strength (CRR_{n15}). 22 different soil profile classes were derived and tested in two case-studies.

A macro-mechanism sub-structuring approach was used for modelling shallow foundation buildings on liquefiable deposits. The approach included the quantification of liquefaction potential of the soil profile in terms of depth and thickness of the liquefiable layer(s) and the resistance to liquefaction, an estimation of the expected level of surface shaking considering the dynamic site response, approximated the soil foundation stiffness using springs and dashpots to account for the change in soil characteristics due to liquefaction and nonlinear shear deformation and estimating the expected load-settlement behaviour of each footing accounting for the build-up of pore pressure. This developed procedure offers a numerical efficient approach for vulnerability assessment.

A procedure for modelling pore pressure, site response and settlement using effective stress analysis with FLAC and PM4Sand was presented and validated against centrifuge tests. Settlement results are in relatively close agreement with the centrifuge test for both experiments and ground motions.

Three simplified methods for the estimation of excess pore pressure were assessed, including a newly developed strain-energy based procedure (Millen et al., 2019) and a stress-based cycle counting procedure. The third procedure considered a dissipated energy method but was shown to have large variation in the capacity with changes in the liquefaction criteria and a lack of formal validation of the complete method, and therefore was not recommended for further use.

Karamitros et al. (2013) and Bray and Macedo (2017) methodologies, provided viable options for efficiently assessing the total dynamic settlement of a building compared with nonlinear effective stress numerical calculations results. The first method showed a good fit with FLAC estimation when the excess pore pressure ratio was calculated with the strain-energy based method excess pore pressure method, while Bray and Macedo (2017) requires to perform a liquefaction triggering assessment, and calculate the safety factor against liquefaction triggering (FS_L).



This project has received funding from the European Union's Horizon 2020 research and innovation programme under grant agreement No. 700748

A simplified procedure called the Stockwell transfer function method was developed to estimate surface ground motion considering the triggering of liquefaction without using a constitutive model. A new cumulative energy-based spectrum was developed to validate the new method against one-dimension nonlinear effective stress analyses. The Stockwell transform method provides a numerical efficient and conceptually simple tool to evaluate the influence the time of liquefaction on the surface motion.

A case-study was used to demonstrate the vulnerability assessment procedure using the macro-mechanism approach. 500 analyses were considered that assessed different soil profile classifications, pore pressure build models, surface acceleration models, settlement models, load-redistribution models, and uncertainties in the ground water level and building material properties. The results were evaluated against six ground motion intensity measures, three measures of peak energy (peak ground acceleration, spectral acceleration at the effective period, average spectral acceleration over a range of periods) and three measures of cumulative energy (cumulative absolute velocity, Arias intensity, unit kinetic energy). The average spectral acceleration or PGA provide the best correlations for peak inter-storey drift and CAV provides the best correlation to tilt. Fragility curves were developed for peak and residual inter-storey drift, foundation tilt, and collapse, for all six intensity measures.

A method for Rapid Risk Identification (RRI) of soil liquefaction and structural damage was introduced, to assess the seismic risk of soil-structure configuration with consideration of soil liquefaction, and to make risk-informed decision, if detailed studies of soil liquefaction are necessary or the issue of soil liquefaction can be disregarded for the investigated case.

An extensive study of the earthquake-liquefaction-induced deformations of traffic embankments was conducted within this work. Numerical analyses were carried out with 2D finite difference code FLAC, using the PM4Sand constitutive model to simulate liquefiable soil behaviour during a seismic event. Fragility curves were prepared for road and railway embankments based on SYNER-G criteria (SYNER-G, 2013), taking into account some model parameters (crest width, embankment height, thickness of liquefiable layer, presence of crust layer and relative density of sandy layer). The presented fragility curves were mostly developed for permanent vertical ground displacement in the middle point of embankment crest as the damage parameter, and PGA at bedrock (alternatively to Arias intensity) for intensity measure. A feasibility study on the prediction of vertical displacement and fragility curves using artificial neural network was performed. Two case-studies in Adapazari, Turkey, allowed to validate the developed fragility curves for traffic embankments to used be for vulnerability assessment of traffic infrastructure on liquefiable ground.

In order to derive a relationship between the structural damage of masonry buildings and soil liquefaction, an empirically based study focused on the effects of liquefaction on structures from the data of about 1,000 private residential masonry buildings located in several municipalities struck by the 2012 Emilia earthquake was presented.

A methodology to develop empirical fragility curves for pipelines was developed built upon a framework provided by Bagriacik et al., (2018) which says pipeline damage is an interaction of earthquake hazard, pipeline exposure and pipeline vulnerability. In the study presented here, earthquake hazard includes Liquefaction Demand Parameters (LDP, synonym for intensity measure for this study). LDPs are permanent



This project has received funding from the European Union's Horizon 2020 research and innovation programme under grant agreement No. 700748

ground deformations (PGD) or measures of liquefaction severity given by settlement, LSN, LPI, LPIsh, which require ground motion, liquefaction susceptibility and groundwater depth data for its computation. These fragility models were calibrated by the extensive data available from the Christchurch Water Supply Network Database.

6.1 NOTES OF ONGOING AND EMERGING STUDIES

Key factors have been neglected in existing empirical procedures to estimate settlement based on free-field conditions (e.g. Tokimatsu & Seed, 1987; Ishihara & Yoshimine, 1992) or in more recent methods that account for the presence of structures, but consider these only as a surcharge load, taking the dimension ratios as an input factor, like the ratio between the foundation width and the thickness of the liquefiable layer (e.g. Liu & Dobry, 1997). Although these last procedures can be adapted to some infrastructures like embankments, levees or pipelines, they have proved to give inaccurate settlement (vertical or lateral spreading, or tilting) predictions near buildings when compared with well documented case histories and physical model studies to yield (e.g. Dashti et al., 2010a, 2010b; Bertalot et al., 2013; Bray et al., 2014).

Probabilistic empirical procedures to estimate reconsolidation volumetric settlements in the free field and evaluate liquefaction triggering potential and subsequent settlement and tilt under structures were proposed (Cetin et al. 2009, 2012) but failed to consider the contribution of various settlement mechanisms and ground motion characteristics (e.g. frequency content and duration) on the building settlement. Similarly, the proposal of recently published works (Bullock et al. 2018), in this project – as described in this deliverable - these mechanisms are taken as important and determinant for the proposed mechanism approach. The non-efficiency or sufficiency of the cyclic stress ratio intensity measure (IM) as a predictor for foundation settlement was taken into account by incorporating energy base pore-pressure time series and the deviatoric deformations based on two-dimensional (2D) numerical analyses.

Without requiring an initial liquefaction triggering analysis (e.g. Youd et al., 2001; Boulanger & Idriss, 2014), it implements automatically a soil softening and likelihood of triggering (even in the absence of full liquefaction) in the underlying susceptible soil layers below the foundation in a clear integrated Soil-Liquefaction-Foundation-Structure Interaction (SLFSI) that are not considered in traditional procedures. The extent and influence of softening (even in the absence of full liquefaction) in the underlying susceptible soil layers are automatically included in the proposed model.

However, it did not included other important factors like tilt and the inertial effects of the structure. The shallow-founded building dynamic properties that control inertial interaction, such as mass, stiffness and height, can influence pore pressure generation and, hence, a building's settlement and particularly tilt potential (e.g. Sancio et al., 2004; Dashti et al., 2010a, 2010b; Olarte et al., 2017).

Some factors are also considered to be determinant in inducing extra damage factors (Karimi et al. 2018, Bullock et al. 2018), like: (i) length/ width ratio (L/B) of the area ($A = B \times L$), for a specific width (B); and, (ii) spatial distribution of liquefiable layers. Meanwhile others, can be important in low intensity shaking, like foundation embedment depth; or, in high intensity shaking, such as low permeability the (silty) cap/crust.



This project has received funding from the European Union's Horizon 2020 research and innovation programme under grant agreement No. 700748

These factors will be incorporated in future works, as to incorporate impact measures, like intolerable settlements or tilting, in the serviceability of buildings, additionally to structural damages themselves.

The probabilistic numerical model used in this project was calibrated for the dynamic settlement using centrifuge experiments, so there is a need to adjust the results to correct for sedimentation and ejecta effects that were not effectively captured by the numerical models. In fact, it is obligatory to combine the predictions of this model with estimates of volumetric and shear-type deformations, incorporating sedimentation or ejecta components in order to cope for the total settlements observed in structures affected by well documented case-histories.

Bray and Macedo (2017) reinforce the idea that while volumetric-induced free-field ground deformation may be estimated with available empirical procedures, nonlinear dynamic soil-structure interaction (SSI) effective stress analyses are required to estimate shear-induced ground deformation (the authors propose a specific formulation for this). These continuum analyses do not capture ejecta-induced building settlement, although this can be significant. This can roughly be estimated by ground failure indices and case-histories experience. The authors report values up to 50% of settlement due to sediment ejecta surrounding the edges of the buildings in Christchurch, during the Darfield 2011 events, while in Adapazari – for the Kocaeli 1999 earthquake - about half of the measured settlement was due to sediment ejecta and half due to shear-induced settlement.

REFERENCES

- Bagriacik, A., Davidson, R., Hughes, M., Bradley, B., & Cubrinovski, M. (2018). Comparison of statistical and machine learning approaches to modeling earthquake damage to water pipelines. *Soil Dynamics and Earthquake Engineering*, 76-88.
- Bertalot, D. & Brennan, A. J. (2015). Influence of initial stress distribution on liquefaction-induced settlement of shallow foundations. *Géotechnique*, 65 (5), 418–428. DOI: 10.1680/geot.SIP.15.P.002.
- Boulanger, R.W. & Idriss, I.M. (2014). CPT and SPT based liquefaction triggering procedures. Report No. UCD/CGM-14/01. Center for Geotechnical Modeling, University of California, Davis. 134 pp. Retrieved from http://nees.ucdavis.edu/publications/Boulanger_Idriss_CPT_and_SPT_Liq_triggering_CGM-14-01_2014.pdf
- Bray, J., Cubrinovski, M., Zupan, J. & Taylor, M. (2014). Liquefaction effects on buildings in the central business district of Christchurch. *Earthquake Spectra* 30 (1), 85–109.
- Bray, J. & Macedo, J. (2017). 6th Ishihara lecture: simplified procedure for estimating liquefaction-induced building settlement. *Soil Dynamics Earthquake Engng* 102, 215–231.
- Bullock, Z., Karimi, Z., Dashti, S., Porter, K., Liel, A. & Frank, K. W. (2018). A physics-informed semi-empirical probabilistic model for the settlement of shallow-founded structures on liquefiable ground. *Géotechnique*, <https://doi.org/10.1680/jgeot.17.P.174>
- Cetin, K. O., Bilge, H. T., Wu, J., Kammerer, A. M. & Seed, R. B. (2009). Probabilistic model for the assessment of cyclically induced reconsolidation (volumetric) settlements. *J. Geotech. Geoenviron. Engng* 135 (3), 387–398.



This project has received funding from the European Union's Horizon 2020 research and innovation programme under grant agreement No. 700748

Methodology for the liquefaction fragility analysis of critical structures and infrastructures: description and case studies

v. 1.0

- Cetin, K. O., Unutmaz, B. & Jeremic, B. (2012). Assessment of seismic soil liquefaction triggering beneath building foundation systems. *Soil Dynamics Earthquake Engng* 43, 160–173.
- Dashti, S., Bray, J. D., Pestana, J. M., Riemer, M. R. & Wilson, D. (2010a). Centrifuge testing to evaluate and mitigate liquefaction induced building settlement mechanisms. *J. Geotech. Geoenviron. Engng* 136 (7), 918–929.
- Dashti, S., Bray, J. D., Pestana, J. M., Riemer, M. R. & Wilson, D. (2010b). Mechanisms of seismically-induced settlement of buildings with shallow foundations on liquefiable soil. *J. Geotech. Geoenviron. Engng* 136 (1), 151–164.
- Ishihara, K. & Yoshimine, M. (1992). Evaluation of settlements in sand deposits following liquefaction during earthquakes. *Soils Found.* 32 (1), 173–188.
- Karamitros, D. K., Bouckovalas, G. D., and Chaloulos, Y. K. (2013). Insight into the Seismic Liquefaction Performance of Shallow Foundations. 139(4):599–607, DOI: 10.1061/(ASCE)GT.1943-5606.0000797.
- Karimi, Z., Dashti, S., Bullock, Z., Porter, K. & Liel, A. (2018). Key predictors of structure settlement on liquefiable ground: a numerical parametric study. *Soil Dynamics Earthquake Engng*.113, 286–308.
- Liu, L. & Dobry, R. (1997). Seismic response of shallow foundation on liquefiable sand. *J. Geotech. Geoenviron. Engng* 123 (6), 557–567.
- Millen, M., Rios, S., Quintero, J., & Viana da Fonseca, A. (2019). Prediction of time of liquefaction using kinetic and strain energy. *Soil Dynamics and Earthquake Engineering, submitted*.
- Olarte, J., Paramasivam, B., Dashti, S., Liel, L. & Zannin, J. (2017). Centrifuge modeling of mitigation–soil–foundation–structure interaction on liquefiable ground. *Soil Dynamics Earthquake Engng* 97, 304–323.
- Sancio, R., Bray, J. D., Durgunoglu, T. & Onalp, A. (2004). Performance of buildings over liquefiable ground in Adapazari, Turkey. *Proceedings of the 13th world conference on earthquake engineering, 13WCEE, Ottawa, ON, Canada*.
- SYNER-G Guidelines for deriving seismic fragility functions of elements at risk: Buildings, lifelines, transportation networks and critical facilities (2013). Kaynia AM (ed.) *Systemic Seismic Vulnerability and Risk Analysis for Buildings, Lifeline Networks and Infrastructures Safety Gain*. Project N°: 244061, Call N°: FP7-ENV-2009-1.
- Tokimatsu, K. & Seed, H. B. (1987). Evaluation of settlements in sands due to earthquake shaking. *J. Geotech. Engng* 113, (8), 861–878.
- Youd, T. L., Idriss, I. M., Andrus, R. D., Arango, I., Castro, G., Christian, J. T., Dobry, R., Finn, W. D. L., Harder, L. F., Hynes, E., Ishihara, K., Koester, J. P., Liao, S. S. C., Marcuson, W. F., Martin, G. R., Mitchell, J. K., Moriwaki, Y., Power, M. S., Robertson, P. K., Seed, R. B. & Stokoe, K. H. (2001). Liquefaction resistance of soils: summary report from the 1996 NCEER and 1998 NCEER /NSF workshops on evaluation of liquefaction resistance of soils. *J. Geotech. Geoenviron. Engng* 127 (10), 817–833.



This project has received funding from the European Union's Horizon 2020 research and innovation programme under grant agreement No. 700748

APPENDICES

A.1 APPENDICES TO SECTION 2.9

A-1.1 CALIBRATION OF THE SIMPLIFIED MODEL FOR THE SOIL SPRING

The calibration of the simplified model for the soil spring was based on results of FLAC 2D SSI analyses of a simple elastic structure located on liquefiable soil profile (Figure A- 1). The calibration was performed using imposed rotation analyses, which were performed for the simplified model in right part of Figure A- 1 with the software OpenSees (2017). The following parameters of the simplified model for the soil spring were part of model calibration:

- The parameters of the OpenSees's uniaxial material "PyLiq1" to be used for simulation of moment-rotational response of shallow foundations ($soilType$, C_d , c , $pRes$, see Section 2.9.3)
- The parameters and procedure for computation of post-liquefaction moment capacity according to the Karamitros et al. (2013a) procedure ($\phi_{2,res}$, $U_{foot,L}$, A , see Section 2.9.3.)
- The parameters which define the degradation of strength during a ground motion that cause liquefaction (t_{init} , $t_{init,deg}$, see Section 2.9.3)

Note that, with the exception of the model for settlements, the remaining components of the simplified model are based on semi-analytical model for existing literature. For these components, the calibration is required only for specific input parameters. The calibration of the model was made assuming that the distribution of pore pressures and the corresponding time of liquefaction are known. The rotation time-histories obtained from FLAC 2D dynamic analyses (see next subsection) were inputted into the simplified model for the soil spring and the parameters of the soil spring were calibrated in order to reproduce (the best as possible) the foundation response in terms of moment time-histories and hysteretic energy. Note that the same set of results was also used for validation of the simplified model for the soil spring (Section 2.9.8).

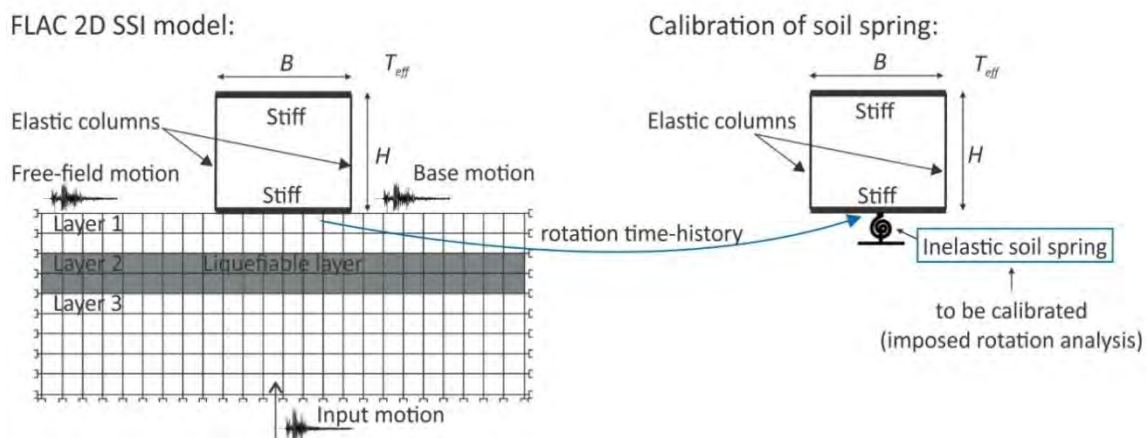


Figure A- 1: Calibration of the inelastic model for the soil spring based on results of FLAC 2D SSI analyses.



This project has received funding from the European Union's Horizon 2020 research and innovation programme under grant agreement No. 700748

A-1.1.1 Description of the FLAC 2D model and results

The FLAC 2D model used to compute the response of the examined SSI problem was developed by UPORTO (left part of Figure A- 1). The model features a simple elastic structure located on a liquefiable soil profile. The soil profile consists of three layers: a non-liquefiable clay crust (layer 1), a liquefiable layer (layer 2), and a stiffer clay layer (layer 3). Three different soil profiles, labelled SP1, SP2 and SP3, are considered in the analyses by specifying different thicknesses of layers. The ground water level is assumed to be located at depth 2 m bellow surface. The material characteristics of the layers are the same for all profiles and are summarized in Table A- 1. The liquefiable layer is model with the constitutive model “PM4Sand” (Boulangier and Ziotopoulou, 2015). The soil domain included in the model has a width of 150 m and a height of 32 m. A compliant base is assumed at the bottom of the model, whereas free-field boundary conditions are used at the two side of the model. The structure is defined specifying its width B , height H , bearing pressure q_b and fixed based period T_{eff} . Two building typologies are examined, i.e. low-rise and mid-rise buildings. The width of the buildings was set to $B=10$ m, whereas the height (H) of the low-rise and mid-rise building amounted to 4 m and 20 m, respectively. The fixed-base periods (T_{eff}) of the two typologies are 0.2 s and 0.6 s, respectively. For each building typology two foundation bearing pressures (q_b) are considered, i.e. 80 kPa and 130 kPa. The foundation and the beam at the top of the building are assumed to be infinitely rigid. The mass of the structure is defined based on foundation bearing pressure and is it assumed to be distributed according to the following distribution: 20 % at foundation level, 70 % at the top beam, and 5 % at the left and right column, respectively. The stiffness of the columns is computed under the condition that the first mode period of the fixed-base structure is equal T_{eff} . The interface between the structure and the soil is assumed to be of non-tension type, and relatively stiff in shear and normal compression. The sliding of the interface is modelled with the Coulomb shear-strength criterion assuming the friction angle of the interface 33°.

Table A- 1: Material characteristics of the examined soil profile.

Material characteristics:	Non-liquefiable clay crust (Layer 1)	Liquefiable sand layer (Layer 2)	Non-liquefiable clay layer (Layer 3)
c_u [kPa]	50	/	200
ϕ' [°]	/	33	/
c' [kPa]	/	0	/
G [MPa]	50	60.4	200
ν	0.4	0.3	0.4
D_r	/	0.55	/
γ [kN/m ³]	15.6	19.7 (saturated)	16.5



This project has received funding from the European Union's Horizon 2020 research and innovation programme under grant agreement No. 700748

In total, 12 models were constructed in FLAC 2D. The characteristics of the models are summarized in **Table A-2**. The seismic response of each model was computed for 5 ground motions. Thus, the total number of dynamic analyses amounted to 60. The most important results of FLAC 2D were: i) acceleration time-history at free field and at the base of the model, ii) pore pressure ratio time-histories in the liquefiable layer under the building and in free-field, and the foundation moment-rotation time-histories.

Table A-2: Characteristic of the FLAC 2D models used for calibration and validation of the simplified model for the soil springs.

No.	Building typology (typology label)	Building width B [m]	Building height H [m]	Fixed-base period T_{eff} [s]	Bearing pressure q_b [kPa]	Soil profile label	Thickness of layer 1 [m]	Thickness of layer2 [m]	Thickness of layer3 [m]
1	Low-rise (v13)	10	4	0.2	80	SP1	4.0	4.8	23.2
2	Low-rise (v13)	10	4	0.2	130	SP1	4.0	4.8	23.2
3	Low-rise (v13)	10	4	0.2	80	SP2	2.0	4.8	25.2
4	Low-rise (v13)	10	4	0.2	130	SP2	2.0	4.8	25.2
5	Low-rise (v13)	10	4	0.2	80	SP3	6.0	4.0	22.0
6	Low-rise (v13)	10	4	0.2	130	SP3	6.0	4.0	22.0
7	Mid-rise (v9)	10	20	0.6	80	SP1	4.0	4.8	23.2
8	Mid-rise (v9)	10	20	0.6	130	SP1	4.0	4.8	23.2
9	Mid-rise (v9)	10	20	0.6	80	SP2	2.0	4.8	25.2
10	Mid-rise (v9)	10	20	0.6	130	SP2	2.0	4.8	25.2
11	Mid-rise (v9)	10	20	0.6	80	SP3	6.0	4.0	22.0
12	Mid-rise (v9)	10	20	0.6	130	SP3	6.0	4.0	22.0

A-1.1.2 Results of model calibration

The rotation time-histories obtained from FLAC 2D dynamic analyses were inputted into the simplified model for the soil spring and the parameters of the soil spring were calibrated in order to reproduce (the best as possible) the foundation response in terms of moment time-histories and hysteretic energy. The final values of the parameters soil spring, which were obtained using a trial-and-error approach, and are presented in **Table A-3**. Due to significant amount of data, the comparison of FLAC 2D dynamic analysis results and results of imposed displacement analysis of the simplified model for the soil spring is graphically presented only for a selected example, i.e. model No. 7 (v9, SP1, $q_b=80$ kPa) from **Table A-2** (see **Figure A-3** to **Figure A-7**). All results of model calibration are summarized in **Figure A-2**, which presents the comparison of predicted and actual maximum moment, hysteretic energy at the end of the analysis, and foundation settlement obtained by imposed displacement analysis of the simplified model and dynamic analysis in FLAC 2D. The mean percentage errors obtained for all 60 analyses are presented at the bottom-right part of figures.



This project has received funding from the European Union's Horizon 2020 research and innovation programme under grant agreement No. 700748

Table A- 3: Recommended values of input parameters for the simplified model for the soil springs.

Parameter:	Recommend value
“PyLiq1” material	$soilType = 1, C_d = 1.0, c = 0, pRes = 0.05 M_{ult,1}$
Post-liquefaction moment capacity	$\phi_{2,res} = 5^\circ, A = 0.9, U_{ff,L} = 0.95, U_{foot,L}$ is estimated at the centre of liquefiable layer
Degradation of strength	$t_{init} = \frac{0.2 t_L}{U_{ff,L}}, t_{init,deg} = f(U_{init,deg})$ is estimate case by case; $U_{init,deg}$ is in range of 0.4 and 0.7 (conservative estimate $U_{init,deg} = 0.3$)

Based on the results presented in Figure A- 3 to Figure A- 7, it can be observed that with the imposed rotation into the soil spring of the simplified SSI model it was possible to reproduce quite well the moment-rotation relationships of soil-foundation system obtained from FLAC 2D dynamic analyses. In the case of ground motion 2 (Figure A- 4), for which liquefaction was not triggered (max pore pressure ratio 0.4), the results obtained for the simplified model match almost perfectly the results of FLAC 2D. In the case of the four remaining ground motions, for which liquefaction was triggered, the simplified model was also capable of predicting the global response of the foundation in terms of moment time-histories, hysteretic energy and foundation settlement. The model for prediction of the average pore pressure ratio in the liquefiable layer match relatively well (at least in the mean sense) to the results of FLAC dynamic analysis (see blue lines). However, the actual distribution of pore pressure ratios is, in general, much more complex than the distribution assumed in the simplified model and varies significantly depending on the ground motion. Sudden fluctuations in pore pressures cause hardening and pinching effects in the soil spring, which can be most clearly observed in the foundation moment time-histories and foundation hysteresis (see e.g. Figure A- 5 and Figure A- 6). In case of sudden drops of the pore pressure ratio, which produce short-term stiffening of the soil (e.g. ground motion 4, see Figure A- 6), the moment capacity of the foundation can be underestimated. It should be noted that the simplified model is intended for simulation of the “average” pore pressure development and as such cannot capture sudden hardening and pinching effects in the hysteretic response of the foundation. Thus, it can be observed that simplified model for the soil spring may in some cases underestimate the maximum foundation moment from FLAC 2D (see Figure A- 2). The results obtained for all 60 dynamic analyses indicate that this influence is moderate, since the average prediction error in maximum moment capacity amounted to -21 %, which is judged to be acceptable considering the simplicity and intended use of the simplified model (as a screening tool). It is worth noting that underestimation of foundation capacity is expected to produce conservative estimates of foundation rotations and settlements, but it may lead to underestimation of seismic demand of the structure. Additional studies would be required in order to better understand how (and if) short-term peaks in the foundation moments (see e.g. Figure A- 6) affect the seismic demand of nonlinear structures.



This project has received funding from the European Union's Horizon 2020 research and innovation programme under grant agreement No. 700748

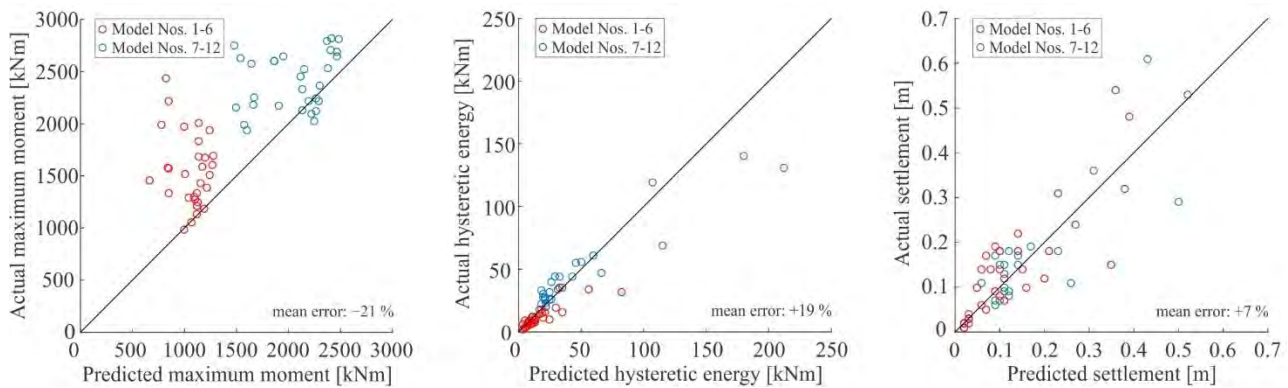


Figure A- 2: Comparison of predicted and actual maximum foundation moment, hysteretic energy, and settlement between the simplified model and FLAC 2D.

The simplified model on average slightly overestimated the total hysteretic energy compared to FLAC 2D dynamic analysis results. The average prediction error of hysteretic energy considering all 60 analyses amounted to +19 % (see **Figure A- 2**). The predicted error was slightly larger in case of the low-rise buildings (models 1-6). In these cases, the over prediction of hysteretic energy was consequence of more pronounced pinching behaviour of the hysteresis, which was not well captured by the simplified model. However, in case of mid-rise buildings alone, the average prediction was only -6 %. The prediction of settlements of the simplified model was in general very accurate, and the mean prediction error of all 60 analyses amounted to +7 % (see **Figure A- 2**). It should be noted that in the case of imposed displacement analysis this conclusion was expected, since the model for settlement was based on the “mean” relationship between cumulative rotation and settlement.

Based on the results of model calibration, it can be concluded that the proposed models for prediction of pore pressure development and degradation of strength, and the selected OpenSees’s hysteretic material “*PyLiq1*” were capable of predicting relatively well (at least in the mean sense) the moment-rotation obtained from FLAC 2D analyses. The results of this section showed some limitations in the current formulation of the model, i.e. the inability to capture softening and hardening effects in the hysteretic response of the foundation due to fluctuations in pore pressures once liquefaction is already triggered. Additional studies are required to better understand the background of such phenomena and to improve the predictive capacity of the simplified model. Nevertheless, as it will be shown in Section 2.9.8 (validation of the model), the simplified model generally produced conservative estimates of foundation settlements and rotations, which are often the decisive parameter for the risk assessment of buildings located on liquefiable soils.



This project has received funding from the European Union's Horizon 2020 research and innovation programme under grant agreement No. 700748

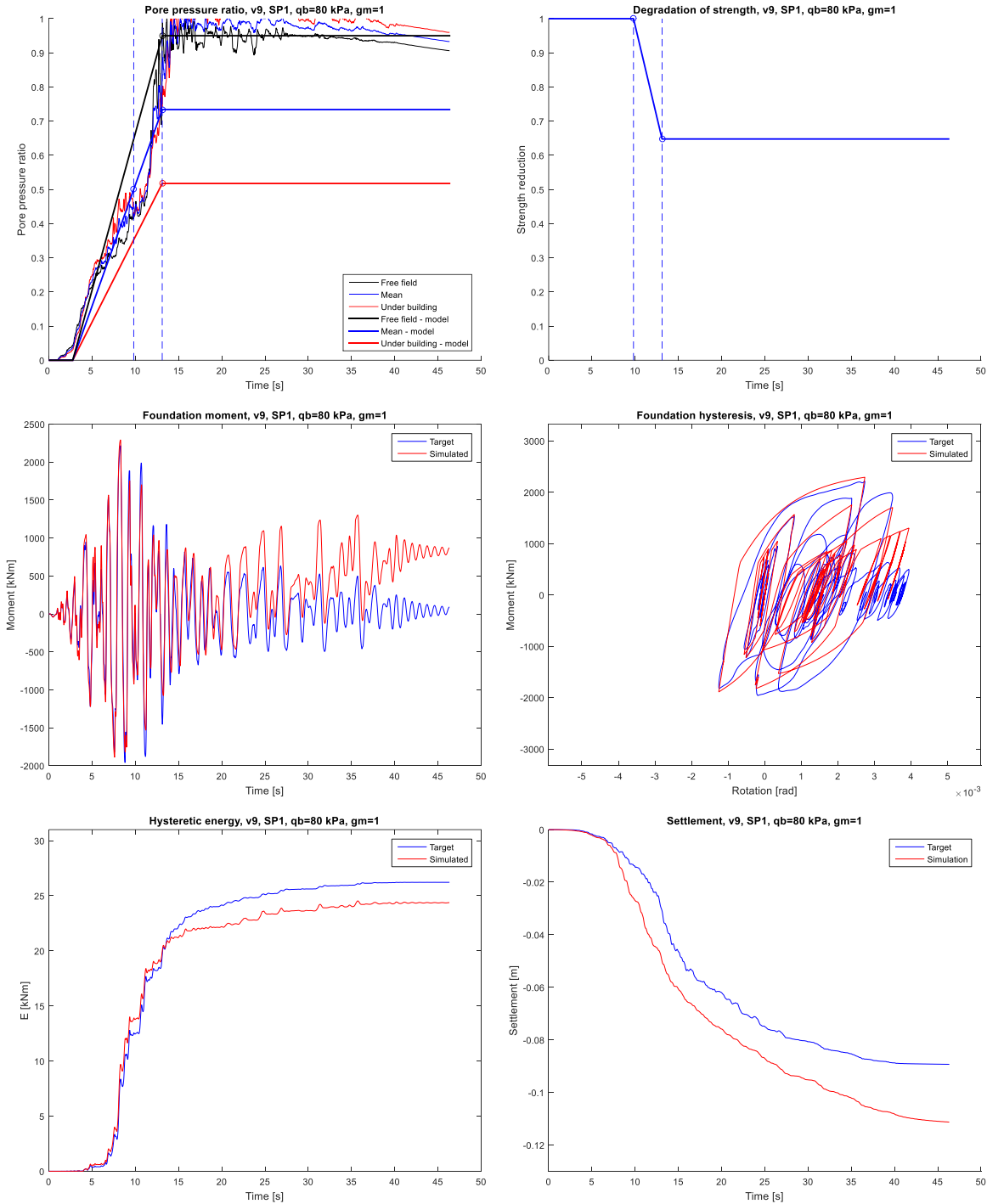


Figure A- 3: Comparison of FLAC 2D dynamic analysis results (blue) and (red) results of imposed displacement analysis of the simplified model for the soil spring (model number 7 (v9, SP1, $q_b = 80$ kPa), subjected to ground motion number 1).



This project has received funding from the European Union's Horizon 2020 research and innovation programme under grant agreement No. 700748

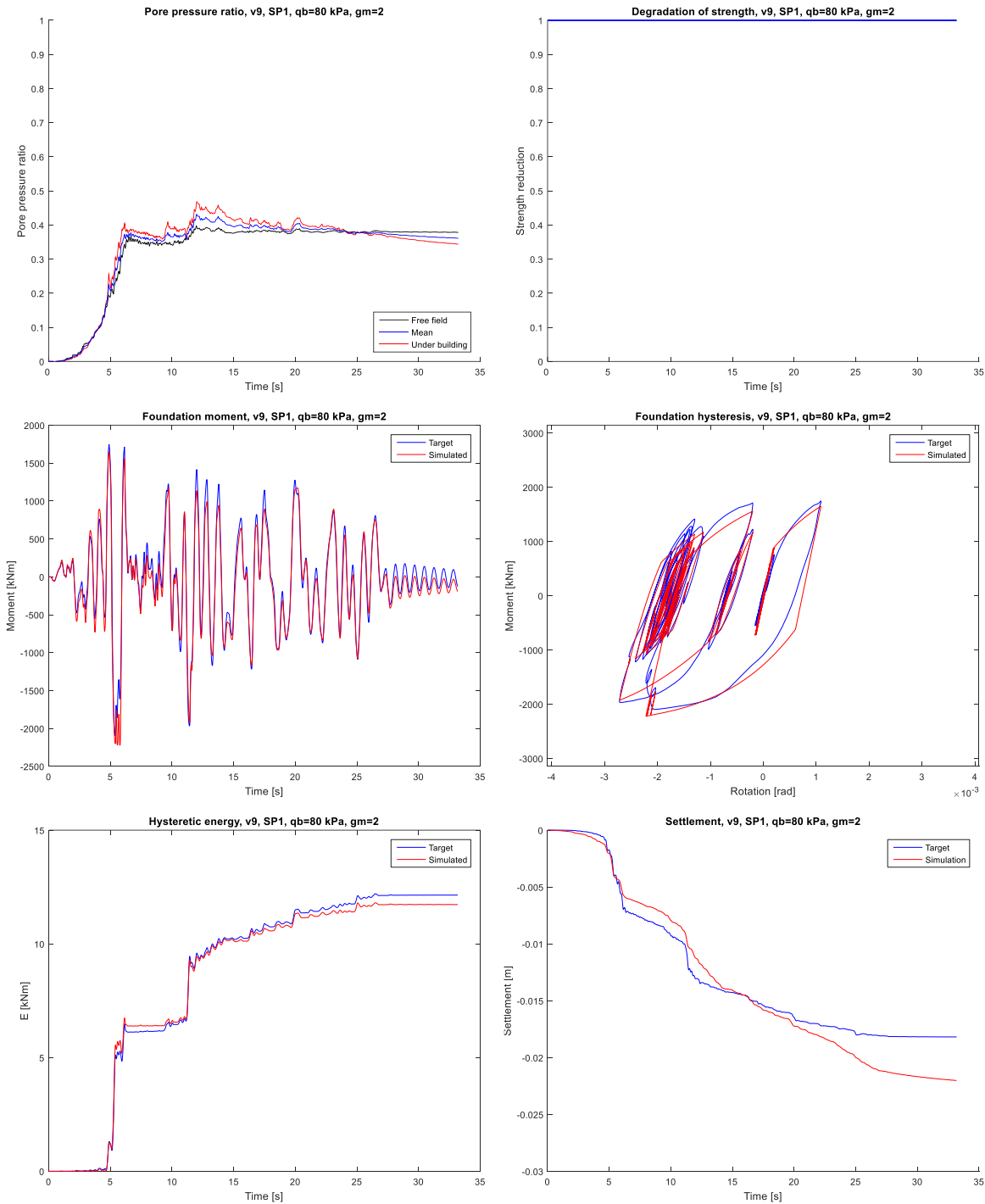


Figure A- 4: Comparison of FLAC 2D dynamic analysis results (blue) and (red) results of imposed displacement analysis of the simplified model for the soil spring (model number 7 (v9, SP1, $q_b=80$ kPa), subjected to ground motion number 2).



This project has received funding from the European Union's Horizon 2020 research and innovation programme under grant agreement No. 700748

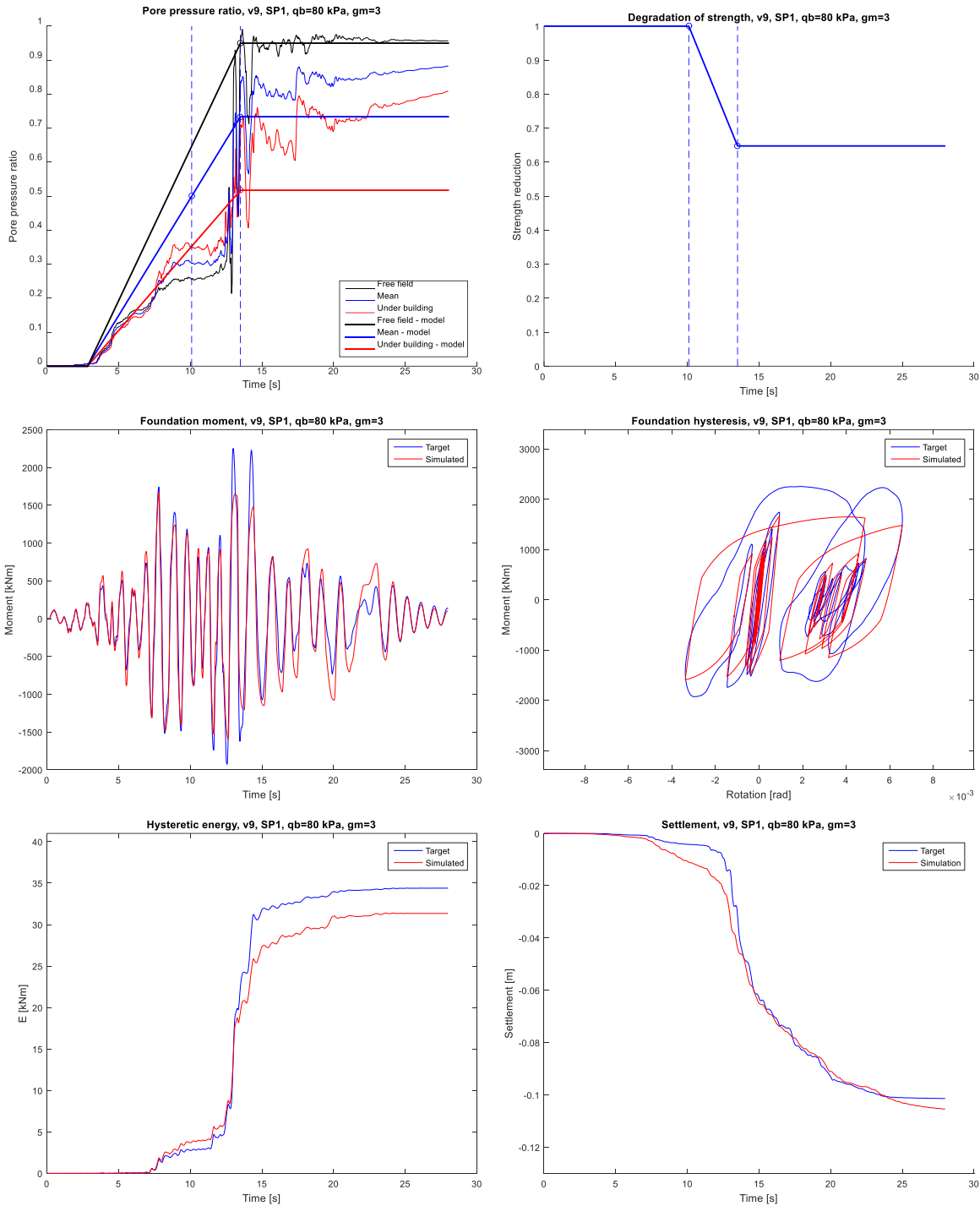


Figure A- 5: Comparison of FLAC 2D dynamic analysis results (blue) and (red) results of imposed displacement analysis of the simplified model for the soil spring (model number 7 (v9, SP1, $q_b=80$ kPa), subjected to ground motion number 3).



This project has received funding from the European Union's Horizon 2020 research and innovation programme under grant agreement No. 700748

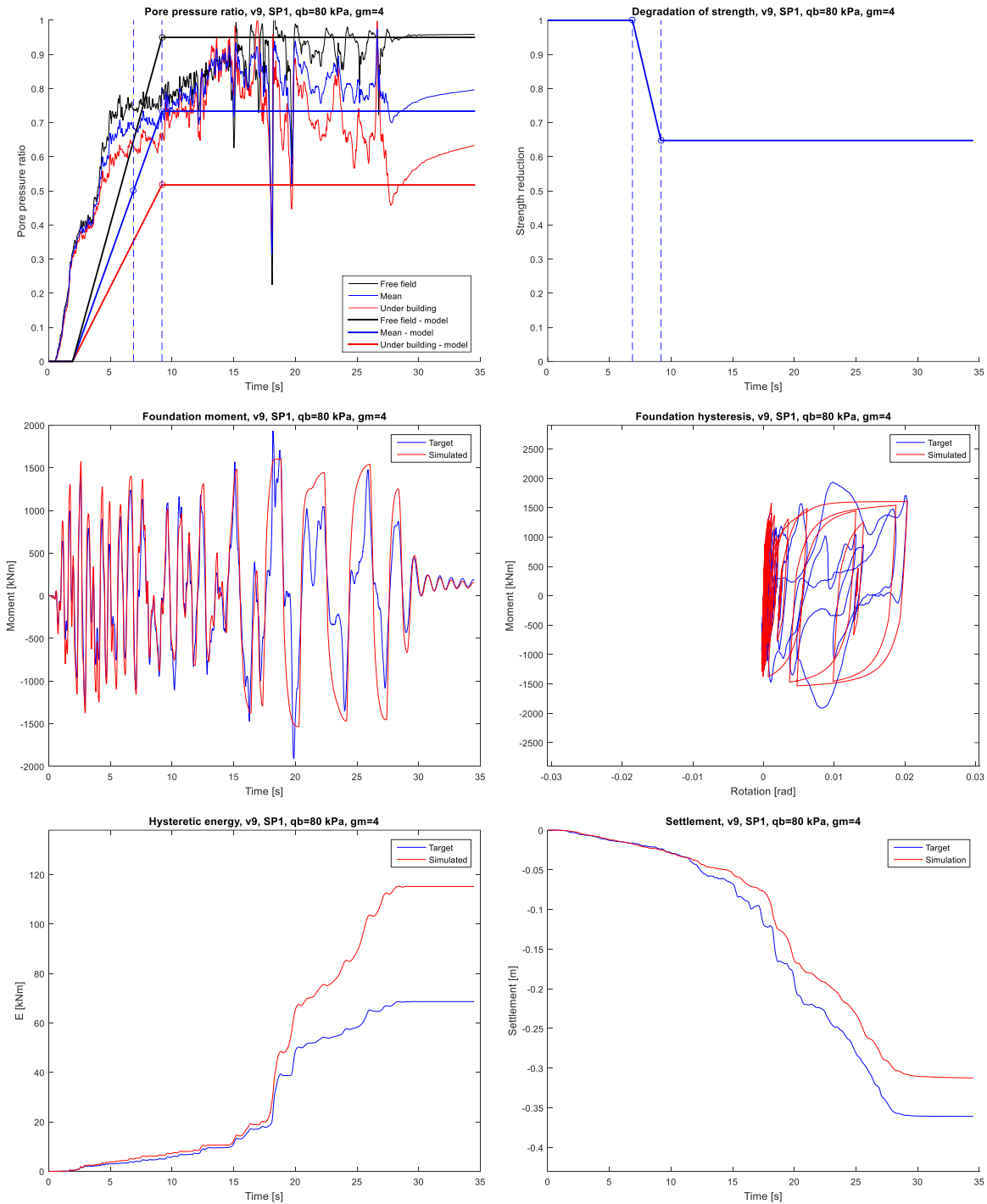


Figure A- 6: Comparison of FLAC 2D dynamic analysis results (blue) and (red) results of imposed displacement analysis of the simplified model for the soil spring (model number 7 (v_9 , $SP1$, $q_b = 80$ kPa), subjected to ground motion number 4).



This project has received funding from the European Union's Horizon 2020 research and innovation programme under grant agreement No. 700748

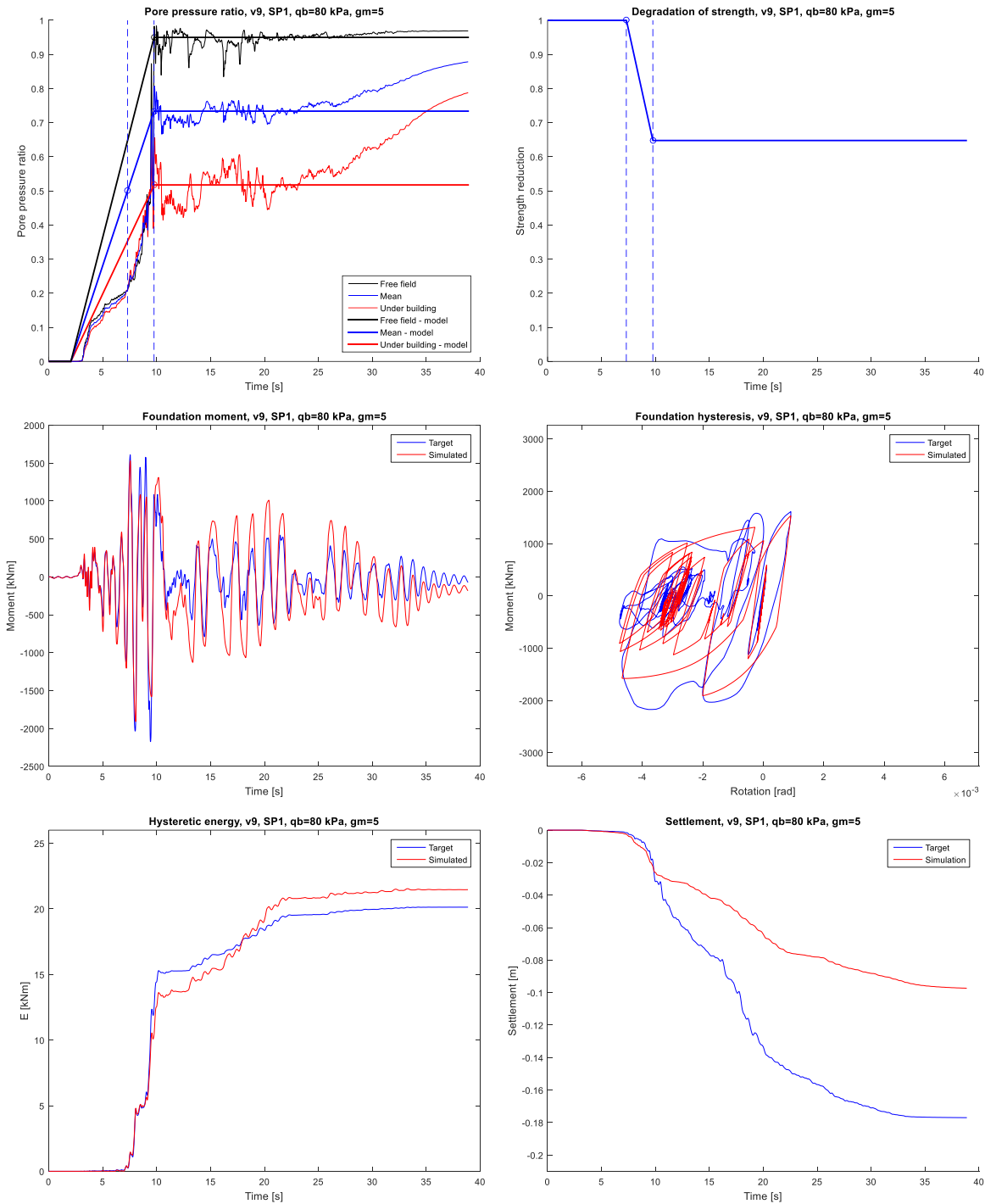


Figure A- 7: Comparison of FLAC 2D dynamic analysis results (blue) and (red) results of imposed displacement analysis of the simplified model for the soil spring (model number 7 (v9, SP1, $q_b=80$ kPa), subjected to ground motion number 5).



This project has received funding from the European Union's Horizon 2020 research and innovation programme under grant agreement No. 700748

A-1.2 CALIBRATION OF INPUT MOTION FOR FRAGILITY ANALYSIS

As explained in Section 2.9.3, in a simplified approach it is convenient to base the assessment on a code-base spectrum, which removes the need for site specific analysis. The standard EC8 (CEN, 2004) does not specify the elastic response spectrum to be used in case of liquefiable soils (class S2), but recommend to perform additional studies. Liquefiable soil profiles are typically composed of loose-to-medium cohesionless soil with or without some soft cohesive layers, which without considering the liquefaction susceptibility match quite well the EC8 definition of soil type D ($v_{s,30} < 180$ m/s, $N_{SPT} < 15$, $c_u < 70$ kPa). Thus, in the following it is examined if, for the examined soil profiles, the input seismic motion for fragility analysis can be based on the EC8 elastic response spectrum for soil type D. Note that a certain level of conservatism is acceptable, since the purpose of the simplified fragility analysis is only decision-making regarding the need for detail studies of soil liquefaction.

In Figure A- 8, the acceleration response spectra (5 % damping) for free-field surface motion computed by 60 FLAC 2D analyses are normalized to peak ground acceleration of 1 g, and are compared to the EC8 elastic response spectrum for soil type D, which is scaled to the same peak ground acceleration. The mean and mean \pm standard deviation spectra from FLAC 2D are presented with red continues and dashed curves, respectively. As it can be observed from Figure A- 8, the EC8 elastic spectrum for soil type D ($T_B = 0.2$ s, $T_C = 0.8$ s, and $T_D = 2.0$ s) provides, in the range of periods of interest (up to 1.5 s, low- to mid-rise structures), conservative estimate of the mean spectrum from FLAC 2D analyses. In the range of periods of interest, the Eurocode 8 spectrum is close to the mean + standard deviation spectrum (84. percentile). Thus, it is expected that the used of the EC8 spectrum for simplified fragility analysis would produce conservative estimates of the mean (median) seismic response for the examined soil profiles, which is crucial for confined decision-making regard the need for detailed studies of soil liquefaction with the RRI.

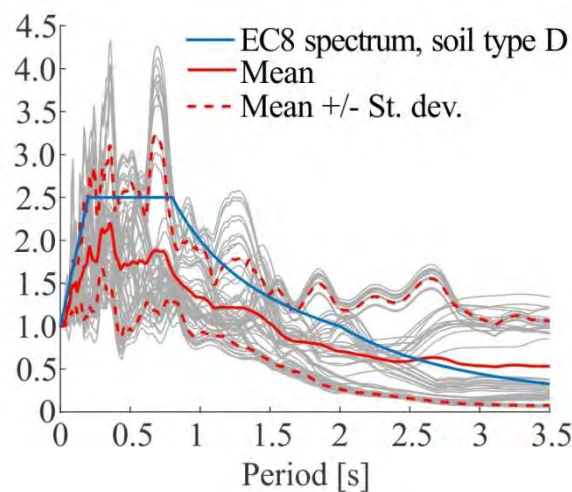


Figure A- 8: Comparison of acceleration response spectra (5 % damping) for free-field surface motion computed from 60 FLAC 2D dynamic analyses the EC8 elastic response spectrum for soil type D, both, normalized to peak ground acceleration of 1 g. The mean and mean \pm standard deviation spectra from FLAC 2D are presented with red continues and dashed curves, respectively.



This project has received funding from the European Union's Horizon 2020 research and innovation programme under grant agreement No. 700748

A-1.3 VALIDATION OF THE SIMPLIFIED MODEL FOR THE SOIL SPRING

A-1.3.1 Methodology

The simplified model for the soil spring, presented in Section 2.9.3, is validated based on dynamic analysis of the simplified SSI model presented in right part of Figure A-9. The goal of the model validation is to assess if the simplified SSI model is capable of reproducing the results of FLAC 2D dynamic analyses, which were described in Section 2.9.6 (model calibration). In the case of the simplified SSI model, the input motion for dynamic analysis was extracted from FLAC 2D results as free-field surface motion. The model of the structure was the same in both models. Note that compared to model calibration (Section 2.9.6), the validation of the model also accounts also for the uncertainty related to approximate definition of input motion, uncertainty related to the time-dependent and ground-motion dependent triggering of liquefaction, and uncertainty related to the prediction of building settlement. Note that in the simplified model, the input motion is defined based on free-field motions, the triggering of liquefaction is assessed based on an empirical triggering procedure, and the foundation settlement is estimated based on a predefined relationship between cumulative rotation and settlement. Additional details regarding the simplified model for the soil spring were presented in Section 2.9.3.

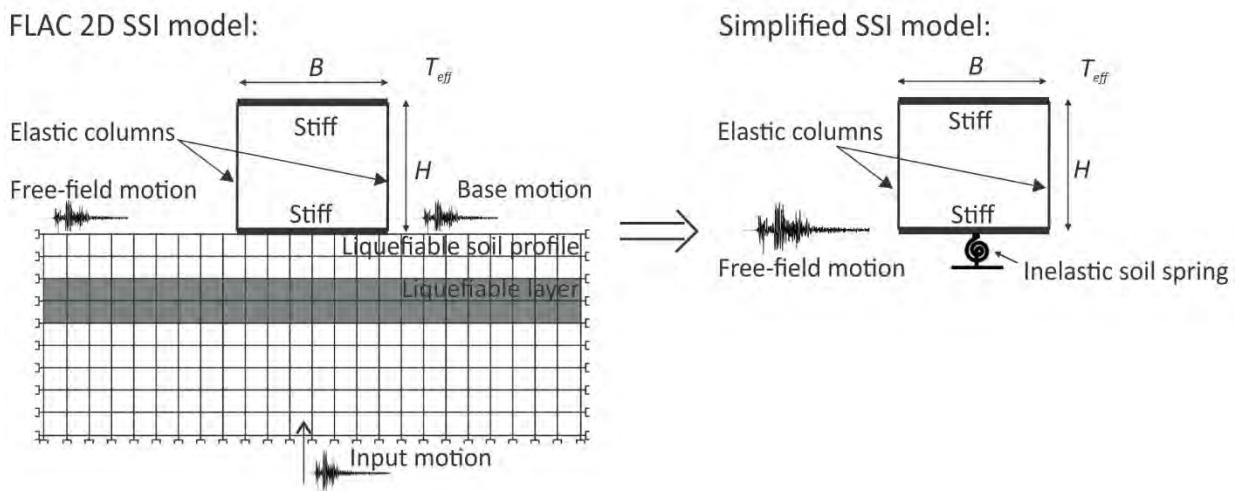


Figure A-9: Validation of the inelastic model for the soil spring based on results of FLAC 2D SSI analyses.

A-1.3.2 Results of model validation

Due to large amount of data, the comparison of the results of dynamic analyses for the simplified model and FLAC 2D is graphically presented only for a selected example, i.e. model No. 7 (v9, SP1, $q_b = 80$ kPa) from Table A-2 (see Figure A-11 to Figure A-15). In figures, the predictive capacity of the simplified model is assessed based on: i) time-dependent and ground-motion dependent triggering of liquefaction, ii) foundation hysteretic response, iii) foundation rotation and moment time-histories, hysteretic energy, and iv) foundation settlements, with results of FLAC 2D analyses. The time of occurrence of liquefaction from FLAC analyses was assumed to correspond to the time where the pore pressure ratio in free-field exceeded the



This project has received funding from the European Union's Horizon 2020 research and innovation programme under grant agreement No. 700748

value $U_{ff,L}=0.95$. All results of model validation are summarized in **Table A- 4** and **Table A- 5** by comparing the limit states of the building predicted based on dynamic analysis of the simplified model and FLAC 2D. The limit states of the building were based on foundation peak rotations and settlements according to Bird et al. (2006) definition (see **Table 2.22** in Section 2.9.4). In addition to this, the comparison of predicted and actual foundation settlements, maximum foundation rotations, and maximum foundation moments is presented in **Figure A- 10**. The mean percentage errors for settlements, maximum rotations and maximum moments, obtained for all 60 analyses, are presented in right-bottom corner of figures.

Based on results of **Figure A- 11** to **Figure A- 15**, it can be observed that the simplified model, in general, predicts quite well the global response of the building, which was obtained by FLAC 2D. The triggering of liquefaction was accurately predicted for all 5 ground motions. Note that liquefaction was not triggered in the case of the ground motion No. 2, which was also well captured by the employed empirical triggering procedure. The time of liquefaction was well estimated for all ground motions (GMs No. 1,3,5) with the exception of ground motion No. 4, for which liquefaction was not triggered early enough. Note that similar results were obtained for all 12 examined models.

For majority of ground motions, the simplified model well predicted the global hysteretic response (see **Figure A- 11** to **Figure A- 15**). Slightly worse prediction was obtained for ground motion No. 4, for which the time of liquefaction was overestimated. The error in the prediction of foundation rotation time-histories is generally larger than the error in the prediction of moment time-histories, which indicate that rotations are more sensitive to modelling uncertainties. Nevertheless, with the exception of ground motions No. 1 and 4, the rotation time-histories obtained by the simplified model match quite well FLAC 2D results. The hysteretic energy obtained for the simplified models match relatively well the results of FLAC 2D analyses. A similar conclusion can also be made for the predictions of foundation settlement. However, in the case of ground motions No.4 and 5, the foundation settlements at the end of the analyses were underestimated.

The results obtained for all 60 analyses indicated that the simplified model (on average) overestimated the foundation settlements and maximum rotations, whereas the foundation maximum moments were slightly underestimated (see **Figure A- 10**). The mean prediction error of all 60 analyses amounted to +34 %, +35 %, and -20 %, in case of foundation settlements, maximum rotations, and maximum foundation moments, respectively. The results of **Table A- 4** and **Table A- 5** indicate that the limit states of the building were mostly related to foundation settlements, and that the foundation maximum rotations were relatively small. It should be noted that the simplified model was in majority of cases able to correctly predict the damage state of the building obtained by FLAC 2D analyses (see green cells (OK) in **Table A- 4** and **Table A- 5**). In some cases, the simplified model overestimated the damage state of the building (blue cells, OK+), which is considered acceptable, since it leads to conservative decision-making when applying RRI method. On the other hand, the simplified model underestimated the damage state of the building in few cases (orange cells, NOT OK). In addition to this, the simplified model slightly underestimated the maximum foundation moment (on average by 20 %), which may result in an underestimation of seismic demand of the structure. Note that the obtained accuracy of the model is judged to be acceptable considering the simplicity and intended use of the simplified model (as a screening tool).



This project has received funding from the European Union's Horizon 2020 research and innovation programme under grant agreement No. 700748

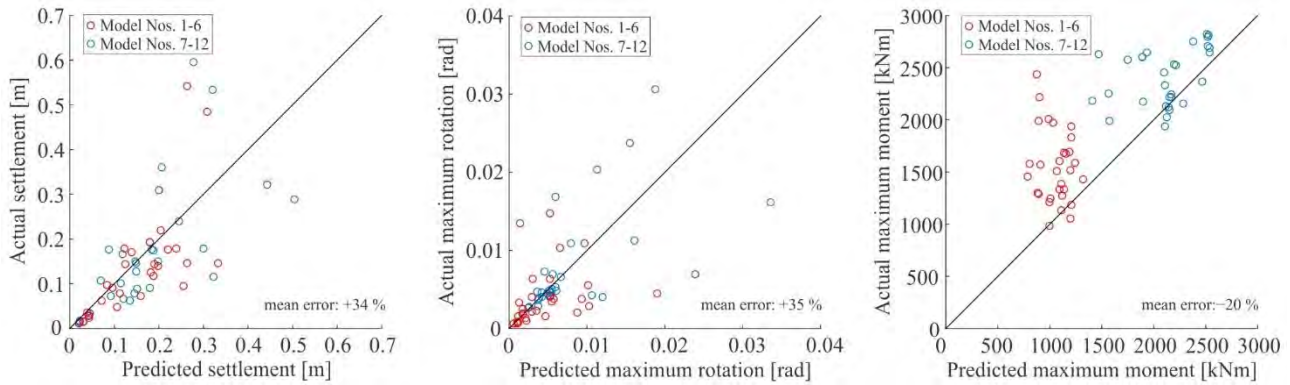


Figure A- 10: Comparison of predicted and actual foundation settlement, maximum rotations, maximum moment between the simplified model and FLAC 2D.

Based on the results of model validation, it can be concluded that the simplified model for the soil spring is able to sufficiently well predict the foundation settlements, maximum rotations and maximum moments obtained by much more complex FLAC 2D dynamic analyses. The simplified model was shown to produce conservative estimates of mean foundation settlements and rotations, which are often the decisive parameter for the risk assessment of buildings located on liquefiable soils.



This project has received funding from the European Union's Horizon 2020 research and innovation programme under grant agreement No. 700748

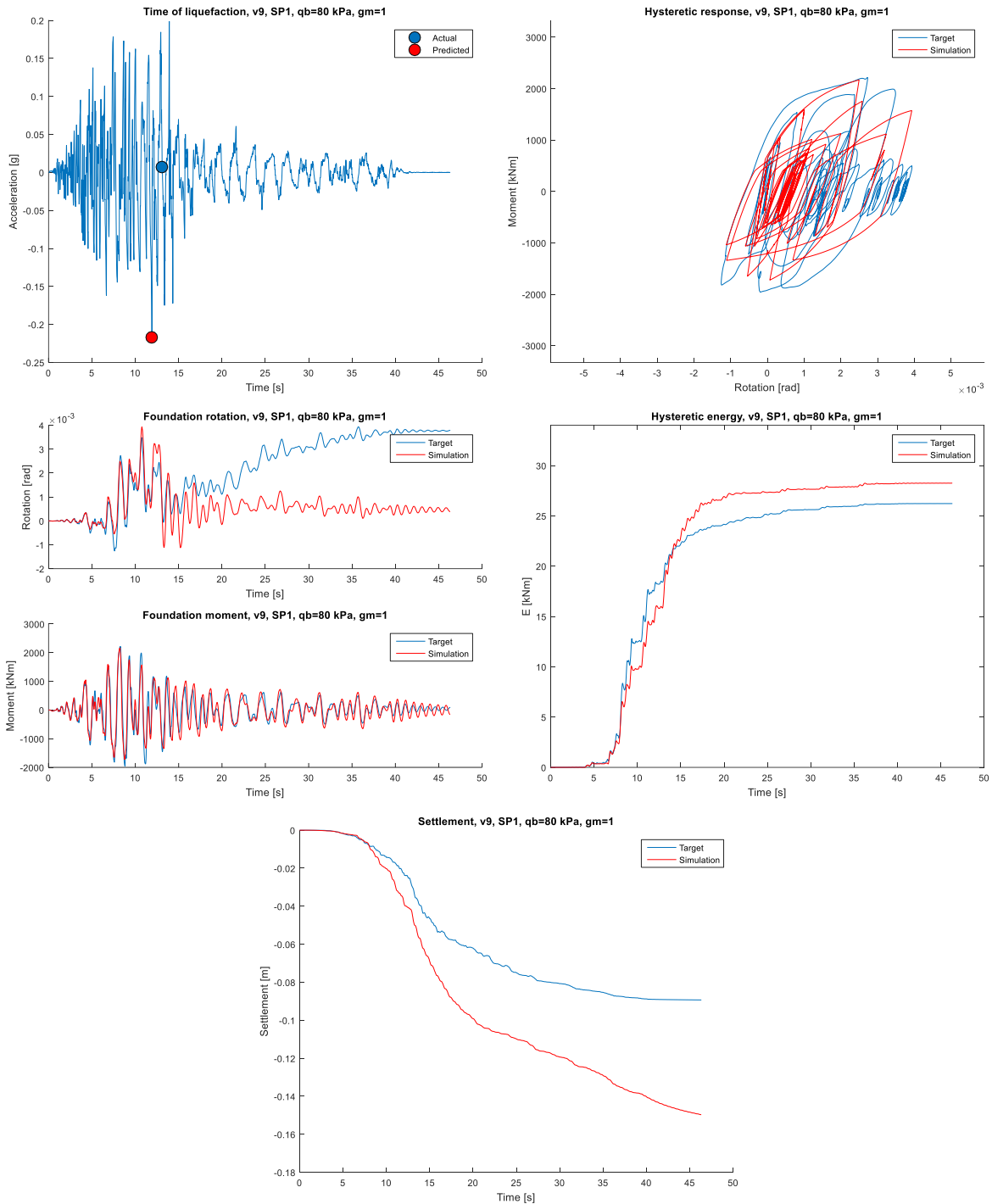


Figure A- 11: Comparison of FLAC 2D dynamic analysis results (blue) and (red) dynamic analysis results of the simplified model for the soil spring (model number 7 (v9, SP1, $q_b=80$ kPa), subjected to ground motion number 1).



This project has received funding from the European Union's Horizon 2020 research and innovation programme under grant agreement No. 700748

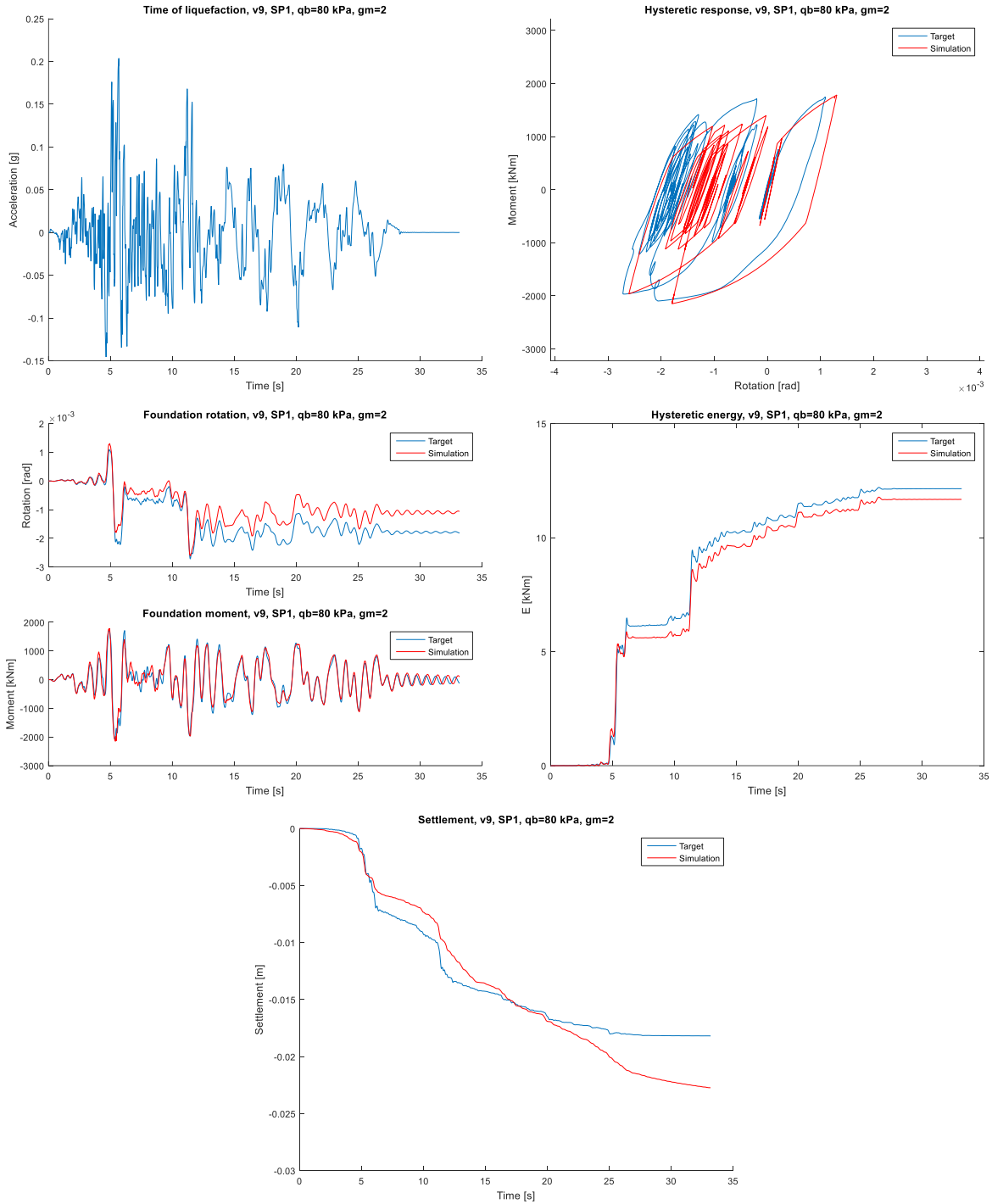


Figure A- 12: Comparison of FLAC 2D dynamic analysis results (blue) and (red) dynamic analysis results of the simplified model for the soil spring (model number 7 (v9, SP1, $q_b=80$ kPa), subjected to ground motion number 2).



This project has received funding from the European Union's Horizon 2020 research and innovation programme under grant agreement No. 700748

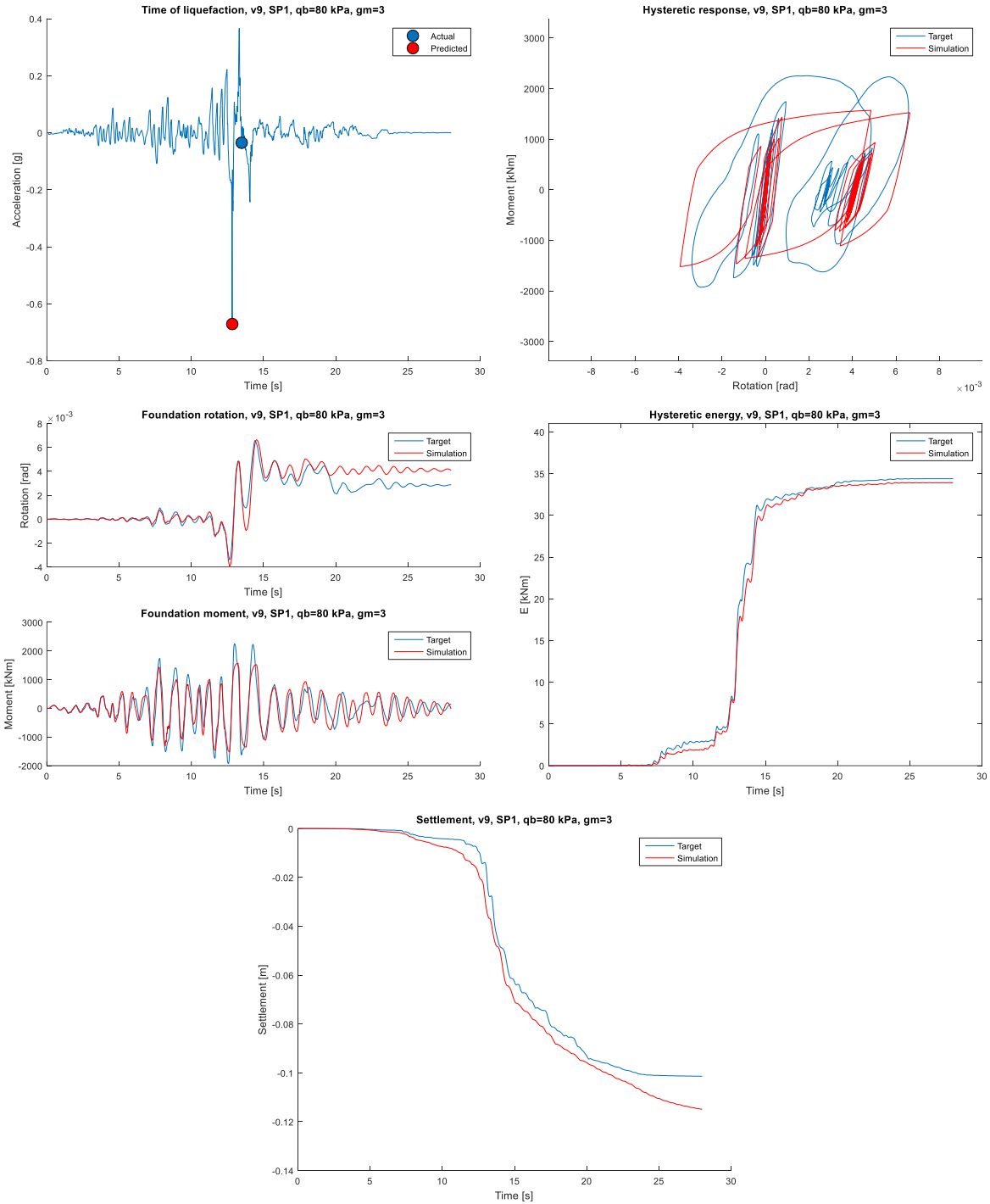


Figure A- 13: Comparison of FLAC 2D dynamic analysis results (blue) and (red) dynamic analysis results of the simplified model for the soil spring (model number 7 (v9, SP1, $q_b=80$ kPa), subjected to ground motion number 3).



This project has received funding from the European Union's Horizon 2020 research and innovation programme under grant agreement No. 700748

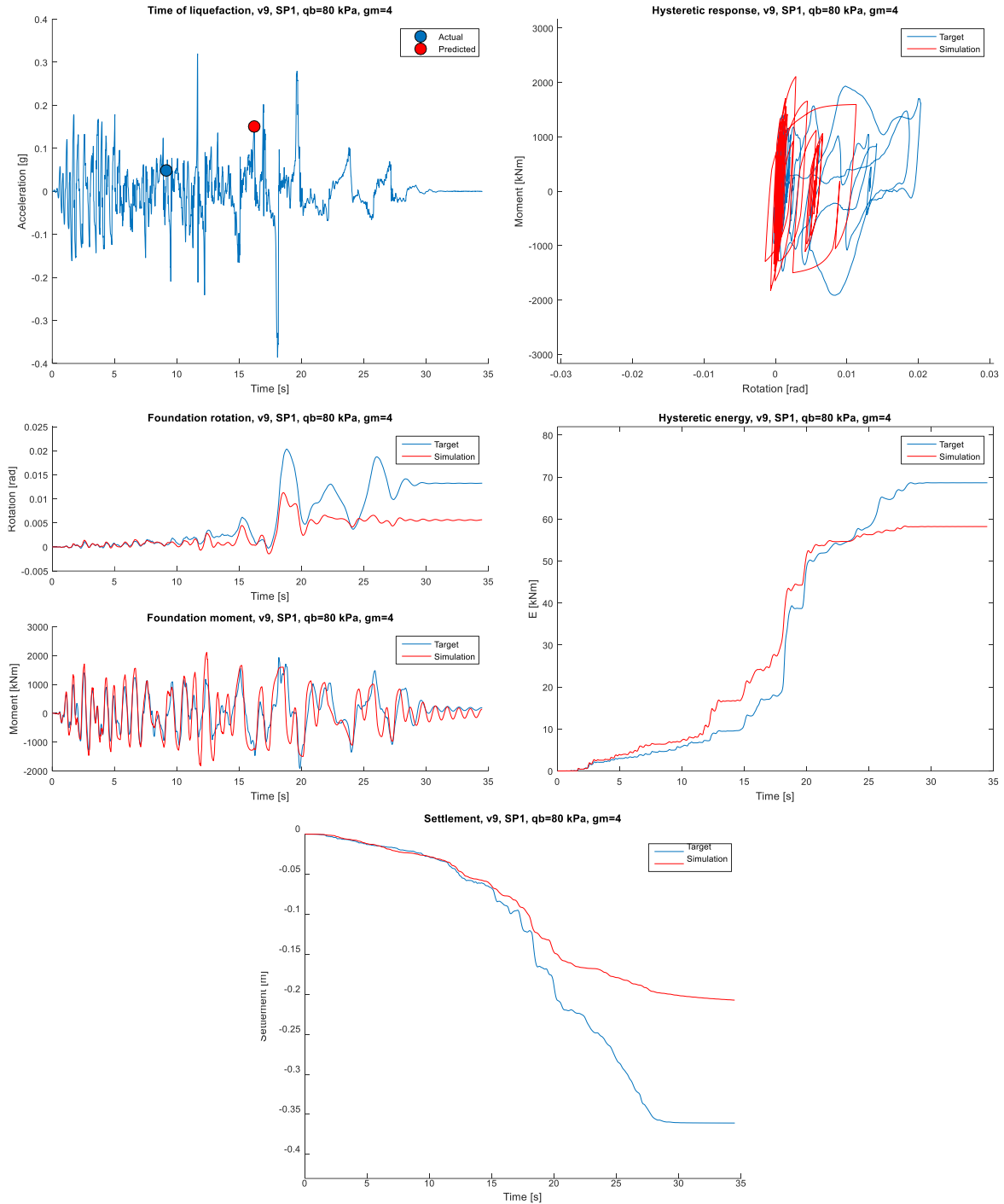


Figure A- 14: Comparison of FLAC 2D dynamic analysis results (blue) and (red) dynamic analysis results of the simplified model for the soil spring (model number 7 (v9, SP1, q_b =80 kPa), subjected to ground motion number 4).



This project has received funding from the European Union's Horizon 2020 research and innovation programme under grant agreement No. 700748

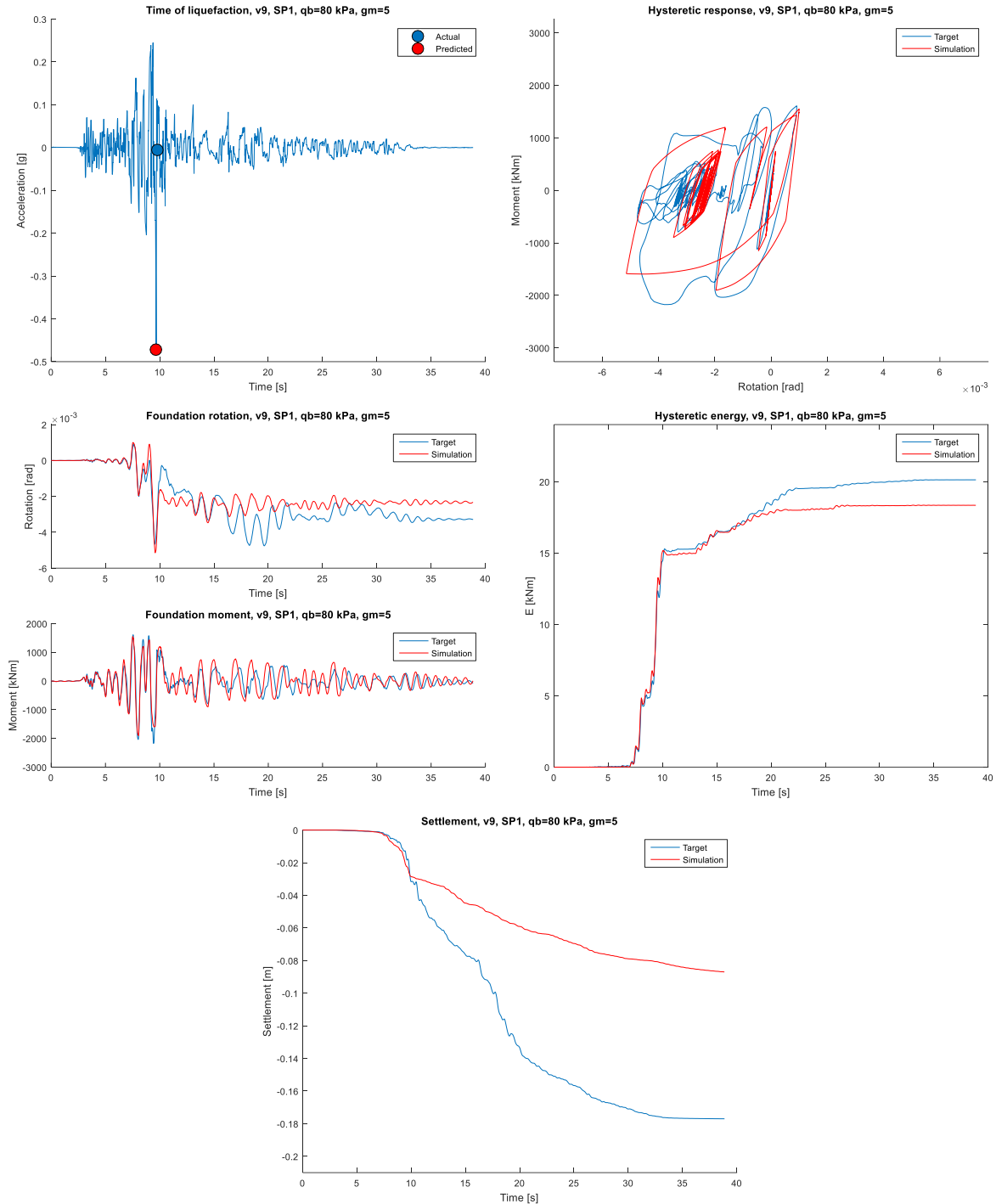


Figure A- 15: Comparison of FLAC 2D dynamic analysis results (blue) and (red) dynamic analysis results of the simplified model for the soil spring (model number 7 (v9, SP1, q_b =80 kPa), subjected to ground motion number 5).



This project has received funding from the European Union's Horizon 2020 research and innovation programme under grant agreement No. 700748

Table A- 4: Comparison of predicted damage states based on dynamic analysis of the simplified model and FLAC 2D for low-rise building topology (models 1-6).

Model No.	Ground motion No.	LSs based on settlements			LSs based on foundation rotations		
		Predicted LS	Actual LS	Decision	Predicted LS	Actual LS	Decision
1	1	DL2	DL1	OK+	0	0	OK
	2	0	0	OK	0	0	OK
	3	DL1	DL1	OK	DL1	0	OK+
	4	DL2	SD	NOT OK	DL1	DL2	NOT OK
	5	DL2	DL2	OK	0	0	OK
2	1	DL2	DL2	OK	0	0	OK
	2	0	0	OK	0	0	OK
	3	DL2	DL2	OK	DL2	DL1	OK+
	4	SD	SD	OK	DL1	DL2	NOT OK
	5	DL2	DL2	OK	DL1	0	OK+
3	1	DL2	DL2	OK	0	0	OK
	2	0	0	OK	0	0	OK
	3	DL2	DL1	OK+	DL1	0	OK+
	4	DL2	DL2	OK	DL2	0	OK+
	5	DL2	DL2	OK	0	0	OK
4	1	SD	DL2	OK+	DL1	DL1	OK
	2	0	0	OK	0	0	OK
	3	DL2	DL1	OK+	DL2	0	OK+
	4	SD	SD	OK	DL2	DL1	OK+
	5	DL2	DL2	OK	DL1	0	OK+
5	1	DL2	0	OK+	0	0	OK
	2	0	0	OK	0	0	OK
	3	DL1	DL1	OK	0	0	OK
	4	DL2	DL2	OK	0	DL2	NOT OK
	5	DL1	DL1	OK	0	0	OK
6	1	DL2	DL2	OK	0	0	OK
	2	0	0	OK	0	0	OK
	3	DL2	DL2	OK	DL1	0	OK+
	4	DL2	SD	NOT OK	DL1	DL2	NOT OK
	5	DL2	DL2	OK	0	DL1	NOT OK



This project has received funding from the European Union's Horizon 2020 research and innovation programme under grant agreement No. 700748

Table A- 5: Comparison of predicted damage states based on dynamic analysis of the simplified model and FLAC 2D for mid-rise building topology (models 7-12).

Model No.	Ground motion No.	LSs based on settlements			LSs based on foundation rotations		
		Predicted LS	Actual LS	Decision	Predicted LS	Actual LS	Decision
7	1	DL2	DL1	OK+	0	0	OK
	2	0	0	OK	0	0	OK
	3	DL2	DL2	OK	DL1	DL1	OK
	4	DL2	SD	NOT OK	DL2	DL2	OK
	5	DL1	DL2	NOT OK	DL1	0	OK+
8	1	SD	DL2	OK+	0	DL1	NOT OK
	2	0	0	OK	DL1	0	OK+
	3	DL2	DL2	OK	DL2	0	OK+
	4	SD	SD	OK	DL2	DL2	OK
	5	DL2	DL2	OK	0	0	OK
9	1	DL2	DL1	OK+	0	0	OK
	2	0	0	OK	0	0	OK
	3	DL2	DL1	OK+	DL1	0	OK+
	4	DL2	DL2	OK	DL2	DL2	OK
	5	DL2	DL2	OK	DL1	DL1	OK
10	1	SD	DL2	OK+	DL1	DL1	OK
	2	0	0	OK	DL1	0	OK+
	3	DL2	DL1	OK+	DL2	0	OK+
	4	SD	DL2	OK+	DL2	DL2	OK
	5	DL2	DL2	OK	0	0	OK
11	1	DL2	DL1	OK+	0	0	OK
	2	0	0	OK	0	0	OK
	3	DL1	DL1	OK	DL1	DL1	OK
	4	DL2	DL2	OK	DL1	DL2	NOT OK
	5	DL1	DL2	NOT OK	0	0	OK
12	1	DL2	DL2	OK	0	0	OK
	2	0	0	OK	DL1	0	OK+
	3	DL2	DL2	OK	DL1	DL2	NOT OK
	4	DL2	SD	NOT OK	DL2	DL2	OK
	5	DL2	DL2	OK	DL1	0	OK+



This project has received funding from the European Union's Horizon 2020 research and innovation programme under grant agreement No. 700748

A.2 APPENDICES TO CHAPTER 3 - SECTION 3.2

The appendices **A-4.1** and **A-4.2** contain graphs of all fragility curves for traffic embankments, generated within WP 3 of LIQUEFACT project.

The titles of the following graphs use the following notation: **H-B-_C-L-_L**

- H – embankment height [m],
- B – crest width [m],
- C – thickness of crust layer [m],
- L – thickness of liquefiable (sandy-silty) layer [m],
- MD or L – medium dense or loose density state of the liquefiable layer

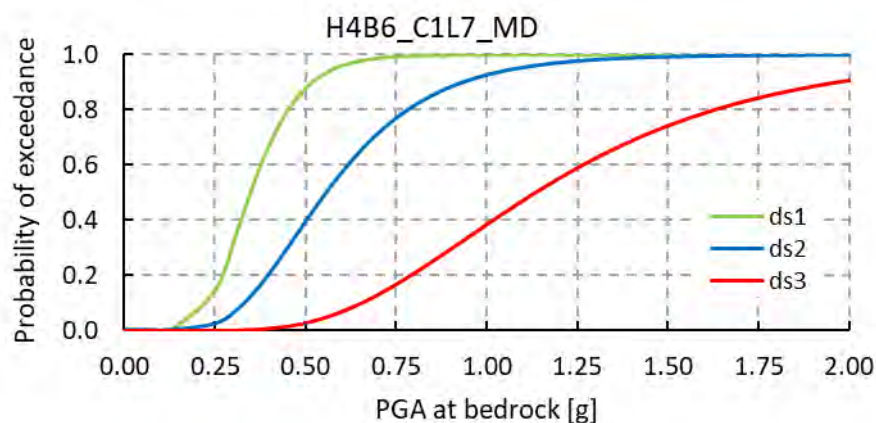
Mean threshold values (presented in bold) of the permanent ground deformations for given damage state of traffic embankments from **Table A-6** were used for the derivation of the fragility curves below.

Table A-6: Damage states for traffic embankments (SYNER-G, 2013).

Road embankments				Railway embankments			
Damage state	Permanent vertical ground displacement [m]			Damage state	Permanent vertical ground displacement [m]		
	min	max	mean		min	max	mean
ds1 – minor	0.02	0.08	0.05	ds1 – minor	0.01	0.05	0.03
ds2 – moderate	0.08	0.22	0.15	ds2 – moderate	0.05	0.10	0.08
ds3 – extensive	0.22	0.58	0.40	ds3 – extensive	0.10	0.30	0.20

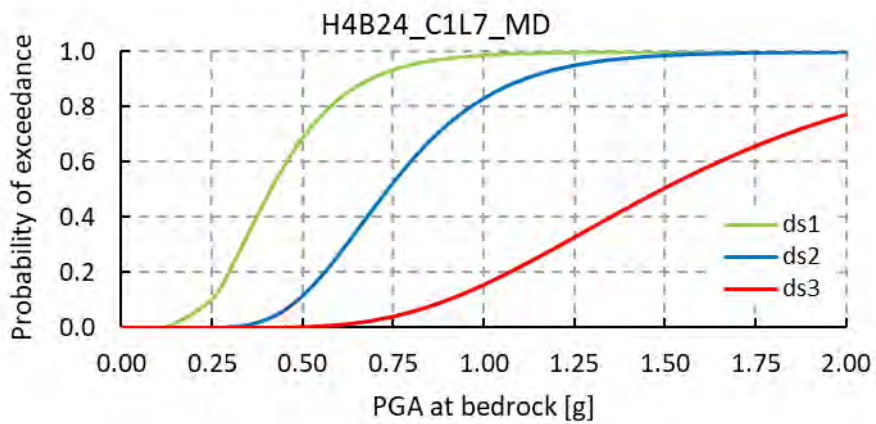
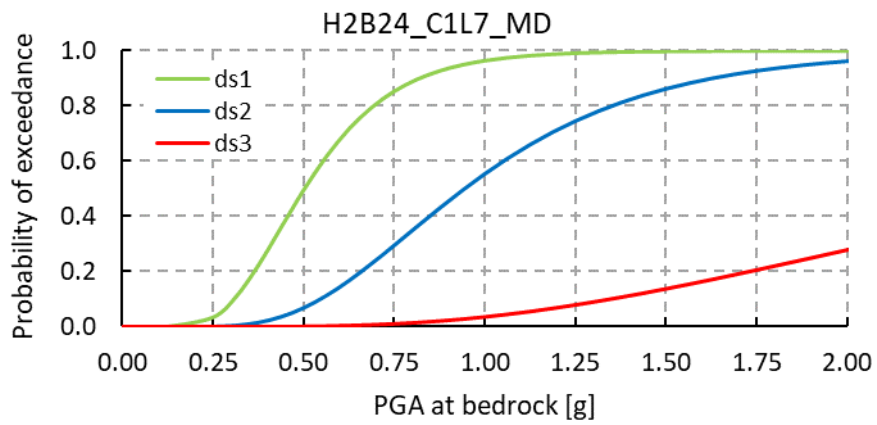
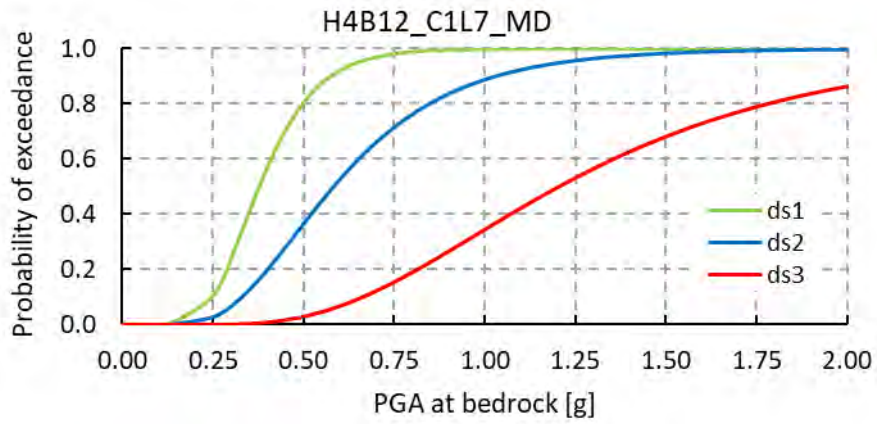
A-2.1 PROPOSED FRAGILITY CURVES TRAFFIC EMBANKMENTS WITH PGA AS INTENSITY

A-2.1.1 Road embankments



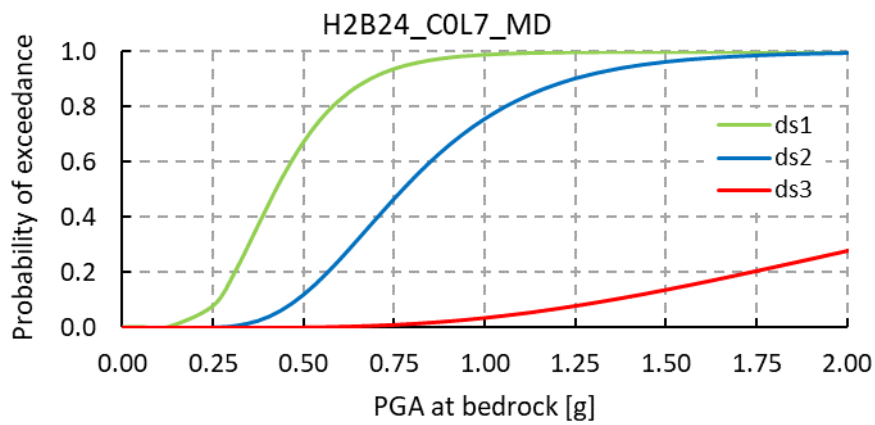
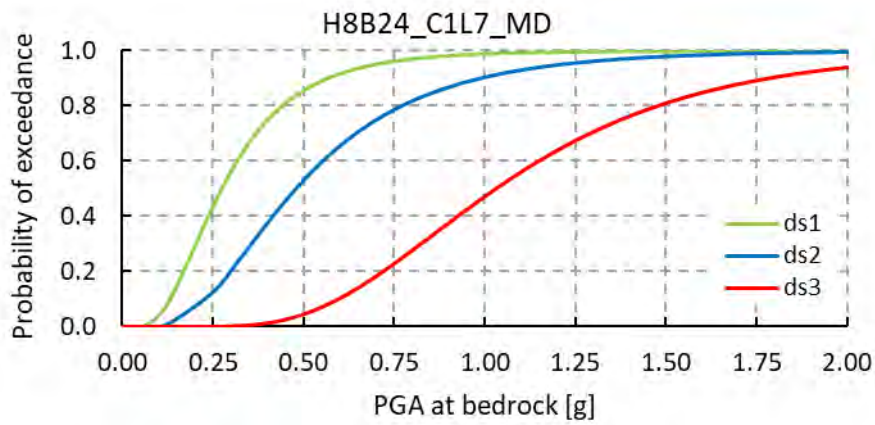
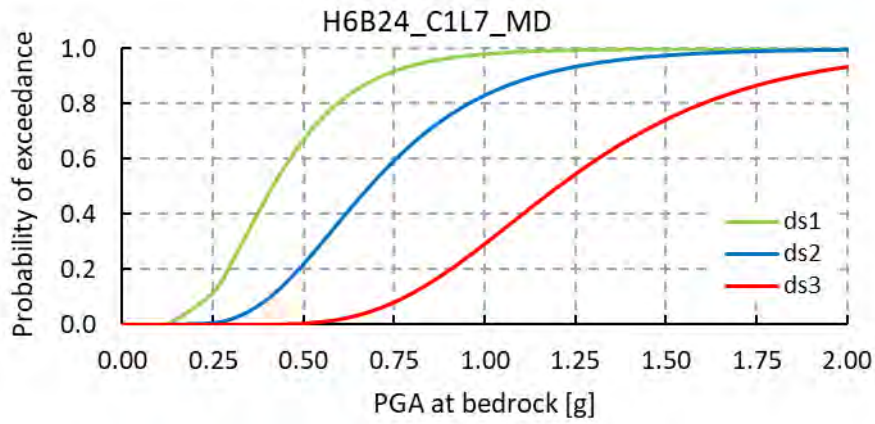


This project has received funding from the European Union's Horizon 2020 research and innovation programme under grant agreement No. 700748



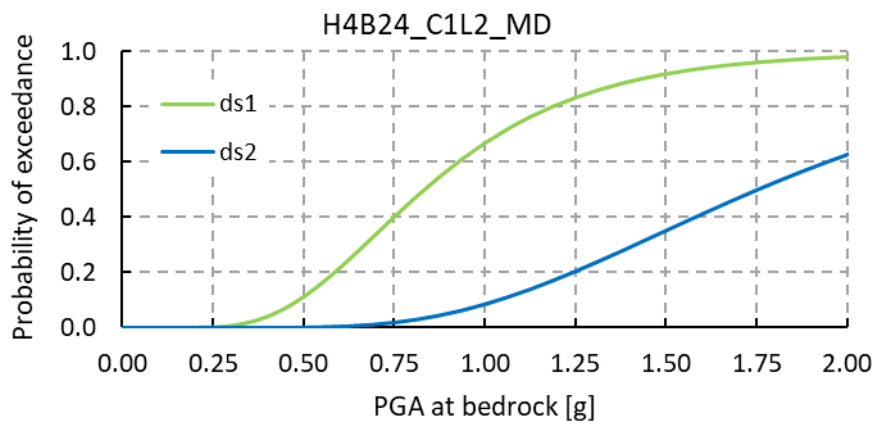
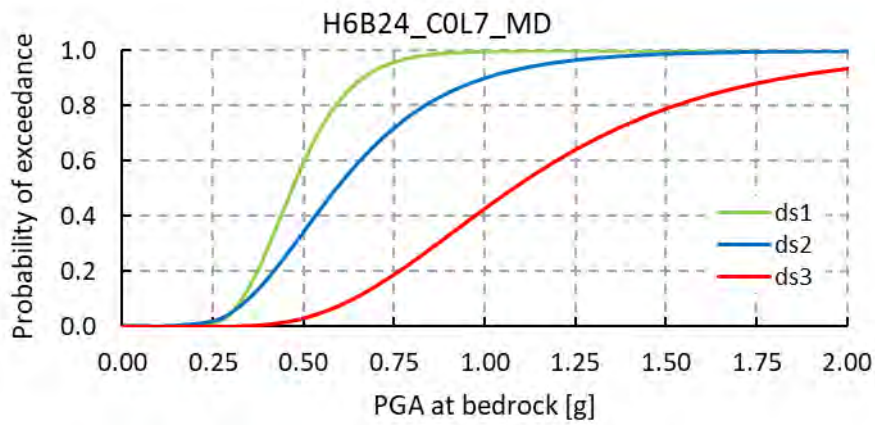
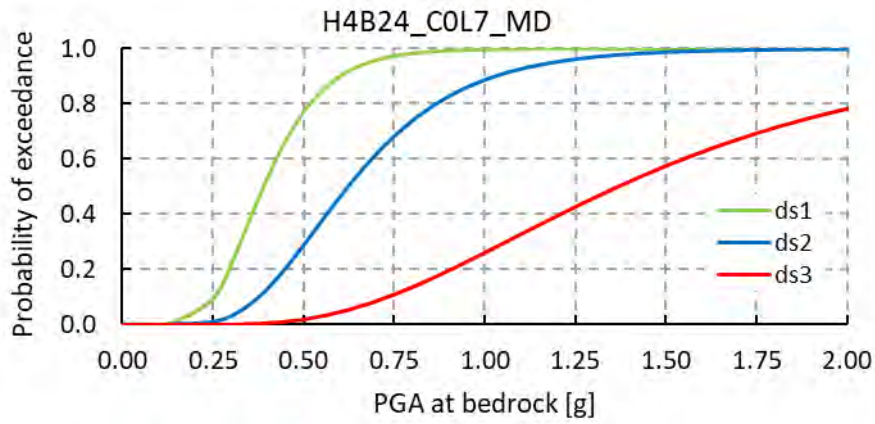


This project has received funding from the European Union's Horizon 2020 research and innovation programme under grant agreement No. 700748



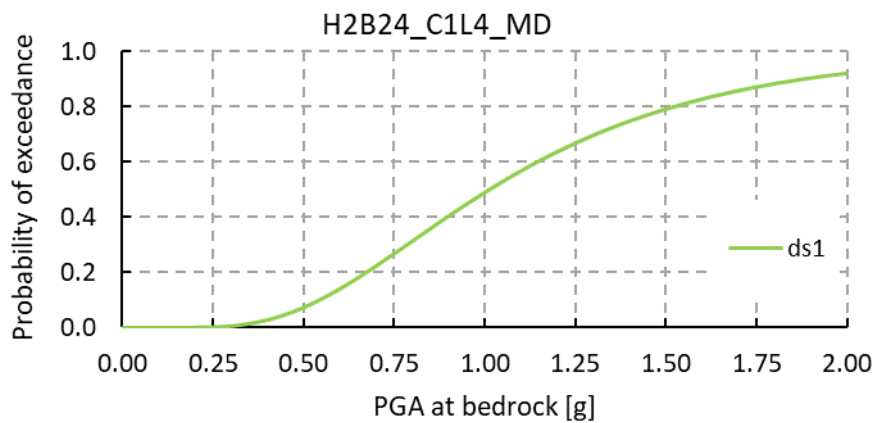
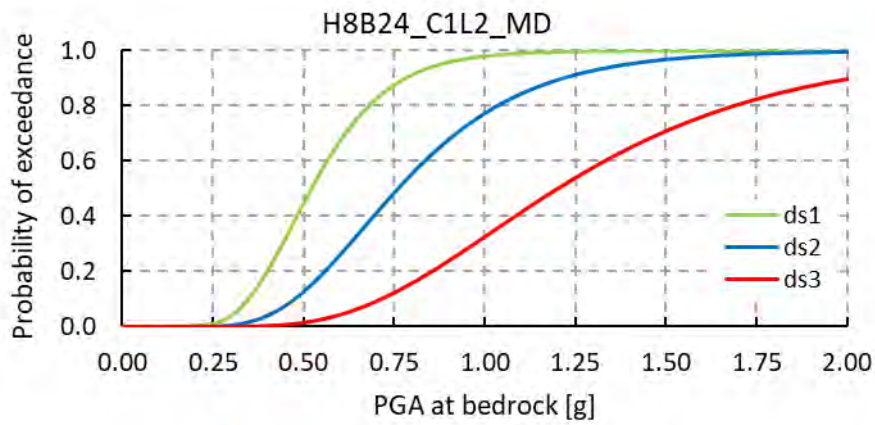
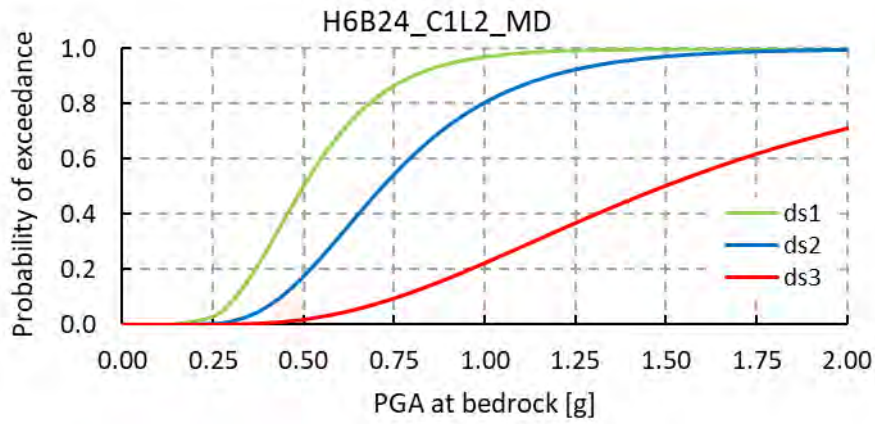


This project has received funding from the European Union's Horizon 2020 research and innovation programme under grant agreement No. 700748



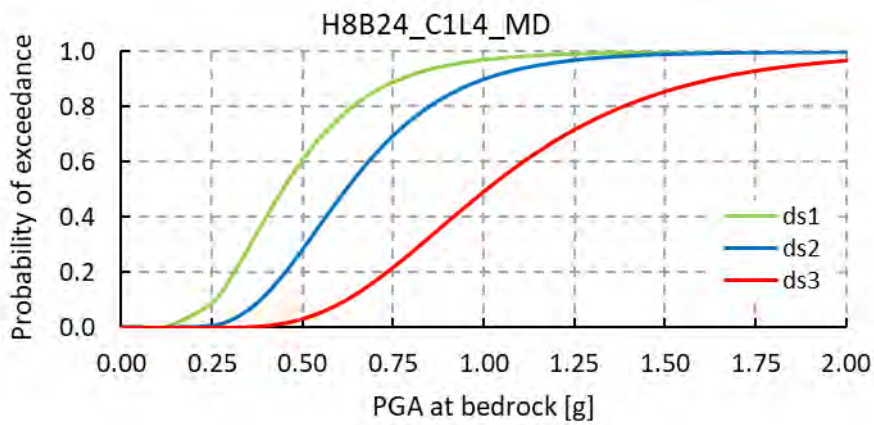
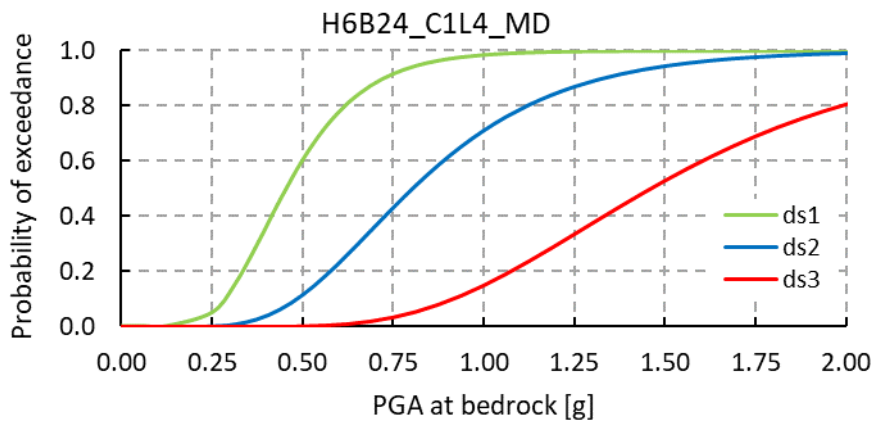
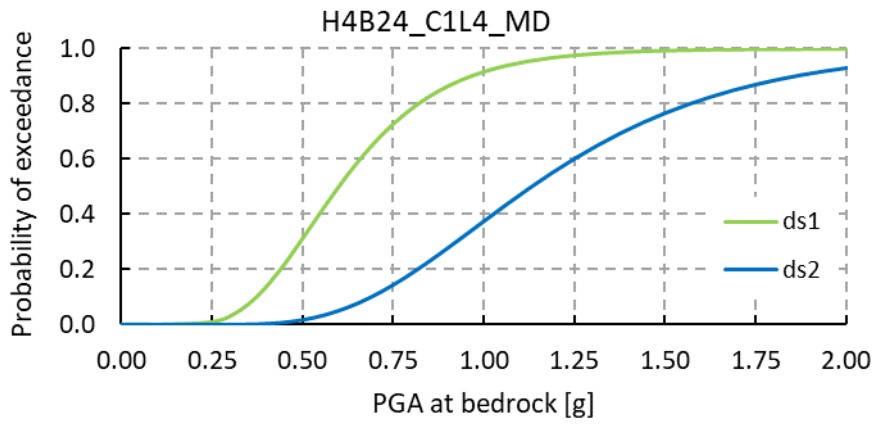


This project has received funding from the European Union's Horizon 2020 research and innovation programme under grant agreement No. 700748





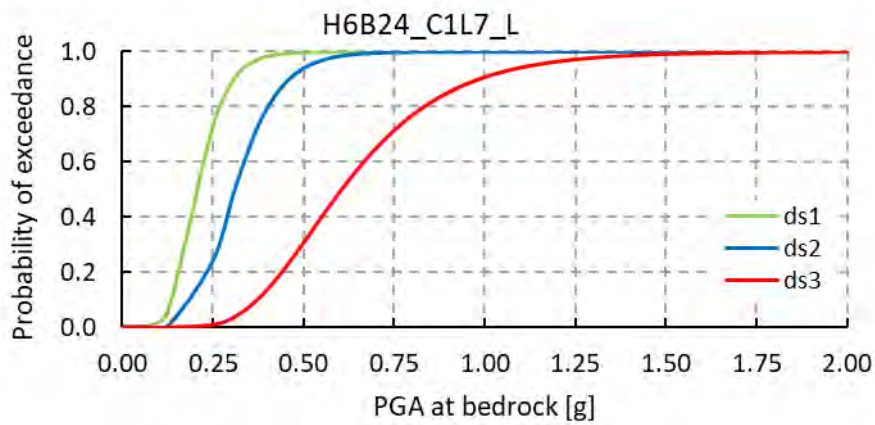
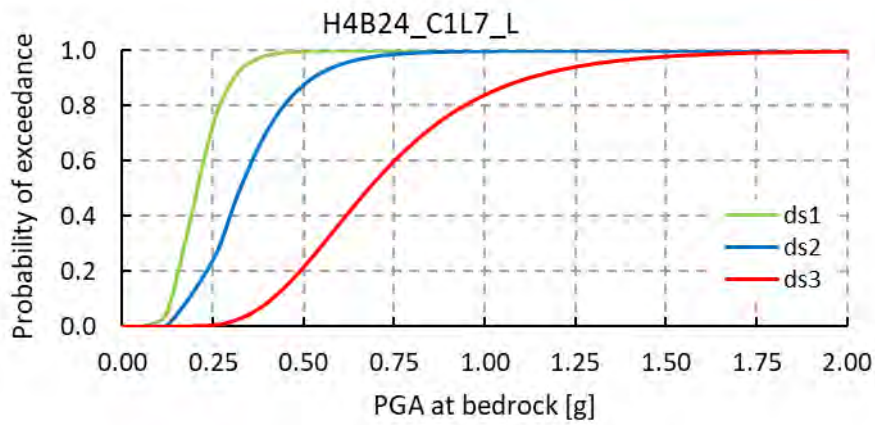
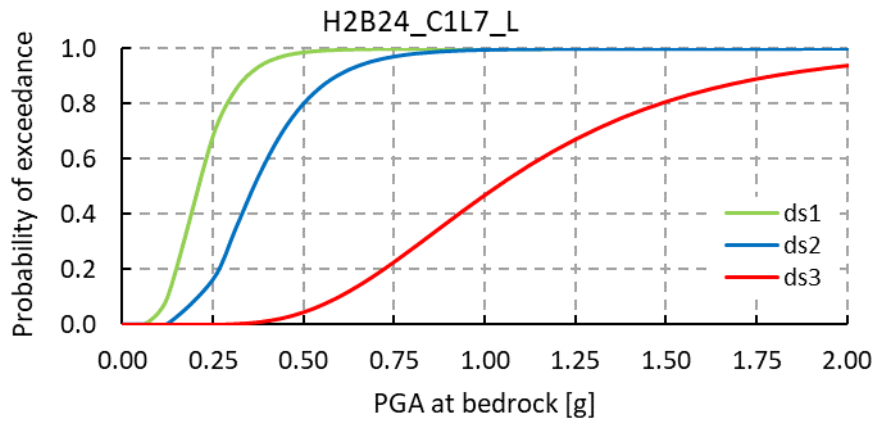
This project has received funding from the European Union's Horizon 2020 research and innovation programme under grant agreement No. 700748





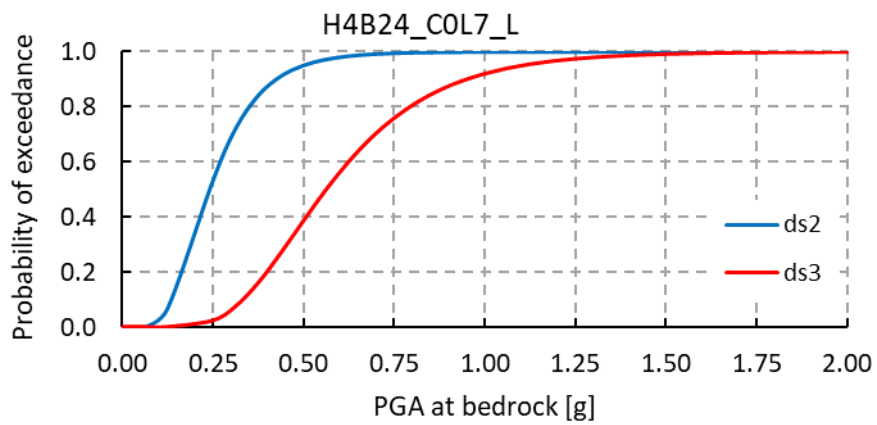
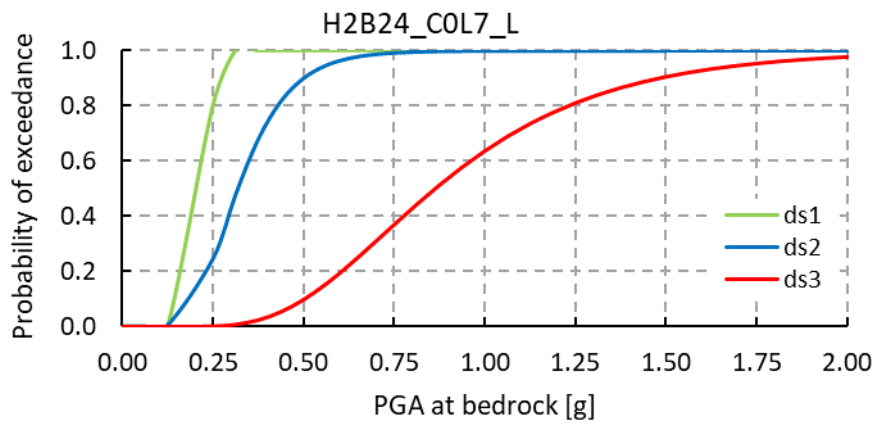
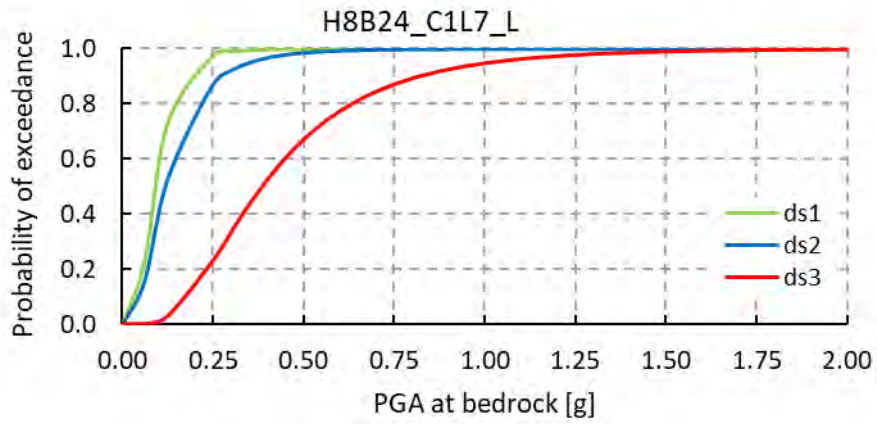
This project has received funding from the European Union's Horizon 2020 research and innovation programme under grant agreement No. 700748

Methodology for the liquefaction fragility analysis of critical structures and infrastructures: description and case studies





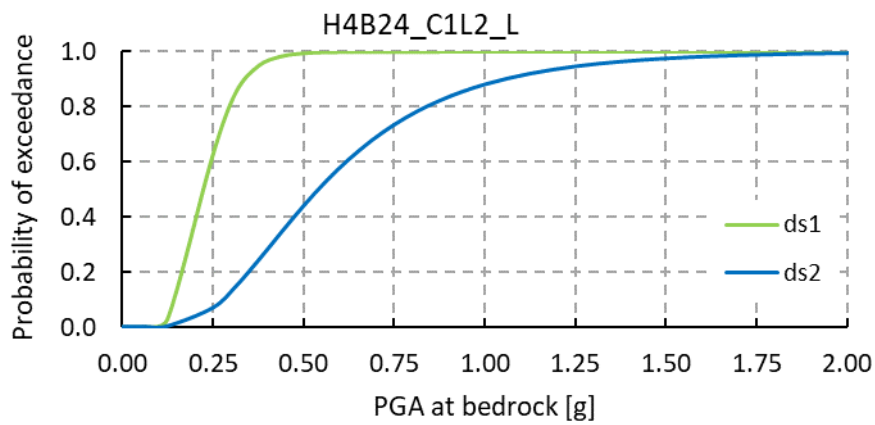
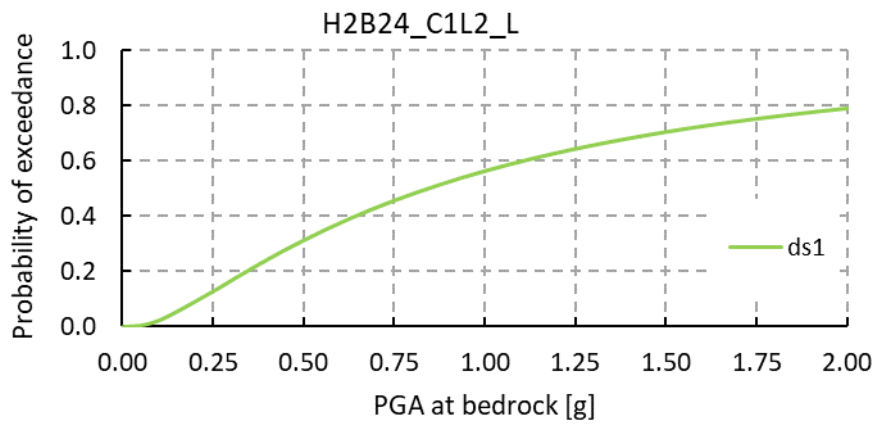
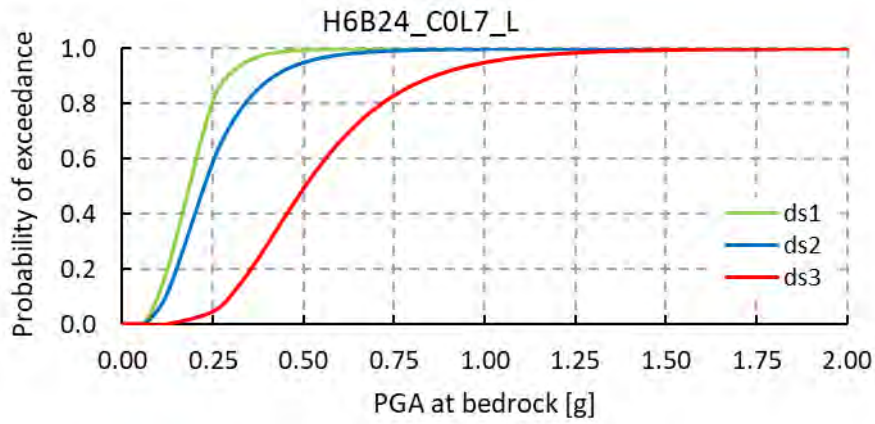
This project has received funding from the European Union's Horizon 2020 research and innovation programme under grant agreement No. 700748





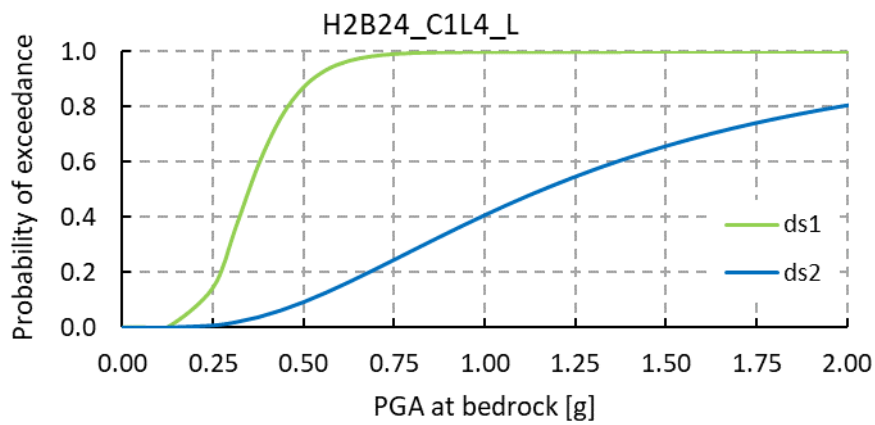
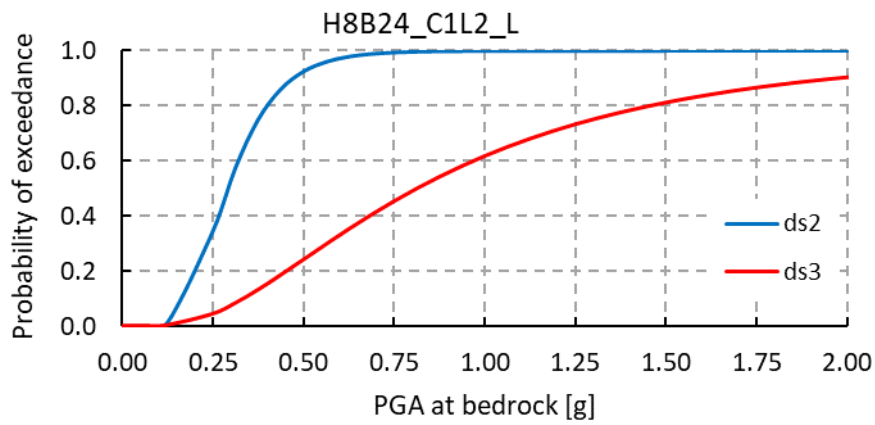
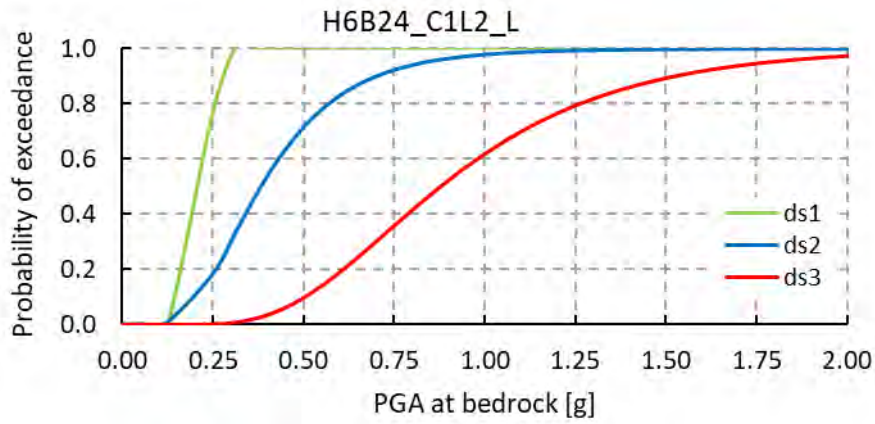
This project has received funding from the European Union's Horizon 2020 research and innovation programme under grant agreement No. 700748

Methodology for the liquefaction fragility analysis of critical structures and infrastructures: description and case studies



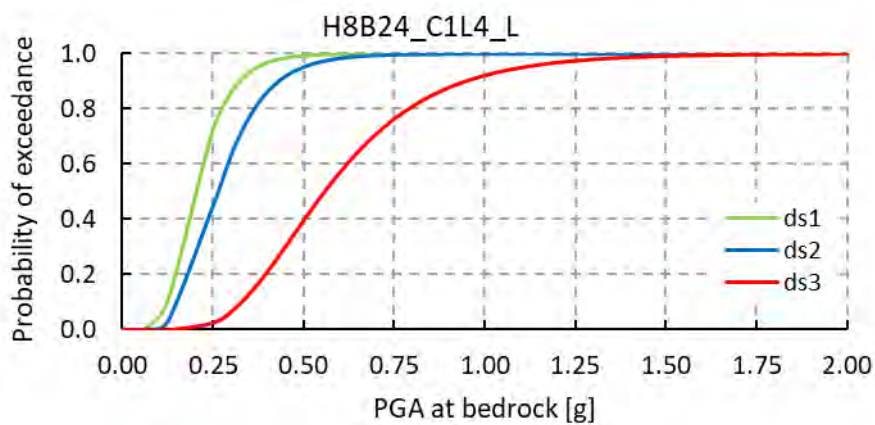
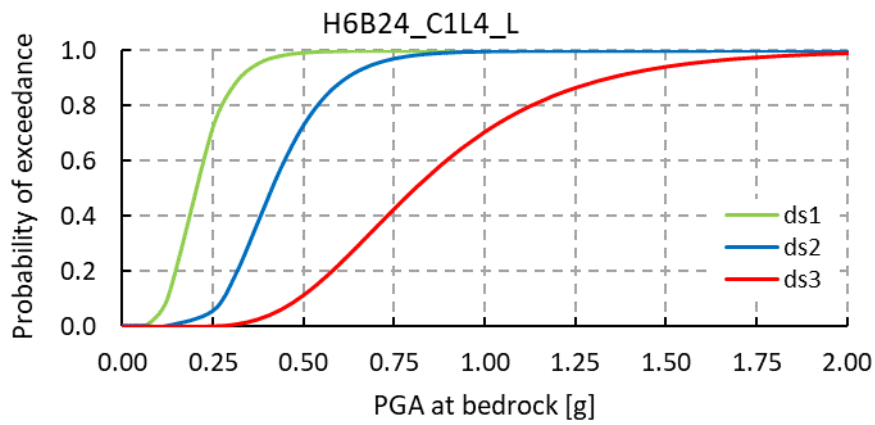
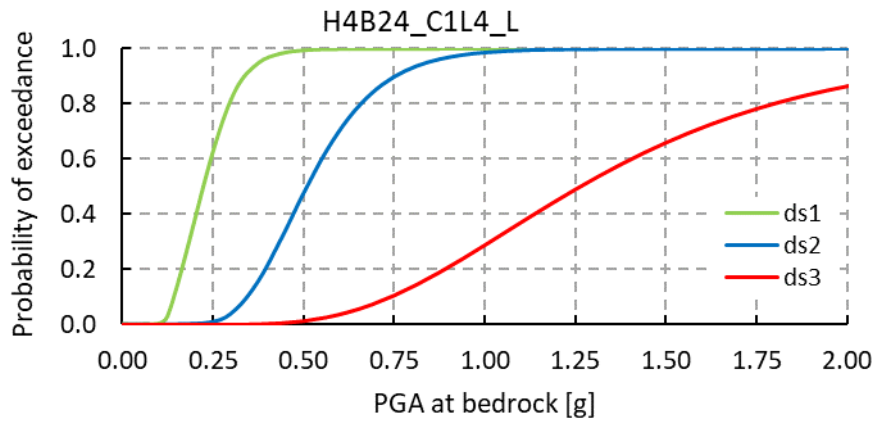


This project has received funding from the European Union's Horizon 2020 research and innovation programme under grant agreement No. 700748





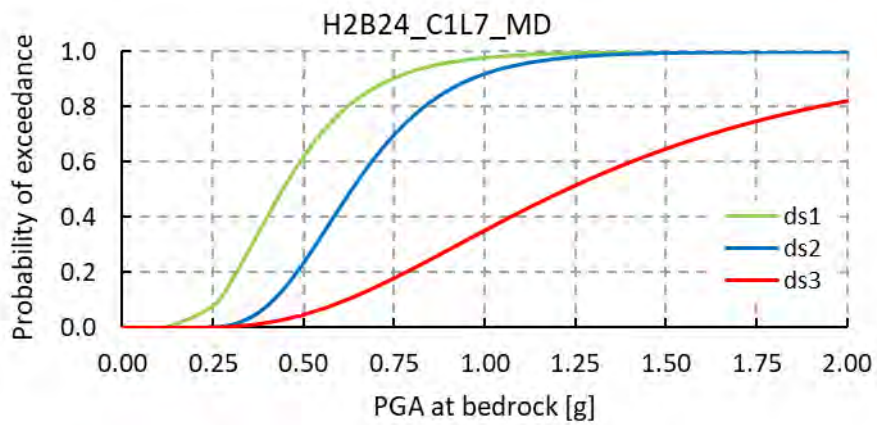
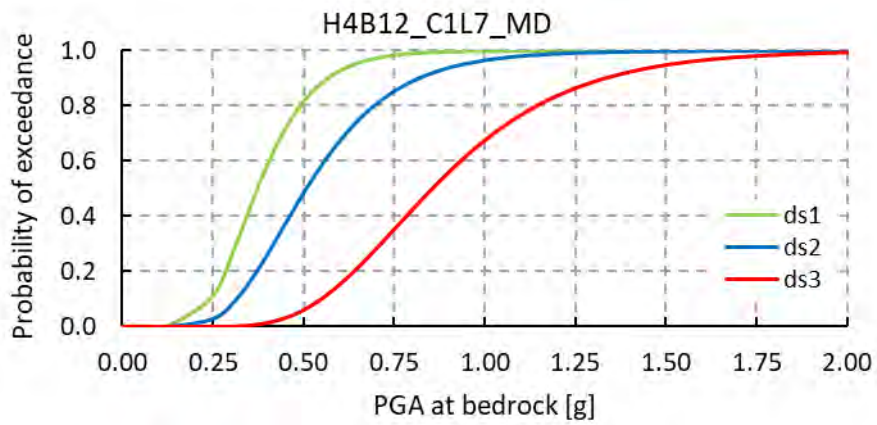
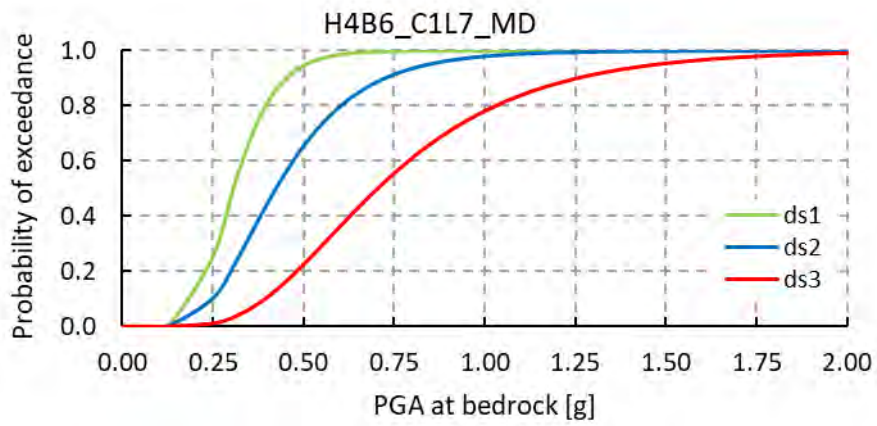
This project has received funding from the European Union's Horizon 2020 research and innovation programme under grant agreement No. 700748



Railway embankments

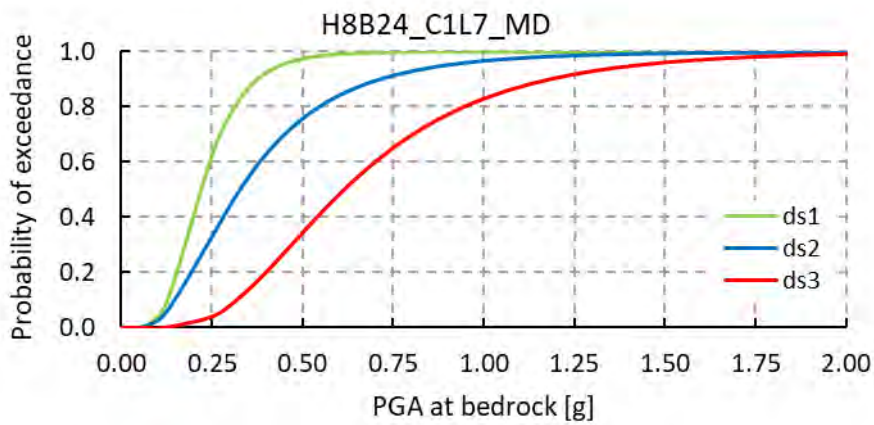
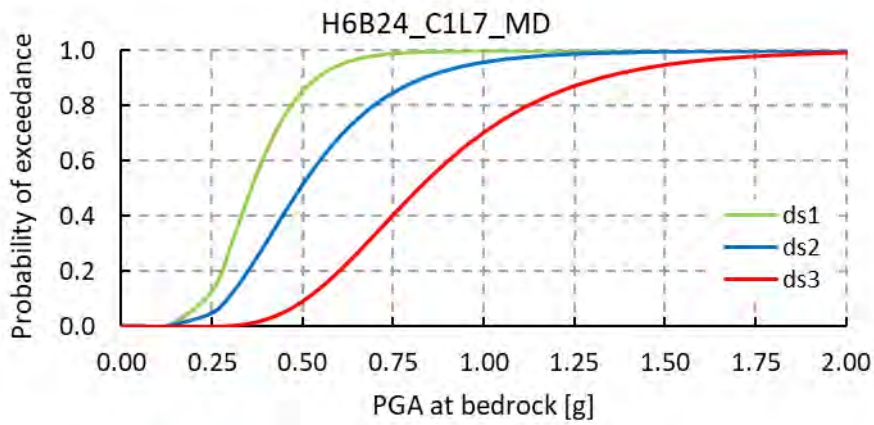
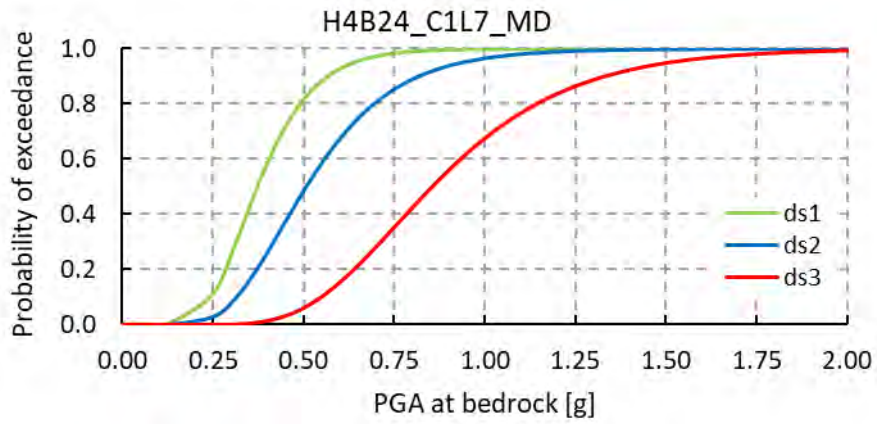


This project has received funding from the European Union's Horizon 2020 research and innovation programme under grant agreement No. 700748



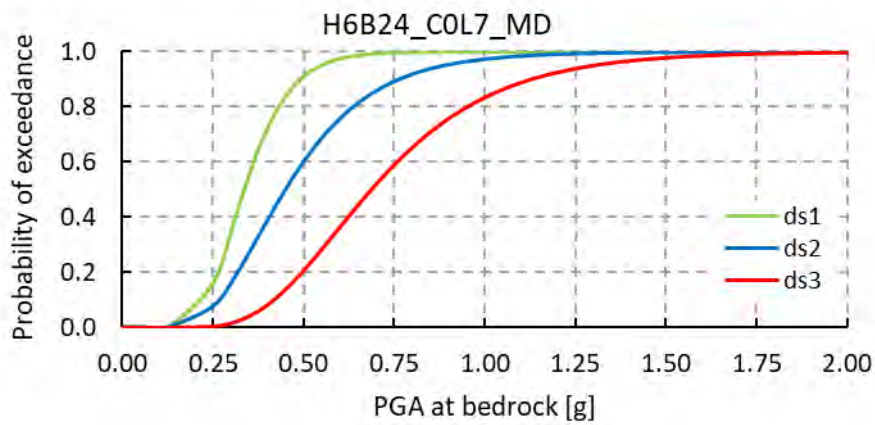
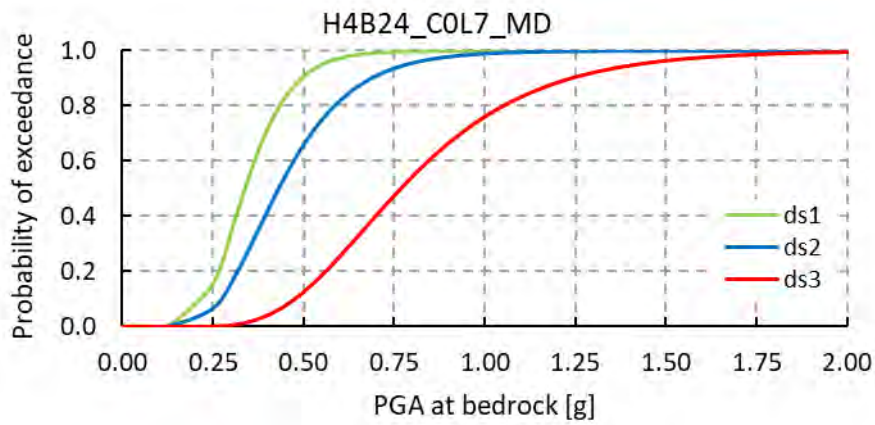
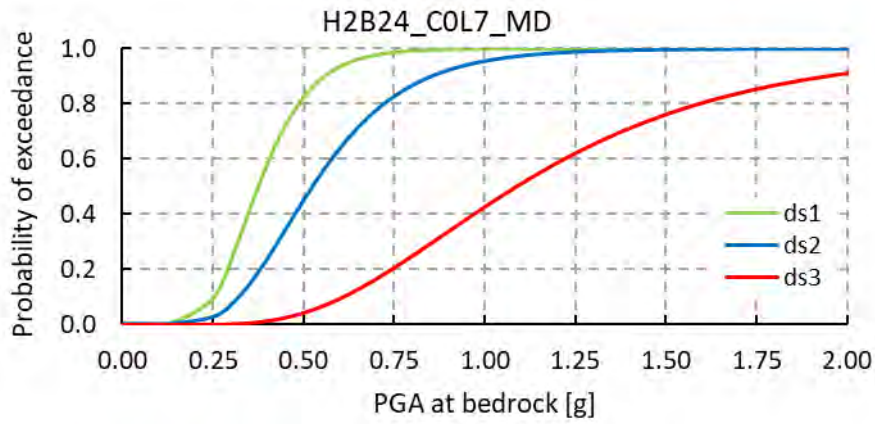


This project has received funding from the European Union's Horizon 2020 research and innovation programme under grant agreement No. 700748



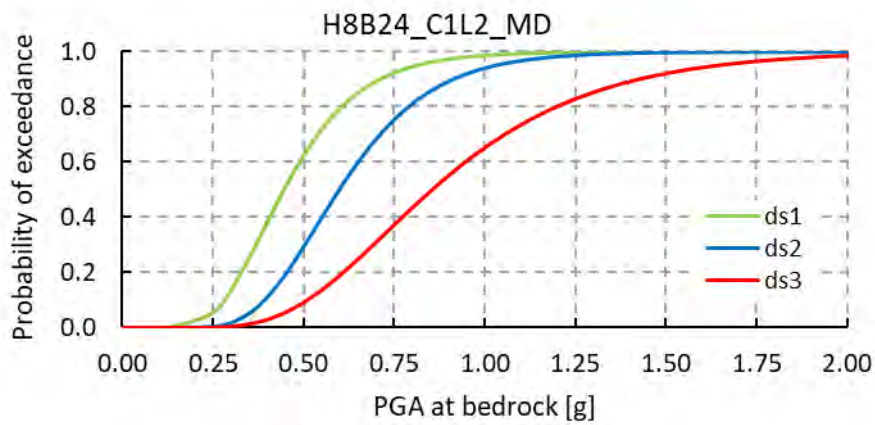
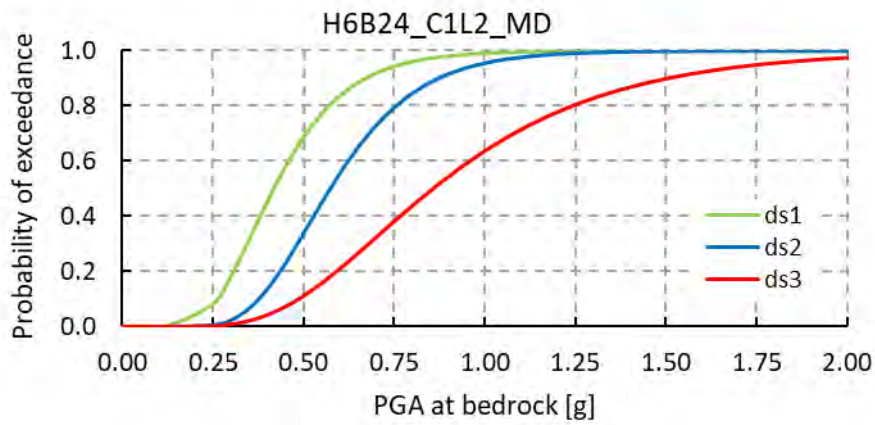
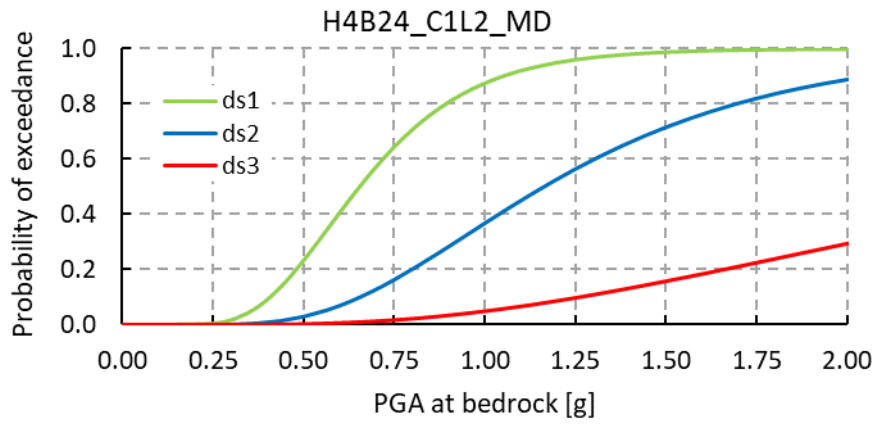


This project has received funding from the European Union's Horizon 2020 research and innovation programme under grant agreement No. 700748



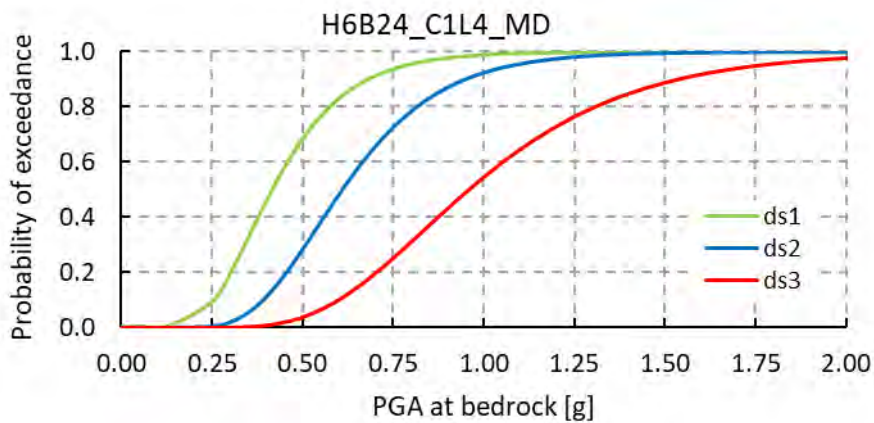
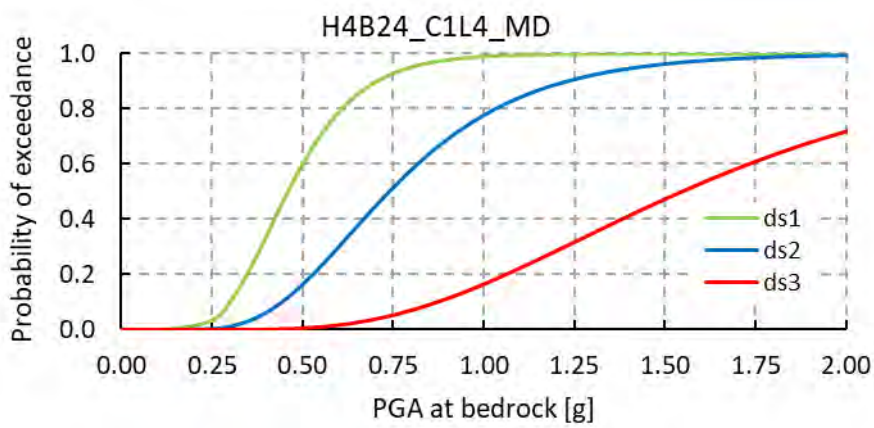
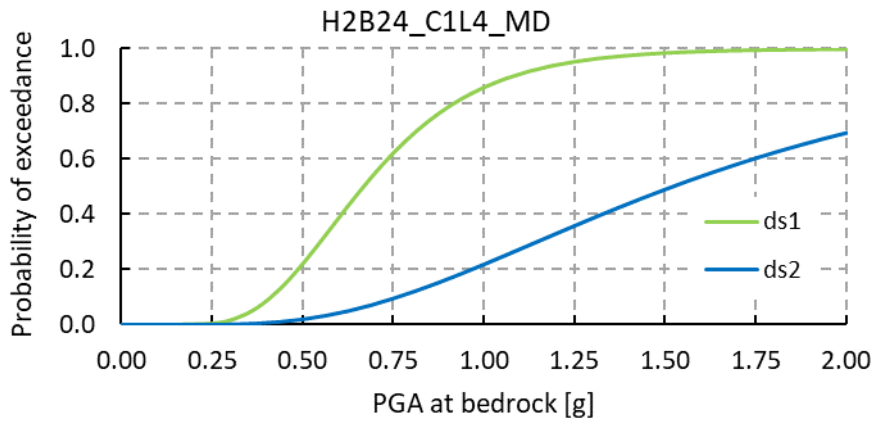


This project has received funding from the European Union's Horizon 2020 research and innovation programme under grant agreement No. 700748



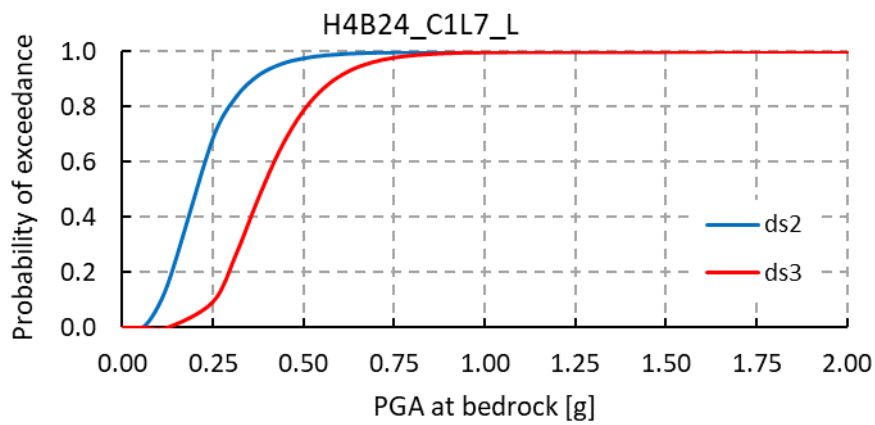
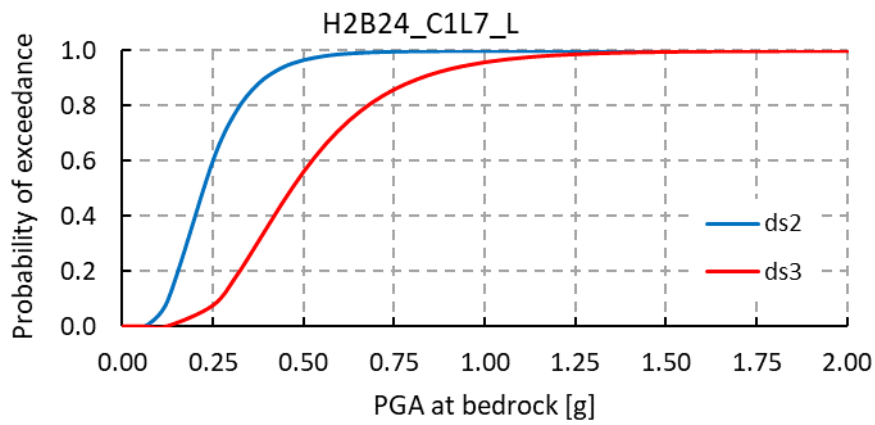
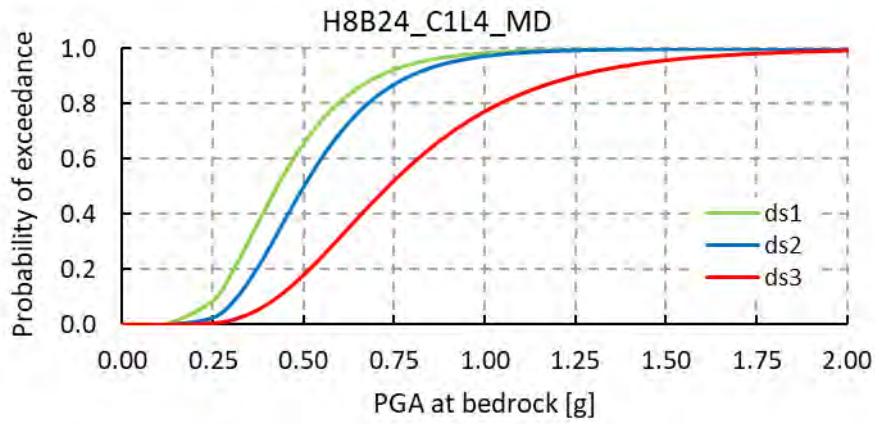


This project has received funding from the European Union's Horizon 2020 research and innovation programme under grant agreement No. 700748





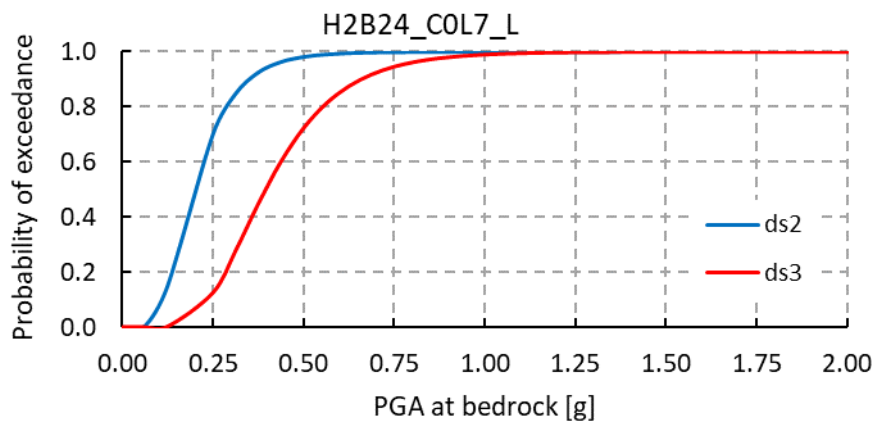
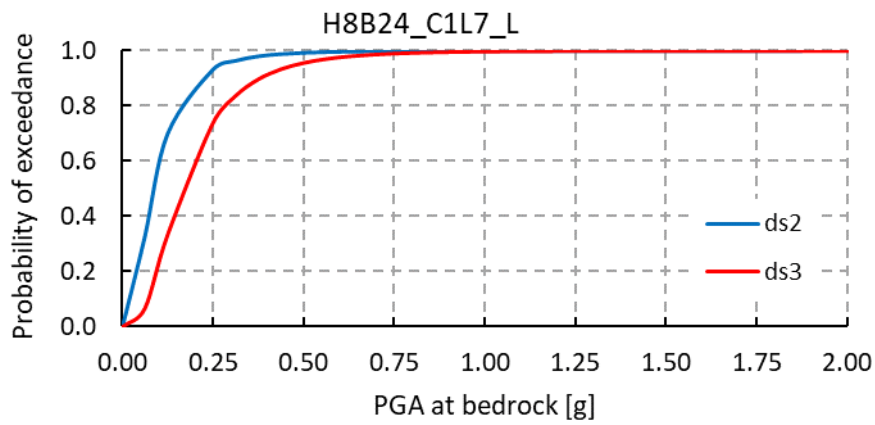
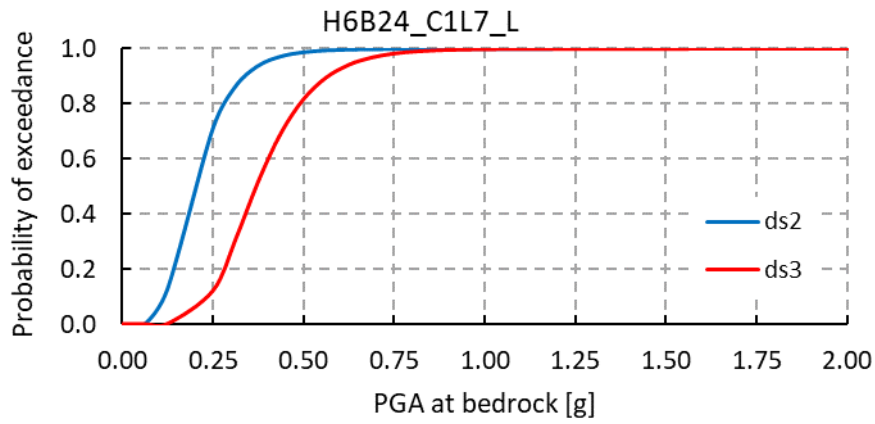
This project has received funding from the European Union's Horizon 2020 research and innovation programme under grant agreement No. 700748





This project has received funding from the European Union's Horizon 2020 research and innovation programme under grant agreement No. 700748

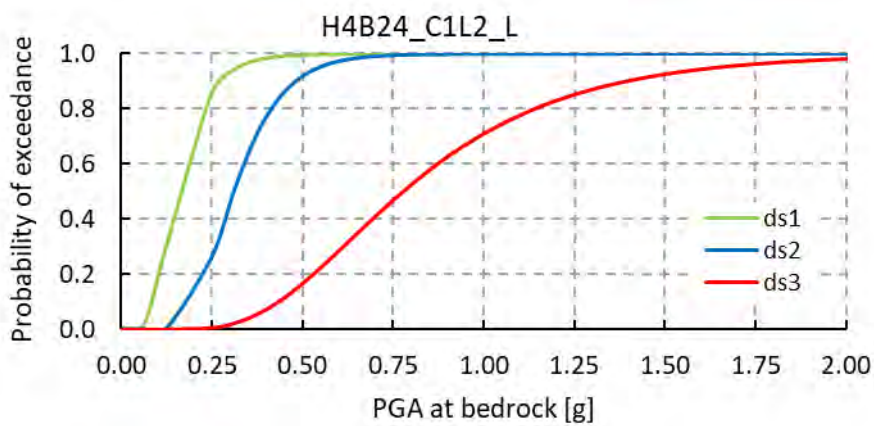
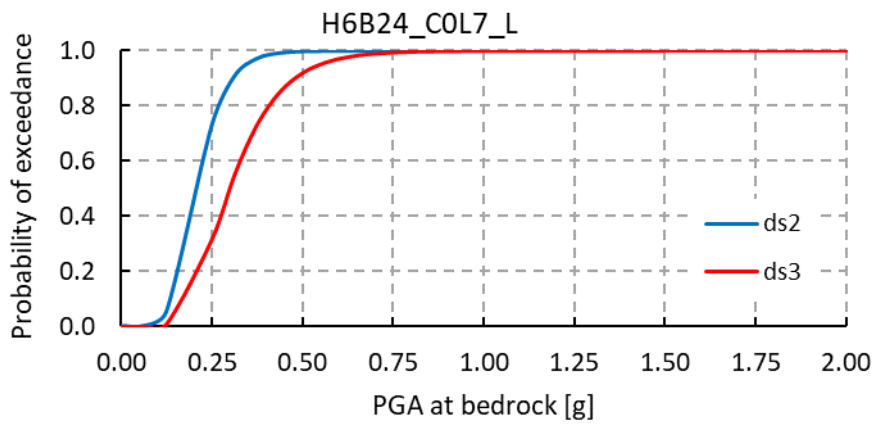
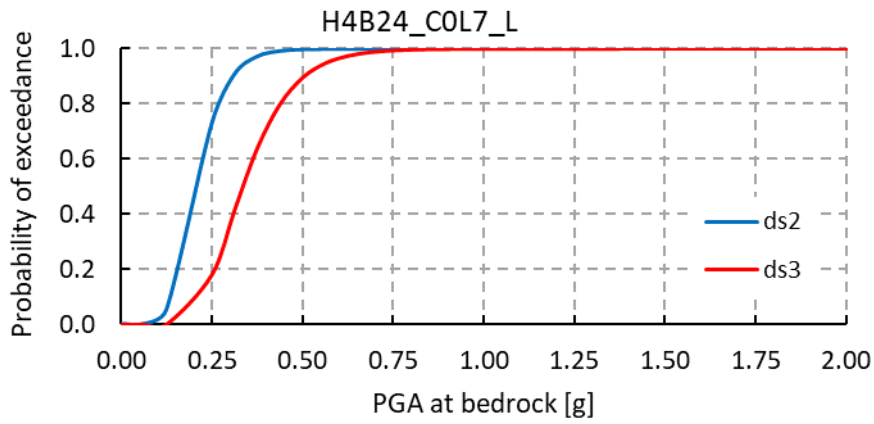
Methodology for the liquefaction fragility analysis of critical structures and infrastructures: description and case studies





This project has received funding from the European Union's Horizon 2020 research and innovation programme under grant agreement No. 700748

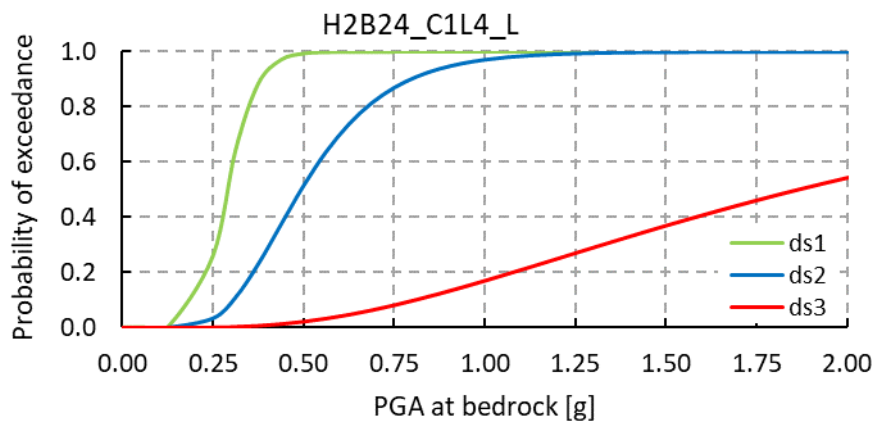
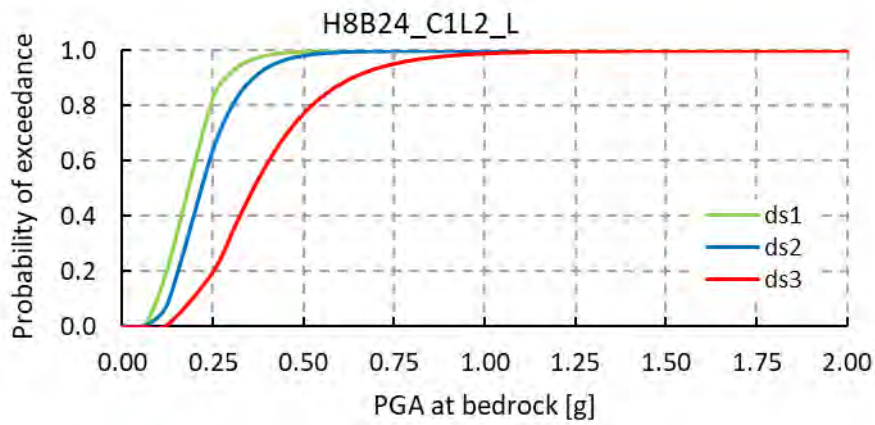
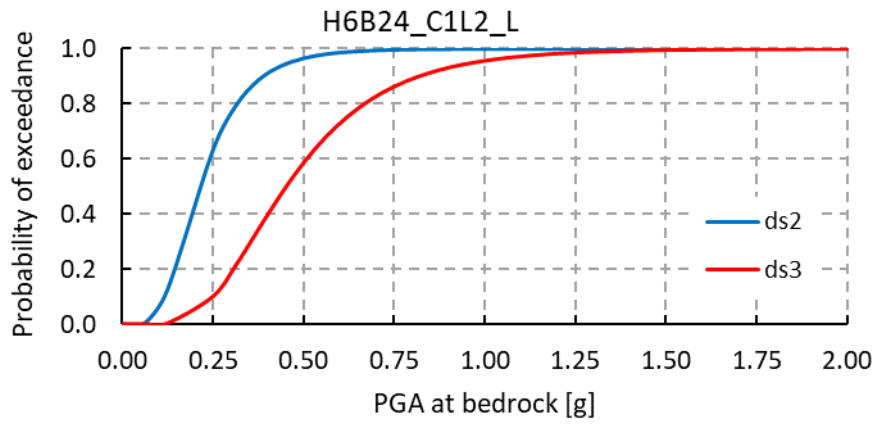
Methodology for the liquefaction fragility analysis of critical structures and infrastructures: description and case studies





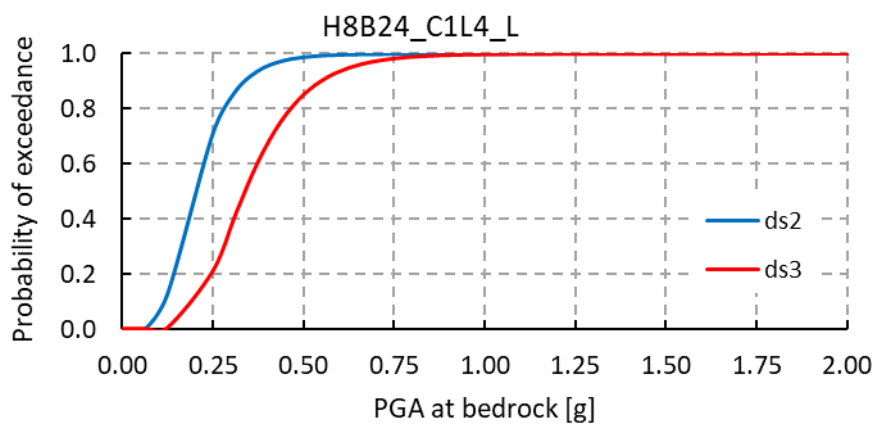
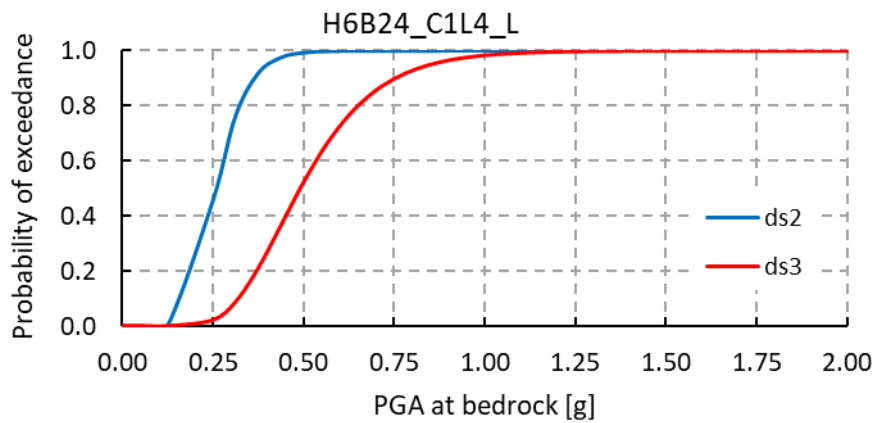
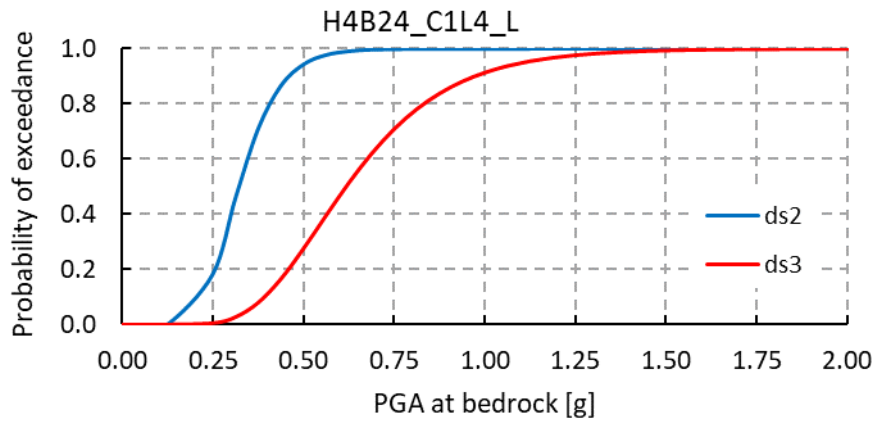
This project has received funding from the European Union's Horizon 2020 research and innovation programme under grant agreement No. 700748

Methodology for the liquefaction fragility analysis of critical structures and infrastructures: description and case studies





This project has received funding from the European Union's Horizon 2020 research and innovation programme under grant agreement No. 700748



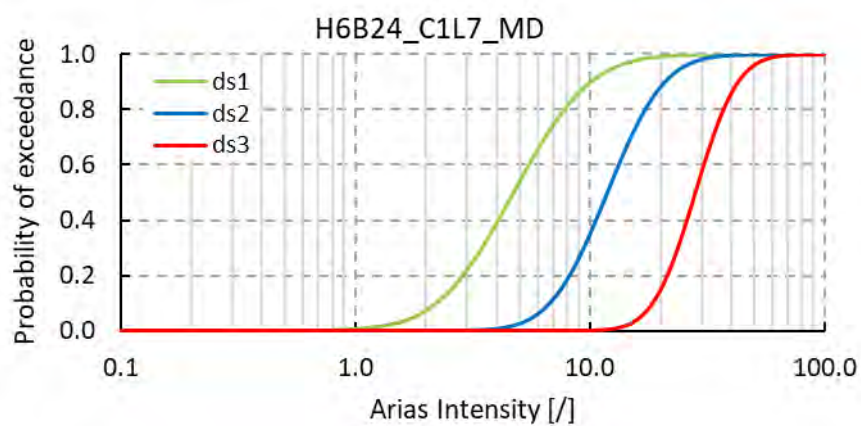
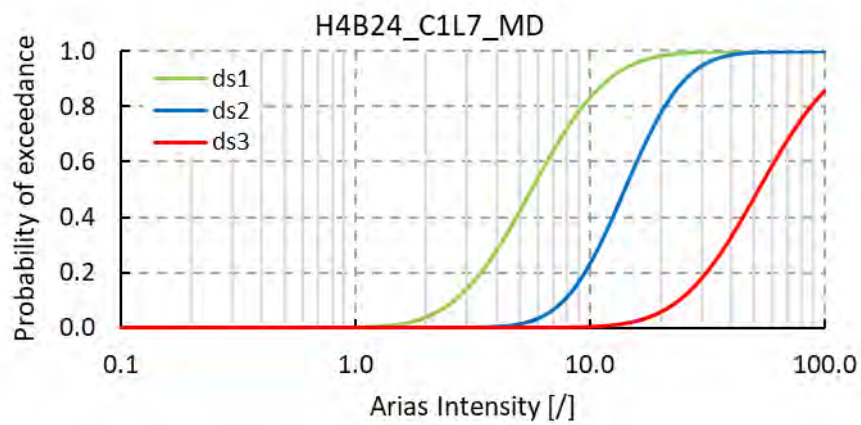
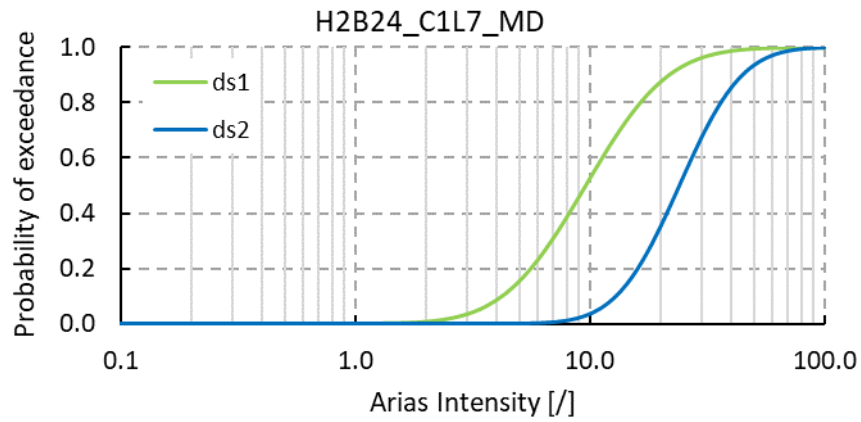
A-4.2 PROPOSED FRAGILITY CURVES TRAFFIC EMBANKMENTS WITH ARIAS INTENSITY AS INTENSITY MEASURE

For the purpose of better distinction, the logarithmic scale on the x axis is used in the graphs below.

Road embankments

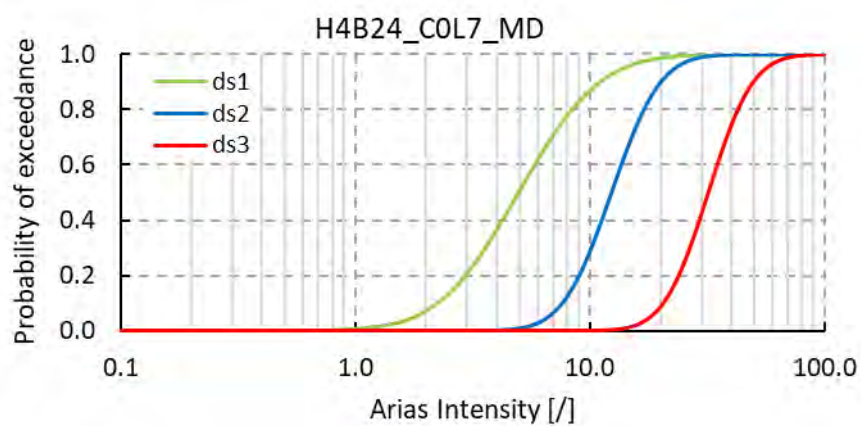
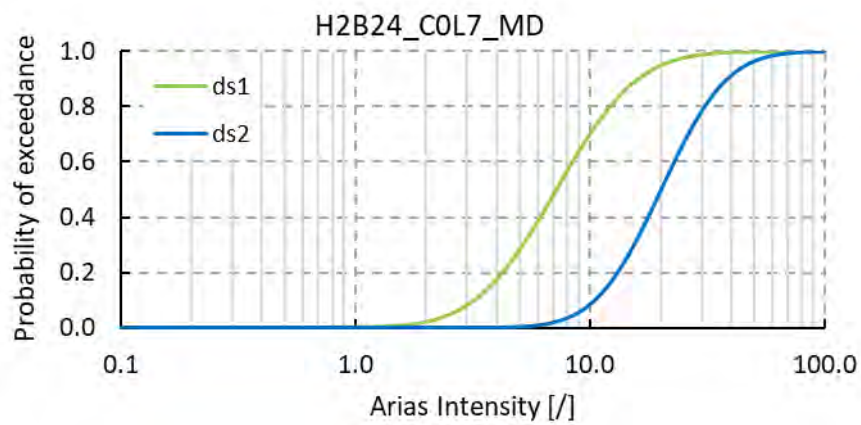
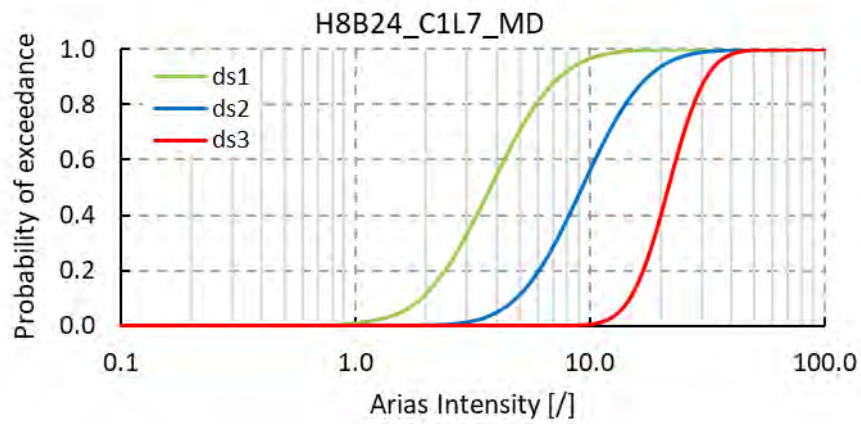


This project has received funding from the European Union's Horizon 2020 research and innovation programme under grant agreement No. 700748



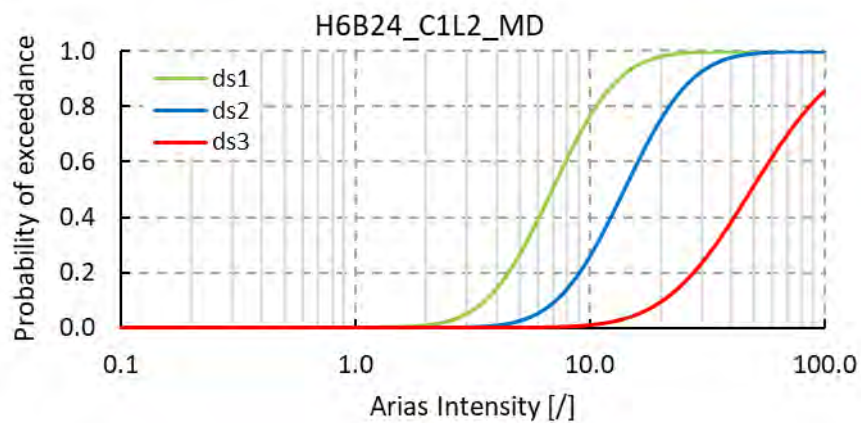
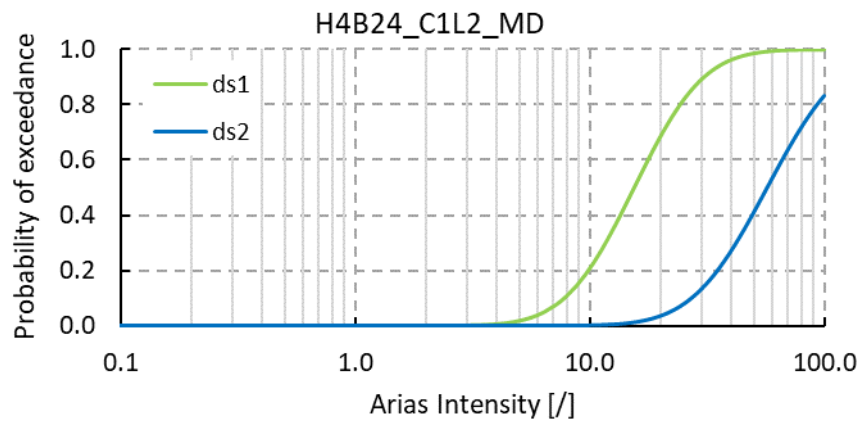
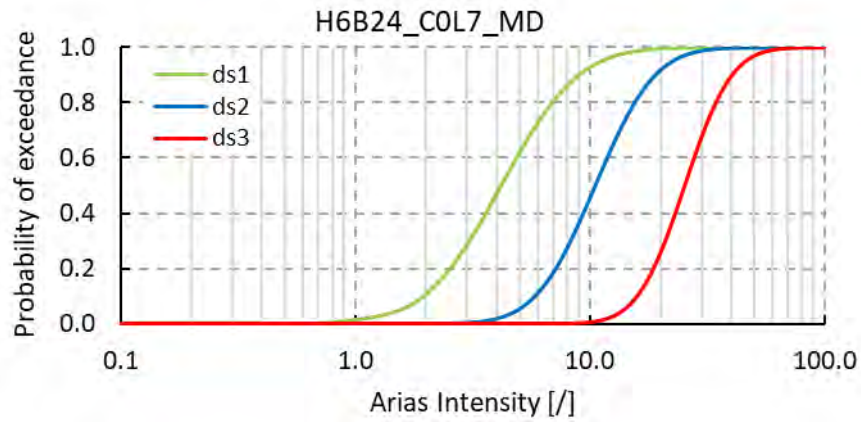


This project has received funding from the European Union's Horizon 2020 research and innovation programme under grant agreement No. 700748



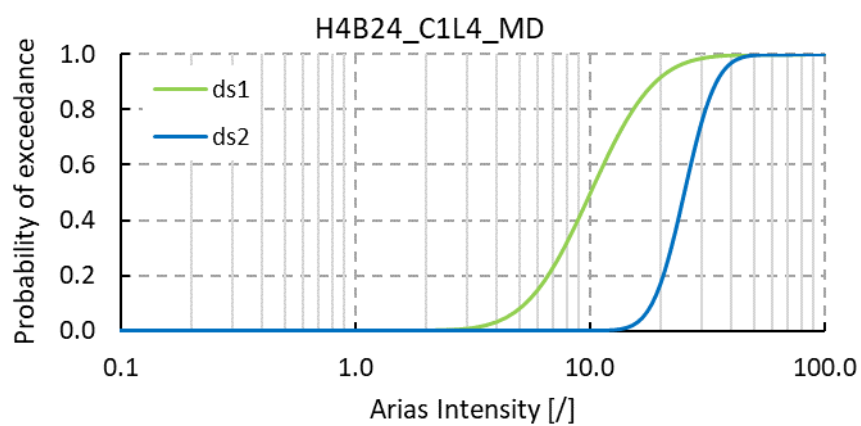
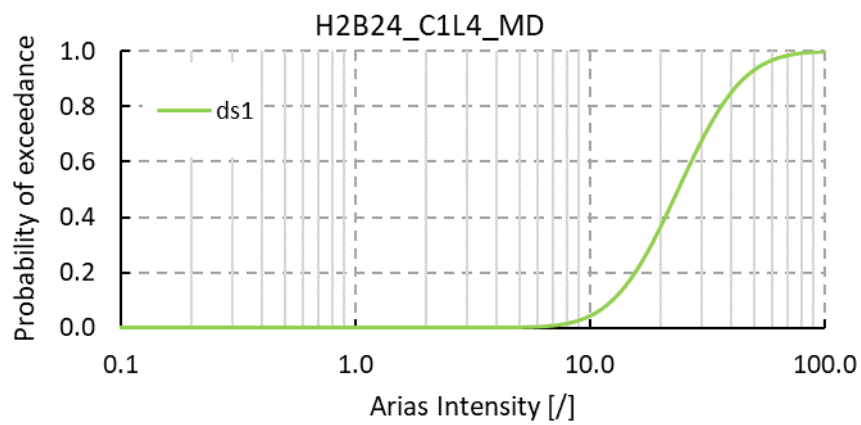
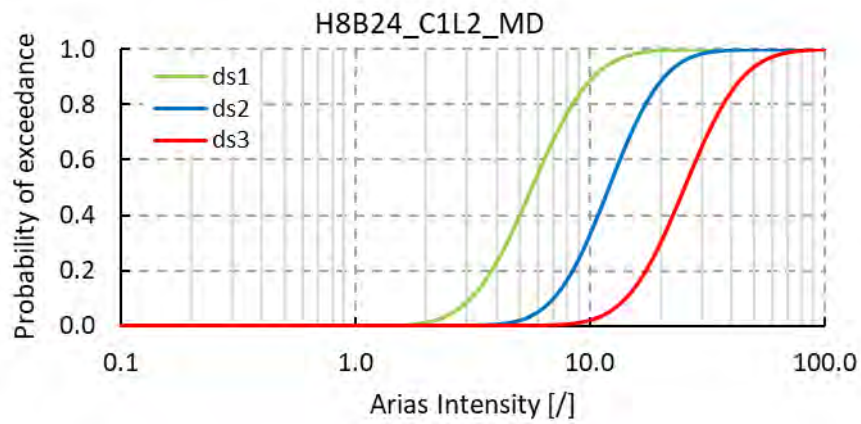


This project has received funding from the European Union's Horizon 2020 research and innovation programme under grant agreement No. 700748



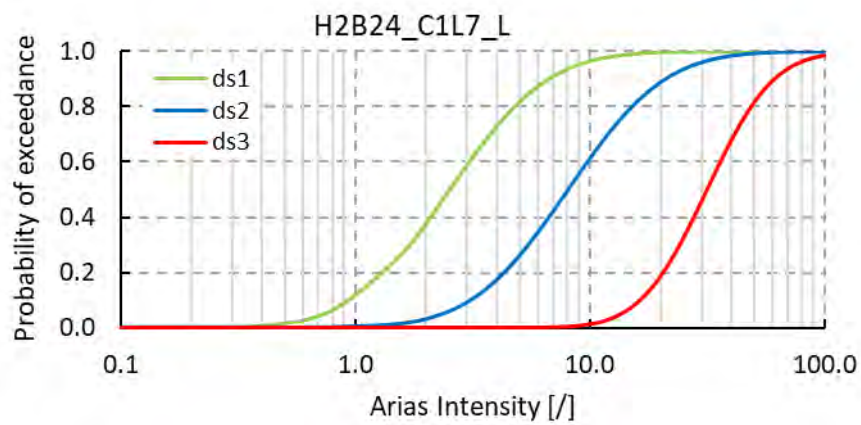
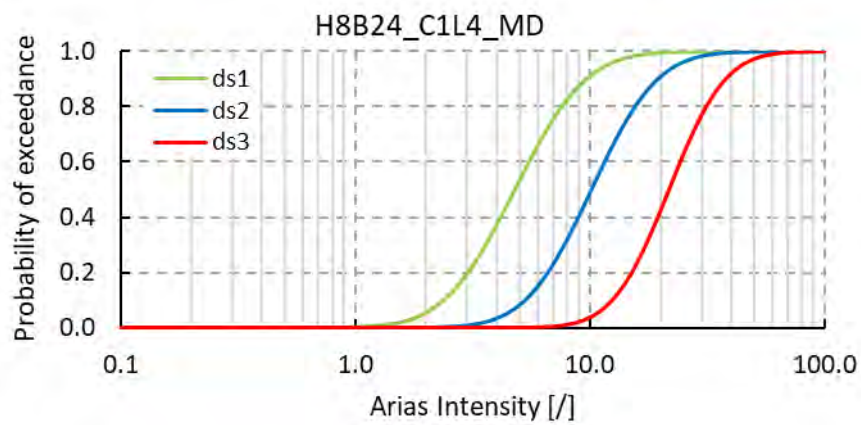
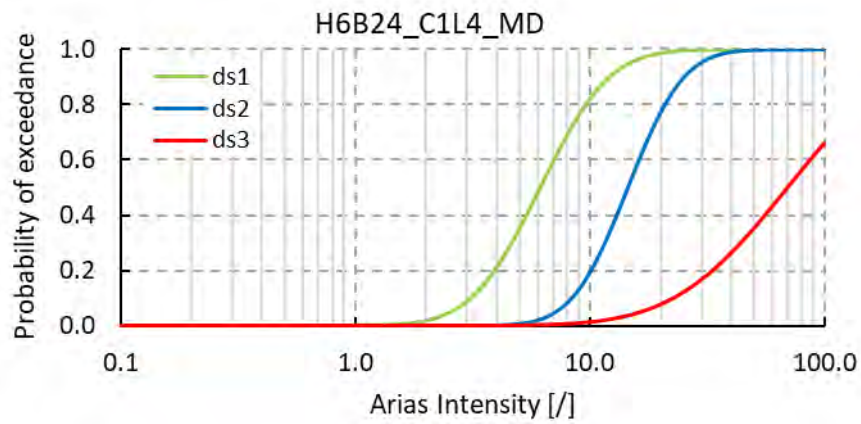


This project has received funding from the European Union's Horizon 2020 research and innovation programme under grant agreement No. 700748



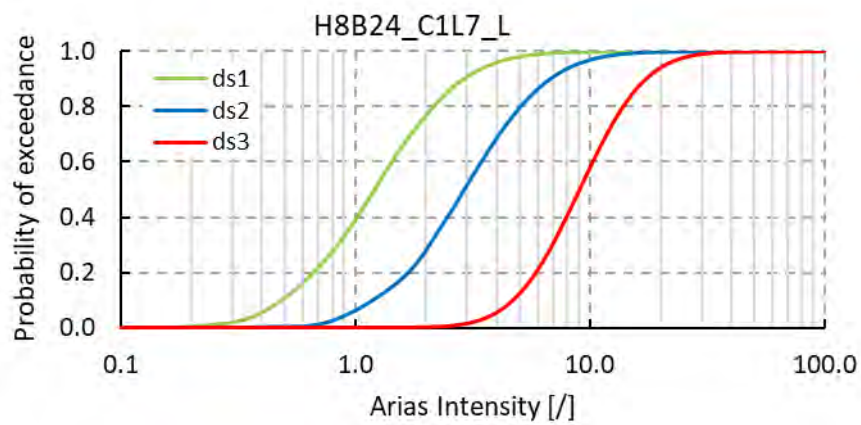
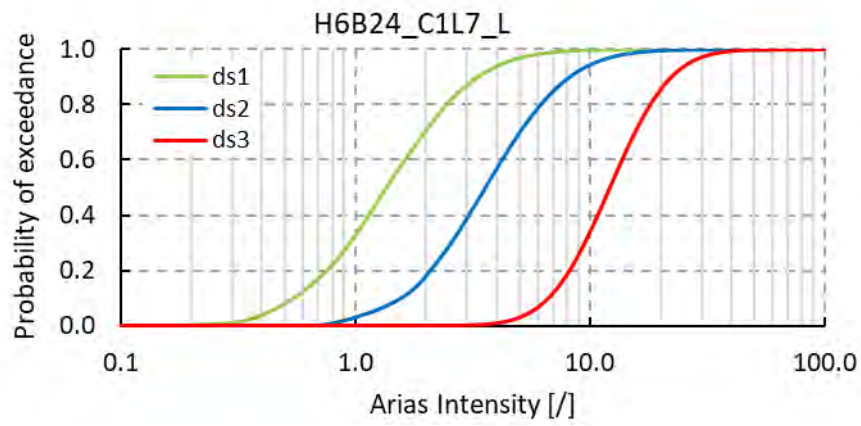
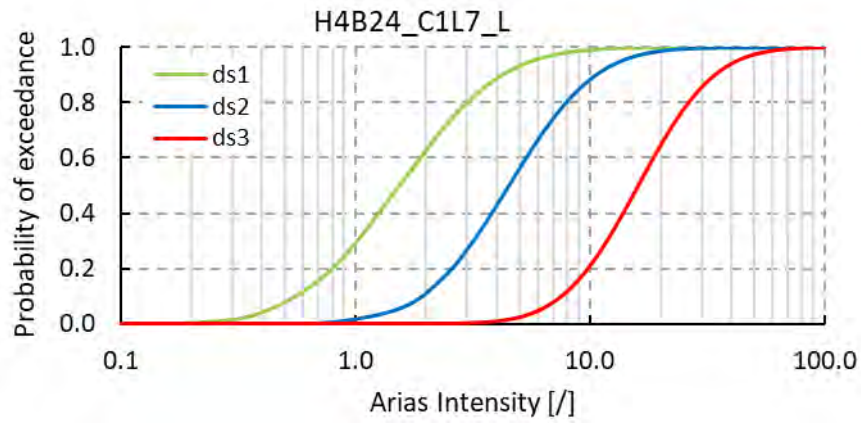


This project has received funding from the European Union's Horizon 2020 research and innovation programme under grant agreement No. 700748



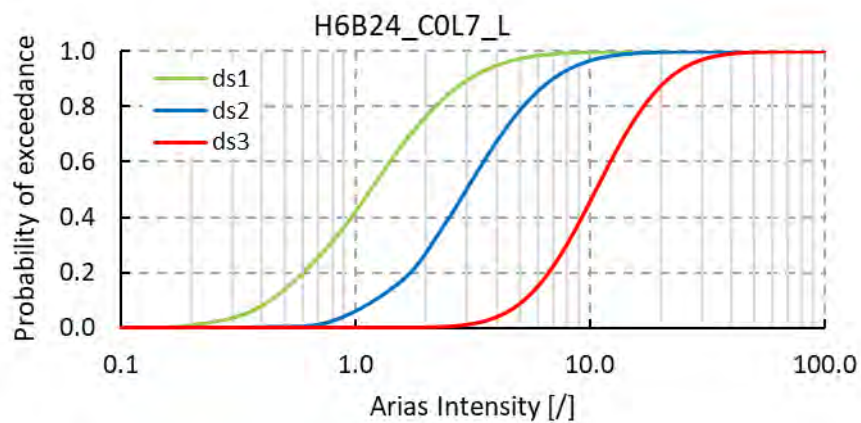
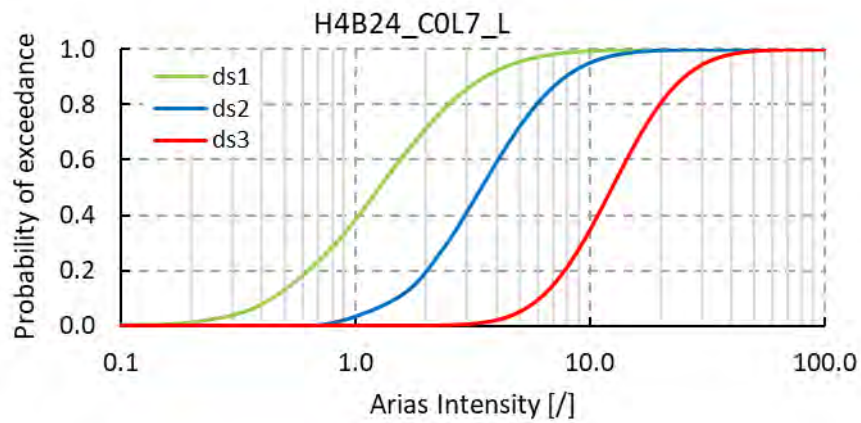
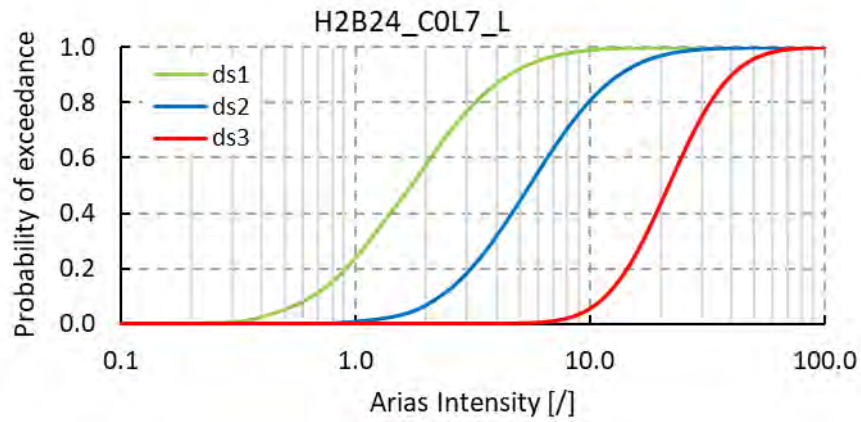


This project has received funding from the European Union's Horizon 2020 research and innovation programme under grant agreement No. 700748



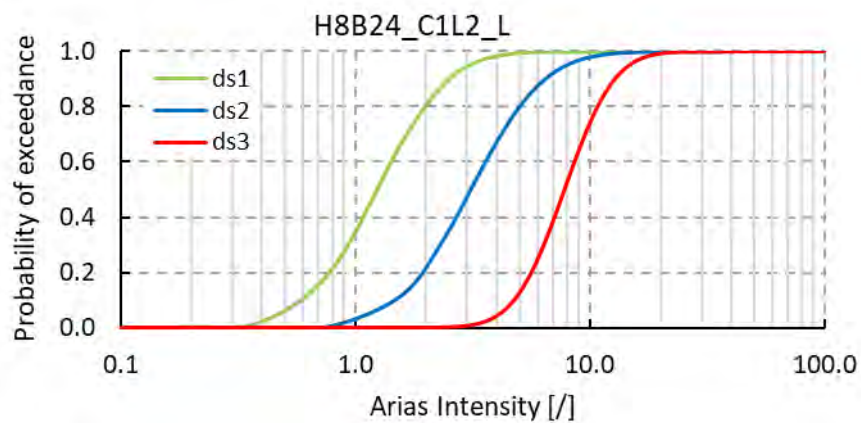
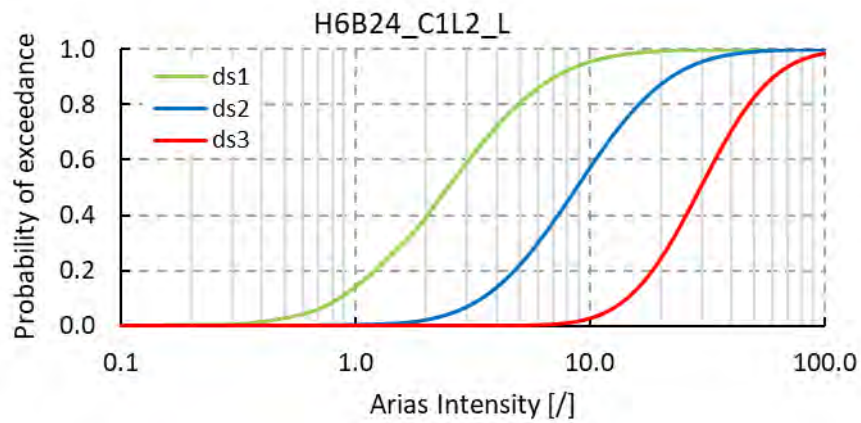
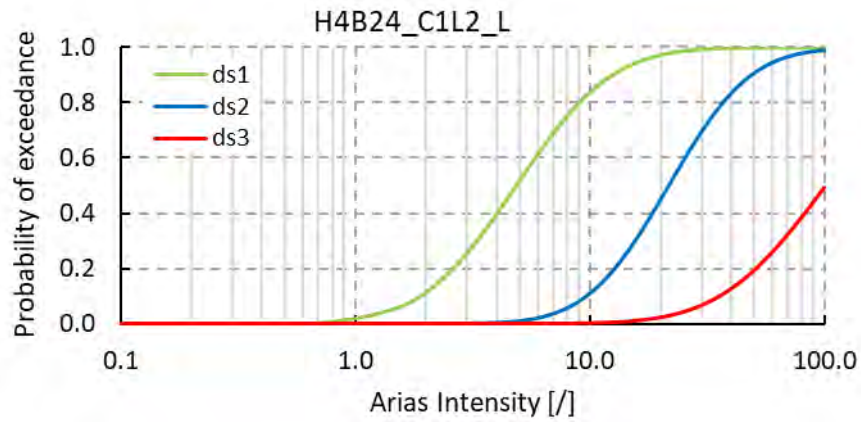


This project has received funding from the European Union's Horizon 2020 research and innovation programme under grant agreement No. 700748



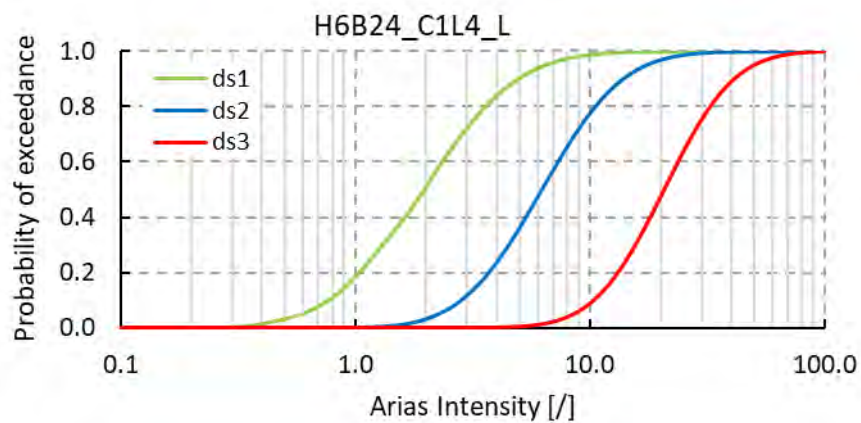
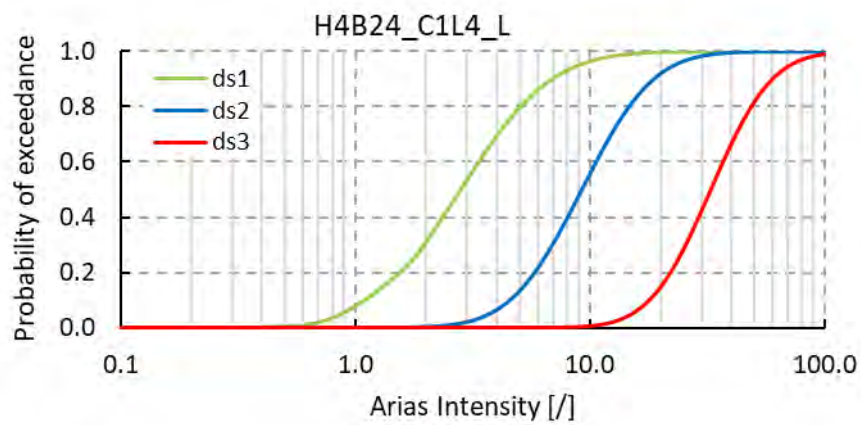
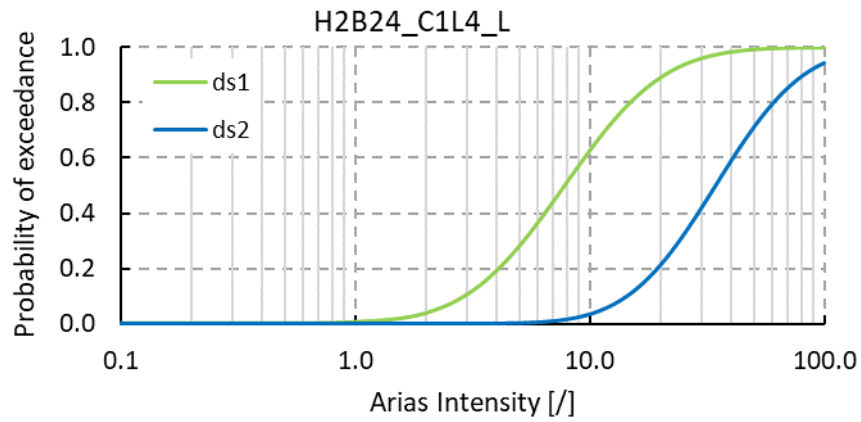


This project has received funding from the European Union's Horizon 2020 research and innovation programme under grant agreement No. 700748



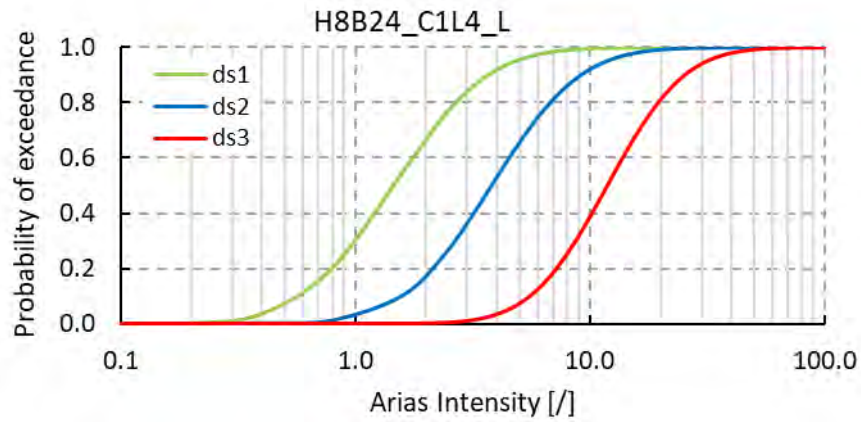


This project has received funding from the European Union's Horizon 2020 research and innovation programme under grant agreement No. 700748

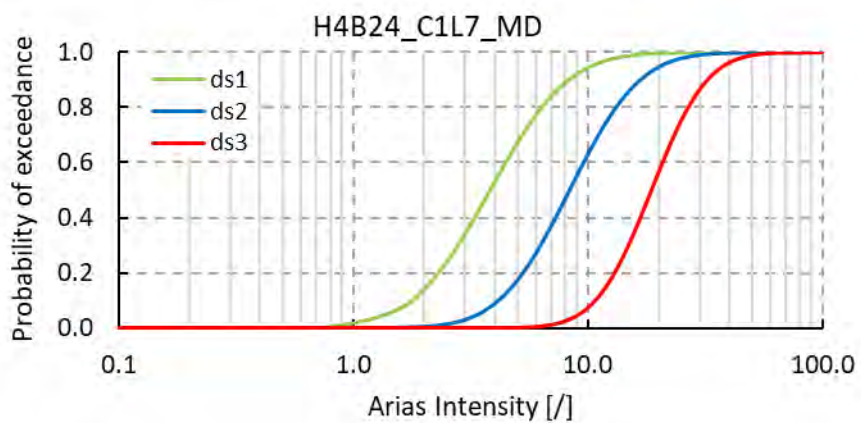
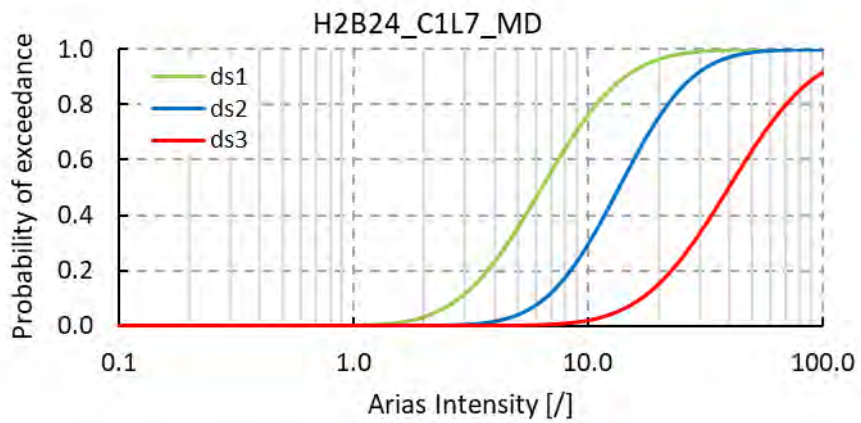




This project has received funding from the European Union's Horizon 2020 research and innovation programme under grant agreement No. 700748

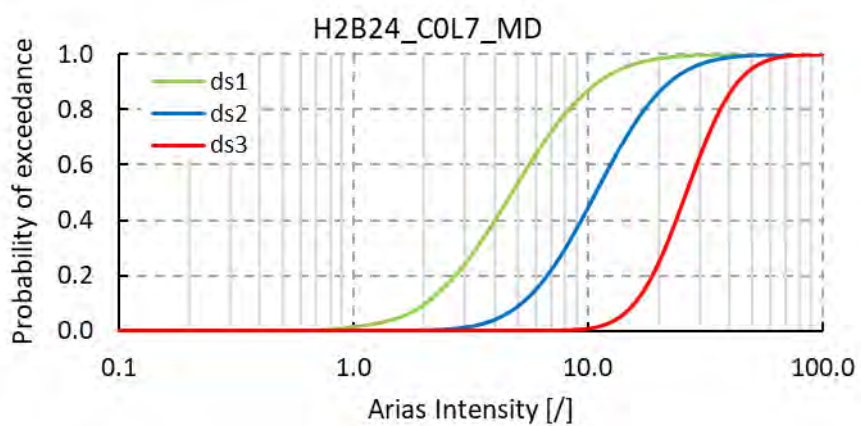
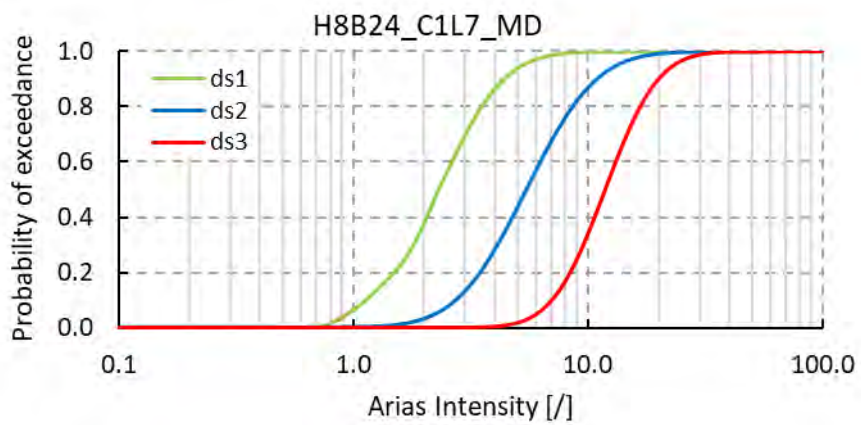
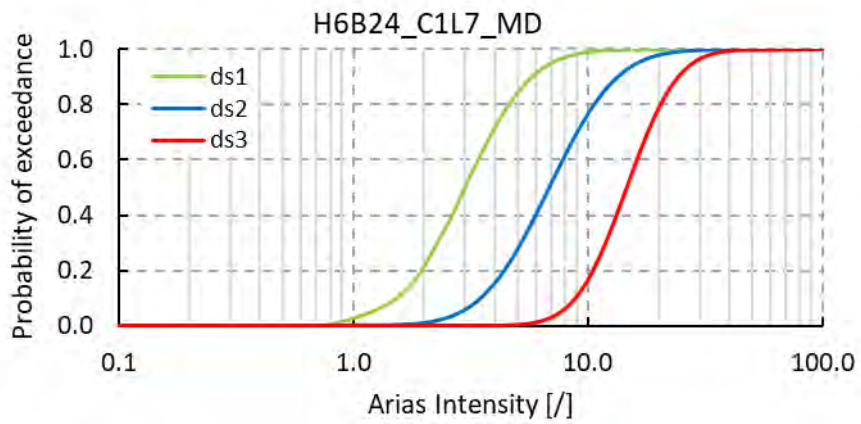


Railway embankments



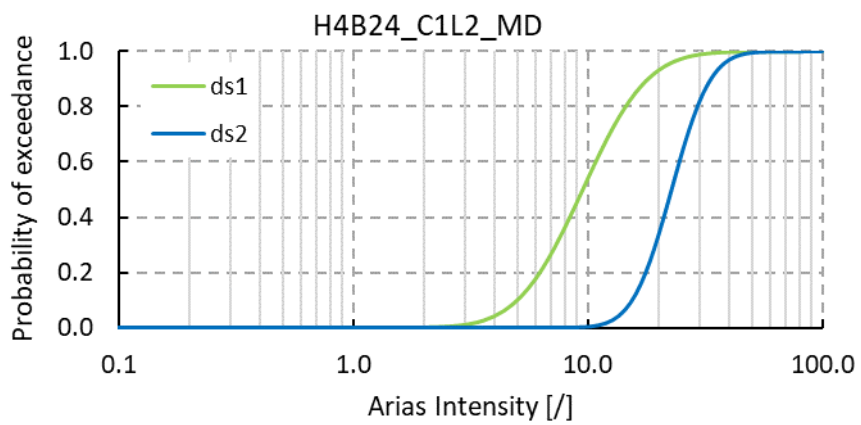
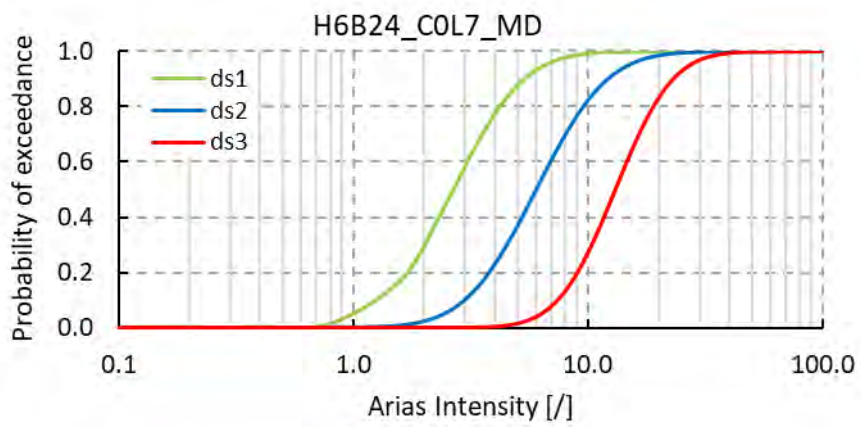
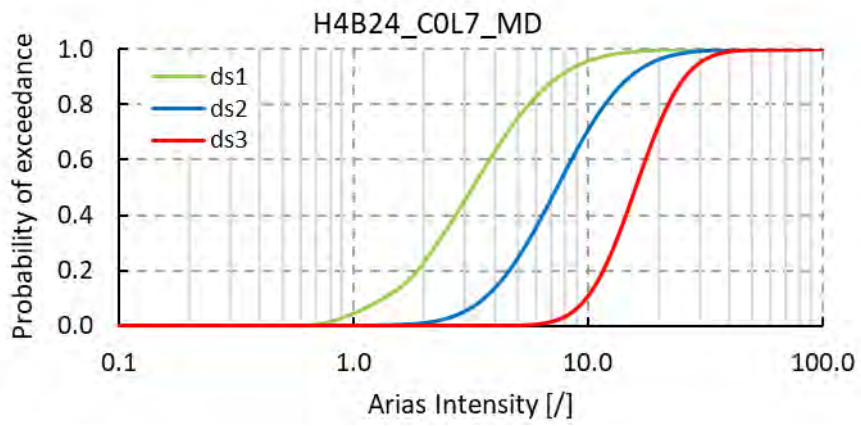


This project has received funding from the European Union's Horizon 2020 research and innovation programme under grant agreement No. 700748



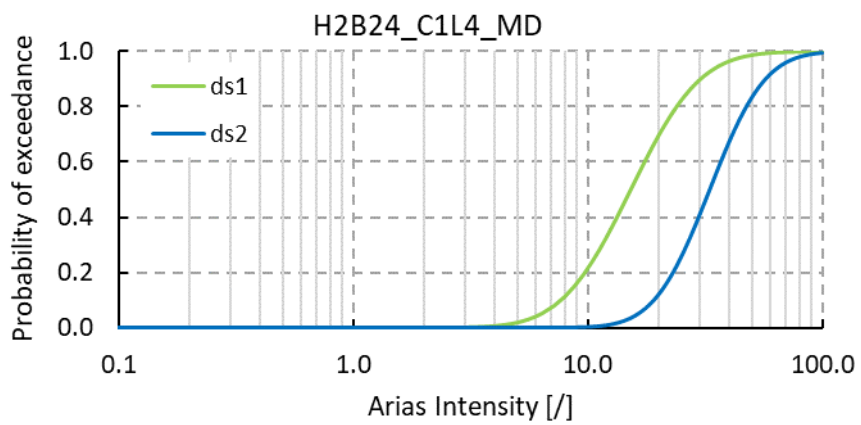
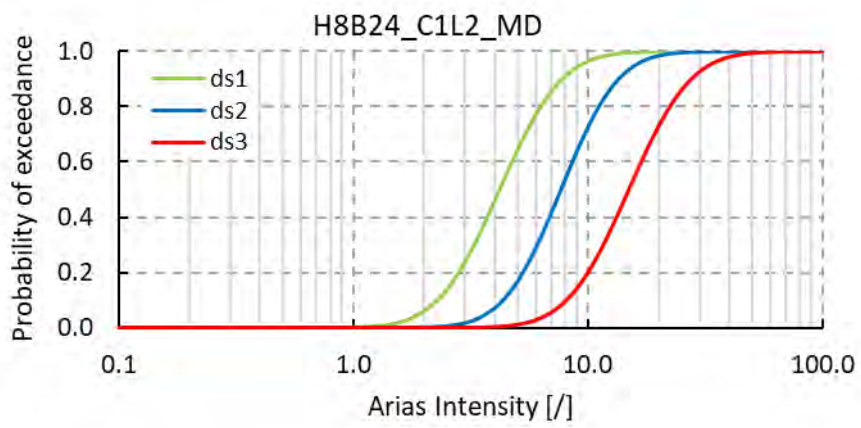
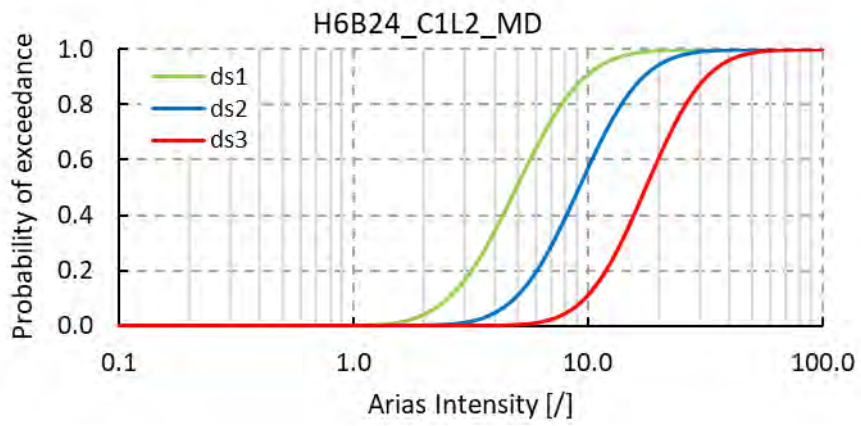


This project has received funding from the European Union's Horizon 2020 research and innovation programme under grant agreement No. 700748



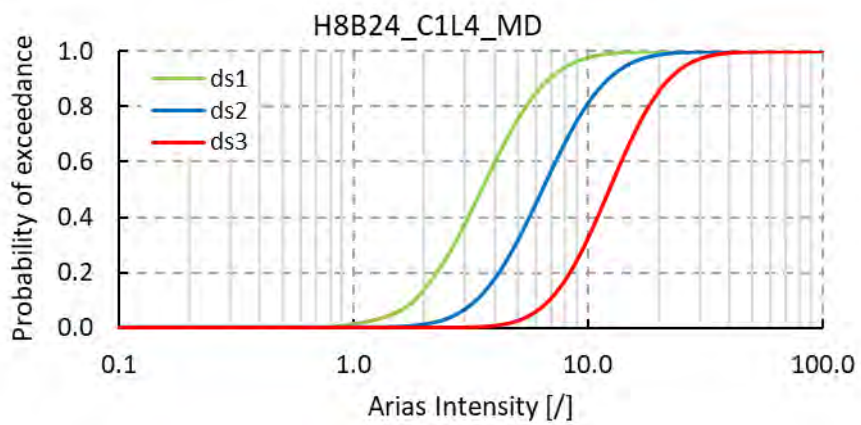
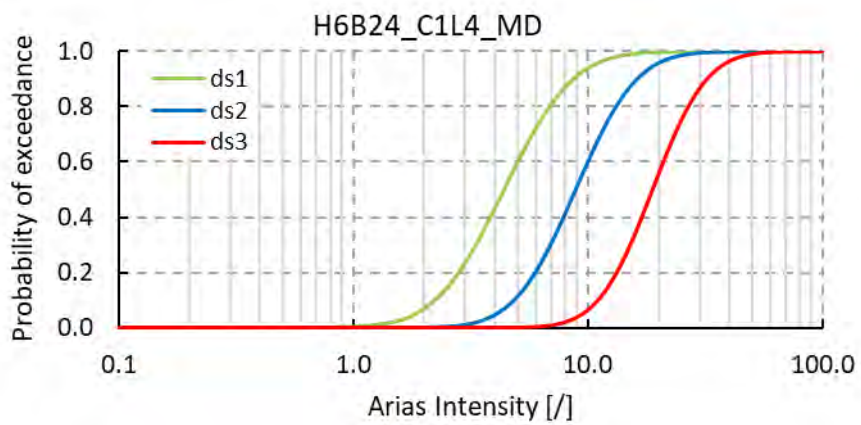
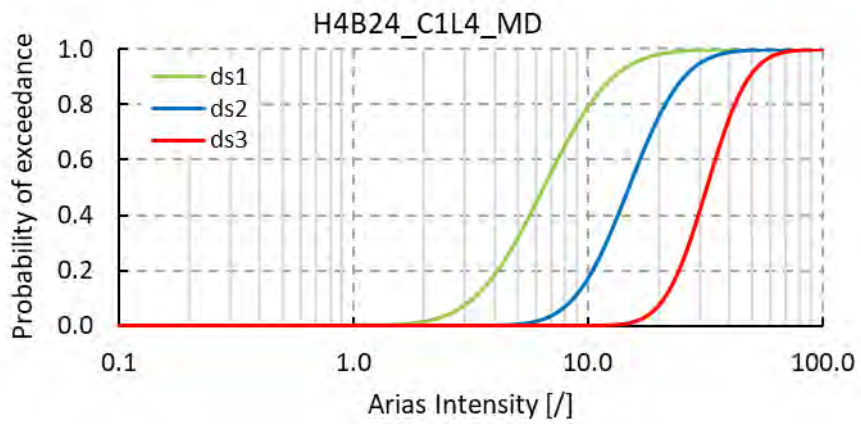


This project has received funding from the European Union's Horizon 2020 research and innovation programme under grant agreement No. 700748



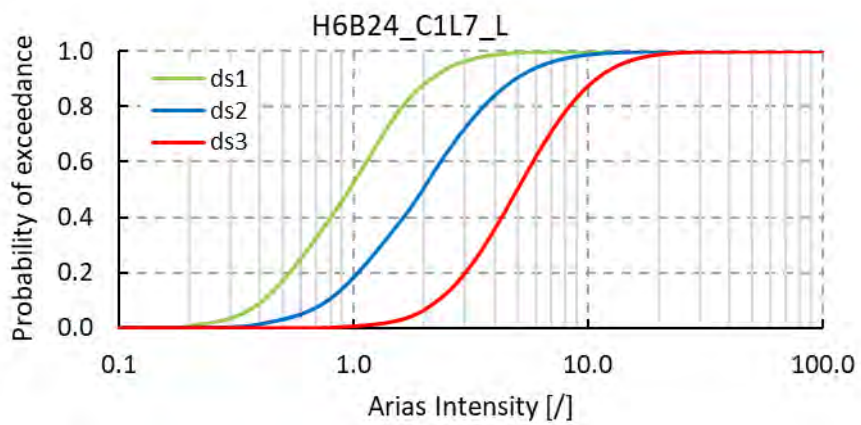
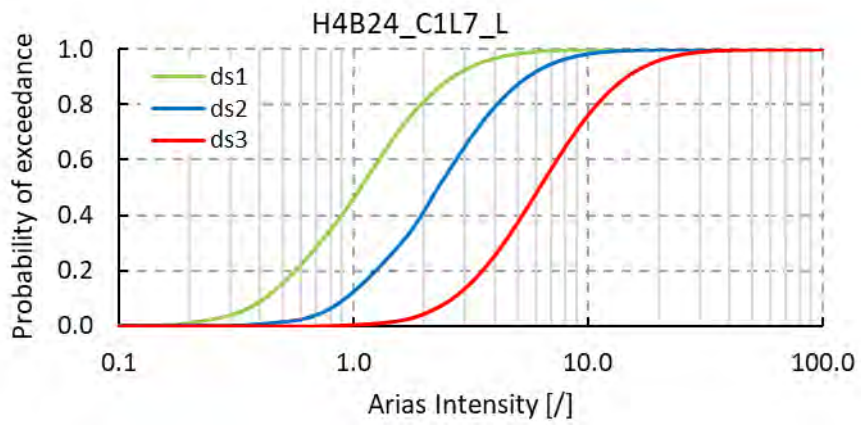
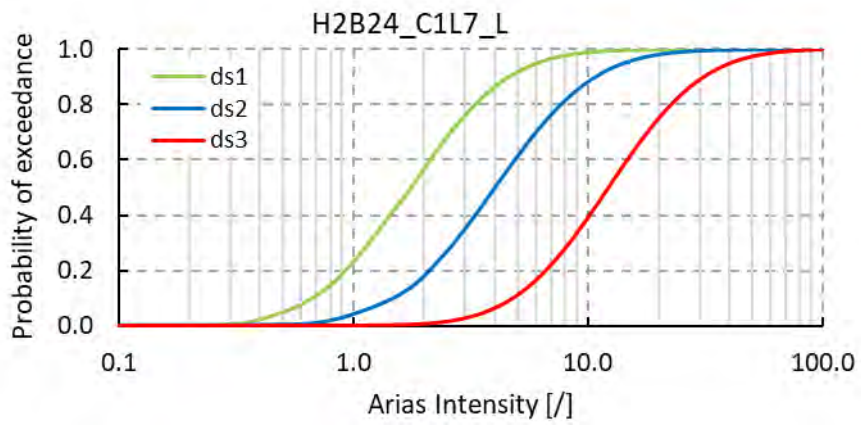


This project has received funding from the European Union's Horizon 2020 research and innovation programme under grant agreement No. 700748



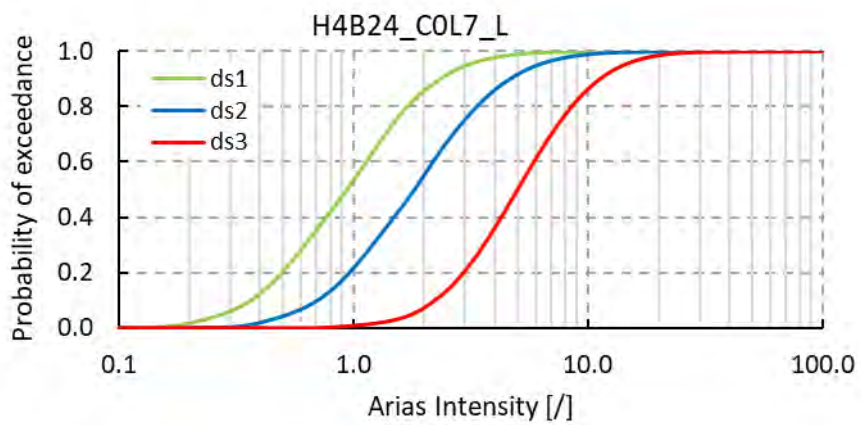
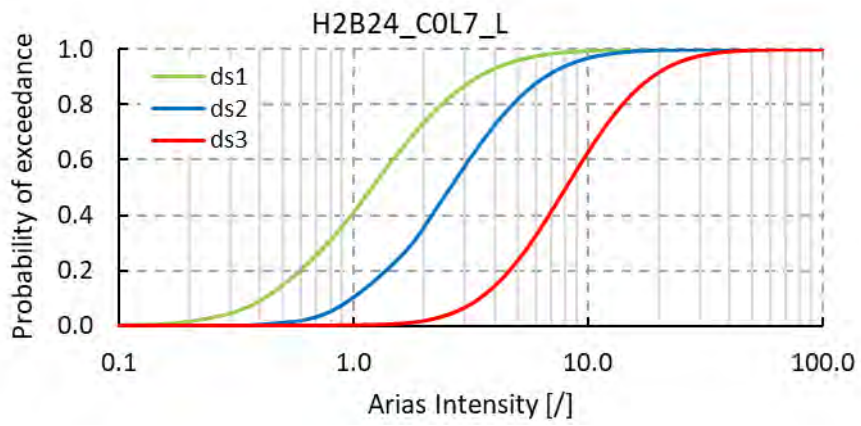
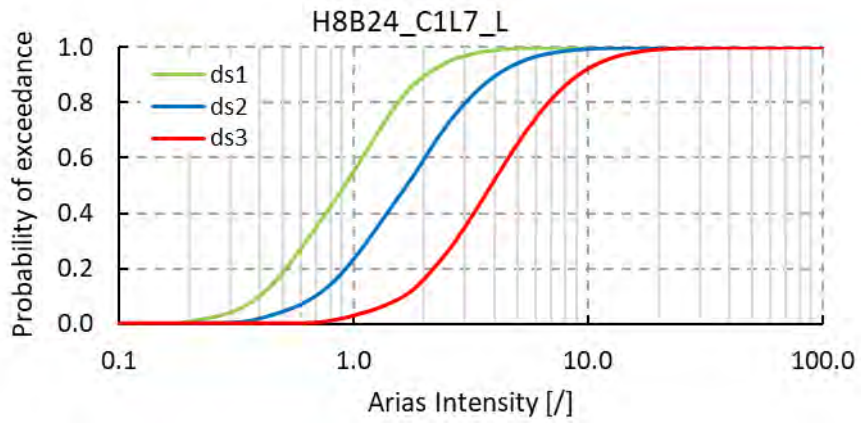


This project has received funding from the European Union's Horizon 2020 research and innovation programme under grant agreement No. 700748



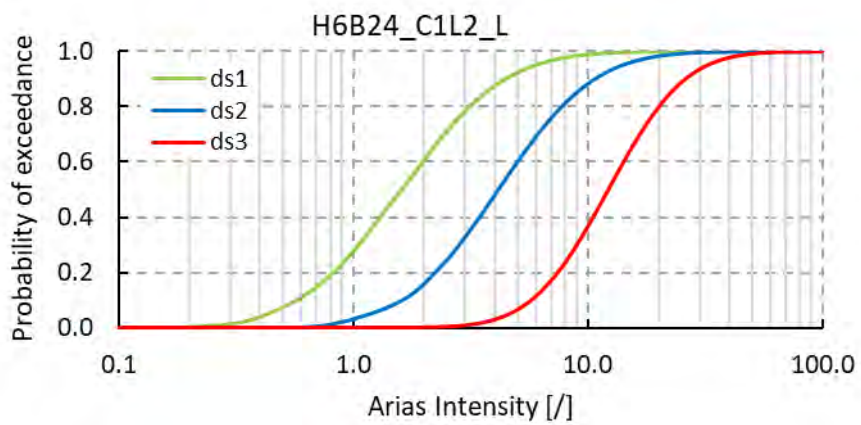
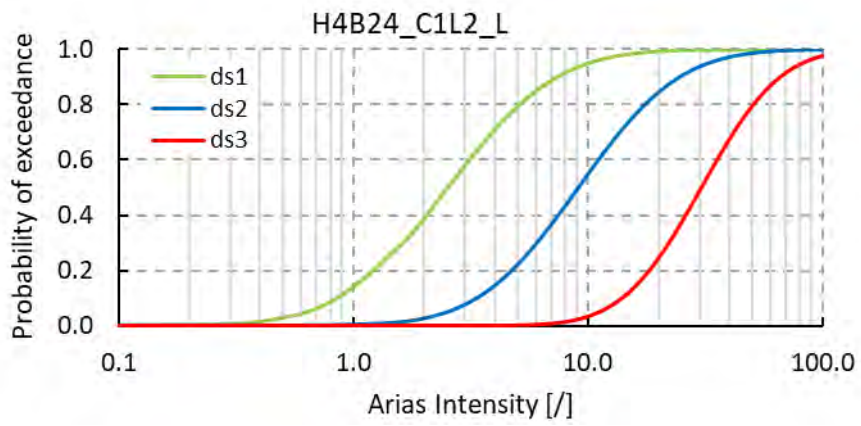
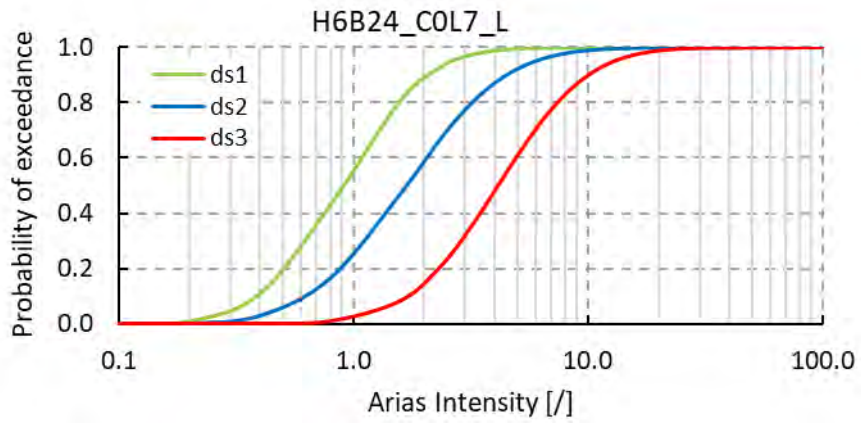


This project has received funding from the European Union's Horizon 2020 research and innovation programme under grant agreement No. 700748



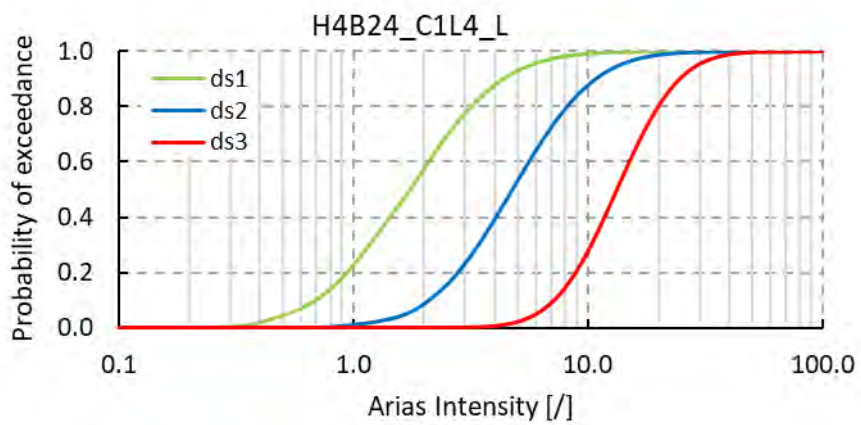
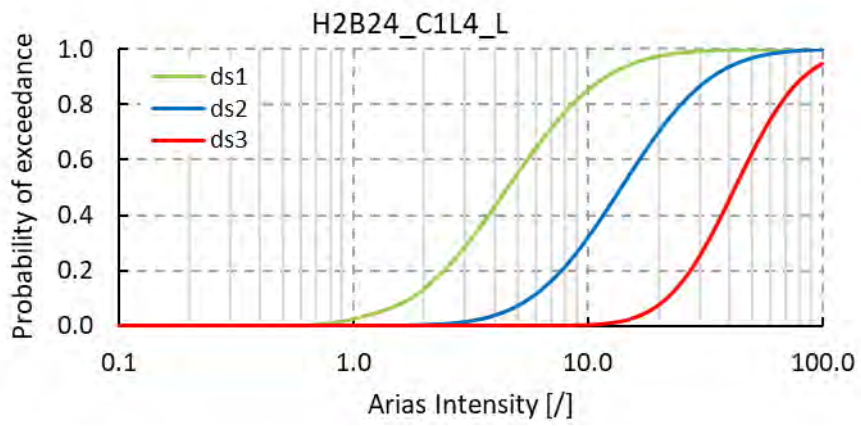
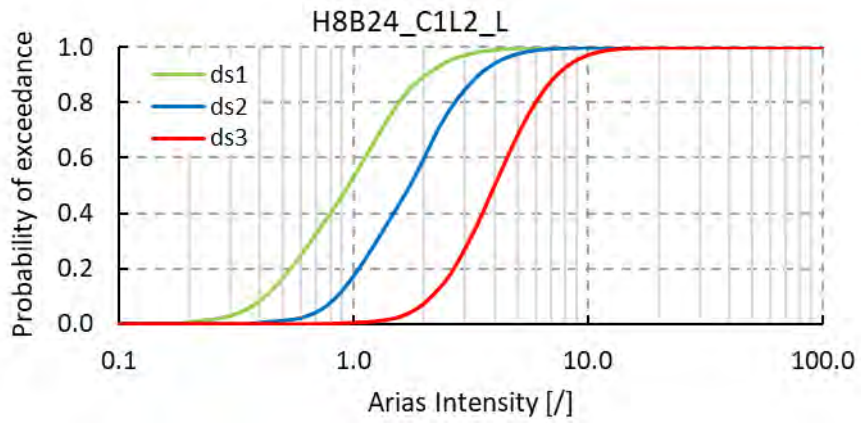


This project has received funding from the European Union's Horizon 2020 research and innovation programme under grant agreement No. 700748





This project has received funding from the European Union's Horizon 2020 research and innovation programme under grant agreement No. 700748





This project has received funding from the European Union's Horizon 2020 research and innovation programme under grant agreement No. 700748

